ISSN 2188-5001

MATERIALS DESIGN AND
CHARACTERIZATION LABORATORY

SUPERCOMPUTER CENTER

ACTIVITY REPORT 2022

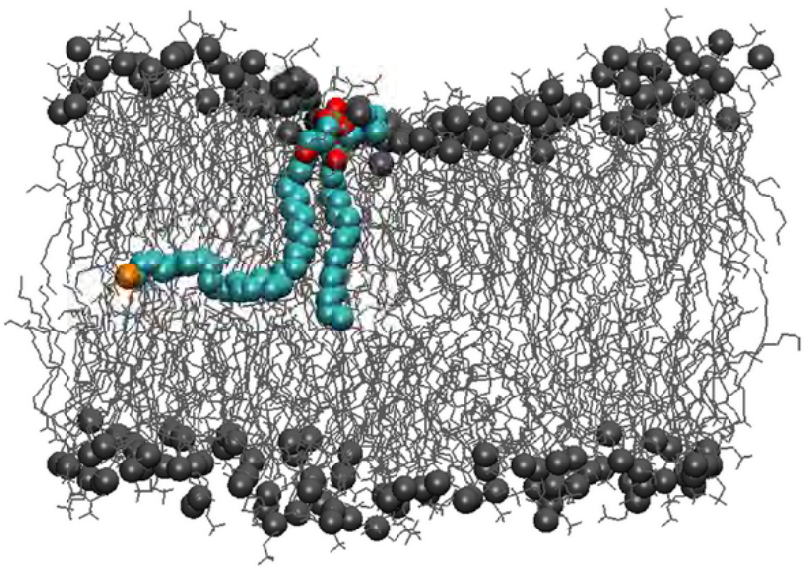

THE UNIVERSITY OF TOKYO

Materials Design and Characterization Laboratory (MDCL)

The MDCL was established as the third research facility of the Institute for Solid State Physics (ISSP) when the latter was reorganized in May 1996. Its aim is to promote material science with an emphasis on the "DSC cycle", where DSC stands for design, synthesis and characterization, three processes for developing new materials.

The MDCL consists of two sections, Materials Design (MD) section and Materials Synthesis and Characterization (MSC) section. The Supercomputer Center of the ISSP (SCC-ISSP) is placed in the MD section, while in the MSC section there are seven laboratories for joint use; Materials Synthesis Laboratory, Chemical Analysis Laboratory, X-ray Diffraction Laboratory, Electron Microscope Laboratory, Electromagnetic Measurement Laboratory, Spectroscopy Laboratory, and High-Pressure Synthesis Laboratory.

Almost all the facilities of the MDCL are open to scientists in Japan through the User Programs conducted by two steering committees of the MDCL. One is the steering committee of the SCC-ISSP, under which the Supercomputer Project Advisory Committee is placed for reviewing proposals. The other is the steering committee of the MSC facilities. More than half of the members of these committees are from the outside of ISSP.

COVER FIGURE

Conformation of an ultra-long chain fatty acid, dTSPC, in DSPC bilayer. The dTSPC molecule is represented by colored spheres.

See Page 35–43, K. Kawaguchi and H. Noguchi, "Molecular dynamics study of ultra-long chain fatty acid in lipid bilayer".

PREFACE

The Supercomputer Center (SCC) is a part of the Materials Design and Characterization Laboratory (MDCL) of ISSP. Its mission is to serve the whole community of computational condensed-matter physics of Japan providing it with high performance computing environment. In particular, the SCC selectively promotes and supports large-scale computations. For this purpose, the SCC invites proposals for supercomputer-aided research projects and hosts the Steering Committee, as mentioned below, that evaluates the proposals.

The ISSP supercomputer system consists of two subsystems: System B, which was last replaced in Oct. 2020, is intended for larger total computational power and has more nodes with relatively loose connections whereas System C is intended for higher communication speed among nodes. System B (ohtaka) consists of 1680 CPU nodes of AMD EPYC 7702 (64 cores) and 8 FAT nodes of Intel Xeon Platinum 8280 (28 cores) with total theoretical performance of 6.881 PFlops. System C was replaced in June 2022 and the current system (kugui) consists of 128 CPU nodes of AMD EPYC 7763 (64 cores) and 8 ACC nodes of AMD EPYC 7763 (64 cores) NVIDIA A100 40GB for HGX with total theoretical performance of 0.973 PFLOPS.

In addition to the hardware administration, the SCC puts increasing effort on the software support. Since 2015, the SCC has been conducting “Project for advancement of software usability in materials science (PASUMS).” In this project, for enhancing the usability of the ISSP supercomputer system, we conduct several software-advancement activities: developing new application software that runs efficiently on the ISSP supercomputer system, adding new functions to existing codes, help releasing private codes for public use, creating/improving manuals for public codes, etc. Two target programs were selected for fiscal year 2022: (1) abICS (proposal made by S. Kasamatsu (Yamagata U.)), and (2) H-wave (proposal made by A. Kobayashi (Nagoya U.)). In addition, since 2021, we have been maintaining the data repository service for secure storage and enhanced usability of results of numerical calculation.

All staff members of university faculties or public research institutes in Japan are invited to propose research projects (called User Program). The proposals are evaluated by the Steering Committee of SCC. Peer-reviewing is done by the Supercomputer Project Advisory Committee. In fiscal year 2022, totally 337 projects were approved including the ones under the framework of Supercomputing Consortium for Computational Materials Science (SCCMS), which specially supports FUGAKU and other major projects in computational materials science.

The research projects are roughly classified into the following three (the number of projects approved):

First-Principles Calculation of Materials Properties (151)
Strongly Correlated Quantum Systems (25)
Cooperative Phenomena in Complex, Macroscopic Systems (141)

In all the three categories, most proposals involve both methodology and applications. The results of the projects are reported in 'Activity Report 2022' of the SCC. Every year 3-4 projects are selected for “invited papers” and published at the beginning of the Activity Report. In the Activity Report 2022, the following three invited papers are included:

``Training method for refinement of machine-learning interatomic potential and its applications",
Kohei SHIMAMURA, Akihide KOURA, and Fuyuki SHIMOJO (Kumamoto Univ.)

``First principles calculation of copper-oxide superconductors exhibiting electron fractionalization",
Masatoshi IMADA (Waseda Univ.)

``Molecular dynamics study of ultra-long chain fatty acid in lipid bilayer",
Kazutomo KAWAGUCHI (Kanazawa Univ.) and Hiroshi NOGUCHI (ISSP)

June 2, 2023

Naoki Kawashima
(Chairman of the steering committee, SCC, ISSP)

CONTENTS

1 OUTLINE

1.1 Supercomputer System

In School year 2022 (SY 2022), the ISSP supercomputer center provided users with System B - Dell PowerEdge C6525/R940 system named "ohtaka" and System C - HPE Apollo 2000 Gen10 Plus/HPE Apollo 6500 Gen10 Plus system named "kugui". System B is a massively-parallel supercomputer with two types of compute nodes: 8 "Fat" nodes and 1680 "CPU" nodes. "Fat" nodes are each comprised of four Intel Xeon Platinum 8280 CPUs (28 cores/CPU) and 3 TB of memory per node. "CPU" nodes have two AMD EPYC 7702 CPUs (64 cores/CPU) and 256 GB of memory per node. System B achieves about 6.881 PFLOPS in theoretical peak performance with high power efficiency. The subsystem comprised of only CPU nodes ranks 87st in the Nov. 2020 Top 500 List, which is a ranking based on total performance measured by the HPL benchmark. The compute nodes communicate to each other through HDR100 Infiniband and are connected in fat tree topology. SY 2022 was the third year of the operation of the current System B. In June 2022, "kugui" was introduced as System C, which will be operated for the next six years. System C is a massively-parallel supercomputer with two types of compute nodes: 128 "CPU" nodes and 8 "ACC" nodes. "CPU" nodes are each comprised of two AMD EPYC 7763 CPUs (64 cores/CPU) and 256 GB of memory. The compute nodes communicate to each other through HDR200 Infiniband and are connected in fat tree topology. "ACC" nodes are each comprised of one AMD EPYC 7763 CPUs (64 cores/CPU), four NVIDIA A100 40GB for HGX GPUs and 256 GB of memory. System C achieves 973 TFLOPS in theoretical peak performance. System C entered official operation in June 14th, 2022. Trial operation of System C continued until July 18th, 2022. SY 2022 was the first year of the operation of the current System C. For further details, please contact ISSP Supercomputer Center (SCC-ISSP).

[Correspondence: center@issp.u-tokyo.ac.jp]

1.2 Project Proposals

The ISSP supercomputer system provides computation resources for scientists working on condensed matter sciences in Japan. All scientific staff members (including post-docs) at universities or public research institutes in Japan can submit proposals for projects related to research activities on materials and condensed matter sciences. These proposals are peer-reviewed by the Advisory Committee members (see Sec. 1.3), and then the computation resources are allocated based on the review reports. The leader of an approved project can set up user accounts for collaborators. Other types of scientists, including graduate students, may also be added. Proposal submissions, peer-review processes, and user registration are all managed via a web system.

The computation resources are distributed in a unit called "point", determined as a function of available CPU utilization time and consumed disk resources. There

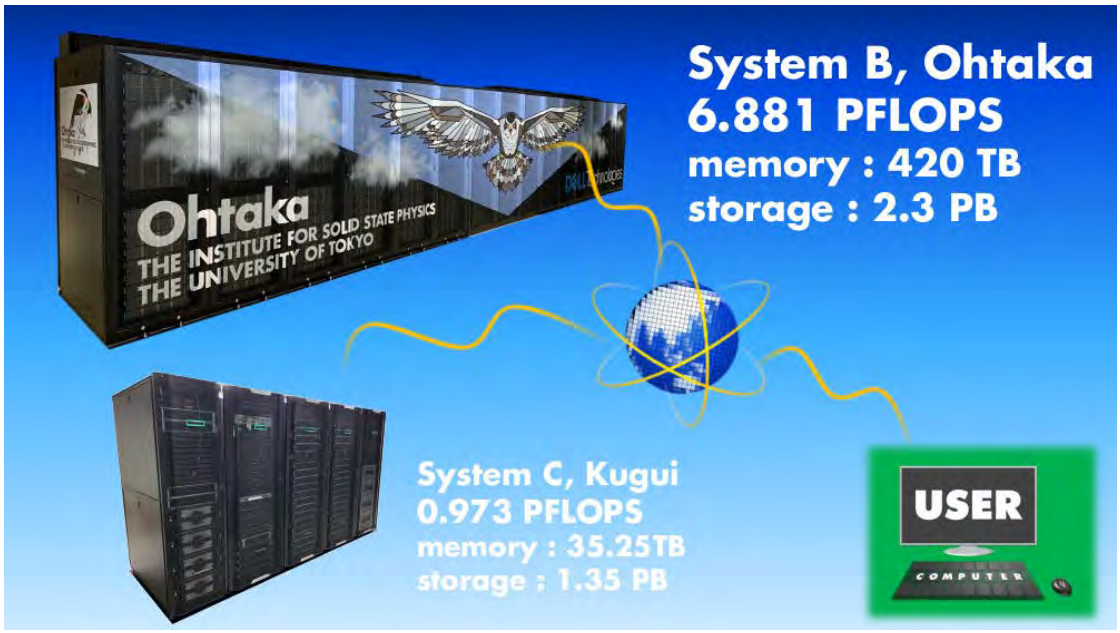

Figure 1: Supercomputer System at the SCC-ISSP

were calls for six classes of research projects in SY 2022. The number of projects and the total number of points that were applied for and approved in this school year are listed in Table 1.

- Class A is for trial use by new users; proposals for Class A projects are accepted throughout the year.
- Proposals for projects in Classes B (small), C (mid-size), E (large-scale), and S (exceptional) can be submitted twice a year. Approved projects in Classes A, B, C, and E continue to the end of the school year.
- In Class D, projects can be proposed on rapidly-developing studies that need to perform urgent and relatively large calculations. An approved project continues for 6 months from its approval.
- Class S is for projects that are considered extremely important for the field of condensed matter physics and requires extremely large-scale computation. The project may be carried out either by one research group or cooperatively by several investigators at different institutions. A project of this class should be applied with at least 10,000 points; there is no maximum. We require group leaders applying for Class S to give a presentation on the proposal to the Steering Committee of the SCC-ISSP. Class S projects are carried out within one year from its approval.
- Project leaders can apply for points so that the points for each system do not exceed the maximum point shown in this table.

Table 1: Classes of research projects in SY 2022. Total points listed in this table are rounded. In Class D, we collect information about the projects ended in each semester.

Class	Maximum Points		Application	# of Proj.	Total points			
					Applied		Approved	
	Sys–B	Sys–C			Sys–B	Sys–C	Sys–B	Sys–C
A	100	50	any time	28	2.8k	1.4k	2.8k	1.4k
B	800	100	twice a year	94	65.9k	6.7k	38.6k	5.5k
C	8k	500	twice a year	176	1092.9k	47.4k	566.8k	35.7k
D	10k	500	any time	6	28.5k	1.2k	23.0k	1.0k
E	24k	1.5k	twice a year	13	273.0k	18.0k	185.5k	14.4k
S	–	–	twice a year	0	0	0	0	0
SCCMS				20	52.3k	5.2k	52.3k	5.2k
Total				337	1515.4k	79.9k	869.0k	63.2k

In addition, from SY 2016, ISSP Supercomputer has been providing 20% of its computational resources for Supercomputing Consortium for Computational Materials Science (SCCMS), which aims at advancing parallel computations in condensed matter, molecular, and materials sciences on the 10-PFlops K Computer and the exascale post-K project. From SY 2020, up to 10% of the computational resources have been provided for SCCMS. Computational resources have also been allotted to Computational Materials Design (CMD) workshops, as well as CCMS hands-on workshops.

1.3 Committees

In order to fairly manage the projects and to smoothly determine the system operation policies, the Materials Design and Characterization Laboratory (MDCL) of the ISSP has organized the Steering Committee of the MDCL and the Steering Committee of the SCC-ISSP, under which the Supercomputer Project Advisory Committee (SPAC) is formed to review proposals. The members of the committees in SY 2022 were as follows:

Steering Committee of the MDCL

KAWASHIMA, Naoki	ISSP (Chair person)
HIROI, Zenji	ISSP
OZAKI, Taisuke	ISSP
NOGUCHI, Hiroshi	ISSP
UWATOKO, Yoshiya	ISSP
OKAMOTO, Yoshihiko	ISSP
SUGINO, Osamu	ISSP
KUBO, Momoji	Tohoku Univ.

HUKUSHIMA, Koji	Univ. of Tokyo
HONDA, Fuminori	Kyushu Univ.
SHIMAKAWA, Yuichi	Kyoto Univ.
MOTOME, Yukitoshi	Univ. of Tokyo
HOSHI, Takeo	Tottori Univ.
ISHIWATA, Shintaro	Osaka Univ.
HASEGAWA, Masashi	Nagoya Univ.
NAKATSUJI, Satoru	ISSP

Steering Committee of the SCC-ISSP

KAWASHIMA, Naoki	ISSP (Chair person)
NOGUCHI, Hiroshi	ISSP
OZAKI, Taisuke	ISSP
SUGINO, Osamu	ISSP
TSUNETSUGU, Hirokazu	ISSP
KATO, Takeo	ISSP
KIMURA, Takashi	ISSP
MORITA, Satoshi	ISSP
FUKUDA, Masahiro	ISSP
IDO, Kota	ISSP
KAWAMURA, Mitsuaki	ISSP
NAKAJIMA, Kengo	Univ. of Tokyo
OTSUKI, Junya	Okayama Univ.
MOTOME, Yukitoshi	Univ. of Tokyo
ONO, Tomoya	Kobe Univ.
TODO, Synge	Univ. of Tokyo
KUBO, Momoji	Tohoku Univ.
OBA, Fumiyasu	Tokyo Tech.
WATANABE, Hiroshi	Keio Univ.
HUKUSHIMA, Koji	Univ. of Tokyo
KITAO, Akio	Tokyo Tech.
HAMADA, Ikutaro	Osaka Univ.
YOSHIMI, Kazuyoshi	ISSP
YATA, Hiroyuki	ISSP
FUKUDA, Takaki	ISSP

Supercomputer Project Advisory Committee

KAWASHIMA, Naoki	ISSP (Chair person)
OZAKI, Taisuke	ISSP
NOGUCHI, Hiroshi	ISSP
SUGINO, Osamu	ISSP
TSUNETSUGU, Hirokazu	ISSP
KIMURA, Takashi	ISSP

KATO, Takeo	ISSP
MORITA, Satoshi	ISSP
FUKUDA, Masahiro	ISSP
IDO, Kota	ISSP
KAWAMURA, Mitsuaki	ISSP
NAKAJIMA, Kengo	Univ. of Tokyo
MOTOME, Yukitoshi	Univ. of Tokyo
TODO, Synge	Univ. of Tokyo
KUBO, Momoji	Tohoku Univ.
OBA, Fumiyasu	Tokyo Tech.
WATANABE, Hiroshi	Keio Univ.
HUKUSHIMA, Koji	Univ. of Tokyo
ONO, Tomoya	Kobe Univ.
OTSUKI, Junya	Okayama Univ.
KITAO, Akio	Tokyo Tech.
HAMADA, Ikutaro	Osaka Univ.
IKUHARA, Yuichi	Univ. of Tokyo
SHIBATA, Naokazu	Tohoku Univ.
AKAGI, Kazuto	Tohoku Univ.
YANASE, Yoichi	Kyoto Univ.
HATSUGAI, Yasuhiro	Univ. of Tsukuba
OKADA, Susumu	Univ. of Tsukuba
KOBAYASHI, Nobuhiko	Univ. of Tsukuba
NAKAYAMA, Takashi	Chiba Univ.
HOTTA, Takashi	Tokyo Metropolitan Univ.
MATSUKAWA, Hiroshi	Aoyama Gakuin Univ.
YAMAUCHI, Jun	Keio Univ.
HAGITA, Katsumi	National Defense Academy
KONTANI, Hiroshi	Nagoya Univ.
SAITO, Mineo	Kanazawa Univ.
YUKAWA, Satoshi	Osaka Univ.
SUGA, Seiichiro	Univ. of Hyogo
YASUDA, Chitoshi	Univ. of the Ryukyus
KIM, Kang	Osaka Univ.
MORIKAWA, Yoshitada	Osaka Univ.
KOGA, Akihisa	Tokyo Tech.
SHIMOJO, Fuyuki	Kumamoto Univ.
TAKETSUGU, Tetsuya	Hokkaido Univ.
TSURUTA, Kenji	Okayama Univ.
HAMAGUCHI, Satoshi	Osaka Univ.
NISHIDATE, Kazume	Iwate Univ.
KAGESHIMA, Hiroyuki	Shimane Univ.
ISHII, Fumiyuki	Kanazawa Univ.
TATETSU, Yasutomi	Meio Univ.
YANAGISAWA, Susumu	Univ. of the Ryukyus

SHUDO, Ken-ichi	Yokohama Natl. Univ.
OHMURA, Satoshi	Hiroshima Inst. Tech.
NOGUCHI, Yoshifumi	Shizuoka Univ.
NAKAMURA, Kazuma	Kyushu Inst. Tech.
GOHDA, Yoshihiro	Tokyo Tech.
RAEBIGER, Hannes	Yokohama Natl. Univ.
KAWARABAYASHI, Tohru	Toho Univ.
KATO, Yusuke	Univ. of Tokyo
NASU, Joji	Tohoku Univ.
HOTTA, Chisa	Univ. of Tokyo
ISOBE, Masaharu	Nagoya Inst. Tech.
HARADA, Ryuhei	Univ. of Tsukuba
TANAKA, Shu	Keio Univ.
KOBAYASHI, Kazuaki	NIMS
TATEYAMA, Yoshitaka	NIMS
TAMURA, Ryo	NIMS
TADA, Tomofumi	Kyushu Univ.
HATANO, Naomichi	Univ. of Tokyo
YOSHINO, Hajime	Osaka Univ.
OKUMURA, Hisashi	NINS-ExCELLS
HOSHI, Takeo	Tottori Univ.
TSUNEYUKI, Shinji	Univ. of Tokyo
SUZUKI, Takafumi	Univ. of Hyogo
YOSHIMOTO, Yoshihide	Univ. of Tokyo
TOHYAMA, Takami	Tokyo Univ. of Sci.
ARITA, Ryotaro	Univ. of Tokyo
OGATA, Masao	Univ. of Tokyo
WATANABE, Satoshi	Univ. of Tokyo
YABANA, Kazuhiro	Univ. of Tsukuba
FURUKAWA, Nobuo	Aoyama Gakuin Univ.
KUROKI, Kazuhiko	Osaka Univ.
TANAKA, Yukio	Nagoya Univ.
KUSAKABE, Koichi	Univ. of Hyogo
SAKAI, Toru	Univ. of Hyogo
ISHIBASHI, Shoji	AIST
OTANI, Minoru	Univ. of Tsukuba
TOMITA, Yusuke	Shibaura Inst. Tech.
SHIRAISHI, Kenji	Nagoya Univ.
OGUCHI, Tamio	Osaka Univ.
KAWAKATSU, Toshihiro	Tohoku Univ.
OTSUKI, Tomi	Sophia Univ.
ODA, Tatsuki	Kanazawa Univ.
ARAI, Noriyoshi	Keio Univ.
UNEYAMA, Takashi	Nagoya Univ.

1.4 Staff

The following staff members of the SCC-ISSP usually administrate the ISSP Supercomputer.

KAWASHIMA, Naoki	Professor (Chair person)
NOGUCHI, Hiroshi	Associate Professor
OZAKI, Taisuke	Professor
SUGINO, Osamu	Professor
IDO, Kota	Research Associate
FUKUDA, Masahiro	Research Associate
KAWAMURA, Mitsuaki	Research Associate
MORITA, Satoshi	Research Associate
NAKANO, Hiroyoshi	Research Associate
YOSHIMI, Kazuyoshi	Project Researcher
AOYAMA, Tatsumi	Project Researcher
MOTOYAMA, Yuichi	Technical Specialist
YATA, Hiroyuki	Technical Specialist
FUKUDA, Takaki	Technical Specialist
ARAKI, Shigeyuki	Project Academic Specialist

2 STATISTICS (SCHOOL YEAR 2022)

2.1 System and User Statistics

In the following, we present statistics for operation time taken in the period from April 1st 2022 to April 3rd 2023 (SY 2022). In Table 2, we show general statistics of the supercomputer system in SY 2022. The total numbers of compute nodes in System B "ohtaka" and System C "kugui" are 1688 and 136, respectively. Consumed disk points amount to about a few percent of the total consumed points in both System B and System C.

In Fig. 2, availabilities, utilization rates, and consumed points in Systems B and C are plotted for each month. Throughout the school year, the availability and the utilization rates were very high : the availability and the utilization rates exceed about 90% and 80% throughout most of the year, respectively.

The user statistics are shown in Fig. 3. The horizontal axis shows the rank of the user/group arranged in the descending order of the execution time (hour×nodes). The execution time of the user/group of the first rank is the longest. The vertical axis shows the sum of the execution time up to the rank. From the saturation points of the graphs, the numbers of "active" users of Systems B and C are around 400 and 100, respectively. The maximum ranks in the graphs correspond to the number of the users/groups that submitted at least one job.

Table 2: Overall statistics of SY 2022

	System B ohtaka	System C kugui
total service time ($\times 10^3$ node·hours)	14420	976
number of executed jobs	476439	108868
total consumed points ($\times 10^3$ point)	502	18
CPU points ($\times 10^3$ point)	489	18
disk points ($\times 10^3$ point)	13	1
total exec. time ($\times 10^3$ node·hours)	13293	790
availability	96.60%	97.38%
utilization rate	92.3%	80.98%

2.2 Queue and Job Statistics

Queue structures of Systems B and C in SY 2022 are shown in Tables 3 and 4, respectively. In System B "ohtaka", users can choose from two types of compute nodes; jobs submitted to queues with "cpu" and "fat" at the end of their queue names are submitted to CPU and Fat nodes, respectively. In System C, there are two types of compute nodes: CPU and ACC nodes. Jobs submitted to queues with "cpu" and "acc" at the end of their queue names are submitted to CPU and ACC nodes, respectively, If users submit a job to queues with "accs" at the end of their queue names, the job runs in the ACC node shared by other jobs of "accs" queues. See Sec. 1.1 for a description of each type of compute node. The user then has to choose the queue according to the number of nodes to use and the duration of their calculation jobs. Queue names starting with "F" are for jobs taking 24 hours or less, while those starting with "L" can run much longer up to 120 hours. More nodes are allotted to "F" queues in order to maximize the turnaround time of user jobs. The queue names starting with "i" are used for interactive debugging of user programs and the elapsed time limit is 30 minutes. The number following "F", "L", or "i" correspond to the number of nodes that can be used by one user job. Although we do not mention here in detail, to promote utilization of the massively parallel supercomputer, background queues (queue name starting with "B") for Systems B and C which charge no points for the jobs have also been open.

To prevent overuse of the storage, points are charged also for usage of disk quota in the three systems, as shown in Table 5. Disk points are revised often for optimal usage of the resources by examining usage tendencies each year.

The number of jobs, average waiting time, and total execution time in each queue are shown in Tables 6 and 7. In Systems B and C, a large portion of jobs have been executed in "F" queues. The largest amount of the execution time has been consumed in the large-scale "F72cpu" and "F16cpu" queues for Systems B and C, respectively. However, substantial number of jobs were run in every queue, suggesting that a wide variety of user needs are met by this queuing scheme. In

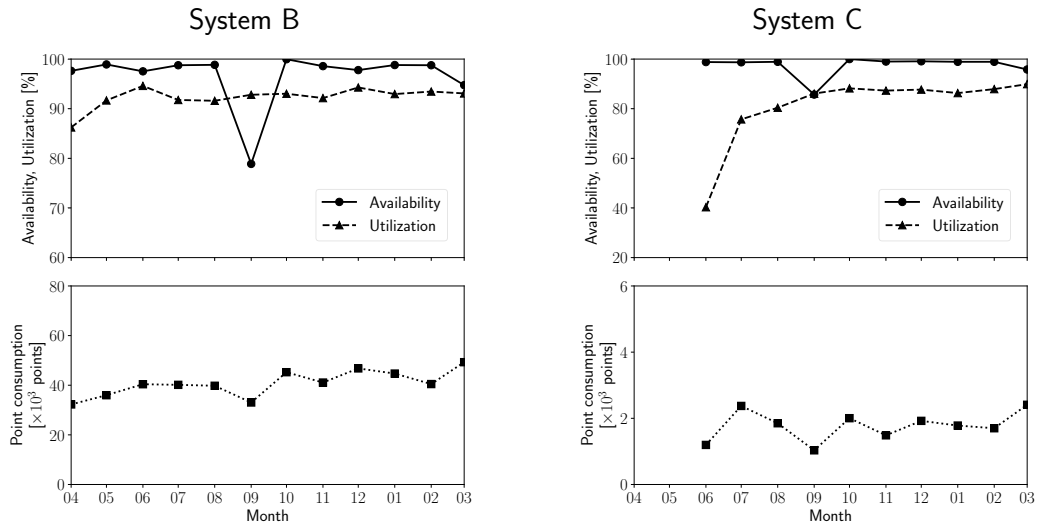

Figure 2: Availabilities, utilization rates and point consumptions of each month during SY 2022.

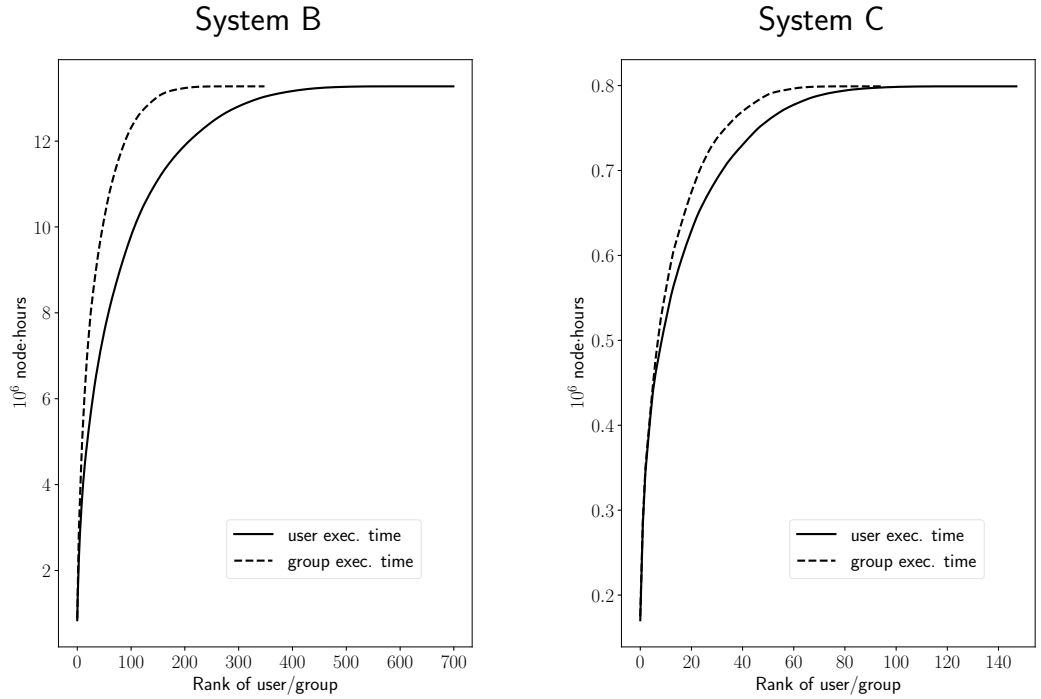

Figure 3: User statistics. The horizontal axis shows the rank of the user/group arranged in the descending order of the execution time (hour×nodes). The vertical axis shows the sum of the execution time up to the rank.

Table 3: Queue structures of System B in SY 2022

System B, ohtaka

queue name	Elapsed time limit (hr)	# of nodes /job	# of nodes /queue	Memory limit (GB)	job points /(node·day)
F1cpu	24	1	600	230/node	1
L1cpu	120	1	300	230/node	1
F4cpu	24	2–4	216	230/node	1
L4cpu	120	2–4	108	230/node	1
F16cpu	24	5–16	288	230/node	1
L16cpu	120	5–16	144	230/node	1
F36cpu	24	17–36	72	230/node	1
L36cpu	120	17–36	36	230/node	1
F72cpu	24	72	576	230/node	1
L72cpu	120	72	288	230/node	1
F144cpu	24	144	432	230/node	1
L144cpu	120	144	144	230/node	1
i8cpu	0.5	1–8	72	230/node	1
F2fat	24	1–2	7	2900/node	4
L2fat	120	1–2	3	2900/node	4
i1fat	0.5	1	1	2900/node	4

most of these queues, the queue settings meet the user's tendencies in that the waiting times are on the order of the elapsed-time limit.

2.3 Project for Advancement of Software Usability in Materials Science

From School Year 2015, the supercomputer center (SCC) has started "Project for advancement of software usability in materials science". In this project, for enhancing the usability of the supercomputer system in ISSP, we perform some software-advancement activity such as implementing a new function to an existing code, releasing a private code on Web, writing manuals. Target programs are publicly offered in December and selected in the review by the Steering Committee of SCC. The projects are carried out by the software development team composed of three members in ISSP. In SY 2022, three projects were selected as listed in Table 8.

Table 4: Queue structures of System C in SY 2022

System C, kugui

queue name	Elapsed time limit (hr)	# of nodes /job	# of nodes /queue	Memory limit (GB)	job points /(node·day)
i2cpu	0.5	1–2	8	240/node	1
F1cpu	24	1	120	240/node	1
L1cpu	120	1	60	240/node	1
F4cpu	24	2–4	32	240/node	1
L4cpu	120	2–4	16	240/node	1
F16cpu	24	5–16	64	240/node	1
L16cpu	120	5–16	32	240/node	1
F1accs	24	1	3	$60\times N_{\mathrm{GPU}}$	1
L1accs	120	1	1	$60\times N_{\mathrm{GPU}}$	1
i1accs	0.5	1	1	$60\times N_{\mathrm{GPU}}$	1
F2acc	24	1–2	4	240/node	1
L2acc	120	1–2	2	240/node	1

* N_{GPU} in ACC queues denotes the number of occupied GPUs.

2.4 ISSP Data Repository

From School Year 2021, the supercomputer center (SCC) has started to operate ISSP Data Repository (ISSP-DR) for accumulating and utilizing research data in materials science. GitLab is used as the data management system, and a portal site is provided as a data registration and search system for the registered data. By using ISSP-DR, it is possible to store and publish research data used in papers and datasets useful in the field of condensed matter science. Users of ISSP Supercomputer are welcome to apply for and use ISSP-DR.

Acknowledgments

The staffs would like to thank Prof. Takafumi Suzuki (now at University of Hyogo) for developing WWW-based system (SCM: SuperComputer Management System) for management of project proposals, peer-review reports by the SPAC committee, and user accounts. We also thank Ms. Reiko Iwafune for creating and maintaining a new WWW page of the ISSP Supercomputer Center.

Table 5: Disk points of Systems B and C

		point/day
System B ohtaka	`/home`	$0.001 \times \theta(q - 600)$
	`/work`	$0.0001 \times \theta(q - 6000)$
System C kugui	`/home`	$0.001 \times \theta(q - 150)$
	`/work`	$0.0001 \times \theta(q - 1500)$

* q is denoted in unit of GB.
* $\theta(x)$ is equal to the Heaviside step function $H(x)$ multiplied by x, i.e., $xH(x)$.

Table 6: Number of jobs, average waiting time, total execution time, and average number of used nodes per job in each queue of System B.

System B, ohtaka

queue	# of Jobs	Waiting Time (hour)	Exec. Time ($\times 10^3$ node·hour)	# of nodes
F1cpu	160175	31.64	290.45	1.00
L1cpu	4726	63.51	207.39	1.00
F4cpu	77846	26.01	1203.73	2.82
L4cpu	4400	58.22	493.38	2.89
F16cpu	44145	12.77	1586.63	9.23
L16cpu	1990	58.49	661.29	9.29
F36cpu	1179	52.79	311.35	28.75
L36cpu	102	69.71	115.50	22.46
F72cpu	8509	19.76	3711.88	72.00
L72cpu	101	40.95	270.27	72.00
F144cpu	3422	18.28	2090.58	144.00
L144cpu	114	257.46	581.50	144.00
i8cpu	143548	0.09	95.25	4.28
F2fat	5698	206.85	36.39	1.24
L2fat	508	60.36	17.51	1.21
i1fat	1003	0.35	0.09	1.00

Table 7: Number of jobs, average waiting time, total execution time, and average number of used nodes per job in each queue of System C.

System C, kugui

queue	# of Jobs	Waiting Time (hour)	Exec. Time ($\times 10^3$ node·hour)	# of nodes
i2cpu	6417	0.39	0.84	1.30
F1cpu	32465	3.03	92.09	1.00
L1cpu	862	24.34	31.42	1.00
F4cpu	3780	6.13	80.44	3.31
L4cpu	374	35.69	45.22	3.44
F16cpu	1837	12.60	134.95	13.53
L16cpu	83	16.11	23.83	12.24
i1accs	3794	0.00	0.20	1.00
F1accs	2946	2.88	10.41	1.00
L1accs	418	1.16	1.57	1.00
F2acc	3225	5.96	4.16	1.04
L2acc	72	2.05	0.63	1.29

Table 8: List of Project for advancement of software usability in materials science for SY 2022.

Project Proposer	Project Name
Shusuke Kasamatsu Yamagata University	Coupling of extended ensemble sampling and first-principles solvers
Akito Kobayashi Nagoya University	Advancement of effective model solvers toward high-throughput calculations — Wavenumber based mean-field approximation and random phase approximation

3 RESEARCH REPORTS

3.1 Invited Articles

Training method for refinement of machine-learning interatomic potential and its applications

Kohei Shimamura, Akihide Koura, and Fuyuki Shimojo
Department of Physics, Kumamoto University,
Kumamoto 860-8555, Japan

Abstract

Machine-learning interatomic potential (MLIP) is based on low-cost ML models trained with first-principles data to achieve high accuracy in molecular dynamics simulations, expanding the range of applicable time-space domains. However, the current widely used training method has limitations in accurately estimating stress and fundamental physical quantities such as free energy and thermal conductivity. We have therefore emphasized the importance of stress training for MLIPs and investigated other issues behind the current training method. The report discusses the role of stress training in reproducing solid-liquid phase transitions and estimating thermal conductivity, as well as the effect of training data with different k points on free energy.

1 Introduction

The machine-learning interatomic potential (MLIP) is used in a wide range of research fields. By training low-cost machine learning models with first-principles molecular dynamics (FPMD) data, the MLIP achieves high accuracy, significantly expanding the applicable space-time domain of MD simulations. MLIP is used to calculate physical quantities that require large statistical amounts, to investigate phenomena occurring in long-term dynamic simulations such as shock waves, and to explore reaction pathways [1, 2, 3].

Under these circumstances, we have been working on the refining the training method of MLIPs. In particular, we have emphasized the importance of stress training to MLIP [4, 5]. Recent mainstream training methods set total potential energy and atomic force as the targets in training [6]. Despite the fact that the accuracy of stress is not guaranteed, some previous studies to investigate high-pressure phenomena have utilized such MLIPs. It is moreover found that the stress training is necessary to accurately estimate fundamental physical quantities such as thermal conductivity (TC), and becomes one of the indispensable training conditions [5]. This report discusses the importance of stress training of MLIPs for reproducing a phase transition and estimating TC. In addition, we also discuss the effect of training data with different k points on thermodynamic quantities obtained through MLIPs, such as free energy. As the MLIP, we adopted an interatomic potential using an artificial neural network (ANN potential).

1.1 Stress training

Originally MLIPs were trained with only total potential energy. Afterward, atomic force, which is crucial for MD simulations, was integrated into the training process, leading to a significant improvement in accuracy compared to MLIPs that only consider the total potential energy. Recently, some MLIPs have been obtained by training with FP data of the total potential energy, atomic force, and stress. However, such MLIPs that target stress in training may still be in a minority. In this report, we show our results that the accuracy of stress is not guaranteed by training with the total potential

energy and atomic force alone, and that the solid-liquid phase transition of Na is accurately reproduced by training with stress [4].

1.2 Free energy calculation

Thermodynamic integration (TI) is a popular method for computing free energy, but when combined with MLIPs such as ANN potentials, some considerations need to be taken for liquids. We discovered a method that involved two steps, using an ideal gas and a soft potential as reference systems [7]. We show how to calculate the free energies of solid and liquid states by the TI method using ANN potential for Na [4].

Furthermore, in numerous previous studies, MLIPs were trained using FP data with multiple k points instead of using of large-scale systems. We however show that as precision requirements increase, larger systems with a greater number of k points will be necessary for the free energy calculation [4].

1.3 TC calculation

The TC calculation method based on the Green-Kubo (GK) formula has been widely used because it can be applied to even disordered systems. However, MLIPs including the ANN potential belong to many-body potentials, and the many-body effects have to be taken into account in the formula of the heat flux [8]. We found that using the rigorous heat flux formula considering the effects together with applying stress training to the ANN potential led to highly accurate TC estimates [9]. Here, we show the result of the TC for the superionic conducting Ag_2Se (α-Ag_2Se) by homogeneous nonequilibrium MD (HNEMD) based on the GK formula [9].

2 Computational Details

In this study, FPMD and MD simulations using MLIPs were conducted using the QXMD code [10].

2.1 ANN potential

The ANN potentials were constructed using ænet [11], which is a training code developed by Artrith *et al.* The ANN potential comprises feed forward neural networks (FFNNs) created for each atomic species. The total potential energy U^{ANN} is defined by the sum of the atomic potential energies $\{\varepsilon_i^{\mathrm{ANN}}\}$ output from FFNNs for all atoms in the system [12].

$$U^{\mathrm{ANN}} = \sum_i^{N_{\mathrm{atom}}} \varepsilon_i^{\mathrm{ANN}}, \tag{1}$$

where N_{atom} denotes the total number of atoms.

The atomic potential energy depends on the structural descriptor used. Chebyshev descriptors [13] were used in this study. The atomic potential energy of the Chebyshev descriptor is only a function of the relative coordinates $\mathbf{r}_{ij}$ [5]

$$\varepsilon_i^{\mathrm{ANN}} = \varepsilon_i^{\mathrm{ANN}}\left(\{\mathbf{r}_{ij}\}_{j\neq i}\right). \tag{2}$$

2.2 Training methods

The following cost function C was used to train the ANN potentials. It consists of three loss functions, i.e., the total potential energy, atomic force, and virial.

$$\begin{aligned} C &= \frac{p_U}{2}\frac{1}{N_I}\sum_I^{N_I}\left(\frac{U_I^{\mathrm{ANN}}-U_I^{\mathrm{Ref}}}{N_{\mathrm{atom}}}\right)^2 \\ &+ \frac{p_F}{2}\frac{1}{N_I}\sum_I^{N_I}\frac{1}{3N_{\mathrm{atom}}}\sum_i^{N_{\mathrm{atom}}}\left(\mathbf{F}_{I,i}^{\mathrm{ANN}}-\mathbf{F}_{I,i}^{\mathrm{Ref}}\right)^2 \\ &+ \frac{p_W}{2}\frac{1}{N_I}\sum_I^{N_I}\frac{1}{6}\sum_j^{6}\left(\frac{W_{I,j}^{\mathrm{ANN}}-W_{I,j}^{\mathrm{Ref}}}{N_{\mathrm{atom}}}\right)^2, \end{aligned} \tag{3}$$

where N_I denotes the number of training data. The symbol "Ref" denotes the training data. Factor 6 for the virial term reflects the number of independent degrees of freedom of the virial tensor $\mathrm{W}_I^{\mathrm{ANN}}$. Because the three loss functions differ in dimension and size, p_U, p_F, and p_W are introduced as adjustable parameters. With appropriate settings of these parameters, highly accurate ANN potentials can be constructed [14].

Note that the training for virial tensor $\mathrm{W}_I^{\mathrm{ANN}}$ is equivalent to that for the stress tensor $\mathrm{P}_I^{\mathrm{ANN}}$ calculated by dividing $\mathrm{W}_I^{\mathrm{ANN}}$ by supercell volume.

The ANN potential trained with total potential energy and atomic force is called EF-fit, while the one trained including virial is called EFP-fit.

2.3 Generation of training data on Na

We obtained the training data of Na by running FPMD simulations. We calculated the electronic states using the projector-augmented-wave (PAW) method [15] within the framework of density functional theory (DFT) [16], in which the generalized gradient approximation (GGA) [17] was used for the exchange-correlation energy. The plane-wave cutoff energies were 10 and 50 Ry for the electronic pseudo-wave functions and pseudo-charge density, respectively. Projector functions were generated for the $3s$, $3p$, and $3d$ state of Na atom.

The FPMD simulations were mainly performed using 128 Na atoms with periodic boundary conditions. For the Brillouin-zone sampling, 4 and 32 special k points were utilized in addition to the Γ point. These are equivalent to sampling at the Γ point in systems consisting of 1024 and 8192 atoms, respectively. For comparison, FPMD simulations were also conducted on 1024 Na atoms using the Γ point. The equations of motion were solved under the isothermal-isobaric (NPT) ensemble through an explicit reversible integrator [18]. The pressure was set to be ambient. The MD time step Δt was 2.9 fs. The simulation temperature was mainly set to 350 K. In addition, FPMD data using 128 atoms with Γ point were prepared for heating and cooling processes in the range between 450 and 200 K to investigate whether the ANN potential can reproduce the melting and solidification processes of Na.

2.4 TI method

In the TI method [4, 7], the interaction energy $U(\lambda)$ with parameter λ and the Helmholtz free energy $F(\lambda)$ are connected by the following relation:

$$\frac{\partial F(\lambda)}{\partial \lambda} = \left\langle \frac{\partial U(\lambda)}{\partial \lambda} \right\rangle_{NVT}, \tag{4}$$

where $\langle \cdots \rangle_{NVT}$ denotes the canonical (NVT) ensemble average. $U(\lambda)$ is given as

$$U(\lambda) = \lambda U_{\mathrm{Na}} + (1-\lambda) U_{\mathrm{ref}} \ \ (0 \le \lambda \le 1), \tag{5}$$

where U_{Na} and U_{ref} are the total potential energies of the target (Na) and reference systems, respectively. By substituting Eq. (5) into Eq. (4), and integrating both sides with respect to λ from 0 to 1, we obtain the following formula:

$$F(\lambda=1) - F(\lambda=0) = \int_0^1 \langle U_{\mathrm{Na}} - U_{\mathrm{Ref}} \rangle_{NVT} \, d\lambda. \tag{6}$$

$F(\lambda=1)$ and $F(\lambda=0)$ are the free energies of the target and reference systems, respectively. As reference systems for the solid and liquid phases, we employed an Einstein solid and an ideal gas, respectively.

In the liquid phase, the soft core (SC) potential U_{SC}, defined as follows, was employed to avoid shortening the interatomic distance as λ approaches zero [7].

$$U_{\mathrm{SC}}(\{\boldsymbol{r}_i\}) = \sum_{i<j}^{N} \mu \left(\frac{\sigma}{r_{ij}} \right)^n. \tag{7}$$

The parameters were used to be $\mu = 7.92 \times 10^{-4}$ hartree, $\sigma = 6.752$ bohr, and $n = 12$. The Helmholtz free energy in the liquid phase was calculated by two TIs. The first TI is calculated along the ideal gas to SC liquid and the second one is from SC to the target liquid Na. In addition, to integrate the first while preventing divergence at smaller λ, we adopted the coordinate transformation from λ to x proposed in the previous study [19]

$$\lambda(x) = \left(\frac{x+1}{2} \right)^{\frac{1}{1-k}}, \tag{8}$$

where the interval of integration is changed from $0 \le \lambda \le 1$ to $-1 \le x \le 1$. We employed the parameter $k = 0.85$. Applying this transformation to the integration with respect to λ, we have the following formula:

$$\int_0^1 f(\lambda) d\lambda = \frac{1}{2(1-k)} \int_{-1}^{1} f(\lambda(x)) \lambda(x)^k dx \,. \tag{9}$$

2.5 Generation of training data on α-Ag_2Se

We generated training data using MD simulations with an empirical interatomic potential (EIP) instead of FPMD. One reason for this is that we can obtain a reference value of TC. The other reason is that the EIP of Ag_2Se proposed by Rino *et al*. [20] is a physically excellent EIP that can describe phase transitions among nonsuperionic, superionic conducting, and liquid phases [21]. The training data were obtained by MD simulation with the NVT ensemble at 500 K for the α-Ag_2Se system that comprises 256 Ag + 128 Se atoms in experimental density [22].

2.6 TC calculation

2.6.1 GK formula and heat flux

According to the GK formula [23, 24], the $\alpha\beta$ component of the TC tensor $\kappa_{\alpha\beta}$ can be estimated as ($\alpha, \beta \in \{x, y, z\}$)

$$\kappa_{\alpha\beta} = \frac{\Omega}{k_{\mathrm{B}}T^2}\int_0^\infty \langle J_{Q,\alpha}(t)J_{Q,\beta}(0)\rangle dt, \quad (10)$$

where T, k_{B}, and Ω are temperature, the Boltzmann constant, and volume of the supercell, respectively. $\langle J_{Q,\alpha}(t)J_{Q,\beta}(0)\rangle$ denotes the auto-correlation function of the heat flux $\mathbf{J}_Q$, and the following expression is employed for both the EIP and ANN potentials:

$$\mathbf{J}_Q = \frac{1}{\Omega}\sum_i^{N_{\mathrm{atom}}} t_i\mathbf{v}_i + \frac{1}{\Omega}\sum_i^{N_{\mathrm{atom}}} \varepsilon_i\mathbf{v}_i + \frac{1}{\Omega}\sum_i^{N_{\mathrm{atom}}} \mathrm{W}_i\mathbf{v}_i \quad , \quad (11)$$

where t_i, $\mathbf{v}_i$, ε_i, and W_i are atomic kinetic energy, velocity, potential energy, and virial tensor for the ith atom, respectively.

2.6.2 Atomic virials in heat flux formula

To derive a rigorous formula of the heat flux for the many-body potentials, an expression for the atomic potential energy is required [8], which corresponds to Eq. (2) for the ANN potentials. In our previous study [5], we have succeeded in deriving the heat flux formula and showed that the atomic virial is expressed as follows.

$$\mathrm{W}_i^{\text{ANN-I}} = \sum_{j\neq i}\mathbf{r}_{ij}\otimes\frac{\partial\varepsilon_j^{\mathrm{ANN}}}{\partial\mathbf{r}_{ji}}. \quad (12)$$

Incidentally, for the many-body potentials such as the ANN potential, there are countless definitions of atomic virial which give identical total virials [9, 5]. We define two more apparently reasonable atomic virials used for heat fluxes in the previous studies.

$$\mathrm{W}_i^{\text{ANN-II}} = \sum_{j\neq i}\mathbf{r}_{ij}\otimes\frac{\partial\varepsilon_i^{\mathrm{ANN}}}{\partial\mathbf{r}_{ji}}, \quad (13)$$

and

$$\mathrm{W}_i^{\text{ANN-III}} = \frac{1}{2}\sum_{j\neq i}\mathbf{r}_{ij}\otimes\left[\frac{\partial\varepsilon_i^{\mathrm{ANN}}}{\partial\mathbf{r}_{ji}} + \frac{\partial\varepsilon_j^{\mathrm{ANN}}}{\partial\mathbf{r}_{ji}}\right]. \quad (14)$$

$\mathrm{W}_i^{\text{ANN-II}}$ appears naturally in the stress-tensor derivation for the ANN potentials [25]. In Ref. [26], $\mathrm{W}_i^{\text{ANN-III}}$ was used because the pairwise force defined as $\mathbf{F}_{ij}^{\mathrm{ANN}} = -\left[\frac{\partial\varepsilon_i^{\mathrm{ANN}}}{\partial\mathbf{r}_{ji}} + \frac{\partial\varepsilon_j^{\mathrm{ANN}}}{\partial\mathbf{r}_{ji}}\right]$ satisfies Newton's third law [8]. The summation $\sum_j^{N_{\mathrm{atom}}}\mathbf{F}_{ij}^{\mathrm{ANN}}$ is equal to $\mathbf{F}_i^{\mathrm{ANN}}$. While the mathematical properties of the three atomic virials differ, their sums over N_{atom} yield the same total virial $\mathrm{W}^{\mathrm{ANN}}$. Hereinafter, the heat flux formulae defined by substituting $\mathrm{W}_i^{\text{ANN-I}}$, $\mathrm{W}_i^{\text{ANN-II}}$, and $\mathrm{W}_i^{\text{ANN-III}}$ into Eq. (11) are referred to as $\mathbf{J}_Q^{\mathrm{I}}$, $\mathbf{J}_Q^{\mathrm{II}}$, and $\mathbf{J}_Q^{\mathrm{III}}$, respectively. Some studies used ANN potentials that estimated TCs with $\mathbf{J}_Q^{\mathrm{II}}$ [27] and $\mathbf{J}_Q^{\mathrm{III}}$ [26]. Recent studies highlighted that the atomic virial can significantly impact the TC when dealing with many-body potentials [8, 28, 29]. It is crucial to compare the TCs obtained from these heat flux formulae.

2.6.3 HNEMD method

The HNEMD method [30], which is based on the GK formula, has successfully reduced the computational cost by enabling the calculation of TC using the time average of the heat flux instead of integrating its auto-correlation function.

$$\kappa = \frac{\Omega}{F_{\mathrm{ext}}T}\lim_{t\to\infty}\langle J_{Q,x}\rangle_t, \quad (15)$$

where F_{ext} denotes a magnitude of perturbation along the x direction of the system. F_{ext} = 0.01 bohr^{-1} was selected for the HNEMD simulations in this study [5].

3 Results

3.1 Solid-liquid phase transition of Na

We first investigated whether the EF-fit and EFP-fit models reproduced the hysteresis of melting and solidification in Na [4]. These two types of ANN potentials were constructed from the FPMD data in the temperature range of 200 to 450 K, performed using 128 atoms with Γ point as mentioned in section 2.3. The EFP-fit was able to accurately reproduce the heating and cooling processes of FPMD. The temperature dependence of radial distribution function $g(r)$ obtained from the MD simulations is shown in Fig. 1. $g(r)$'s by the EFP-fit (green dashed lines) are quite consistent with the FPMD results (black solid lines). In contrast, the $g(r)$ obtained from the MD simulations using EF-fit (red dashed lines) showed a significant deviation from those obtained from FPMD . The above results demonstrate the risk by using MLIPs such as EF-fit, which do not guarantee the accuracy of stress.

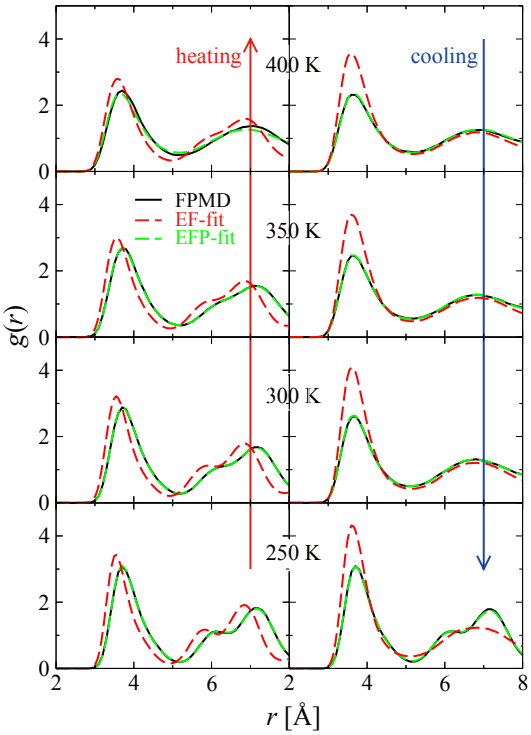

Figure 1: Temperature dependence of the radial distribution function $g(r)$ in the heating and cooling processes. The black solid lines correspond to the results from FPMD simulations. The red and green dashed lines correspond to those from MD simulations with EF-fit and EFP-fit, respectively. Taken from Ref. [4].

3.2 Size dependence of the free energy of Na

In many previous studies, the training data of MLIPs were created by FP calculation with many k points to avoid using large-scale systems. However, it is not obvious whether the respective MLIPs constructed from the training data obtained with a specific number of k points and corresponding system sizes show equivalent accuracy. Therefore, we conducted the following analysis to clarify the influence of training conditions such as system size and the number of k points on thermodynamic quantities such as free energy [4].

We created the four types of EFP-fit models. These were trained with the FPMD data obtained from the 128-atom system with Γ point, 128-atom system with 4k points, 128-atom system with 32k points, and 1024-atom system with Γ point, which are hereinafter referred to as 128-ΓANN, 128-4kANN, 128-32kANN, and 1024-ΓANN potentials, respectively. To investigate the size-dependent behavior of thermodynamic quantities, we calculated the Helmholtz free energy for 128 and 1024 atoms using 128-ΓANN and 128-4kANN potentials. Additionally, for comparison, we computed the same quantities for 1024 atoms using 1024-ΓANN and 128-32kANN potentials. Figure 2 shows the (a) Helmholtz free energy F, (b) total potential energy U, and (c) product of entropy and temperature TS as a function of the number of atoms N. The triangles and circles represent the solid and liquid phases, respectively. The black, red, green, and blue symbols de-

note the values calculated using the 1024-ΓANN, 128-4kANN, 128-ΓANN, and 128-32kANN potentials, respectively. As observed from this figure, the outcomes obtained using the128-ΓANN potential exhibit significant deviation from the others. Moreover, the values computed using the 1024-ΓANN, 128-4kANN, and 128-32kANN potentials are nearly identical with regard to the vertical axis.

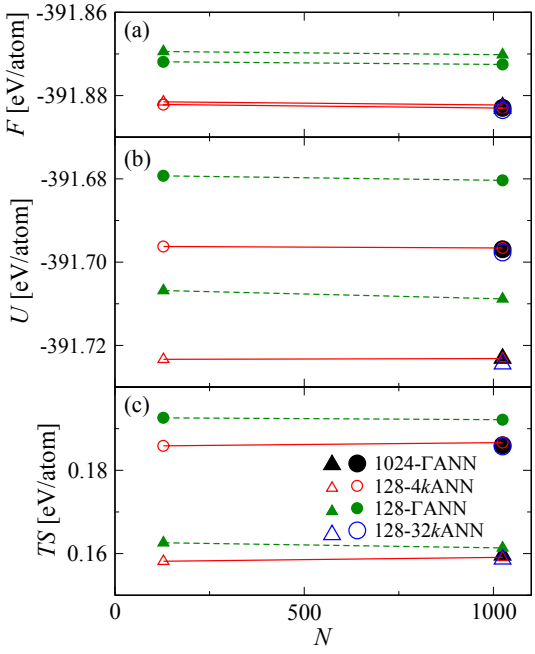

Figure 2: (a) Helmholtz free energy F, (b) total potential energy U, and (c) product of entropy and temperature TS obtained using the TI method at 350 K as a function of the number of atoms N. Triangles and circles correspond to the solid and liquid states, respectively. The black, red, green, and blue symbols indicate the values calculated using the 1024-ΓANN, 128-4kANN, 128-ΓANN, and 128-32kANN potentials, respectively. Taken from Ref. [4].

To further examine the size dependence, we computed the differences in Helmholtz free energy between the solid and liquid states $\Delta F = F_{\rm liq} - F_{\rm sol}$, as shown in Table 1. From the table, we obtained the following findings: (i) the values obtained from the 128-ΓANN potential differs largely from the others; (ii) the difference in ΔF between 128 and 1024 atoms is merely 0.13 and 0.11 meV/atom when calculated with the 128-ΓANN and 128-4kANN, respectively, suggesting that for systems with more than 128 atoms, the size dependence on ΔF is almost negligible in comparison with the difference of Helmholtz free energy; (iii) the difference between the ΔF values computed using the128-4kANN and 1024-ΓANN potentials is relatively small, with a difference of only 0.50 meV/atom for 1024 atoms; (iv) the value of ΔF obtained using the 128-32kANN is more similar to that obtained using the 1024-ΓANN than to that obtained using the 128-4kANN. Despite being trained with FPMD data at a single temperature of 350 K, the 128-4kANN potential is capable of accurately calculating ΔF with an error of only a few tenths of meV/atom. However, if higher precision is required, larger systems with more k points will be necessary.

Table 1: Differences of Helmholtz free energy $\Delta F = F_{\rm liq} - F_{\rm sol}$ between the solid and liquid states at 350 K in meV/atom. Taken from Ref. [4]

Atoms	128-Γ	128-4k	1024-Γ	128-32k
128	-2.47	-0.63	-	-
1024	-2.34	-0.74	-0.24	-0.33

3.3 TC calculation of α-Ag_2Se

The stress training is also associated with the accuracy of TC. Here, we present the results of an investigation of the influence of the heat flux formulae ($\mathbf{J}^{\rm I}_Q$, $\mathbf{J}^{\rm II}_Q$, and $\mathbf{J}^{\rm III}_Q$) and stress training on TC, using α-Ag_2Se as the test system [5].

To examine the effect of stress training, we used the EF-fit and EFP-fit models, and also took into account the dependence of the initial weight parameters in ANN. We constructed five each of the EF-fit and EFP-fit with different initial weight parameters. Figure 3 plots five TCs ($\kappa^{\rm ANN}$) obtained from the respective EF-fit and EFP-fit models as a function of root mean square errors of stress for the validation data ($\Delta P_{\rm valid}$). The vertical axis shows the absolute value $|\kappa^{\rm ANN} - \kappa^{\rm EIP}|$,

where κ^{EIP} is the reference TC obtained from the EIP (0.274 $\mathrm{Wm^{-1}K^{-1}}$). For the EF-fit, while three TCs calculated by $\mathbf{J}^{\mathrm{I}}_Q$ are sufficiently close to 0, all of the five $\Delta P_{\mathrm{valid}}$ are larger than 0.47 GPa. Furthermore, $|\kappa^{\mathrm{ANN}} - \kappa^{\mathrm{EIP}}|$ exhibits a large value of ~ 0.2 $\mathrm{Wm^{-1}K^{-1}}$ with higher values of $\Delta P_{\mathrm{valid}}$ when using $\mathbf{J}^{\mathrm{I}}_Q$. $\mathbf{J}^{\mathrm{II}}_Q$ gives large errors of the TCs $\sim$0.25 $\mathrm{Wm^{-1}K^{-1}}$ with higher $\Delta P_{\mathrm{valid}}$. In the case of the TC calculated with $\mathbf{J}^{\mathrm{III}}_Q$, the deviation in the TC is larger than 0.02 $\mathrm{Wm^{-1}K^{-1}}$. The plots in Fig. 3 indicate that when $\Delta P_{\mathrm{valid}}$ is larger, errors in TC become larger and sometimes result in significant deviations.

The good agreement with the reference values suggests that stress training plays a crucial role as anticipated. For EFP-fit, all $|\kappa^{\mathrm{ANN}} - \kappa^{\mathrm{EIP}}|$ calculated with $\mathbf{J}^{\mathrm{I}}_Q$ is plotted near the origin as shown in Fig. 3. There are no cases showing larger TC errors as seen in the EF-fit. The maximum value of $|\kappa^{\mathrm{ANN}} - \kappa^{\mathrm{EIP}}|$ is $\sim$0.005 W $\mathrm{m^{-1}K^{-1}}$, which is much smaller than even the minimum values of $|\kappa^{\mathrm{ANN}} - \kappa^{\mathrm{EIP}}|$ calculated with $\mathbf{J}^{\mathrm{II}}_Q$ and $\mathbf{J}^{\mathrm{III}}_Q$, i.e. 0.055 and 0.041 W $\mathrm{m^{-1}K^{-1}}$, respectively.

From the above results, only $\mathbf{J}^{\mathrm{I}}_Q$ gives a correct estimation of TC. Further, the correct TC may not be obtained even with $\mathbf{J}^{\mathrm{I}}_Q$ unless $\Delta P_{\mathrm{valid}}$ is sufficiently minimized through stress training.

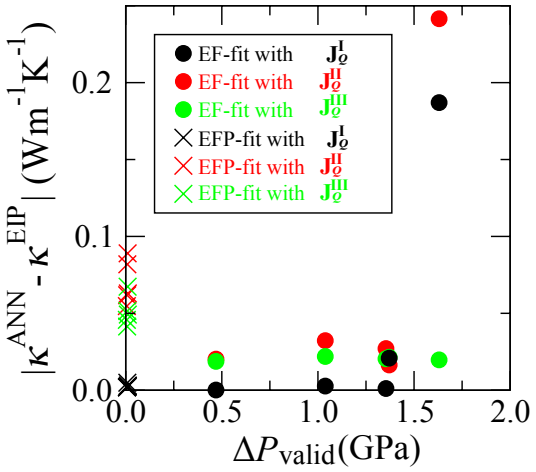

Figure 3: Absolute difference between the TC calculated from the ANN potentials (κ^{ANN}) and the EIP (κ^{EIP}) as a function of root mean square errors for the validation data ($\Delta P_{\mathrm{valid}}$) of five ANN potentials belonging EF-fit (filled circles) and EFP-fit (cross marks) for the validation data. κ^{ANN} and κ^{EIP} are calculated from HNEMD simulations. κ^{ANN} are computed using heat flux formulae $\mathbf{J}^{\mathrm{I}}_Q$ (black), $\mathbf{J}^{\mathrm{II}}_Q$ (red), and $\mathbf{J}^{\mathrm{III}}_Q$ (green). Taken from Ref. [5].

4 Summary

In this report, we have investigated and discussed issues that are unverified with the current training method of MLIPs. Specifically, we reported that the stress training is necessary to accurately reproduce the solid-liquid phase transition of Na and the TC of α-Ag_2Se. In addition, it was suggested that in order to construct more accurate MLIPs from the viewpoint of free energy calculations, increasing the number of k points is not the only solution, and a large-scale system is also necessary.

We would like here to comment on other unestablished aspects of MLIP training methods. It is important to recognize that adjusting the coefficients of the cost function can dramatically alter the accuracy of MLIPs [14]. The heat flux regularization method [31] introduced into the cost-function to estimate partial TCs may also lead to improved robustness of MLIPs. It should be emphasized that more attention should be paid to the importance of the modification of the cost function for the improvement of MLIPs as well as the developments in their architectures and descriptors.

Ackwnowledgements

This study was supported by MEXT/JSPS KAKENHI Grant Numbers Nos. 22K03454, 21H01766, and 19K14676, and JST CREST Grant Number JPMJCR18I2, Japan. The authors thank the Supercomputer Center, the Institute for Solid State Physics, University of Tokyo for the use of the facilities. The computations were also carried out using the facilities of the Research Institute for Information Technology, Kyushu University.

References

[1] Morawietz T and Artrith N 2021 *J. Comput. Aided Mol. Des.* **35** 557–586

[2] Misawa M, Fukushima S, Koura A, Shimamura K, Shimojo F, Tiwari S, Nomura K i, Kalia R K, Nakano A and Vashishta P 2020 *J. Phys. Chem. Lett.* **11** 4536–4541

[3] Yang M, Bonati L, Polino D and Parrinello M 2022 *Catal. Today* **387** 143–149

[4] Irie A, Fukushima S, Koura A, Shimamura K and Shimojo F 2021 *J. Phys. Soc. Jpn* **90** 094603

[5] Shimamura K, Takeshita Y, Fukushima S, Koura A and Shimojo F 2021 *Chem. Phys. Lett.* **778** 138748

[6] Behler J 2021 *Chem. Rev.* **121** 10037–10072

[7] Fukushima S, Ushijima E, Kumazoe H, Koura A, Shimojo F, Shimamura K, Misawa M, Kalia R K, Nakano A and Vashishta P 2019 *Phys. Rev. B* **100**(21) 214108

[8] Fan Z, Pereira L F C, Wang H Q, Zheng J C, Donadio D and Harju A 2015 *Phys. Rev. B* **92**(9) 094301

[9] Shimamura K, Takeshita Y, Fukushima S, Koura A and Shimojo F 2020 *J. Chem. Phys.* **153** 234301

[10] Shimojo F, Fukushima S, Kumazoe H, Misawa M, Ohmura S, Rajak P, Shimamura K, Bassman L, Tiwari S, Kalia R K, Nakano A and Vashishta P 2019 *SoftwareX* **10** 100307

[11] Artrith N and Urban A 2016 *Comput. Mater. Sci.* **114** 135 – 150

[12] Behler J and Parrinello M 2007 *Phys. Rev. Lett.* **98**(14) 146401

[13] Artrith N, Urban A and Ceder G 2017 *Phys. Rev. B* **96**(1) 014112

[14] Irie A, Shimamura K, Koura A and Shimojo F 2022 *J. Phys. Soc. Jpn.* **91** 045002

[15] Kresse G and Joubert D 1999 *Phys. Rev. B* **59** 1758–1775

[16] Hohenberg P and Kohn W 1964 *Phys. Rev.* **136** B864

[17] Perdew J P, Burke K and Ernzerhof M 1996 *Phys. Rev. Lett.* **77** 3865–3868

[18] Tuckerman M, Berne B J and Martyna G J 1992 *J. Chem. Phys.* **97** 1990–2001

[19] Rang M and Kresse G 2019 *Phys. Rev. B* **99**(18) 184103

[20] Rino J P, Hornos Y M M, Antonio G A, Ebbsjö I, Kalia R K and Vashishta P 1988 *J. Chem. Phys.* **89** 7542–7555

[21] Shimojo F and Okazaki H 1991 *J. Phys. Soc. Jpn.* **60** 3745–3753

[22] Okazaki H 1967 *J. Phys. Soc. Jpn.* **23** 355–360

[23] Kubo R 1957 *J. Phys. Soc. Jpn.* **12** 570–586

[24] Green M S 1952 *J. Chem. Phys.* **20** 1281–1295

[25] Behler J 2011 *J. Chem. Phys.* **134** 074106

[26] Mangold C, Chen S, Barbalinardo G, Behler J, Pochet P, Termentzidis K, Han Y, Chaput L, Lacroix D and Donadio D 2020 *J. Appl. Phys.* **127** 244901

[27] Sosso G C, Donadio D, Caravati S, Behler J and Bernasconi M 2012 *Phys. Rev. B* **86**(10) 104301

[28] Surblys D, Matsubara H, Kikugawa G and Ohara T 2019 *Phys. Rev. E* **99**(5) 051301

[29] Boone P, Babaei H and Wilmer C E 2019 *J. Chem. Theory Comput.* **15** 5579–5587

[30] Evans D J 1982 *Phys. Lett. A* **91** 457 – 460

[31] Shimamura K, Koura A and Shimojo F 2022 *arXiv*: 2101.10468

First principles calculation of copper-oxide superconductors exhibiting electron fractionalization

Masatoshi IMADA
Research Institute for Sicence and Engineering, Waseda University,
3-4-1 Okubo, Shinjuku-ku, Tokyo, 169-8555
Department of Engineering and Applied Sciences, Sophia University.
7-1 Kioi-cho, Chiyoda-ku Tokyo, 102-8554
and
Toyota Physical and Chemical Research Institute,
41-1 Yokomichi, Nagakute, Aichi, 480-1192

Abstract

We review recent *ab initio* studies on high-T_c superconductivity in copper oxides and insights into basic science of strongly correlated electron systems gained by extensive simulations enabled by supercomputers. After deriving effective Hamiltonians for a number of copper oxide compounds, they were solved by a state-of-the-art quantum many-body solver. The solutions show d-wave superconducting states correctly as the ground states. They are severely competing with the charge inhomogeneous states such as spin/charge stripes in accordance with the experimental indications. The amplitude of the superconducting order parameter and its carrier concentration dependence in the ground state well reproduce the experimental trend. The results further show that the diverse materials dependence is well captured. From the understanding of the materials dependence, we successfully extract the principal component that controls the strength of the superconductivity. We will also clarify how the superconductivity can be enhanced in the present mechanism beyond the existing materials. The *ab initio* solution also offers insights into electron fractionalization, which was recently proposed based on photoemission and resonant inelastic X-ray scattering results. The quantum entanglement found in the cuprate superconductors is shown to share a common underlying concept with the quantum spin liquids, which show another type of fractionalization described as an electronic spin splintered into two spinons. A unified understanding of the different two fractionalizations is sketched.

1 Introduction

Since the discovery of superconductivity in 1986 in copper oxides with quasi-two-dimensional perovskite structure, more than 35 years have already passed. Although a number of new superconductors were discovered since then, the copper oxides still hold the record of the highest critical temperature at ambient pressure. However, its mechanism has not converged to consensus in the community. Nevertheless, new ideas and concepts from the viewpoint of the basic science have been proposed even now. In this sense, the cuprate superconductors occupy a special position in materials science for decades. Among all, the cuprates show strong electron correlation even at temperatures well above the superconducting transition temperature T_c, character-

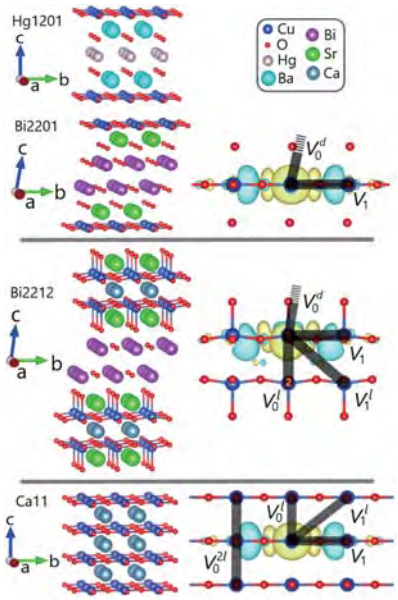

Figure 1: Crystal structure of four cuprate compounds [3]。

ized as the pseudogap in the underdoped region. In addition, the superconducting phase is severely competing with charge inhomogeneous states such as charge striped phases and antiferromagnetic phase. These features invalidate naive mean-field approximations, perturbative treatments from the simple metal and conventional density functional theory, which makes the study difficult. Physical properties including superconductivity itself and its diverse materials dependence of T_c need to be treated from first principles by accurate quantum many-body solvers by taking account of quantum entanglement properly.

Recently, numerical methods to study the strongly correlated electron systems have largely been developed [1], in which effective Hamiltonians derived by an *ab initio* framework starting from given crystal structure without resorting to adjustable parameters have been solved by accurate quantum many-body solvers. We summarize the essence of the results in this report.

In accordance with thus obtained *ab initio* results, electron fractionalization is independently identified as an important origin of the superconductivity and the pseudogap. Namely, it was found that an electron that is an elementary particle in vacuum is emergently splintered in strongly correlated electron systems. Thus generated particles are mutually tunneling quantum mechanically, in other words, hybridizing each other. The fractionalization well accounts for experimental data otherwise puzzling, that was revealed by combining experimental and computational results.

The achievement reviewed in this report would not be reached without the extensive simulations with the aid of supercomputer and the algorithmic progress, where technical details are quite important. However, from the viewpoint of the basic science, the most important achievement is how innovative idea and concept are established as the outcome and how new avenue is opened. In this review, we focus on the understanding of physics achieved in the recent studies by our group. We also address the relation of the electron fractionalization to the electronic spin fractionalization established in *ab initio* as well as model studies of quantum spin liquids.

2 *Ab initio* calculations

Numerical method to properly treat the strongly correlated electron systems by deriving effective Hamiltonians describing computationally tractable small degrees of freedom near the Fermi level has been developed for recent two decades [1, 2]. This method is called MACE (multiscale *ab initio* scheme for correlated electrons). Recently MACE has been further improved by using the constrained GW method supplemented by the self-interaction correction [5–7] instead of the conventional constrained random phase approximation (cRPA) [2] to allow better starting point of the global band structure with the proper removal of the double counting of the correlation effect. It is further improved by

introducing the level renormalization feedback (LRFB) to take into account the global self-consistency of the charge density [8].

With these refined procedures, effective Hamiltonians for four families of cuprate superconductors were derived [3], which are carrier doped $CaCuO_2$ (Ca11) (highest suprerconducting transition temperature is $T_c^{\rm opt} \sim 110$K at the optimum carrier doping), $Bi_2Sr_2CuO_6$ abbreviated hereafter as Bi2201 ($T_c^{\rm opt} \sim$ 10-40 K), $Bi_2Sr_2CaCu_2O_8$ abbreviated as Bi2212 ($T_c^{\rm opt} \sim$ 85-100 K), and $HgBa_2CuO_4$ ($T_c^{\rm opt} \sim$ 90K). These four materials share common stacked quasi-two-dimensional CuO_2 planes as viewed from the crystal structures in Fig. 1. Although the similar common CuO_2 planes are responsible for the superconductivity, the superconducting critical temperatures have diversity as mentioned above. To pursuit the origin of the diversity, conventional density functional theory (DFT) refined by the GW method was applied and global electronic structure was obtained as is shown in Fig. 2. There, a very similar band is crossing the Fermi level E_F (zero energy in Fig. 2), which is identified as the antibonding band (AB band) generated by a strong hybridization of Cu $3d_{x^2-y^2}$ and O $2p_\sigma$ orbitals in the same CuO_2 plane. However, other bands away from E_F are largely different.

Since physical properties below room temperatures are determined by the band near the Fermi level in the conventional understanding, the diversity of $T_c^{\rm opt}$ is hardly understood from the similar AB bands. However, the effect of renormalization from the scattered bands may affect the electronic strucure of the AB band due to electron correlation and the original GW band alone is not sufficient to understand the properties below room temperature in the strongly correlated systems. After taking account the effects of the bands away from E_F, which renormalizes the AB band, the effective Hamiltonian for the AB band was derived by following the refined MACE procedure [3].

The derived Hamiltonian has the form

$$\mathcal{H} = \sum_{i,j,\sigma} t_{ij} c^\dagger_{i\sigma} c_{j\sigma} + \sum_i U n_{i\uparrow} n_{i\downarrow} + \frac{1}{2} \sum_{i \neq j} V_{ij} n_i n_j, \tag{1}$$

where i, j denotes the Wannier orbital sites of the AB orbital in the CuO_2 plane, which are assigned one per Cu atom. By using these site coordinates, i, j dependent hopping t_{ij}, onsite interaction, U and interaction V_{ij} between i and j sites are obtained. Here, $c^\dagger_{i\sigma}(c_{i\sigma})$ is the creation (annihilation) operator of the AB orbital electron at i site with the spin σ.

By taking into account up to the 9th neighbor hopping and interactions in this Hamiltonian without adjustable parameters, the ground states of the 4 families of the cuprate superconductors are obtained [4] by using the many-variable variational Monte Carlo method [9, 10]. Below by considering translational and C_4 rotational symmetries of Cu square lattice, we take the notation of t_1 to t_9 and V_1 to V_9 in the order of distance for the hopping and interaction, respectively.

In Fig. 3, superconducting pair-pair correlation function $P_d(r)$ is plotted as a function of distance for several choices of $L \times L$ size AB-orbital square lattices and for a number of hole concentrations δ in the case of hole doped $CaCuO_2$. By using these data, we define $\bar{P}_d(L)$ as $P_d(r)$ converged at long distance for $L \times L$ lattice, which are extrapolated to the thermodynamic limit $L \to \infty$ as one can see in the insets of Fig. 3. Thus obtained $\bar{P}_d^\infty = \lim_{L\to\infty} \bar{P}_d(L)$ show nonzero values indicating d-wave superconducting long range order in agreement with the experimental indications.

Hole concentration dependence of the superconducting order parameter $F_{\rm SC}^\infty = \sqrt{\bar{P}_d^\infty}$ obtained from Fig. 3 is shown in Fig. 4, which has the maximum at around $\delta = 0.05$-0.1 with a dome structure. It shows monotonic decrease for $\delta > 0.1$, which is consistent with the hole concentration dependence of the superconducting gap observed in the measurement

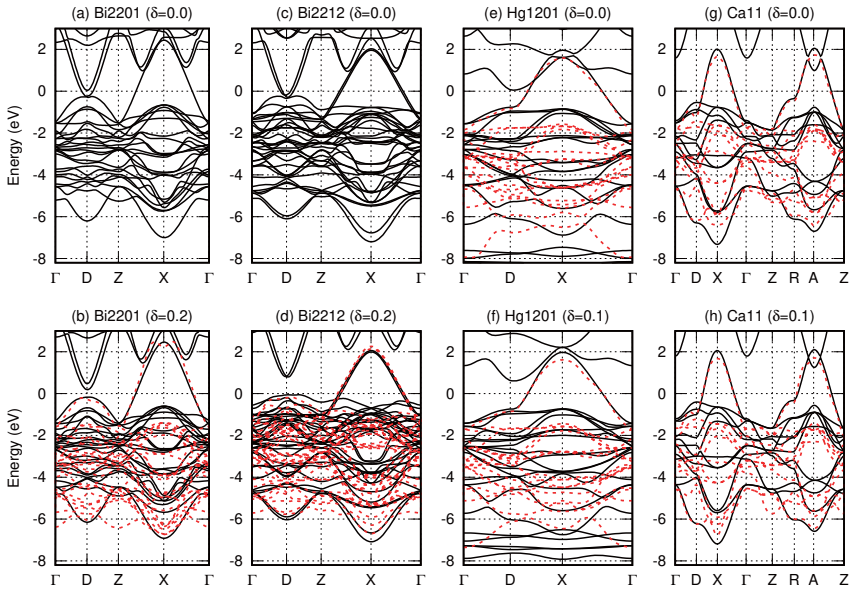

Figure 2: Electronic band structure of 4 cuprate compounds calculated by the GW method [3]. Abscissa represents the wavenumber along the symmetry line and the ordinate is the energy in the unit of eV.

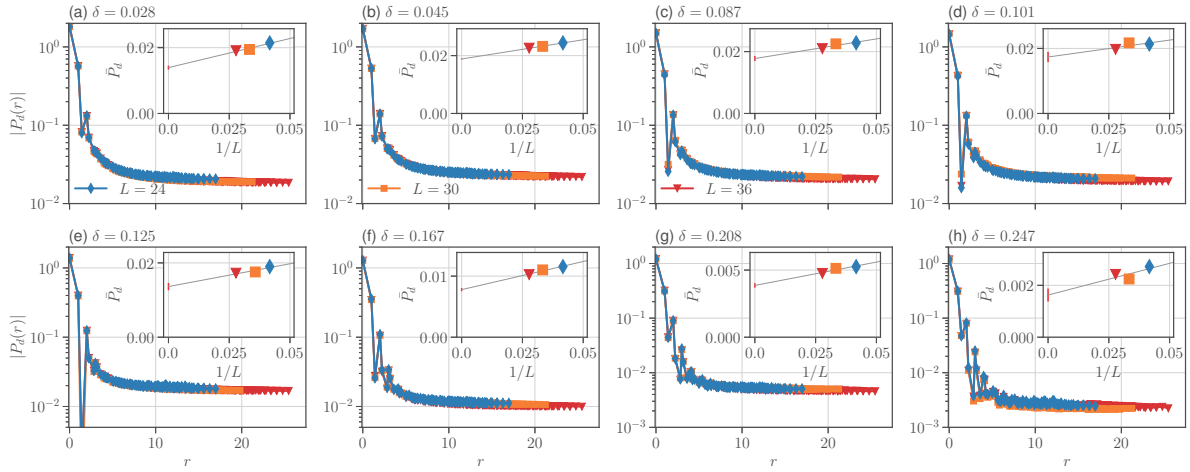

Figure 3: Superconducting correlation of carrier doped $CaCuO_2$ as a function of distance for various system sizes and doping concentrations. Insets show the size extrapolation taken by using the converged value at long distance of each lattice [4].

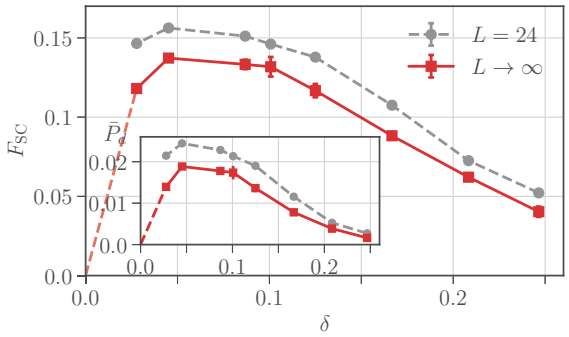

Figure 4: Hole concentration (δ) dependence of superconducting order parameter $F_{\rm SC}^{\infty}$ [4]. Gray symbols are the result of 24×24 lattice and red symbols are values in the thermodynamic limit [4].

by angle-resolved photoemission spectroscopy (ARPES) and scanning tunneling microscope (STM) [11, 12]. The order parameter at the optimal doping $F_{\rm SC}^{\infty} \sim 0.1$ is also in agreement with the superfluid density determined from the penetration depth measured by the muon spin resonance [13].

On the other hand, this superconducting ground states are severely competing with non-superconducting charge inhomogeneous states with spin-charge stripe orders illustrated in Fig. 5 in the excitation energy scale below 10meV. This also reproduces the widely observed competition in the cuprates.

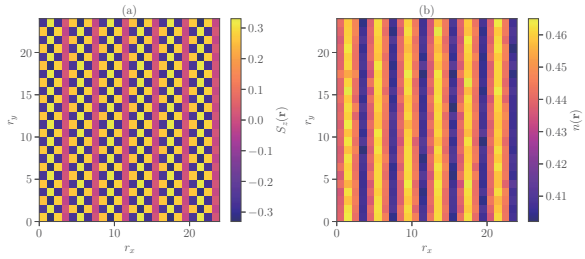

Figure 5: Example of charge and spin density distribution in the real space view of a stripe ordered excited state [4]. (a): Spin density configuration. (b): Chaegr density configuration.

Since the calculated results well reproduce the experimental properties quantitatively, it is now possible to position the status of the cuprate superconductivity in the global perspective, to clarify the superconducting mechanism and to examine the controllability of the superconducting strength all on a realistic ground. In fact, by examining relation between the material dependent diversity of the superconductivity and the parameters of the *ab intio* paramters of the effective Hamiltonians, it was found that the amplitude of the superconducting order parameter $F_{\rm SC}^{\infty}$ is mainly determined by $U/|t_1|$. $U/|t_1|$ is distributed and concentrated between 7 and 9 in the 4 compounds, and they are similar. However, if we plot the relation between $F_{\rm SC}^{\infty}$ and $U/|t_1|$ as one sees in Fig. 6, $F_{\rm SC}^{\infty}$ rapidly and systematically increases with $U/|t_1|$ in the range $7 < U/|t_1| < 8$. Namely if one wants to enhance the superconductivity in most of the realistic compounds, one can do simply by increasing $U/|t_1|$.

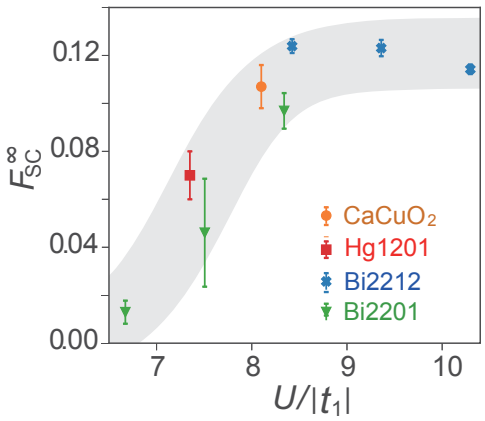

Figure 6: Relation between superconducting order parameter $F_{\rm SC}^{\infty}$ and the *ab initio* parameter $U/|t_1|$ for the 4 family of the cuprates [4].

To understand this trend more clearly, $F_{\rm SC}^{\infty}$ was calculated for the Hamiltonian beyond the *ab initio* parameter values by scaling the on-site U and intersite V_n interactions as αU and ξV_n, respectively as shown in Fig. 7. The scaling of $U/|t_1|$ by α indicates that, if we start from the carrier doped $CaCuO_2$, there exists the maximal enhancement of $F_{\rm SC}^{\infty}$ at slightly larger $U/|t_1|$ than the *ab initio* value, while

it is better to decrease V_n as much as possible and $F_{\rm SC}^{\infty}$ increases to more than twice of the *ab initio* value when ξ vanishes. Within the realistic materials, larger $U/|t_1|$ makes $F_{\rm SC}^{\infty}$ larger. However, if α is increased further, $F_{\rm SC}^{\infty}$ becomes suppressed. In fact, if $U/|t_1|$ is too large, excitonic as well as spin-singlet fluctuations, which generate the quantum entanglement are suppressed and the superconductivity growing from the entanglement are naturally suppressed. Then $\alpha \sim 1.2$ and small ξ beyond the real available material are understood as the optimum condition for the enhancement of superconductivity in the present case. Of course simultaneous tuning toward larger α and smaller ξ is not an easy task in reality, while it provides us with a useful basic guide line for the materials design by the strong-coupling superconducting mechanism.

Now let us come back to the analyses of real materials. It was shown that $T_c^{\rm opt}$ at the optimal doping concentration is well represented by

$$T_c^{\rm opt} \sim 0.16 t_1 F_{\rm SC}^{\infty} \qquad (2)$$

for all the 4 families of the cuprates studied as shown in Fig. 8.

For the Cooper pair formation needed for the superconductivity, effective attractive interaction between electrons is required. To gain insight into the origin of the attraction, carrier concentration (δ) dependence of the energy is plotted in Fig. 9. The total energy of the effective Hamiltonian has of course convex curve with positive curvature for the δ dependence as is required for the thermodynamic stability for the spatially uniform phase. However, the local energy proportional to U denoted as E_U shows a concave (negative curvature) curve as is shown in Figs. 9 (c) and (d). Therefore, if we expand it with respect to δ as $E_U = E_0 + a\delta + b\delta^2 + \cdots$, b becomes negative, which immediately means the local attraction because the quadratic coefficient represents the effective carrier interaction. The origin of this emergent local attraction is the following: The

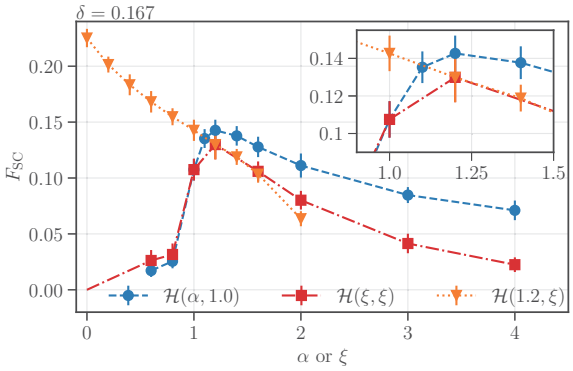

Figure 7: Parameter search of superconducting order parameter $F_{\rm SC}^{\infty}$ in an example starting from *ab initio* parameters of carrier doped $CaCuO_2$ at the hole concentration $\delta = 0.167$. The parameters U and V_n are monitored by scaling U as αU, and all the intersite interactions $V_n, n = 1, \cdots 9$ as ξV_n All the hopping parameters t_n are retained at the *ab initio* values [4]. The case with the monitoring only by α is shown as blue circles, where $F_{\rm SC}^{\infty}$ shows the maximum at $\alpha = 1.2$, with nearly 40 % enhancement from the real hole-doped $CaCuO_2$. On the other hand, if α and ξ are scaled simultaneously, $F_{\rm SC}^{\infty}$ becomes the maximum with 30% enhancement from the *ab initio* value at $\alpha = \xi = 1.2$. The orange upside down triangles show the case by scaling ξ with α fixed at 1.2.

carriers are incoherent and has a large self-energy originally arising from U, while the evolution of the carrier doping makes the carriers rapidly coherent (Fermi-liquid like) and the local repulsive interaction energy is reduced nonlinearly causing the negative b, which can be regarded as the consequence of the release from the Mottness.

3 Electron fractionalization

When the local energy shows such a concave curve, locally bistable energy structure emerges consisting of one stable point in the underdoped side in the left of the concave curve

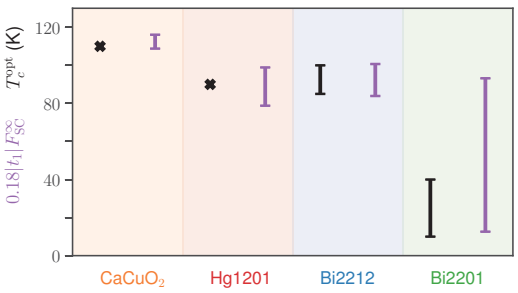

Figure 8: Comparison of experimental $T_c^{\rm opt}$ and the scaling formula $0.16 t_1 F_{\rm SC}^{\infty}$ obtained from the *ab initio* parameter t_1 and the calculated order parameter $F_{\rm SC}^{\infty}$. Purple symbols are the prediction by the scaling from the calculation, while the black symbols are the experimental values [4]. For Bi2201 and Bi2212, the error bars are mainly coming from the experimental uncertainty of crystal structure.

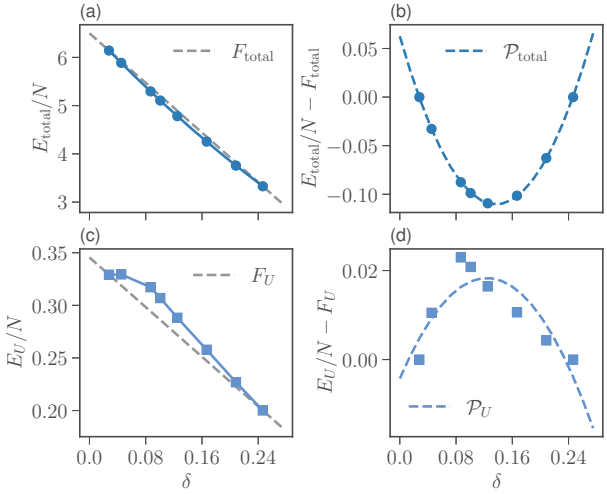

Figure 9: δ dependence of total energy of the effective Hamiltonian of carrier doped $CaCuO_2$, $E_{\rm tot}$ (a,b) and the energy proportional to U denoted as E_u (c,d) [4]。 In (b,d), δ-linear function F is subtracted for better visibility.

and the other in the overdoped side of the concave curve, which may also be interpreted as the tendency toward the local phase separation. If we introduce the creation (annihilation) of fermion operators to represent the excitation around the two stable region as $c^\dagger, (c)$ for the overdoped region and $d^\dagger, (d)$ for the underdoped region, a simplified two-component fermion model (TCFM) becomes emergently relevant in the following form of a phenomenological Hamiltonian:

$$\begin{aligned} H &= \sum_{k,\sigma}[\epsilon_c(k)c^\dagger_{k,\sigma}c_{k,\sigma} + \epsilon_d(k)d^\dagger_{k,\sigma}d_{k,\sigma} \\ &+ \Lambda(k)(c^\dagger_{k,\sigma}d_{k,\sigma} + \text{H.c.})] \\ &+ \sum_{ij}(v_c(r_{ij})n_{ci}n_{cj} \\ &+ v_d(r_{ij})n_{di}n_{dj} + v_{cd}(r_{ij})n_{ci}n_{dj}). \end{aligned} \tag{3}$$

Here, $\epsilon_c(k)$ and $\epsilon_d(k)$ are the dispersions of c fermion and d fermion, respectively and $\Lambda(k)$ is their hybridization amplitude representing quantum tunneling between these fermions. v_c, v_d and v_{cd} are repulsive interactions between two c fermions, between two d fermions and between c and d fermions, respectively. Here, n_c and n_d are the number operators for c and d, respectively. If the effects of v_{cd} dominates over v_c, v_d and Λ, segregation of c and d is favored and charge inhomogeneous states such as stripe states in real space become stable. On the contrary, if the effect of Λ is dominant, c and d hybridize and make the hybridization gap. This gap is nothing but the pseudogap known in the cuprate superconductors. This Hamiltonian is the simplest one to represent the electron fractionalization into two fermions c and d, which is distinct from the earlier proposals of slave boson and slave fermion formalism of fractionalization.

When we introduce the anomalous term $\Delta_c(k)$ and $\Delta_d(k)$ representing the superconducting pairing on the mean-field level, and ignore the interaction between c and d by as-

suming it is small, the TCFM becomes

$$\begin{aligned} H &= \sum_{k,\sigma}[\epsilon_c(k)c^\dagger_{k,\sigma}c_{k,\sigma} + \epsilon_d(k)d^\dagger_{k,\sigma}d_{k,\sigma} \\ &+ \Lambda(k)(c^\dagger_{k,\sigma}d_{k,\sigma} + \text{H.c.}) \\ &+ (\Delta_c(k)c^\dagger_{k,\sigma}c^\dagger_{-k,-\sigma} + \Delta_d(k)d^\dagger_{k,\sigma}d^\dagger_{-k,-\sigma} \\ &+ \text{H.c})], \end{aligned} \tag{4}$$

The Green's function for the c fermion (which can be regarded as the conventional quasiparticle) of the TCFM (4) is given by

$$G_c(k,\omega) = \frac{1}{\omega - \epsilon_c(k) - \Sigma^{\text{nor}}(k,\omega) - W(k,\omega)}. \tag{5}$$

The self-energy contributed from the paired electron and the normal self-energy contributed from the interaction with the normal electrons are

$$W(k,\omega) = \frac{\Sigma^{\text{ano}}(k,\omega)^2}{\omega + \epsilon_c(k) + \Sigma^{\text{nor}}(k,-\omega)^*}, \tag{6}$$

and

$$\Sigma^{\text{nor}}(k,\omega) = \frac{\Lambda(k)^2(\omega + \epsilon_d(k))}{\omega^2 - \epsilon_d(k)^2 - \Delta_d(k)^2}, \tag{7}$$

respectively. Here the anomalous self-energy itself is

$$\Sigma^{\text{ano}}(k,\omega) = \Delta_c(k) + \frac{\Lambda(k)^2\Delta_d(k)}{\omega^2 - \epsilon_d(k)^2 - \Delta_d(k)^2}. \tag{8}$$

In the superconducting state of the TCFM, the normal and anomalous self-energies both have prominent poles (or peaks in the imaginary part) at the same energy $\omega = \pm\sqrt{\epsilon_d(k)^2 + \Delta_d(k)^2}$. However, it was shown that these contributions completely cancel in the total Green' function [14, 15]. Nevertheless, the peak in the anoomalous self-energy is the main origin of the high-T_c superconductivity [14, 16]. Because of the cancellation in the observable Green's function, it has been hidden in the experimental measurements such as ARPES and STM. However, with the help of machie-learning technique, the anomalous and normal contributions were separately extracted from the ARPES data [17] and supported the emergence of the prominet peaks and their cancellations in accordance with the TCFM results [16]. Since the emergence of the peaks accompanied by the cancellation is a unique property of the fractionalized electron, this identification by the machine learning is evidence of the fractionalization.

However, the ARPES data have their own background, noise, and the limitation in the measurable range in the momentum and energy. Therefore, the machine-learning result is not necessarily 100% secured. Therefore, stringent tests by using other independent measurements with different probe are desirable. Recently, the consequence of electron fractionalization on the resonant inelastic X-ray scattering (RIXS) measurement, which can measure the exciton dynamics, was examined. The analysis was made by using TCFM parameters fit by the ARPES data together with the machine learning result. The prediction was that the exciton resonance peak intensity is enhanced in the superconducting phase in comparison to the normal pseudogap phase as one can see in Fig. 10, if the fractionalization is at work [18]. The origin of this enhancement is the increase of the occupied c component below the fermi level in the superconducting phase, because only the c component decays to the core electron and forms an exciton. This prediction was tested experimentally at the NSRRC facility in Taiwan and as in Fig. 11 the exciton peak enhancement in the order of 10% was detected at the optimum doping, where the fractionalization is expected and the normal phase has the pseudogap, in agreement with the prediction, while the enhancement was not observed in the overdoped sample where the fractionalization is not expected [19]. This result further establishes the existence of the electron fractionalization.

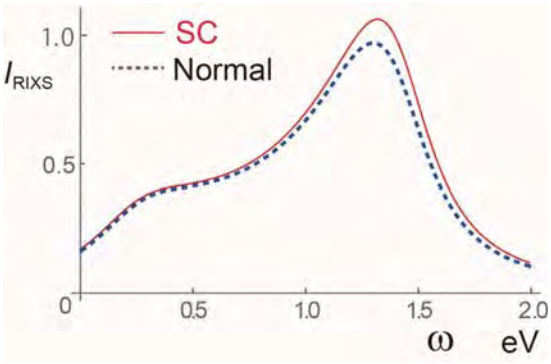

Figure 10: Prediction of the exciton resonance peak in the superconducting phase (red curve) as compared to that in the normal phase (dashed curve) in the presence of the electron fractionalization. The peak is enhanced in the superconducting phase only when the fractionalization is at work [19].

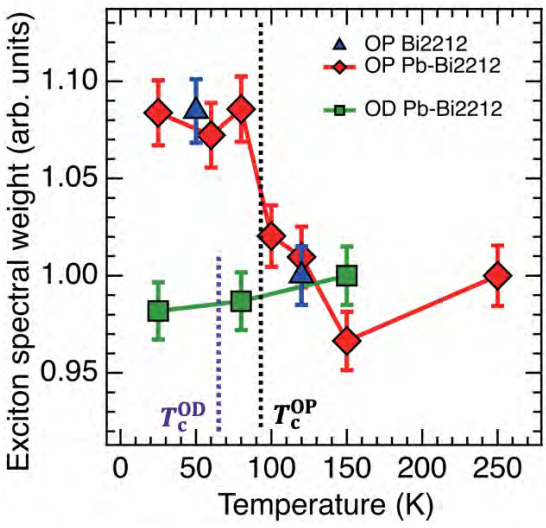

Figure 11: Temperature dependence of the exciton resonance peak measured by RIIXS. The peak is enhanced below T_c only for the sample at the optimum doping (red diamond and blue triangle symbols), where the fractionalization is expected. The intensity does not change in the overdoped sample (green squares), where the fractionalization is not expected [19].

4 Summary and outlook – toward unified understanding of fractionalization for high T_c superconductivity and quantum spin liquid

Another challenge of condensed matter physics is the nature of quantum fluids, especially, the quantum spin liquid since the first proposal half a century ago [24]. It was already shown with the aid of supercomputers that the quantum spin liquid phase indeed exists and the spin excitations are well described by the fractionalized spinions in gapless quantum spin liquids, where the spinon has the Dirac-type gapless excitation and an observable spin excitation is represented by the two composite excitations of the spinon [20,21]. *Ab initio* calculations of molecular solid called dmit salts indeed demonstrated that this picture holds [20]. The existence of the quantum spin liquid was also established in a theoretical touchstone model, J_1-J_2 Heisenberg Hamiltonian on the square lattice, where essentially the same structure of the fractionalized excitation is obtained [21]. These findings were made it possible by the progress in quantum many-body solver using the neural network [25].

The electron fractionalization found in the cuprate superconductors and the fractionalization of an electronic spin into two spinons in the quantum spin liquid look quite different at a glance. However, the essence of the superconducting state as well as the quantum spin liquid lies in the way of constructing quantum mechanically entangled state, the element of which is commonly the paired state of two electrons with further entanglement of the pairs. Figure 12 illustrate a state consisting of the two sites and two electrons with one up and one down electrons, represented by a linear combination of the 4 states, which expand the full Hilbert space composed of the 4 states, with the weight of a_1, a_2 a_3, and a_4. If $a_3 = a_4 = 0$

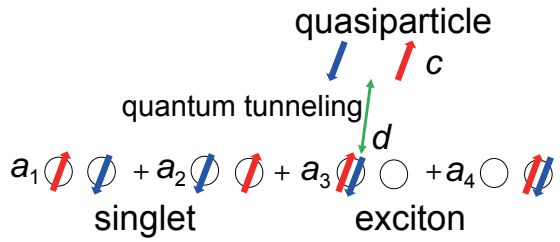

Figure 12: Illustration of the full Hilbert space as a simplified but comprehensive view containing the electron fractionalization in the strong coupling superconductor and the quantum spin liquid in the Mott insulator for two electrons on two sites.

holds in the Mott insulator, the ground state satisfies $a_1 = -a_2$ through the superexchange interaction, which generates the quantum entanglement of the singlet as a component of the quantum spin liquid. On the other hand, if $a_1 = a_2 = 0$ is satisfied, the component with a_3 and a_4 represents the quantum entanglement of an exciton and a dark fermion d as a fermionic component of the exciton emerges due to the Mottness, where d drives the high-T_c superconductivity. In this sense, the quantum spin liquid and high-T_c Cooper pair are connected as the different component of the originally same entanglement. In Fig. 12, the quasiparticle (c fermion) is spatially extended, which appears when the electron is released from the 4 bound states and is distinct from the dark fermion d, while they transform each other by the hybridization, meaning c and d have finite lifetime. In this way, the quantum entanglement by the spin singlet constituting the quantum spin liquid and by the exciton leading to the electron fractionalization are represented in the extended Hilbert space in a unified fashion and the singlet and exciton take on different aspect of the same entanglement.

Ab initio calculations of strongly correlated electron systems needed for quantitative understanding and predictive power had faced with large difficulty for decades. In particular, high-T_c superconductivity and quantum mechanically entangled spin liquid had been major challenging targets. However, MACE scheme has one after another suceeded in reproducing first the superconducting properties of strong coupling superconductors such as the iron-based superconductors [22] and the cuprate superconductors [3, 4, 23]. MACE has also succeeded in reproducing the quantum spin liquid in an *ab initio* fashion [20]. The *ab initio* calculations are crucially important in the sense that the understanding of the universal mechanisms that produces the high-T_c superconductivity and the quantum spin liquids as well as materials design become possible only by understanding material dependence quantitatively based only on the crystal structure. On the other hand, the *ab initio* results obtained after solving by sophisticated quantum many-body solvers are, in a sense, black box outcome and its nature is sometimes not intuitively easily understandable. Therefore, to reveal the underlying physics hidden in the calculated results, simplified phenomenological models which capture the essence are quite useful and also help comparisons with experiments.

Next subject to understand electron fractionalization is to derive phenomenological two-component fermion model microscopically from *ab initio* Hamiltonians. On the other hand, determination of the parameters of TCFM are now being made possible from the fitting to the experimental spectroscopic data [15, 18]. To enhance the accuracy of quantitative estimates and predictability, combined analyses of different spectroscopic tools such as the combination of ARPES, RIXS and quasiparticle interference (QPI) derived from STM data have already started. Integrated spectroscopy combined with the *ab initio* calculations and the machine learning aided by supercomputer facility is the future avenue to be pursuied to attack difficult strongly correlated electron systems.

Acknowledgements

This activity report is based on the collaborations with Michael Schmid, Jean-Baptiste Moree, Youhei Yamaji, Motoaki Hirayama, Yusuke Nomura, Di-Jing Huang, Atsushi Fujimori, Teppei Yoshida, Kota Ido, Takahiro Misawa, and Kazuyoshi Yoshimi. To perform the numerical simulation, computer resources of "Fugaku" (hp190145, hp200132, hp210163, hp220166) under the MEXT project JPMXP1020200104 were utilized. We also thank the facility supported by Supercomputer Center, Institute for Solid State Physics, University of Tokyo. We are also grateful to the financial support of JSPS Kakenhi Grant No. 16H06345, No. 22A202 ("Foundation of Machine Learning Physics ") and No, 22H05114 ("Frontiers of Condensed Matter Physics Pioneered by Neural Network").

References

[1] M. Imada, and T. Miyake: J. Phys. Soc. Jpn. **79** (2010) 112001.

[2] F. Aryasetiawan, M. Imada, A. Georges, G. Kotliar, S. Biermann, and A.I. Lichtenstein: Phys. Rev. B **70** (2004) 195104.

[3] J.-B. Morèe, M. Hirayama, M. T. Schmid, Y. Yamaji, and M. Imada: Phys. Rev. B **106**, (2022) 235150.

[4] M. T. Schmid, J.-B. Morèe, Y. Yamaji, and M. Imada: unpublished.

[5] M. Hirayama, T. Miyake and M. Imada: Phys. Rev. B **87** (2013) 195144.

[6] M. Hirayama, T. Miyake, M. Imada, and S. Biermann: Phys. Rev. B. **96** (2017) 075102.

[7] M. Hirayama, Y. Yamaji, T. Misawa, and M. Imada: Phys. Rev. B **98** (2018) 134501.

[8] M. Hirayama, T. Misawa, T. Ohgoe, Y. Yamaji, M. Imada: Phys. Rev. B **99** (2019) 245155.

[9] D. Tahara and M. Imada: J. Phys. Soc. Jpn. **77** (2008) 114701.

[10] T. Misawa, S. Morita, K. Yoshimi, M. Kawamura, Y. Motoyama, K. Ido, T. Ohgoe, M. Imada, T. Kato: Comput. Phys. Commun. **235**, (2019) 447.

[11] K. Tanaka, W. S. Lee, D. H. Lu, A. Fujimor, T. Fujii, Risdiana, I. Terasaki, D. J. Scalapino, T. P. Devereaux, Z. Hussain, and Z.-X. Shen: Science **314**, (2006) 1910.

[12] J. Alldredge, J. Lee, K. McElroy, M. Wang, K. Fujita, Y. Kohsaka, C. Taylor, H. Eisaki, S. Uchida, P. Hirschfeld, and J. Davis: Nat. Phys. **4**, (2008) 319.

[13] Y. J. Uemura, G. M. Luke, B. J. Sternlieb, J. H. Brewer, J. F. Carolan, W. N. Hardy, R. Kadono, J. R. Kempton, R. F. Kiefl, S. R. Kreitzman, P. Mulhern, T. M. Riseman, D. L. Williams, B. X. Yang, S. Uchida, H. Takagi, J. Gopalakrishnan, A. W. Sleight, M. A. Subramanian, C. L. Chien, M. Z. Cieplak, G. Xiao, V. Y. Lee, B. W. Statt, C. E. Stronach, W. J. Kossler, and X. H. Yu, Phys. Rev. Lett. **62**, (1989) 2317.

[14] S. Sakai, M. Civelli, and M. Imada: Phys. Rev. Lett. 116 (2016) 057003; Phys. Rev. B. **94** (2016) 115130.

[15] M. Imada: J. Phys. Soc. Jpn. **90** (2021) 111009.

[16] Y. Yamaji, T. Yoshida, A. Fujimori, M. Imada: Phys. Rev. Research **3** (2021) 043099.

[17] T. Kondo, Y. Hamaya, A. D. Palczewski, T. Takeuchi, J. Wen, Z. Xu, G. Gu, J. Schmalian, and A. Kaminski, Nat. Phys. **7** (2011) 21.

[18] M. Imada: J. Phys. Soc. Jpn. **90** (2021) 074702.

[19] A. Singh, H. Y. Huang, J. D. Xie, J. Okamoto, C. T. Chen, T. Watanabe, A. Fujimori, M. Imada, D. J. Huang: Nat. Commun. **13** (2022) 7906.

[20] K. Ido, K. Yoshimi, T. Misawa, and M. Imada: npj Quantum Mater. **7** (2022) 48.

[21] Y. Nomura and M. Imada: Phys. Rev. X **11** (2021) 031034.

[22] T. Misawa and M. Imada: Nat. Commun. **5** (2014) 5738.

[23] T. Ohgoe, M. Hirayama, T. Misawa, K. Ido, Y. Yamaji, M. Imada Phys. Rev. B **101**, 045124 (2020).

[24] P. Fazekas and P. W. Anderson: Phil. Mag. **30** (1974) 423.

[25] Y. Nomura, A. S. Darmawan, Y. Yamaji and M. Imada: Phys. Rev. B **96** (2017) 205152.

Molecular Dynamics Study of Ultra-Long Chain Fatty Acid in Lipid Bilayer

Kazutomo KAWAGUCHI[1], and Hiroshi NOGUCHI[2]
[1]*Institute of Science and Engineering, Kanazawa University*
Kanazawa, Ishikawa 920-1192
[2]*Institute for Solid State Physics, University of Tokyo*
Kashiwa-no-ha, Kashiwa, Chiba 277-8581

Abstract

Although ultra-long-chain fatty acids (ULCFAs) exist in biomembranes in certain types of tissues, their biological roles remain unknown. In this report, we review our recent study on the molecular conformation of ULCFAs in lipid bilayers using molecular dynamics simulations. Their long chains exhibit characteristic fluctuations between elongated, L-shaped, and turned conformations. The ratios of these conformations are changed in response to the lipid-density differences between upper and lower leaflets. This response is faster than the flip–flop of cholesterols.

1 Introduction

Biological membranes consist of various types of lipids and proteins [1]. Phospholipids are the most abundant lipids in biological membranes and have a polar head group and two hydrocarbon tails (fatty acids). Phospholipids are biosynthesized by a combination of a polar head group and two hydrocarbon tails and have a range of structural and functional roles in biological cells [2, 3]. Each tail typically contains between 14 and 22 carbon atoms. Fatty acids containing more than 22 carbons are called very-long-chain fatty acids (VLCFAs). Moreover, much longer chains containing more than 32 carbons were found at the sn-1 position of phosphatidylcholine (PC) in photoreceptors, fibroblasts, and keratinocytes [4, 5, 6]. These fatty acids are called ultra-long-chain fatty acids (ULCFAs). It is considered that ULCFAs are stored as a precursor of bioactive lipid mediators [7] and derivatives of C32:6 and C34:6 are neuroprotective in retina [8]. However, the physicochemical properties of ULCFAs with respect to their structures and the biological roles of ULCFA-containing phospholipids are still unclear.

Molecular simulations have been widely applied to study lipid membranes [9, 10, 11, 12, 13]. All-atom molecular dynamics (MD) simulations for VLCFAs, in which the tail length of the sn-1 chain is maximally 24, have also been performed by a few groups [14, 15, 16, 17, 18]. It has been shown that the long hydrocarbon chain is slightly interdigitated into the opposite leaflet [14, 16, 17]. However, ULCFAs had not been simulated yet. To examine the effects of ultra-long chains, we have conducted all-atom MD simulations for ULCFAs [19, 20]. Our study revealed that the longer chains of ULCFAs have more strongly interacted with the opposite leaflet than those of VLCFAs. The ultra-long sn-1 chain of ULCFAs takes elongated, L-shaped, and turned conformations in lipid bilayers and that these conformational change can reduce the lipid-density difference between upper and lower leaflets.

Three types of ULCFAs are used in this

study. The chain length and number of unsaturated bonds are varied. Lipid molecules composing Host bilayer membranes consist of single or two types of phospholipids. Moreover, cholesterols (CHOLs) are embedded in the bilayer membrane to examine the effect of the flip–flop of cholesterols.

2 Methods

2.1 ULCFAs

The molecular structures of ULCFAs used in this study are shown in Fig. 1. Dotriacontahexaenoic acid containing phosphatidylcholine (dTSPC, C32:6-C18:0), which has an ultra-long chain of 32 carbons with six double bonds at the sn-1 position [Fig. 1(a)]. Hexacosatetraenoic acid containing phosphatidylcholine (HSPC, C26:4-C18:0), which has a very-long chain of 26 carbons with four double bonds at the sn-1 position [Fig. 1(b)]. Lacceroic acid containing phosphatidylcholine (LSPC, C32:0-C18:0), which has an ultra-long chain of 32 carbons with no double bonds at the sn-1 position [Fig. 1(c)]. All of the ULCFAs have a stearoyl chain at the sn-2 position. HSPC is constructed by truncating the long hydrocarbon chain of dTSPC at C26, and LSPC is constructed by the saturation of the long hydrocarbon chain of dTSPC. A single ULCFA molecule (dTSPC, HSPC, or LSPC) was inserted into the lipid bilayers described in the next section.

2.2 Lipid Bilayer

The molecular structures of lipids composing bilayer membranes are shown in Fig. 2. Distearoyl phosphatidylcholine (DSPC, C18:0-C18:0) contains two saturated stearoyl chains. Stearoyl-DHA phosphatidylcholine (SDPC, C18:0-C22:6) contains a steroyl chain and a docosahexaenoyl chain with six double bonds at the sn-1 and sn-2 positions, respectively. Stearoyl-oleoyl phosphatidylcholine

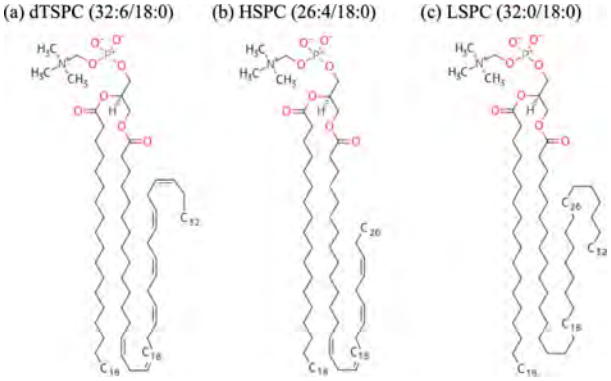

Figure 1: Molecular structures of ULCFAs. (a) dTSPC (C32:6-C18:0), (b) HSPC (C26:4-C18:0), and (c) LSPC (C32:0-C18:0).

(SOPC, C18:0-C18:1) contains a steroyl chain and an oleoyl chain with a double bond at the sn-1 and sn-2 positions, respectively.

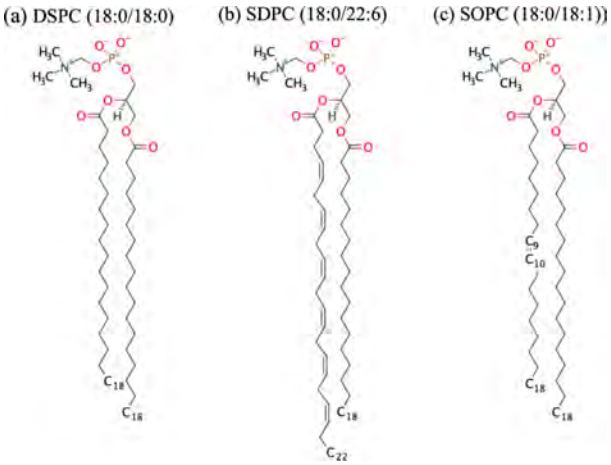

Figure 2: Molecular structures of lipids composing bilayer membranes. (a) DSPC (C18:0-C18:0), (b) SDPC (C18:0-C22:6), and (c) SOPC (C18:0-C18:1).

We considered three types of host lipid bilayers for embedding a single ULCFA molecule: (1) single-component bilayers. (2) asymmetric-component bilayers, in which each leaflet is composed of a single type of phospholipids. (3) two-component bilayers composed of a single type of phospholipids and cholesterols.

(1) DSPC, SDPC, and SOPC were used for single-component host bilayers and dTSPC was used as ULCFA. A membrane bilayer consisting of 100 lipid molecules per leaflet was prepared for each membrane system. The membrane was connected by its periodic images in the xy plane under the periodic boundary conditions. A single lipid molecule in the upper leaflet was replaced by a single dTSPC molecule for each single-component bilayer, in order to examine the influence of the difference between upper and lower leaflets on the long sn-1 chain of dTSPC (see Table 1). Ten lipid molecules in the upper (lower) leaflet were removed in the '189u' ('189l') system. Four lipid molecules in the upper (lower) leaflet were removed in the '195u' ('195l') system. Two lipid molecules in the upper (lower) leaflet were removed in the '197u' ('197l') system. Labels 189, 195, and 197 represent the total number of the host lipid molecules. The number of water molecules per lipid was fixed at 50 in all cases. The lipids do not flip–flop to the opposite leaflets on a simulation time scale (the flip–flop time is typically hours or days [21]). The difference of the lipid numbers between the two leaflets results in the deviation of the lipid density from a stable value even under zero surface tension, as described by an area-difference-elasticity model [22, 23]. Thus, the lipids in the leaflet with higher density are more compressed, although a flat membrane connected by the periodic boundary does not bend because of the symmetry. The DSPC/dTSPC and SDPC/dTSPC mixtures were equilibrated for 200 ns, which was followed by 800-ns production runs at 343 K. to avoid the gel phase of DSPC and SDPC. The SOPC/dTSPC mixtures were equilibrated for 400 ns, which was followed by 1.6 μs-production runs at 303 K.

Table 1: Numbers of phospholipids in single-component host bilayers. A single dTSPC molecule was embedded.

Model	Upper leaflet	Lower leaflet
DS189u	89 DSPCs	100 DSPCs
DS189l	99 DSPCs	90 DSPCs
DS197u	97 DSPCs	100 DSPCs
DS197l	99 DSPCs	98 DSPCs
SD189u	89 SDPCs	100 SDPCs
SD189l	99 SDPCs	90 SDPCs
SD197u	97 SDPCs	100 SDPCs
SD197l	99 SDPCs	98 SDPCs
SO189u	89 SOPCs	100 SOPCs
SO189l	99 SOPCs	90 SOPCs
SO195u	95 SOPCs	100 SOPCs
SO195l	99 SOPCs	96 SOPCs
SO197u	97 SOPCs	100 SOPCs
SO197l	99 SOPCs	98 SOPCs

Table 2: Numbers of phospholipids in asymmetric-component host bilayer membranes. Three types of ULCFAs were embedded in the bilayers.

Membrane	Upper leaflet	Lower leaflet
DS89-SD100	89 DSPCs	100 SDPCs
DS99-SD90	99 DSPCs	90 SDPCs
DS99-SD98	99 DSPCs	98 SDPCs
SD89-DS100	89 SDPCs	100 DSPCs
SD99-DS90	99 SDPCs	90 DSPCs
SD99-DS98	99 SDPCs	98 DSPCs

(2) A DSPC/SDPC mixture asymmetric bilayer was used as a host lipid bilayer. We prepared six types of host lipid bilayers with different numbers of lipids, as shown in Table 2. A single ULCFA molecule was inserted into the upper leaflet. The system temperature was controlled at 343 K to avoid the gel phase of DSPC and SDPC. The membranes were equilibrated for 200 ns, followed by 800 ns production runs.

(3) We added cholesterols to both the upper and lower leaflets of the bilayer to investigate the effects of cholesterols on the conformation of the ULCFAs. DSPC and SDPC were used as the host lipid molecules. The number of host lipid molecules is 89 in the upper leaflet, and 100 in the lower leaflet. In the initial state, 20 or 40 cholesterols are added in both upper

Table 3: Numbers of lipids in bilayers containing cholesterols. A single dTSPC molecule was embedded.

Membrane	Upper leaflet	Lower leaflet
DS/CHOL20	89 + 20	100 + 20
DS/CHOL40	89 + 40	100 + 40
SD/CHOL20	89 + 20	100 + 20
SD/CHOL40	89 + 40	100 + 40

and lower leaflets, as listed in Table 3. The system temperature was controlled at 343 K to avoid the gel phase of DSPC and SDPC. The DS/CHOL and SD/CHOL mixtures were equilibrated for 1 μs and 3 μs, respectively.

2.3 MD Simulations

The system pressure of all simulations was controlled at 0.101 MPa. The CHARMM 36 force field [24] and TIP3P water model [25] were used to represent lipid and water molecules, respectively. All MD simulations were performed using GROMACS [26].

To calculate the lipid area in the tensionless membranes, we performed MD simulations for a pure symmetric membrane consisting of 100 DSPCs or 100 SDPCs per leaflet. From these MD simulations, we obtained that the area per lipid of DSPC and SDPC are 0.63 and 0.74 nm^2, respectively. Thus, SDPCs have a slightly larger area than DSPCs because of their unsaturated bonds.

3 Results and Discussion

3.1 Conformation of the sn-1 chain of ULCFAs

Figure 3 shows three types of conformations of the sn-1 chain of dTSPC embedded in SD189u bilayer. A turned conformation, in which the C_3-C_{18}-C_{32} angle in the sn-1 chain is approximately 0° is shown in Fig. 3(a). The terminal carbon atom (C_{32}) is located in the upper leaflet. An L-shaped conformation, in which the angle is approximately 90°, is shown in Fig. 3(b). The C_{32} atom is located at the boundary of the two leaflets. An elongated conformation, in which the angle is approximately 180°, is shown in Fig. 3(c). The C_{32} is located in the lower leaflet. The sn-1 chain temporally fluctuates among these conformations. That is, it moves between the upper and lower leaflets and also lies along with the interface between the two leaflets. This conformational fluctuation is rapid, and the transit time between two leaflets is $\sim$ 10 ns. This large conformational fluctuation has not been observed in the other lipids and is specific to ULCFAs. In particular, the elongated conformation penetrates deeply into the opposite leaflet.

These three types of conformations were also observed for dTSPC, HSPC, and LSPC embedded in asymmetric membranes (case 2) under all simulated conditions. Three types of conformations of dTSPC, HSPC, and LSPC are shown in Fig. 4(a), (b), and (c), respectively. The long chain of LSPC is more elongated than that of dTSPC owing to the saturated bonds of the chain.

3.2 Distribution of atoms

The distribution of atoms in the sn-1 chain of ULCFA in a lipid bilayer was calculated along the z-axis, which is parallel to the bilayer normal. The origin of the z-axis is set at the center of the lipid bilayer. Figure 5 shows the probability distribution of C_3, C_{18}, and C_{32} atoms of the sn-1 chain of dTSPC and phosphate (P) atoms of DSPC, SDPC, and SOPC in single-component bilayers (case 1). The terminal carbon C_{32} of the sn-1 chain is widely distributed from z of -2 to 2 nm, corresponding with the conformation fluctuations observed in the snapshots. The free-energy difference $F(z)$ between two conformations were calculated using $F(z) = -k_{\mathrm{B}}T\ln(p(z))$. The estimated value was less than $1.2k_{\mathrm{B}}T$ from $p(z)$ of C_{32}, indicating no apparent free-energy barrier among them.

The distributions of P in DS189u, SD189u,

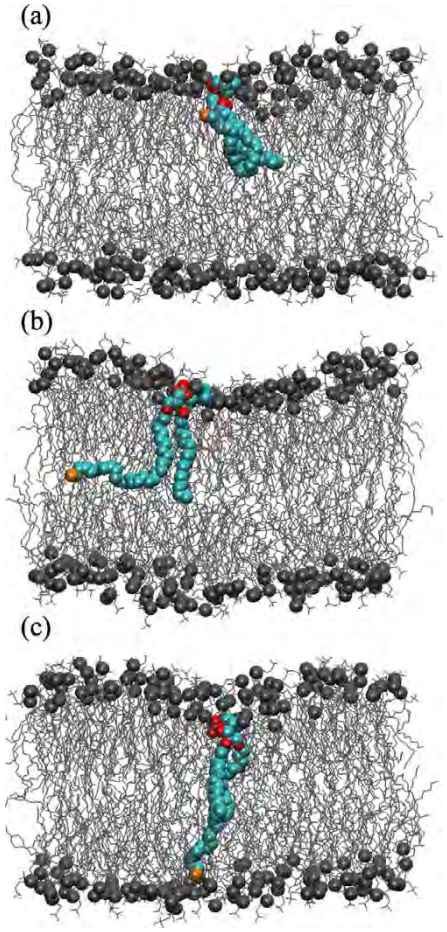

Figure 3: Snapshots of dTSPC in DS189l membrane. (a) Turned conformation. (b) L-shaped conformation. (c) Elongated conformation. dTSPC are represented by colored spheres. Host lipid molecules are shown in gray (spheres represent the phosphate atoms). Water molecules are not shown for clarity.

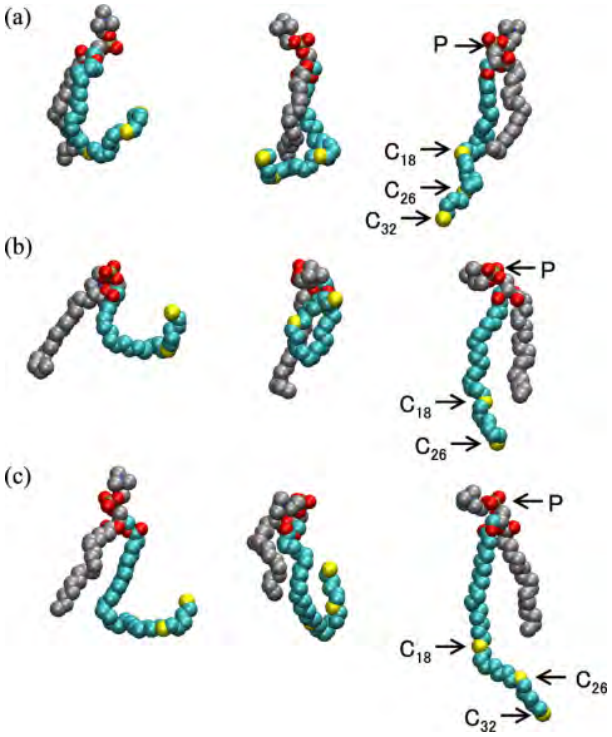

Figure 4: Snapshots of (a) dTSPC, (b) HSPC, and (c) LSPC embedded in lipid bilayers (DS89-SD100). Carbon atoms in the sn-1 chain are shown in cyan and other carbon atoms are shown in gray. Hydrogen atoms are not shown for clarity. Reproduced from Ref. [20].

and SO198u were similar to those in DS189l, SD189l, and SO198l, respectively. as shown in Fig. 5. These results indicate that the membrane thickness does not depend on the lipid-density difference between the two leaflets. Thus, the host lipid bilayer structure is not significantly modified in the examined range of the density difference.

In contrast, the distribution of carbon atoms in the sn-1 chain of dTSPC depends on the lipid-density difference between the two leaflets. As the lipid density relatively decreases in the lower leaflet, the distribution of C_{32} largely shifts toward the lower leaflet. The peak position of C_{18} shifts toward the lower leaflet as observed in C_{32}, but the shift magnitude is smaller. The distribution of C_3 shifts slightly toward the lower leaflet as the lipid density relatively decreases in the lower leaflet. Thus, the longer region ($C_{18} \sim C_{32}$) of the sn-1 chain exhibits larger changes arising from the lipid-density difference between the two leaflets.

To quantitatively investigate the effects of the lipid-density differences on the conformation of the sn-1 chain, we calculated the mean z-position of the C atoms normalized by the mean z-position the P atoms as a function of the lipid density ratio. The lipid density ratio

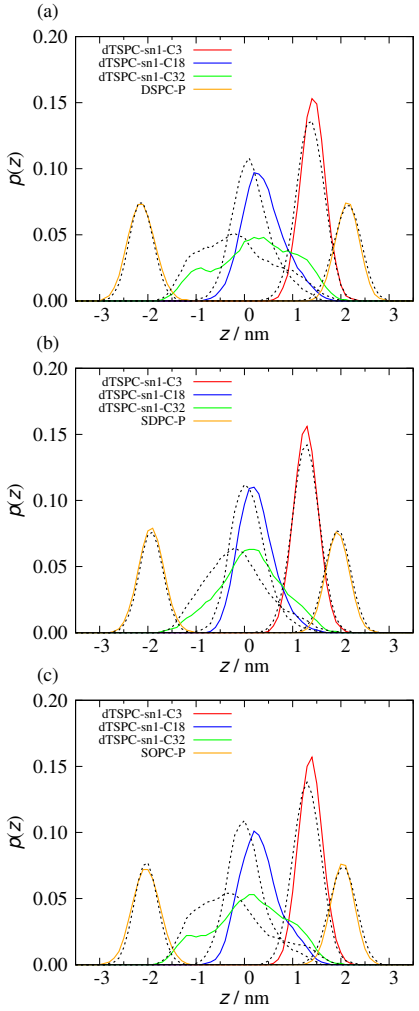

Figure 5: Probability distribution of atoms in (a) DS189u/l, (b) SD189u/l, and (c) SO189u/l systems. The solid and dotted lines represent the probability distributions in 'u' and 'l', respectively. Reproduced from Ref. [19].

is defined as $N_{\rm l}S_{\rm l}/N_{\rm u}S_{\rm u}$, where $N_{\rm l}$ and $N_{\rm u}$ are the numbers of host lipid molecules in the lower and upper leaflets, respectively. $S_{\rm l}$ and $S_{\rm u}$ represent the area per lipid of DSPC or SDPC in the lower and upper leaflets, respectively, obtained from the MD simulations for a pure symmetric membrane.

Figure 6 shows the correlation between the normalized z-position ($z_{\rm C}/z_{\rm P}$) and the lipid density ratio $N_{\rm l}S_{\rm l}/N_{\rm u}S_{\rm u}$ for dTSPC in the DSPC/SDPC asymmetric bilayer (case 2). A positive linear correlation was found between the normalized z-positions of carbon atoms and the lipid density ratio.

From the least-squares fitting (represented by dashed lines), we found that the value of $z_{\rm C}/z_{\rm P}$ was almost 0 for C_{32} at $N_{\rm l}S_{\rm l}/N_{\rm u}S_{\rm u} = 1$. Thus, the terminal carbon is located in the middle of the lipid bilayer in the absence of lipid-density difference and moves to the upper (lower) leaflet as the lipid density of the upper (lower) leaflet decreases. Therefore, the conformational change of the sn-1 chain in dTSPC reduces the lipid-density differences.

In the cases of HSPC and LSPC, we found similar behavior. The ratio of the elongated conformation increases as the lipid density of the opposite leaflet decreases. The position the terminal atom C_{26} of HSPC is almost identical to that of C_{26} in dTSPC. The sn-1 chain of LSPC is more deeply in the lower leaflet than that of dTSPC. We concluded that the reduction of the lipid-density differences between the two leaflets by the change in the ultra-long sn-1 chain conformation is a general property of ULCFAs.

3.3 Order parameters

We calculated the lipid order parameters, $S_{\rm CD}$, using the following equation:

$$S_{\rm CD} = \langle \frac{3\cos^2\alpha - 1}{2} \rangle, \qquad (1)$$

where α is the angle between C-H bond vector and the bilayer normal. The brackets indicate the average over time and lipid molecules. Calculated order parameter profiles, $-S_{\rm CD}$, for ULCFAs embedded in the DS89-SD100 bilayer are shown in Fig. 7. These profiles were not sensitive to lipid-density differences. The order profiles of the sn-1 chain decreased to 0 at C_{15} and exhibited a low order in the longer region until the terminal. The order of the sn-2 chain was similar to that of the sn-2 chain in DSPC, because the sn-2 chain in ULCFAs are equivalent to the sn-2 chain in DSPC. In the case of HSPC, the order profile of the sn-1

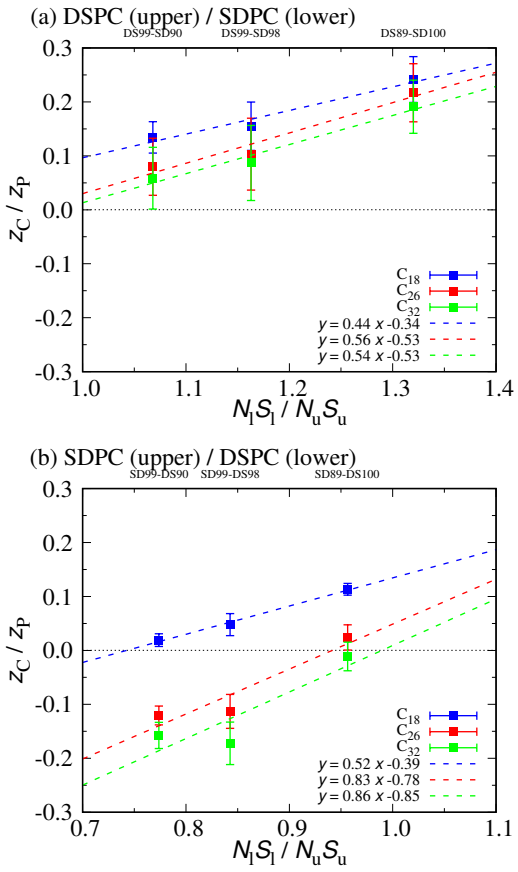

Figure 6: Correlation between normalized z-position of C atoms and lipid-density ratio for dTSPC. Reproduced from Ref. [20].

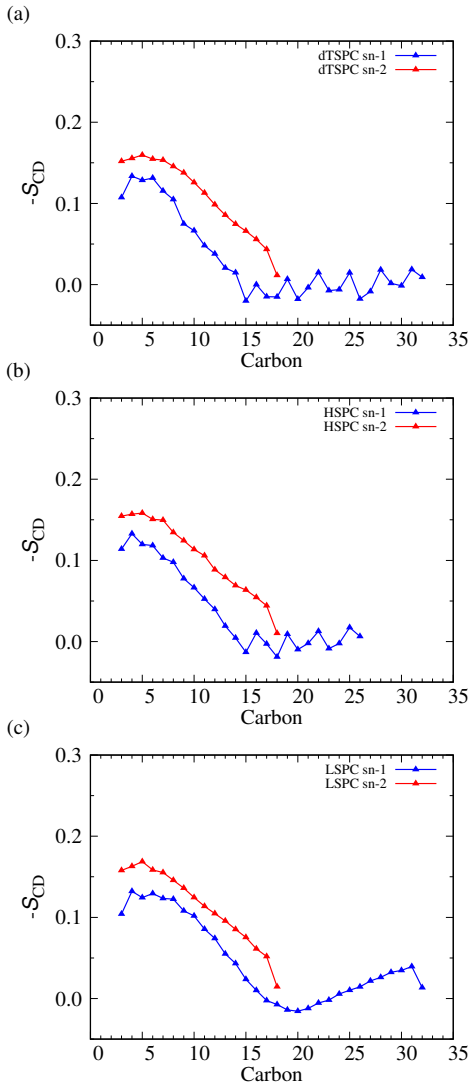

Figure 7: Order parameter profiles, $-S_{CD}$, of (a) dTSPC, (b) HSPC, and (c) LSPC for DS89-SD100. Reproduced from Ref. [20].

chain exhibited a similar profile to that in dTSPC, because the sn-1 chain in HSPC is equivalent to the sn-1 chain until C_{26} in dTSPC. In contrast, the order profile of LSPC becomes higher toward the terminal, because the sn-1 chain of the LSPC has no double bonds. It is indicated that the saturated long chain takes a more elongated conformation than unsaturated long chains.

3.4 dTSPC with Cholesterols

We analyzed the interactions between dTSPC and cholesterols in asymmetric bilayers. Cholesterol molecules were embedded in the asymmetric bilayers with number fractions of 20 % or 40 %, as shown in Table 3. In the initial state of each simulation, the cholesterol fraction in the upper leaflet ($N_{\mathrm{upper}}/N_{\mathrm{total}}$) was set to 0.5.

In the case of the DSPC bilayers, the cholesterol fraction is almost constant (0.5) during 1 μs, showing that the flip–flop time of cholesterols is much longer than 1 μs. On the other hand, in the case of the SDPC bilayers, the fraction frequently changed during 3 μs, showing that the lipid-density difference between the two leaflets was reduced by cholesterols. The flip–flop times per cholesterol molecule were 0.52 and 0.66 μs for SD/CHOL20 and

SD/CHOL40, respectively. These values of flip–flop time are much faster than those of phospholipids (hours or days) but slower than those of ULCFAs. A similar time scale of the cholesterol flip–flop was previously reported in the MD simulations of other lipid compositions [27, 28, 29]. After the cholesterol flip–flop, the conformation distribution of ULCFAs becomes close to that in the absence of the area difference in the two leaflets. Therefore, the area difference is responded by ULCFAs first and later by cholesterols. ULCFAs is a rapid sensor of the area difference.

4 Summary

In this report, we have shown the conformational change of ULCFAs in single-component and asymmetric bilayer membranes using MD simulations. The ultra-long sn-1 chain largely fluctuates between upper and lower leaflets and takes elongated, L-shaped, and turned conformations. ULCFAs can rapidly reduce the lipid-density differences between the two leaflets via the ratio change of these conformations.

References

[1] G. van Meer, D. R. Voelker, and G. W. Feigenson, Nature Rev. Mol. Cell Biol. **9**, 112 (2008).

[2] H. Shindou and T. Shimizu, J. Biol. Chem. **287**, 1 (2009).

[3] B. Anthony, S. Vanni, H. Shindou, and T. Ferreira, Trends Cell Biol. **25**, 427 (2015).

[4] J. P. SanGiovanni and E. Y. Chew, Prog. Retin. Eye Res. **24**, 87 (2005).

[5] A. McMahon and W. Kedzierski, Br. J. Ophthalmol. 1127 (2009).

[6] P. Barabas, A. Liu, W. Xing, C. Chen, Z. Tong, C. B. Watt, B. W. Jones, P. Bernstein, and D. Križaj, Proc. Natl. Acad. Sci. USA **110**, 5181 (2013).

[7] B. Jun, P. K. Mukherjee, A. Asatryan, M. A. Kautzmann, J. Heap, W. C. Gordon, S. Bhattacharjee, R. Yang, N. A. Petasis, N. G. Bazan, Sci. Rep. **7**, 5279 (2017).

[8] F. Deák, R. E. Anderson, J. L. Fessler, D. M. Sherry, Front Cell Neurosci. **13**, 428 (2019).

[9] M. Müller, K. Katsov, and M. Schick, Phys. Rep. **434**, 113 (2006).

[10] M. Venturoli, M. M. Sperotto, M. Kranenburg, and B. Smit, Phys. Rep. **437**, 1 (2006).

[11] H. Noguchi, J. Phys. Soc. Jpn. **78**, 041007 (2009).

[12] R. M. Venable, F. L. H. Brown, and R. W.Pastor, Chem. Phys. Lipids **192**, 60 (2015).

[13] S. J. Marrink, V. Corradi, P. C. T. Souza, H. I. Ingólfsson, D. P. Tieleman and M. S.P. Sansom, Chem. Rev. **119**, 6184 (2019).

[14] A. P. Ramos, P. Lagë, G. Lamoureux, and Michel Lafleur, J. Phys. Chem. B **120**, 6951 (2016).

[15] R. Gupta, B. S. Dwadasi, and B. Rai, J. Phys. Chem. B **120**, 12536 (2016).

[16] T. Róg, A. Orłowski, A. Llorente, T. Skotland, T. Sylvänne, D. Kauhanen, K. Ekroos, K. Sandvig, and I. Vattulainen, Biochim. Biophys. Acta **1858**, 281 (2016).

[17] M. Manna, M. Javanainen, H. M. Monne, H. Gabius, T. Rog, and I. Vattulainen, Biochim. Biophys. Acta **1859**, 870 (2017).

[18] E. Wang and J. B. Klauda, J. Phys. Chem. B **122**, 2757 (2018).

[19] K. Kawaguchi, K. M. Nakagawa, S. Nakagawa, H. Shindou, H. Nagao, and H. Noguchi, J. Chem. Phys. **153**, 165101 (2020).

[20] K. Kawaguchi, H. Nagao, H. Shindou, and H. Noguchi, J. Phys. Chem. B **126**, 9316 (2022).

[21] R. D. Kornberg and H. M. McConnell, Biochemistry **10**, 1111 (1971).

[22] U. Seifert, Adv. Phys. **46**, 13 (1997).

[23] S. Svetina and B. Žekš, Adv. Colloid Interface Sci. **208**, 189 (2014).

[24] J. B. Klauda, I. M. Venable, J. A. Freites, J. W. O'Connor, D. J. Tobias, C. Mondragon-Ramirez, I. Vorobyov, A. D. MacKerell Jr., and R. W. Pastor, J. Phys. Chem. B **114**, 7830 (2010).

[25] A. D. MacKerell Jr. and P. W. Pastor, J. Phys. Chem. B **102**, 3586 (2010).

[26] M. J. Abraham, T. Murtola, R. Schulz, S. Páll, J. C. Smith, B. Hess, and E. Lindahl, SoftwareX **1**, 19 (2015).

[27] S. Jo, H. Rui, J. B. Lim, J. B. Klauda, and W. Im, J. Phys. Chem. B **114**, 13342 (2010).

[28] F. Ogushi, R. Ishitsuka, T. Kobayashi, and Y. Sugita, Chem. Phys. Lett. **522**, 96 (2012).

[29] R. Gu, S. Baoukina, and D. P. Tieleman, J. Chem. Theory Comput. **15**, 2064 (2019).

3.2 First-Principles Calculation of Material Properties

Theoretical study on dynamical processes in heterogeneous catalysis using density functional theory and machine learning methods

H. H. HALIM, T. N. PHAM,Y.-L. WANG, T. OTA, S. E. M. PUTRA
Y. HAMAMOTO, K. INAGAKI, I. HAMADA, and Y. MORIKAWA
Department of Precision Engineering, Graduate School of Engineering, Osaka University, 2-1 Yamadaoka Suita, Osaka 565-0871

In 2022-2023, we carried out theoretical investigation of chemical processes at surfaces and interfaces, Cu-Zn surface alloy formation on Cu(997), Hydrogenation of formate species using atomic hydrogen on a Cu(111) model catalyst, oxygen vacancy migration in $SrFeO_{3-\delta}$ and $Sr_3Fe_2O_{7-\delta}$, NO-H2O coadsorption on Cu(111), and activity and selectivity of N_2 fixation on B doped g-C_9N_{10}.

In this report, we report Cu-Zn surface alloy formation on Cu(997)[1]. The catalysts based on metal-alloys are well recognized in the field of heterogenous catalysis considering the emerging of unique properties upon alloying. Given the optimal composition and environment, these catalysts can offer high catalytic performance that outperform their alloy constituents. There have been notorious examples on the application of metal-alloy based catalysts in heterogenous catalysis. In the present study, we focus on Cu-Zn surface alloy which has been reported to be very active for methanol synthesis by hydrogenation of CO_2. Experimental studies have shown that the deposition of Zn on Cu(111) promotes the activity of methanol production by an order of magnitude at Zn coverage of 0.197. In addition, the Cu-Zn alloy has been reported as a good model of $Cu/ZnO/Al_2O_3$ (CZA), the industrial catalyst used to synthesize methanol by hydrogenation of CO_2. Thus, this alloy has been extensively involved in the investigation of the true active site of CZA which remains under controversy.

Recently, it was reported that by coupling Molecular Dynamics (MD), active-learning, and automated event detection, Lim et al. have successfully reveal the restructuring mechanisms of Pd deposited on Ag. By adopting similar methodologies, we performed MD simulation of Zn depositions on Cu(997) surface to explicitly capture the mechanisms that are responsible to the Cu-Zn surface alloying. The MD simulations were implemented based on force-field that was trained by means of Gaussian Process (GP). The database, containing information of atomic forces acting on various environments, were obtained from DFT calculations. The task of training was done by using Fast Learning of Atomistic Rare Events (FLARE) code which utilizes the uncertainty information from GP, together with active on-the-fly learning scheme to build the force-field efficiently.

We used DFT calculations to provide forces of the central atom on each atomic environment. All DFT calculations were performed using the STATE code. The electron-ion interaction was described by ultrasoft pseudopotentials. We took into account the van der Waals (vdW) interactions by applying optB86b-vdW exchange correlation functional as implemented in the STATE code.

To construct GP force-field, we used FLARE

code with two- and three-body multispecies kernels. The interaction cutoffs for two- and three-body kernels are set to 7.0 Å and 4.5 Å, respectively. The hyperparameters embedded to these kernels, namely two-body signal variances (σ_2), two-body length scale (l_2), three-body signal variances (σ_3), three-body length scale (l_3), and noise hyperparameter (σ_n) was optimized by maximizing the log marginal likelihood using BFGS algorithm as implemented in SciPy used inside the FLARE code. The database is constructed by employing active and on-the-fly learning scheme that update the database based on uncertainty information calculated by GP. In order to provide new atomic environments to be candidate for the database, MD code internal to FLARE is used to evolve atomic structures with 1 fs timestep within canonical (NVT) ensemble. The temperature is set up at 700 K with all atoms are allowed to move. To obtain more diverse atomic environments, we manually changed the initial structure after certain MD steps during the on-the-fly learning when no significance improvement in the Mean Absolute Error (MAE) was found. The details of this procedure and the resulting database are reported in the next section.

To observe the alloying process of Cu-Zn, we performed MD simulations within NVT ensemble at temperature 700 K for up to 6.25 μs. Figure 1 shows the evolution of deposited Zn atoms on Cu(997) until the Cu-Zn surface alloy is formed. To clearly observed the number of Zn atoms that substituted at the terrace, we also plotted the composition of Cu and Zn atoms as a function of rows for every certain timesteps. Such plots accompany each MD snapshots in Figure 1. The snapshots of the MD simulation are also presented as video in the Supporting Information. In the beginning (Figure 6a), the Zn atoms are found to localize at the step edge, covering the original Cu step adatoms. The profile of boundary between Cu and Zn is still fairly linear. After 1.25 μs, some of the Zn atoms are incorporated

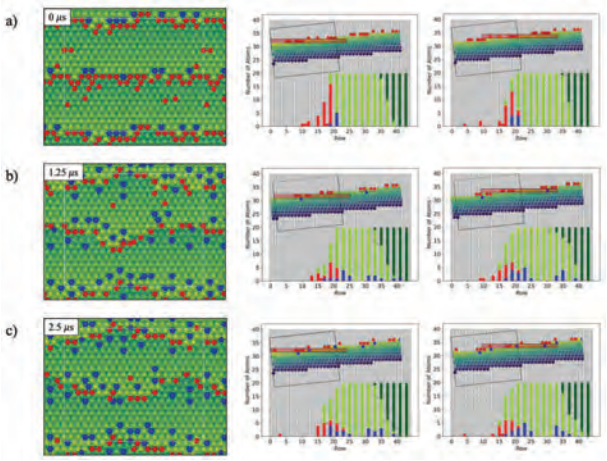

Figure 1: The snapshots of MD simulations showing the evolution of deposited Zn atoms on Cu(997). The green to yellow atom indicates the Cu atom, the red atom indicates Zn as adatom, and blue atom indicates substituted Zn atom. The two plots accompanied each snapshot show the composition of atom as a function of row. In each plot, the red, blue, light green, and dark green bars indicate the number of Zn as adatom, Zn as incorporated atom, Cu as surface atom, and Cu atom which is covered by additional Cu or Zn layer.

at the upper and lower terrace near the step edge (Figure 1b). At this stage, almost no Zn atoms are incorporated at the middle terrace. We also noticed Zn atoms are dominantly incorporated to the upper terrace whereas only few incorporated Zn atoms found at the lower terrace. After 2.5 μs (Figure 1c), the distribution of the Zn on the surface and the number of incorporated Zn atom are still relatively similar.

References

[1] Harry Handoko Halim and Yoshitada Morikawa: ACS Physical Chemistry Au **2**, 430-447 (2022).

Prediction of Material Properties using Density Functional Theory

Osamu Sugino

Institute for Solid State Physics,

The University of Tokyo, Kashiwa-no-ha, Kashiwa, Chiba 277-8581

We have studied properties of cuprate superconductors and zirconia cathode materials using the SCAN and PBE exchange-correlation (xc) functionals, respectively, of the density functional theory (DFT). Our DFT calculations of cuprates reproduced lattice properties and electronic band structures consistent with available experimental data and predicted properties of layered ones [1]. Our calculated free energy landscape for the oxygen reduction reaction occurring on the zirconia surface suggested that a high reactivity appears not only when doped with nitrogen atoms and oxygen vacancies also in the pristine conditions. It is therefore possible that the role of defects may be increase of the carrier conductivity rather than enhancement of the reactivity [2].

We have used for the electronic structure calculations the packages VASP and Quantum Espresso implemented in the ISSP supercomputers. We have used for modeling the defective zirconia the abICS package developed by S. Kasamatsu [3].

The accuracy of the xc functionals is essential in providing reliable prediction of material properties. We tried to improve the accuracy using a machine learning method. We used the accurate electronic structures of small molecules provided by a quantum chemical calculation together with the theoretically derived properties of the xc functionals [4]. Those different data of molecules and theory are found to play a complementary role in increasing the accuracy and numerical stability of the functional as demonstrated by calculation of various crystals.

References

[1] A. N. Tatan, et al., AIP Advances 12, 105308 (2022).

[2] S. Muhammady, et al., J. Phys. Chem. C 126, 15662 (2022).

[3] https://www.pasums.issp.u-tokyo.ac.jp/abics

[4] R. Nagai et al., Phys. Rev. Research 4, 013106 (2022); Electron. Struct. 1, 37-38 (2022).

Clarification of Microscopic Mechanisms of Semiconductor Epitaxial Growth and Device-Interface Formation by Large-Scale Quantum-Theory-Based Computations

Atsushi Oshiyama

Institute of Materials and Systems for Sustainability, Nagoya University

Furo-cho, Chikusa-ku, Nagoya 464-8601

In the fiscal year of 2022, on the basis of the total-energy electronic-structure calculations and molecular dynamics simulations within the density-functional theory (DFT), we have studied the epitaxial growth of wide-gap semiconductors and graphene sheets, atomic and electronic structures of semiconductor surfaces and their interfaces with insulators. The main computational tools are our RSDFT (Real Space DFT) code and RS-CPMD (Car-Parrinello Molecular Dynamics) code as well as VASP code. Specifically, we have studied 1) the atom-scale mechanism of GaN epitaxial growth [1,2], 2) the mechanism of graphene growth on SiC surfaces [3], 3) atomic and electronic structures of stepped SiC surfaces [4] and GaN/AlSiO interfaces [5], and 5) the role of point defects in SiN which have been speculated to be the principal element of current flash memories. The below is the explanation of the issues 2) and 5) above.

Initial stage of graphene formation on SiC(0001) Surfaces

Graphene has a consolidated background as an innovative two-dimensional (2D) material because of the peculiar electronic and mechanical properties. Several methods have been proposed to produce graphene sheets. Among them, an emerging technology consists in the thermal decomposition of silicon carbide (SiC). The major advantage of this technique is the possibility of growing graphene directly on a semiconducting substrate, thus avoiding the difficult step of extracting and transferring graphene sheets on a substrate. From a scientific standpoint, the formation of graphene from a SiC crystal, possibly

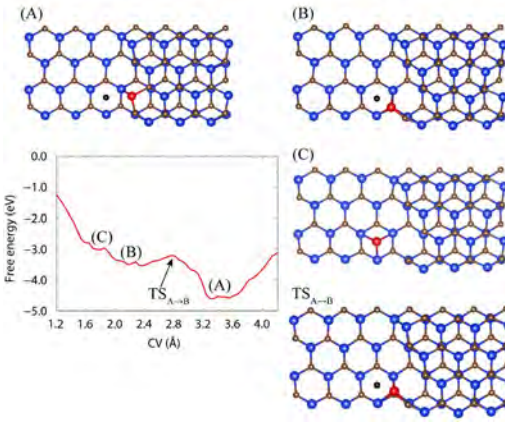

Fig. 1: Free-energy profile of Si desorption from the step edge and major relevant configurations. The color code for the atoms is blue for Si and brown for C. The collective variable (CV) used in the meta-dynamics is the distance between a desorbing Si (red sphere) and the center of mass (black sphere) of the lower terrace site formed by three C atoms.

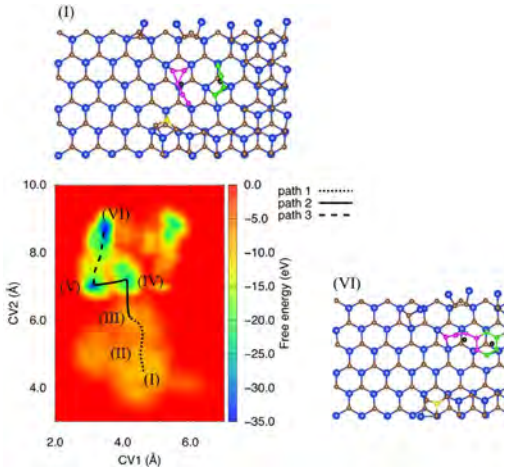

Fig. 2: Free-energy landscape (the bottom-left) and minimum free-energy reaction pathway (path1 + path2 + path3: the dotted, solid and dashed lines) for the clustering of carbon atoms. The labels from (I) to (VI) in the landscape indicate the positions of the (meta) stable configurations along the pathway. The stable configurations (I) and (VI) are shown in the top-left and the bottom-right, respectively. In (I), C5 and C4 clusters are highlighted with magenta and green spheres, respectively. Those clusters become a single cluster C9 in the final configuration (VI). The CV1 is the distance between the COM of C5 (left black sphere) and COM of C4 (right black sphere) and the CV2 is the distance between the COM of C5 and a C atom (yellow sphere).

accompanied by a selective removal of Si atoms and subsequent condensation of C atoms, is still an unexplored issue.

Based on the first principles molecular dynamics empowered by free energy sampling methods, we have clarified atomistic processes of the initial stage of graphene formation on SiC(0001). Our simulations have shown that the desorption of a Si atom from a step edge and its subsequent migration to a stable site on the nearby terrace is an endothermic reaction (Fig. 1). Yet, this step is an essential initial trigger to the process that eventually will lead to the formation of a graphene sheet. We have found that a subsequent Si desorption leaves behind under-coordinated C atoms and this, in turn, triggers the formation of three stable C-C bonds via an exothermic reaction. This second step paves the route to the formation of larger carbon structure at the SiC(0001) surface. Following the guidelines that these simulations indicate, we focused on the processes occurring upon desorption of several Si atoms. We have clarified how small C clusters formed at the exposed surface can merge into a larger structure presenting a C6 ring, the expected seed of a graphene-like conformation (Fig. 2). The extension of this carbon bond network realized in this way is accompanied by a remarkable energy gain, leading to an exothermic reaction and to a stable carbon structure precursor of an actual graphene flake.

Nitrogen Vacancy in Silicon Nitride: Emergence of Floating Gap States

Silicon nitride（SiN）thin films are fabricated near interfaces of Si-MOS structures, and utilized as memory elements in non-volatile flash memories which sustain our energy-saving society. The microscopic mechanism of the memory function is unknown, however. We have performed DFT calculations with hybrid approximation to the exchange-correlation functional and clarified the atomic and electronic structures of nitrogen vacancy (V_N) in SiN. The results indicate that the floating electron state inherent to host SiN is localized near V_N and induce a gap state which is free from energy

barriers upon electron capture and emission, thus being a strong candidate for the memory unit.

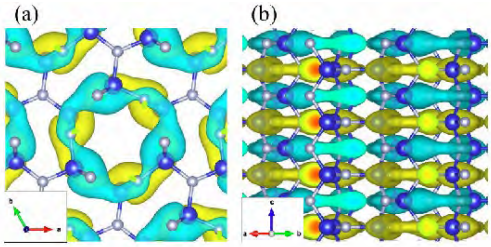

Fig. 3: KS orbital of the CBB of β-Si_3N_4 viewed from *c* axis (a) and from its perpendicular direction (b). The isovalue surface of the KS orbital is shown by the yellow (+) and bluegreen (-) blobs. The blue and gray balls depict Si and N atoms, respectively.

Figure 3 shows the Kohn-Sham (KS) orbital of the conduction-band bottom (CBB) of SiN (its crystalline form β-Si_3N_4). The orbital is distributed not near atomic sites but in the internal space, showing the *floating* character. We have found from the DFT calculations that the floating state is ubiquitous in various sparse materials such as carbon nanomaterials and even in typical tetrahedral-symmetry semiconductors [Matsushita, Oshiyama: PRL 2012, 2014, Nano Lett. 2017].

When a single N atom is removed from SiN (i.e., V_N), the nearest neighbor three Si atoms lose their partner, inducing 3 Si dangling bonds (DBs). These DB states are linear combined and induce a totally symmetric state in the valence band and remaining two states in the gap. Depending on the position of the Fermi level in the gap, V_N changes its charge state from +1 to -3, showing interesting competition between the Jahn-Teller splitting and the exchange splitting.

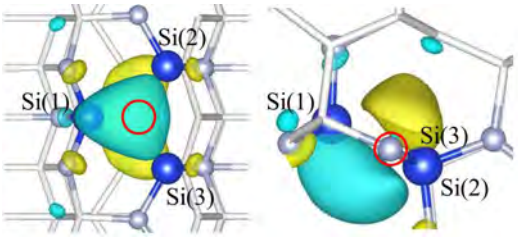

Fig. 4: KS orbital of localized the floating state in the gap of SiN. Isovalue surface of the orbital from (a) a perpendicular and (b) a parallel directions to a plane consisting of 3 neighbor Si atoms.

More interestingly, the floating state near CBB (Fig. 3) capture additional electrons and localized near V_N (Fig. 4). This is due to the ionicity of SiN: The N atom in SiN is an anion so that V_N is effectively positive, thus attracting electrons. This generates additional gap states, making V_N multiply charged. The floating state localized in the N-deficit region may be responsible for the memory function.

The group id codes for the achievements above are k0042 and m0037.

Related publications

[1] M. Boero, K. M. Bui, K. Shiraishi, K. Ishisone, Y. Kangawaa, and A. Oshiyama, Appl. Surf. Sci. **599**, 153935 (2022).
[2] K. M. Bui, K. Shiraishi and A. Oshiyama, Appl. Surf. Sci. **613**, 155840 (2023).
[3] M. Boero, F. Imoto and A. Oshiyama, Phys. Rev. Materials **6**, 093403 (2022).
[4] T. Kimura, K. Chokawa, K. Shiraishi, and A. Oshiyama, Phys. Rev. B **106**, 035309 (2022).
[5] K. Chokawa, K. Shiraishi and A. Oshiyama, J. Appl. Phys **133**, 065301 (2023).
[6] F. Nanataki, K. Shiraishi, J.-I. Iwata, Y.-i. Matsushita, and A. Oshiyama, Phys. Rev. B **106**, 155201 (2022)

Understanding structure-property relationships of disordered materials using first-principles based high-throughput simulation framework

Shusuke KASAMATSU

Academic Assembly (Faculty of Science),

Yamagata University, Kojirakawa, Yamagata-shi, Yamagata 990-8560

Characterizing the order within disorder of atomic arrangements in materials is imperative for predicting, understanding, and designing a wide variety of materials functionalities such as electronic, ionic, and thermal conductivity/insulation and catalytic activity. Recently, we have been focusing on developing methods to perform sufficient statistical thermodynamics sampling in disordered systems, and we have also started to consider how to analyze such huge amounts of data to extract meaningful structure-property relationships.

For sampling of disordered crystalline systems, we had already introduced our abICS (ab Initio Configuration Sampling) framework for deriving an on-lattice neural network model from first-principles calculations in past Activity Reports [1]. This year, we benchmarked its performance on calculating temperature-dependent disorder in the cation sublattice of three spinel oxides. The efficiency of the approach in an active-learning setting was demonstrated clearly against random sampling, and issues such as accuracy degradation vs. lattice relaxation and the ability to learn energetics for varying compositions were discussed [2].

As a first application to an unsolved materials science problem, abICS was used to understand the hydration behavior of heavily Sc-doped $BaZrO_3$, known as a promising perovskite proton conductor for solid oxide fuel cells. Although this class of materials has been known as a good proton conductor for 40 years, the local structure that activates the hydration reaction, which is the key reaction to introduce protons into the system, remained unknown. Using abICS, we simulated the ratio of Sc-V_O-Sc, Sc-V_O-Zr, and Zr-V_O-Zr that contribute to hydration under experimental thermodynamic conditions. We also obtained a machine-learning model for lattice volumes and predicted doping and hydration-dependent lattice constants in excellent agreement with experiment. Careful comparison with *in situ* XAS and thermogravimetry measurements lead to the conclusion that Sc-V_O-Sc and Sc-V_O-Zr are the active sites for hydration [3].

In the case of liquid and amorphous systems, we have been relying on available software for neural network potential training such as

Simple-NN [4]. Training a reliable model for liquid and amorphous systems up to two components is now relatively easy to achieve, and for such systems, we have now started to consider how to understand the order within disorder. Towards this end, we have been examining the applicability of topological data analysis [5], which characterizes the structure in terms of the size and shapes of rings and cavities. Figure 1 shows the temperature-dependent first order persistence diagram for liquid and amorphous $ZnCl_2$, where each dot corresponds to a ring of Zn atoms; the "birth" axis corresponds to the bond distance for forming the rings, and the "death axis" roughly corresponds to the roundness of the rings. A clear change is seen in the ring distribution vs. temperature, suggesting that we can characterize the subtle difference between liquid and amorphous $ZnCl_2$ in terms of the intermediate-range order, which may be related to the exponential decay in viscosity at the glass transition.

References

[1] S. Kasamatsu, ISSP Supercomputer Center Activity Report 2020, pp. 16-26.

[2] S. Kasamatsu et al., J. Chem. Phys. **157**, 104114 (2022).

[3] K. Hoshino, S. Kasamatsu, et al., Chem. Mater. **35**, 2289-2301 (2023).

[4] K. Lee et al., Comp. Phys. Comm. **242**, 95 (2019).

[5] I. Obayashi et al., J. Phys. Soc. Jpn., **91**, 091013 (2022).

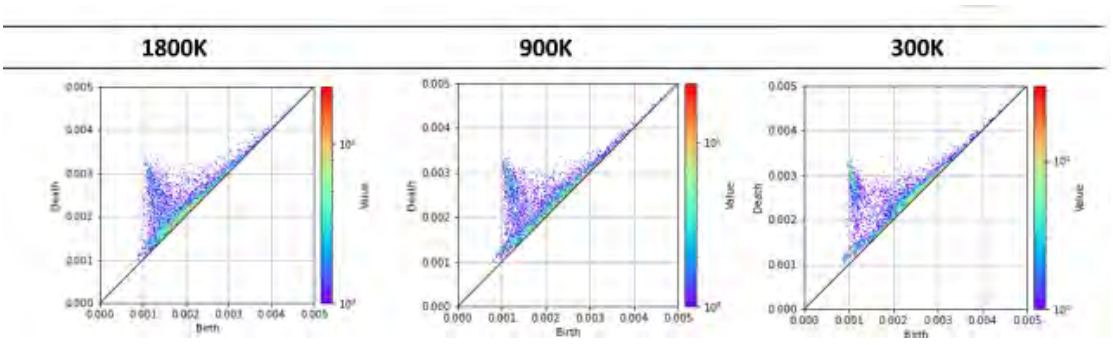

Fig. 1: First order persistence diagrams of liquid and amorphous $ZnCl_2$.

Development of first-principles calculation code RSPACE and design of highly functional interface

Tomoya ONO
Graduate School of Engineering, Kobe University
Rokkodai-cho, Nada, Kobe 657-8501

4H-silicon carbide (4H-SiC) is an IV-IV type semiconductor with a wide band gap of 3.2 eV, and the 4H-SiC based metal-oxide-semiconductor field-effect transistor (MOSFET) is expected to be used in next generation switching devices operating at high power and high frequency applications. However, the potential of 4H-SiC has not been fully utilized owing to the low on current of MOSFETs, which is caused by defects at the 4H-SiC/SiO_2 interface. The post-oxidation annealing process using N_2O, NO, or N_2 gas has been proposed to reduce the density of interface defects and increase the on current. In our previous study, we investigated the total energies and electronic structures of the nitride layers by density functional theory (DFT) calculation using the surface models, where the 4H-SiC/SiO_2 interfaces are modeled by the OH terminated surfaces. However, the surface models do not include the effect of the SiO_2 networks on the interface atomic structure. In this project of 2022, we employ the models containing the SiO_2 layers on the SiC substrate.

Figure 1 shows our computational models, where the surface of the 4H-SiC substrate is terminated with the SiO_2 layer and the other side of the substrate is terminated with H atoms. The rectangular supercells of 10.1 Å × 5.3 Å × 26.3 Å for the *a*-face model, 10.1 Å × 6.2 Å × 27.3 Å for the *m*-face model, and 18.5 Å × 5.3 Å × 26.8 Å for the Si-face model were employed. The *z*-axis was taken to be the direction perpendicular to the surface. We considered the modification incorporating four Si vacancies (V_{Si}s) and 16 N atoms at C sites (N_Cs). The cases in which V_{Si}s were arranged parallel to the surface were investigated to evaluate the anisotropy of the formation energy of the nitride layer. In our model, the areal N-atom density was on the order of 10^{14} cm^{-1}, which is consistent with the experimental results. Although there are two inequivalent lattice sites of 4H-SiC, i.e., *h* (hexagonal) and *k* (quasi-cubic) sites, our previous studies have shown that nitride layers tend to grow at the *k* site. Thus, we consider the cases in which V_{Si}s are arranged at the *k* site. We also investigated the interfaces with the nitride layer at the second layer for all the faces. For the first-principles calculation, we used the RSPACE code[1, 2], which is based on the real-space finite-difference approach within the frameworks of density functional theory (DFT) and is developed in this project. We employed the local density approximation of the DFT to describe the exchange and correlation effects. Electron-ion interactions were approximated by the projector-augmented wave method. The structural optimization was performed until the residual forces are smaller than 0.001 Hartree/Bohr radius.

The formation energy of the above interaction for generating one V_{Si} to insert a nitride layer was obtained as

$$E_{\rm form} = E_{\rm total}^{(\rm w/\ mod)}/4 + E(SiO_2) + 4\mu_{CO} + 2\mu_N - E_{\rm total}^{(\rm w/o\ mod)}/4 - 6\mu_{NO}, \quad (1)$$

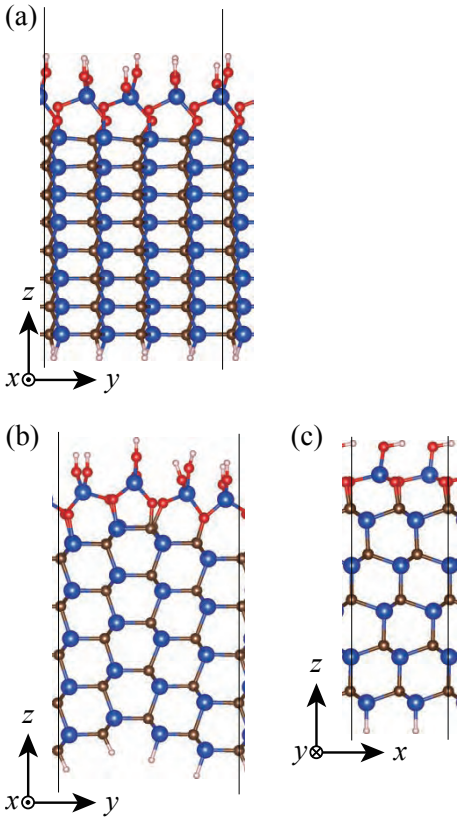

Figure 1: Interface atomic structures with CO bonds for (a) a-, (b) m-, and (c) C-face models before N-atom incorporation. Blue, brown, red, and gray spheres are Si, C, O, and H atoms, respectively. Black lines are the boundaries of the supercell.

where $E(SiO_2)$ is the total energy of a SiO_2 unit in a bulk of quartz SiO_2. $E_{\rm total}^{(\rm w/o\ mod)}$ and $E_{\rm total}^{(\rm w/\ mod)}$ represent the total energies of the interface without and with N-atom incorporation, respectively. In addition, $\mu_{\rm NO}$, $\mu_{\rm CO}$, and $\mu_{\rm N}$ are the chemical potentials of a NO molecule, a CO molecule, and N atoms in a N_2 molecule, respectively. We set the temperature at 1000 K and the partial pressure of NO gas ($p_{\rm NO}$) at 1 atm. The partial pressures of CO ($p_{\rm CO}$) and N_2 (p_{N_2}) gases were set at 10^{-5} atm and 0.25×10^{-5} atm.

The formation energies of the nitride layers are shown in Fig. 2. All the reactions are exothermic and the nitride layers growing along the a face are the most stable among

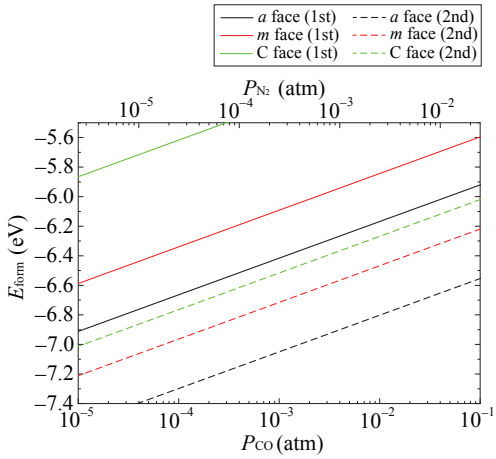

Figure 2: Formation energies $E_{\rm form}$ defined Eq. (1) for interface with CO bonds with respect to partial pressures of CO and N_2. Reprinted from Ref. 3.

those along the a, m, and Si faces. The formation energy of the nitride layer at the topmost layer is smaller than that at the second layer, resulting in the localization of the N atoms at the interface. Note that the NO annealing generates the nitride layers immediately below the SiO_2 layers without any transition layers. It was found that the effect from the SiO_2 layer on the interface atomic structure after the NO annealing and our conclusions derived by the surface models do not change when the SiO_2 layers are attached to the substrates.

References

[1] T. Ono and K. Hirose, Phys. Rev. Lett. **82**, 5016 (1999).

[2] K. Hirose, T. Ono, Y. Fujimoto, and S. Tsukamoto, *First Principles Calculations in Real-Space Formalism, Electronic Configurations and Transport Properties of Nanostructures* (Imperial College, London, 2005).

[3] N. Komatsu, M. Ohmoto, M. Uemoto, and T. Ono, J. Appl. Phys. **132**, 155701 (2022).

First-Principles Study on Carrier Mobility of SiC_6 Nanoribbons

Yoshiyuki EGAMI
Division of Applied Physics, Faculty of Engineering, Hokkaido University
Kita 13, Nishi 8, Kita-ku, Sapporo, Hokkaido 060-8628

In recent years, as semiconductor electronic devices have become smaller, a remarkable reduction in carrier mobility due to the thinning of silicon channels has become an important issue. Therefore, two-dimensional materials that can maintain high carrier mobility even with thin films have been attracting attention. A typical 2-dimensional material, graphene, has a carrier mobility of about 100 times that of silicon, and is therefore expected to become a post-silicon material. However, since the energy band gap of graphene is zero, it is difficult to apply it to semiconductor devices. So, several studies have been performed to open the gap. Among them, this work focuses on siligraphene, in which graphene is doped with silicon atoms. In particular, it is shown that SiC_6 siligraphene has a negative Poisson's ratio and a unique property that the carrier mobility changes significantly with strain. On the other hand, the carrier mobility of SiC_6 nanoribbons fabricated by cutting SiC_6 siligraphene as a channel material has not yet been clarified.

In this work, the carrier mobility of SiC_6 nanoribbon considering acoustic phonon scattering at room temperature is evaluated using the effective mass, elastic modulus, and deformation potential obtained by first-principles calculations [1]. As a result, the electron mobility of SiC_6 nanoribbons is significantly lower than that of SiC_6 siligraphene, but the hole mobility is sufficiently improved to be applied to n-type transistor materials. For future work, it is necessary to investigate the dependence of carrier mobility on the width and edge structure of the nanoribbon.

Ballistic electron transport properties in SiC_6 nanoribbons connected to semi-infinite electrodes consisting of graphene are also evaluated [1, 2]. There are two types of conduction channels: in the 1st channel, the scattering wave function is extended throughout the system via the delocalized π orbitals of carbon atoms (Fig. 1(a)), resulting in a conduction channel with high transmission. On the other hand, in the 2nd channel, the scattering wave propagates via states consisting of sp^3 orbitals of silicon atoms, but most of the wave is reflected at nanoribbon region (Fig. 1(b)) and the transmission is quite small.

This work has been performed on System B of the Supercomputer Center, the Institute for Solid State Physics, the University of Tokyo.

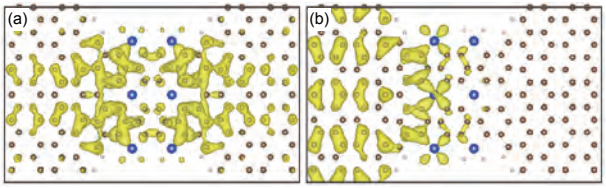

Figure 1: Charge density distribhutions of scattering wave functions.

References

[1] K. Hirose *et al.*: First-principles calculations in real-space formalism (Imperial College Press, 2005).

[2] Y. Egami, S. Tsukamoto and T. Ono: Phys. Rev. Res. **3**, 013038 (2021).

Analyses related to atomic structures and atom dynamics at complex structures such as surfaces, interfaces and defects

Satoshi WATANABE
Department of Materials Engineering, the University of Tokyo
7-3-1 Hongo, Bunkyo-ku, Tokyo, 113-8656

1 Introduction

To deepen our understanding on atomic arrangements and dynamics in/at complex structures such as surfaces, interfaces and defects is crucial for further development of novel information and energy devices. We have been tackling this issue using various simulation methods including multi-scale or machine-learning approaches. In the following, two of our results in fiscal year 2022 are described.

2 Defect structures in WS_2 thin films

Investigations on WS_2 aiming at electronic devices have been active recently. However, the performance of prototype devices were much lower than expected because of structural defects in fabricated WS_2 thin films. We examined [1] defect structures of WS_2 thin films using the high-dimiensional neural network potential (HDNNP). We successfully generated HDNNP with the root mean square error of energy from density functional theory (DFT) calculation of about 6 meV/atom. Molecular dynamics (MD) simulations using the HDNNP and WS_2 slab models reveal that S vacancies introduced in the slab are transformed into structures consisting of 5-memberd and 9-membered rings or other structures including rings different from 6-membered one spontaneously.

3 Electrical conductivity and Seebeck coefficient of organic semiconductors

Organic semiconductors have attracted much attention recently as thermoelectric materials. However, their power generation efficency is still insufficient for practical applications. We developed [2] a realistic evaluation method of the electrical conductivity and Seebeck coefficient of organic semiconductors using electronic structure calculations based on DFT. In our method, many structures were obtained using MD simulations with an empirical force field to consider thermal fluctuation in a crystal explicitly. The Seebeck coefficient and carrier mobility were obtained from the average of the density states and transfer integrals between adjacent moleculres calculated for each structure, respectively. We applied our scheme to pentacene and rubrene. Our results agree well with experimental data.

References

[1] R. Otsuka, K. Shimizu, H. Wakabayashi, S. Watanabe: 70th JPSJ Spring Meeting 2023, 16p-B414-7 (in Japanese).

[2] M. Ohno, K. Shimizu, and S. Watanabe: Appl. Phys. Express **16** (2023) 011005.

Theoretical study of point defects in visible-light-driven semiconductor photocatalysts using first-principles calculations

Seiichiro L. TEN-NO
Graduate School of System Informatics, Kobe University
Rokkodai-Cho, Nada-Ku, Kobe 657-8501

Point Defect in Layered Perovskite Photocatalyst $Y_2Ti_2O_5S_2$

Layered perovskite $Y_2Ti_2O_5S_2$ (YTOS) is a strong candidate for semiconductor photocatalysts for overall water splitting under visible light. Although YTOS has a band gap sutable for absorption of visible light and valence/conduction band positions useful for overall water splitting, structural defects during synthesis should be controlled to promote photocatalytic performance [1, 2, 3].

We have investigated the point defects and electronic structures using first-principles calculations based on the density functional theory (DFT). The DFT calculations were performed within the PBE+U (Perdew–Burke–Ernzerhof functional with Hubbard U correction) functional using the projector augmented wave (PAW) method, as implemented in the Vienna ab initio simulation package (VASP).

We have evaluated the formation energy of anion vacancies $E_{\rm form}$ using the chemical potentials $\Delta\mu_i$ relative to bulk precipitate. $\Delta\mu_i$ were determined by the phase diagram of the relevant compounds in the synthesis of YTOS. Fig. 1(a) shows the phase diagrams as functions of $\Delta\mu_{\rm Ti}$ and $\Delta\mu_{\rm Y}$ for S-rich conditions, in which YTOS is stable within the area of the ABC triangle. In Fig. 1(b), $E_{\rm form}$ of V_S, V_{O_c}, and $V_{O_{ab}}$ for S-rich conditions is shown as a function of the Fermi level $E_{\rm F}$ measured from the valence band maximum $E_{\rm V}$. The evaluation of $E_{\rm form}$ suggests that the S-defect (O-defect) is easy to form when $E_{\rm F}$ is near the valence (conduction) band.

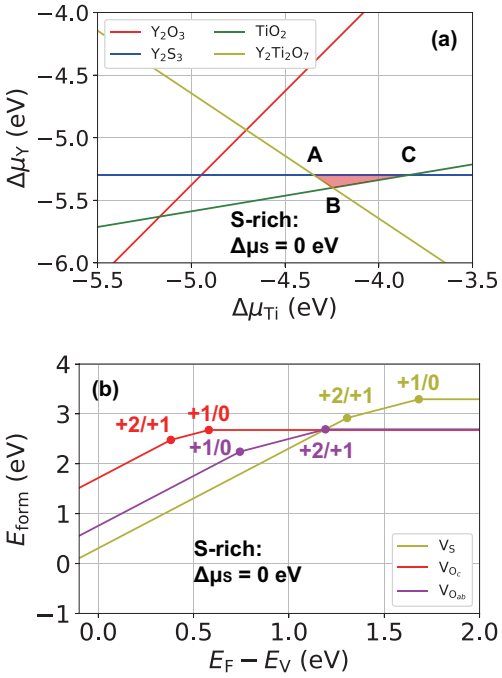

Figure 1: (a) Quaternary phase diagram of YTOS with respect to $\Delta\mu_{\rm Ti}$ and $\Delta\mu_{\rm Y}$ for S-rich conditions. (b) Formation energy of anion vacancies $E_{\rm form}$ against $E_{\rm F} - E_{\rm V}$.

Chemical Doping in Perovskite Photocatalyst $SrTiO_3$

Perovskite $SrTiO_3$ (STO) is a typical semiconductor photocatalyst for overall water split-

ting under ultraviolet. According to the recent experiment [5], it is observed that Al-doped STO can enable a quantum efficiency of almost unity at wavelengths between 350 and 360 nm.

To explore more efficient dopants for higher-performance photocatalysts, we have studied the dopant effects on the electronic structures of STO using the first-principles analysis. The DFT calculations were performed within the PBE+U functional using PAW method as implemented in VASP. We treated the supercell models including one V_O and two X_{Ti} (one Mg_{Ti}) with X being B, Al, Ga, In, Tl, Sc.

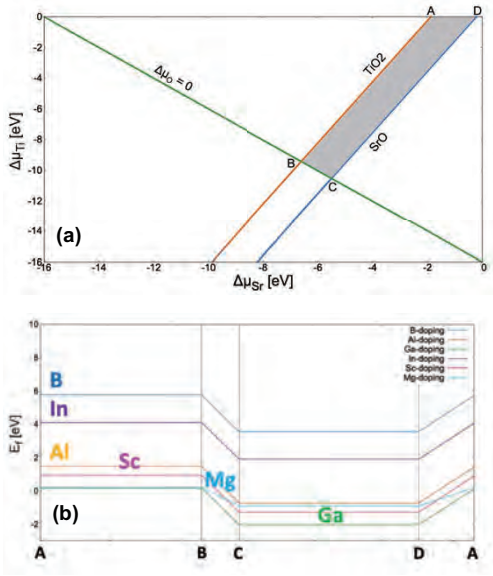

Figure 2: (a) Ternary phase diagram of STO with respect to $\Delta\mu_{Sr}$ and $\Delta\mu_{Ti}$. (b) Dopant formation energy of each dopnat E_f along ABCD points.

The supercell calculations showed that each dopant except for Tl can cancel the defect level arising from the V_O. We have also evaluated the formation energy of each dopant E_f using the chemical potentials $\Delta\mu_i$ relative to bulk precipitate. $\Delta\mu_i$ were determined by the phase diagram of the relevant compounds of STO. Fig. 2(a) shows the phase diagrams as functions of $\Delta\mu_{Sr}$ and $\Delta\mu_{Ti}$, in which STO is stable within the area of the ABCD square. In Fig. 2(b), E_f of each dopant is shown along ABCD points.

Water oxidation reaction on $BiVO_4$

Perovskite $BiVO_4$ (BVO) is used as an O_2-evolution photocatalyst for overall water splitting. We have investigated the reaction processes of the water oxidation on BVO using the first-principles calculations. The DFT calculations were performed within PBE and revised PBE (RPBE) using the slab models with (110) facet. Fig. 3 shows the energy diagram of O_2- and H_2O_2-evolution on BVO (110) surface, which suggests that H_2O_2-evolution is expected to be favorable on the (110) facet compared to O_2-evolution.

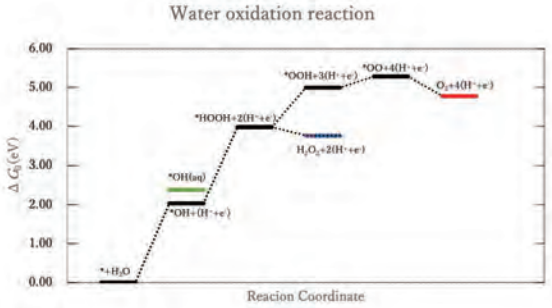

Figure 3: Energy diagram of O_2- and H_2O_2-evolution

References

[1] Q. Wang *et. al.*: Nat. Mater. **18**, 827 (2019).

[2] Z. Pan *et. al.*: Res. Chem. Intermed. **47**, 225 (2021).

[3] M. Nakabayashi, K. Nishiguchi *et. al.*: J. Phys. Chem. C (in press: https://doi.org/10.1021/acs.jpcc.3c00820).

[4] M. Cococcioni *et. al.*: Phys. Rev. B **71**, 035105 (2005).

[5] T. Takata *et. al.*: Nature **581**, 413 (2020).

Development of Thermal Functional Materials Based on First-principles Simulations

Wenyang DING[1], and Junichiro SHIOMI[1,2]

1. Department of Mechanical Engineering, The University of Tokyo, Japan

2. Institute of Engineering Innovation, The University of Tokyo, Japan

Manipulating thermal conductivity of crystalline materials by phonon engineering has attracted tremendous attention. Van der Waals (vdW) heterostructures are an ideal candidate to realize low thermal conductivity in their through-thickness direction due to its weak interlayer interactions and prominent disorder by alternating stacking orders.[1] However, previous studies have not been able to characterize phonon propagation thought vdW heterostructures in mode-wise fashion, which has limited the understanding and engineering of the heat conduction. Herein, for the first time, heat conduction in vdW heterostructures are resolved to the level of individual phonon polarizations, whose incident angles are utilized to elucidate the role that phonon interference and phonon tunneling play in vdW heterostructures.

First, we searched for vdW graphene-WS_2 heterostructure with the ultralow thermal conductivity by combining Bayesian optimization and non-equilibrium molecular dynamics (NEMD) including all the orders of anharmonicity. It is found that the lowest thermal conductivity of optimized heterostructure is 0.04 W/m-K, only 5% of graphite thermal conductivity and 13% of pristine WS_2 thermal conductivity (Fig. 1). Interestingly, the thermal conductivity of optimized heterostructure possesses only half of the thermal conductivity of the corresponding periodic superlattice. Moreover, the lattice thermal conductivity of pristine WS_2, pristine graphite, periodic superlattice, and the optimized heterostructure are also calculated by utilizing mode-resolved atomistic Green's function (AGF) method. Since AGF only considers harmonic interatomic force constants, it serves to probe the characteristics of elastic phonon scattering whose influence on thermal conductivity is partial but significant as can be seen in the comparison with NEMD results (Fig. 1). To further study the characteristics of elastic phonon scattering, the mode-resovled phonon transmissions are calculated using the S-matrix analysis.[2]

References

(1) Liu, Y.; Weiss, N. O.; Duan, X.; Cheng, H.-C.; Huang, Y.; Duan, X. Van der Waals heterostructures and devices. *Nature Reviews Materials* **2016**, *1* (9), 16042.

(2) Ong, Z.-Y. Atomistic S-matrix method for numerical simulation of phonon reflection, transmission, and boundary scattering. *Physical Review B* **2018**, *98* (19), 195301.

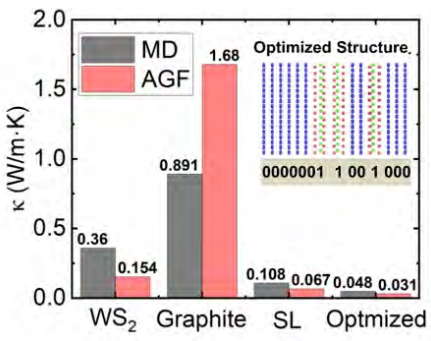

Fig. 1 Comparison of the thermal conductivity of difference. structures and methods.

First-principles study of energy and spintronics materials

Fumiyuki ISHII, Naoya YAMAGUCHI, Rifky SYARIATI,
Hikaru SAWAHATA, Hana Pratiwi KADARISMAN, Kaiki SHIBATA,
Yaotang ZHANG, Vierta SARASWATI, Takahiro TOMINAGA,
Yedija Yusua Sibuea TEWENG, Juhri HENDRAWAN,
Yume MORISHIMA, Khusnul YAKIN, Wardah AMALIA,
Syifa Fauzia Hariyanti PUTURI, Ahmad GHIFFARI, Salsabila Amanda PUTRI
Nanomaterials Research Institute, Kanazawa University
Kanazawa, 920-1192, Japan

1. *$MnBi_2Te_4$ van der Waals layers*[1]

The transverse thermoelectric effect, which produces an electric field in the direction of the cross product of the temperature gradient and magnetization of magnetic materials, has attracted much attention in recent years because of its potential applicability to a large area. Since $MnBi_2Te_4$ was predicted to have antiferromagnetic order in the interlayer and to be a ferrimagnetic semiconductor with quantized anomalous Hall conductivity in an odd number of three or more septuple layers, it is expected to generate a transverse thermoelectric effect. We have performed first-principles calculations by using OpenMX code[2] for ultrathin $MnBi_2Te_4$ films and estimating the coefficient representing the magnitude of the transverse thermoelectric effect. The anomalous Hall and Nernst effect were calculated by using our developed efficient methods by local Berry phase in momentum space[3]. A large enhancement in transverse thermoelectric effect, anomalous Nernst coefficient, larger than 20μV/K, was obtained by the Seebeck term for a wide range of carrier concentrations. The present results motivate further studies on the anomalous Nernst effect in intrinsically or doped magnetic semiconductors.

2. *Hapkeite Fe_2Si*[4]

In order to obtain a guideline for exploring new inexpensive and high-performance thermoelectric materials, the first-principles calculations were performed to clarify the thermoelectric properties of Fe-Si alloys, which are the most abundant iron-based compounds. As a result, we obtained a large transverse thermoelectric transport coefficient α_{xy} of 2.06 A/mK for the model crystal structure of a mineral Hapkeite Fe_2Si contained in a meteorite Dhofar 280, which is believed to originate from the Moon. Calculated results show that the model structure, Hapkite Fe_2Si, exhibits a more significant transverse thermoelectric transport coefficient than bcc-Fe and hexagonal Fe_2Si. Detailed analysis of the electronic states and transport coefficients indicates that the significant transverse thermoelectric effect is due to an anomaly in the density of states (DOS) at the interface between the Fe layer and the Si-Fe alternating layer. The band-edge type van Hove singularity contributed to the DOS at the Fermi level. Several previous studies have attempted to generate transverse thermoelectric effect through multi-layered structures with each layer on the order of 1 nm scale. A similar interfacial effect that enhances the transverse thermoelectric ef-

fect may be observed. Therefore, this finding is promising for the design of new transverse thermoelectric materials.

3. *Persistent spin helix in diamond*[5]
Density functional theory (DFT) simulations were performed to investigate the diamond (111) surface. We investigated how different terminations such as hydroxyl (OH) and hydrogen (H) affect the strength of the spin-orbit coupling on the diamond surface and the spin structure in momentum space. The calculation results reveal that the OH-terminated state contributes to the valence band maximum (VBM), while the H-terminated state contributes to the conduction band minimum (CBM). Due to the OH termination, persistent spin helix spintexture is obtained and the spin-orbit coupling coefficient is found to be 14.2 meV·Å at the valence band maximum (VBM). This is significant compared to the ZnO($10\bar{1}0$) surface and slightly larger than various n-type sphalerite quantum wells. Moreover, it is larger than the 3.6 meV·Å resulting from the hydrogen termination of diamond. Due to the large spin-orbit coupling coefficient, the wavelength of persistent spin helix is shortened, and miniaturization of spin field effect transistors can be expected.

4. *The Rashba effect of PbS/Au(111)*
We have performed the first-principles calculation of the PbS(111) which has buckled honeycomb structure on the Au(111) surfaces. The broken inversion symmetry due to the buckling of the system shifted the energy and caused the Rashba effect. The orientation or contact at the interface highly controls the Rashba effect at heterostructures. For the metal-metal contact, Pb-Au, allows the Rashba effect at the interface, while metal-insulator contact, S-Au, does not. The PbS(111) can be used to generate the Rashba effect surface state of thin noble metals.

References

[1] Y. Morishima, N. Yamaguchi, H. Sawahata, and F. Ishii, Appl. Phys. Express, **16** 043003 (2023).

[2] H. Sawahata, N. Yamaguchi, S. Minami, and F. Ishii, Phys. Rev. B **107**, 024404 (2023).

[3] T. Ozaki *et al.*, http://www.openmx-square.org/

[4] T. Tominaga N. Yamaguchi, H. Sawahata, and F. Ishii, Jpn. J. Appl. Phys. **62** SD1019(2023).

[5] H.P. Kadarisman, N. Yamaguchi, and F. Ishii, Appl. Phys. Express, **16** 023001(2023).

First Principles Studies on Spin Tranfer Torque Magnetic Randum Access Memory (STT-MRAM)

Kenji SHIRAISHI

Institute for Materials and Systems for Sustainability,

Nagoya University, Furo-cho, Chikusa-ku, Nagoya, 464-8601

Spin-transfer torque magnetic random-access memory (STT-MRAM) is expected to be a non-volatile memory that replaces SRAM and DRAM currently in use. MgO layer in CoFeB/MgO/CoFeB MTJ consists of irregularly shaped grains with a diameter of 10 to 15 nm, and the presence of mainly the Σ5 (210) [001] grain boundaries was observed at the interface between the grains. iPMA is generally known to be sensitive to the cleanliness of the interface between the ferromagnetic layer and the insulator [1]. In this study, we focus on the grain boundary which occurred most frequently in MgO film and investigated the influence of the grain boundary for iPMA by performing the first principles calculations.

Near grain boundary (within a 4 Å range from the center line of grain boundary, the magnitude of iPMA strongly decreases. It is because the DOS peaks in the down spin channel for "|m|=1" above Fermi energy are decreased. It causes the spin orbit coupling hybridization of (|1|×|1|) changes from perpendicular magnetic anisotropy to in-plane magnetic anisotropy. In the DOS peaks in the down spin channel above Fermi energy in ideal model, the wave functions mainly form the bonding orbitals between interfacial Fe atoms and second layer Fe atoms. Near grain boundary, the in-plane symmetry is broken by the grain boundary and the hybridization between interfacial Fe atoms and second layer Fe atoms weakens. It causes that the unoccupied down spin states of "|m|=1" extend above Fermi energy. We suggest that it is necessary to keep the d orbital hybridization around Fe atoms for further microfabrication.

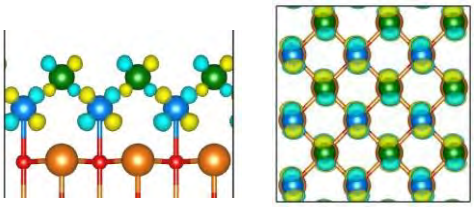

Fig.1: Wave functions at Γ point in down spin states

References

[1] A. Hallal, H. X. Yang, B. Dieny, and M. Chshiev, Phys. Rev. B 88, (2013) 184423.

First Principles Studies on Si-rich a-SiN for Flash Memory Application

Kenji SHIRAISHI

Institute for Materials and Systems for Sustainability,

Nagoya University, Furo-cho, Chikusa-ku, Nagoya, 464-8601

SiN is a useful material under harsh environments due to its high thermal stability and toughness against fracture, and lately utilized as passivation layer in Si solar cells. To advance our understanding of the memory function in SiN, however, the most important task never achieved so far is the determination of the thermodynamic level (TD) induced by V_N. This TD level is responsible for the electron capture and emission and its determination involves assessment of roles of hybridization, spin polarization and ionicity of V_N in SiN. We find that the appearance of this TD level is promoted by the spontaneous structural transformation near V_N, resulting in multiple charge states of nitrogen vacancy.

We have performed the density-functional calculations with the hybrid approximation that clarify the atomic and electronic structures of the N vacancy (V_N) in Si_3N_4. We have found that the floating state hidden in the conduction bands create a new π-like state in collaboration with the dangling-bond states around the V_N(, (Fig.1) thus rendering the V_N being multiple charge states from +1 to -5 (Fig.2). The newly found π state is unprecedented in the sense that it has the origin of the floating state distributed not around atomic sites but in the internal space of the material. The multiple charge states we have found may be utilized as an active element in information technology.

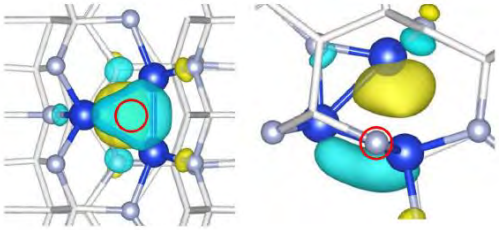

Fig.1: π-like state appeared in V_N in Si_3N_4

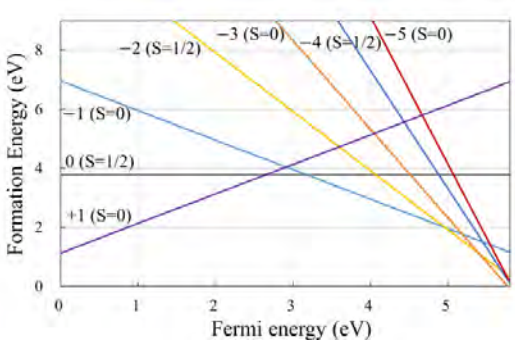

Fig.2: formation energy of V_N in Si_3N_4.

References

[1] F. Nanataki, K. Shiraishi, J. Iwata, Y. Matsushita, A. Oshiyama, Phys. Rev. B 88, (2013) 184423.

Hydrogen production by water splitting on CeO_2 (100) facet

Akira YOKO

Advanced Institute for Materials Research,

Tohoku University, Katahira 2-1-1,Aoba-ku, Sendai, Miyagi 980-8577

CeO_2 nanocubes with (100) facet have been synthesized by supercritical method, and it was found to have high oxygen storage capacity. In this study, the redox property of the (100) facet was studied by using first-principles calculations.

In this study, first principles simulations based on density functional theory (DFT) was conducted. Plane wave basis DFT simulations were conducted using VASP code. Structures of CeO_2 at surface and bulk were calculated with generalized gradient approximation proposed by Perdew, Burke, and Ernzerhof (PBE) [1]. The valence configurations of the pseudopotentials were $5s^2 5p^6 4f^1 5d^1 6s^2$ for Ce and $2s^2 2p^6$ for O. The DFT+U method introduced by Dudarev et al. [2] was used to treat electron localization. The parameter U-J was set to 5.0 eV for Ce4f and 5.5 eV for O2p states, respectively, based on previous studies of CeO_2 [3]. The Monkhorst-Pack k-point mesh of 4×4×4 was used for the unit cell of CeO_2. The slab model exposing (100) facet includes 60 atoms, and that for (111) facet includes 108 atoms. The Monkhorst -Pack k-point mesh for the slab model was 4×4×1.

Figure 1(a) and 1(b) show CeO_2 (100) bare surface and hydroxylated surface, respectively. For the (100) facet model, half of the oxygen was moved to the other side to exclude polarity keeping the CeO_2 composition. When CeO_2 is fully hydroxylated by water adsorption and dissociation, the surface state is changed as Figure 1(b). Interestingly, the lattice expansion observed inside of the bare surface model (Fig. 1(a)) was relaxed with surface hydroxylation owing to the surface stabilization.

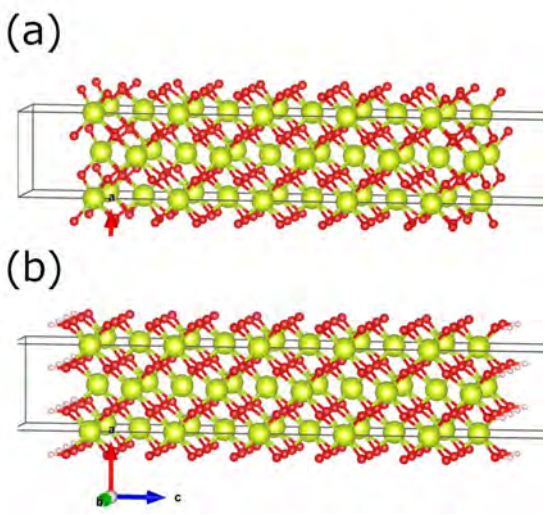

Fig. 1: CeO_2 (100) bare surface and hydroxylated (100) surface.

References

[1] J.P. Perdew, K. Burke, M. Ernzerhof, Phys. Rev. Lett., 77 (1996), p. 38650. [2] S. Dudarev, G. Botton, S. Savrasov, C. Humphreys, A. Sutton, Phys. Rev. B, 57 (1998), p. 1505. [3] P.R. Keating, D.O. Scanlon, B.J. Morgan, N.M. Galea, G.W. Watson, J. Phys. Chem. C, 116 (2012), pp. 2443-2452

Electronic structure analysis of SiC/SiO_2 interface under gated electric field

Yu-ichiro MATSUSHITA

Laboratory for Materials and Structures, Institute of Innovative Research, Tokyo Institute of Technology, Ookayama, Meguro-ku, Tokyo 152-8552

SiC-MOS devices have attracted much attention as next-generation power devices due to their excellent characteristics. However, the device characteristics are at most 10% of the theoretical performance value of SiC, which is thought to be due to high-density interface defects. However, we have proposed a new type of mechanism for the generation of interfacial levels, which originates from the peculiarity of the wave function at the lower end of the conduction band of SiC.

In this study, we have performed a comparative study of the electronic structure of the SiC/SiO_2 interfaces under a gated electric field by means of theoretical calculations based on density functional theory, including the dependence of the electronic structure on the plane orientation. It is found [1] that the wavefunction at the conduction band minimum (CBM) at the $SiC(0001)/SiO_2$ interface tends to be localized at the cubic site closest to the interface. On the other hand, we found that such localization of the wavefunction cannot be observed on nonpolar interfaces such as the (11-20) plane. We found that this is related to the structural channel near the interface. Of particular importance, the localization of the wavefunction at this (0001) interface is distributed much closer to the interface (<5 Å) than expected from the effective mass approximation (EMA), and thus is expected to be more sensitively scattered by interface defects. This result may explain why the channel mobility of the (0001) plane is particularly low compared to the other planes (e.g., (1120)), which is well known from experiments.

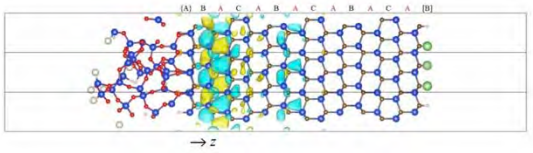

FIG 1. Isosurface at 38% of the peak value of wavefunction localized at outermost cubic site (F = 1.0 MV/cm, CBM). The blue, brown, red, and small white balls depict Si, C, O, and H atoms, respectively.

We have also clarified that the

deviation from the EMA, which is a frequently used method to analyze the electronic structures in semiconducting devices, is attributed to the long structural periodicity along the [0001] direction in the SiC crystals.

Furthermore, in actual SiC-MOS interfaces, the introduction of nitrogen is used to improve the interface properties. However, its microscopic mechanism has not been elucidated. In addition, considering the recent experimental results that the introduced nitrogen also diffuses to the SiC side. We study how the electronic states at the SiC / SiO2 interface are affected when nitrogen is introduced as a dopant based on first-principles calculations. As a result, we found that the deep doping of nitrogen relaxes the confinement potential near the interface and the localization of the wavefunction, which is expected to improve the device properties. We succeeded in proposing a new way to improve SiC-MOS devices.

Fig. 1: Supercomputer System B at SCC-ISSP.

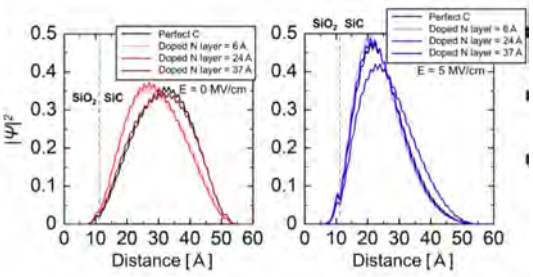

FIG 2. Local density of states (LDOS) of the CBM in slabs with di↵erent N-doped regions. For clarity, averaging was done over the atomic layer thickness period. Applied electric fields are 0, 5, and 10 MV/cm, respectively.

References

[1] K. Tachiki, Y. Nishiya, J.-I. Iwata, and Y. Matsushita, arXiv:2303.08527 (2023).

[2] H. Yoshioka, J.-I. Iwata, and Y. Matsushita, arXiv:2303.05085 (2023).

Density functional theory study of adsorption and reaction of molecules on metal surfaces

Ikutaro Hamada

Department of Engineering, Graduate School of Engineering,

Osaka University, 2-1 Yamada-Oka, Suita, Osaka 565-0871

Graphene doped with foreign elements has attracted enormous attention because of emergent electronic properties, besides its own unique structural, electronic, and mechanical properties, as well as its stack(s) with the same and/or different two-dimensional materials.

Graphene doped with nitrogen has been shown to exhibit catalytic activity toward electrochemical oxygen reduction reaction (ORR). To understand the mechanism of ORR on nitrogen-doped graphene, it is important to understand the interaction between graphene and water, a common solvent in electrochemistry. However, density functional theory with the conventional semilocal approximation fails to describe the weak water-graphene interaction accurately. In this work [1], we use rev-vdW-DF2 [2], one of the van der Waals density functionals, which has been shown to be able to describe the water-graphene interaction accurately [3], to study the interaction between water molecule and nitrogen-doped graphene. We consider different water orientations and different nitrogen configurations and obtain the preferred orientations of the water molecule, depending on the nitrogen configuration. We reveal that graphitic and pyridinic nitrogen atoms are charged positively and negatively respectively, which lead to different water orientations. The interaction energy curves obtained in this work may serve as references for future studies and be useful for modeling of graphene/water interfaces with hybrid quantum-mechanics/molecular mechanics-type methods.

Nitrogen-doped graphene with a single transition metal atom (single atom catalyst, SAC) has also been attracted much attention as it shows ORR activity comparable to platinum, and there have been numerous studies both experimentally and theoretically. However, the mechanism of ORR on SAC is not yet fully resolved. In this study [4], we focus on the exchange-correlation functional to be used to study ORR on SAC, in particular Fe and Co SAC embedded in a nitrogen-doped graphene (Fe/Co-N_4-C). By choosing the results obtained using the Bayesian error estimate functional with van der Waals correlation (BEEF-vdW) [5] as references, we perform systematical calculations of the ORR intermediates on Fe-N_4-C and Co-N_4-C using commonly used semilocal exchange-correlation functionals with and without dispersion correction and find that revised Perdew-Burke-Ernzerhof (RPBE) [6,7] functional with Grimme's dispersion correction [8] (RPBE-D3) gives the results consistent with those obtained using BEEF-vdW. The conclusion drawn in this work as well as the strategy taken there will be useful to choose an appropriate (low-cost) exchange-correlation function to study electrochemical and heterogeneous reactions.

References

[1] A. F. Z. Abidin and I. Hamada, Phys. Rev. B **105**, 075416 (2022).

[2] I. Hamada, Phys. Rev. B **89**, 121103 (R) (2014).

[3] J. G. Brandenburg, A. Zen, D. Alfé, and A. Michaelides, J. Chem. Phys. **151**, 164702 (2019).

[4] A. F. Z. Abidin and I. Hamada, Surf. Sci. **724**, 122144 (2022).

[5] J. Wellendorff, *et al*., Phys. Rev. B **85**, 235149 (2012).

[6] J. P. Perdew, K. Burke, and M. Ernzerhof, Phys. Rev. Lett. **77**, 3865 (1996).

[7] B. Hammer, L. B. Hansen, and J. K. Norskøv, Phys. Rev. B **59**, 7413 (1999).

[8] S. Grimme, J. Antony, S. Ehrlich, and H. Krieg, J. Chem. Phys. **132**, 154104 (2010).

Theoretical determination of charge injection levels in organic semiconductor films

Ryo Uza and Susumu Yanagisawa
Department of Physics and Earth Sciences, University of the Ryukyus
Senbaru 1, Nishihara Okinawa 903-0213

Zinc phthalocyanine (ZnPc) can be used as a p-type semiconductor with hole carriers. Fluorinated zinc phthalocyanine (F_{16}ZnPc) can also be used as an n-type semiconductor. ZnPc and F_{16}ZnPc are attracting attention as organic solar cell materials. Fundamental understanding on the formation mechanism of charge injection levels is urgent for their practical application. In the present work, Vienna Ab-initio Simulation Package (VASP) was used to determine from first-principles the lattice parameters of the crystals and the atomistic structure of molecular films by the van der Waals (vdW) density functional[1]. Subsequently, the band energy calculations were performed with the GW approximation, which included the effects of electronic polarization. The ionization potential (I) or electron affinity (A) of any molecule depends on the electronic polarization of the surrounding molecules and the electrostatic interactions upon the ionized molecule from its surroundings[2]. The effect induced by the molecules surrounding an ionized molecule, which stabilizes the charge injected into the molecule by the polarization clouds with an opposite charge, is called electronic polarization. In this work, both the effects of the electrostatic interaction and the electronic polarization were included in the calculations to quantitatively predict the level of charge injection.

The result indicates that in case of ZnPc thin film the energy levels are relatively shifted up in the standing configuration and shifted down in the lying configuration. This comes from the electric quadrupole moment of the neutral molecule. Electric quadrupoles generate electrostatic potentials in crystals and films. The generated electrostatic potential is governed by the electric quadrupole tensor and depends on the distance between molecules and the orientation angle of the constituent molecule. Therefore, the shift is opposite for the standing and lying configurations, as the orientation angle of the molecules relative to the nearest neighbor molecules changes and the sign of the electrostatic potential is different. Similarly, given the opposite signs of the zz component of the electric quadrupole tensor, the signs of the electrostatic potential for ZnPc and F_{16}ZnPc are opposite.

The effect of electronic polarization was determined using the GW approximation to calculate I and A, and the density of states was obtained by matching the corresponding energy levels to the peak of the density of states. It was found that the positions of the density of states peaks are in good agreement with the experimental photoelectron/inverse photoelectron spectra[3] (Fig. 1). The calculated energy gap is slightly shallower than the experimental results, which can be corrected by improving the accuracy of the GW approximation.

Overall, it is concluded that the present theoretical method is of practical use in predicting the frontier energy levels of organic semiconductor thin film. Prediction of the charge injection levels in mixed films of ZnPc and

F_{16}ZnPc is in progress.

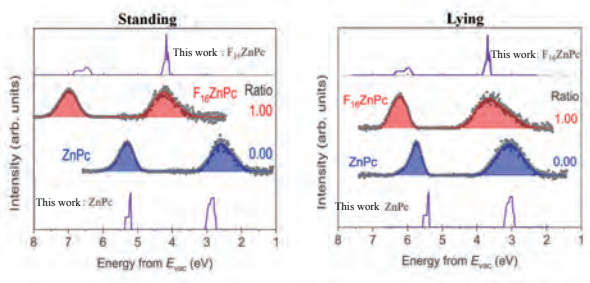

Figure 1: Theoretical density of states (DOS) of ZnPc and F_{16}ZnPc thin films with standing and lying configurations. The experimental DOS measured with direct/inverse photoemission[3] are also displayed.

References

[1] I. Hamada: Phys. Rev. B **89**, 121103 (2014).

[2] K. Yamada, S. Yanagisawa, T. Koganezwa, K. Mase, N. Sato, and H. Yoshida: Phys. Rev. B **97**, 245206 (2018).

[3] Y. Uemura, S. A. Abd-Rahman, S. Yanagisawa, and H. Yoshida: Phys. Rev. B **102**, 125302 (2020).

Reduction of Rare Metals in Fuel Cell and Formic Acid Decomposition Catalysts

Norihito Sakaguchi

Center for Advanced Research of Energy and Materials, Faculty of Engineering, Hokkaido University, Sapporo, Hokkaido 060-8628

We investigated the adsorption and diffusion properties of single-atom catalysts on light-element doped graphene supported on the metal substrates, with the aid of the first-principles calculation based on the density functional theory (DFT). We also investigated the catalytic activities of the considered systems in oxygen reduction and formic acid decomposition reactions.

At first, we investigated the stabilities of single Pt and Cu atoms on light-element doped graphene supported on the metal substrates. We considered Fe, Ni, and Cu as metal substrates. We performed the total energy and electronic structure calculations using The Vienna Ab initio Simulation Package (VASP). We installed a parallelized VASP with Intel® MPI Library and Intel® Math Kernel Library. We have reported that the adsorption of Pt and Cu atoms on light-element doped graphene with flat structures became stronger through supporting the magnetic substrates, i.e., Fe and Ni substrates, last year. We reinvestigated the adsorption properties of Pt and Cu atoms on light-element doped graphene with flat structures on non-magnetic substrates, i.e., Cu substrates. We revealed that the ferromagnetic electronic structures of metal substrates are not required to enhance the chemical bonding between single-atom catalysts and light-element doped graphene light-element doped graphene. In most cases of steric light-element doped graphene, the non-magnetic substrates also weaken the Pt and Cu adsorption and enhance the catalyst diffusion on the light-element doped graphene in the same way as the magnetic substrates.

Based on the previously reported volcano plots, we also investigated the catalytic activities of the considered systems in oxygen reduction and formic acid decomposition reactions from the adsorption energies of the components of the reactants. Although the strong chemical bonds between catalysts and supports are expected to lead to higher catalytic activities, the enhancements of catalytic reactions have been found only in a few systems.

References

[1] Y. Kunisada, N. Sakaguchi, Nano Express 3 (2022) 042001.

Development of Efficient Oxygen Storage Materials and Hydrogen Permeation Barrier Materials

Yuji Kunisada

Center for Advanced Research of Energy and Materials, Faculty of Engineering, Hokkaido University, Sapporo, Hokkaido 060-8628

We investigated the doping effects on the oxygen absorption/desorption properties of brownmillerite-type oxides,[1] with the aid of the first-principles calculation based on the density functional theory (DFT). We also performed O K-edge electron energy loss spectroscopy (EELS) simulations to build the EELS database for characterizing the experimental EELS spectra obtained with transmission electron microscopy. Besides, the solubility and diffusion properties of hydrogen isotopes in amorphous ceramic materials were also investigated to validate its application as hydrogen permeation barrier materials.

We investigated the oxygen absorption energies with various heteroatom substitutions in Ca_2AlMnO_5 using The Vienna Ab initio Simulation Package (VASP). We installed a parallelized VASP with Intel® MPI Library and Intel® Math Kernel Library. We revealed the effects of local atomic distortions induced by dopants on the oxygen absorption energies. We also performed EELS simulations of nonequivalent O atoms using Z+1 approximation to construct the database of the O K-edge EELS spectra.

We also investigated the hydrogen isotope solubility and diffusion properties in the amorphous ceramic materials. We considered Al_2O_3 as the hydrogen permeation membrane. We performed melt-quenching technique to obtain the amorphous structure last year. However, the obtained structures are not fully in the amorphous phase due to insufficient melting. Therefore, we obtained the atomic structures of the amorphous Al_2O_3 using higher melting temperatures and longer time steps for molecular dynamics simulations. Next, we performed 2000 DFT calculations with various hydrogen positions in amorphous Al_2O_3 to determine the relationship between the dissolution energies and the local structures. Using the Voronoi analysis, we evaluate the volume occupied by the hydrogen atoms. Finally, we revealed the dependence of the dissolution energies and diffusion barriers on the volume occupied by the hydrogen atoms.

References

[1] K. Tanahashi, Y. Omura, H. Naya, Y. Kunisada, N. Sakaguchi, A. Kurniawan, T. Nomura, ISIJ International 62 (2022) 2578-2586.

Densest binary/ternary sphere packings and prediction of quaternary hydrides

Ryotaro Koshoji, Masahiro Fukuda, Mutsuaki Kawamura, Taisuke Ozaki
Institute for Solid State Physics, University of Tokyo
Kashiwa-no-ha, Kashiwa, Chiba 277-8581

It was widely accepted in the 2000s that the Barlow packings such as FCC structure are the densest unary sphere packings. Despite the simpleness of the problem, it is also too difficult to identificate the densest binary sphere packings (DBSPs), however, the development of computers has been enabling us to explore the DBSPs by computer simulations. If we only explore the periodic dense packings of spheres of n different sizes by computer, the packing fraction at given sphere-composition ratio is maximized by filling the space with not more than n kinds of periodic packings. In 2012, Hopkins *et al.* explored the DBSPs under the restriction that the number of spheres in the unit cell with periodic boundary condition is not more than 12 and constructed the phase diagram for the first time. They also showed that in some radius and composition ratios a considerable number of the structures have competitive packing fractions, so it is necessary to optimize the packing structure precisely with small distortions.

We developed the structural optimization algorithm based on the steepest-decent method that is easy to implement. The computational cost is small and we showed that it is as precise as the Torquato-Jiao algorithm. Our algorithm, which produces initial structures as layer-by-layer stacking structures, completely revisit the previous studies with small corrections, and we successfully found the 12 putative DBSPs since the maximum number of spheres in unit cell is set to be double. As a result, a total of 28 putative DBSPs are known at the present time.

In ternary systems, the DBSPs are the candidates for the phase separations as well as the FCC packings of small, medium, and large spheres. Following our studies, we constructed the phase diagrams for the first time since previous studies on the dense ternary sphere packings (DTSPs) do not construct the phase diagrams. As a result, we totally discovered the 59 putative DTSPs [1]. One of the well-ordered DTSPs is the (13-2-1) structure shown in Fig. 1(a). The structure is the DTSP at several radius ratios such as 0.44 : 0.64 : 1.00, at which small and medium spheres are too large to be placed in the tetrahedral and octahedral sites if large spheres comprising the fcc structure contact with each other. The clathrate network of small spheres correspond to that of boron in UB_{12}, and the (13-2-1) structure has one additional small sphere placed in the cuboctahedron of small spheres. A medium sphere is placed in the tetrahedral site as CaF_2.

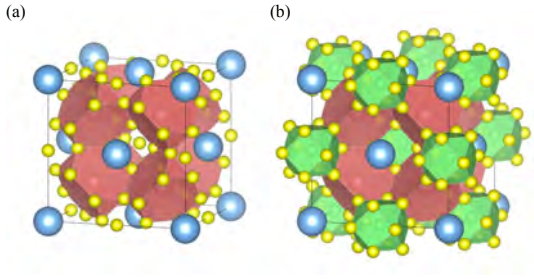

Figure 1: (a) The (13-2-1) structure. (b) The (12-1-2-1) structure.

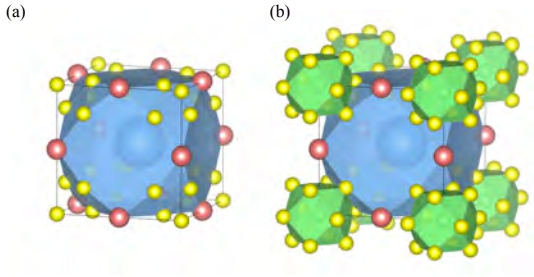

Figure 2: (a) The (13-3-1) structure. (b) The (12-1-3-1) structure.

The clathrate network has structural similarity with LaH_{10} and YH_6. The crystal structures of

Table 1: The list of substitution atoms for spheres, where the symbol E corresponds to empty.

sphere size	elements
small	H
semi-small	E, H, Li, Be, Na, Mg, Al, K, Ca, Sc, Ti, V, Cr, Mn, Fe, Co, Ni, Cu, Zn
medium	From Li to Hg (except for B to Ne, Si to Ar, Br, Kr, Xe, Ce to Lu, Pt)
large	From K to Hg (except for Br, Kr, Xe, Ce to Lu, Pt)

the binary hydrides correspond to the DBSPs of the XY_{10} and (6-1) structures, respectively. Therefore, we can expect that the (13-2-1) structure also correspond the hydrides under high pressure. However, crystal structures tend to prefer the coordination polyhedron [72]. Therefore, we replace the small sphere at the center of the cuboctahedron with metallic atoms so that the metallic atoms should be coordinated by 12 small spheres comprising a cuboctahedron. We call the quaternary structure shown in Fig. 1(b) as the (12-1-2-1) structure. This structure also has the $Fm\bar{3}m$ symmetry. We also focus on the (13-3-1) structure shown in Fig. 2(a). It is the DTSP at several radius ratios such as 0.30 : 0.40 : 1.00 and can be derived by substituting an atom at the vertex of the unit cell of the perovskite structure with a cuboctahedron of 13 small spheres. To produce the structural prototype of hydrides, we replace the small sphere at the center of the cuboctahedron with metallic atoms as shown in Fig. 2(b), and we call it as the (12-1-3-1) structure.

Table 1 shows the list of substitution atoms for spheres in the (12-1-2-1) and (12-1-3-1) structures. Small spheres are substituted with only hydrogen atoms. The number of chemical compositions for each structural prototype is 36652. To screen out unstable candidates, we execute the structural optimizations and molecular dynamic simulations with static/dynamic crystal lattices. We use the standard enthalpies of formations (SEFs) to estimate the structural stabilities. We calculate the phonon dispersions for some of hydrides which have lower SEFs and no spin polarization.

As a result, we confirm that at least 23 hydrides are dynamically stable [2]. We found that many hydrides prefer the $(12\text{-}1\text{-}2\text{-}1)_V$ structure shown in Fig. 3 to the (12-1-2-1) structure. It it worth mentioning that the $(12\text{-}1\text{-}2\text{-}1)_V$ structure is isotypic to the $Pm\bar{3}$ structure of $ScYH_6$ (cP8). Importantly, the previous study indicated that cP8-$ScYH_6$ may possess the lowest enthalpy in the pressure range of 50150 GPa. Since several quaternary hydrides

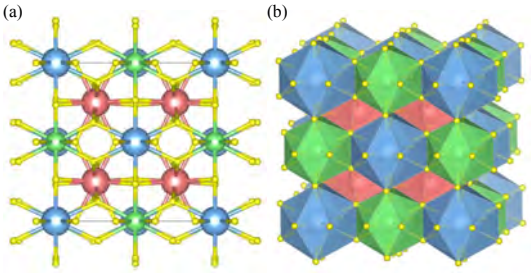

Figure 3: The $(12\text{-}1\text{-}2\text{-}1)_V$ structure.

of which we confirm the dynamic stabilities are the superstructures of cP8-$ScYH_6$, we can expect that they may also have the lowest enthalpies under higher pressures. In fact, the SEFs under 10 GPa of the four kinds of the decomposition paths from $H_{12}ScY_2Ca$:

$$ScH_2 + 2YH_2 + CaH_2 + 2H_2, \quad (1)$$
$$ScH_2 + 2YH_3 + CaH_2 + H_2, \quad (2)$$
$$ScH_3 + 2YH_2 + CaH_2 + 1.5H_2, \quad (3)$$
$$ScH_3 + 2YH_3 + CaH_2 + 0.5H_2, \quad (4)$$

are calculated, and we found that $H_{12}ScY_2Ca$ are considerably stable since it has almost the same enthalpy as the decomposition of Eqs. (1) and (3) while it is less stable than the decompositions of Eqs. (2) and (4) by about 1.2 eV/f.u., corresponding to the thermodynamic instability of 78.6 meV/atom compared to the case of Eq. (4).

Finally, we calculate the superconducting transition temperatures T_c by density functional theory for superconductors, are found to be 5.7 and 6.7 K for the selected two hydrides $H_{12}ScY_2Ca$ and $H_{12}ScY_2Sr$, respectively [2].

References

[1] R. Koshoji and T. Ozaki: J. Phys. Commun. **6**, 075002 (2022).

[2] R. Koshoji, M. Fukuda, M. Kawamura, T. Ozaki: Phys. Rev. Materials. **6**, 114802 (2022).

Control of magnetic anisotropy by strain and electric polarization at interfaces

Yoshihiro GOHDA

Department of Materials Science and Engineering, Tokyo Institute of Technology
J1-3, Nagatsuta-cho 4259, Midori-ku, Yokohama 226-8502, Japan

Magnetocrystalline-anisotropy (MCA) energy is of importance in controlling the direction of magnetic moments. The dependence of the magnetic anisotropy on lattice constants can be utilized for magnetoelectric couplings via domain modulations of ferroelectric materials under ferromagnetic ones. Such interface multiferroicity is promising for the reduction of energy consumptions in magnetic devices avoiding the Joule heating by the electric current. The magnetoelectric effect of Co_2FeSi was found to be much larger than that of Fe_3Si [2], albeit its origin is yet to be clarified.

In this project, we performed first-principles calculations of ferromagnetic Heusler compounds to clarify the microscopic origin behind the strain-mediated modulation of the MCA energy E_{MCA}. In Co_2FeSi, site-projected E_{MCA} of both Co and Fe decrease with an isotropic expansion of the in-plane lattice as shown in Fig. 1(a). This can be compared with a formulation connectable to X-ray magnetic circular dichroism observations via the quadrupole moment of the spin-density distribution (quadrupole term) and changes in orbital magnetic moments (Bruno term) [1]. As is clear from the figure, the quadrupole term is dominant for Co_2FeSi corresponding to the $\uparrow\downarrow$ spin-flip term, i.e., couplings between up-spin unperturbed states and down-spin virtual states, in Fig. 1(b). In contrast, the MCA energy modulation in Fe_3Si was found to be attributed to neither Bruno nor quadruple terms.

In addition, phase equilibria in permanent magnets were discussed through first-principles thermodynamics [3, 4].

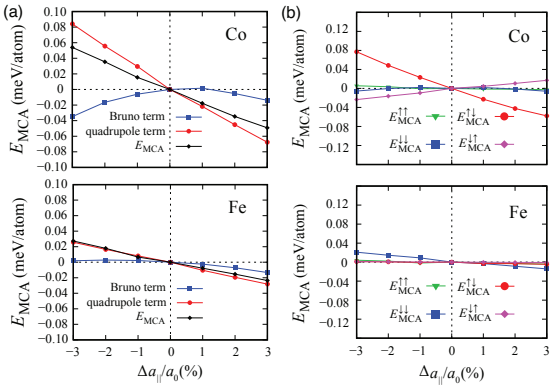

Figure 1: Site-resolved E_{MCA} of Co_2FeSi as a function of the distortion ratio $\Delta a_{||}/a_0$: (a) total E_{MCA} and contributions from the Bruno and quadrupole terms; (b) $E^{\uparrow\uparrow}_{\mathrm{MCA}}$, $E^{\downarrow\downarrow}_{\mathrm{MCA}}$, $E^{\uparrow\downarrow}_{\mathrm{MCA}}$, and $E^{\downarrow\uparrow}_{\mathrm{MCA}}$

[1] J. Stöhr, J. Magn. Magn. Mater. **200**, 470 (1999).
[2] S. Fujii, Y. Gohda, *et al.*, NPG Asia Mater. **14**, 43 (2022).
[3] S. Tsuna and Y. Gohda, J. Appl. Phys. **133**, 115103 (2023).
[4] S. Nishino and Y. Gohda, Jpn. J. Appl. Phys. **62**, 030902 (2023).

Discovery of Super-Composite Electrical Insulating Materials Based on Multiscale Physics and Deep Learning of Polymers

Hajime SHIMAKAWA, Haruto SUZUKI, Chihiro TATEYAME, Yuki MORI,
Akiko KUMADA, and Masahiro SATO
Department of Electrical Engineering & Information Systems
The University of Tokyo, Hongo, Bunkyo-ku, Tokyo 113-8656

Materials Informatics (MI), a data-driven material design method, is considered effective for designing polymer materials that require a vast amount of manufacturing information. However, although sample information including fillers and measurement conditions have a great influence on material properties, the methods for extracting them as features have not been sufficiently investigated, and the use of MI is currently limited [1]. In this study, we investigated electrical and thermal feature extraction for polymers using multi-scale physics based on first-principles and molecular dynamics calculations. We also used machine learning to predict the electrical and thermal properties of composite polymer materials. Furthermore, the importance of each material information was examined based on feature engineering.

In multiscale electrical feature computation, we successfully developed computational methods of ionic charge mobility in polymer matrix and hole trapping barrier between polymer matrix and nano-filler. In machine learning, experimental results of thermal and electrical conductivity of the composite materials in PoLyInfo [2] were used. The thermal and electrical conductivities were learned by adding polymer information, filler information, volume fraction, measurement temperature, sample thickness, and process conditions, and the prediction accuracy improved with each additional feature. The prediction accuracy increased significantly when filler information was added for thermal conductivity, and when process information was added for electrical conductivity. While filler volume fraction had a significant effect on prediction of thermal conductivity, it was not sufficient for prediction of electrical conductivity, indicating that input of process conditions is necessary in predicting electrical conductivity. Our results show a new potential of materials informatics for the prediction of complex polymer properties.

References

[1] L. Chen, et al.: Mater. Sci. Eng. R Rep., 144, 100595 (2021)
[2] https://polymer.nims.go.jp/en/

First-principles study of photoresponsive functional materials

Shinji TSUNEYUKI

Department of Physics, The University of Tokyo

Hongo, Bunkyo-ku, Tokyo 113-0033

The technology to connect and control semiconductor or magnetic devices with light is attracting attention as an essential technology in the era of 5G and beyond 5G. The development of materials and devices necessary for this purpose is required. This research aims to develop and demonstrate a first-principles simulation method for the optical responsivity of materials, which will serve as a basis for such research and development.

This academic year, we developed a first-principles method to calculate the dielectric properties of crystals with significant anharmonic effect in phonon in the sub-THz to THz range and applied the technique to rutile TiO_2 [1].

The method is based on Cowley's lattice dynamics theory on dielectric properties [2]. We calculate the Born effective charges of ions from the Berry phase and employ the modified self-consistent phonon approach to calculate phonon frequencies and linewidths, including third and fourth-order anharmonicity.

We find that the optical phonon frequencies and line widths at the gamma point better agree with experimental measurements than those obtained by the perturbative approach (Fig.1). We also find that the four-phonon scattering process contributes as much to the phonon linewidths of some phonon modes as the third-order anharmonic term. This method is versatile and relatively computationally inexpensive, and will be useful for future development of dielectric materials.

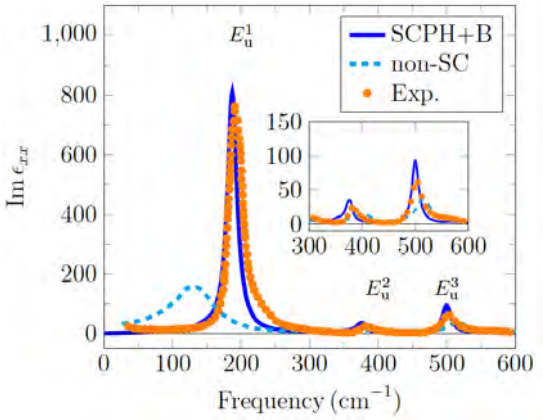

Fig.1 The imaginary part of the dielectric function ε_{xx}. The results of the present method and a perturbative approach are show in a solid line and a dashed line, respectively (from Ref. [1]).

References

[1] T. Amano, T. Yamazaki, R. Akashi, T. Tadano and S. Tsuneyuki, Phys. Rev. B, 107, 094305 (2023).

[2] R. Cowley, Adv. Phy. 12, 421 (1963).

Analyses on electronic and magnetic structure and parallelization development in quasi-particle self-consistent *GW* code

Tatsuki ODA[1,2], Kazuki MURANAKA[2], Chandro PARDEDE[2], Jakub LUTSINEC[2], Ko HYODO[2], Masao OBATA[1,2]

[1]*Institute of Science and Engineering, Kanazawa University, Kanazawa, Ishikawa 920-1192*

[2]*Graduate School of Natural Science and Technology, Kanazawa University, Kanazawa, Ishikawa, 920-1192*

We have studied electronic structure in several systems of magnetic material. In one of the investigations, we found new foundations of magnetic shape memory alloy on the electronic instability to modulated phases using the quasi-particles self-consistent GW method (QSGW) in which the electron-correlation of random phase approximation is explicitly included in the self-energy part of one particle energy level. This method was used in the software *ecalj* [1] which has been developed by the researcher T. Kotani. Our group has developed its highly parallelized code, achieving a one-order faster using the computer facilitated in ISSP. We have also developed the density functional theory (DFT) code optimized for GPU architecture.

(A) Application to Ni_2MnGa by QSGW method

According to the QSGW approach, the Ni e_g orbitals in the cubic (austenite) phase, which lead to martensite phase transition by band Jahn-Teller effect, were found to locate just on the Fermi level. This implies a clear definitive origin of band Jahn-Teller (JT) effect in comparison with the results obtained by the density functional approach of generalized gradient approximation (GGA). From the analysis of generalized susceptibility in the cubic phase, the instabilities responsible for the modulated structures of 10M, 14M, and 6M were found to be an intrinsic property in the electronic states [2]. These states may stabilize the modulated one, accompanied by tetragonal local JT distortions. Their property of Fermi surface nesting sensitively depends on a subtle change in the magnetic moment, corresponding to the experimental fact that the modulated structure appears depending on temperature and the composition of the magnetic element. We also found that there is another secondary peak in the generalized susceptibility.

The results of QSGW show a lot of improved features in the electronic structure. The Ni 3d e_g component, appearing just at the Fermi level, can be definitive theoretical evidence for the existence of phase instability at low temperatures. Compared with the GGA +U or GGA results, the eigenvalue levels of the minority spin state shift to higher energies,

indicating an increase in exchange splitting and, thus, an increasing total magnetic moment. The energy level shift in the minority spin state is small but makes a drastic change in the generalized susceptibility. The change is quantitative, but the meaning of its result provides a qualitative conclusion in the martensite phase of 10M or 14M appearing at low temperatures. Such an instability indicated from the investigation of susceptibility is found to be much more sensitive to the magnetic moment, implying a close relationship with the composition of the magnetic element and the external magnetic field.

(B) Optimization of DFT code for GPU

The use of GPU parallelization has shown a great promise in accelerating DFT calculations and reducing the computational cost. The results obtained from our GPU-accelerated DFT code demonstrate its potential to accelerate electronic structure calculations, making it a promising tool for studying large-scale systems in materials science, physics, and chemistry.

Several of the subprogram in the DFT code need a lot of memory data for accomplishing their operations. In a plane-wave-basis code, the routines of fast Fourier transformation (FFT) and matrix-matrix multiplication (MMM) are essential in the total computational cost. The problem has been a large amount of data transfer between GPU and CPU. Such problem may be resolved in our plane wave code with a currently available GPU equipped at ISSP computer.

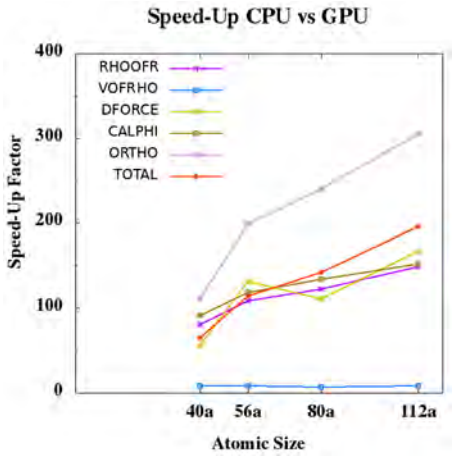

Fig. 1: Time ratio of GPU vs. CPU.

We combined the use of OpenACC programming and CUDA library that provides the routines of FFT and MMM. The OpenACC can manage data transfer from host to device and vice versa easily and parallelize some kinds of calculations with simple directive. We performed DFT calculations on the different system size; modulated magnetic shape memory alloy Ni_2MnGa (NMG); $(NMG)_{10}$(40 atoms), $(NMG)_{20}$(80 atoms), $(NMG)_{14}$(56 atoms), $(NMG)_{28}$(112 atoms). Our code gained speed-up 65-195-fold depending on its system size. However, we faced memory limitation due to memory capacity on the GPU. As the larger system we calculate, the large memory capacity we need to perform the calculation.

References

[1] T. Kotani, J. Phys. Soc. Jpn. **83**, 094711 (2014); *ecalj*: https://github.com/tkotani/ecalj/.

[2] M. Obata, T. Kotani, and T. Oda, Phys. Rev. Mater. **7**, 024413 (2023).

Systematic elucidation of structure and electronic state of π-electron-proton coupled molecular conductors under pressure

Shun DEKURA†
Institute for Solid State Physics, The University of Tokyo,
Kashiwanoha 5-1-5, Kashiwa, Chiba 277-8581

κ-H_3(Cat-EDT-TTF)$_2$ (= H-TTF) and its analogues, which have been recently developed in our group, show unique π-electron–proton coupled physical properties owing to the strongly correlated electrons and dynamics of protons in the H-bonds: such as quantum spin liquid / quantum paraelectric states or charge ordering transition coupled to the dynamics of protons.[1–4] Although H-TTF shows charge ordering with proton localization under hydrostatic pressure, it was very recently found that S/Se substituted H-TTF analogue, H-ST, shows metallization and superconducting transition under hydrostatic pressure, and shows metal–insulator transition under uniaxial pressure. To understand the π-electron–proton coupled physical properties of H-ST under physical pressure, in this study, the author performed first-principles structural optimization of H-ST under hydrostatic and uniaxial pressure, using OpenMX software (Ver. 3.9) on the ISSP Supercomputer System B (ohtaka), using GGA-PBE exchange-correlation functional.

Structural optimizations were performed by minimizing the enthalpy under hydrostatic or uniaxial pressures up to 2.0 GPa. The optimized structures under hydrostatic pressures did not show proton localization up to 2.0 GPa. On the other hand, the optimized structures under uniaxial pressures showed proton localization below 2.0 GPa. The results are consistent with the experimentally observed behavior, and suggests that isotropy of the applied pressure, in addition to the band width increase, is key to cause metallization in H-ST. However, structural optimization of H-TTF under hydrostatic pressure did not result in proton localization unlike the experimental observation, which indicates the importance of quantum nature of protons to fully understand the behavior of H-TTF analogues under pressure.

References

1) H. Mori, S. Yokomori, S. Dekura, and A. Ueda, Chem. Commun. **58**, 5668 (2022).
2) A. Ueda, S. Yamada, T. Isono, H. Kamo, A. Nakao, R. Kumai, H. Nakao, Y. Murakami, K. Yamamoto, Y. Nishio, and H. Mori, J. Am. Chem. Soc. **136**, 12184 (2014).
3) A. Ueda, K. Kishimoto, T. Isono, S. Yamada, H. Kamo, K. Kobayashi, R. Kumai, Y. Murakami, J. Gouchi, Y. Uwatoko, Y. Nishio, and H. Mori, RSC Adv. **9**, 18353 (2019).
4) M. Shimozawa, K. Hashimoto, A. Ueda, Y. Suzuki, K. Sugii, S. Yamada, Y. Imai, R. Kobayashi, K. Itoh, S. Iguchi, M. Naka, S. Ishihara, H. Mori, T. Sasaki, and M. Yamashita, Nat. Commun. **8**, 1821 (2017).

†Current address: Institute of Multidisciplinary Research for Advanced Materials (IMRAM), Tohoku University, 2-1-1 Katahira, Aoba-ku, Sendai 980-8577

Elucidation of the mechanism of fast proton conduction based on proton tautomerism in molecular crystals by using first-principles calculations

Shun DEKURA†

Institute for Solid State Physics, The University of Tokyo,

Kashiwanoha 5-1-5, Kashiwa, Chiba 277-8581

The author has been developing anhydrous superprotonic conductors based on single-crystalline molecular solids, and elucidating their peculiar conduction mechanism involving molecular internal degrees of freedom.[1–4] In this study, we elucidated the mechanism of anhydrous superprotonic conduction ($\sigma > 10^{-3}$ S/cm) with the low activation energy (E_a) of ca. 1.0 eV based on proton tautomerism in 1,2,3-triazolium phosphate. To evaluate the activation energies accompanied with the proton conduction in the crystal structure, first-principles NEB calculations were performed using OpenMX software (Ver. 3.9) on the ISSP Supercomputer System B (ohtaka), using a generalized gradient approximation (GGA) proposed by Perdew, Burke, and Ernzerhof to the exchange-correlation functional.

At first, the experimentally obtained X-ray structure was optimized fixing the unit-cell geometry for the initial state, where all the four 1,2,3-triazolium in the unit cell are 1*H*,3*H*-tautomer. Then, the structure with one 2*H*,3*H*-tautomer out of four 1,2,3-triazolium in the unit cell was optimized as final state. The NEB calculation for this step suggested that this tautomerization occurs via hydrogen-bond formation with transient proton transfer to phosphate in the adjacent layer. The corresponding E_a was ca. 1.2 eV, consistent with the experimentally observed one. The result strongly supports the low-barrier anhydrous proton conduction realized by proton tautomerism. However, only one step of whole proton conduction process has been elucidated in this research; the other processes are now under consideration.

References

1) Y. Sunairi, S. Dekura, A. Ueda, T. Ida, M. Mizuno, and H. Mori, J. Phys. Soc. Jpn. **89**, 051008 (2020).

2) S. Dekura, Y. Sunairi, K. Okamoto, F. Takeiri, G. Kobayashi, Y. Hori, Y. Shigeta, and H. Mori, Solid State Ionics **372**, 115775 (2021).

3) Y. Hori, S. Dekura, Y. Sunairi, T. Ida, M. Mizuno, H. Mori, and Y. Shigeta, J. Phys. Chem. Lett. **12**, 5390 (2021).

4) S. Dekura, M. Mizuno, and H. Mori, Angew. Chem. Int. Ed. **61**, e202212872 (2022).

†Current address: Institute of Multidisciplinary Research for Advanced Materials (IMRAM), Tohoku University, 2-1-1 Katahira, Aoba-ku, Sendai 980-8577

First-principles calculations of electron correlation parameters to elucidate π-electron–proton coupled physical properties of the unconventional molecular conductors Cat-TTF analogues

Shun DEKURA†

Institute for Solid State Physics, The University of Tokyo,
Kashiwanoha 5-1-5, Kashiwa, Chiba 277-8581

κ-H_3(Cat-EDT-TTF)$_2$ (= H-TTF) and its analogues, which have been recently developed in our group, show unique π-electron–proton coupled physical properties owing to the strongly correlated electrons and dynamics of protons in the H-bonds.[1)] In particular, a charge-ordering (CO) phase transition coupled to the localization of D in H-bonds occurs in H/D isotope substituted analogue.[2)] The CO transition temperature varies upon the S/Se substitution in the π-electron framework and the application of physical pressure;[3,4)] however, the mechanism had not been revealed. In this study, to investigate the impact of electron correlation on the π-electron–proton coupled CO transition, the author evaluated the bandwidth *W*, on-site Coulomb repulsion *U*, and inter-site Coulomb repulsion *V* of the H-TTF analogues by first-principles DFT calculations based on the experimental X-ray structures.

All the calculations were performed on the ISSP Supercomputer System B (ohtaka). The electronic band structures were calculated by using Quantum Espresso (version 6.8), where the half-filled HOMO–HOMO antibonding band crosses the Fermi level. The maximally localized Wannier functions (MLWFs) with the shapes consistent with HOMO–HOMO antibonding orbitals were successfully obtained from the band crossing the Fermi level using RESPACK software. Then, *U* and *V* for each analogue were evaluated by the screened direct integrals between two MLWFs in the crystals. Based on the comparison of the obtained electronic parameters and CO transition temperature (T_{CO}), *W* and *V* were found to be correlated with T_{CO}. Considering that the CO transition occurs between CO and Mott insulating states, the author concluded that V plays important role to determine T_{CO} although previously H(D) in the H-bonds governs and triggers the CO transition.

References

1) H. Mori, S. Yokomori, S. Dekura, and A. Ueda, Chem. Commun. **58**, 5668 (2022).
2) A. Ueda, S. Yamada, T. Isono, H. Kamo, A. Nakao, R. Kumai, H. Nakao, Y. Murakami, K. Yamamoto, Y. Nishio, and H. Mori, J. Am. Chem. Soc. **136**, 12184 (2014).
3) A. Ueda, A. Hatakeyama, M. Enomoto, R. Kumai, Y. Murakami, and H. Mori, Chem. Eur. J. **21**, 15020 (2015).
4) A. Ueda, K. Kishimoto, T. Isono, S. Yamada, H. Kamo, K. Kobayashi, R. Kumai, Y. Murakami, J. Gouchi, Y. Uwatoko, Y. Nishio, and H. Mori, RSC Adv. **9**, 18353 (2019).

†Current address: Institute of Multidisciplinary Research for Advanced Materials (IMRAM), Tohoku University, 2-1-1 Katahira, Aoba-ku, Sendai 980-8577

Structural analysis on twist grain-boundaries

Kazutoshi INOUE[1], Mitsuhiro SAITO[2], and Yuichi IKUHARA[1,2,*]
[1] *Advanced Institute for Materials Research, Tohoku University, Sendai, Miyagi, 980-8577*
[2] *Institute of Engineering Innovation, The University of Tokyo, Yayoi, Tokyo, 113-8656*

Revealing the relationship between atomic structure and macroscopic properties is one of the most important issues in materials science. Grain boundaries (GBs) are especially important for their complex atomic structures and contribution to the properties. Historically, atomic structures of tilt GBs have been discussed by structural unit model. However, it is essential to consider the 3D atomic structure for twist GBs. The polyhedral unit model, which is an updated version of the structural unit model, rigorously describes the 3D GB atomic structure using a combination of atomic polyhedra. In this study, atomic models for [001] twist GBs in metals with $\Sigma \leq 53$ were built with a 3D periodic boundary condition. The translation models are systematically constructed by the 0.1 Å steps within the Displacement-Complete-Shift lattice to screen the stable atomic structures. Each model was firstly calculated to obtain GB energy without relaxation to screen the translation states. We applied the first-principles DFT calculations with the plane-wave basis projector-augmented wave method included in VASP to screen and determine the stable atomic structure by using cpu nodes in System B. The generalized gradient approximation was used for the exchange-correlation potentials in the Perdew-Burke-Ernzerhof form, employing an ultrasoft pseudopotential. The cutoff energy was set 400 eV for all plane-wave basis sets. The Brillouin-zone integrations were performed over a $4 \times 4 \times 1$ k-point mesh generated by the Monkhorst-Pack scheme. The GB energy is the interfacial excess free energy calculated by

$$\Delta E = \frac{1}{2A} \left(E_{\text{total}} - N\sigma_i \right),$$

where E_{total} is the total energy of the system including GBs, σ_i is the energy of the unit cell of the bulk crystal, N is the number of unit cells contained in the supercell, and A is the area of the GB. The GB energies for a fixed intergrain separation are within 0.1 J/m^2, indicating the energy landscape is almost flat. Then, atomic positions as well as the supercell volume of the most stable structure were relaxed such that all forces were $< 1.0 \times 10^{-5}$ eV/Å, and the residual force on each relaxed atom was 0.05 eV/Åunder the constant pressure of 0 Pa and constant temperature of 0 K. Then, interstitial voids in each model are calculated by Voronoi analysis, placing the sphere of maximal radius at the Voronoi vertex. The maximum diameter for each void center can be calculated within the hard sphere model and their maximum values vary from 0.30 to 0.50 in the unit of the lattice constant a_0. We show that the GB energies and the maximum void volumes have relatively high correlation, suggesting that the maximum void volume can be used to screen low energy translation states for twist GBs [1].

References

[1] K. Inoue, K. Kawahara, M. Saito, M. Kotani, Y. Ikuhara: preprint (2022).

First-Principles Lattice-Dynamics Calculations and Thermal Expansion Behavior for NASICONs

Yasuhide MOCHIZUKI[1], Takayuki NAGAI[2], Suguru YOSHIDA[3], Tsuyoshi KIMURA[2]

[1] Department of Materials Science and Engineering, Tokyo Institute of Technology, 2-12-1 O-okayama, Meguro-ku, Tokyo

[2] Department of Advanced Materials Science, University of Tokyo, Kashiwa 277-8561 Chiba, Japan

[3] Materials Research Institute, Pennsylvania State University, University Park, Pennsylvania 16802, United States

Negative-thermal-expansion materials have attracted considerable attention because they contribute to sustain the lifespan of largely expanding materials and also because of their fascinating and counter-intuitive thermal properties. The well-known and representative NTE materials are Si [1], ReO_3 [2], ScF_3 [3] ZrW_2O_8 [4] and $KZr_2P_3O_{12}$ (NASICON) [5]. Since the reports of NTE in various materials in the past few decades, it has been widely known that the mechanism for NTE is the transverse acoustic phonon modes, which have negative Grüneisen parameters. However, the detailed mechanisms for the NTE properties are uncovered ever since now. Here, we report our progress for elucidating the microscopic origin of NTE in $KZr_2P_3O_{12}$ and the relevant compounds.

Our first-principles calculations were performed by using the projector augmented-wave method [6], and the PBEsol functional within the generalized gradient approximation [7] as implemented in VASP [8]. The phonon band structures were derived from the calculated force constants using PHONOPY [9].

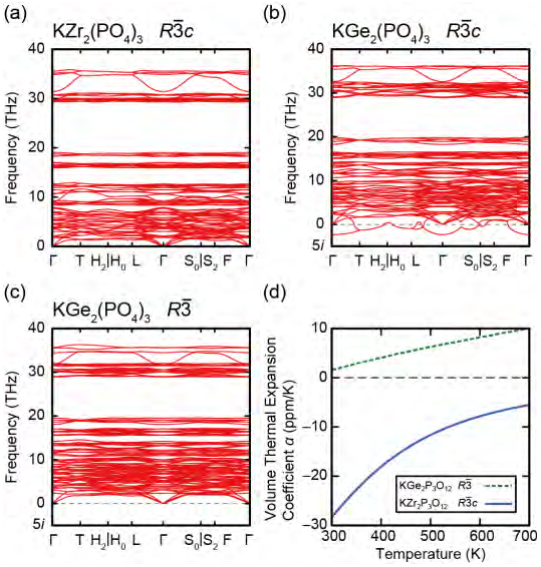

Fig. 1: Calculated phonon bands for the $R\bar{3}c$ phases of (a) $KZr_2(PO_4)_3$, (b) $KGe_2(PO_4)_3$, and the $R\bar{3}$ phase of (c) $KGe_2(PO_4)_3$. Calculated thermal expansion coefficients of $KZr_2(PO_4)_3$ and $KGe_2(PO_4)_3$ are also shown.

We present the calculation results of phonon bands for the $R\bar{3}c$ phases of $KZr_2(PO_4)_3$ (KZP) and $KGe_2(PO_4)_3$ (KGP) as shown in Fig. 1(a, b).

We can see that KZP is dynamically stable, whereas KGP is dynamically unstable. We found that the imaginary phonon mode in the $R\bar{3}c$ phase of KGP is Γ_2^+ (A_{2g}) phonon mode leading to dynamically stable $R\bar{3}$ phase, which is shown in Fig. 1(c). In our previous report, we found that the Γ_2^+ phonon mode (the rotational modes of ZrO_6 octahedra and PO_4 tetrahedra) is the most important for realizing negative thermal expansion in KZP [10] since the Γ_2^+ phonon mode has the largest negative value of Grüneisen parameter. By substituting *d*-block element Zr with *p*-block element Ge, the Γ_2^+ phonon mode became unstable because the rotational Γ_2^+ mode of GeO_6 octahedra and PO_4 tetrahedra trigger second-order Jahn-Teller effect, which lowers the electrons energy [11]. Here, as shown in Fig. 1(d), we have calculated the thermal expansion coefficients for KZP ($R\bar{3}c$ phase) and KGP ($R\bar{3}$ phase) by using quasi-harmonic approximation. We found that the $R\bar{3}$ phase of KGP has positive thermal expansion coefficients above room temperature because the Γ_2^+ phonon mode was transformed into Γ_1^+ (A_g) phonon in $R\bar{3}$, the negative Grüneisen parameter value of which was weakened.

In conclusion, we have shown that substituting Zr site with *p*-block element Ge makes the $R\bar{3}c$ phase (NASICON structure) dynamically unstable because the rotational phonon mode transforming as irreducible representation Γ_2^+ triggers second-order Jahn-Teller effect which lowers the electrons energy. Further, because the Γ_2^+ phonon mode is crucial for realizing negative thermal expansion, the lowered symmetry structure of KGP ($R\bar{3}$ phase) was transformed into a positive thermal expansion material.

References

[1] S. Biernacki and M. Scheffler, *Phys. Rev. Lett.* **63**, 290 (1989).

[2] T. Chatterji *et al.*, *Phys. Rev. B* **78**, 134105 (2008).

[3] B. K. Greve *et al.*, *J. Am. Chem. Soc.* **132**, 15496 (2010).

[4] C. Martinek and F. Hummel, *J. Am. Ceram. Soc.* **51**, 227 (1968); T. A. Mary *et al.*, *Science* **272**, 90 (1996).

[5] W. Miller et al., J. Mater. Sci. 44, 5441 (2009).

[6] P. E. Blöchl, *Phys. Rev. B* **50**, 17953 (1994).

[7] J. P. Perdew *et al.*, *Phys. Rev. Lett.* **100**, 136406 (2008).

[8] G. Kresse and J. Furthmüller, *Phys. Rev. B* **54**, 11169 (1996); G. Kresse and D. Joubert, *ibid* **59**, 1758 (1999).

[9] A. Togo and I. Tanaka, *Scr. Mater.* **108**, 1 (2015).

[10] Y. Mochizuki, S. Bae, and H. Raebiger, Activity Report of Supercomputer Center Institute for Solid State Physics 2021.

[11] T. Nagai, Y. Mochizuki, S. Yoshida, and T. Kimura, *J. Am. Chem. Soc.* **145**, 8090 (2023).

Prediction of CO Adsorption Energy on Single Atom Catalysts Embedded in TiO_2 by Machine Learning

Kyoichi SAWABE
Graduate School of Engineering, Nagoya University, Chikusa, Nagoya 464-8603

This year, we conducted a feature analysis for machine learning (ML) prediction of CO adsorption energy on single-atom catalysts (SAC) using TiO_2 substrates.

We used the VASP program for spin polarization DFT calculations. Slab units with n ($n = 2 - 6$) layers were used as models of TiO_2 surfaces. The electronic states of the SAC were modulated by changing both the thickness of the slab unit and the single metals embedded in TiO_2.

Good features for ML would require parameters of a chemically meaningful nature sufficient to describe the adsorption. In the case of CO adsorption on the SAC, σ donation, π back donation, and structural relaxation due to the adsorption are involved in the adsorption strength. Therefore, ML should use features that can describe these properties. Furthermore, data with a sufficient variation of these features must be used for ML. The σ donation is related to the Lewis acidity of the adsorption site. The strength of CH_3CN adsorption is often used experimentally and theoretically in order to measure the strength of Lewis acidity. Therefore, we calculated the strength of CH_3CN adsorption on SACs. A linear regression of CO adsorption energy, $E_{ads}(CO)$, on r-TiO_2 (rutile type TiO_2) with respect to $E_{ads}(CH_3CN)$ was obtained with good accuracy, as shown in Fig. 1a. This means that σ donation is dominant for the CO adsorption on r-TiO_2. In other words, information on π back donation and structural relaxation was not available in the CO adsorption data on r-TiO_2. Applying the learning model obtained with the CO/r-TiO_2 data to the case of CO/a-TiO_2 (anatase type TiO_2), we obtained Figure 1b, in which the deviation of data points from the straight line of the prediction model appears as CO adsorption becomes stronger. Thus, the features of π back donation and structural relaxation for the CO adsorption can be extracted from the additional data for a-TiO_2.

By eliminating the parameters that are highly correlated with each other using a Lasso regression, etc., a multiple linear regression (MR) model shown in Figure 1c was obtained. We used six parameters: $E_{ads}(CH_3CN)$, Charge, melting point, the heat of melting, crystalline system, and RMO, which is the distance between the embedded metal and the horizontally neighboring oxygen. Although the melting point and the heat of melting do not appear to have any chemical significance for CO adsorption, the above analysis indicated that they relate to the π back donation and/or the structural relaxation.

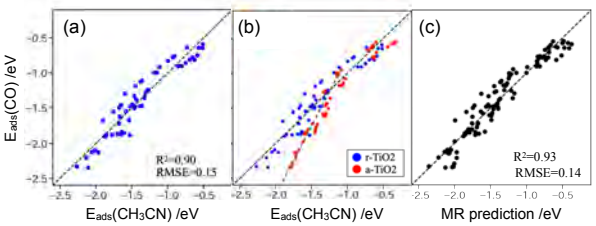

Figure 1: Linear regression model for $E_{ads}(CO)$ on (a) r-TiO_2 and (b) both r-TiO_2 and a-TiO_2 using $E_{ads}(CH_3CN)$. (c) Multiple linear regression model.

Quantum transport theory based on large-scale first-principles electron transport calculations

NOBUHIKO KOBAYASHI
Department of Applied Physics, University of Tsukuba
1-1-1 Tennodai Tsukuba Ibaraki 305-8573

Analysis of transport properties from the atomistic level is an important issue from the viewpoint of materials science and technology. The purpose of this project is to analyze and predict the transport properties of materials from first-principles. We have developed the nonequilibrium Green's function (NEGF) method and the O(N) time dependent wave-packet diffusion (TD-WPD) method on the basis of the density functional theory (DFT). By using these methods, we have investigated charge, head and spin transport properties of materials. [1]

We have developed a Simulation code for Atomistic Kohn-sham Equation (SAKE) for the ab-initio electron transport calculation based on the DFT and NEGF formalism. [2] We have applied the method to analysis of thermoelectricity of Heusler compounds, chalcopyrite, and skutterudites. High performance systems are designed based on analysis of electronic structures and thermoelectric properties.

Organic semiconductors have attracted much attention for their applications to flexible, printable, lightweight, and low-cost electronic devices. They are crystals that are assemblies of π-conjugated molecules weakly bonded by van der Waals interactions, and electron transport properties are significantly influenced by electron-phonon interactions. We developed the O(N) TD-WPD method for the quantum transport calculation of huge systems of up to 100 million atoms a decade ago, and have been applied organic semiconductors. [3] It is possible to calculate the conductivity and the mobility of the system with micron-order lengths at room temperature at the atomistic levels, and also to analyze the transport properties of materials weakly bonded by van der Waals interactions. The electron and hole mobilities of the pentacene thin-film are calculated taking the effect of intramolecular vibrations on both the partially dressed polaron and the dynamic disorder into consideration by using TD-WPD method. It is demonstrate that electron mobility in high-mobility organic semiconductors is indeed limited by polaron formation. [4]

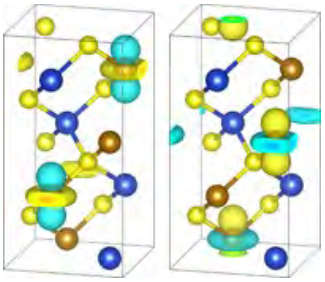

Figure 1: Wavefunctions of chalcopyrite CuFeS2.

References

[1] N. Kobayashi, H. Ishii, K. Hirose, in *3D Local Structure and Functionality Design of Materials* eds H. Daimon, Y. C. Sasaki (World Scientific, 2018) p133.

[2] H.Takaki, N.Kobayashi, K.Hirose, *J. Phys.: Condens. Matter.* 32 325901(2020)

[3] H. Ishii, S. Obata, N. Niitsu, S. Watanabe, H. Goto, K. Hirose, N. Kobayashi, T. Okamoto, and J. Takeya, *Sci. Rep.* 10, 2524 (2020)

[4] H. Sato, S. A. Abd. Rahman, Y. Yamada, H. Ishii and H. Yoshida *Nat. Mater.* 21, 910 (2022).

First-principles simulation of interfacial reactions using density functional theory and classical liquid theory

Minoru OTANI
Center for Computational Sciences, University of Tsukuba
1-1-1, Tenno-dai, Tsukuba, Ibaraki 305-8577, Japan

The electrochemical properties at the interface between electrode and electrolyte have much attention to improving the electrochemical performances of rechargeable batteries, fuel cells, and electrochemical catalysts. Because the electrochemical properties depend on the material properties constructing the electrochemical interface and environmental parameters such as the bias voltage, an exhaustive study is indispensable to understand the details of physical phenomena at the electrochemical interfaces.

To simulate the physical phenomena at the electrochemical interface, we have continuously developed the ESM-RISM method [1] that combines density functional theory using the effective screening medium technique (ESM) [2] and reference interaction site model (RISM) [3]. In this method, we treat the electrode surface and the reactants using the quantum mechanical theory and the solvation system using the classical solution theory. The electrostatic and van der Waals-type potentials describe the interaction between the quantum mechanical particles and classical solution. Because ESM-RISM is formulated under the grand-canonical ensemble, we can naturally address the formation of an electric double layer at the electrochemical interface using the half-cell system.

Although the modeling of the ESM-RISM method is physically reasonable, there is a well-known drawback of the RISM theory that underestimates the dielectric constant of a solution with dipolar solvent molecules. The dielectrically consistent RISM (DRISM) is one of the solutions to overcome the drawback of the RISM theory. This year, we have combined DRISM with the ESM-RISM framework to increase the accuracy of electrochemical interface simulations and applied it to the Pt(111)/aqueous water interface as a benchmark calculation [4].

First, to check the results of DRISM, we calculated the salt-concentration dependence of the activity coefficients for the bulk NaCl aqueous solution. The results of the conventional RISM underestimate the activity coefficients compared to the experiment, but DRISM well reproduces the experiment. Thus, DRISM improves the dielectric properties of the bulk solution. The results of electrochemical properties at the interface, such as the potential of zero charges, standard hydrogen electrode potential, double-layer capacitance, and thickness of the contact layer, are improved by DRISM and in reasonable agreement with the previous experiments and theories.

Further application results such as the theoretical analysis of oxide electrode degradations and the electrochemical catalysts will be reported elsewhere.

References

[1] S. Nishihara and M. Otani: Phys. Rev. B **96**, 115429 (2017).

[2] M. Otani and O. Sugino: Phys. Rev. B **72**, 115407 (2006).

[3] A. Kovalenko and F. Hirata: Chem. Phys. Lett. **290**, 237 (1998).

[4] S Hagiwara, S Nishihara, F Kuroda, and M Otani: Phys. Rev. Mater. **6**, 093802 (2022).

Theory of tunneling currents at semiconductor pn junctions in electric fields based on first-principles calculation

Takashi NAKAYAMA
Department of Physics, Chiba University
1-33 Yayoi, Inage, Chiba 263-8522

The tunnel field-effect transistor (TFET) is one of promising candidates for future energy-saving devices, due to its much steeper on-off switching features compared to conventional MOS FETs. Recently, we showed by the first-principles and one-dimensional wave-packet model calculations that the cooping of Al and N atoms around the Si-pn junctions produces impurity states in Si band gap and such states make the resonance with conduction-band states under the electric field of pn-junction, which shortens the tunneling length between p- and n-Si layers and markedly increases tunneling currents, in agreement with experiments.

The purposes of this work are to study (i) the tunneling current at Al-N co-doped Si-pn junctions by the three-dimensional more realistic calculations and (ii) how such tunneling current changes by the N-atom doping into the pn junctions made of direct band-gap semiconductors such as InP.

We consider the (100)-directed 2x2 pn junctions with 104 atom-layers of 5 typical semiconductors like Si and InP, as shown in Fig.1. The N-atom impurity is inserted in this junction. To simulate electronic structures of pn junctions, we adopt the conventional $sp^3d^5s^*$ tight-binding model, whose parameters are determined so as to reproduce electronic structures by the first- principles hybrid-DFT calculation. The calculation of the tunneling currents are performed using the non-equilibrium Green's function (NEGF) method, where the semi-infinite electrodes are attached to the left and right sides of the present junction in Fig.1.

Figures 2(a)-(b) show calculated tunneling currents as a function of the electric field, for Si, Ge, and GaP, and for InP and GaAs, respectively.

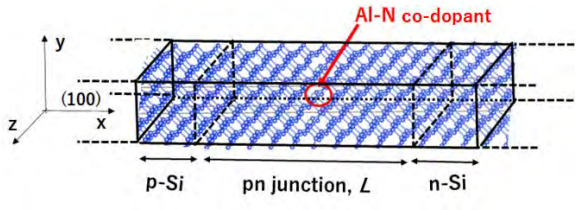

Fig.1. Schematic view of Al-N doped (100) Si-pn junction employed in this work.

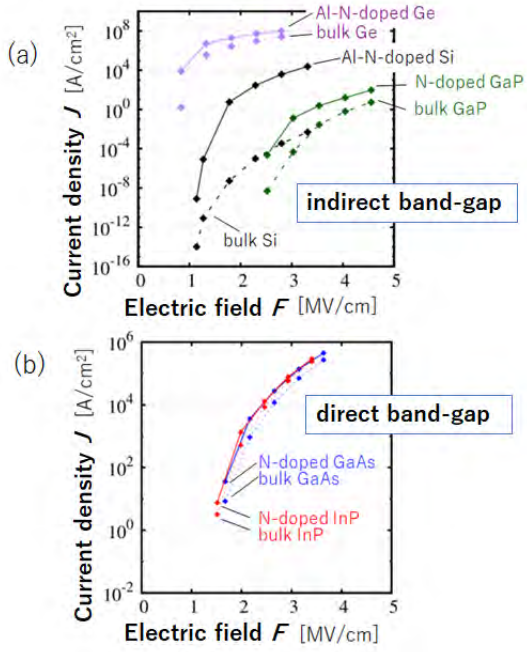

Fig.2. Calculated tunneling current as a function of electric field in pn junctions made of (a) Al-N-doped Si and Ge and N-doped GaP, and (b) N-doped GaAs and InP. The results for non-doped cases are also shown by dashed lines.

Here, both the currents in the cases with and without Al-N/N impurity atoms are shown. It is clearly seen that the Al-N/N-atom doping markedly increases the current by about 10^2-10^7 times for the former indirect band-gap systems, while induces a slight current change for the latter

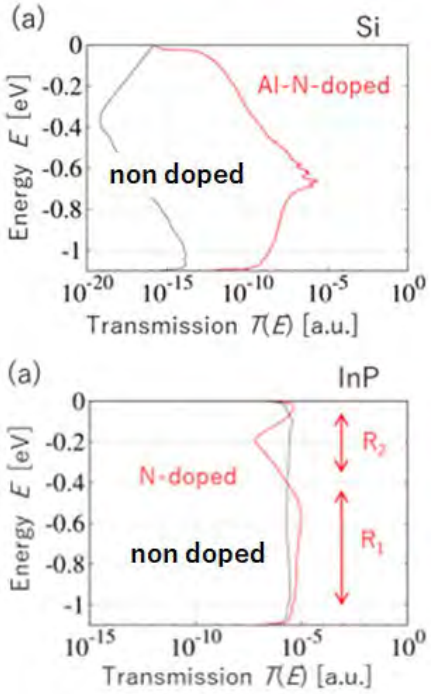

Fig.3. Calculated transmission spectra across pn junctions with and without Al-N/N impurity atoms by red and black lines, respectively, as a function of the energy in the tunneling energy window, for (a) Si and (b) InP.

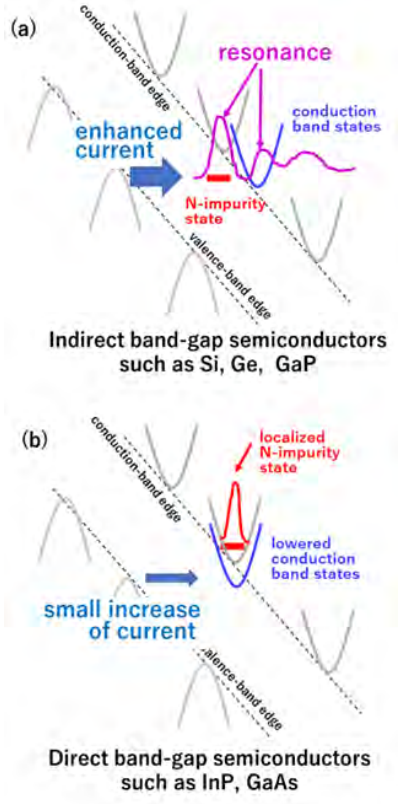

Fig.4. Schematic pictures to explain the effects of Al-N/N-atom doping on tunneling currents at pn junctions made of (a) indirect band-gap semiconductors like Si, Ge, and GaP, and (b) direct band-gap ones like InP and GaP.

direct band-gap systems.

To clarify the origin of current enhancement, we show in Fig.3(a) the transmission spectra of electrons for Si. It is seen that the transmission becomes much larger when impurity atoms are present, and its spectra have an extremely large peak around E=-0.66. By analyzing the local density of states around the pn junction, as shown in Fig.4(a), we found that the electric field in pn junctions produces the resonance between isolated Al-N/N states in the band gap and conduction-band states. These resonance states shorten the tunneling length and markedly enhances the tunneling current, which is in good agreement with experiments.

With respect to direct band-gap systems, we show in Fig.3(b) the transmission spectra for InP. It is seen that the transmission spectra have flat shape not depending on the energy without impurities, while they show small modulation around E=-0.4eV for the N-doped junctions. We found that, since the N-impurity states are located in the conduction bands for the direct band-gap systems as shown in Fig.4(b), the impurity doping only modulates the bands of host semiconductors, resulting in the slight change of tunneling currents.

All these calculations were performed using the xTAPP, VASP, and our original pspwf and NEGF codes. In order to realize the calculations for the present pn-junction systems, because the system is made of a large number of atoms (1000-2000 atoms), the advanced computing facility having multi-task and higher-speed CPU (more than 1280 cores × 2.0G Hz), larger-size memory (around 256GB), and larger-size strange (more than 2 TB) is indispensable. These conditions are realized only by the present ISSP supercomputing systems.

Data-driven materials development using anharmonic phonon database

Masato OHNISHI

Department of Mechanical Engineering, The University of Tokyo, Japan

In recent years, Materials Informatics (MI) technology, which integrates informatics and materials science, has been rapidly developing. However, there is still a lack of databases for anharmonic phonon properties, which are crucial for the development of thermal functional materials, such as thermal insulators, thermoelectric materials, and thermal interface materials. In addition, because mechanical properties are closely linked to phonon properties, atomic vibrations, the availability of an anharmonic phonon property database would be valuable also for the design and development of various structural materials.

In this project, we have been developing an anharmonic phonon property database (APDB) for data-driven materials development. During the previous fiscal year (April 2022 to March 2023), we focused on establishing an automated workflow for calculating the thermal conductivity of the stable materials, those without negative (imaginary) phonon frequencies, in Phonondb[1]. We also generated thermal conductivity data for many materials using the developed automation code.

The developed automation code, written in Python, efficiently handles crystal structures and calls first-principles software (VASP[2]) and phonon analysis software (ALAMODE[3]). The established workflow is illustrated in Figure 1. Although multiple processes are involved in the entire calculation, the most computationally expensive one is calculating forces using the first-principles approach. As we aim to analyze

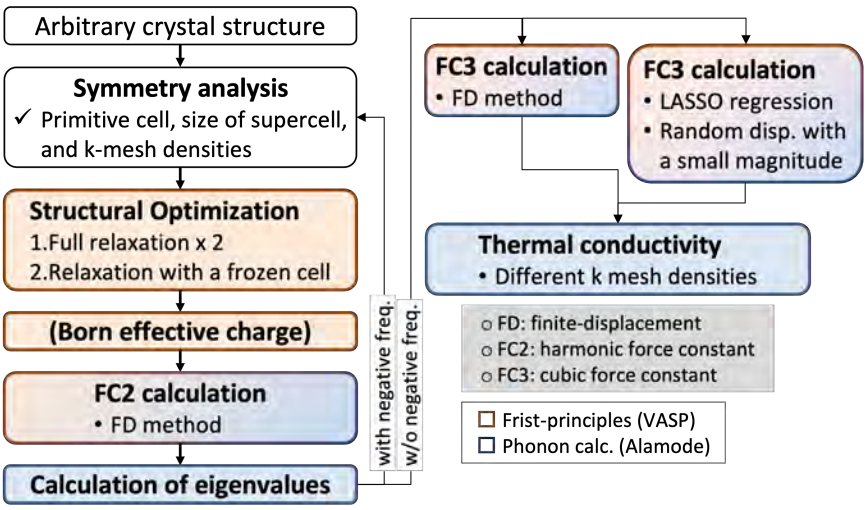

Fig. 1 Workflow for the automation calculation of anharmonic phonon properties

many materials, parallelizing the calculation for each material is unnecessary. Instead, the "bulk" job, which allows the submission of numerous similar jobs as a single job, is optimal for our simulation. Using the "bulk" job, we can analyze up to 144 materials simultaneously in ISSP supercomputer. As a result, we have calculated thermal conductivities for approximately 2,000 materials using the ISSP supercomputer as well as HPCI supercomputers. Moreover, we have shared the developed automation code with collaborators worldwide so that they can also work on data generation.

After finishing the calculation for the stable materials in Phonondb in the fiscal year of 2023, we will release the developed database with computational details. The released database should allow easy accessibility to anharmonic phonon properties, enabling accurate prediction of material properties as well as material design for target properties.

References

[1] Togo, http://phonondb.mtl.kyoto-u.ac.jp.

[2] G. Kresse and J. Hafner, Phys. Rev. B 47 , 558 (1993); ibid. 49 , 14 251 (1994).

[3] T. Tadano, Y. Gohda, and S. Tsuneyuki, J. Phys.: Condens. Matter 26, 225402 (2014)

Impurity effects on TiO_2 and X-ray emission spectra of molecules by all-electron *GW* calculations using TOMBO

Kaoru OHNO

Graduate School of Engineering, Yokohama National University

79-5 Tokiwadai, Hodogaya-ku, Yokohama 240-8501

We found a new stable phase of anatase TiO_2 codoped with C and N having a relatively small band gap in our *GW* calculations [1] using the all-electron mixed basis program, TOMBO, which uses both plane waves and numerical atomic orbitals as basis functions [2]. Under intermediate oxygen pressure, the band gap of TiO_2 codoped with C and N was found to be 2.28 eV. Therefore, this phase can be used as a visible-light-response photocatalyst.

The initial state of X-ray emission spectroscopy (XES) and resonant inelastic X-ray scattering (RIXS) is an excited eigenstate with a deep core hole after the X-ray photoelectron spectroscopy (XPS) and X-ray photoabsorption spectroscopy (XAS), so that their calculations offer a good example of extended quasiparticle theory (EQPT) [3] in many-body perturbation theory (MBPT). Moreover, to overcome the basis set incompleteness problem, we adopt the all-electron mixed basis program, TOMBO. Here we applied the one-shot *GW* + Bethe--Salpeter equation (BSE) approach in MBPT to this problem on the basis of EQPT and analyze XES and RIXS energies for CH_4, NH_3, H_2O, and CH_3OH molecules [4]. Figure 1 shows the RIXS spectra of a CH_3OH molecule calculated by our method together with the experimental data [5]. The agreement is excellent without introducing any empirical fitting parameter.

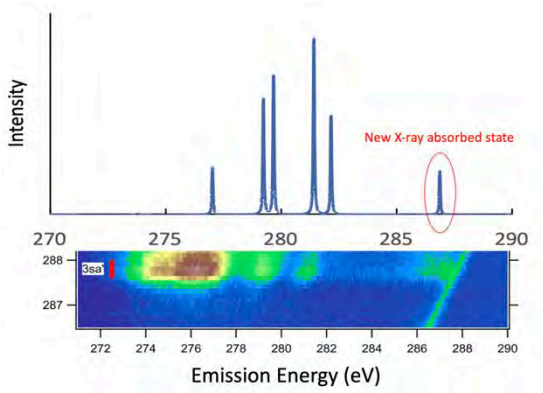

Fig. 1: Calculated [4] (above) and experimental [5] (below) RIXS spectra of a CH_3OH molecule.

References

[1] T. Ishikawa, R. Sahara, K. Ohno, K. Ueda, & T. Narushima: Comp. Mat. Sci. **220** (2023) 112059.

[2] S. Ono, Y. Noguchi, R. Sahara, Y. Kawazoe, & K. Ohno, Comp. Phys. Comm. **189** (2015) 20.

[3] K. Ohno, S. Ono, & T. Isobe: J. Chem. Phys. **146** (2017) 084108.

[4] K. Ohno & T. Aoki: PCCP **24** (2022) 16586.

[5] A. Benkert, F. Meyer, D. Hauschild, M. Blum, W. Yang, R. G. Wilks, M. Bär, F. Reinert, C. Heske & L. Weinhardt,: J. Phys. Chem. A **120** (2016) 2260.

Development of a first-principles calculation software for a many-body wave function theory

Masayuki OCHI
Forefront Research Center, Osaka University
1-1 Machikaneyama-cho, Toyonaka, Osaka 560-0043

We have developed a first-principles electronic structure calculation software using the transcorrelated (TC) method [1, 2]. The TC method is a many-body wave function theory, where Hamiltonian is similarity-transformed with the Jastrow correlation factor. By this transformation, electron correlation effects are efficiently considered. In particular, one-electron orbitals in the Jastrow-Slater-type wave function can be optimized in the same manner as the Hartree–Fock (HF) method, to say, by solving a one-body self-consistent-field (SCF) equation. It is advantageous that the computational cost for this process is the same order as that for the HF method [3].

In this year, we have published our computational code TC++ on github [4] together with its technical details [5], including efficient treatment of the three-body interactions included in the similarity-transformed Hamiltonian and accurate correction terms for the divergence of the effective potentials in the reciprocal space. One can perform the TC calculation using TC++ by reading some output files dumped by DFT calculation using the Quantum-Espresso package [6]. TC++ supports the following functionalities: HF, TC, and biorthogonal TC (BITC) calculations, SCF and band calculations, solids and homogeneous electron gas, a plane-wave-basis set, and norm-conserving pseudopotentials. At present, the Jastrow factor has a simple random-phase-approximation-type form, but TC++ will support more general types of the Jastrow factor soon. Calculation is MPI-parallelized for the k-point and band indices. Using supercomputers of ISSP, we have performed several test calculations on several kinds of solids, to check the applicability of our code and verify the accuracy of calculated quantities, e.g., a band structure and a total energy. As reported in our previous studies (e.g., [3]), calculated band gaps are more accurate than LDA and GGA, but the total energy is at present less accurate. Now we have tested the accuracy using a polynomial-type Jastrow factor including a larger number of optimizable parameters.

References

[1] S. F. Boys and N. C. Handy, Proc. R. Soc. London Ser. A **309**, 209 (1969); *ibid.* **310**, 43 (1969); *ibid.* **310**, 63 (1969); *ibid.* **311**, 309 (1969).

[2] N. C. Handy, Mol. Phys. **21**, 817 (1971).

[3] M. Ochi, K. Sodeyama, R. Sakuma, and S. Tsuneyuki, J. Chem. Phys. **136**, 094108 (2012).

[4] https://github.com/masaochi/TC

[5] M. Ochi, Comput. Phys. Commun. **287**, 108687 (2023).

[6] https://www.quantum-espresso.org/

Development of Polymer Electret Materials for Energy Harvesting Using Machine Learning

Yucheng ZHANG, Zeitan MAO, Kuniko SUZUKI, and Yuji SUZUKI

Department of Mechanical Engineering

The University of Tokyo, Hongo, Bunkyo-ku, Tokyo 113-8656

Electret is a dielectric material with quasi-permanent charges and can trap charges stably for decades. Vibrational electret energy harvester (VEEH) can generate electricity efficiently from kinetic energy via the electrostatic induction. The VEEH with bipolar (both positively and negatively charged) electret leads to four times output power theoretically, thus specifying the importance of designing high-performance bipolar polymer electrets.

CYTOP (Cyclic Transparent Optical Polymer, AGC Chemicals) is one of the best polymer electret materials as shown in Fig. 1. Recently, we utilized quantum chemical analysis for evaluating the charge trap of CYTOP electrets [1]. It is found that although the repeat-unit-number of CTX-A is above 1000, the trapped charge is localized at the amide bond, which is formed by dehydration reaction between the carboxyl end group and the amine introduced.

Recently, by employing the de novo molecule generation and the functional group enrichment analysis, we successfully proposed the electret CTX-A/APDEA with high bipolar charging performance via combining CTX-A with N-(3-aminopropyl) diethanolamine [2].

This result encouraged us to move further to search new amines in the open-source database PubChem, aimed at designing better bipolar polymer electret based on CYTOP CTX-A after the dehydration reaction. It is also shown that the ionization potentials (IPs) computed by the density functional theory (DFT) with polarizable continuum model (PCM) correction agree well with the trends of the surface charge density and charge stability measured by the wet experiments [3,4].

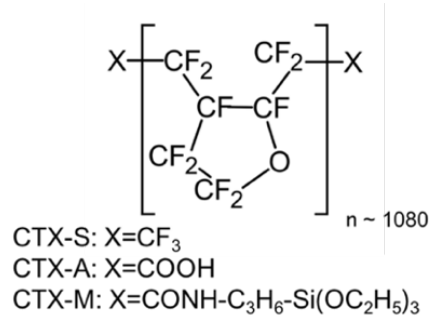

Fig. 1. Chemical structure of CYTOP series.

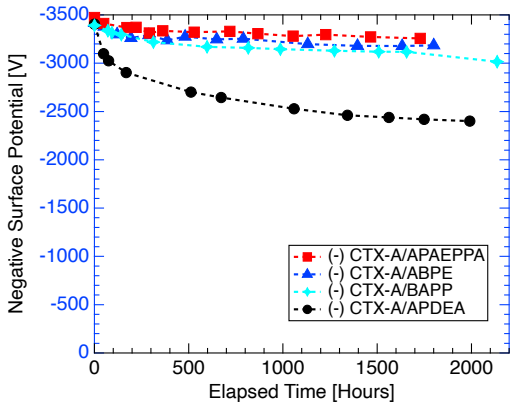

Figure 2. Surface potential decay versus elapsed time for negatively-charged with -3.5 kV, stored under room temperature.

To prepare the labeled data, 5522 amines were initially sampled from the PubChem. Thereafter, the virtual dehydration reaction was conducted and PCM-DFT computation was automatically made. Subsequently, 80% of the data for solid-state IPs and the information on molecules and bonds was employed to teach the deep learning model named MEGNet [5]. Two sets of the data (10 % each) were used as the validation/test sets. As a result, the mean absolute error (MAE) of solid-state IP is found to be as small as 0.326 eV. The computational cost with this approach is significantly lower than PCM-DFT, enabling rapid screening of huge databases to find candidates for new high-performance bipolar polymer electrets.

We also made another MEGNet to predict the boiling point, because the amines should not be evaporated at the thermal curing temperature of the CYTOP polymer.

Candidates are re-examined with PCM-DFT to get accurate solid-state IP. Three amines APAEPPA, ABPE, and BAPP have finally been selected. Figure 2 shows the surface potential for those films (15 μm in thickness) after charging to -3.5 kV. It is found that the materials obtained in this study are superior to our previous CTX-A/APDEA in terms of charge stability [4].

All the quantum chemical calculations are made with the software GAUSSIAN [5] at the DFT level with the CAM-B3LYP functional and 6-31+G(d,p) basis set, while PCM is combined for solid-state analysis due to the solvation effect correction.

This work was partially supported by JST CREST Grant Number JPMJCR15Q3 and JPMJCR19Q1. The calculations are performed with SGI ICE XA ISSP system B with 1 node (24 CPUs).

References

[1] Kim S., et al., J. Phys. Chem. B, Vol. 124, No. 46, pp. 10507-10513 (2020).

[2] Zhang, Y., et al., Appl. Phy. Lett., 118, 223904 (2021).

[3] Mao, Z., et al., IEEE Conf. Electr. Insul. Dielectr. Phenom., pp. 667-670 (2021).

[4] Mao, Z., et al., Adv. Mater., submitted.

[5] M. Frisch et al., “Gaussian 09, Rev. A. 1,” Gaussian, Inc. Wellingford, CT, (2009).

Design and Understanding of Catalysts Realized by Theory and Machine Learning

Hao Li

Advanced Institute for Materials Research (WPI-AIMR),

Tohoku University, Sendai 980-8577, Japan

1. Introduction

Catalyst design is essential for realizing a sustainable society. However, it is sometimes challenging due to the complicated reaction networks and surface phases under reaction conditions. To address this challenge, *ab initio* calculations, molecular dynamics, and microkinetic modeling can help better understand the reaction and make predictions.

2. Computational Methods

In this project, DFT calculations were performed using VASP with the exchange–correlation energetics described by the Perdew, Burke, and Ernzerhof (PBE) or the revised PBE (RPBE) functional. The generalized gradient approximation was employed. Ion–electron interactions were described by the framework of projector-augmented plane-wave method. The energy cutoff was set to at least 400 eV. Spin-polarization was included when necessary. Brillouin zone was sampled by the Monkhorst-Pack method. Transition states were located by the climbing-image nudged elastic band.

3. Results and Discussion

3.1. Surface state analysis

Due to the equilibrium between water and adsorbate, the surface state of an electrocatalyst is usually different from its pristine form at operating conditions. Meanwhile, the electrochemical surface state of a catalyst is essential in determining the catalyst activity. In this project, we analyzed the surface states of typical transition metal X-ides (TMXs) and emerging M-N-C catalysts, and found that their catalytic surfaces generally differ from their stoichiometric forms [1-2]. A typical example is shown in Fig. 1, where the surfaces of dual-atom M-N-C are usually pre-covered [1]. These show that we should probe the surface state before analyzing the electrocatalytic activity.

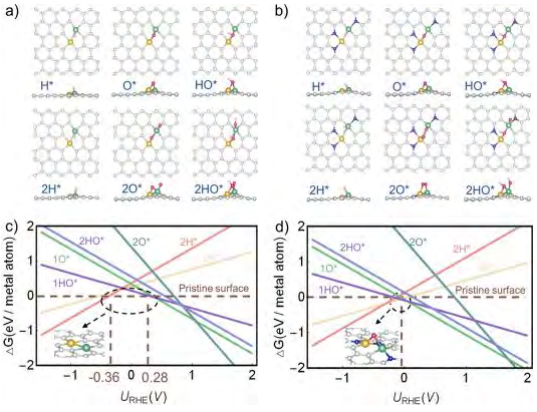

Fig. 1: Examples of the calculated surface Pourbaix diagrams of dual-atom M-N-C catalysts. (a-b) Optimized structures. (c-d) Surface Pourbaix diagrams. Reprinted with

permission from Ref. [1].

3.2. Catalysis theory development

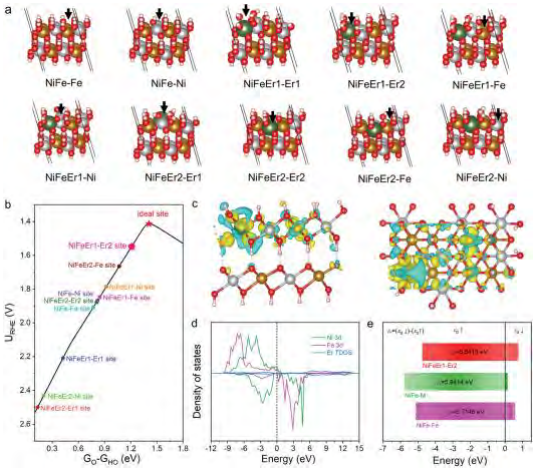

Fig. 2: (a) The Er-NiFe-LDH considered for simulations. (b) Microkinetic modeling to analyze OER activities of various sites at Er-NiFe-LDH. (c) Charge density differences. (d) Projected density of states. (e) Calculated spin-polarized *d*-band centers of different systems. Reprinted with permission from Ref. [3].

We also analyzed various catalysts and their performances based on catalysis modeling. The analyzed catalyst systems include TMXs and single-atom catalysts. The analyzed reactions include oxygen evolution (OER) [3], oxygen reduction [4], and nitrogen reduction [5]. An example is shown in Fig. 2 [3], in which we analyzed the OER activities of Er-doped NiFe layered double-hydroxide (LDH). Besides, we also studied thermal catalysis, such as Hg^0 oxidation.

3.3. Machine learning (ML) analysis

In addition to DFT-based analysis, this project performed explainable ML modeling to identify the role of element La as the active center of ORR in alkaline media [6]. Based on ~7800 experimental data, we derived the key role of La and found that those materials with La could possess good ORR performance. These show that ML can not only provide prediction, but also unravel the structure-performance relation of electrocatalysts.

4. Conclusion

Through this ISSP project, we performed comprehensive analyses to understand some promising electrocatalytic materials. We found that surface state is an essential factor in electrocatalysis that should not be dismissed before the activity analyses of many catalysts. Also, explainable ML can help identify the critical factor of a material in electrocatalysis.

References

[1] W. Yang, J. He, B. Zhou, L. Wei, Z. Gao*, H. Li, Commun. Chem. **6**, 6 (2023).

[2] H. Liu, X. Jia, A. Cao, L. Wei, C. D'agostino, H. Li, J. Chem. Phys. **158** (2023).

[3] Y. Zhu, X. Wang, X. Zhu, Z. Wu, D. Zhao, F. Wang, D. Sun, Y. Tang, H. Li, G. Fu, Small, **19**, 5 (2023).

[4] C. Liu, Z. Yu, F. She, J. Chen, F. Liu, J. Qu, J. M. Cairney, C. Wu, K. Liu, W. Yang, H. Zheng, Y. Chen, H. Li, L. Wei, Energy Environ. Sci. **16**, 446 (2023).

[5] Y. Zhang, Z. Yu, F. She, L. Wei, Z. Zeng, H. Li, J. Colloid Inter. Sci. **640**, 15 (2023).

[6] R. Zhao, Z. Chen, Q. Li, X. Wang; Y. Tang, G. Fu, H. Li, J-M. Lee, S. Huang, Chem. Catal. **2**, 3590 (2022).

First principles study of the adsorption structure of helicene on the Ag(111) surface

Yuji HAMAMOTO

Department of Precision Engineering, Graduate School of Engineering

Osaka University, Yamada-oka, Suita, Osaka 565-0871

Molecular chiral recognition has drawn growing attention due to its importance in biochemistry and pharmacology, and has been studied using a model system composed of chiral molecules adsorbed on a solid surface. The molecular adsorption structure provides a key to the origin of chiral recognition, whereas its detail is beyond the reach of experimental techniques such as scanning tunneling microscopy.

Here we resort to density functional theory (DFT) calculations to investigate the adsorption structure of 7-thiaheterohelicene (7TH) on the Ag(111) surface. Although 7TH forms a one-dimensional chain on Ag(111), we focus on single molecule adsorption to clarify the interaction of the S atoms of 7TH with the Ag surface. The van der Waals interaction between 7TH and Ag(111) is considered by using the van der Waals density functional (vdW-DF) method [1] and the rev-vdW-DF2 functional [2].

We first estimate the adsorption site and orientation of a 3TH molecule on Ag(111). The optimal site and orientation for 3TH are used to make an initial guess on the local structure of 7TH near Ag(111). We then optimize the adsorption height and relax the whole system to determine the adsorption structure of 7TH on Ag(111). The adsorption structure shown in Fig. 1 indicates that 7TH physisorbs on Ag(111), i.e., the S atoms play a minor role in the molecular adsorption. This allows us to use classical molecular dynamics (MD), which is computationally much cheaper than DFT, to investigate the formation of a 7TH chain on Ag(111). The results for the MD simulations will be discussed in more detail elsewhere [3].

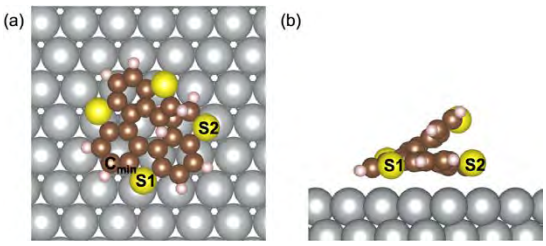

Fig. 1: Adsorption structure of 7TH on Ag(111). Top (a) and side (b) views are shown.

References

[1] M. Dion, H. Rydberg, E. Schröder, D. C. Langreth, and B. I. Lundqvist, Phys. Rev. Lett. **92**, 246401 (2004).

[2] I. Hamada, Phys. Rev. B **89**, 121103(R) (2014).

[3] C. Ye et al., in preparation.

Global search for metastable structures of silicene on the Ag(111) surface by Gaussian process regression

Yuji HAMAMOTO

Department of Precision Engineering, Graduate School of Engineering

Osaka University, Yamada-oka, Suita, Osaka 565-0871

Silicene, a silicon analog of graphene, has been intensively studied in the last decade, because of its peculiar phenomena, as well as its better compatibility with the silicon-based electronics than graphene. Density functional theory (DFT) calculations reveal that freestanding silicene is characterized by the alternately buckled honeycomb lattice, whereas silicene grown on the Ag(111) surface exhibits a variety of nontrivial buckling patterns, which makes it difficult to theoretically predict stable structures of silicene on Ag(111). To overcome the difficulty, we here adopt a structure search method based on an evolutionary algorithm (EA) and the Gaussian process (GP) regression [2]. This method accelerates the structure search by relaxing the structures generated with EA, using the energy landscape predicted with GP instead of that obtained by computationally expensive DFT calculations.

Our results demonstrate that the method not only reproduces the well-known buckled structures of silicene on Ag(111), but also predict new structures that have never been reported as far as we know. For example, our results predict at least seven phases for the $\sqrt{13} \times \sqrt{13}R19.1°$ unit cell relative to Ag(111), which are classified into type-II [Figs. 1(a)-1(c)] and type-I [Figs. 1(d)-(g)] phases based on the angle between the Ag[110] and Si[110] directions. The type-I phases are characterized by one, two, or three protruded Si atoms, and are energetically comparable with each other. These behaviors are analogous to the so-called T phase, whose structures is hard to identify experimentally and still under discussion.

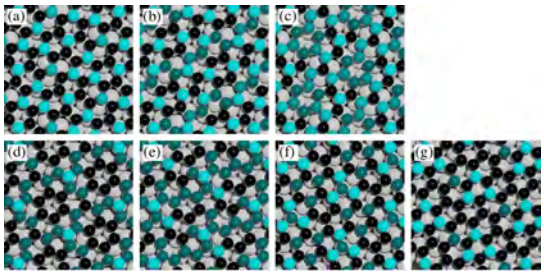

Fig. 1: $\sqrt{13} \times \sqrt{13}R19.1°$ phases obtained with the structure search method. The bright (dark) cyan balls denote higher (lower) Si atoms.

References

[1] K. Takeda and K. Shiraishi, Phys. Rev. B **50**, 14916 (1994).

[2] M. K. Bisbo and B. Hammer, Phys. Rev. Lett. **124**, 086102 (2020).

High-accuracy machine-learning interatomic potential and massively large-scale molecular simulation for microscopic mechanisms of grain-boundary-dislocation interactions

Tatsuya YOKOI

Department of Materials Physics

Nagoya University, Furo-cho, Chikusa-ku, Nagoya, Aichi, 464-8601

In polycrystalline metals and alloys, grain boundaries (GBs) exist and generally interact with dislocations, thereby having great impacts on mechanical properties though GB strengthening. It is thus essential to understand the relationship between GB structures, their interaction with dislocations and mechanical properties at various length scales, with the goal of optimal design of polycrystalline microstructure in metals and alloys.

For this purpose, previous theoretical studies performed large-scale molecular simulations based on classical empirical interatomic potentials, in order to determine atomic structure and energetics at GBs. However, their adjustable parameters are fitted only to bulk properties without consideration of atomic environments of GBs. This often leads to critical errors in predicting atomic structures and energetics of these lattice defects. In addition, classical empirical potentials are typically based on simple analytic functions and thus show limited transferability to various atomic environments for lattice defects.

To tackle the above issue, this work constructed an artificial-neural-network (ANN) interatomic potential and combined it with molecular simulations. For a preliminary analysis, aluminum was chosen as a model system [1,2]. The ANN potential was used to predict favorable atomic structures and energetics for symmetric tilt GBs. The predicted results were then validated by performing density-functional-theory (DFT) calculations.

As illustrated by Fig. 1, the ANN potential was constructed by following the architecture reported by Behler and Parinello [3] and Behler [4], with two hidden layers each having 48 nodes.

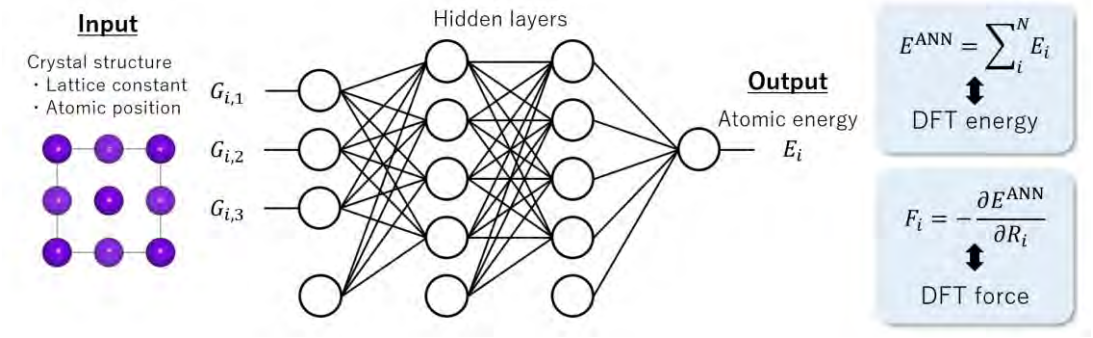

Fig. 1 Schematic illustration of an ANN potential.

Two- and three-body symmetry functions were employed to encode the atomic environment of each atom and to provide the input value for the ANN potential. In order to generate training datasets, DFT calculations were performed using the projector augmented wave (PAW) method in the VASP [5,6]. The exchange-correlation energy was calculated using a revised version of the generalized gradient approximation parameterized by Perdew, Burke and Ernzerhof (GGA-PBEsol) [7].

In order to cover a wide range of atomic environments, not only single crystals but also lattice defects including point defects, surfaces and GBs were used as references for generating the training datasets. With those reference structures, structural relaxation and molecular dynamic simulations were performed, and snapshots were extracted from the calculated results. The total potential energy and atomic force were used as the training datasets. The ANN potential was trained using an extended Kalman filter and then combined with structural relaxation and molecular dynamics.

It was found that all training datasets exhibit sufficient small errors, including the GBs in the training datasets. The mean absolute errors (MAEs) were evaluated to be 1.46 meV/atom and 17.1 meV/Å for the total energies and atomic forces, respectively, which are comparable to previous studies. It is thus expected that the present ANN potential exhibits an excellent accuracy to predict GBs.

Then structural relaxation calculations with the ANN potential were performed to predict the relationship between atomic structures and GB energies for symmetric tilt GBs with the $[001]$ and $[\bar{1}10]$ rotational axes. The predicted atomic structures were used to perform DFT calculations and to calculate their GB energies in the DFT level. As a result, the ANN potential is found to accurately predict GB energies from low to high energy states for all the GBs examined. In addition, the lowest-energy structures predicted by the ANN potential were the same as those for DFT calculations. These results suggest that the ANN potential can be used to predict the lowest-energy structures and their GB energies prior to DFT validation, which will greatly reduce computational cost for searching for energetically favorable atomic structures for GBs.

In future research, the ANN potential will be applied to dislocations, in order to evaluate its ability to predict core structures and formation energies for dislocations.

References

[1] T. Yokoi et al., submitted.
[2] T. Yokoi et al., prepared.
[3] J. Behler, M. Parrinello, Phys. Rev. Lett. 98, 146401 (2007).
[4] J. Behler, Int. J. Quantum Chem. 115, 1032-1050 (2015).
[5] G. Kresse, D. Joubert, Phys. Rev. B **59**, 1758-1775 (1999).
[6] G. Kresse, J. Furthmüller, Comput. Mater. Sci. **6**, 15-50 (1996).
[7] J. P. Perdew et al., Phys. Rev. Lett. **100**, 136406 (2008).

Development of crystal structure prediction method and material search

Tomoki YAMASHITA
Top Runner Incubation Center for Academia-Industry Fusion, Nagaoka University of Technology
1603-1 Kamitomioka-machi, Nagaoka, Niigata, 940-218

We have studied the structural stability of SrO on MgO substrates since SrO with unknown crystal structure synthesized on MgO substrate has been reported [1]. There is an approximately 20 percent mismatch between the lattice parameters of SrO (5.16 Å) and MgO (4.22 Å), which could affect the structural stability of SrO We performed crystal structure prediction (CSP) simulations for Sr_4O_4 using CrySPY [2]. Four hundred structures of tetragonal Sr_4O_4 were randomly generated with the lattice constant of the MgO(100) substrate. Only the lattice constant c was relaxed during structural optimization using Quantum ESPRESSO. Here, GGA is used for the exchange-correlation functional. The results of the search showed that the rocksalt-type structure was not the most stable under the constraint on the lattice constant a. The four-coordinated structures were more stable than others. Alhough the predicted structure differs from that obtained experimentally, we found that the lattice constraints make the rocksalt structure unstable.

We have also searched for solid electrolyte materials that can be synthesized in the systems of Li-Mg-P_2O_7 using CSP with CrySPY [2]. We perfromed randam search simulations for $LiMg_{1.5}P_2O_7$, $Li_2MgP_2O_7$, and $Li_3Mg_{0.5}P_2O_7$. In each composition, 1000 random structures were locally optimized using the VASP code. The CSP simulations were conducted using GGA-PBE, and PBEsol was also used for the structures with low energy. We obtained a structure with a hull distance of 2 meV/atom for $Li_2MgP_2O_7$, and structures with a hull distance of about 20 meV/atom for $LiMg_{1.5}P_2O_7$ and $Li_3Mg_{0.5}P_2O_7$. In addition to the randam search simulations, DFT calculations were also performed to evaluate the energy of $Li_2MgP_2O_7$ with the P_2O_7 framework in the $Li_{2.2}Zn_{0.8}P_2O_7$ (LZ) structure [3]. From a vast number of combinations of cation sites in the LZ structure, the top 10 structures with the lowest Mardelung energy were adopted for DFT calculations. The lowest energy of the LZ structure was only a few meV higher than the energy of the structure found in RS simulations (RS structure). The RS structure become unstable when the cationic site changes, which increases the energy. On the other hand, the LZ structure have almost no change in energy when the cation site was exchanged.

References

[1] K. Komatsu, T. Shirai, A. Nakamura, A. Kato, S. Ohshio, N. Nambu, I. Toda, H. Muramatsu, H. Saitoh, Ceramics International **39**, 7115 (2013).

[2] T. Yamashita, S. Kanehira, N. Sato, H. Kino, H. Sawahata, T. Sato, F. Utsuno, K. Tsuda, T. Miyake, and T. Oguchi, Sci. Technol. Adv. Mater. Meth. **1** (2021) 87.

[3] A. E. Lapshin and M. A. Petrova, Glass Physics and Chemistry, **36**,75 (2010).

Study of the Principle of Photothermal Conversion by *Ab Initio* Calculations

Mizuho ONO[1], Hiroki GONOME[2]

[1]*Graduate School of Engineering,*

Tohoku University, Aoba-ku, Sendai, Miyagi 980-0845

[2]*Graduate School of Science and Engineering,*

Yamagata University, Jonan, Yonezawa, Yamagata 992-8510

In light-matter interactions, the electrons and nuclei that composes matter interact with each other, but the physical processes are extremely complex and fast. In simulations of matter that reproduce this situation, the Born-Oppenheimer approximation is typically applied and the motion of the electrons is decoupled from that of the nucleus. On the other hand, it has been reported that non-negligible non-adiabatic effects between the electrons and the nucleus can act on molecules moving under a strong external field [1]. The objective of this work is to evaluate the effect of the external field on the energy of the system by performing coupled calculations of the electron and lattice (nuclear) systems without applying the Born-Oppenheimer approximation. The coupled calculations treat non-adiabatic motion by applying Ehrenfest dynamics with time-dependent density functional theory and classical molecular dynamics (TDDFT-MD) for the electron and lattice. The time waveform of the incident electric field in the simulation is shown in Figure 1. The light intensity is 10^{13} W/cm^2 and the central frequency is 3.10 eV. Figure 2 shows the total energy excluding the kinetic energy of the lattice and the kinetic energy of the lattice in the TDDFT-MD simulation results for the silicon crystal. During the application of an electric field, the energy of the system increases rapidly, while the kinetic energy of the lattice remains almost unchanged. In other words, the energy increase of the system is dominated by the interaction between the electromagnetic waves and the electrons. The kinetic energy of the lattice then begins to fluctuate after 300 fs due to electron-lattice interactions. The numerical analysis therefore shows that the lattice system is hardly displaced

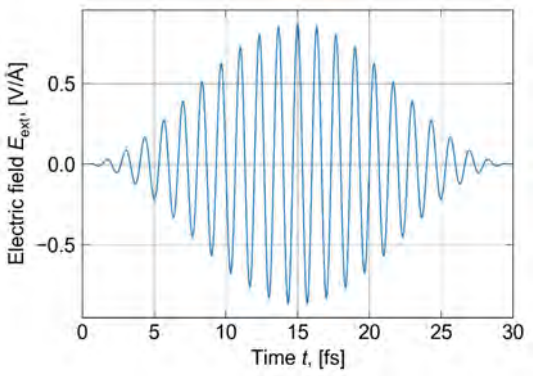

Fig. 1: Incident electric field

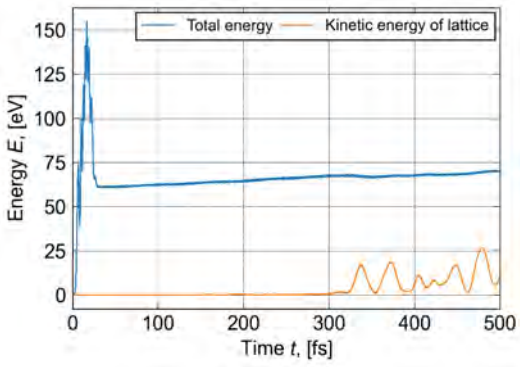

Fig. 2: Total energy and kinetic energy of lattice.

directly by the applied electric field but receives energy through the interaction with the electron system.

References

[1] C. Lian, S.B. Zhang and S. Meng, Phys. Rev. B. **94**, 184310 (2016).

Development of a full *GW* electron-hole interaction kernel for the Bethe-Salpeter equation

Yoshifumi NOGUCHI

Department of Applied Chemistry and Biochemical Engineering, Graduate School of Engineering, Shizuoka University, Johoku 3-5-1, Hamamatsu, Shizuoka 432-8561, Japan

In 1995, Onida, et al., initiated the first-principles *GW*+Bethe-Salpeter simulations for a Na_4 cluster [1]. Since then, the method has been applied to a wide-range of materials in which it has demonstrated its accuracy and reliability. However, the conventional simulations need to employ an additional approximation to a *GW* electron-hole interaction kernel (Ξ^{GW}) without exception solving the equation. Specifically, the employed approximation neglects the two second-order exchange terms in the *GW* electron-hole interaction kernel based on an unconfirmed assumption that the second-order terms have a negligibly small contribution. Therefore, it is evident that the conventional *GW*+Bethe-Salpeter method does not satisfy the Baym-Kadanoff conservation low [2].

Considering not only the first-order direct and exchange terms but also the two second-order exchange terms, we have developed a *GW*+Bethe-Salpeter method with a full *GW* electron-hole interaction kernel and implemented it into our original all-electron mixed basis program [3]. Figure 1 shows the Feynman diagrams of the full *GW* electron-hole interaction kernel. We simulated the S_1 optical gap of 28 typical organic molecules in Thiel's set [4] and revealed the contributions of the two second-order exchange terms. The effects of the method with a full *GW* electron-hole interaction kernel are 0.2 eV maximum for the $n \rightarrow \pi^*$ excitations and negligibly small for the $\pi \rightarrow \pi^*$

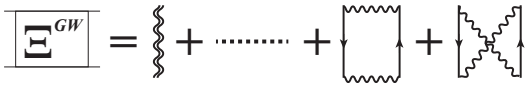

Figure 1. Full *GW* electron-hole interaction kernel.

and $\pi \rightarrow$Rydberg excitations compared with the those of the conventional method. The results of our exciton analysis method suggest that the contribution of the second-order exchange terms tends to be larger for higher exciton binding energies.

References

[1] G. Onida, et al., Phys. Rev. Lett. **75**, 818 (1995).

[2] G. Baym and P. Kadanoff, Phys. Rev. **124**, 287 (1961).

[3] S. Yamada, et al., Phys. Rev. B. **105**, 045113 (2022).

[4] M. R. Silva-Junior and W. Thiel, J. Chem. Theory Comput. **6**, 1546 (2010).

Ab-initio research on nano structures of magnetic nano particles

Yasutomi TATETSU

Meio University, Biimata, Nago, Okinawa 905-8585

The search for advanced materials that possess both thermodynamic stability and instability for different applications has become a hot topic in recent years. With the advancements in technology, chemical synthesis techniques are being developed to control nanoparticles with precision, allowing the discovery of new functional materials with unique properties. Teranishi's team at Kyoto University has recently made an important breakthrough by discovering a new behavior of crystal structure transformation in an ionic nanocrystal [1]. Moreover, the team was able to synthesize a new $Z3$-type Fe(Pd, In)$_3$ crystal structure by introducing indium as a third element into $L1_2$-FePd$_3$, which could have significant implications for the development of new technologies [2]. The discovery of these new materials is critical for advancements in various fields such as medicine, energy, electronics, etc.

In this report, we have conducted first-principles calculations to explore the stability of compounds with $Z3$-type structures. Our research aimed to estimate the formation energies for various $Z3$-Fe(Pd, M)$_3$ structures, where M represents different transition metals. To perform these calculations, we utilized the ab-initio code, OpenMX [3], to compute the ground states of $L1_2$-(Fe, M)Pd$_3$ and $L1_2$-(Fe, M)Pd$_3$ structures. We compared the energies obtained to analyze the stability of these structures. Our results indicated that some $Z3$-type structures exhibit lower energies compared to the $L1_2$-type structures, indicating that they could be synthesized experimentally. Further theoretical investigations are required to explain the coercivity mechanism in the $Z3$-Fe(Pd, M)$_3$ structures.

References

[1] Z. Li, M. Saruyama, T. Asaka, Y. Tatetsu, and T. Teranishi, Science, **373**, 332 (2021).

[2] K. Matsumoto *et al.*, Nat. Commun., **13**, 1047 (2022).

[3] http://www.openmx-square.org

Machine Learning Based Optimized Polymer for Thermal Function Materials

Bin XU

Department of Mechanical Engineering,

The University of Tokyo, 7-3-1, Hongo, Bunkyo-ku, Tokyo 113-8656

Polymer informatic is an emerging filed where the AI and machine learning are being used in the efficient discovery and design of polymer with target properties and has large impact on several aspect of human life, science, and technology. Cellulose is an organic compound with the formula $(C_6H_{10}O_5)_n$, a polysaccharide consisting of a linear chain of several hundred to many thousands of β linked D-glucose units. Cellulose is an important structural component of the primary cell wall of green plants, many forms of algae and the oomycetes. In this work, we applied the molecular dynamics simulation in combination with the machine learning to explore the effect of strain, hydrogen bonds, and structure ordering on thermal transport in cellulose. The structure for the simulation is shown in Fig. 1.

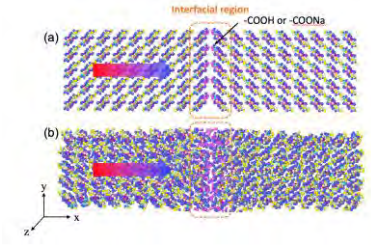

Figure 1 Schematic illustration of structure used for non-equilibrium molecular dynamics simulation.

The temperature dependent thermal conductivity of cellulose polymer with the temperature up to 300 K is shown in Fig. 2. The thermal conductivity of filaments with lower crystallinity index (CI) also increases with a similar slope until 240 K, but then saturates to a constant value until 300 K. Temperature-dependence thermal conductivity reveal that the filaments exhibit phonon transport at effective dimension between 2D and 3D.

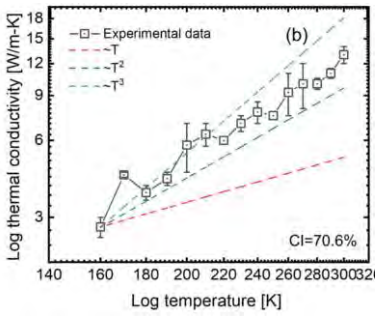

Figure 2 temperature dependent thermal conductivity of cellulose nanofiber.

References

[1] Mu, Fengwen, **Bin Xu**, Xinhua Wang, Runhua Gao, Sen Huang, Ke Wei, Kai Takeuchi et al. Journal of Alloys and Compounds **905** 164076 (2022).

[2] Wang, G., Kudo, M., Daicho, K., Harish, S., **Xu, B**., Shao, C., Lee, Y., Liao, Y., Matsushima, N., Kodama, T. and Lundell, F., Nano Letters, **22**, 8406-8412 (2021).

Theoretical study of quantum effects in nanographene devices

Koichi KUSAKABE
Graduate School of Science, University of Hyogo
Kouto, Kamigori, Hyogo 5-8581

1 Introduction

New quantum devices for quantum information and quantum electronics are being developed by exploring various quantum effects. We are studying graphene-based quantum computation resources,[1] and graphene-based spin-electronic devices.[2, 3] We have developed theoretical approaches to study stubility of adsorbed molecules on graphene in solvents,[4] acceleration methods utilizing evolutionary algorithms,[5] and light-induced structural transformation of nanomaterials.[6]

2 Quantum computation resources by poly-PTM

The design of a hydrogenated poly-PTM measurement-based quantum computation resources was promoted by evaluating decice behavior based on proton NMR simulations on adsorbed hydrogen on the poly-PTM. The design of a two-dimensional $S = 3/2$ antiferromagnetic Heisenberg system was promoted based on the design of a two-dimensional honeycomb poly-PTM network. We concluded that possible computational resource states in a two-dimensional hydrogenated nanographene requires control of the effective many-body interaction between localized spins.

3 Stability and functions of nanographene devices

The structural stability of hydrogenated nanograpehe structures was evaluated, as well as the activation energy barrier heights on the hydrogen diffusion path. To evaluate decoherence, which is the central concern of quantum information operation, we developed a theory of spin-current-rotation coupling and the effect of inserting insulating hBN between metallic Ni substrate and graphene. We concluded that control of the decoherence process requires the control of the interaction between electron spins and current rotation.

Acknowledgement

The author acknowledges the big contributions of Dr. N. Morishita, Mr. K. Komatsu, and Prof. M. Kitatani on nanographene quantum computation resorces. He also thanks Dr. Y. Wicaksono, Ms. H. Harfah, Dr. G. K. Sunnardianto, and Prof. M. A. Majidi for collaboration on graphene quantum spintronics devices, and all collaborators for theoretical approaches to nanomaterial device structures.

References

[1] N. Morishita, Y. Oishi, T. Yamaguchi, K. Kusakabe, Appl. Phys. Express **14**, 121005 (2021).

[2] Y. Wicaksono, H. Harfah, G. K. Sunnardianto, M. A. Majidi, and K. Kusakabe, RSC Adv., **12**, 13985 (2022).

[3] Y. Wicaksono, H. Harfah, G. K. Sunnardianto, M. A. Majidi, and K. Kusakabe, Magnetochem. **9**, 113 (2023).

[4] Y. Oishi, H. Ogi, S. Hagiwara, M. Otani, and K. Kusakabe, ACS Omega, **7**, 35, 31120 (2022).

[5] T. Ishikawa, K. Kusakabe, Y. Makino, S. Sakamoto, N. Okuyama, J. Phys. Chem. A, **126**, 8082 (2022).

[6] M. Nagai, Y. Higashitani, M. Ashida, K. Kusakabe, H. Niioka, A. Hattori, H. Tanaka, G. Isoyama, N. Ozaki, Commun. Phys., in press (2023).

Electrochemical reaction analysis using density functional calculation + implicit solvation model 3

Jun HARUYAMA

Institute for Solid State Physics,

The University of Tokyo, Kashiwa-no-ha, Kashiwa, Chiba 277-8581

We have studied H_2O adsorption monolayer on Pt(111). The understanding of this metal/water interface system is important for basic electrochemical reactions such as the oxygen reduction reaction. This year, we focused on the calculation method for the second-order nonlinear susceptibility $\chi^{(2)}$ in this system.

Fig. 1a shows the most stable adsorption monolayer structure, √39×√39 cell including 5- and 7-membered rings on Pt(111). By employing the density functional perturbation theory combined with the effective screening medium [1] + explicit electric field approach, we obtained $\chi^{(2)}_{zzz}$ as shown in Fig. 1(b). [2] The negative and positive signs of Im $\chi^{(2)}_{zzz}$ in the high (3000–3500 cm^{-1}) and low (600 –2400 cm^{-1}) frequency regions, respectively, were obtained. The spectra show negative double peaks in the high-frequency region, consistent with those obtained by heterodyne-detected sum-frequency generation spectroscopy. [3] The peaks at approximately 2000–3500, 1600, and 600–1200 cm^{-1} are composed of the OH stretching, H_2O bending, and H_2O libration modes, respectively. This study provides a fundamental basis for structure analysis of H_2O adsorption on metal surfaces.

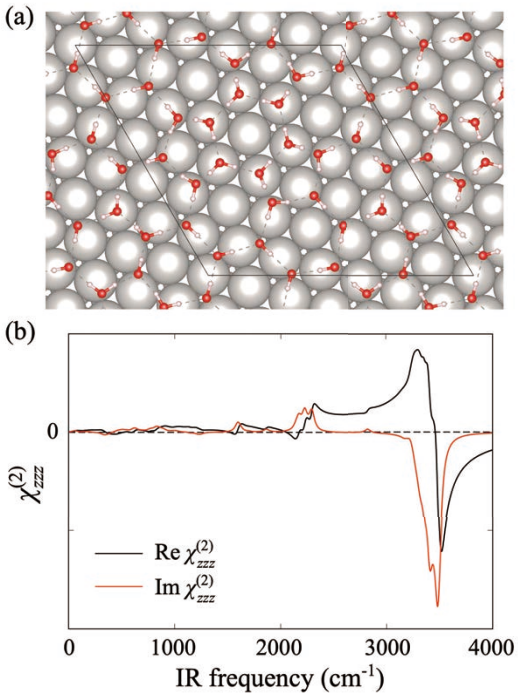

Fig. 1: (a) H_2O adsorption monolayer structure. (b) Second-order nonlinear susceptibility $\chi^{(2)}_{zzz}$.

References

[1] M. Otani and O. Sugino: Phys. Rev. B **73** (2006) 115407.

[2] J. Haruyama, T. Sugimoto, and O. Sugino, *submitted.*; https://isspns-gitlab.issp.u-tokyo.ac.jp/j-haruyama/Pt111_H2O-monolayer

[3] T. Sugimoto and Y. Matsumoto, Phys. Chem. Chem. Phys. 22, 16453 (2020).

Discovery of Fast Anhydrous Proton Conduction in α-MoO_3

Atsuo YAMADA

Department of Chemical System Engineering,

The University of Tokyo, Bunkyo-ku, Hongo, Tokyo 113-8656

Aqueous proton batteries show potential as high-power energy storage devices because of the small size of the protons and their high mobility in aqueous solutions. Among various transition metal oxides, orthorhombic MoO_3 (α-MoO_3) is one of the most promising proton hosts with fast kinetics and large capacities. Herein, we investigated the mechanism of proton intercalation and transportation in α-MoO_3 based on theoretical calculations [1].

The spin-polarized DFT calculation was adopted to trace the H^+ dynamics in α-MoO_3 with VASP program. Based on a 2 × 1 × 2 supercell ($Mo_{16}O_{48}$), a series of H-intercalated structures of H_xMoO_3 ($0 \le x \le 3.0$) was calculated. The CI-NEB method was used to calculate proton diffusion pathways.

The energy profiles of H^+ diffusion in MoO_3 are shown in Fig. 1. At the early stages of protonation and deprotonation, the activation barriers for proton diffusion between the oxygen arrays of MoO_3 were below 0.4 eV, which is comparable to that of Grotthuss mechanism in water. Therefore, further exploration of other host materials with dense and continuous oxygen arrays capable of fast anhydrous proton conduction is an important challenge for the practical application of high-power aqueous proton batteries.

References

[1] Z. Ma, X. M. Shi, S. Nishimura, S. Ko, M. Okubo, A. Yamada, *Adv. Mater.*, **34**, 2203335 (2022).

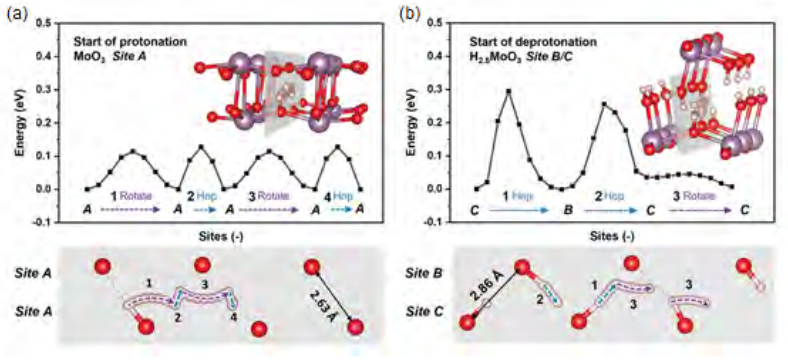

Figure 1 Anhydrous proton transport via hydrogen bond network and corresponding energy barriers at the early stages of protonation (a) and deprotonation (b). The three most stable H^+ absorption sites in MoO_3 are labeled as A, B, and C, respectively.

First-principles prediction of anomalous Hall effect in antiferromagnetic perovskites

Kunihiko Yamauchi

Department of Precision Engineering, Graduate School of Engineering, Osaka University, 2-1 Yamadaoka, Suita, Osaka 565-0871

Recently, large anomalous Hall conductivity in noncollinear antiferromagnetic (AFM) systems has been recently observed and attracted much attention while the anomalous Hall effect takes place typically in ferromagnetic (FM) materials with the finite magnetization.

In this study, by using DFT calculation, we predict the anomalous Hall effect (AHE) in perovskite $CaCrO_3$ as a representative of collinear antiferromagnetic materials [1]. We showed that the C-type AFM ordering (Fig. (a)) generates the sizable anomalous Hall conductivity and revealed two essential roles of the non-symmorphic *Pbnm* symmetry. (i) The screw and glide symmetry operations bind the AFM and FM order parameters in the same irreducible representation so that AHE is active in the AFM order. (ii) The band-sticking effect at the Brillouin-zone surface makes Cr-t_{2g} state form the narrow bands near the Fermi energy; a couple of those bands cause anticrossing and enhancement of the Berry curvature (Fig. (b)).

In this year, we also studied 2D magnetism as reported in Ref. [2] and [3] in collaboration with theoretical and experimental groups in Italy and Germany.

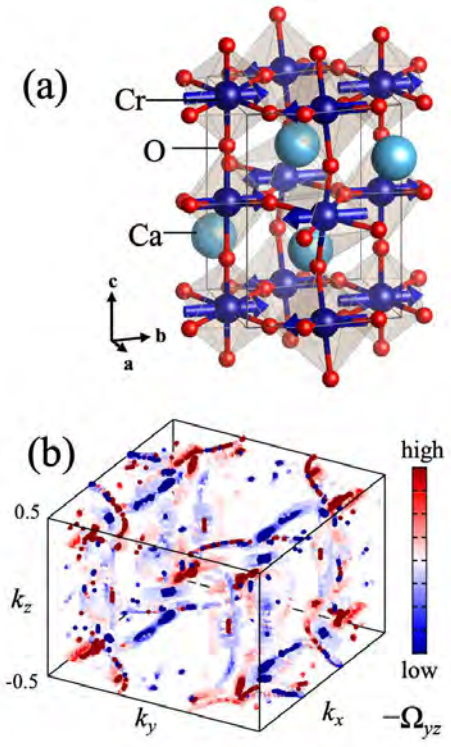

Figure: (a) C-type AFM ordering in *Pbnm* crystal structure of $CaCrO_3$. (b) Berry curvatures in the orthorhombic Brillouin zone.

References

[1] Thi Phuong Thao Nguyen and Kunihiko Yamauchi, Phys. Rev. B. **107**, 155126 (2023).

[2] A. D. Vita, T. T. P. Nguyen, .., K. Yamauchi, *et al*., Nano Letter **22**, 7034 (2022).

[3] K. Riedl, .., T. T. P. Nguyen, K. Yamauchi, *et al.*, Phys. Rev. B **106**, 035156 (2022).

Ab-initio electron dynamics simulation for nonlinear optical phenomena in solids

Shunsuke SATO

Center for Computational Sciences

University of Tsukuba, Tsukuba, Ibaraki 305-8577, Japan

We have studied light-induced electron dynamics in solids based on the time-dependent density functional theory. This year, we focused on the development of a novel analysis technique for light-induced linear and nonlinear optical phenomena in solids based on the time-dependent current density [1]. Here, we first compute the time-dependent current density as

$$\boldsymbol{j}(\boldsymbol{r},t) = -\frac{e}{\Omega \mathrm{m_e}} \int_{FBZ} d\boldsymbol{k} \sum_b f_{b\boldsymbol{k}} \times \psi^*_{b\boldsymbol{k}(\boldsymbol{r},t)}\big(\boldsymbol{p} + \boldsymbol{A}(t)\big)\, \psi_{b\boldsymbol{k}}(\boldsymbol{r},t), \quad (1)$$

where $\psi_{b\boldsymbol{k}}(\boldsymbol{r},t)$ are time-dependent Kohn-Sham orbitals, and $\boldsymbol{A}(t)$ is the vector potential that is related to the applied external electric field as $\boldsymbol{A}(t) = -\int^t dt' \boldsymbol{E}(t')$. By applying Fourier transform to the computed current density in Eq. (1), we obtain the frequency-resolved microscopic current density as

$$\tilde{\boldsymbol{j}}(\boldsymbol{r},\omega) = \int dt\, e^{i\omega t} \boldsymbol{j}(\boldsymbol{r},t). \quad (2)$$

The frequency-resolved microscopic current density contains the atomic scale real-space information of light-induced linear and optical phenomena. In Ref. [1], we demonstrated that the developed current-density analysis captures microscopic insight into optical phenomena in both delocalized and bound electrons in solids. We further plan to apply the developed method for the investigation of nonlinear optical phenomena in solids in order to develop the microscopic interpretation of perturbative and nonperturbative nonlinear phenomena.

In addition to the development of the above theoretical scheme, we have studied transient optical properties of solids under the presence of intense femtosecond laser fields. For the investigation of nickel, we analyzed the light-induced spin-dynamics and transient absorption based on the pump-probe technique, and we found that the local spin-density dynamics causes the change of the photoabsorption around the absorption edge. Based on this finding, we further proposed the attosecond spin-dynamics spectroscopy to investigate the element-specific light-induced spin-dynamics in the attosecond time-scale.

References

[1] Shunsuke A. Sato, “"Frequency-resolved microscopic current density analysis of linear and nonlinear optical phenomena in solids", arXiv:2302.05859 [cond-mat.mtrl-sci].

First-principles study on the structure of water/graphene interfaces depending on the number of graphene layers

Tatsuhiko OHTO

Graduate School of Engineering Science,

Osaka University, 1-3 Machikaneyama, Toyonaka, Osaka 560-8531

Ab initio molecular dynamics (AIMD) simulation is a powerful tool to describe heterogeneous systems such as the water/solid interface. Although AIMD is computationally expensive, it describes electronic states beyond classical force fields,[1] which is important for interfacial structures.

We have simulated sum-frequency generation (SFG) spectra of isotopically diluted water at the water-graphene sheet interfaces using ab initio molecular dynamics simulations, with changing the number of the graphene layers from one to three. The simulation of water-single graphene interface has already been performed using ISSP.[2] A sharp 'dangling' O-D peak around ~2640 cm-1 appearing in simulated SFG spectra evidences that graphene is hydrophobic. Although the results obtained so far are still preliminary, the dangling O-D peak is blue-shifted by increasing the number of the graphene layer. This frequency difference manifests a weaker O-D…C intermolecular interaction between water and thicker graphene, indicating that graphite is more hydrophobic than graphene.

The simulations were performed using the CP2K code [3]. After obtaining the sufficient length of trajectories, we are going to construct machine learning force field to simulate larger scale interfaces between carbon/water.

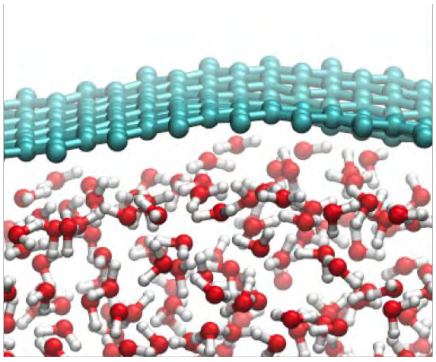

Fig. 1: Structures of the graphene-water interface.

References

[1] T. Ohto et al. Phys. Chem. Chem. Phys. **19**, 6909 (2017).

[2] T. Ohto et al. Phys. Chem. Chem. Phys. **20**, 12979 (2018)

[3] The CP2K developers group, http://cp2k.berlios.de/

Multiscale simulations for magnetic materials

Hung Ba TRAN
Laboratory for Materials and Structures, Institute of Innovative Research, Tokyo Institute of Technology, Midori-ku, Yokohama 226-8503, Japan

Our previous works have studied the magnetocaloric effect by multiscale simulations. The magnetic parameters, such as magnetic exchange coupling constants J_{ij} and magnetic anisotropy energy, are calculated from first–principles calculations. Then, the Monte-Carlo simulations are performed to estimate the magnetic properties at thermal equilibrium, such as magnetization curves and isothermal magnetic entropy change. Several types of the magnetocaloric effect, such as conventional (direct) magnetocaloric effect, giant magnetocaloric effect, anisotropic magnetocaloric effect, and inverse magnetocaloric effect, can be considered using our in–house program[1, 2, 3, 4, 5, 6].

In our recent works, we consider the spin reorientation effect in $Nd_2Fe_{14}B$ material based on first–principles calculations[7]. $Nd_2Fe_{14}B$ is famous material for permanent magnets that are widely used in power generation, motors, and so on due to the high magnetic anisotropy energy, saturation magnetization, and Curie temperature. However, the material has a problem at low temperatures. It is spin reorientation from the easy axis (z–direction) to cone magnetization (where the magnetization is tilted). In previous theoretical works, the spin reorientation in $Nd_2Fe_{14}B$ is usually considered using empirical parameters as crystal–electric field term. In contrast, in this work, we calculate the Dzyaloshinskii–Moriya interactions (DMI) by first–principles calculations for the first time. We found that the DMI is the origin of spin reorientation in $Nd_2Fe_{14}B$. The spin reorientation in $Nd_2Fe_{14}B$ can be reproduced in Figure. 1 (a) by introducing the DMI. In addition, the peak like in magnetic anisotropy energy of experimental work can be

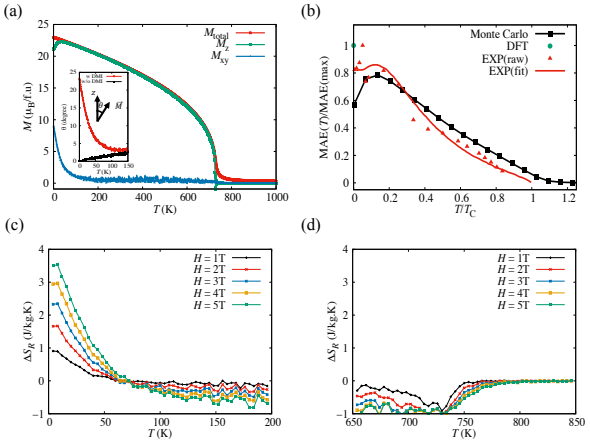

Figure 1: (a) Total (red) and projected spontaneous magnetization in the out–of–plane (green) and in–plane (blue) directions as a function of the temperature of $Nd_2Fe_{14}B$ (inset figure: Temperature dependence of the tilt angle between the magnetization direction and z–direction in the case of switching on (red) and switching off (black) the Dzyaloshinskii–Moriya interaction). (b) The magnetic anisotropy energy obtained is based on DFT (green) and Monte Carlo method by integrating the M–H curves (black) and experimental raw data (red dots) and that derived from anisotropy constants (continuous red curves). (c) Rotating magnetic entropy change as a function of temperature and the magnetic field around the spin reorientation temperature and (d) Curie temperature.

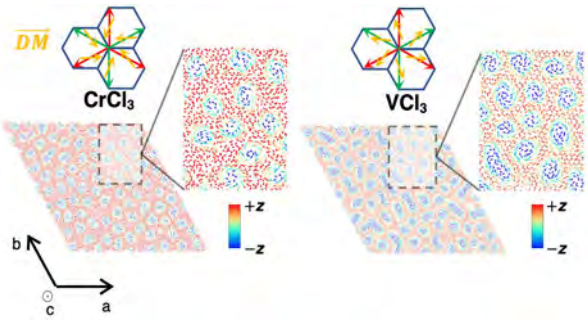

Figure 2: In–plane components of Dzyaloshinskii–Moriya vector for the second nearest neighbor of intra–layer of $CrCl_3$ and VCl_3, where the red and green arrows indicate pairs with different sub–lattices, and the yellow arrow indicates the direction of Dzyaloshinskii–Moriya vector. Snapshot of Monte Carlo simulation of $CrCl_3$ at 10 K with external magnetic field equal to 4 T along the positive z–direction. Snapshot of the Monte Carlo simulation of VCl_3 at 10 K with external magnetic field equal to 6 T along the positive z–direction.

reproduced quantitatively, as shown in Figure. 1 (b). The spin reorientation in the material is usually not desirable for the application of a permanent magnet. However, we found that the rotating entropy change around spin reorientation is almost four times higher than at the Curie temperature, as shown in Figure. 1 (c, d) due to the peculiar properties of spin reorientation.

On the other hand, we also consider the skyrmions in van der Waals centrosymmetric MX_3 (M: V, Cr, Mn, Fe, Co; X: Cl, Br, I) [8]. Skyrmions usually appear in non–centrosymmetric material due to the DMI lacking inversion symmetry. Although MX_3 has space group $R\bar{3}$ being centrosymmetric with honeycomb lattice, the broken local inversion symmetric of the second nearest neighbor of intra–layer stabilizes the finite DMI. It leads to ultra-small skyrmions with a diameter being 2.0 nm, as shown in Figure. 2. In addition, two types of helicity can be realized in $CrCl_3$ and VCl_3 due to the nearly opposite direction in Dzyaloshinskii–Moriya vector. Not only skyrmions but also antiferromagnetic skyrmions and meron are observed in MX_3.

References

[1] H. B. Tran, T. Fukushima, K. Sato, Y. Makino, and T. Oguchi, J. Alloys Compd. **854**, 157063 (2021).

[2] H. B. Tran, T. Fukushima, Y. Makino, and T. Oguchi, Solid State Commun. **323**, 114077 (2021).

[3] H. B. Tran, T. Fukushima, H. Momida, K. Sato, Y. Makino, and T. Oguchi, Comput. Mater. Sci. **188**, 110227 (2021).

[4] H. B. Tran, T. Fukushima, H. Momida, K. Sato, Y. Makino, and T. Oguchi, J. Alloys Compd. **926**, 166718 (2022).

[5] H. B. Tran, H. Momida, Y. Matsushita, K. Sato, Y. Makino, K. Shirai, and T. Oguchi, Phys. Rev. B **105**, 134402 (2022).

[6] H. B. Tran, H. Momida, Y. Matsushita, K. Shirai, and T. Oguchi, Acta Mater. **231**, 117851 (2022).

[7] H. B. Tran, Y. Matsushita, Appl. Mater. Today **32**, 101825 (2023).

[8] H. B. Tran, Y. Matsushita, Skyrmions in van der Waals centrosymmetric materials with Dzyaloshinskii-Moriya interactions, arXiv:2209.02333 (2022) (under review).

Theoretical design of novel functional materials based on abundant elements for energy conversion and storage.

Tetsuya TAKETSUGU
Faculty of Science, Hokkaido University
N10W8, Sapporo, Hokkaido 060-0810

DFT computations using QuantumEspresso and VASP packages are used to gain physical-chemical insights and to design novel functional materials with abundant elements for energy conversion and storage processes. This helps to reduce costs and dependences on precious metals in energy-related industrial applications.

We have demonstrated that oxygen-functionalized hexagonal boron nitride (h-BN) can be an efficient catalyst for oxidative dehydrogenation (ODH) of light alkanes, specifically ethane (C_2H_6), propane (C_3H_8), butane (C_4H_{10}), and isobutane ($HC(CH_3)_3$) [1]. This is particularly interesting because it is commonly accepted that hexagonal boron nitride is an inert material. However, we have demonstrated that h-BN can be functionalized and serve as an active catalyst. It has been found that the reaction pathway involves two H atom transfer steps with small activation energies. We demonstrate that the synergy of two active sites, *B-O-O-B* and *B-O-B* (Figure 1), is crucial for the first and second H-transfer, respectively. With the increase in molecular mass of the considered light alkanes, the ODH reaction temperature decreases. The charge redistribution during H-transfers and localized oxygen atomic states in the conduction band are explored to suggest possible descriptors for the rational design of new catalysts. The universal action of the *B-O-O-B* and *B-O-B* active sites for ODH of the light alkanes paves the way for metal-free BN-based materials for future catalytic applications.

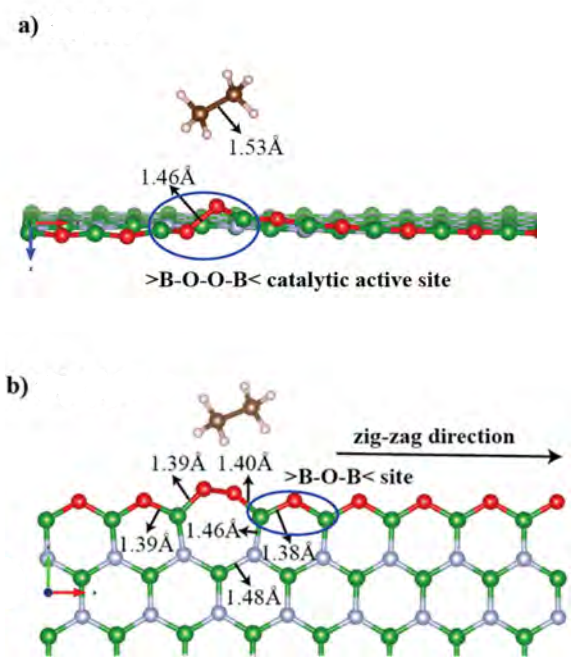

Figure 1: Catalyticaly active (a) *B-O-O-B* and (b) *B-O-B* sites [1].

The multielectron transfer is a key process being indispensable for a wide spectrum of modern electrochemical energy technology. Finding promising multielectron-transfer materials with abundant elements is especially important to advance the present rechargeable battery technology mainly relies on single electron transfer type electrodes. To date,

a few oxide-based materials can reach an electron-transfer number per metal-cation (e) larger than 2 upon a (de)intercalation mechanism. However, these oxide-based electrodes face challenges in improving electrochemical properties as they still suffer from considerable degradation during charge/discharge reactions due to irreversible rearrangements of bonds between metallic cation and anionic oxygen. Furthermore, these high-performance multielectron-transfer oxides are mainly constituted of precious metals. As it is well-known, these elements are limited, and therefore, electrode materials based on precious metals are inappropriate candidates to replace the present cathode materials.

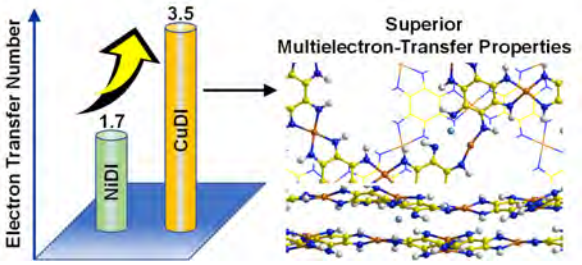

Figure 2: A significantly reversible multielectron-transfer is demonstrated by using only abundant elements [2].

We have demonstrated that the non-oxide electrode based on the bis(diimino)copper framework can show e = 3.5 with cation/anion co-redox mechanism together with a dual-ion mechanism (Figure 2). In this study, the role of the cation-anion interactions has been unveiled by using an experiment/theory collaboration applied to a series of the model non-oxide abundant electrode systems based on different metal-nitrogen bonds. These models provide a route for the design of the multielectron transfer materials based on the tunable π-d conjugated electronic structures. It is found that the Cu-nitrogen bonds show a unique reversible rearrangement upon Li-intercalation, and this process responds to acquire a significant reversible multielectron-transfer. This work provides new insights into the affordable multielectron-transfer electrodes and uncovers an alternative strategy to advance the electrochemical energy storage reactions.

References

[1] S. Kumar, A. Lyalin, Z. Huang, and T. Taketsugu, *Catalytic Oxidative Dehydrogenation of Light Alkanes over Oxygen Functionalized Hexagonal Boron Nitride*, ChemistrySelect **7**, e202103795 (2022).

[2] D. Xia, K. Sakaushi, A. Lyalin, K. Wada, S. Kumar, M. Amores, H. Maeda, S. Sasaki, T. Taketsugu and H. Nishihara, *Superior Multielectron-Transferring Energy Storage by π-d Conjugated Frameworks*, Small **18**, 2202861 (2022).

Microscopic structure of water/CeO_2 interface

Akira NAKAYAMA

Department of Chemical System Engineering,

The University of Tokyo, Tokyo 113-8656, JAPAN

The structural properties and dynamical behaviors of the interface between water and cerium oxide (CeO_2) are investigated by reactive molecular dynamics (MD) simulations employing the neural network potentials (NNP)[1][2] that are trained to reproduce density functional theory (DFT) results. In the construction of the neural network potentials, DFT-based MD (DFT-MD) simulations with enhanced sampling schemes[3] are employed to efficiently acquire training data that include diverse hydrogen-bonding configurations caused by proton hopping events. The water interfaces with three low-index surfaces of (111), (110), and (100) are explored with these neural network potentials, and structure and long-range proton and hydroxide ion transfer dynamics are examined with unprecedented system sizes and long simulation times.

The time step for DFT-MD simulations was set to 1 fs and the temperature was controlled at 360 K. RPBE was used for the DFT functional. The DFT-D3[4] and DFT+U methods was used to incorporate dispersion interaction and electron correlations for Ce 4f electrons, respectively. *k*-point sampling was performed at Γ points only. CP2K was used for DFT-MD calculations. For each interface, a slab model was created with a surface size of $p(4\times4)$ and a water thickness of 30 Å. The conventional and enhanced sampling DFT-MD methods were performed for 20 ps, yielding a total of 8000 configurations as training data.

We mainly discuss the results for the water/CeO_2(110) interface. The z-axis projection of the density distribution of O and H atoms on the CeO_2 surface and in the first hydration layer obtained from the NNP-MD simulations is shown in Figure 1. Note that the average position of the topmost Ce atoms is set to z = 0 Å. The large-scale and long-time simulations provide sufficient statistics to analyze the interface structure in more detail compared to previous studies.

The mechanism of proton transfer occurring at the water/CeO_2(110) interface is then analyzed. Proton transfer can be roughly divided into surface proton transfer (SPT), in which proton transfer occurs between a water molecule coordinated on a Ce atom and a surface O_S atom, and adlayer proton transfer (APT), in which proton transfer occurs between a water molecule and hydroxide ion coordinated on a Ce atom. The proton transfer

between surface species is further classified into direct and indirect transfer that involves neighboring water molecules.

At the water/CeO_2(110) interface, a total of 863 proton transfers were observed during 4 ns of trajectory, when thermal equilibrium is considered to have been reached. Table 1 shows the observed ratio of each proton transfer. Since the structure of the CeO_2(110) surface is not symmetric with respect to the *x*-axis and *y*-axis directions, the APT were also classified according to whether the proton transfer occurred in the *x*- or *y*-axis direction.

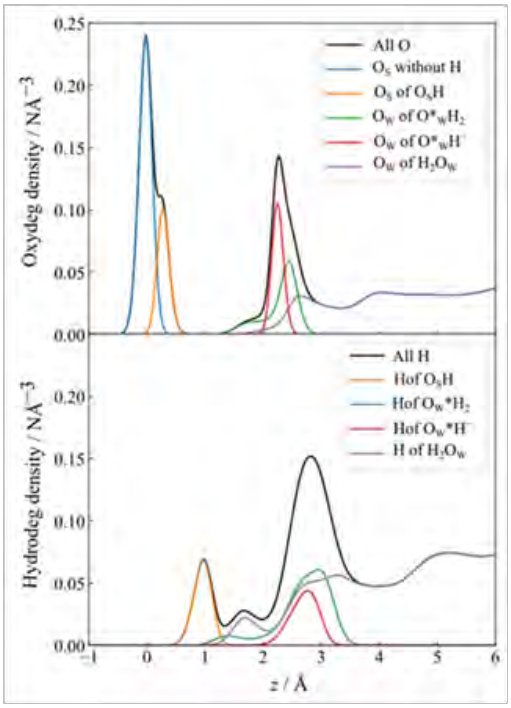

Fig. 1: Density profiles of oxygen and hydrogen at the water/CeO_2(110) interface.

As seen, APT occurred more frequently than SPT, possibly because the distance between surface O atoms is closer. H atoms bonded to surface O atoms are stabilized by forming hydrogen bonds with neighboring surface O atoms, thus making SPT less likely to occur. In addition, more migration was observed in the *y*-direction since the distance between surface Ce is closer.

In summary, we have generated training data using DFT-MD calculations with enhanced sampling scheme and constructed NNPs for the water/CeO_2 interface. Using the constructed NNPs, we performed large-scale and long-time simulations and obtained the detailed information on the structure and proton transfer mechanisms near the interface, which were difficult to obtain using the conventional DFT-MD simulations.

Table 1: Proton hopping machanims

プロトン移動機構		割合
APT direct	x direction	13.2%
	y direction	25.6%
APT indirect	x direction	6.3%
	y direction	18.2%
SPT direct	Forward	0.8%
	Backward	0.9%
SPT direct	Forward	13.0%
	Backward	12.4%
Others		9.4%

References

[1] J. Behler and M. Parrinello, Phys. Rev. Lett. **98**, 146401 (2007).

[2] J. Behler, J. Chem. Phys. **145**, 170901 (2016).

[3] L. Maragliano and E. Vanden-Eijnden, Chem. Phys. Lett. **426**, 168 (2006).

[4] S. Grimme, J. Antony, S. Ehrlich, and H. Krieg, J. Chem. Phys. **132**, 154104 (2010).

Prediction of properties of organic ferroelectrics and piezoelectrics by first-principles calculation

Shoji ISHIBASHI
National Institute of Advanced Industrial Science and Technology (AIST)
Tsukuba, Ibaraki 305-8568

Many azole compounds such as imidazoles and tetrazoles contain polar and bistable hydrogen-bonded molecular sequences suitable for ferroelectricity or antiferroelectricity. In this study, we have computationally investigated relative stabilities of possible ferroelectric (FE) and antiferroelectric (AFE) phases in eight azole compounds: 5-(4-aminophenyl)-1H-tetrazole (APHTZ), 5-(4-fluorophenyl)-1H-tetrazole (FPHTZ), 5-(4-chlorophenyl)-1H-tetrazole (CPHTZ), 5-(4-methylphenyl)-1H-tetrazole (MPHTZ), 5-phenyl-1H-tetrazole (PHTZ), 2-phenyl-1H-imidazole (PHIM), 2,4,5-tribromo-1H-imidazole (TBIM), and 2-bromo-4,5-dimethyl-1H-imidazole (DM-BIM) [1].

The Perdew-Burke-Ernzerhof (PBE) version of the generalized gradient approximation (GGA) [2] was used to describe the electronic exchange-correlation energy. Starting from the experimental structures, the atomic positions were optimized. The convergence criterion was set to 5×10^{-5} Ha/bohr for the maximum force. All the calculations were performed using the QMAS code based on the projector augmented-wave method [3] and the plane-wave basis set.

The obtained results are shown in Fig. 1 together with schematic illustrations of various states in a zero field based on the polarization hysteresis experiments as well as the structural analyses. It is confirmed that the computational and experimetal results are consistent with each other.

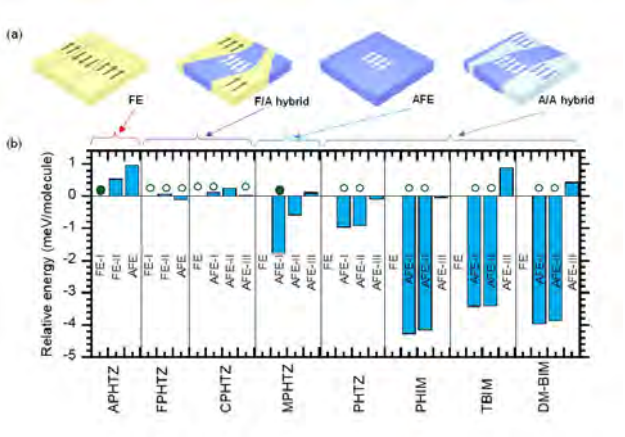

Figure 1: Ferroelectric (FE), antiferroelectric (AFE), and phase-coexisting (F/A hybrid and A/A hybrid) states in the PHTZs crystals. (a) Schematic illustrations of various states in a zero field. (b) Energy histogram of the candidate H-ordered states relative to each FE (or FE-I) form. Filled and open circles point to the non-degenerate and nearly degenerate ground states, respectively (S. Horiuchi, H. Minemawari, and S. Ishibashi, Mater. Horizons, Advance Article (2023), DOI: 10.1039/d2mh01530g).

References

[1] S. Horiuchi, H. Minemawari, and S. Ishibashi, Mater. Horizons, Advance Article (2023).

[2] J.P. Perdew, K. Burke, and M. Ernzerhof, Phys. Rev. Lett. **77**, 3865 (1996).

[3] P. E. Blöchl, Phys. Rev. B **50**, 17953 (1994).

Ab initio calculation for transition-metal-oxide interface

Kazuma NAKAMURA
Quantum Physics Section, Kyushu Institute of Technology
1-1 Sensui-cho, Tobata, Kitakyushu, Fukuoka, 804-8550

In the present study, we investigate electronic structures of interfaces and surfaces of transition-metal oxides using first-principles calculations based on density functional theory. In material science, important physical properties often occur at the surfaces and interfaces of materials. Currently, it is possible to predict physical and chemical properties of the surfaces and interfaces by using *ab initio* electronic structure calculations. On the other hand, since the size of systems including the surface and interface becomes large, and complicated problems such as the generation of an artificial electric field in the surface system are known to occur, so it is necessary to accumulate detailed know-how to perform stable *ab initio* calculations.

Here, we focus on a representative oxide interface system of $SrTiO_3/SrVO_3$ (STO/SVO) hetero structure, and study its microscopic electronic structure and optical properties in details. The STO/SVO system is a fascinating system realizing a metal-insulator transition at the interface [1, 2], especially small thickness of SVO block. In this study, we analyzed this system with *ab initio* calculations, particularly focusing on optical spectra.

We performed *ab initio* self-consistent pseudopotential calculations in which wavefunctions were expanded in a plane-wave basis [3]. We employed norm-conserving pseudopotentials, and the generalized-gradient approximation for exchange-correlation energy. The cutoff energies for the wavefunction and charge density are 100 Ry and 400 Ry, respectively. The atomic geometry was fully optimized with kept at inplane lattice constant $a = 3.9451$ Å, where the force on each ion were relaxed to less than 0.001 a.u. and a Monkhorst-Pack k-grid of $10\times10\times2$ was employed. Optical calculations were performed with using RESPACK [4]: The energy cutoff for the polarization function was set to 3 Ry. The total number of bands considered in the polarization calculation was determined to cover unoccupied states up to 10-15 eV above the Fermi level. The integral over the Brillouin zone was calculated with the generalized tetrahedron technique with a smearing of 0.01 eV.

Figure 1 shows our structure models to be analyzed, where we consider a multilayer model consisting of SVO and STO blocks [panel (a)] and a symmetric slab model [(b)]. The slab model includes a vacuum region with 20 Å, and has a mirror symmetry with respect to the central TiO_2 plane. Then, artificial electric fields due to asymmetry in the both ends of the slab do not occur. The structural models include several SVO blocks, where we specify the number of the blocks as n. In the present study, we consider the structural models until $n = 4$. The number of the STO blocks was fixed to 5 for the multilayer and 8.5 for the slab (0.5 indicates an additional central TiO_2 layer).

Figure 2 shows our calculated band structures of the multilayer (a) and slab (b), where the band diagrams for the $n = 2$ model are

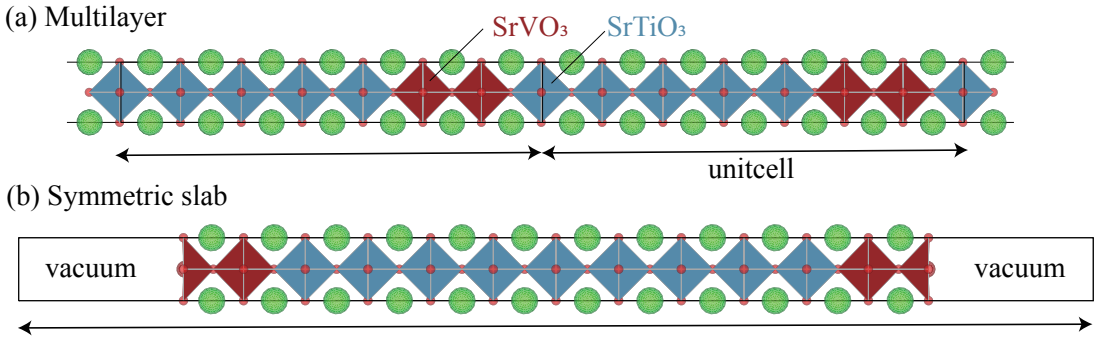

Figure 1: Two structural model: (a) Multilayer consisting of $SrTiO_3$ and $SrVO_3$ blocks. (b) Symmetric slab having a mirror symmetry with respect to the center TiO_2 plane.

displayed. From the band structures, we see that both two systems are metal; the SVO t_{2g} bands cross the Fermi level, and the STO t_{2g} band is about 1 eV above from the Fermi level.

Figures 2(c) and (d) show our calculated reflectance spectra for the multilayer and slab models, respectively. We see that the both spectra exhibit a lowering of the plasma edge compared to the bulk SVO one. We also see the appreciable n dependence of the plasma edge. The difference between the multilayer and slab results seems to be small.

In summary, we have calculated electronic structures and reflectance spectra of the STO/SVO system from first principles. In the experiments, the system is insulator at small thickness of the SVO blocks, and this origin should be further investigated from view of strongly correlation physics. To this end, we need to perform *ab initio* derivations of the low-energy model of SVO-t_{2g} bands near the interface, which leaves as a next step.

[1] D. H. Kim, *et al.*, Solid State Commun. 114, 473 (2000).

[2] K. Yoshimatsu, *et al.*, Phys. Rev. Lett. 104, 147601 (2010).

[3] P. Giannozzi, *et al.*, J. Phys. Condens. Matter 29, 465901 (2017).

[4] K. Nakamura, *et al.*, Comput. Phys. Commun. 261, 107781 (2021).

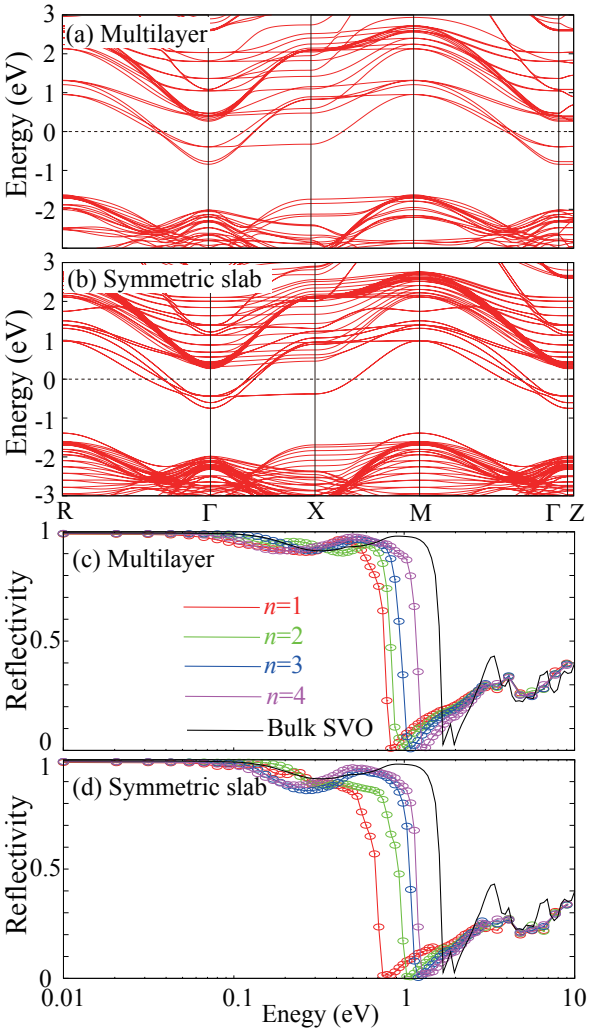

Figure 2: Our calculated band structures of (a) multilayer and (b) slab model where we show $n = 2$ case. Panels (c) and (d) show our calculated reflectance spectra of multilayer and slab models, respectively.

Two-color mixing enhancement of nonlinear optical absorption for a semiconductor

Yasushi SHINOHARA[1,2], and Mizuki TANI[3]

[1]*Photon Science Center,*

The University of Tokyo, Hongo, Bunkyo-ku, Tokyo 113-8656.

[2]*NTT Basic Research Laboratories,*

NTT Corporation, 3-1 Morinosato Wakamiya, Atsugi, Kanagawa 243-0198.

[3]*Department of Nuclear Engineering and Management*

The University of Tokyo, Hongo, Bunkyo-ku, Tokyo 113-8656.

We have theoretically studied dielectrics exposed to strong laser fields using a first-principles theoretical framework based on time-dependent density-functional theory (TDDFT) within SALMON-TDDFT [1]. The real-time solution of the time-dependent quantum system is one of the most accurate schemes to evaluate nonlinear optical responses that perturbative expansions cannot describe.

One of the most prominent features of the nonpertubative response of the material is the complex mixing of multiple frequencies of an applied field. We do not have a simple formula to model the response written as a combination of amplitudes depending on the frequency of the field, i.e., the Fourier component of the field, in contrast to simple power expansion within the perturbation theory. We need a theoretical description capable of nonperturbative responses to evaluate the response.

We have performed TDDFT simulations for energy absorption of Si crystals exposed to strong laser field that has two color components, 1.6 eV, and 3.2 eV [2]:

$$E(t) = f(t)\left[E_{1.6\ \mathrm{eV}}\cos\left(\frac{1.6\ \mathrm{eV}}{\hbar}t\right) + E_{3.2\ \mathrm{eV}}\cos\left(\frac{3.2\ \mathrm{eV}}{\hbar}t\right)\right],$$

where $f(t)$ is an envelope function that has 14.4 fs full-width-half-maximum. The second color, 3.2 eV, is slightly above the direct gap of the crystal. To model an experimental setup of frequency conversion for 3.2 eV from 1.6 eV via second harmonic generation, we change the relative power ratio such that the sum of two components is kept constant:

$$I_{\mathrm{tot}} = I_{1.6\ \mathrm{eV}} + I_{3.2\ \mathrm{eV}},$$

$$I_i = \frac{1}{2}\epsilon_0 c|E_i|^2, i = 1.6\ \mathrm{eV}, 3.2\ \mathrm{eV},$$

where ϵ_0 and c are the vacuum permittivity and the speed of light. The criteria of nonperturbative response based on the Keldysh

parameter [3] is 6.91 TW/cm^2 and 27.2 TW/cm^2 for 1.6 eV and 3.2 eV. The absorbed energy is evaluated by the total work from the field to the system

$$E_{\mathrm{abs}} = \int_0^{\infty} \mathrm{d}t\, \boldsymbol{J}(t) \cdot \boldsymbol{E}(t)$$

where $\boldsymbol{J}(t)$ is the induced charge current evaluated by TDDFT.

Our simulation shows maximal energy absorption is realized by a condition $I_{1.6\ \mathrm{eV}}/I_{3.2\ \mathrm{eV}} \sim 1.0$, when we have $I_{\mathrm{tot}} = 1\ \mathrm{TW/cm^2}$. This fact is hardly explained by perturbative expansion because the lower-order nonlinear response is expected to dominate the dynamics for such weak intensity compared to the atomic unit value of 35 PW/cm^2. The perturbative expansion predicts $I_{1.6\ \mathrm{eV}}/I_{3.2\ \mathrm{eV}} \sim 0.0$ for the maximal absorption condition.

This nontrivial maximal energy absorption mixing ratio appears for other combinations (0.2 eV, 3.2 eV), (0.8 eV, 3.2 eV). This generic behavior is explained by energy detuning due to the lower frequency components with the strong resonant excitation due to the 3.2 eV component. When the lower frequency component does not exist, 3.2 eV component cause Rabi oscillation because of the strong field. Rabi oscillation leads to saturation of absorption in a pulse. By the lower frequency driving for intraband motion, a resonant point undergoes off-resonant condition by the detuning. Then another off-resonant state becomes resonant. This sequence avoids saturation, and the number of excited electrons increases with the two-color mixture for the driving field.

References

[1] https://salmon-tddft.jp/, M. Noda, S.A. Sato, et al., Computer Physics Communications. **235**, 356 (2019).

[2] Mizuki Tani, Kakeru Sasaki, Yasushi Shinohara, and Kenichi L. Ishikawa, Phys. Rev. B **106**, 195141 (2022).

[3] L. V. Keldysh, Sov. Phys. JETP **20**, 1307 (1965).

First-principles calculations of complex metallic alloy surfaces

Kazuki NOZAWA
Department of Physics and Astronomy, Kagoshima University
1-21-35, Korimoto, Kagoshima 890-0065

High-resolution transmission electron microscopy experiments observed the formation of small ZnO patches on the PdZn(111) surface during the methanol steam reforming reaction, indicating the ZnO patches plays an important role in the CO_2 selectivity of this catalyst [1]. Last year we obtained an oxidized PdZn(111) surface having a distorted hexagonal Zn-O structure at the top layer [2]. In this fiscal year, we studied the dehydrogenation of water on this oxidized PdZn(111) surface. Calculations are performed with VASP program package as flat MPI jobs on system B and C.

Because the obtained Zn-O layer on the oxidized PdZn(111) surface is corrugated as shown in the figure, first we calculated the potential energy surface (PES) of water with fixing atomic positions to find out promising candidates for the starting structure of the structural relaxation. We investigated the PES for water with its molecular plane parallel and perpendicular to the surface, keeping the distance to the nearest surface atom at 2.0 and 2.5 Å. Many of these calculations were done as bulk jobs on system B. Next, we performed structural relaxation from 20 stable starting structures obtained. We performed similar calculations for the hydroxyl and hydrogen on the same surface to determine the stable coadsorption structure. The stable adsorption site of water was found on a Zn atom forming the hexagonal Zn-O ring. The obtained adsorption energy of water was larger than that on the non-oxidized PdZn(111) surface but smaller than that on ZnO(0001) surface [3]. However, the coadsorption energy of hydroxyl and hydrogen obtained in this calculation was larger than that on the non-oxydized PdZn(111) surface [3]. It means this surface is not active for the hydrogenation of water.

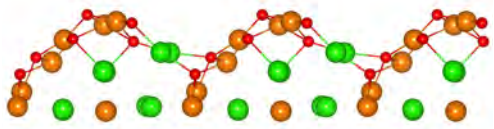

Figure 1: Side view of the oxidized PdZn(111) surface.

In addition to the above work, we studied pentacene adsorption on the twofold surface of the icosahedral Ag-In-Yb quasicrystal [4] and the electronic structure of trace (Pt, Ni, Pd)-doped $Al_{13}Fe_4$ intermetallic compounds.

References

[1] M. Friedrich *et al.*, Angew. Chem. **52**, 4389 (2013).

[2] K. Iwamura, Master Thesis (Kagoshima University, 2023).

[3] G. K. Smith *et al.*, Surf. Sci. **605**, 750 (2011).

[4] M. Sato *et al.*, J. Phys.:Conf. Ser., **2461**, 012016(2023).

Adsorption States of Oxygen on Pt Nanoparticles

Takehiko SASAKI and Yasumasa IMAI

Department of Complexity Science and Engineering, Graduate School of Frontier Sciences, The University of Tokyo, Kashiwa-no-ha, Kashiwa, Chiba 277-8561

The surface state of the catalyst platinum nanoparticles determines the performance of polymer electrolyte fuel cells (PEFC). Characterization of the electrochemical cycle and oxygen adsorption state on the surface of platinum nanoparticles, as well as the high-coverage oxygen adsorption state with subsurface oxygen generation, has been investigated using synchrotron radiation transient response XAFS and resonant inelastic X-ray scattering (RIXS). Although computational studies on oxygen species on Pt surfaces have been published [1,2], it is necessary to determine the oxygen adsorption structure on the Pt nanoparticles in order to conduct spectral analysis.

The Pt nanoparticles to be calculated are Pt nanoparticles composed of 586 atoms of the cuboctahedron type corresponding to the actual catalyst particle size range of 2.5 nm in order to study the high-coverage oxygen adsorption state where subsurface oxygen atoms also exist. The primary purpose is to obtain the adsorption structure by VASP calculation and provide the coordinates for FDMNES simulation. The unit cell has a volume of 22.13×44.26×33.19 ($Å^3$) and contains 215 Pt atoms and oxygen atoms. After optimization of this unit cell, cuboctahadral nanoparticle is obtained by symmetry operation. The structure optimization calculation was performed by allowing the relaxation of the first and second neighbors of oxygen atoms. The energy cutoff is 400 eV and the k-point mesh is 3x2x2. The representative models are shown in Fig. 1.

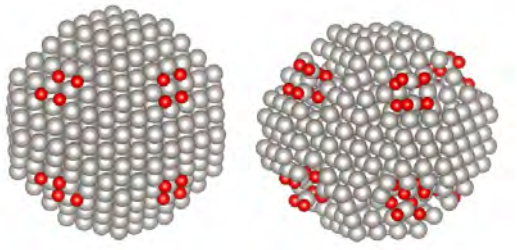

Fig. 1 Obtained models $Pt_{586}O_{32}$ and $Pt_{586}O_{64}$.

Now calculations to determine chemical potential for each species under electrochemical processes are in progress.

References

[1] J.K. Norskov et al. , J. Phys. Chem. B **108**, 17886 (2004).

[2] R. Jinnouchi et al., Catal. Today **262**, 100 (2016).

Modeling of the Ammonia Decomposition Reaction on Iron-based Material Surfaces

Peijie FENG, Minhyeok LEE, and Yuji SUZUKI

Department of Mechanical Engineering, School of Engineering,

The University of Tokyo, 7-3-1 Hongo, Bunkyo-ku, Tokyo 113-8656

Ammonia is expected as a next-generation green energy carrier due to its high hydrogen density and ease of liquifying for storage and transportation. However, the direct application of ammonia as a fuel suffers from its low flammability and potential NOx emission [1]. A fundamental understanding of ammonia reaction kinetics is necessary to overcome these issues. On the other hand, since ammonia-related reaction kinetics has been developed and validated mainly focusing on DeNOx applications, the kinetics model often loses its robustness in absence of oxygen, where thermal decomposition mainly occurs [2].

Therefore, we conducted density functional theory (DFT) calculations using the Vienna Ab initio Simulation Package (VASP) with the aid of the supercomputer system at ISSP to evaluate the rate-determining step of ammonia surface decomposition on iron-based materials.

It has been demonstrated that the nitrogen recombination reaction shows the largest activation energy on metal surfaces such as Fe, Co, and Ni [3], and accordingly, it can be assumed as the rate-determining step. Any surface offering a lower N-N recombination activation barrier would significantly facilitate ammonia decomposition. To estimate the reactivity of ammonia on iron nitride and compare it with that on iron, DFT calculations are performed that illustrate the activation barrier of the rate-determining step on iron and iron nitride. Firstly, the surface energy is calculated to identify the most common lattice surface where the reaction happens. Secondly, the adsorption conformation of N_2 and atomic N is calculated to obtain the system's total energy. Finally, the calculated conformation for the reactant and product is used to estimate the total energy of transition states. Based on a series of calculations, the activation energy can be estimated from the energy difference between the transition state and the initial reactant state.

The surface energy calculation on iron nitride (FeN) is performed on lattice surfaces 100, 110 (with Fe or N at the top layer), and 111 (with Fe or N at the top layer). The result shows the lattice surface 110 has the lowest surface energy at around $0.086 eV/Å^2$ as shown in Table 1. The lower the surface energy, the more stable the surface is and the more common it is on the catalyst surface as

experimentally prepared. On the other hand, a closed-packed surface (110) can be found on iron surfaces, which usually possess the lowest surface energy. Thus, FeN with lattice surface 110 and Fe with lattice surface 110 are used to estimate and compare the heterogeneous reaction of ammonia.

Table 1: Surface energy of iron nitride FeN.

Lattice Surface	110	100		111	
Top Element	-	Fe	N	Fe	N
Surface Energy [eV/Å^2]	**0.086**	0.186	0.361	0.361	0.093

Since N-N recombination is the key rate-determining step of ammonia decomposition, the most stable adsorption site for N is found by placing N atoms at all possible adsorption sites (as shown in Fig. 1) on the surface both for FeN-110 and Fe-110. Among all possible adsorption sites, the Fe-top site on FeN-110 and the Hollow site on Fe-110 showed the lowest adsorption energy, indicating they are the most preferable active site to adsorb free N atoms.

By defining the product conformation for N_2 molecules on the surface, the climbing image

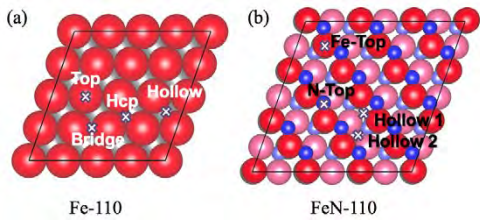

Fig. 1: Adsorption site of (a) Fe-110 and (b) FeN-110 surfaces.

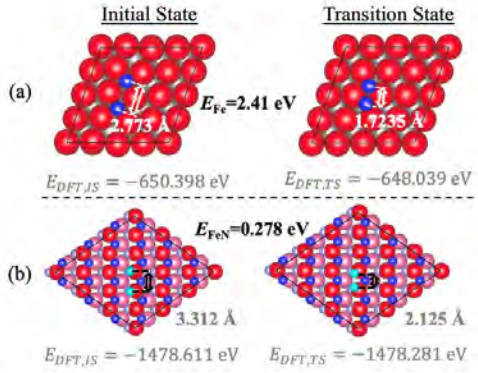

Fig. 2: Initial and transition states of N-N recombination for (a) Fe-110 and (b) FeN-110 surfaces.

nudged elastic band (CI-NEB) method [4] calculation can be performed first-principally, which yields the transition states and the total energies of the reaction between the given reactants and the products. As shown in Fig. 2, the FeN surface provides a lower activation energy (0.278 eV) than the Fe surface (2.41 eV), indicating a promising catalyst for ammonia decomposition reaction.

Further improvements in finding the reaction kinetics shall be made through the harmonic transition state method.

References

[1] M.V. Manna, P. Sabia, R. Ragucci, and M. de Joannon, Fuel **264,** 116768 (2020).

[2] P. Glarborg, H. Hashemi, and P. Marshall, Fuel Commun. **10**, 100049 (2022).

[3] X. Duan *et al.*, J. Mol. Catal. A Chem. **357**, 81 (2012) .

[4] G. Henkelman and H. Jónsson, J. Chem. Phys. **111**, 7010 (1999).

Study on the Catalytic Mechanism of RuTi Alloy in Catalyst-Referred Etching Method

Pho Van BUI, Daisetsu TOH, Kouji INAGAKI, Yoshitada MORIKAWA

Grad. School of Engineering,

Osaka University, 2-1 Yamada-oka, Suita, Osaka 565-0871

Polishing is an extremely important technique used in the finishing processes for optical and semiconductor surfaces and determines the performance of the final products. To produce smooth surface without introducing any crystallographically damaged surface, only pure chemical etching method is desired. Recently, catalyst-referred etching (CARE) method using Pt catalyst and water (as an etchant) has been proposed [1]. CARE can planarize SiC and various crystalline semiconductor materials to atomically smooth surfaces [2,3]. The main role of the catalyst is to dissociate water molecules and to stabilize the five-fold coordinated states. After a Si was removed from the material, silicic acid is formed and bonded to the catalyst surface.

To improve the removal rate (RR) and stability, many catalyst metals have tested their capability as a catalyst metal in CARE. Our recent studies found that Ni and Ru alloy are the best catalysts in terms of RR [4]. However, the RR is decayed in time due to poisoning by removal products. Our recent experimental results have shown that alloying Ru with Ti could effectively improve its stability for several hours of polishing compared to Ni or Ru itself [5]. The long-term stability of a catalyst could reduce the cost and increase the reliability of CARE to be a practical ultraprecision polishing method for next-generation optical devices. Therefore, purpose

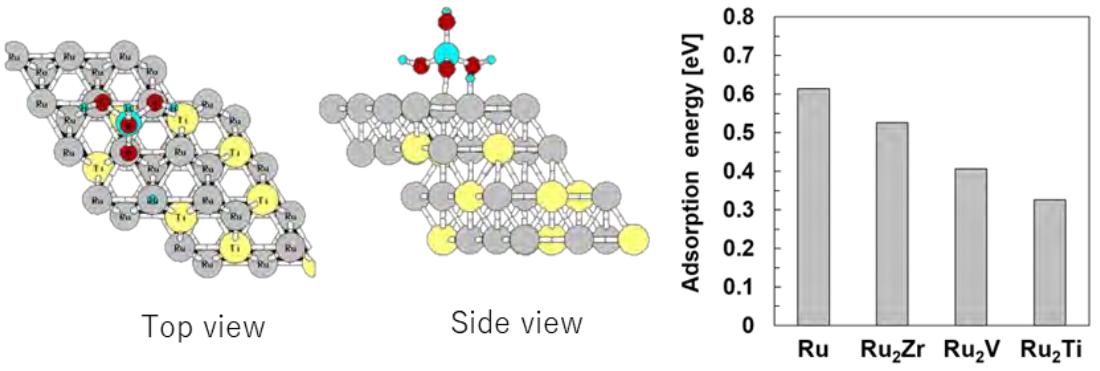

Fig. 1: Top and side views of the Ru_2M slab model with silicic acid. Adsorption energy of silicic acid.

of the proposed research is to elucidate the catalytic mechanism of RuTi alloy and general understanding of the catalytic decay using first principles calculations.

The DFT calculations were performed using the Simulation Tool for Atom Technology package, which has clarified the adsorption and dissociative reaction on metal surfaces [6-8]. The electron–ion charge interactions were described by an ultra-soft pseudopotential. The wavefunction and charge density were expanded by a plane-wave basis set with 25 and 225 Ry cut-off energies, respectively. Optimization was iteratively performed until the residual forces acting on all atoms at the saddle point were reduced to below 10^{-3} E_h/a_0, where E_h = 27.211 eV and a_0 = 0.529 Å.

In this study, we used the 3×4×4 supercell model of Ru with (0001) surface as the host metal catalyst model, as shown in Fig. 1. A few Ru atoms are substituted by a transition metal atom, such as Zr, V, and Ti, creating a Ru-based alloy catalyst model. The adsorption energy, E_{adsorb}, of silicic acid on Ru, Ru-V, Ru-Ti, and Ru-Zr alloy catalyst surfaces was calculated by,

$$E_{adsorb} = |E_{Ru+silicic\ acid} - (E_{Ru} + E_{silicic\ acid})|,$$

where $E_{Ru+silicic}$ acid, E_{Ru}, and $E_{sicilic\ acid}$ are the total energies of the Ru-based catalyst with adsorbed silicic acid, the Ru-based catalyst, and silicic acid, respectively.

The adsorption energies of silicic acid on the Ru catalyst and Ru-based alloy catalyst are shown in Fig. 1. The adsorption energy of silicic acid on RuTi alloy is the lowest among the investigated catalysts. DFT calculations showed that Ti doping to Ru reduces the adsorption energy of silicic acid on the Ru site from 0.61 to 0.32 eV and efficiently restores the active Ru sites.

References

[1] H. Hara, Y. Sano, H. Mimura, K. Arima, K. Kubota, K. Yagi, J. Murata, and K. Yamauchi, J. Electron Mater. **35**, L11 (2006).

[2] D. Toh, P.V. Bui, N. Kidani, S. Matsuyama, Y. Sano, Y. Morikawa, and K. Yamauchi, K. Rev. Sci. Instrum. **90**, 045115 (2019).

[3] A. Isohashi, P.V. Bui, D. Toh, S. Matsuyama, Y. Sano, K. Inagaki, Y. Morikawa, and K. Yamauchi, Appl. Phys. Lett. **110**, 201601 (2017).

[4] D. Toh, P.V. Bui, A. Isohashi, S. Matsuyama, K. Yamauchi, and Y. Sano, Rev. Sci. Instrum. **91**, 045108 (2020).

[5] D. Toh, K. Kayao, P.V. Bui, K. Inagaki, Y. Morikawa, K. Yamauchi, and Y. Sano, Pre. Eng. submitted.

[6] T. Hayashi, Y. Morikawa, and H. Nozoya, J. Chem. Phys. **114**, 7615 (2001).

[7] Y. Hamamoto, I. Hamada, K. Inagaki, and Y. Morikawa, Phys. Rev. B **93**, 245440 (2016).

[8] J. Quan, F. Muttaqien, T. Kondo, T. Kozaeashi, T. Mogi, T. Imabayashi, Y. Hamamoto, K. Inagaki, I. Hamada, Y. Morikawa, and J. Nakamura, Nature Chem. **11**, 722 (2019).

Proton Storage in Ruddlesden–Popper-type $Sr_3Fe_2O_7$

Kosuke Kawai, Masashi Okubo

Department of Electrical Engineering and Bioscience, School of Advanced Science and Engineering, Waseda University, 3-4-1 Okubo, Shinjuku-ku, Tokyo 169-8555

We investigated proton storage properties of Ruddlesden–Popper-type $Sr_3Fe_2O_7$ using density functional theory (DFT) calculations. This year, we focused on thermodynamically stable sites of proton in the lattice of $Sr_3Fe_2O_7$.

DFT calculations were performed with the Vienna ab initio simulation package (VASP). The projected augmented wave method and a plane basis set implemented in the VASP code were utilized with a cutoff energy of 520 eV and *k*-point sampling on a 6×6×2 grid.[1] The generalized gradient approximation of the Perdew–Burke–Ernzerhof exchange-correlation functional was used with Hubbard U = 4.0 eV for Fe to correct the self-interaction error of correlated d electrons.[2,3] An initial structure model of $Sr_3Fe_2O_7$ was obtained from the Materials Project (ID: mp-18820), and expanded to a superstructure of 2×2×1 ($Sr_{24}Fe_{16}O_{56}$, **Fig.1a**). Structure optimization was performed with a convergence condition of ΔF < 0.01 eV/Å. A H atom was located manually near an O atom with a H–O distance of < 1 Å, and then structure optimization was performed in the same way. Graphics of crystal structures were drawn by VESTA software.[4]

Three thermodynamically stable H^+ sites were identified around interlayer space after structure optimization. Site A is bridged to the nearest O atom in the same FeO_6 octahedron, and the most thermodynamically stable. Site B in the interlayer space is directed to an O atom in neighboring Fe_2O_7 layer. Site C is also in the interlayer space but directed to a Sr atom, resulting in high electrostatic energy.

References

[1] G. Kresse and J. Furthmüller, *Phys. Rev. B* **54**, 11169−11186 (1996).

[2] J. P. Perdew, et al., *Phys. Rev. Lett.* **77**, 3865−3868 (1996).

[3] F. Zhou, et al., P*hys. Rev. B - Condens. Matter Mater. Phys.* **70**, 1–8 (2004).

[4] K. Momma and F. Izumi, *J. Appl. Crystallogr.* **41**, 653−658 (2008).

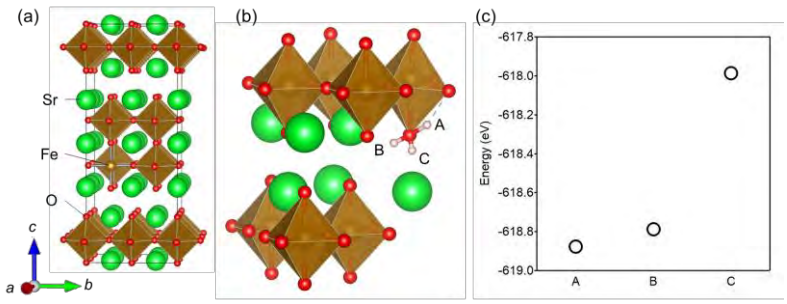

Fig.1 (a) Crystal structure of Ruddlesden–Popper-type $Sr_3Fe_2O_7$, (b) typical H^+ sites, and (c) total energies of $HSr_{24}Fe_{16}O_{56}$.

Ultrafast adsorption states of two-dimensional metal-organic-frameworks and semiconductors

Kenichi SHUDO

Fac. of Eng/Sci, Yokohama Nat'l Univ.

The University of Tokyo, Kashiwa-no-ha, Kashiwa, Chiba 277-8581

We performed calculation for elucidation of a nonlinear optical effect of a typical transition metal dichalcogenides, $MoSe_2$, using Vienna *ab initio* Simulation Package (VASP). Molecular dynamics produces well the atomic trajectories from an initial kick due to potential deformation caused by photo-transition. Hyperlinear components gives a sum frequency and harmonics of fundamental oscillation (Fig.1). These Fourier components are contrary to the linear normal modes reachable either *via* experimental cw-Raman spectroscopy and theoretical diagonalization of atomic potential along with the displacement of each atom. The nonlinear optical effect derived by atomic motion was thus clarified.

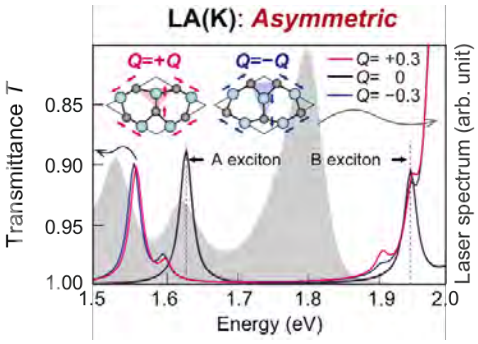

Fig. 1: Example of nonlinear vibronic modes of $MoSe_2$ simulated by means of molecular dynamics at femtosecond scale. See Ref [1] for detail.

Metastable-atom electron spectroscopy (MAES) reveals electric states of a surface, exclusively giving information of the electron cloud protrude into the vacuum. We measured the spectra of such electrons of a typical topological insulator, Bi_2Se_3. Our preliminary calculation of one to a few layers of this crystal, using VASP. The obtained results are analyzed based on the local density of state dependent on the distance from the top-most surface atoms. The spectral features of the MAES applied to the crystal are concluded to be originated from concurrent processes of resonance ionization and Auger neutralization.

Similar local electron distribution curves are obtained also for layler-by-layer structures of metal-organic framework (MOF) of 5,10,15,20-Tetrakis(4-carboxyphenyl)-porphyrin.

References

[1] S. Bae, K. Matsumoto, H. Raebiger, K. Shudo, Y.-H. Kim, Ø.S. Handegård, T. Nagao, M. Kitajima, Y. Sakai, X. Zhang, R. Vajtai, P. Ajayan, J. Kono, J. Takeda, I. Katayama: Nature Communications 13, 4279 (2022)

Analyzing Reaction Mechanism of Charge Transfer in Catalysis by Electronic Structure Calculations

Tatsuya JOUTSUKA

Institute of Quantum Beam Science, Graduate School of Science and Engineering, Ibaraki University, Hitachi, 316-8511 Ibaraki, Japan.

Frontier Research Center for Applied Atomic Sciences, Ibaraki University, 162-1 Shirakata, Tokai, Ibaraki 319-1106, Japan.

Carbon Recycle Energy Research Center, Ibaraki University, Hitachi, 316-8511 Ibaraki, Japan.

Focusing on the selectivity of zirconia-catalyzed methanol synthesis, we calculated adsorption and reaction energies to clarify the reaction mechanism. [1-2] In addition, polaron transfer rate constants in bulk titanium dioxide (TiO_2) and $SrTiO_3$ were calculated by the constrained density functional theory (CDFT) method. Then, the electronic structure calculation was used to elucidate the photocatalytic reaction mechanism and crystal plane selectivity in photocatalysts.

A zirconia-based solid solution catalyst $ZnZrO_x$ was prepared by substituting Zn with Zr, which has high catalytic activity. The correlation between the binding strength of the substituted elements and adsorbates (reactants, products, and intermediates) and methanol synthesis capacity was clarified. The DFT calculations using cp2k program package showed that the Zn species in the clusters are more likely to be exposed on the surface. This result is consistent with experimental results, suggesting that Zn species are unevenly distributed on the surface and deposited near the surface; by adding excess Zn to ZrO_2, both Zn-containing clusters and ZnO nanoparticles were formed. We also analyzed the dynamics in adsorption and chemical reactions by molecular dynamics simulation and develop a method to analyze charge transfer. In addition, we elucidated the mechanism of Cu nanoparticle formation with a size <10 nm using DFT calculations.[3] Furthermore, we analyzed theoretical methods for proton transfer in liquid water,[4] cross-coupling of arylboronic acid and imidazole on *t*-ZrO_2,[5] and Cu deposition by chemical vapor deposition using a CuI precursor[6] using VASP and cp2k program packages.

In addition, the polaron transfer rate constants in bulk TiO_2 and $SrTiO_3$ (Fig. 1) was calculated by the CDFT method along the several directions (such as [101] direction in TiO_2) using cp2k program package. We found

that the CDFT method can evaluate the potential energy profile more accurately than linear interpolation of structures that has been frequently employed for bulk TiO_2. We next moved on to the $SrTiO_3$ (001) and (110) surfaces to understand the porlaron transfer at the surface. We are now studying the relation with the oxygen vacancy and electron polaron to discuss the photocatalytic mechanism further using cp2k program package.

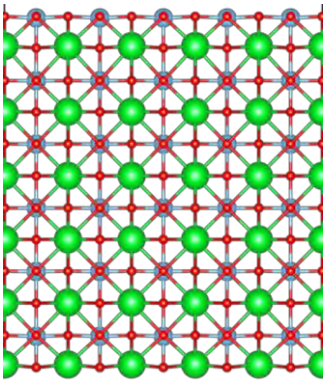

Fig. 1: Bulk $SrTiO_3$.

References

[1] Shohei Tada, Nagomu Ochiai, Hiroka Kinoshita, Mitsuhiro Yoshida, Natsumi Shimada, Tatsuya Joutsuka, Masahiko Nishijima, Tetsuo Honma, Noriko Yamauchi, Yoshio Kobayashi, and Kenta Iyoki, ACS Catal., **12**, 7748–7759 (2022).

[2] Tatsuya Joutsuka and Shohei Tada,* J. Phys. Chem. C, **127**, 6998–7008 (2023)

[3] Tatsuya Joutsuka, Ryu Hamamura, Kakeru Fujiwara, Tetsuo Honma, Masahiko Nishijima, and Shohei Tada, Int. J. Hydrog. Energy, **47**, 21369–21374 (2022).

[4] Tatsuya Joutsuka, J. Phys. Chem. B, **126**, 24, 4565–4571 (2022).

[5] Masaru Kondo, Tatsuya Joutsuka, Kakeru Fujiwara, Tetsuo Honma, and Shohei Tada, Catal. Sci. Technol., **13**, 2247-2254 (2023).

[6] Gento Toyoda, Hikari Kikuchi, Satoshi Yamauchi, Tatsuya Joutsuka, Takashi Fuse, and Yusuke Kubota, Jpn. J. Appl. Phys., **62**, SH1002 (2023).

First-principles calculation of oxygen defects on the surface of titanium dioxide TiO_2

Shoya Kawano

Department of Electrical and Electronic Engineering, Kyushu Institute of Technology, Kitakyushu, Fukuoka, 804-8550

We have studied stability of oxygen defects on TiO_2 surface by density functional calculations in this project. Oxygen defects in TiO_2 significantly changes its catalytic performance, carrier transport, hydrophilicity, and other functions. Therefore, if we can successfully control these oxygen defects, it will be possible to design the function of TiO_2. For this purpose, we have studied the configuration of oxygen defects on TiO_2 surface using scanning probe microscopy (SPM) image with template matching method. This SPM image analysis indicated typical configuration of oxygen defects. Therefore, we investigated stability of configuration of oxygen defects on TiO_2 surface by density functional calculations.

We performed density functional calculations for slab models of rutile TiO_2 (110) by using Quantum ESPRESSO code [1,2]. The slab models have two oxygen defects on surface and 1 nm vacuum gaps. The unit cell included 144, 240, 300 and 450 atoms are considered for slab models without defects. In Quantum ESPRESSO, we use the norm-conserving pseudo potentials generated by the code ONCVPSP (Optimized Norm Conserving Vanderbilt PSeudopotential), and are obtained them from the PseudoDojo [3]. The exchange-correlation function is used Perdew-Burke-Ernzerhof type. For example, Γ-point-centered 2×2×1 k-points sampling were used for 2×2×4 surface unit cell of TiO_2 (110) included 238 atoms. We use the energy cutoff of 96 Ry for the wave function, a convergence criterion for the electronic self-consistency loop of 10^{-10} Ry, and the Gaussian smearing method with a smearing width of 0.002 Ry. Lattice parameters of TiO_2 is referred to previous report [4].

Figure 1 shows calculated structure of TiO_2 surface model of 2×2×4 surface unit cell with two defects (238 atoms) and their defect energy E_{vac}. E_{vac} is defined as follows

$$E_{vac} = E_{Ti_nO_{2n-1}} + E_{O_2} - E_{Ti_nO_{2n}},$$

where $E_{Ti_nO_{2n-1}}$, E_{O_2} and $E_{Ti_nO_{2n}}$ are total energy of slab with defects, total energy of oxygen molecule and total energy of slab without defects. We considered five configurations for two defects introduced at bridge oxygen on the surface. The bridge oxygen is bonded with titanium along the parallel axis in Fig. 1. Configurations of defects like Fig. 1 (a)-(c) are more stable than defects along parallel axis in Fig.1 (d) and (e). This

trend of results is consistent with our STM image analysis.

We have used the L4cpu of system B with 512 parallel computing for 144 and 240 atoms unit cell, the L16cpu of system B with 2048 parallel computing for 300 and 450 atoms unit cell.

References

[1] P. Giannozzi *et. al*. J. Phys. Condens. Matter. **21**, 395502 (2009).

[2] P. Giannozzi *et. al*. J. Phys. Condens. Matter. **29**, 465901 (2017)

[3] M. J. van Setten, M. Giantomassi, E. Bousquet, M. J. Verstraete, D. R. Hamann, X. Gonze, G.-M. Rignanese, Computer Physics Communications **226**, 39-54 (2018)

[4] X. W. Wang, B. H. Zhang, L. Y. Sun, W. N. Qiao, Y. D. Hao, Y. C. Hu, and X. E. Wang, Journal of Alloys and Compounds **745**, 856 (2018).

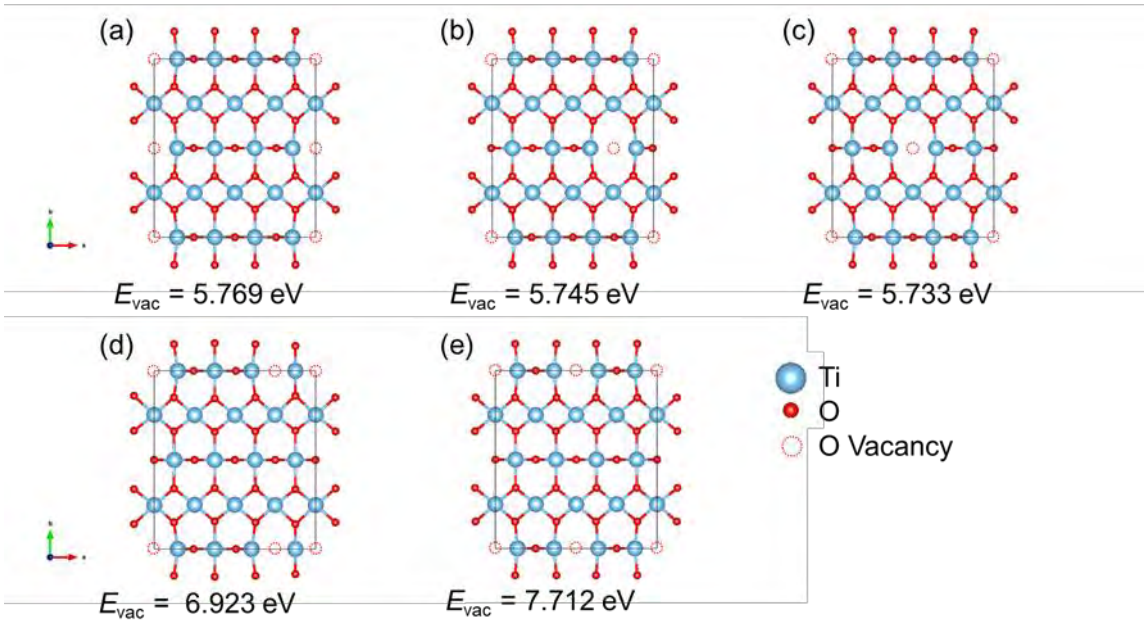

Fig. 1 Calculated structure of TiO_2 surface model and their defect energy.

Thermal conductivity calculation for high thermal conductive insulator

Shoya Kawano

Department of Electrical and Electronic Engineering, Kyushu Institute of Technology, Kitakyushu, Fukuoka, 804-8550

We have computed the lattice thermal conductivity of several materials to create a database for the design of high thermal conductive insulators. High thermal conductivity insulators are essential for the substrate of power devices. To develop high-performance power devices, it is necessary to discover new substrate materials with high thermal conductivity insulators. In this project, we created a database of lattice thermal conductivity for materials informatics.

We performed density functional phonon calculations using the ALAMODE code [1] with the Quantum ESPRESSO code [2,3] to compute the lattice thermal conductivity. We calculated the second- and third-order force constants from density functional theory. The second-order force constants were calculated using the finite displacement method, while the third-order force constants were calculated using the random displacement method implemented in ALAMODE. In the density functional calculations, we used norm-conserving pseudo-potentials generated by the Optimized Norm Conserving Vanderbilt Pseudopotential code, obtained from PseudoDojo [4]. We used the Perdew-Burke-Ernzerhof type exchange-correlation function. For finite displacement and random displacement approaches, we used displacement distances of 0.02 and 0.04 Å, respectively.

We calculated the lattice thermal conductivity of AlAs, CaO, SrO, YN, CeO_2, AlN, CaF_2, $MgBe_2N_2$, $TaGaFe_2$, and BN. These structures were collected from the Materials Project [5]. For the random displacement approach, we used 20-500 structures and compared their thermal conductivity accuracy. We found that a set of 20 structures satisfied the accuracy for the lattice thermal conductivity database. We continue to calculate the lattice thermal conductivity with the obtained parameters in this project to create a database.

We used the F16CPU of system B with 2048 parallel computing by MPI for the density functional calculations for each displacement. For thermal conductivity calculation, MPI/OpenMP hybrid parallelization was used with the F16CPU of system B.

References

[1] T. Tadano, Y. Gohda, and S. Tsuneyuki, J. Phys.: Condens. Matter **26**, 225402 (2014)

[2] P. Giannozzi *et*. *al*. J. Phys. Condens. Matter. **21**, 395502 (2009).

[3] P. Giannozzi *et*. *al*. J. Phys. Condens. Matter. **29**, 465901 (2017)

[4] M. J. van Setten, M. Giantomassi, E. Bousquet, M. J. Verstraete, D. R. Hamann, X. Gonze, G.-M. Rignanese, Computer Physics Communications **226**, 39-54 (2018)

[5] https://materialsproject.org/

Stable structures of low-dimensional systems from first-principles

Shota ONO
Department of Electrical, Electronic and Computer Engineering, Gifu University
Gifu 501-1193

In this project, we have studied (i) stable structures of two-dimensional (2D) hexagonal materials [1], (ii) structural and electronic properties of 2D ionic crystals [2], and (iii) surface rippling on non-close-packed metal surfaces [3] using density functional theory (DFT) and machine-learning approaches.

For the case (i), we have explored the stable configurations of atomic species on a hexagonal plane in 2D binary systems. The configuration search was accelerated by using the Bayesian optimization (BO) approach. For the 2D copper-based systems of Cu-X, we have shown that the structures having a hexagonal or elongated ring of Cu (or X) atoms containing a X (or Cu) cluster in the unit cell are relatively stable, in particular, for X = Be, Pd, and Au (see Fig. 1(a)). The binary Lennard-Jones model was used to interpret the optimized structures predicted by DFT calculations.

For the case (ii), we have shown that 4 and 12 IA-VII alkali halides in the 2D hexagonal and tetragonal structures (see Fig. 1(b)) are dynamically stable, respectively. The electronic band gaps range from 6.8 eV for LiF to 3.9 eV for RbI and CsI in the tetragonal structure within the generalized gradient approximation. A hard sphere model that considers the Madelung energy and the core-core repulsion explains the nearest-neighbor bond length and the cohesive energy of 2D alkali halides.

For the case (iii), we have studied surface rippling of $X/A(100)$ (see Fig. 1(c)), assuming X = H to Bi except for noble gases and A = Cu, Ag, and Au. We have shown that small atoms (such as H, C, N, O and F) attract electrons from the substrate due to the large electronegativity, which prevent them from passing through voids in the (100) surface. We have also discussed a breakdown of the hard sphere model for predicting the surface rippling amplitude.

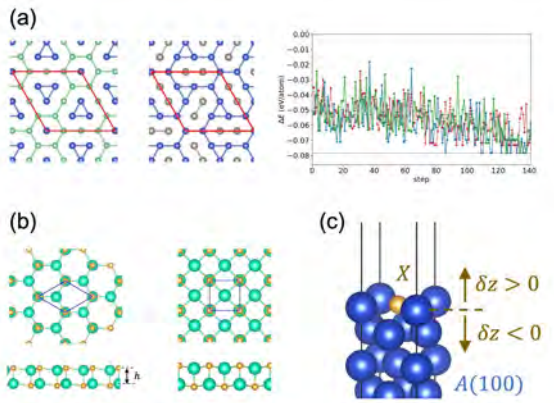

Figure 1: Stable structures (a), (b), and (c) studied in Refs [1], [2], and [3], respectively. The structures in (a) were found by using BO.

References

[1] S. Ono: AIP Advances **12**, 085313 (2022).

[2] S. Ono: J. Phys. Soc. Jpn. **91**, 094606 (2022).

[3] S. Ono, H. Satomi, and J. Yuhara: Comp. Mater. Sci. **218**, 111959 (2023).

Stable structure of vacancy cluster in tungsten and iron trapping multiple hydrogen atoms

Kazuhito Ohsawa

Institute for Applied Mechanics, Kyushu University,

Kasuga-koen, Kasuga, Fukuoka 816-8580

Introduction

Tungsten (W) and Iron (Fe) are important materials for plasma facing materials (PFMs) used in fusion reactors. In particular, W shows promise as divertor armor tiles exposed to the most intense plasma particle irradiation. Vacancy (V) and vacancy clusters nucleated in the metals under the irradiation circumstance are considered to be a large amount of hydrogen (H) and hydrogen isotope trap sites. In particular, tritium (T) retention in the PFMs is a serious problem for safety operation of fusion reactor because T is radio isotope whose half-life is about 12 years. So, the investigation of the vacancy clusters in the metals and H trapping are important subjects in the field of PFMs. In the present work, stable structures of vacancy clusters and their interaction with multiple H atoms in W and Fe lattice are investigated by computational methods. A difference of vacancy clusters in W and Fe was clarified. Besides, positions of multiple H atoms trapped in the vacancy type lattice defects are examined. The effects of H were investigated on the stable structures of the vacancy clusters.

Simulation method

Stable vacancy cluster structures and positions of multiple H atoms trapped in the vacancy clusters in W and Fe specimen were calculated in terms of first-principle calculations based on density functional theory (DFT). We used the Vienna ab-initio simulation package (VASP) for the DFT simulations. A large simulation cell, composed of 5x5x5 bcc lattice (250 atoms), were used in order to reduce the effects of periodic boundary condition imposed on the simulation cell. The cut-off energy of plane wave was 350eV.

The binding energy E_b of di-vacancy V_2 was defined as

$$E_b(V_2) = 2E[V]-E[V_2]-E_{ref}, \qquad (1)$$

where E is cohesive energy of the supercell and E_{ref} indicates energy of perfect crystal. For example, $E[V]$ and $E[V_2]$ mean cohesive energies of supercells containing mono- and di-vacancy, respectively. Positive binding energy E_b corresponds to attractive interaction of the two vacancies. Similarly, the binding energy of V-H complex V_2H_2 i.e., di-vacancy trapping two H atoms, is defined as

$$E_b(V_2H_2) = 2E[VH]-E[V_2H_2]-E_{ref},. \qquad (2)$$

Results and discussion

Stable structures of di-vacancy in W and Fe are different, as shown in Fig.1. The most stable arrangements of two vacancies are <111> in W and <100> in Fe, respectively. Actually, binding energy between two vacancies arranged in <100> direction is larger than that of <111> in Fe estimated in Eq. (1), according to Fig. 2. However, <111> arrangement of di-vacancy trapping two H are more stable than <100> one estimated in Eq. (2). Therefore, stable structure of di-vacancy in Fe is changed from <100> to <111> arrangement by the H trapping. By the way, the most stable structure of di-vacancy in W is <111> arrangement in both cases. Figure 3 shows two H atoms trapped in di-vacancy in W and Fe. H atoms trapped in the vacancy type lattice defects are allocated in the vicinity of octahedral interstitial (O-site). In addition to it, H atoms preferentially occupy O-sites located in the center of the di-vacancy where two vacancies are in contact with each other.

In the present work, H trapping are supposed to play important roles for stabilization of vacancy clusters. The binding energy of vacancy clusters increase and structure of di-vacancy are changed by the H trapping in Fe.

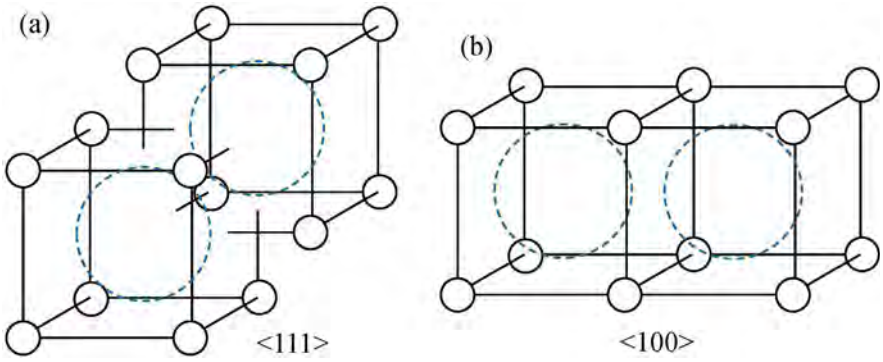

Fig. 1: Most stable structure of di-vacancy in bcc lattice. Arrangements of two vacancies are (a) <111> in W and (b) <100> in Fe, respectively.

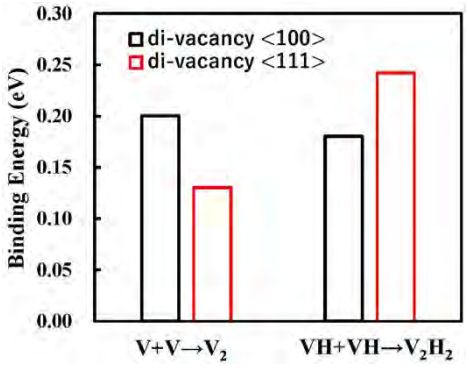

Fig. 2: Binding energy of di-vacancy and di-vacancy trapping two H atoms in Fe.

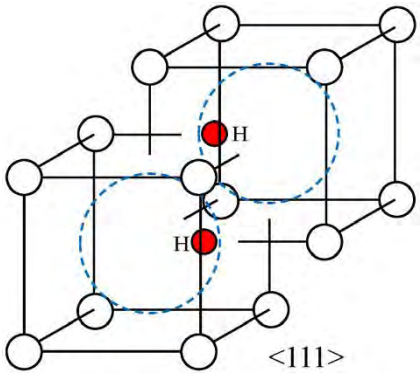

Fig. 3: Positions of two H atoms trapped in di-vacancy in W and Fe.

Ab initio molecular-dynamics study of structural and transport properties of liquid mixtures containing hydrocarbon under ultra-high pressure

Satoshi OHMURA

Department of Civil and Environmental Engineering,

Hiroshima Institute of Technology, Saeki-ku, Hiroshima 731-5193

Understanding the structures and physical properties of the C-H system at higher pressures is essential to constrain the interiors of the ice giant planets (extrasolar planet). Therefore, it is important for planetary science to understand the behavior of this important material in extreme conditions. For this reason, we have performed ab initio molecular-dynamics (MD) simulations for liquid Methane (CH_4) under high pressures. We used a 500-atom system consisting of 400 hydrogen and 100 carbon atoms in a cubic supercell with periodic boundary conditions.

Figure 1 shows the pressure dependence of the pair distribution functions $g_{\alpha\beta}(r)$ of liquid CH_4 obtained from the MD simulation. Since methane molecules remain intact up to 100 GPa, the shape of $g_{CC}(r)$, $g_{CH}(r)$ and, $g_{HH}(r)$ at 55 and 100 GPa are almost the same. Above 150 GPa, in $g_{CC}(r)$, a new peak appears at approximately 1.4 Å and its position gradually shifts to a smaller r with increasing pressure. Moreover, the first peak of $g_{CC}(r)$ is clearly separated from a second peak at pressures of 150 GPa, suggesting that the C-C bonds contributing to the first peak are highly stable and strong. The simulation found that the interaction remains even under ultrahigh pressure conditions of 1300 GPa. For hydrogen, molecular hydrogen is observed after methane dissociation (at 150 GPa). When the pressure becomes higher, hydrogen molecule becomes unstable.

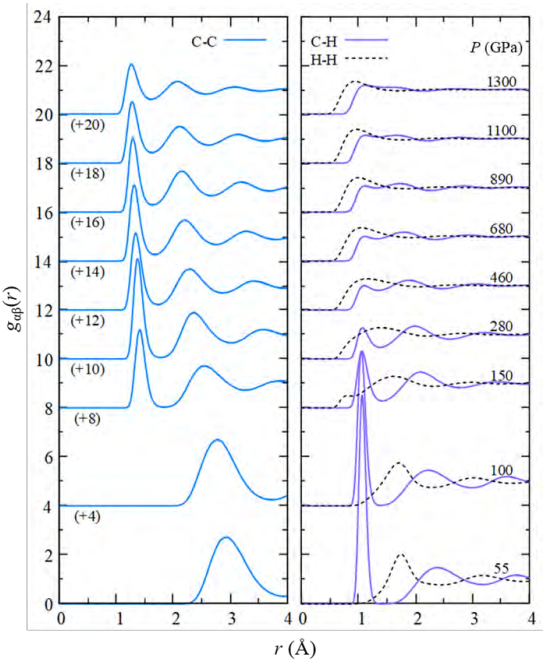

Fig. 1: Pressure dependence of the pair distribution functions $g_{\alpha\beta}(r)$ of liquid CH_4.

Temperature dependence of structural and electronic properties of organic molecular thin film surfaces

Kaori Niki

Graduate school of science

Chiba University, Yayoi-cho, Inage-ku, Chiba 263-8522

In recent years, it has been reported that organic molecules' electronic and physical properties interact with the surface using Wave number space-resolved Photoelectron Spectroscopy. We have investigated the copper (Ⅱ) phthalocyanine (CuPc) - monolayer substrate system. This year, we investigated molecular motion depending on the terminal. Monolayer $TiSe_2$ has two typical phases depending on the temperature. A (1 × 1) structure (normal phase) is shown at room temperature, and a (2 × 2) superstructure (CDW phase) is realized under the 200 K. Each phase has a band gap of 83 meV and 153 meV, respectively [1, 2]. We have adopted this interesting thin film as the substrate and reported the structural changes depending on the temperature in the previous year and structure optimization, resulting in an adsorption distance of 3.16 Å.

This time, we performed Molecular dynamics (MD) simulation using these structures as the ground state, and clarified the structures after temperature change.

MD calcuration of CuPc on $TiSe_2$

We performed density functional theory (DFT) calculations using the Vienna Ab Initio Software Package (VASP) version 5.4.4 [3,4]. The Generalized Gradient Approximation (GGA) within the Perdew-Burke-Ernzerhof (PBE) formalism described the exchange-correlation effects. We used a unit cell with lattice constants a = b = 3.53 Å, c = 20.0 Å, α = β = 90° and γ = 120°, and plane-wave basis set with the projector augmented wave (PAW) approach with an energy cutoff of 380 eV. The Brillouin zone integration was performed on a Monkhorst-Pack of 18×18×1 grid of k-points. The energy convergence criterion chosen for the self-consistency cycle was 1×10^{-7} eV. To account for Fermi surface broadening, temperature parameter σ for Methfessel-Paxton smearing was applied [5]. So far, we have found the parameter set (U = 3.9 eV and σ = 0.01 eV), which reproduces the experimental result [6]. We used these parameters for the MD simulation of the CuPc / $TiSe_2$ structure. After relaxing the geometries at 0 K, the systems were brought up to 654 K by repeated velocity rescaling using the spin-polarized PBE+U DFT-D3 functional at the Γ-point. Then 5 ps microcanonical MD trajectories were generated with a 1 fs time step.

Molecural rotation of CuPc/$TiSe_2$

Figure 1 shows the geometry of CuPc on

TiSe2 at 0 K. S1 and S2 indicate the axis of the surface. “Center, " one of the molecular axes, is tilted 30 degrees from the axis s2.

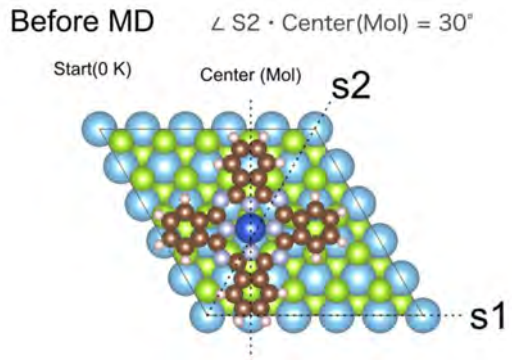

Figure 1. Geometry of CuPc/TiSe2

Figure 2 shows the geometry of CuPc/TiSe2 after MD. A temperature of 654 K is assumed. We can see the motion of the molecule to the lower left. The angle between the central and s2 is magnified to 60 degrees.

After MD

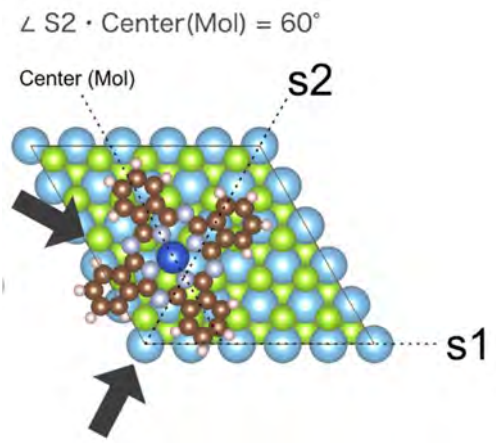

Figure 2. Geometry of CuPc/TiSe2

Cu is adsorbed between Ti and Se atoms before MD simulation. At this time, charge repulsion occurs between Cu and surrounding Se, and between carbon and Se near the center at lower temperatures.

On the other hand, after MD calculation, the number of Se electrons in TiSe2 is slightly larger than before calculation. On the other hand, the number of electrons in Cu atom decreases. A stable structure is due to the close distance between Cu and Ti creates. Nitrogen closer to the center has additional electrons and approaches Ti atoms. This also creates a stable structure.

Conclusion

By performing MD calculations using VASP, we clarified changes in the charge distribution of molecules and substrates and molecular motions with increasing temperature.

References

[1] J.-P. Peng *et. al.*, Phys. Rev. B **91**, 121113 (2015).

[2] P. Chen *et. al.*, Nat. Commun **6**, 8943 (2015).

[3] G. Kresse and J. Furthmuller, Phys. Rev. B, **54**, 11169 (1996).

[4] G. Kresse and J. Hafner, Phys. Rev. B, 49 14251 (1994).

[5] M. Methfessel and A. T. Paxton, Phys. Rev. B **40**, 3616 (1989).

[6] R. Bianco *et.al.*, Phys. Rev. B **92**, 094107 (2015).

Development of First Principles methods for Light-Matter Interaction

Hiroki KATOW

Photon Science Center, Graduate School of Engineering,

The University of Tokyo, Bunkyo-ku, Tokyo 113-8656, Japan

The electronic dipole moment calculation is a fundamental of the light-matter interaction. In isolated systems, the dipole moment is defined by an expectation value of dipole operator and no ambiguities in its definition. Contrarily in periodic systems, ambiguity of the choice of cell boundary leads to the indefiniteness of its definition. Modern understanding of this issue is that the ambiguity is rooted in the indefinite complex phase factor of one-particle orbitals, which is called gauge degrees of freedom. A solution is proposed for ground states by King-Smith and Vanderbilt where the dipole moment is reformulated to exclude explicit dependency on the gauge [1].

A same obstacle is present in excitonic systems. The author of this report and colleagues have developed a gauge-free method for excitonic systems [2] as an extension of King-Smith and Vanderbilt's formula. We demonstrated the validity of our gauge-free dipole calculation of Graphane exciton by using System B. We employed Quantum ESPRESSO [3] and BerkeleyGW [4] package to compute excitonic wave functions based on GW+BSE method. In this project we calculated excitonic states of monolayer (ML) and bulk hexagonal boron nitride (hBN) for further systematic study. Massively parallelized calculations using 2048 cpu in F16cpu class were conducted. We show the exciton energy spectrum of ML- and bulk-hBN in Figure 1. Due to the weak screening of two-dimensional system ML-hBN possesses larger GW gap (8.12 eV) than bulk-hBN (5.54 eV). We also confirmed huge exciton binding energy of ML-hBN. As a future prospect, we apply our gauge-free method to ML- and bulk-hBN by utilizing the excitonic wave functions computed in this project.

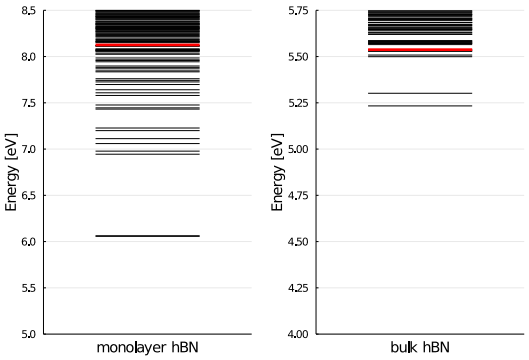

Fig. 1 Exciton energy spectrum of the monolayer hBN (left) and bulk hBN (right) calculated by using BerkeleyGW package [4] which is based on GW+BSE method. Red lines indicate GW gap.

References

[1] R.D. King-Smith et al., Phys. Rev. B 47, 1651(R) (1993).

[2] H. Katow et al., Phys. Rev. Lett. **129**, 047401 (2022).

[3] P. Giannozzi et al., J. Phys. Condens. Matter 21, 395502 (2009).

[4] J. Deslippe et al., Comput. Phys. Commun. 183, 1269 (2012).

Fig. 1: Supercomputer System B at SCC-ISSP.

Study on structural elementary excitations at semiconductor surfaces and interfaces

Hiroyuki KAGESHIMA
Graduate School of Natural Science and Technology, Shimane University
1060 Nishi-Kawatsucho, Matsue, Shimane 690-8504

In this project, we have been focused on physical properties of structural elementary excitations of semiconductor surfaces and interfaces. In this year, we have focused on the physical properties of SiO self-interstitial in SiO_2. [1] The calculations were performed based on the first-principles calculation. Program package PHASE/0 was employed. [2]

When Si is oxidized, a large volume expansion occurs at the interface, so Si is released into the oxide film in order to relax the generated strain. This is because a slightly denser and Si-rich region is formed near the interface, and a concentration gradient of excess Si is generated, which tends to promote the migration and diffusion of excess Si toward the oxide film side. Moreover, the presence of excess Si is thought to induce and to enhance structural deformation of the oxide film. Therefore, the behavior of excess Si in the near-interface oxide film governs strain relaxation in two ways. In this study, we traced the path of the migration and diffusion of excess Si at the atomic level, and investigated the energy profile by the first-principles calculations.

A quartz/Si(100) interface model with four Si layers and four SiO_2 layers was used for the calculation. The front and back surfaces are terminated by H, and superslab geometry with a sufficient vacuum layer is prepared. The in-plane periodicity is $2\sqrt{2} \times 2\sqrt{2}$, which is sufficiently large. The unit cell contains 142 atoms. We used plane wave bases with the cutoff of 30 Ry, and norm-conserving pseudopotentials for Si and H as well as an ultrasoft pseudopotential for O. We also used the exchange-correlation density functional of generalized gradient approximation (GGAPBE). We employed the Monkhorst-Pack k-point sampling of $4\times4\times1$. Using the structure with interstitial SiO placed at the interface as the initial structure (Fig. 1), we searched for migration diffusion paths. In the route search, the structure optimization calculation was performed by fixing one Si layer and H on the back surface. For comparison, a SiO_2 crystal model equivalent to one in which only the oxide film was taken out and arranged periodically was also used to investigate the characteristics of the interface.

We assumed that the excess Si is interstitial SiO in the oxide film, and that migration diffusion consists of three elementary processes. These are O vacancy transfer, Si coordination number conversion, and Si bond order conversion. All of these elementary processes are effective only for migration diffusion of interstitial SiO, and are not considered for other forms of excess Si. In particular, O vacancy transfer and Si coordination number conversion are essential. In order for Si coordination number conversion to occur, O vacancy transfer must be repeated to move O vacancies to appropriate positions. Si bond order conversion can be substituted by these two, but it has the effect of shortening several steps at once.

Based on these assumptions, we succeeded in constructing a transport diffusion path of the excess Si from the interface to the oxide film

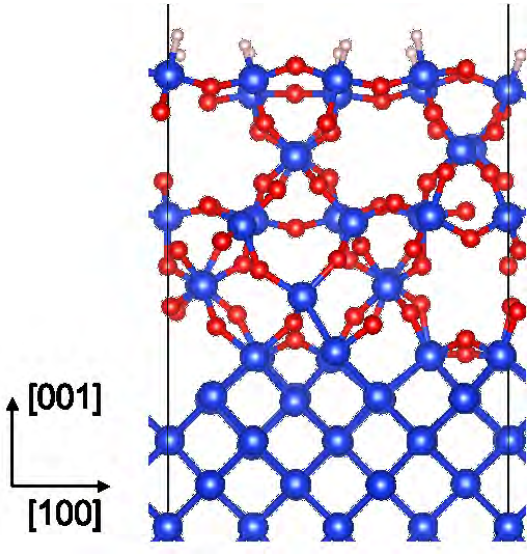

Figure 1: Starting atomic structure for the migration diffusion path of the SiO interstitial. Large, middle, and small spheres indicate Si, O, and H atoms, respectively.

surface. Moreover, the energy profile is numerically consistent with previous experimental results. It was also found that near the interface, migration diffusion is difficult due to strong structural constraint from the Si crystal side. The highest energy is 2.37 eV for the initial structure, and the energy drops to −1.47 eV when interstitial SiO reaches the surface. This diffusion path we found consists of 10 steps of O vacancy transfer, 15 steps of Si coordination number conversion, and 1 step of Si bond order conversion. It should be noted that Si and O belonging to SiO interstitaial at the final structure is different from those at the starting structure. SiO interstitial moves with sequentially kicking the neighboring Si and O like a billiards, and the kicked-out Si and O become new interstitial SiO, while Si and O belonging to the old intersititial SiO are absorbed as a part of the oxide.

So far, we have reported that, by the first-principles molecular dynamics method, the migration and diffusion of atoms in Si-rich SiO_2 is enhanced under compressive strain, [3] and by the first-principles nudged-elastic-band (NEB) method, the migration and diffusion of the O vacancies in SiO_2 is conversely reduced. [4] Therefore, we have speculated that the movement and diffusion of atoms in SiO_2, which has a large Si composition, is governed not by the movement and diffusion of O vacancies but by the Si coordination number conversion due to interstitial SiO. Our results are numerically consistent with these calculation results, which supports our speculation, and suggests the importance of the behavior of interstitial SiO in Si oxidation.

In this calculation, the barrier height in each elementary process is not calculated yet. For this reason, the comparison of our results with the experimental results and our previous computational results is unfortunately still insufficient. We are planning to calculate barrier heights by using the first-principles NEB method, and to compare numerical values much more in detail.

References

[1] H. Kageshima, T. Akiyama, and K. Shiraishi, Matter. Sci. Semicon. Process. **162** (2023) 107527 (7 pages).

[2] https://azuma.nims.go.jp

[3] H. Kageshima, Y. Yajima, K. Shiraishi, and T. Endoh, Jpn. J. Appl. Phys. **58** (2019) 111004 (11 pages).

[4] K. Yata and H. Kageshima, Jpn. J. Appl. Phys., **60** (2021) 035504 (6 pages).

Exponent puzzle for metal-insulator transition in doped semiconductors

Yosuke HARASHIMA
Division of Materials Science, Nara Institute of Science and Technology
Takayama-cho, Ikoma, Nara 630-0192

The zero temperature conductivity is zero at low impurity concentrations, and it becomes finite at high impurity concentrations. A metal-insulator transition occurs at concentrations in between. This metal-insulator transition is a general phenomenon of quantum transport and is known to occur in many semiconductors. Understanding the mechanism of the metal-insulator transition leads to an understanding of the general theory of quantum transport.

Here, electrons are scattered by randomly configurated impurities, and the phases of wavefunctions are randomly shifted out. Those waves interfere each other and propagation is inhibited, resulting in the appearance of localized states. This is called Anderson localization and a metal-insulator transition driven by disorder is called Anderson transition. Anderson transition is a continuous transition, and the correlation length ξ diverges at the transition point as $\propto |n - n_{\rm c}|^{-\nu}$. The critical exponent, ν, which characterizes this divergence, plays an important role in understanding the physical characteristics of the system. Since the critical exponent is universal and independent of the details of the system, the critical exponent can be used to classify systems. In other words, when two systems have different critical exponents, it means that they have different intrinsic physical features and are completely different physical phenomena.

Although there have been several experimental reports on the critical exponent of the metal-insulator transition, the proposed mechanism has not yet been clarified. There are two values of $\nu \simeq 0.5$ and $\simeq 1.0$–1.3 that have been reported experimentally. This problem is called the "exponent puzzle" and the origin of descripancy has been studied for long time. One possible origin is the effect of carrier compensation due to unintentionally introduced impurities or lattice defects, but this has not been confirmed theoretically. The purpose of this study is to elucidate the exponent puzzle by conducting a theoretical analysis considering the compensation effect in order to clarify the essential factor that causes the descripancy in the critical exponent.

Figure 1 is a calculated electronic density in a randomly distributed impurity system. The calculation is based on the density functional theory and local density approximation. We performed electronic structure calculations of compensated systems with spin configurations by using a program code used in our previous work. Positive ions and negative ions are randomly distributed in three dimensional space. They represent donors and acceptors. We solve the electronic states such that charge neutrality is satisfied, i.e., the number of electrons is equal to the difference between the number of donors and acceptors.

We also have examined stable impurity configurations in doped systems. The results are opened in Refs. [1, 2].

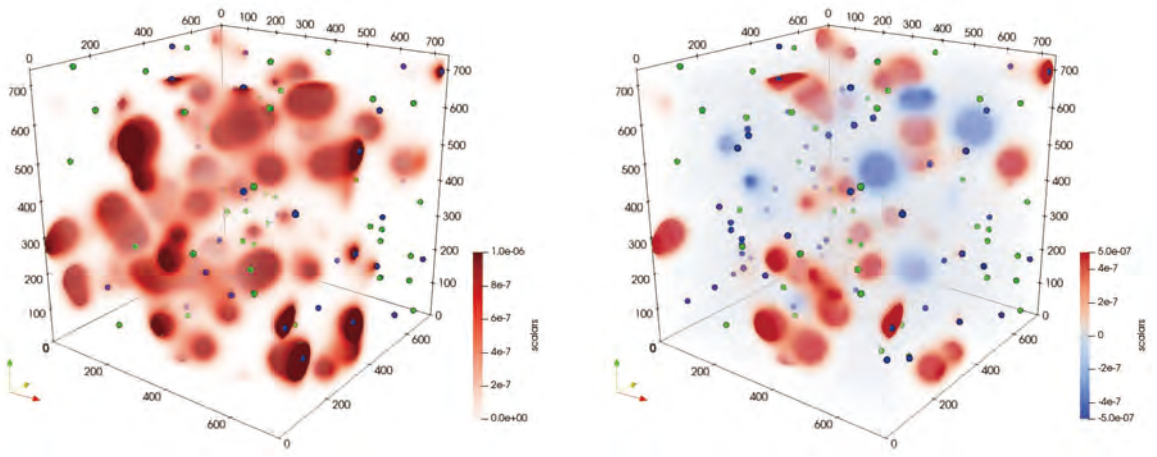

Figure 1: Total electronic density (left panel) and spin density (right panel) in a three dimensional system. Donor and acceptor ions are shown as blue and green points, respectively. In the right panel, positive and negative values denote up and down spin, respectively. The number of donor ions is 100, and that of acceptor ions is 50.

References

[1] Y. Harashima, *et. al.*: IEEE Trans. Semicon. Man., accepted, DOI:10.1109/TSM.2023.3265658.

[2] Y. Harashima, *et. al.*: arXiv:2303.14891.

Phase stability of high-entropy alloys

Yoko Yamabe-Mitarai

Frontier Science Graduate School,

The University of Tokyo, Kashiwa-no-ha, Kashiwa, Chiba 277-8561

High-entropy alloys (HEAs) comprise multiple elements with near-atomic composition and have high configurational entropy of constituent elements. HEAs have been attracted as new generation structural and functional materials since this new paradigm was proposed in 2004 [1]. Most of HEAs have a single face-center-cubic (fcc), body-center-cubic (bcc) structures or their mixtures. Due to limited slip system, hexagonal-close-pack (hcp) structure is expected to be high temperature materials. Large solid-solution hardening is also expected for HEAs. Then, we are applying to find HEAs with hcp structure experimentally and by using DFT calculation. Ti is focused on one of constituent element because Ti is used as high-temperature materials due to its small density and high specific strength. Phase stability of alloys was experimentally investigated, and a few alloys were found to be a hcp structure [2]. To investigate the effect of alloying elements and composition dependence on phase stability, phase stability change of bcc and hcp structures in Ti by 6 different alloying elements was calculated using DFT. Supercell model with 128 atoms was used to indicate solid solution phase. Special Quasirandom Structure was used to simulate random atomic position for ternary alloys as shown in Fig. 1. The internal coordinates was optimized using Quantum Expresso (QE). The total energy and density of states was calculated on the optimized coordinates. The formation energy calculated from the total energy indicated Al, Sn, Hf and Zr stabilized hcp structure, while Nb and Mo stabilized bcc structure.

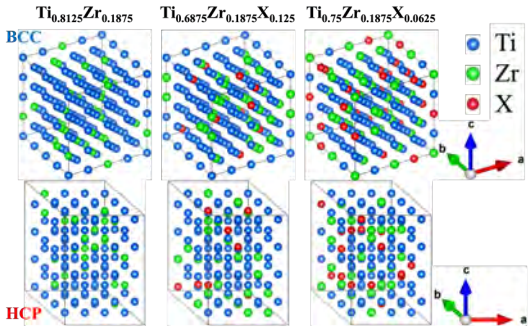

Fig. 1:BCC (top) and HCP (bottom) SQS model. X is alloying elements.

References

[1] B. Cantor, I. T. H. Chang, P. Knight, A. J. B. Vincent, Mater. Sci. Eng. A, **375-377**, 213 (2004).

[2] Y, Yamabe-Mitarai, K. Yanao, Y. Toda, I. Ohnuma, T. Matsunaga, JALCOM, **911**, 164849 (2022).

Analysis of the electronic structure of magnetic shape memory alloy by quasiparticle self-consistent *GW* approach

Masao OBATA[1,2]

[1]*Institute of Science and Engineering, Kanazawa University, Kanazawa, Ishikawa 920-1192*

[2]*Graduate School of Natural Science and Technology, Kanazawa University, Kanazawa, Ishikawa, 920-1192*

Magnetic shape memory (MSM) alloy of Ni-Mn-Ga [1] has attracted attention, showing an enormous magnetic field-induced strain (MFIS) effect of up to around 10%. This unique property comes from transitions among energetically close structures involving nanoscale-modulated structures attributed to magnetic and electronic stats. The MFIS effect is experimentally observed in the modulated structure of 10M or 14M, which has a long-period crystal structure in the *ab* plane. Although many investigations of the electronic structure based on density functional theory (DFT) within local density approximation or generalized gradient approximation (GGA) were reported, the results did not fully incorporate the experimental facts: for example, the stabilization mechanism of the modulated structures is still unclear. The importance of electron correlation effects in this material was recently indicated [2]. Thus, we employed one of the post-DFT methods, the quasiparticle self-consistent *GW* (QSGW) approach, to investigate the electronic structure beyond the GGA level. This study investigated the electronic and magnetic structure of the stoichiometric Ni_2MnGa in austenite (cubic) and non-modulate martensite (tetragonal) phases by using the first-principles calculation package ecalj [3].

As the result of the QSGW calculation, the obtained energy level of the Ni e_g orbital of the cubic phase is higher than that of GGA and almost coincided with the Fermi level. The state moves from the Fermi level in the tetragonal phase. This result strongly supports martensitic transformation due to the Jahn-Teller effect. Analysis of the Fermi surfaces nesting through generalized susceptibility revealed that its electronic state of cubic phase possesses intrinsic instabilities corresponding to 10M and 14M, which are not observed in the previous GGA calculation [4].

References

[1] K. Ullakko et al, Appl. Phys. Lett. 69, 1966 (1996).

[2] M. Zelený et al., Mater. Des., **209**, 109917 (2021).

[3] https://github.com/tkotani/ecalj/

[4] M. Obata, T. Kotani, T. Oda, Phys. Rev. Materials 7, 024413 (2023)

Calculation and comparison of adsorption energies of perfluoro molecules on Cu(111) and Cu(100) using first-principles calculation

Yuji Ohkubo, Misa Nishino, Hiroki Toujima, and Kouji Inagaki

Graduate School of Engineering,

Osaka University, 2-1 Yamadaoka Suita, Osaka 565-0871

Recently, increasing frequency of the digital signals is necessary because the amount of information communication is increasing. However, the higher the frequency is, the greater the transmission loss is. Therefore, polytetrafluoroethylene (PTFE) which has much low relative dielectric constant and dielectric loss tangent is considered as a suitable dielectric of high frequency printed wiring boards. However, PTFE has low adhesion property, so adhering PTFE to Cu is difficult. We have achieved generation of oxygen-containing functional groups and adhesion strength of 0.94 N/mm between PTFE and Cu when PTFE was He-plasma-treated at over 200℃ under atmospheric pressure[1]. Also, from the calculations of the adsorption energy between Cu(111) and fluorinated molecules, the functional groups containing COO˙ is possible to generate PTFE surface having high adhesion property. However, the calculations about Cu surface having different orientations are not performed. Therefore, in this study, the adsorption energy between Cu(100) and fluorinated molecules was calculated and the effect of orientation was investigated.

Our calculations were performed using the STATE (Simulation tool for atom technology) code with plane-wave basis and ultra-soft pseudopotential[2, 3]. The wave function and the charge density of cutoff energies were 36 and 400 Ry, respectively. Generalized gradient exchange-correlation functional based on Predew-Burke-Ernzerhof (PBE) was used for the exchange-correlation functional and DFT-D2 was used for the dispersion correction method[2, 3]. Cu surface was modeled Cu(100) 3×3 slab composed of 3 atomic layers. As the model of as-received PTFE, CF_3–CF_3 was calculated. In addition, CF_3–CF=O, CF_3–CF_2–OH, CF_2=CF_2, and CF_3–CF_2–OO˙ were calculated as the model of plasma-treated PTFE. These were the models of molecule containing oxygen-containing functional groups observed by C1s-XPS spectrum of the plasma-treated PTFE surface. Cu surface, fluorinated molecules, and adsorption systems were optimized then total energies were calculated. The adsorption energy was defined as the difference between the sum of total energy of Cu surface and fluorinated molecules and total energy of adsorption system.

Fig. 1 shows the values of adsorption

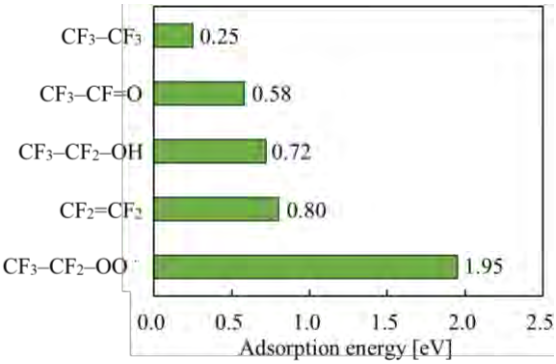

Fig. 1 Values of adsorption energies.

energies by calculation. The values of adsorption energies of CF_3–CF_3, CF_3–CF=O, CF_3–CF_2–OH, CF_2=CF_2, and CF_3–CF_2–OO· was 0.25, 0.58, 0.72, 0.80, and 1.95 eV, respectively. In the case of molecules containing COO·, the adsorption energy was the highest and the molecule was stable as with Cu(100). However, in the case of Cu(111), the value of adsorption energy was 4.73 eV[2]. The value of Cu(100) was lower than that of Cu(111). **Fig. 2** shows the optimized atomic geometries for Cu(111) and Cu(100). In the case of Cu(111), CF_3–CF_2–OO· was dissociated to CF_3–CF_2–O· and O, then they adsorbed. However, in the case of Cu(100), CF_3–CF_2–OO· was adsorbed without dissociation. This is because the adsorption energy of Cu(100) was lower. The adsorption energy was calculated when CF_3–CF_2–OO· was dissociated and adsorbed on Cu(100) as shown in **Fig. 3**. The adsorption energy was 5.27 eV. This value was close to Cu(111). These results suggest that it is important to dissociate CF_3–CF_2–O· and O and adsorb to Cu surface, in order to further improve the adhesion property.

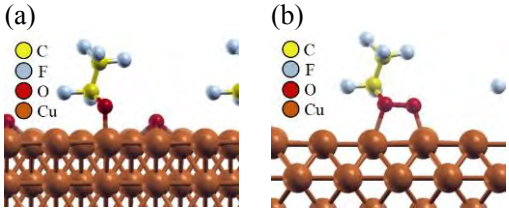

Fig. 2 Atomic geometries for CF_3–CF_2OO· model (a) on Cu(111) and (b) on Cu(100).

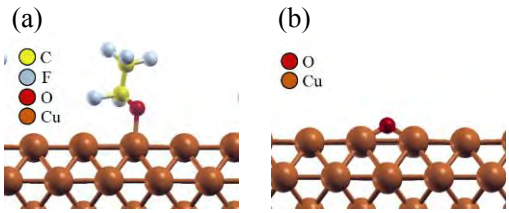

Fig. 3 Atomic geometries for (a) CF_3–CF_2O· model and (b) O model.

In this study, the functional groups contributing to improvement in adhesion property were explored by calculating the adsorption energies between fluorinated molecules and Cu(100) and comparing the result of Cu(111). In the result of calculations, generating the functional groups containing COO· is possible to generate PTFE surface having high adhesion property, regardless of orientations. Also, in order to further improve the adhesion property, it is important to dissociate CO· and O and adsorb to Cu surface. On the other hands, the calculations of Cu(110) and copper oxide is not performed. Therefore, these calculations are needed in the future.

References

[1] M. Nishino et al., INTERFINISH2020 Abstract, C-SEP06-004 (2021) 210.

[2] K. Toyoda et al., *J. Chem. Phys*. **132** (2010) 134703.

[3] K. Toyoda et al., *J. Nanosci. Nanotechnol*. **11** (2011) 2836–2843.

Development of Efficient Evaluation Methods of Berry-phase-mediated Physical Properties for Large Scale Systems Using the First-principles LCPAO Method

Naoya YAMAGUCHI
Nanomaterials Research Institute (NanoMaRi), Kanazawa University
Kakuma-machi, Kanazawa, Ishikawa 920-1192

We did the following researches about the following topics in this subject: (i) development of a linear-combination-of-pseudo-atomic-orbital (LCPAO) scheme of a Berry phase method to apply electric fields [1] and (ii) development of a new scheme to the anomalous Hall and Nernst conductivity applicable to metallic systems [2].

For (i), we have developed a first-principles LCPAO scheme of a homogeneous and finite electric field method based on the modern theory of polarization and density functional theory (DFT), so that one can consider electric field effects even for periodic systems such as bulk insulators. We validated our scheme by calculating the electronic and static dielectric constants and Born effective charges of III-V and II-VI semiconductors and group IV insulating materials. The calculated values coincided with the reported computational values, and they were an agreement with the experimental values. For the Born effective charges, we confirmed that the values obtained from our scheme are consisted with those obtained from the finite difference method (i.e. numerical differentiation of electric polarization with respect to atomic positions.) The spin-orbit interaction (SOI) has a non-negligible influence on the dielectric constants of cases including the heavy elements. We applied our scheme with the SOI to evaluate the Born effective charges characterizing the bond properties, covalency and ionicity in new semi-stable phases of BiTeI including a wide-gap topological insulating phase [3]. Our LCPAO implementation will make it easy to investigate the electronic structures and physical properties under an electric field even for the large system including hundreds of atoms. In addition, we also developed the spin texture code for insulators under electric fields through the Berry phase scheme. We did test calculations by applying the spin texture code to bulk diamond. Bulk diamond is a system keeping the spatial inversion symmetry, but a strong electric field can break the symmetry to induce the spin splitting through the Rashba effect (see Fig. 1 and 2).

For (ii), we also developed the new evaluation scheme for the anomalous Hall and Nernst conductivity without constructing the Wannier functions or explicit evaluation of the Kubo formula [2]. We reproduced the intrinsic contribution of typical anomalous Hall systems such as body-centered-cubic iron. Our scheme has advantages of efficiency so that it is the non-iterative scheme unlike Wannierization. Therefore, our scheme can easily address not only large scale cases but also high-throughput calculations. We applied the scheme to evaluate the peculiar magnetic thermoelectricity in the ferrimagnetic phases of $MnBi_2Te_4$ layers [4]

and a ferromagnetic superlattice of tetragonal-Fe_2Si, that is, Hapkeite [5]. We also developed another version of the scheme based on the improved tetrahedron method. It is possible to directly evaluate the pure term of anomalous Nernst conductivity (ANC) even for systems with too low the Curie temperature to obtain the convergent values of the pure term through the numerical differentiation of the anomalous Hall conductivity with respect to the chemical potential.

We also improved the spin texture code by changing the eigenvalue solver so that k-space spin density matrices can be calculated more stably and efficiently. Through the code, we investigated a hydroxyl-terminated diamond surface and found the electronic structure with the persistent spin helix that is important to spintronic applications [6].

We implemented them to the OpenMX code [7], and they will be released in the future.

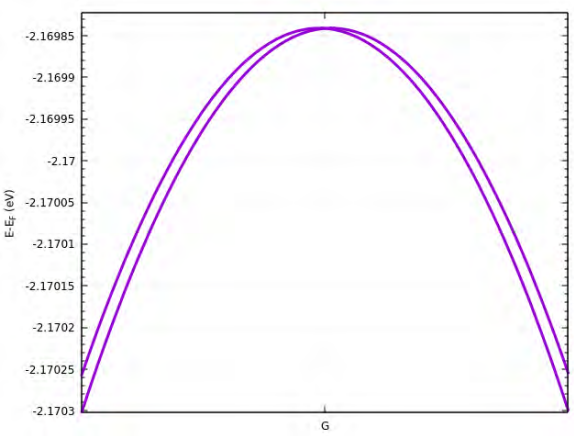

Figure 1: Band structure with the Rashba spin splitting around the valence band top at the Γ-point induced by an electric field of 3.5 GV/m perpendicular to one of the faces in bulk diamond. The momentum shift Δk was 2.99×10^{-4} Å^{-1}, and the induced electric polarization was 12.58 μC/cm^2.

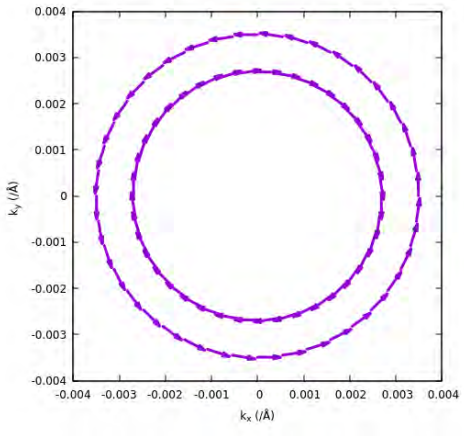

Figure 2: Spin texture for the Rashba spin splitting around the valence band top at the Γ-point induced by an electric field of 3.5 GV/m perpendicular to one of the faces in bulk diamond. The length and direction of arrows represent the magnitude and direction of the expectation values of the spin every k-point, respectively.

References

[1] N. Yamaguchi, F. Ishii, Comput. Phys. Commun. **280**, 108487 (2022).

[2] H. Sawahata, N. Yamaguchi, S. Minami, F. Ishii, Phys. Rev. B **107**, 024404 (2023).

[3] Y. Zhang, N. Yamaguchi, H. Sawahata, F. Ishii, Appl. Phys. Express, in press, DOI: 10.35848/1882-0786/acccd3 (2023).

[4] Y. Morishima, N. Yamaguchi, H. Sawahata, F. Ishii, Appl. Phys. Express **16**, 043003 (2023).

[5] T. Tominaga, N. Yamaguchi, H. Sawahata, F. Ishii, Jpn. J. Appl. Phys. **62**, SD1019 (2023).

[6] H. P. Kadarisman, N. Yamaguchi, F. Ishii, Appl. Phys. Express **16**, 023001 (2023).

[7] http://openmx-square.org.

Electronic structure investigation of the Ba_2PrBiO_6 photocatalyst

Kazume NISHIDATE
Faculty of Science and Engineering, Iwate University
Ueda 4-3-5, Morioka, Iwate 020-8551

A large number of double-perovskite oxides, $A_2B'^{\,III}B''^{\,V}O_6$, have been studied due to their intriguing physical and chemical properties originating in their mixed valence nature. Where the small cations occupy the B' and B" sites with the different valencies. Recently, it was found that the Ba_2PrBiO_6 double-perovskite has a photo catalytic activity in the visible light. However, theoretical analysis on the electronic properties of its surface has not been performed. In this work, we perfomed the first-principles density functional computation of the surface of Ba_2PrBiO_6. We used the **Quantum ESPRESSO** (QE) package. We applied the Heyd-Scuseria-Ernzerhof hybrid functional (HSE06) formalism for the exchange-correlation to evaluate the band gap as well as the work function.

The surface electronic states are calculated using a slab model, which consists of stacked three unit cells and the vacuum region of 16 Å . Where Ba_2PrBiO_6 has the Ba-O and the Pr-Bi polar planes alternately stacked in one direction. The top and the bottom planes are terminated with the same polar surface to prevent the artificial dipole-dipole interactions over the cyclic boundary. The work function ϕ is defined as the difference between the vacuum level (ϕ_{vac}) and the Fermi level E_F (Figure. 1).

We also performed the Born-Oppenheimer Molecular Dynamics simulations of the slab to investigate its reactiveness to the water. In this stage, we used the PBE functional for the exchange-correlation and employed only the Γ

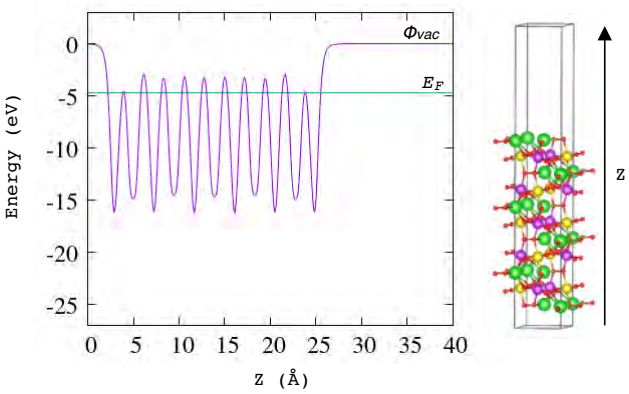

Figure 1: Averaged electronic potentials for the Ba-O polar plane along the Z axis of the super-cell.

point for the reciprocal space integration to suppress the computational time. Temperature was regulated to be 300 K throughout the simulation time steps using the velocity scaling method. And H_2O molecule was placed at 5 Å over the Ba-O surface. There are three stages in the adsorption process. First, a H_2O molecule approaches the surface as the result of the Coulomb interaction between the oxygen and the surface Ba atoms (I). Then, the oxygen atom makes a bond with Ba by releasing its hydrogen atom and thereby forming a hydroxyl group. The released hydrogen atom also makes a bond with the oxygen atom of the slab (II). In this adsorption process, two hydroxyl groups were created. We have been focusing on the detailed analysis on the calculated results.

Theoretical Study on Electronic Properties in New Nanoscale Surfaces and Interfaces

Katsuyoshi KOBAYASHI
Department of Physics, Ochanomizu University
2-1-1 Otsuka, Bunkyo-ku, Tokyo 112-8610

We theoretically studied the photoemission spectra of V_5Se_8 monolayers. V_5Se_8 is a layered material composed of VSe_2 layers and V intercalant layers. It is known that bulk V_5Se_8 has an antiferromagnetic structure at low temperatures. However, a recent experiment showed ferromagnetic behavior in V_5Se_8 thin films [1]. We studied the electronic structure of V_5Se_8 monolayers in 2022 [2].

It may be assumed that V_5Se_8 monolayers have a structure composed of two VSe_2 layers and a V intercalant layer as shown in Fig. 1(a). However, a recent experiment [3] showed a structure that the surfaces of V_5Se_8 monolayers are covered with the V intercalant layers. In order to investigate the surface structures of V_5Se_8 monolayers we performed a density-functional calculation. We used the program package VASP for density-functional calculations.

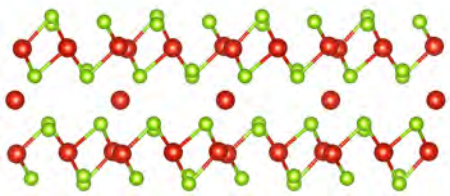

Figure 1: Side view of the atomic structure of a V_5Se_8 monolayer.

Figure 2 shows the photoemission intensity calculated for the structure shown in Fig. 1. The photoemission intensity is a calculated band structure weighted by the $\mathbf{G}_{\parallel} = 0$ component of wave functions, where $\mathbf{G}_{\parallel}$ are the components of reciprocal lattice vectors parallel to the surface. This is due to that the wave functions in vacuum regions are mainly connected to the $\mathbf{G}_{\parallel} = 0$ component in materials. The band structure is calculated in a nonmagnetic state because the photoemission experiment was performed at room temperatures. The energy bands are broadened with a width of 0.1 eV. The calculated intensity has good agreement with the experimental one [2]. The photoemission intensity calculated for the structure with a V-adsorbed surface is similar to Fig. 2. But, Fig. 2 better reproduces a characteristic feature of the experimental band dispersion. Therefore it is concluded that the V_5Se_8 monolayers in the experiment of Ref. [2] have the structure shown in Fig. 1.

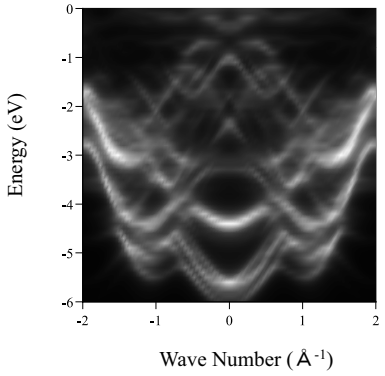

Figure 2: Calculated photoemission intensity of the V_5Se_8 monolayer. The origin of energy is the Fermi energy. The wave number is along the direction perpendicular to the side view plane in Fig. 1.

References

[1] M. Nakano *et al.*: Nano Lett. **19** (2019) 8806.

[2] K. Sumida *et al.*: Phys. Rev. B **106** (2022) 195421.

[3] Q. Meng *et al.*: Phys. Status Solidi RRL **16** (2022) 2100601.

Interaction of magnetic metal phthalocyanines with metal surfaces

Tetsuya ARUGA
Department of Chemistry, Kyoto University
Kitashirakawa-Oiwakecho, Sakyo, Kyoto 606-8502

Phthalocyanine ($C_{32}H_{18}N_8$) is a planar molecule with an extended π electron system. Two hydrogen atoms in the central "hole" of the molecule can easily be substitutid by a 2+ transition metal ion, giving rise to metal phthalocyanine (MPc), and thus the molecule has two significant electronic motifs, conjugated π electrons of a Pc molecule and an open-shell d orbital of the central transition metal ion.

In this work, we studied the interaction and interface structure of the metal phthalocyanine molecules adsorbed on bi-layer indium films fabricated on Si(111)-(1× 1) substrate [1] and studied the ordering and the interaction of the molecule with the indium substrate. Experimentally, the adsorbed molecules form a two-dimensional close-packed lattice. No second adsorption layer is formed at room temperature, suggesting that the energy gain associated with the planar stacking is weak. On the other hand, the interaction of phthalocyanine with In substrate appears to be strong, as implied by the formation of close-packed lattice and the stability against the temperature increase.

In order to clarify the origin of the molecule–surface interaction, we performed a computational work by using VASP [2, 3, 4, 5]. We used optB86b-vdW van der Waals density functional (vdW-DF) [6] in order to treat the interaction of the extended π-electron system of the molecule with the sp bands of the In substrate. We used DFT+U method in order to properly describe the electronic state of the Fe^{2+} ion in the molecule. The value of U was set so that the magnetic moment of the Fe^{2+} ion in a free FePc molecule is reproduced.

The adsorption structure predicted by the calculation indicates that the adsorption is governed by two different molecule–surface interactions. The structure obtained by the minimization of the total energy indicated two significant characteristics that are not found in H_2Pc, which is only weakly bound to the surface by vdW-like interaction with the metallic substrate. Firstly, the Pc molecule is deformed to a bowl-like structure with the molecular center down and closest to the substrate. Secondly, the Fe ion in the center of the molecule protrude further downward and appears to be associatively interacting with the In atoms below. These characteristics are not found for H_2Pc and CuPc, suggesting that these are characteristic to MPc molecules with open d-shell M ions. The interaction between the molecule and the substrate may differ depending on the number of d electrons. The effect of these interaction on the superconductivity of the In film[7, 8] is intriguing.

References

[1] E. Rotenberg et al.: Phys. Rev. Lett. **91**, 246404 (2003).

[2] G. Kresse and J. Hafner, Phys. Rev. B **47**, 558 (1993); ibid. 49, 14251 (1994).

[3] G. Kresse and J. Furthmüller, Comput. Mat. Sci. **6**, 15 (1996).

[4] G. Kresse and J. Furthmüller, Phys. Rev. B **54**, 11169 (1996).

[5] G. Kresse and D. Joubert, Phys. Rev. **59**, 1758 (1999).

[6] J. Klimeš et al., Phys. Rev. B 83, 195131 (2011).

[7] T. Zhang et al., Nat. Phys. 6, 104 (2010).

[8] T. Uchihashi et al., Phys. Rev. Lett. 107, 207001 (2011).

In-plane interaction of π-conjugated molecules

Tetsuya ARUGA
Department of Chemistry, Kyoto University
Kitashirakawa-Oiwakecho, Sakyo, Kyoto 606-8502

Phthalocyanine ($C_{32}H_{18}N_8$) is a planar molecule with a 2D extended π-conjugated electron system. Two hydrogen atoms in the central "hole" of the molecule can easily be substituted by a 2+ transition metal ion, giving rise to metal phthalocyanine (MPc).

The adsorption of MPc on single-crystalline metal surfaces has been studied by several groups. In these works, irrespective of the substrate, MPc molecules form ordered two-dimensional lattice, which has common characteristics as below: (1) the molecule adsorbs with its molecular plane parallel to the surface, (2) the molecules form nearly square lattice that is commensurate with the substrate lattice, (3) the molecules are rotated in plane by $\sim 20^\circ$ from the symmetrical direction of the substrates and forms a staggered structure.

The first point is understood by the fact that the adsorption is mostly governed by the van der Waals interaction between the surface and the molecule. The second point is due to the shape of the molecule, which prefers square-like lattice to maximize the coverage. The third point is not obvious. Previous authors claimed that this is due to the direct chemical interaction of N atoms in the molecule with a particular atoms of the surface, which however has not been confirmed by quantitative methods.

In this work, we studied (1) the interaction among metal phthalocyanine molecules adsorbed on bi-layer indium films fabricated on Si(111)-(1$\times$ 1) substrate [1] and (2) the interaction among metal phthalocyanine molecules in the same geometry as in (1) but without the substrate.

The total energy was computed by using VASP code [2, 3, 4, 5] as a function of azimuthal rotation angle. The total energy for the case (1) shows decrease with increasing azimuthal angle from 0° and get minimum at $\sim 20^\circ$. Further increase of the azimuthal angle leads to the divergence of the total energy due to the direct contact of the neighboring molecules. The energy minimum at $\sim 20^\circ$ is in good agreement with the observation. The case (2) gave rise to an almost the same angular dependence but with the amplitude 60% $\sim$ 70% of the case (1).

The results indicates that the rotation of the molecule is induced by the intermolecular interaction, which most probably is dipole-dipole interaction between C-H groups of the molecule. The energy minimum is achieved when the C-H bonds with opposite direction of neighboring molecules approach with each other most closely. Our calculation does not indicate any significant contribution of the direct interaction of molecular N atom with the substrate. The reduced interaction in the case (2) suggests that the image dipoles induced in the substrate (bilayer In) are smaller in strength, which is most probably due to the ultra-thinness of the substrate In bilayer, in which the metallicity of the lower In layer is mostly lost due to the bonding with substrate Si atoms.

References

[1] E. Rotenberg et al.: Phys. Rev. Lett. **91**, 246404 (2003).

[2] G. Kresse and J. Hafner, Phys. Rev. B **47**, 558 (1993); ibid. 49, 14251 (1994).

[3] G. Kresse and J. Furthmüller, Comput. Mat. Sci. **6**, 15 (1996).

[4] G. Kresse and J. Furthmüller, Phys. Rev. B **54**, 11169 (1996).

[5] G. Kresse and D. Joubert, Phys. Rev. **59**, 1758 (1999).

Atomic structures and electronic properties of nanocarbon-based materials

Yoshitaka FUJIMOTO
School of Engineering, Kyushu University
Moto-oka, Fukuoka-city, Fukuoka 819-0395

Graphene is one of the most promissing materials for electronics devices such as field effect transistors and molecular sensors. It has been reported that the boron atom in graphene could act as a reactive site for the adsorptions of environmetally polluting NO and NO_2 molecules. [1] Furthermore, the B atoms in bilayer graphenes are also reported to enhance the adsorption properties of several molecules, leading to the possibility to fabricate the highly sensitive NO_x sensors. [2, 3, 4] However, it might be difficult to detect harmful CO molecules using B-doped graphene. Carbon nanotube (CNT) is also expected to be one of the most promising materials for development of sensors due to its high surface-to-volume ratio of one-dimensional nanostructures and its excellent electrical conductivity. Here, we report the adsorption properties of environmetally polluting NO_x and harmful CO molecules on CNTs. [5]

We examine the atomic structures of B-doped and N-doped (10,0) CNTs without the adsorbed molecules. The zigzag nanotubes such as the (10,0) CNT have two kinds of C-C bonds around each atom. In the B-doped case, two kinds of the B-C bond lengths are found to be 1.47 Å and 1.50 Å. In the case of the N-doped case, the C-N bond lengths are 1.37 Å and 1.40 Å. The B-C bond lengths are much longer compared with two kinds of the C-C bond lengths (1.40 Å and 1.41 Å) in a pristine (10,0) CNT, while the two kinds of N-C bond lengths are slightly shorter than the corresponding C-C bond lengths. In addition, the B-C and N-C bond lengths are longer and shorter than those of B-doped graphene (1.47 Å) and N-doped graphene (1.40 Å), respectively.

We also examine the adsorption properties of various molecules including environmentally toxic molecules on the B-doped and N-doped (10,0) CNTs. Table I lists the adsorption energy and the distance between the molecule and the B (C) atom in the B (N)-doped (10,0) CNTs. For the B-doped cases, CO, NO, NO_2 and O_2 molecules are found to be strongly adsorbed with relatively large adsorption energies as well as the short binding distances, while CO_2 and N_2 molecules are weakly adsorbed. For the N-doped CNT, it is reported that the adsorption energy of a H atom at a neighboring C atom is larger than that at the dopant N atom itself. Here, we examine the adsorption of all six types of molecules at the C atom sites next to N-dopant atoms in the N-doped CNTs. It is found that only NO and NO_2 molecules are strongly adsorbed, while the adsorption energies of the remaining four molecules (CO, CO_2, O_2, and N_2) are relatively small and at the same time the binding distances between molecule and C atom are relatively long. It is interesting that the adsorption energies of these molecules on the B-doped and N-doped CNTs are overall larger than those on the B-doped and N-doped graphenes, respectively, due to the curvature effects of the nanotubes.

In summary, we have investigated the adsorption effects of environmentally toxic molecules on atomic structures and energetics of B-doped and N-doped (10,0) CNTs based on the first-principles electronic structure study. The B-doped CNTs can strongly bind with CO, NO, NO_2 and O_2 molecules, while CO_2 and N_2 molecules are not strongly but weakly

Table 1: Adsorption energy E_a (eV) and distance d (Å) from the B (C) atom for each molecule adsorbed on B (N)-doped (10,0) CNTs.

		NO	NO_2	CO	CO_2	O_2	N_2
B-doped	E_a	−1.32	−1.82	−0.46	−0.06	−0.36	−0.23
	d	1.75	1.56	1.54	2.77	1.59	2.71
N-doped	E_a	−0.97	−0.91	−0.08	−0.07	−0.13	−0.23
	d	1.66	1.53	2.74	2.75	1.70	2.84

adsorbed. The N-doped CNTs can strongly bind with only NO and NO_2 molecules in air. The environmentally harmful NO and NO_2 and toxic CO molecules are individually detectable by using B-doped and/or N-doped CNTs.

References

[1] Y. Fujimoto and S. Saito, Jpn. J. Appl. Phys. **58**, 015005 (2019).

[2] Y. Fujimoto and S. Saito, Chem. Phys. **478**, 55 (2016).

[3] Y. Fujimoto and S. Saito, Appl. Surf. Sci. Adv. **1**, 100028 (2020).

[4] Y. Fujimoto, Mod. Phys. Lett. B **35**, 2130001 (2021).

[5] Y. Fujimoto and S. Saito, J. Electrochem. Soc. **169**, 037512 (2022).

Effects of Element Substitution on Molecular Packing and Band Structures in Single-component Molecular Conductors with Canted Antiferromagnetism

So YOKOMORI

Department of Chemistry, College of Science

Rikkyo University, 3-34-1 Nishi-Ikebukuro, Toshima, Tokyo, 171-8501

We have investigated the syntheses and electronic properties of single-component molecular conductors exhibiting canted antiferromagnetism (CAF). The occurrence of CAF in molecular conductors is exceedingly uncommon [1], and as a result, the corresponding structure-property relationships have yet to be fully disclosed. Recently, a single-component molecular conductor with CAF was produced through the use of a diethoxybenzene-fused gold dithiolene complex (see Fig. 1). In this investigation, we centered our attention on the high modulatory capability of substituting elements in the complex. To enable an effective evaluation of the systematic structure-property relationship in CAF molecular conductors, we computed the band structures of element-substituted complexes to aid in the synthesis of new compounds.

Band calculations for three kinds of element-substituted complexes (as depicted in Fig. 1) were executed using OpenMX 3.9 software. For these calculations, the crystal structures were optimized by means of the DFT-D3 method which involved vdW- and dispersion energy-correction, by exchanging the original elements in the crystal structure of the diethoxybenzene-fused gold dithiolene complex with other elements. As a result, the following findings were unveiled: substituting Se led to a reversal of the magnitude of J_1 and J_2, as well as a decrease in the bandwidth. This suggests that Se substitution would significantly affect the CAF behavior. In the S-substituted complex, an interaction appeared along the inter-conducting layer direction and the bandwidth increased. This outcome implies that the dimensionality of spin-spin interaction is stronger than that of the original complex, and thus, the transition temperature of CAF ordering transition could be expected. For the N-substituted complex, no significant changes were observed except for a slight decrease in the bandwidth. Therefore, it can be concluded that the priority of synthesizing this complex is low. Accordingly, in this investigation, we successfully gained insights into which complexes should be synthesized next.

References

[1] R. Ishikawa *et al.*, *J. Phys. Soc. Jpn.*, **87**, 064701 (2018).

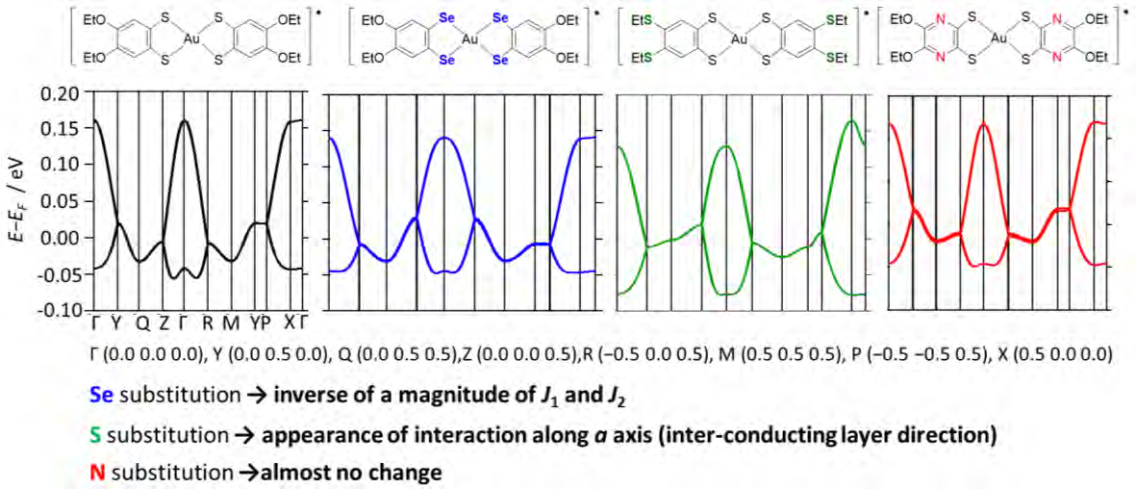

Fig. 1. Structural formula of the complex of CAF molecular conductor and newly designed element-substituted complexes, and calculated band structures. An explanation of band structure changes for each result are shown in the bottom.

First principles study on the band structures of high entropy compounds

Hidetomo USUI

Department of Physics and Materials Science,

Shimane University, Nishikawatsu-cho, Matsue, Shimane 690-8504

High-entropy alloys are alloys containing five or more elements at one site. Recently, high-entropy compounds have attracted much attention not only from a mechanical point of view but also as functional materials such as thermoelectric and superconducting materials.[1,2] We have investigated the electronic structure of a high entropy compound *M*Te (*M* = Ag, In, Sn, Pb, Bi), which exhibits robustness of superconductivity to external pressure[3, 4]. This year, we calculated the electronic band structure of *M*Te in the rock salt typed crystal structure using the VASP package within the PBE-exchange correlation functional with spin-orbit coupling included. We used a 2×2×2 supercell of MTe ($Sn_{16}Pb_{16}Te_{32}$, $In_{11}Pb_{10}Bi_{11}Te_{32}$, $In_8Sn_8Pb_8Bi_8Te_{32}$, and $Ag_8In_6Bi_6Sn_6Pb_6Te_{32}$). We calculated the site arrangement of *M* atoms using the special-quasi random structure implemented in Alloy Theoretic Automated Toolkit. We took a *k*-mesh spacing of 0.1 $Å^{-1}$ and a cut-off energy of 330 Ry. The unfolded electronic band structure of *M*Te is shown in Fig. 1. It is found that the band structure for M=Sn, Pb exhibits sharp spectral lines, but for M = Ag, In, Sn, Pb, and Bi, due to a mixture of various elements, spectral weight is reduced. It can be understood that substitution by elements in other groups can suppress the quasiparticle lifetime but can control the band structure around the Fermi level.

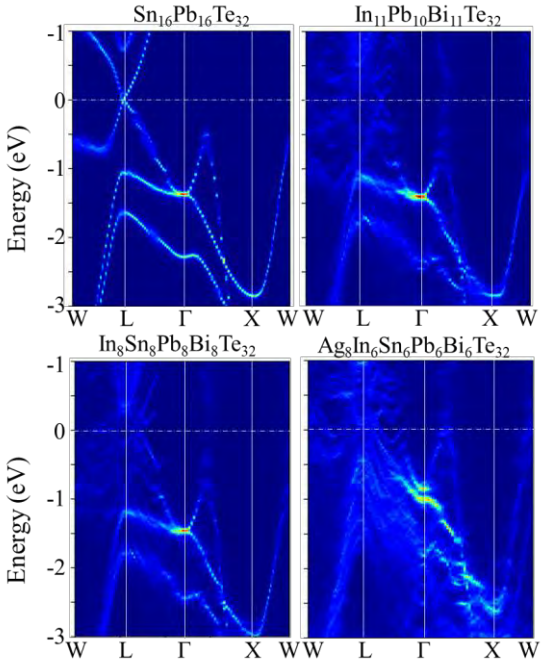

Fig. 1: Electronic band structure of MTe

References

[1] B. Jiang et al., Science **371**, 830 (2021)

[2] P. Koželj *et al*., Phys. Rev. Lett., **113,** 107001 (2014).

[3] Md R. Kasem *et al*., Sci. Rep **12**, 7789 (2022)

[4] Y. Mizuguchi *et al*., Mater. Today Pnys. **32**, 101019 (2023)

First-principles study of interfacial magnetic structure in topological magnets

Susumu MINAMI[†,‡], Yuta TOGA[†], Katsuhiro TANAKA[†]
[†]*Department of Physics, Univeristy of Tokyo, Hongo, Bunkyo-ku, Tokyo 113-0033*
[‡]*Department of Mechanical Engineering and Science, Kyoto University, Nishikyo-ku, Kyoto 615-8540*

Topological magnetic materials such as Mn_3Sn and Mn_3Ge exhibit unique properties due to their particular band structures (Berry phase) and have attracted attention as core elements for antiferromagnetic spintronics devices. Recently, finite tunneling magnetoresistance (TMR) effects have been observed at room temperature in the magnetic tunneling junctions (MTJs) with Mn_3Sn [1] and Mn_3Pt [2], increasing the demand for research on the interface in antiferromagnetic MTJs.

This research project employed the QUANTUM ESPRESSO, a first-principles calculation code, to analyze the Mn_3Ge/MgO MTJ and its interface, which have the non-collinear magnetic configuration. Due to its non-collinear magnetic structure, the computational cost and output data volume significantly increased, and the convergence worsened, necessitating the use of the ISSP Supercomputer.

The study presents the magnetic moments of the Mn layers at the vacuum surface and within the MgO multilayer film, with energy-based optimization of interfacial distances. Figure 1 shows the layer dependence of the magnetic moments of the Mn atoms. While the magnetic moments increase at the vacuum surface due to increased electron localization, this increase is not observed at the MgO interface for some Mn positions. The different surface states influence the magnetic moments of Mn atoms inside the interface.

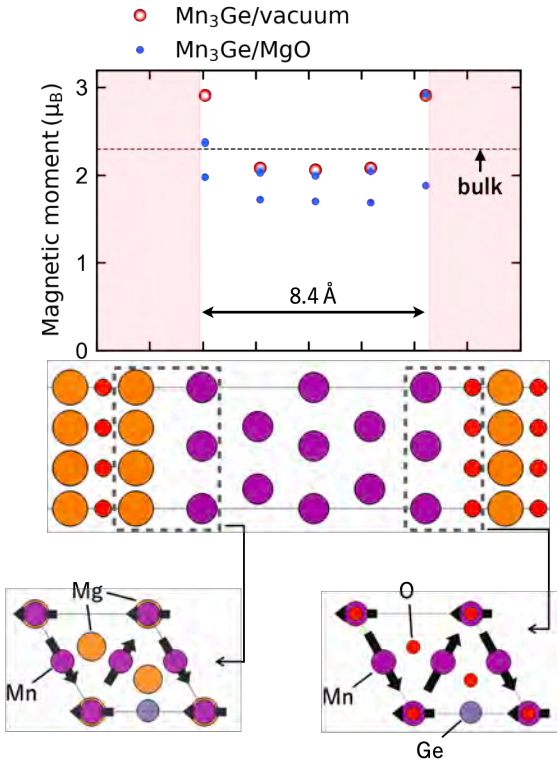

Figure 1: Magnetic moments of the Mn atoms near the surface and the interface.

As the performance of MTJs is influenced by the magnetic state near the interface, future research will investigate charge transfer, film thickness dependence, and their relation to the tunnel conductance.

References

[1] X. Chen *et al.*, Nature **613**, 490 (2023).

[2] P. Qin *et al.*, Nature **613**, 485 (2023).

RSDFT calculation of atomic displacements detected through energy dissipation measurement on noncontact atomic force microscopy

Toyoko ARAI[1], Takahiro Kato[1], Jun-Ichi Iwata[2], Atsushi Oshiyama[3]

[1]*Graduate school of Natural Science and Technology, Kanazawa University, Kanazawa, Ishikawa, 920-1192*

[2] *Institute of Innovative Research, Tokyo Institute of Technology, Tokyo 152-8550*

[3]*IMaSS, Nagoya University, Nagoya, Aichi 464-8601*

We had experimentally found that, when non-contact atomic force microscopy (nc-AFM) images showed the high resolution for the individual adatoms on a Si(111)-(7×7) surface, the simultaneously obtained energy dissipation signal increased in close proximity over the hollow sites surrounded by a Si adatom and a Si rest atom with a dangling bond per each [1]. To clarify the role of the dangling bonds on the Si adatom and the Si rest atom, we partially terminated the Si(111)-(7×7) surface with H, leading to chemical inactivation of some of the dangling bonds. Some distinct bright regions in the dissipation image were lost, which coincided with the hollow sites next to H-terminated rest atoms and/or H-terminated adatom (Fig. 1). This indicates that the dangling bonds of the rest atom and adatom around the

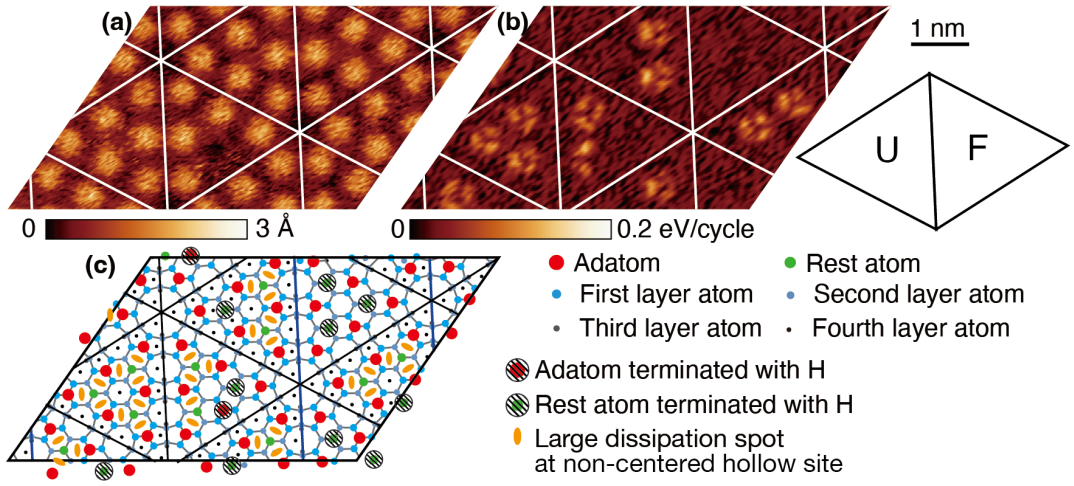

Fig. 1: (a) nc-AFM image of a partly H-terminated Si(111)-(7×7) surface in a constant Δf mode obtained simultaneously with (b) the dissipation image at Δf_{set} = –30 Hz with a cantilever of f_0 = 199 kHz. The image area was 6.0×3.5 nm^2, sheared at 35° for drift compensation. The white meshes denote the unit cells. (c) Atomistic model of the H-terminated Si(111)-(7×7). The estimated H-terminated sites are hatched.

hollow site can change the dissipation. In this study, to elucicate the phenomena, the forces between Si tip and Si(111)-(7×7) surface were calculated using real-space density functional theory (RSDFT) [2]. RSDFT is a first-principles program developed by Oshiyama and Iwata, which uses a real-space difference method and a pseudopotential method.

First, we optimized the structure of a Si(111)-(7×7) reconstructed surface consisting of 298 Si atoms, the back surface of which was terminated with 49 H atoms, and the structure of a [001]-oriented Si tip by RSDFT; the tip consisted of 30 Si atoms having a Si dimer at the tip apex, the back side of which was terminated with 18 H atoms, named “dimer tip”

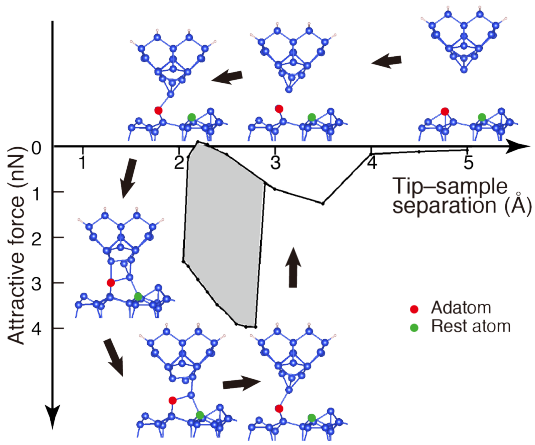

Fig. 2 Force–distance (separation) curve with the optimized structures of the Si tip and Si(111)-(7×7) surface, calculated by RSDFT.

[3]. Next, we calculated the structure changes and the forces acting between the tip and the Si surface during tip approaching and retracting over the hollow site at the separations between the tip apex atom and the Si adatom on the surface from 5.0 to 2.0 Å, as shown in Fig. 2. The atom structure and the force-distance curves exhibited hysteresis. The greyed area surrounding by the force-distance curve should correspond to the nonconservative dissipation energy that was experimentally measured. Furthermore, the calculations with Si(111)-(7×7) surface with H-terminated rest atoms or H-terminated adatom did not show such hysteresis during one cycle of tip travel. This calculation for the hydrogen termination was also in good agreement with the experiment.

References

[1] T. Arai, R. Inamura, D. Kura, and M. Tomitori, Phys. Rev. B **97**, 115428 (2018).

[2] J.-I. Iwata, D. Takahashi, A. Oshiyama, T. Boku, K. Shiraishi, S. Okada, and K. Yabana, J. Comput. Phys. **229**, 2339 (2010).

[3] P. Pou, S. A. Ghasemi, P. Jelinek, T. Lenosky, S. Goedecker and R. Perez, Nanotechnology **20**, 264015 (2009).

A study of nickelate superconductors in first-principles

Hirofumi SAKAKIBARA
Department of Engineering,
Tottori University, Tottori, Tottori 680-8525

A recently discovered superconductor $NdNiO_2$ [1] attracts broad interests among the field of low-temperature physics because of its cuprate-like electronic structure. Namely, $NdNiO_2$ has infinite layered structure to have monovalent nickel atoms in which the electron configuration is $3d^9$, the same with the copper site of cuprates. This striking similarity motivates researchers to compare the nickelates and the cuprates for the purpose of unveiling the high-T_c pairing mechanism [2].

However, the nickelates also have several dissimilarity: (1) T_c is lower (up to 20K, where that of cuprates are up to 135K), (2) no long-range magnetism on the vicinity of superconducting dome in the carrier-temperature phase diagram, (3) no superconductivity in the bulk materials [3]. Even the feature (1) and (3) is still under intense debate, however, some consensus for (2) is being formed. Namely, since the energy bands formed by lanthanoid atoms overlaps with 3*d* bands of nickelate unlike cuprates, the self-doped holes from the lanthanoid site break magnetic order so that no magnetic phase is observed [4,5].

A theory is proposed to interpret the feature (1) based on the combination of many-body theory and first-principles calculation [5]. In the theory, by applying fluctuation exchange approximation (FLEX, Ref. 6) on a seven-orbital model constructed in first-principle with maximally localized Wannier orbital [7], it is revealed that the first-principles Hubbard U obtained in constrained random phase approximation (cRPA, Ref. 8) is much stronger than that of cuprates. Therefore, the self-energy induced by spin-fluctuation damps quasi-particles weight to degrade T_c. The main reason of this larger U in the nickelates is the much larger energetical splitting Δ_{dp} between nickel ion and oxygen.

Considering the above numerical results, we can easily imagine that T_c in nickelates goes up by applying hydrostatic pressure that may lower U and/or U/t values, where t is the hopping integrals of the $3d_{x2-y2}$ orbitals between nearest neighbor sites. In this research, to confirm this idea, I have constructed the seven-orbital model by obtaining stable crystal structure under hydrostatic pressure (0GPa--20GPa). For computational details, quantum espresso package (QE, Ref. 9) and RESPACK [10] officially implemented in the system B are employed and the bulk crystal structure is

assumed. It is found that the *U/t* value becomes smaller by hydrostatic pressure, where the value of *t* is simply scaled by the lattice constant along the *a*-axis (along the layers). By performing FLEX calculation assuming such smaller *U/t* value, the larger λ, the eigenvalues of Eliashberg equation, is obtained. This means that T_c may get higher if the hydrostatic pressure is applied on nickelates.

Interestingly, the value of *U* itself remains almost constant (or, slightly gets larger) when the applied pressure gets stronger. To give deeper insight to this result, I have calculated the value of *U* in cRPA by varying the valence of nickel atoms. Namely, I have performed virtual crystal approximation (VCA) for two Sr-doped systems $La_{1-x}Sr_xNiO_2$ and $Nd_{1-x}Sr_xNiO_2$, where the nickel's valence is simply formulated as $1+x$. In this calculation, the value of *U* gets smaller as the valence gets smaller. By constructing the so-called *d-p* model considering all of the 3*d*-orbitals and 3*p*-orbitals, it is found that Δ_{dp} is roughly scaled by the valence of nickel atoms.

To summarized, I have performed mainly two types of calculations employing QE+ R ESPACK to capture the possible variation of *U/t* value in the infinite layered nickelates: structural optimization under pressure and VCA calculation nickelates. The value of *U/t* may decrease by hydrostatic pressure while *U* itself possibly remains constant. By VCA calculation, it is found that *U* itself is roughly scaled by the valence of nickel atom. These results give us a hint to optimize *U/t* value for seeking higher T_c materials such as cuprates. As a future task, I will challenge to theoretically explain the recent experimental result of praseodymium nickelate thin firm in which T_c gets significantly higher by applying pressure [11].

References

[1] D. Li et al., Nature (London) 572, 624 (2019).

[2] M. R. Norman, Physic 13, 85 (2020).

[3] Q. Li et al., Communications Materials 1, 1(2020).

[4] A. S. Botana and M. R. Norman, Phys. Rev. X 10, 011024 (2020).

[5] H. Sakakibara et al., Phys. Rev. Lett. 125, 077003 (2020).

[6] N. E. Bickers et al., Phys. Rev. Lett 62, 961 (1989).

[7] N. Marzari and D. Vanderbilt, Phys. Rev. B 56, 12947 (1997).

[8] F. Aryasetiawan, Phys. Rev. B 70, 195104 (2004).

[9] P. Giannozzi et al., J. Phys.: Condens. Matter 21, 395502 (2009)

[10] K. Nakamura et al., Comp. Phys. Comun. 261, 107781 (2021).

[11] N. N. Wang et al., Nat. Commun. 13, 4367 (2022).

Growth mechanism of MoS_2/MoO_2 core shell nanowires studied by DFT calculation

Toshihiro SHIMADA

Division of Applied Chemistry, Faculty of Engineering, Hokkaido University,

Kita 13 Nishi 8, Kita-ku, Sapporo, Hokkaido 060-8628

We have experimentally found that MoS_2 nanotubes with rectangular cross sections are grown in certain conditions by chemical vapor deposition. After the detailed study of the growth conditions using turbulent flow, we found that MoO_2 nanowires are formed first, and the surface is sulfurized to make MoS_2/MoO_2 core shell nanowires as shown in electron microscopy images in Fig. 1[1].

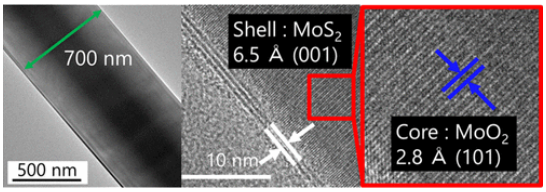

Fig. 1 : Transmission electron microscope images of MoS_2/MoO_2 core shell nanowires. (reprinted with permission: American Chemical Society[1])

In order to elucidate the mechanism of this growth feature, we used DFT calculation (VASP). We studied the surface energies of the precursor MoO_2 (Table 1 and Fig. 2).

We found that the surface energies do not so differ with each other as to explain the nanowire growth by surface stability effect. We concluded that the MoO_2 nanowires are grown from some other precursors with excess oxygen.

Table 1. Surface Energies of Various Faces of MoO_2

Faces	Surface energy /Jm^{-2}
(011)	2.25
(101)	1.84
(110)	2.36
(-111)	2.55
(11-1)	2.55
(010)	1.30
(-101)	1.75

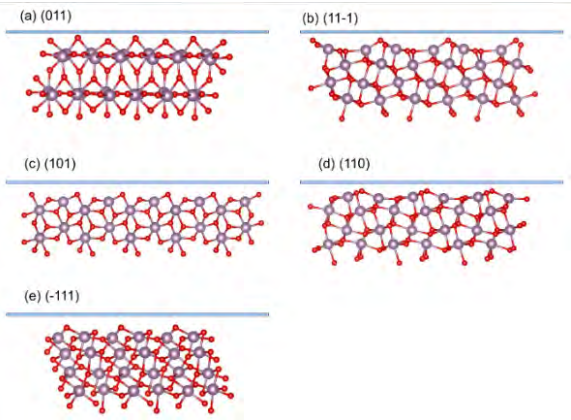

Fig. 2 : Optimized structures of MoO_2 surfaces.

References

[1] M. Goto, I. Yamane, S. Arasawa, T. YAnase, S. Yokokura, T. Nagahama, Y.Chueh, Y. Shin, Y. Kim and T. Shimada, ACS Omega **7**, 39362-39369 (2022).

First-principles calculation of graphitization of diamond surface and its exfoliation process

Kouji INAGAKI

Graduate School of Engineering, Osaka University

Yamadaoka 2-1, Suita, Osaka 565-087

Diamond is a material with a highest mechanical strength and has been applied as cutting tools. However, serious wear occurs in cutting ferrous materials. As the cause, oxidation of the diamond surface, diffusion of carbon atoms into iron, graphitization and its exfoliation, etc. have been proposed, but they are still unclear. It is well known that graphite is generally formed on diamond surfaces. The wear is most likely caused by the exfoliation of this graphite layer. Following the study of diamond surface oxidation [1], graphitization and its exfoliation on diamond surfaces were investigated. We found that for a simple diamond-Iron interface, the diamond surface is not significantly changed by the separation of the interface. However, it was found that the C-C bonds at the diamond-Fe interface can be cleaved by Fe with a low activation barrier of less than 1 eV, as in catalytic reactions. Furthermore, at the interface where the reaction takes place, the graphitized layer is found to be exfoliated by the subsequent interface separation. This study will be submitted for publication soon.

References

[1] J. I. Enriquez, F. Muttaqien, M. Michiuchi, K. Inagaki, M. Geshi, I. Hamada, and Y. Morikawa Carbon 174, 36-51 (2021).

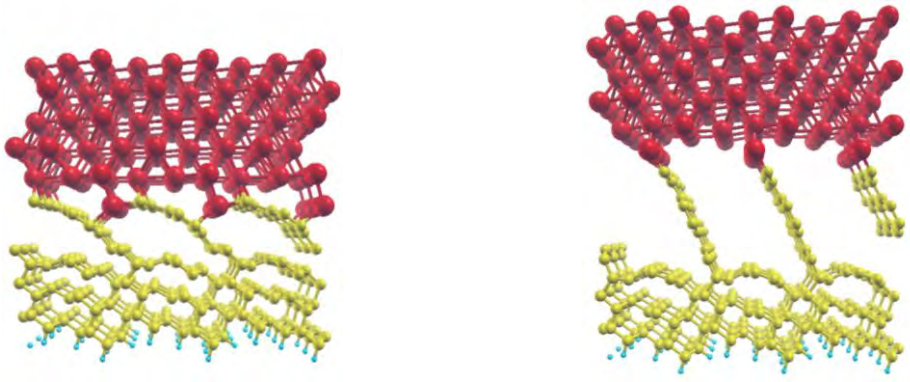

(a) (b)

Fig. 1: Peeling of graphitized diamond surface in the separation of diamond and iron interface. Yellow and red spheres represent carbon and Fe atom. (a) Formed interface between stepped diamond (111) and Fe (110) surfaces. (b) After interface separated.

AB type 2D materials database construction by DFT

Masahiro FUKUDA

Institute for Solid State Physics,

The University of Tokyo, Kashiwa-no-ha, Kashiwa, Chiba 277-8581

Demand for high-throughput calculations based on the DFT is increasing rapidly due to developments in data science and artificial intelligence. In our previous research, we constructed a structure map [1] and a web-based database [2] of AB_2 type monolayers by high-throughput DFT calculations using OpenMX. These data also provided on the ISSP data repository [3].

In this project, a program code to perform high throughput electronic and phonon band and DOS calculations by using OpenMX [4] and Alamode [5] with Spglib [6] were developed to construct materials database. In addition, the developed job scripts for massive parallel bulk jobs using GNU parallel package enable us to perform high throughput DFT calculations on the ISSP supercomputer ohtaka effectively and comfortably.

These developed program codes are applied to the AB type structure map (Fig.1) construction, basic materials database construction [7], material search for quaternary metal hydrides [8], and AFM simulations to determine atomic arrangement of Si adatom on the Silicene/Ag(111) surface [9]. Au_2X type monolayer study is currently being carried out.

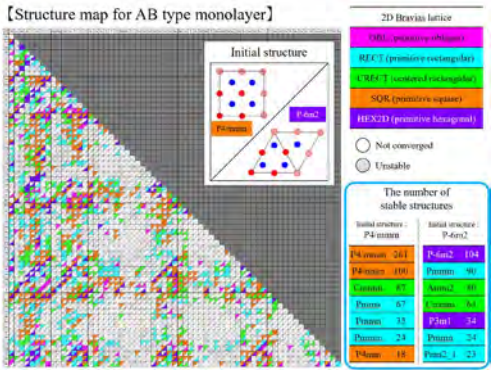

Fig.1: Structures map of AB type monolayers.

References

[1] M. Fukuda, J. Zhang, Y.-T. Lee, T. Ozaki, Mater. Adv., 2, 4392 (2021).

[2] Structure map and database of AB_2 type 2D materials (www.openmx-square.org/2d-ab2/).

[3] Structure map of AB2 type 2D materials by high-throughput DFT calculations

[4] OpenMX, http://www.openmx-square.org

[5] T. Tadano, Y. Gohda, and S. Tsuneyuki, J. Phys.: Condens. Matter 26, 225402 (2014).

[6] Spglib package (github.com/atztogo/spglib/).

[7] OpenMX database of Atoms using standard basis sets, OpenMX database of bulks using standard basis set

[8] R. Koshoji, M. Fukuda, M. Kawamura, T. Ozaki, Phys. Rev. Materials 6, 114802 (2022).

[9] Y. Adachi, Z. Runnan, W. Xinbo, M. Fukuda, T. Ozaki, Y. Sugimoto, Applied Surface Science, 157336 (2023).

Exploring dopants aiming at achieving high bulk insulation in Pb-based topological insulators

Yuki TOKUMOTO

Institute of Industrial Science,

The University of Tokyo, Komaba, Meguro-ku, Tokyo 153-8505

$PbBi_2Te_4$ topological insulator (TI) is considered as one of the promising candidates for future spintronics material with a large spin current density. However, experimental studies of its surface transport properties have not yet been reported, owing to a lack of bulk insulating crystals. So far, we achieved bulk insulating states in $Pb(Bi,Sb)_2Te_4$ topological insulators by tuning compositional ratio of Bi and Sb [1]. Furthermore, we recently revealed that In doping for $Pb(Bi,Sb)_2Te_4$ TI is effective for further lowering carrier concentrations and bulk resistivities, which is considered to be die to a localized impurity band that acts as a charge buffer occurring inside the bulk band gap.

We carried out band structure calculation of $PbBi_2Te_4$ based on density functional theory (DFT) using Vienna ab-initio simulation package (VASP) version 6.2.1. We adopted generalized gradient approximation (GGA) proposed by Perdew, Burke, and Ernzerhof (PBE) as the exchange correlation energy functional. For all calculations, we included spin-orbit coupling (SOC). We obtained band gap of 115 meV for $PbBi_2Te_4$, which is much lower than experimentally reported value ~230 meV. In order to estimate band gap more accurately, the Heyd-Scuseria-Ernzerhof (HSE06) and HSE03 hybrid functional was employed. As a result, band gap was further underestimated. We found that the HSE is not effective for accurate estimation of band gap of narrow-gap semiconductors.

In future, we plan to calculate electronic structure of In-doped $Pb(Bi,Sb)_2Te_4$ using GGA-PBE including SOC.

References

[1] Y. Hattori, Y. Tokumoto, and K. Edagawa: Phys. Rev. Mater. **1** (2017) 074201.

Dielectric function calculations in rare-earth-metal monoxides

Takayuki MAKINO

Research Center for Development of Far-Infrared Region,

University of Fukui, Bunkyo, Fukui, 910-8507

Oxygen in metals is an important and rapidly expanding field of theoretical and experimental study. One of studies is characterization of the electronic structure of metals containing a dissolved oxygen or ordered oxide phases. Compared to the oxygen adsorption metals, an ordered oxygen is more manageable because it can be handled within the framework of band theory. Owing to the metastable open-shell divalent ions, the ground state of rare-earth-metal monoxides are not trivial. In some cases, it results in a metallic ground state, while in other cases, it yields in an insulator. These monoxides can be viewed as prototypes of the large number of metallic monoxides which form in the same NaCl structure.

According to pioneering work [1], lineshape analysis of the spectra revealed that a certain rare-earth monoxide is an indirect-type narrow-gap Mott-Hubbard insulator, having a gap of *ca*. 0.2 eV [1]. The author has tried to reproduce this in the DFT- based calculation. To open the gap, there are representative three knocks. First, we should introduce an on-site Coulomb energy, which is otherwise known as the Hubbard energy [2]. Recently this has been turned out to be able to determine in *ab-initio* manner. Second, we should also introduce the Hubbard energy on the oxygen. We used a HP executable included in the Quantum ESPRESSO package [3]. Finally, the introduction of the antiferromagnetic order tends to open the gap even with smaller Hubbard energy. To reconcile with this experimental result (paramagnetic), we should assume the antiferromagnetic order is effective only within a short-range. To check this, we confirmed that the antiferromagnetic insulating ground state is energetically favored.

The Hubbard energy for the rare-earth is evaluated to be *ca.* 1 eV. The calculation under this condition yielded in a metallic ground state. If we wish to open the gap, the Hubbard energy must be 9 eV. This fact made the authors reconsider about a ground state of our rare-earth-metal monoxide system.

We used a 50 Ry energy cutoff for the electronic wave functions and a small smearing width of 0.02 Ry which required a 6×6×6 *k*-point mesh. Adopted pseudopotentials are based on the projector augmented-wave method.

We introduced that (Up) on the p orbital of the oxygen atom. The value of Up (*ca*. 21 eV) has been determined by the self-consistent linear response approach. To implement the antiferromagnetic ordering, we adopted four-atom-configuration including two cations with up and down spins.

The judgement for narrow-gap insulator has been based on the absorption spectrum. The Drude edges are less noticeable viewed in this spectrum. It is no longer true in cases of photoconductivity or dielectric function, dominated by large Drude tails. The authors [1] have presented the dependence of the electrical conductivity on the partial oxygen pressure during the growth. They identified that the specimen showing the lowest conductivity should be classified into a narrow-gap insulator rather than a (correlated) bad metal. We speculate that even this one should be a gapless compound. In the measurement of thin films, it is impossible to accurately and precisely quantify the small optical absorption coefficient region. Accurate information in the region of small coefficients is essential for determining whether it is indirect or direct transitions. This condition cannot be satisfied in the case of a metastable substance that can only be synthesized in a thin film state. Then, we are interested in the Hubbard energy dependence of the optical conductivity and dielectric function spectra for this compound.

We are now calculating various types of the optical spectra for this rare-earth-metal monoxide. We used the Wannier executable included in the Quantum ESPRESSO package [3]. By increasing the Hubbard energy in the DFT calculation, the infrared divergence in the conductivity spectrum is suppressed. On one hand, in addition to the optical absorption spectrum, we are now constructing the optical conductivity spectrum based on the same set of the measured data, i.e., transmissivity and reflectivity.

References

[1] K. Kaminaga *et al.*, ACS Omega 2018, 3, 10, 12501.

[2] B. Himmetoglu *et al.*, Phys. Rev. B. 84, 115108 (2011).

[3] P. Giannozzi *et al.*, J. Phys.: Condens. Matter 21, 395502 (2009).

Electronic Structure and Fermiology of d- and f-electron compounds

Isaki Kinjo, Juno Iraha, Yasutomi Tatetsu[1], and Takahiro Maehira[2]
Graduate school of Engineering and Science, Nishihara, Okinawa 903-0213
[1]*Center for Liberal Arts Education, Meio University, Nago, Okinawa 905-8585*
[2]*Faculty of Science, University of the Ryukyus, Nishihara, Okinawa 903-0213*

The calculation for an energy band structure of TaC was carried out using a relativistic linear augmented-plane-wave (RLAPW) method. f electrons are assumed to be itinerant and the calculation is performed in the paramagnetic phase. Note here that relativity should be taken into account, because of large atomic numbers of the constituent atoms. The spatial shape of the one-electron potential is determined in the muffin-tin approximation, and we use the exchange and correlation potential in the local density approximation (LDA)[1]. The crystal structure of TaC is categorized into the NaCl-type structure, which is characterized by the space group Fm3m[2, 3, 4, 5, 6, 7]. The iteration process for solving the Dirac one-electron equation starts with the crystal charge density that is constructed by superposing the relativistic atomic charge densities for neutral atoms Ta($[\mathrm{Xe}]4f^{14}5d^{3}6s^{2}$), and C($2s^{2}2p^{2}$), where [Xe] symbolically indicate the closed electronic configuration for xenon. In Figure 1, we show the energy band structure for TaC along the symmetry axes in the Brillouin zone in the range from 0.0 to 2.0 Ryd. First note that in the vicinity of the Fermi level E_{F} located at 1.2860 Ryd., there occurs hybridization between Ta 5d and C 2p states. The number of the valence electrons in the APW sphere partitoned into the angular momenta is 0.612 (s), 0.993 (p), 3.327 (d) and 0.381 (f) in the Ta sphere, 0.570 (s), 1.044 (p), 0.006 (d) and 0.000 (f) in the C sphere. There are 2.012 valence electrons outside the APW sphere in the primitive cell.

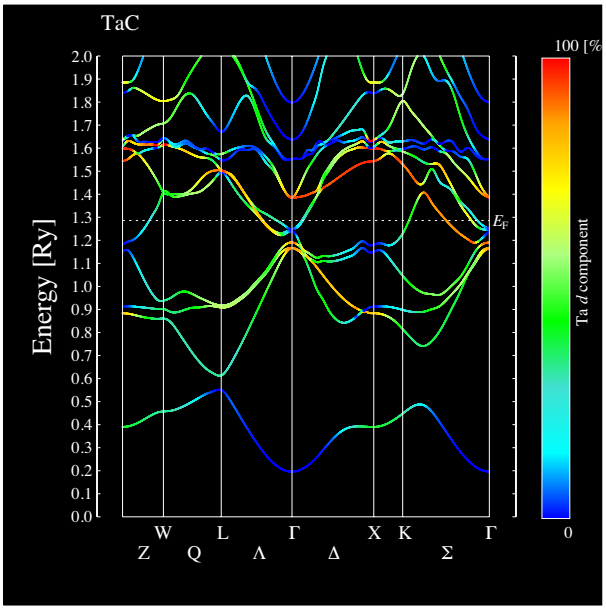

Figure 1: Energy band structure for TaC calculated by using the self-consistent RLAPW method.E_{F} indicate the position of the Fermi level.The contribution of Ta-5d electrons to the Energy band is illustrated by color, where red corresponds to 100% (Ta-5d).

Now we discuss the Fermi surfaces of TaC. Since the lowest four bands are fully occupied, as shown in Figure 1, the next three bands are partially occupied, while higher bands are empty. Namely, the 5th, 6th, and 7th bands crossing the Fermi level construct the hole or electron sheet of the Fermi surface, as shown

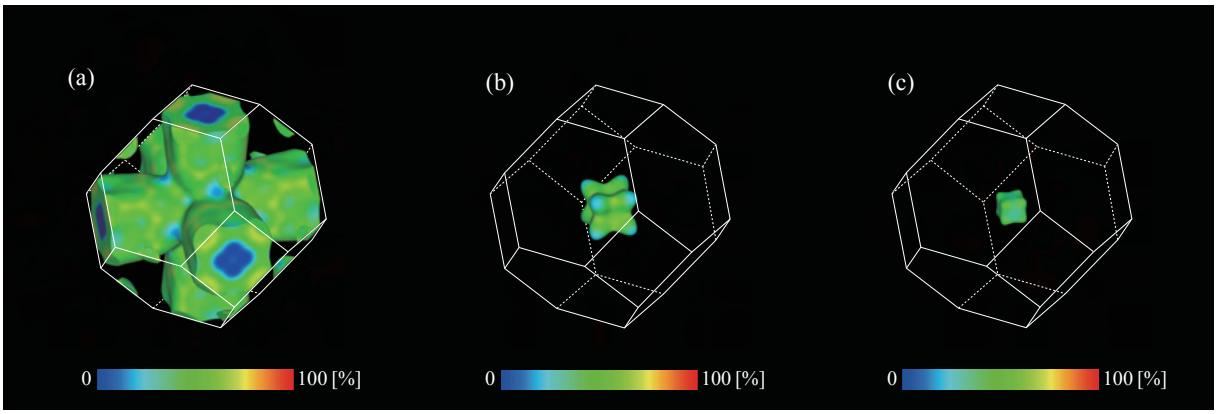

Figure 2: Calculated Fermi surfaces of TaC for (a) 5th band hole sheets, (b) 6th band electron sheets, and (c) 7th band electron sheets. Colors indicate the amount of 5d angular momentum character on each sheet of the Fermi surface. Red-shift indicate the increase of the admixture of d electrons. The center of the Brillouin zone is set at the Γ point.

in Figure 2. Note that the Fermi surfaces from 5th, 6th, and 7th bands are shown in (a), (b), and (c). The Fermi surface from the 5th band consists of two equivalent small hole sheets centered at the K points and one large hole sheet centered at the Γ point. The 5th band constructs a large hole sheet centered at the Γ point, which exhibits a complex network consisting of big "arms" which lie along the edges of Brillouin zone, as observed in Figure 2(a). The hole sheet centered at the Γ point is shown in Figure 2(b). It looks like a rounded cube having eight bumps in the <111> directions. The 7th band constructs a small electron sheet, which is centered at the Γ point is shown in Figure 2(c). The total number of holes is not equal to that of electrons, which represents that TaC is a uncompensated metal. Let us turn our attention to the analysis of the angular momentum character of the states forming various sheets of the Fermi surface. Here the most important quantity is the amount of Ta 5d character, which is the partial density of states for Ta 5d state for each point in k-space on the Fermi surface. This quantity is visualized in Figure 2, where the admixture of the Ta 5d states is increased as the red shift in color, as shown in the scale diagram. The broad variation of the color from blue to red reflects a substantial variation of the 5d contribution for different groups of states which change in the range from about 15% to about 80%. However, this distribution is different from part to part on the Fermi surface.

References

[1] O. Gunnarsson and B. I. Lundqvist: Phys. Rev. B 13 (1976) 4274.

[2] Nowotny H., and Kieffer R.Z.: Metallkd. **38** (1947) 257.

[3] Allen P.B., and Cohen M.L.: Phys. Rev. Lett. B29 (1972) 1593.

[4] Klein B.M., and Papaconstantopoulos D.A.: Phys. Rev. Lett. B32 (1974) 1193.

[5] Mulokozi A.M.: J. Less-Common Met. **79** (1981) 139.

[6] Allison C.Y., Finch C.B., Foegelle M.D., and Modine F.A.: Solid State Commun. **68** (1988) 387.

[7] Frisk K., and Fernandez Guillermet A: J. Alloys Compd. **238** (1996) 167.

Electronic Structure of 2D Boron Monosulfide

Masayuki TOYODA
Department of Physics, Tokyo Institute of Technology
Ookayama 2-12-1, Meguro-ku, Tokyo 152-8551

Ultrathin two-dimensional (2D) materials are a class of nanomaterials that exhibit unique mechanical, physical and chemical properties. Among them, 2D materials consisting of boron has been now attracting increasing interest due to their polymorphic properties. Recently, ultrathin boron monosulfied (BS) nanosheets have been successfully synthesized by the physical exfoliation of rhombohedral boron monosulfide (r-BS) [1]. The discovery of the BS nanosheets raised attention to their bulk layers. We have investigated the electronic and lattice vibrational properties of r-BS by performing first-principles density-functional theory (DFT) and density-functional perturbation theory calculations. The results agrees well with the experimental measurements including the infrared absorption spectroscopy [2] and microfocused angle-resolved photoemission spectroscopy [3]. By incorporating with the experiment, we have revealed the detailed electronic structure of r-BS and its *p*-type semiconductivity. In this study, we have utilized the efficient parallel computing power of ISSP Supercomputer System B (ohtaka).

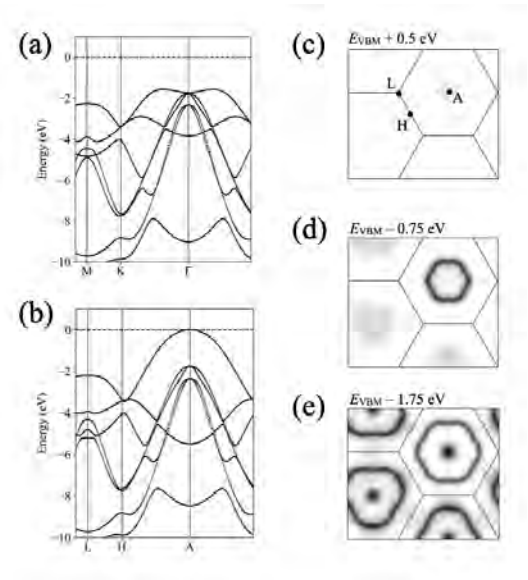

Figure 1: Calculated electronic structure of r-BS. The band dispersion (a and b) and 2D cross-section at different energies (c, d, and e) are shown.

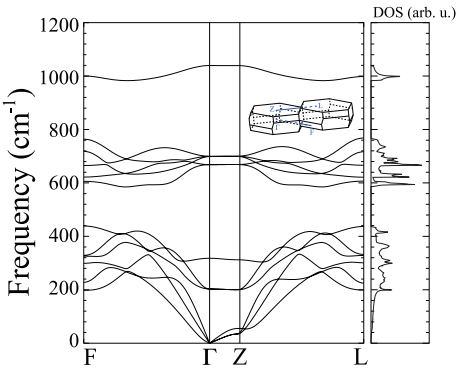

Figure 2: Calculated phonon dispersion of r-BS.

References

[1] H. Kusaka, R. Ishibiki, M. Toyodaet al., J. Mater. Chem. A **9**, 24631-24640 (2021); J. Mater. Chem. A **10**, 4999 (2022).

[2] 0 N. Watanabe, K. Miyazaki, M. Toyoda et al., Molecules **28**, 1896 (2023).

[3] K. Sugawara, H. Kusaka, T. Kawakami et al., Nano Lett. **23**, 1673-1679 (2023).

Exploration of exotic surface sites for catalyst informatics

Yoyo HINUMA

National Institute of Advanced Industrial Science and Technology (AIST)

1-8-31, Midorigaoka, Ikeda, Osaka 563-8577

Surface point defects of metal oxides, for instance O vacancies, have a dominant effect on heterogeneous catalysis. The Mars-Van Krevelen mechanism is one of the most frequently encountered catalytic process. In one example, O vacancies on a metal oxide catalyst surface act as reaction sites. The energy minimum required to remove O from a surface, which is denoted as the surface O vacancy formation energy (E_{Ovac}), can be used to rationalize and predict catalytic performance in such a catalytic process. Calculation of E_{Ovac} requires a slab-and-vacuum model with sufficient spacing between O vacancies, hence some estimation of E_{Ovac} from less costly calculations, such as slab-and-vacuum model calculations with minimum cell size and even bulk calculations, will be effective in screening materials for a given purpose.

Computational exploration of previously unknown reactive sites is a powerful strategy for emergence of new catalytic reactions. The surface energies of experimentally known perovskite oxides with B-site cations with redox capability (Ti-Fe). The A-cation and B-cation terminated (100) surfaces were studied. The symmetry was reduced by hand to obtain the lowest energy structure. Fig. 1 shows $CaTiO_3$ shown in the setting of a 2x2x2 supercell of the cubic 5-atom.

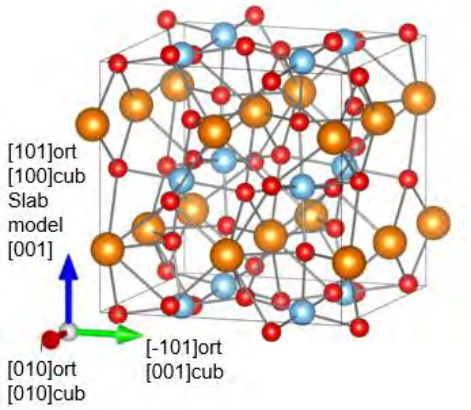

Fig. 1. Crystallographic conventional cell of CaTiO3 (space group type Pnma, number 62). Orange, blue, and red balls represent Ca, Ti, and O, respectively. The directions of basis vectors are shown in the orthorhombic (ort) and cubic (cubic) settings/

The following trends were found:

-Metallic compounds had small E_{Ovac}; less than 2 eV and 1 eV for A-cation and B-cation terminated surfaces, respectively.

-Ti-containing compounds had very high E_{Ovac} with more than 4 eV for the B(Ti)-cation layer. This result implies that Ti-containing perovskites are not very reactive.

-Other compounds were in-between, with the trend of higher A-cation layer E_{Ovac} when the B-cation contains more 3*d* electrons

Atom correlation of two-dimensional Cu-Ni alloy on the Ni(110) and Cu(110) surfaces

Tsuneo FUKUDA

Division of Electronics and Physics, Graduate School of Engineering,

Osaka Metropolitan University, 3-3-138 Sugimoto, Sumiyoshi-Ku, Osaka 558-8585

Copper-Nickel alloys are ubiquitous materials, and they are widely used as construction materials such as piping and various coinages. Cu and Ni are both simple fcc metals and form a uniform solid solution without any intermetallic compounds. The interaction energy is, however, known to be positive, resulting in a spinodal decomposition which has been established theoretically and experimentally. However, due to the lack of definitive experimental studies, no quantitative evaluation of the interaction energy between Cu and Ni has ever been conducted.

Here we studied atom correlation of two-dimensional alloy on Ni(110) and Cu(110) surfaces. The (110) face of fcc metals have a unique one-dimensional atom chain, and we have experimentally demonstrated one-dimensional attractive interaction of Cu-Cu on the Ni(110) surface.[1] The aim of this study is to evaluate the interaction energy from the first-principles. We used VASP, and by changing the Cu-Cu (Ni-Ni) distance on the Ni(110) (Cu(110)) surfaces the interaction energies were extracted as a function of Cu-Cu (Ni-Ni) distance (n). Atomic structures and the calculation parameters are respectively shown in the inset of Fig. 1 and Table 1.

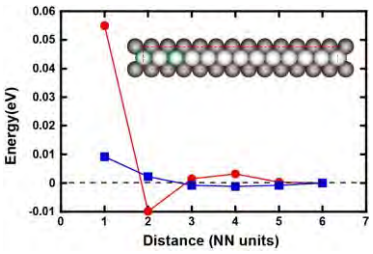

Fig. 1: Interaction energy as function of atomic distance. Red circles are for Cu-Cu pairs on the Ni(110) surface, and blue squares are for Ni-Ni pairs on the Cu(110) surface. Unit cell is indicated by a red broken rectangle in inset, and embedded Cu atoms for n=2 are indicated by green.

Table 1 Parameters for the present calculation

VASP Version	6.3.2
slab geometry	1×12 units 9 layers
k-points	32×4
potential	PBE [2]
cut off energy	384.08 eV
Fermi level smearing	Methfessel & Paxton σ = 0.12(Ni), 0.3 (Cu) eV
convergence condition	Electronic:10^{-6} eV Ionic: 0.01 eV/Ang.
SCF mixing parameters	AMIX = 0.02,BMIX = 0.0001 AMIX_MAG = 0.08 BMIX_MAG = 0.0001

The results shown in Fig. 1 clearly indicate attractive interaction both Ni-Ni and Cu-Cu pairs, which is direct confirmation of the clustering behavior of the two-dimensional Cu-Ni alloy.

References

[1] T. Fukuda, T. Saito, I. Kishida, ACSIN-14, Sendai 2019, 23E28.

[2] J. P. Perdew, K. Burke, and M. Ernzerhof, Phys. Rev. Lett. 77 (1996) 3865.

Search and realization of novel electronic properties of surfaces and interfaces and of nanostructures

Takeshi INAOKA
Department of Physics and Earth Sciences, Faculty of Science, University of the Ryukyus, 1 Senbaru, Nishihara, Okinawa 903-0213

This academic year, using the van-der-Waals density-functional theory, we investigated the electronic structure of the x-form phthalocyanine (Pc) crystal and the iodine doping effect on this structure. The Pc is a planar π-conjugated macrocyclic molecule which can include an atom of various species at its center. The x-form is one of several typical stacking forms of Pc in which molecular planes are perpendicular to the stacking axis. The x-form crystal is composed of a simple tetragonal lattice.

In each primitive unit cell of x-LiPc or x-NiPc, there are two molecules which are stacked along the c axis with a staggered angle of about 40° . The x-LiPc or x-NiPc is considered to be a Mott insulator because of its half-filled band. On iodine (I) doping, I atoms penetrate into one-dimensional (1D) open channels between x-form molecular chains, which results in x-LiPcI [1] or x-NiPcI [2]. Although x-LiPc or x-NiPc is a Mott insulator because of its half-filled band, doped I atoms oxidize partially Pc chains, shift the band occupancy from half-filling, and consequently leads to metallic nature [1]. In this analysis, we chosen SiPc and SiPcI, because a monomer of SiPc has a Si p_z-derived orbital just above the LUMO, and we expected x-SiPc to be 1D Si metal. However, as described below, dimerization of Si turns out to prevent formation of a metallic band.

We employed the program package 'Vienna Ab initio Simulation Package' (VASP) [3,4] on system B to optimize our structures.

To visualize our system, we show the optimized x-SiPcI structure in Fig. 1.

First, we consider the case without I doping. If we assume one period in the stacking direction, namely, one molecule in each primitive unit cell, we obtain a metallic band with about one-third occupied, and the cohesive energy per molecule of 1.82 eV. However, this is not the ground state.

In a single SiPc chain with two period, two Pc molecules in each primitive unit cell are stacked with a staggered angle 45° where eight C atoms nearest to the center Si atom in one molecule accord with those in the other molecule in projected position. This angle relation enables overlapping of p_z orbitals of adjacent molecules at these C-atom positions. The cohesive energy is 3.41 eV which is larger than that of the above one-period system.

In the x-SiPc crystal without I doping, which includes intermolecular interaction, the staggered angle deviates to 38.4° . Although this angle is somewhat unfavorable in terms of the above-mentioned overlap of C-atom p_z orbitals, s-orbital overlap occurs between two H atoms at the outer edges of neighboring molecule planes, as shown in the total electron density distribution in Fig. 2. This overlap can be ascribed to the fact that a number of k-states in some σ-bond dominant bands about 7 eV below the

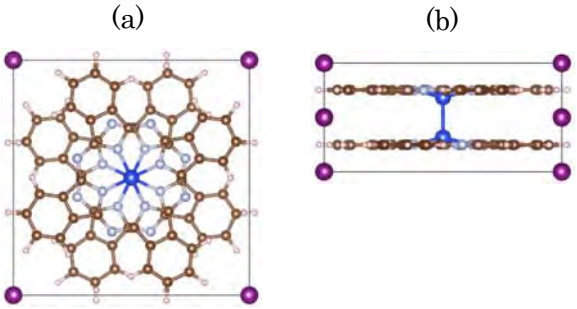

Fig. 1 Optimized x-SiPcI crystal structure. (a) top view, (b) side view. As for circles, blue: Si, gray: N, brown: C, white: H, purple: I.

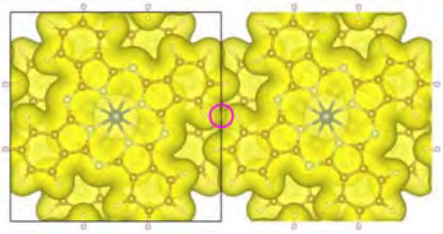

Fig. 2 Total electron-density distribution of x-SiPc. The purple circle shows s-orbital overlap between two H atoms.

Fermi level have local orbitals like H molecules. The Si atoms dimerize in the stacking direction, as in Fig. 1 (b), which prevents formation of a metallic band owing to Si p_z orbitals. The molecule cohesive energy is as large as 4.01 eV. Figure 3 (a) exhibits the band dispersion along the Γ–Z line in the stacking direction. The band b185, which is fully occupied, derives from Si p_z orbitals. Two almost degenerate bands, each of which is spin-degenerate, are half-filled ones, which leads to Mott insulators, according to the experimental results of x-LiPc [1] or x-NiPc [2].

Iodine (I) doping to x-SiPc turns this insulator into a metal. Figure 3 (b) displays the band dispersion along the Γ–Z line for x-SiPcI. We can identify the I-derived bands by following the energy levels labeled red in this panel. The highest one of these band dispersions that passes the levels b199 and b195 decreases rapidly in energy and intersects the Fermi level. Since this implies appearance of a metallic band, we analyzed the electronic structure. Figures 4 (a) and (b) shows the top and side views of the electron density distribution of the state at the Fermi level which is arrowed and marked b195 in red in Fig. 3 (b). The metallic states along the I atomic chains are connected to π-electron systems extending around the outer edges of Pc molecular planes. We consider that I doping makes a wide range of x-form Pc crystals metallic, including LiPcI and NiPcI.

To verify existence of 1D metallic bands due to I atomic chains, we are performing further calculations taking more k points in the Brillouin zone and upgrading the calculational scheme to the hybrid density functional method with higher accuracy. We will report the confirmed results in a near future [5].

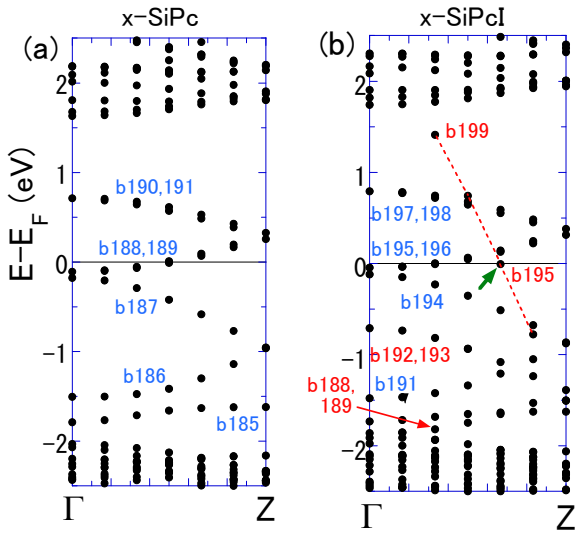

Fig. 3 Band dispersion of (a) x-SiPc and (b) x-SiPcI along the c axis. The bands labeled in red in (b) stem from the I-atomic chains, and one of these bands crosses the Fermi level, as is eye-guided by a red broken line.

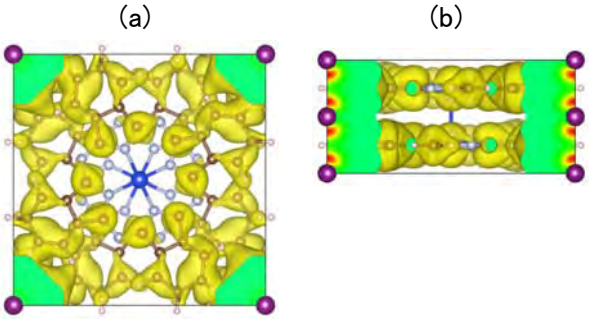

Fig. 4 Electron-density distribution of the state at the Fermi level that is arrowed and labeled b195 in red in Fig. 3 (b). (a) top view, (b) side view.

References

[1] R. Teruya et al., Angew. Chem. Int. Ed. **61**, e202206428 (1–6) (2022).
[2] C. J. Schramm et al., J. Am. Chem. Soc. **102**, 6702–6713 (1980).
[3] G. Kresse and J. Hafner: Phys. Rev. B **47**, 558–561 (1993).
[4] G. Kresse and J. Furthmüller: Comput. Mat. Sci. **6**, 15–50 (1996).
[5] T. Inaoka, to be submitted.

DFT calculations of organic halogen molecules and their reaction products on metal surfaces

Noriyuki TSUKAHARA

National Institute of Technology, Gunma College, Toriba-machi 580, Maebashi, Gunma, 371-0845, Japan.

In this study, DFT calculations were carried out to clarify the contribution of intermolecular halogen and hydrogen bonds to the structures of the 1,3,5-tris(bromophenyl)benzene (TBB) molecular film on Ag(111) and Si(111) (! 3"! 3)-Ag surfaces [1]. In combination with STM experiments, the structure of TBB molecular films and the intermolecular interactions are clarified. Fig. 1 shows the spatial distribution of the differential charge density for the isolated TBB molecule and TBB assembly on Ag(111). The difference in the distribution between the isolated molecule and the TBB assembly is derived from electrostatic attraction with a Br atom in the neighboring TBB molecule for the TBB assembly. It indicates intermolecular halogen bond. Similar calculation indicates the intermolecular hydrogen bond on Si(111) (! 3" ! 3)-Ag.

In addition, STM and DFT calculations were carried out to clarify the growth mechanism of the metal cluster using the metal-organic layer obtained by coupling reaction of TBB molecules on Ag(111) as a template [2].

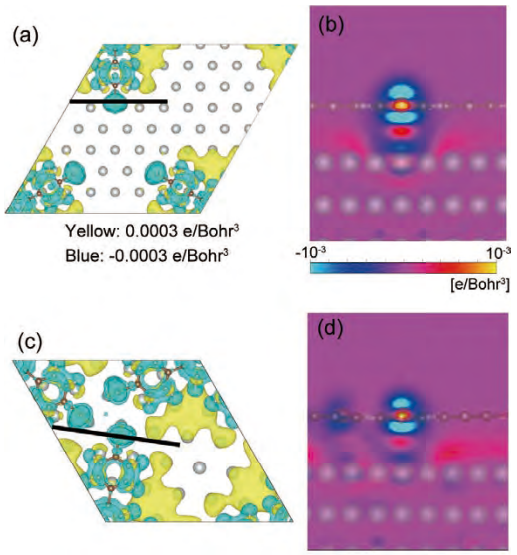

Fig. 1: The spatial distribution of the differential charge density for the isolated TBB molecule and the TBB assembly on Ag(111), and the vertical cross section of the distribution along the line in (a) and (c). Reprinted with permission from N. Tsukahara and J. Yoshinobu, Langmuir, **38**, 8881 (2022). Copyright 2022, American Chemical Society.

References

[1] N. Tsukahara and J. Yoshinobu, Langmuir, **38**, 8881 (2022).

[2] N. Tsukahara, R. Arafune, and J. Yoshinobu, Langmuir, to be submitted.

3.3 Strongly Correlated Quantum Systems

Numerical Studies on Superconductivity of Bilaye Cuprates and Mott Insulating States of Kitaev Materials

Youhei YAMAJI
Research Center for Materials Nanoarchitectonics, National Institute for Materials Science
Namiki, Tsukuba-shi, Ibaraki 305-0044

We have studied properties of two families of typical correlated electron systems, cuprate high-temperature superconductors and quantum-spin-liquid candidates, by using many-variable variational Monte Carlo methods [1]. As detailed below, we found that adjacent CuO_2 layer does not improve stability of the d-wave superconductivity in Hubbard-type hamiltonians [2], which are effective hamiltonians for the bilayer cuprates. We also studied propertie of an *ab initio* hamiltonian of a Kitaev material, Na_2IrO_3 [3, 4].

We studied the superconducting correlation function at long distance, P_d, for the bilayer t-t' Hubbard model around $U/t = 10$ and $t'/t \sim -0.3$. When we change a hole concentration, we found that the maximum P_d is quantitatively similar for the single-layer and bilayer t-t' Hubbard models [2]. From the momentum distribution functions, $n_{\boldsymbol{k}}$, we estimated the size of the superconducting gap Δ. Then, the effective attractive interaction, V_d, can be inferred by $V_d = \Delta/\sqrt{P_d}$. For both of the single-layer and bilayer systems, we obtain $V_d \sim 1.7t$. The variety of the optimal critical temperatures of cuprates may originate from the screening from apical oxygen and, thus, mainly from the Hubbard U [5, 6].

We also studied the properties of Na_2IrO_3 beyond low-energy spin degrees of freedom. First, we clarified the ground state of the *ab initio* t_{2g} hamiltonian [3]. We confirmed that the ground state shows the zigzag magnetic order, and found that the the amplitude of the Mott gap is 750 meV, which is larger than 340 meV reported by combining the optical conductivity and photoemission spectroscopy [7]. The discrepancy originates from the Mott-Andern nature of the experimentally observed samples of Na_2IrO_3 due to disorders, where the Mott gap is filled by in-gap localized states. When the principle energy scales, the on-site (off-site) Coulomb repulsion U (V_{ij}) and spin-orbit coupling $\zeta_{\rm so}$, are deviated from the *ab initio* values, the first order phase transitions from the zigzag state to ferromagnetic and charge ordered states are found.

References

[1] T. Misawa, *et al.*: Comput. Phys. Commun. **235**, 447 (2019).

[2] A. Iwano and Y. Yamaji: J. Phys. Soc. Jpn. **91**, 094702 (2022).

[3] Y. Yamaji, *et al.*: Phys. Rev. Lett. **113**, 107201 (2014).

[4] C. Xu and Y. Yamaji: in preparation.

[5] J.-B. Morée, *et al.*: Phys. Rev. B **106**, 235150 (2022).

[6] M. T. Schmid, *et al.*: arXiv:2303.06672.

[7] R. Comin, *et al.*: Phys. Rev. Lett. **109**, 266406 (2012).

Theoretical study of strongly-correlated topological phenomena by exploiting first-principles calculations and machine learning

Yukitoshi MOTOME

Department of Applied Physics,

The University of Tokyo, Bunkyo, Tokyo 113-8656

We have theoretically studied a variety of intriguing topological phenomena in strongly-correlated electron systems by using numerical methods including first-principles calculations and machine learning (project numbers: 2022-Ca-0013 and 2022-Cb-0013). During the last fiscal year, we have achieved substantial progress on the following topics. We summarize the main results below.

(i) *Development of new theoretical methods*: We developed a new framework to solve "inverse problem", namely to construct a proper Hamiltonian which exhibits desired physical properties, by using automatic differentiation [1]. We also proposed a new scheme for physical reservoir computing by exploiting frustrated magnets, which is useful to realize efficient parallel computing in both space and time [2,3].

(ii) *Topological properties of thin films of Weyl semimetals*: Studying the structural, electronic, and magnetic properties of atomically thin films of Co-based shandite by first-principles calculations, we clarified the changes of magnetism and band topology with respect to the number of Co kagome layers and the surface termination, which will be useful for future experimental fabrication [4].

(iii) *Topological spin crystals as spin moire*: Extending the research in last year, we clarified the effect of phase shift on skyrmion and hedgehog crystals and elucidated the topological phase diagrams [5]. We also showed that hedgehog crystals can be stabilized in centrosymmetric cubic lattices by itinerant frustration mechanism [6]. In addition, we developed a new exact method to solve thermodynamics of effective infinite-range interaction models [7], and by applying it we unveiled hidden topological transitions associated with pair creation and annihilation of emergent magnetic monopoles [8].

(iv) *Kitaev quantum spin liquids*: By using the pseudo-fermion functional renormalization group (PFFRG) method, we clarified the feasibility of Kitaev quantum spin liquids in ultracold polar molecules [9], a complete phase diagram for the Kitaev-Heisenberg model with arbitrary spin length S [10], and the phase diagram for the S=1/2 Kitaev-Heisenberg

model on a three-dimensional hyperhoneycomb lattice [11]. We also unveiled several exotic phases, including multiple-q chiral phases and chiral spin liquid, in competing region between spin nematics and spin liuqids in the S=1 Kitaev model with bilinear-biquadratic interactions by using the SU(3) formalism [12]. We elucidated linear and nonlinear thermal transport in the presence of both uniform and staggered magnetic fields [13]. In addition, we clarified that the dynamical spin transport induced by an AC magnetic field applied to an edge of the system is useful for the identification of fractional excitations in the Kitaev quantum spin liquids [14]. Furthermore, we found a phase transition in the quantum spin liquid phase under a magnetic field in α-$RuCl_3$ in collaboration with experimentalists [15]. We also wrote a review article (in Japanese) [16] in a special issue for “New Developments on the Physics of Kitaev Spin Liquids” edited by the author and coworkers [17].

References

[1] K. Inui and Y. Motome, Commun. Phys. **6**, 37 (2023).

[2] K. Kobayashi and Y. Motome, preprint (arXiv:2302.14496).

[3] 特願 2023-025883「情報処理システム、情報処理方法およびプログラム」求 幸年、小林海翔（2023 年 2 月 22 日出願）

[4] K. Nakazawa, Y. Kato, and Y. Motome, preprint (arXiv:2212.09026).

[5] K. Shimizu, S. Okumura, Y. Kato, and Y. Motome, Phys. Rev. B **105**, 224405 (2022).

[6] S. Okumura, S. Hayami, Y. Kato, and Y. Motome, J. Phys. Soc. Jpn. **91**, 093702 (2022).

[7] Y. Kato and Y. Motome, Phys. Rev. B **105**, 174413 (2022).

[8] Y. Kato and Y. Motome, Phys. Rev. B **107**, 094437 (2023).

[9] K. Fukui, Y. Kato, J. Nasu, and Y. Motome, Phys. Rev. B **106**, 014419 (2022).

[10] K. Fukui, Y. Kato, J. Nasu, and Y. Motome, Phys. Rev. B **106**, 174416 (2022).

[11] K. Fukui, Y. Kato, and Y. Motome, preprint (arXiv:2303.09156).

[12] R. Pohle, N. Shannon, and Y. Motome, Phys. Rev. B **107**, L140403 (2023).

[13] K. Nakazawa, Y. Kato, and Y. Motome, Phys. Rev. B **105**, 165152 (2022).

[14] T. Misawa, J. Nasu, and Y. Motome, preprint (arXiv:2304.00528).

[15] S. Suetsugu, Y. Ukai, M. Shimomura, M. Kamimura, T. Asaba, Y. Kasahara, N. Kurita, H. Tanaka, T. Shibauchi, J. Nasu, Y. Motome, and Y. Matsuda, J. Phys. Soc. Jpn. **91**, 124703 (2022).

[16] 張 成燻、求 幸年：固体物理 **57**, 757 (2022).

[17] 固体物理特集号 **57**, 613-784 (2022), "キタエフスピン液体の新展開" (編集委員：芝内孝禎・遠山貴巳・求 幸年)

Theoretical study on elementaly excitations and optical control of topological phases in the spin-charge coupled magnets

Rintaro ETO and Masahito MOCHIZUKI
Department of Applied Physics, Waseda University
Okubo, Shinjuku-ku, Tokyo 169-8555

We have theoretically studied elementaly excitations and photoinduced topological phases in the Kondo-lattice magnets with couplings between spin and charge degrees of freedom (project ID: 2022-Ca-0012, 2022-Cb-0014). Results of these projects are listed below.

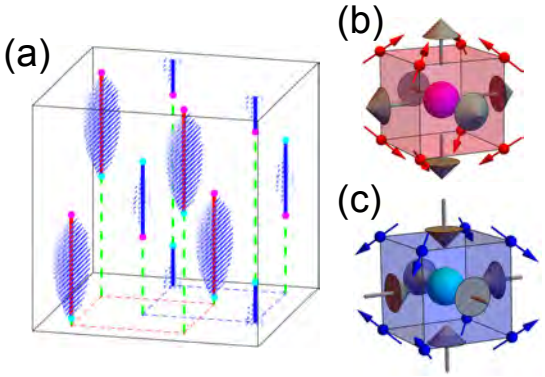

Figure 1: (a) Schematic of the quadruple-Q hedgehog lattice. Magenta and cyan balls represent hedgehogs and antihedgehogs, respectively. Red and blue dashed lines represent the Dirac strings A (vortex type) and B (antivortex type), respectively. (b),(c) Enlargements of the (b) hedgehog and (c) antihedgehog. Gray arrows denote local emergent magnetic fields.

(i) *Spin-wave excitations in the quadruple-Q magnetic hedgehog lattices in 3D chiral magnets*: We have theoretically studied the spin-wave modes of the quadruple-Q magnetic hedgehog lattices in 3D chiral magnets [Fig. 1(a)] [1]. First, we constructed a microscopic Kondo-lattice model on the 3D cubic lattice, which hosts the quadruple-Q hedgehog lattice spin textures as the ground state. In this model, interplay of the second- and fourth-order spin-spin interactions mediated by nested Fermi surfaces is a key to stabilizing the hedgehog lattice spin textures. The hedgehog lattice spin textures in this model have two types of Dirac strings connecting a hedgehog [Fig. 1(b)] and an antihedgehog [Fig. 1(c)], the vortex-type strings A and the antivortex-type strings B. Using this model, we studied the spin-wave excitations of the hedgehog lattice spin textures under an external magnetic field ($\parallel$ [001]) by using large-scale adiabatic spin-dynamics simulations based on the kernel polynomial method. By calculating the microwave absorption spectra for microwave polarization parallel to the Dirac strings (i.e. $\parallel$ [001]), we found three spin-wave nmodes, which are named L1, L2, and L3, in order from the lowest to highest frequency. These modes are spatially localized at the Dirac strings and are associated with translational motion of the Dirac strings. In particular, the disappearance of L2 mode, which is localized at the strings B, is observed simultaneously with the field-induced hedgehog-antihedgehog pair annihilation at the strings B.

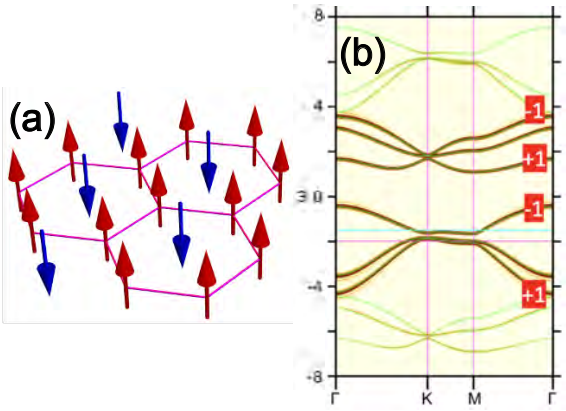

Figure 2: (a) Schematic of the three-sublattice ferrimagnetic order. Majority spins form a honeycomb network. (b) Single-particle spectrum of a Floquet Chern insulator state. Green lines represent the Floquet states. Numbers are the Chern numbers of the corresponding bands.

(ii) *Floquet topological phases in the Dirac half-metallic ferrimagnet*: We have theoretically investigated photoinduced topological phases in the Dirac half-metallic state in the spin-charge coupled Kondo-lattice magnets [2]. We here considered the three-sublattice ferrimagnetic order on the 2D triangular lattice which appears spontaneously when the conduction electron filling is 1/3 [Fig. 2(a)]. We analyzed this model using the Floquet theory and found two types of Floquet Chern insulator (FCI) states with gapped spin-polarized Dirac bands. One is associated with the gap opening at K point [Fig. 2(b)], whereas the other originates from the gap closing and reopening at M point. The appearance of the former FCI state was also confirmed in our analysis of the periodic Anderson model, from which the Kondo-lattice model is derived via the perturbational calculation. Both of these FCI states are induced not by the first-order but by the higher-order terms in the high-frequency expansion, and are distinct from conventional ones induced by the first-order terms associated with the original sublattice degrees of freedom of the honeycomb lattice. This work will extend the scope of Floquet engineering to magnetic materials with sublattice degrees of freedom of magnetic origin.

References

[1] R. Eto and M. Mochizuki, in preparation.

[2] R. Eto and M. Mochizuki, in preparation.

Studies on superconductivity in trestle-type lattices

KAZUHIKO KUROKI
Department of Physics, Osaka University
1-1 Machikaneyama, Toyonaka, Osaka, 560-0043, Japan

INTRODUCTION

Most cuprate superconductors possess CuO_2 planes, which are considered to play the main role in the occurrence of superconductivity. One exception is $(Sr,Ca)_{14}Cu_{24}O_{41}$[1], which consists of two-leg ladder and chain structures. Yet another possible example is $Pr_2Ba_4Cu_7O_{15-\delta}$[2]. This material is constructed from alternating stacking of $PrBa_2Cu_3O_7$ and $PrBa_2Cu_4O_8$, and does have CuO_2 planes, but they are considered to be insulating. There have been suggestions that the double-chain structure in $PrBa_2Cu_4O_8$ is responsible for the superconductivity, and some theoretical studies support this possibility[3–5]. Quite recently, there has been stronger evidences that the double-chain structure is responsible for the occurrence of superconductivity[6].

FLEX STUDIES ON THE HUBBARD MODEL ON A TRESTLE-TYPE LATTICE

The double-chain structure can be modeled by a Hubbard model on a trestle-type lattice, with intra-chain hopping t_2 and interchain hopping t_1. This model can further be considered as a single band one-dimensional system with nearest (t_1) and next nearest (t_2) neighbor hoppings. We theoretically studied this model using the fluctuation exchange (FLEX) approximation. We have varied t_2/t_1 as well as the band filling, and obtained the eigenvalue of the Eliashberg equation at a fixed temperature, which measures tendency towards superconductivity. Depending on the parameter values, there can be either two or four Fermi points because the band structure has a double-well shape. The case where there are four Fermi points resembles the situation for the two-leg ladder systems. We find that the eigenvalue of the Eliashberg equation becomes the largest when the band intersects the Fermi level at two Fermi points and also barely touches the Fermi level at two other points. This is in fact reminiscent of the situation where one of the bands is incipient in the two-leg ladder system[7]. Studies applying other many-body methods to this model are underway in order to verify these FLEX results.

FIRST-PRINCIPLES MODEL CONSTRUCTION OF $PR_2BA_4CU_7O_{15-\delta}$

In order to obtain a realistic model of $Pr_2Ba_4Cu_7O_{15-\delta}$, we have performed first principles band calculation of this material using VASP, and obtained a tightbinding model for the double-chain structure through wannierization. A relatively large t_1/t_2 ratio is obtained, consistent with previous studies[3–5]. Many-body study of this realistic model is now underway. An important point we are focusing on is (i) the band filling of the double-chain structure as a function of oxygen deficiency δ and (ii) the origin of the relatively large t_1/t_2, which is essential in obtaining the tendency toward superconductivity.

[1] M. Uehara *et al.*, J. Phys. Soc. Jpn. **65**, 2764 (1996).
[2] M. Matsukawa *et al.*, Physica C **411**, 1011 (2004).
[3] K. Sano, Y.Ono, and Y. Yamada, J. Phys. Soc. Jpn. **74**, 2885 (2005).
[4] T. Nakano and K. Kuroki, Phys. Rev. B **76**, 014515 (2007).
[5] T. Habaguchi *et al.*, J. Phys. Soc. Jpn. **80**, 024708 (2011).
[6] S. Nishioka *et al.*, Appl. Phys. Exp. **15**, 023001 (2022).
[7] K. Matsumoto, D. Ogura, and K. Kuroki, Phys. Rev. B **97**, 014516 (2018).

First-principles calculations of dynamical susceptibilities for strongly correlated materials

Hiroshi SHINAOKA
Department of Physics, Saitama University, Saitama 338-8570

This report details our recent computational investigation of $SrRu_2O_6$, a material around the boundary between covalent and Mott insulators. Our study aimed to compare the results with those of inelastic scattering experiments, and for this purpose, we employed the density functional theory plus the dynamical mean-field theory (DFT+DMFT) approach. We used DCore [1] and ALPS/CT-HYB [2] for DFT+DMFT calculations. The codes are parallelized by MPI. We constructed the tight-binding model using Wien2k.

We successfully created a phase diagram as a function of temperature. Notably, we observed an antiferromagnetic phase at low temperatures consistent with experimental findings. Figure 1 plots the temperature dependence of the magnetic moment.

Currently, we are calculating the dynamic susceptibility in the low-temperature phase by solving the Bethe-Salpeter equation. We expect to release our results as a preprint [3].

It is important to acknowledge that this research has been conducted as a collaboration between Prof. Atsushi Hariki at Osaka City University and the group of Jan Kuneš at TU Wien.

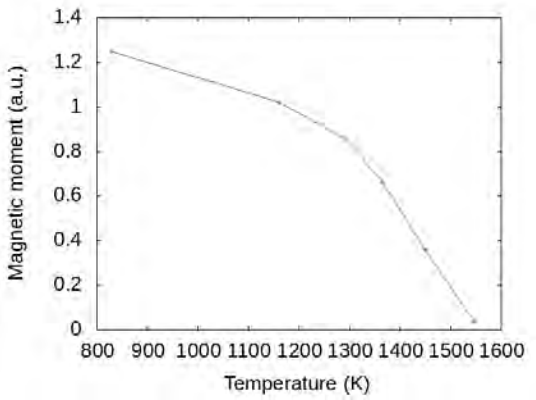

Fig. 1: Temperature dependence of magnetic moment

References

[1] H. Shinaoka, J. Otsuki, M. Kawamura, N. Takemori, K. Yoshimi, SciPost Phys. 10, 117 (2021).

[2] H. Shinaoka, E. Gull, P. Werner, Comput. Phys. Commun. 215, 128 (2017).

[3] Diana Csontosová, H. Shinaoka, A. Hariki, and J. Kuneš, in preparation.

Nonlocal correlation effects in a Hund Ferromagnet

Yusuke NOMURA

Department of Applied Physics and Physico-Informatics, Keio University,

3-14-1 Hiyoshi, Kohoku-ku, Yokohama, 223-8522, Japan

Understanding electron correlation effects beyond Fermi liquid theory is a fundamental problem in condensed matter physics, since various intriguing phenomena such as superconductivity and magnetism emerge from pseudogap and strange-metal states.

A well-known example is the pseudogap behavior observed in doped cuprates, where strong nonlocal antiferromagnetic fluctuations are believed to play an important role. This phenomenon has been intensively studied by the cluster extension of the dynamical mean-field theory.

However, nonlocal correlation effects in multi-orbital systems remain largely elusive. In particular, the influence of ferromagnetic fluctuations in the strong-coupling regime is still poorly understood compared to the antiferromagnetic case.

Such a strong-coupling ferromagnetic regime is expected in the multiorbital Hubbard model. Therefore, we study the two-orbital Hubbard model on the two-dimensional square lattice using cellular dynamical mean-field theory. Although the cluster extension in multiorbital systems is computationally expensive, we have managed to accomplish the calculations thanks to the efficient continuous-time quantum Monte Carlo methods developed in Refs. [1-4].

We find that the Fermi surface expands even above the Curie temperature as if the spin polarization occurred, contrary to a naïve view that the Fermi surface should recover non-spin-polarized behavior. Behind this phenomenon, effective “Hund’s physics” works in momentum space; ferromagnetic spin correlations induce effective Hund’s coupling in momentum space, leading to a large modulation of the momentum space occupancy. The reconstruction of the Fermi surface differs from the antiferromagnetic case, where it creates hot and cold spots in the Fermi surface. Our finding will give a deeper insight into the physics of Hund’s ferromagnets above the Curie temperature.

References

[1] Y. Nomura, S. Sakai, and R. Arita, Phys. Rev. B **89**, 195146 (2014)

[2] H. Shinaoka, Y. Nomura et al., Phys. Rev. B **92**, 195126 (2015)

[3] Y. Nomura, S. Sakai, and R. Arita, Phys. Rev. B **91**, 235107 (2015)

[4] H. Shinaoka, Y. Nomura and E. Gull,

Comput. Phys. Commun. **252**, 106826 (2020)

[5] Y. Nomura, S. Sakai, and R. Arita, Phys. Rev. Lett. **128**, 206401 (2022)

Transient absorption spectrum in photo-excited one-dimensional Mott insulators

Takami TOHYAMA
Department of Applied Physics, Tokyo University of Science, Tokyo 125-8585

The elucidation of nonequilibrium states in strongly correlated systems is of great interest since it promises to open a door to the emergence of novel quantum phases. One of the most significant challenges is how to preserve nonequilibrium states, such as the Floquet states, from thermalization, for which the realization of many-body localization may hold the key. Also, the nonequilibrium-induced insulator-to-metal transition studied extensively in the one-dimensional (1D) Mott insulator is a fundamental issue associated with competition between itinerancy and localization of charge degrees of freedom. Similarly, non-absorbable terahertz photons with strong intensity may induce a metallic state via quantum tunneling. Until now it has been commonly accepted that the breakdown of the Mott insulators via electric pulses leads to metallic states. However, we raise question about the validity of this understanding.

To answer this question, in this project we focus on the possibility of the emergence of novel quantum phases such as glass phases with intermediate properties between itinerancy and many-body localization. We investigate pulse-excited states of the half-filled 1D extended Hubbard model using the time-dependent density-matrix renormalization group (tDMRG). Our tDMRG makes use of the Legendre polynomial for the calculation of time-evolution operator. We use two target states at a given time t and $t + \Delta t$ to construct a basis set that can express wavefunctions in the time-dependent Hilbert space. With the two-target tDMRG procedure, we can calculate time-dependent physical quantities with high accuracy even when the Hamiltonian varies rapidly with time.

From our tDMRG simulations, we propose a Mott transition to glassy states induced by mono- and half-cycle terahertz pulses **??**. If we excite the Mott insulating state via photon absorption, we obtain metallic states with large Drude weight. In contrast, we find that strong electric fields inducing the Zener breakdown strongly suppress the Drude weight even in the presence of a large number of carriers. We consider that the Hilbert-space fragmentation due to high fields leads to glassy dynamics as seen in fracton systems. The glassy state is accompanied by electric polarization that breaks inversion symmetry **??**. We also demonstrate a steady electric current induced by an ultrashort subcycle pulse. This is due to an Aharonov-Bohm flux introduced through the phase of an electric field. Consequently, time-reversal symmetry is broken. Both symmetry breakings can be monitored by second harmonic generation. These findings propose a new methodology for designing the symmetries of electronic states and open up a new field of subcycle-pulse engineering.

References

[1] K. Shinjo, S. Sota, and T. Tohyama: Phys. Rev. Res **4** (2022) L032019.

[2] K. Shinjo, S. Sota, S. Yunoki, and T. Tohyama: arVix:2211.08694.

Research of Three-Channel Kondo Effect Emerging from Holmium Ions

Takashi HOTTA
Department of Physics, Tokyo Metropolitan University
1-1 Minami-Osawa, Hachioji, Tokyo 192-0397

In 2021, we have discovered the three-channel Kondo effect emerging from Ho ions [1]. Here we briefly report the subsequent development of the research, in particular, the magnitude of the effective impurity spin of the three-channel Kondo effect.

First we explain the model Hamiltonian. For the construction of the model, we define one f-electron state by the eigenstate of spin-orbit and crystalline electric field (CEF) potential terms. We obtain Γ_7 doublet and Γ_8 quartet from $j = 5/2$ sextet whereas we find Γ_6 doublet, Γ_7 doublet, and Γ_8 quartet from $j = 7/2$ octet under the cubic CEF potential. Then, we include the Γ_7 and Γ_8 conduction electron bands. Here we consider only the hybridization between the conduction and $j = 7/2$ electrons. The model Hamiltonian is given by

$$\begin{aligned} H &= \sum_{\boldsymbol{k},\mu,\tau} \varepsilon_{\boldsymbol{k}} c^\dagger_{\boldsymbol{k}\mu\tau} c_{\boldsymbol{k}\mu\tau} + \sum_{\boldsymbol{k},\mu,\tau} V(c^\dagger_{\boldsymbol{k}\mu\tau} f_{b\mu\tau} + \text{h.c.}) \\ &+ nE_f + \sum_{j,\mu,\tau} (\lambda_j + B_{j,\mu}) f^\dagger_{j\mu\tau} f_{j\mu\tau} \\ &+ \sum_{j_1\sim j_4} \sum_{\mu_1\sim\mu_4} \sum_{\tau_1\sim\tau_4} I^{j_1 j_2, j_3 j_4}_{\mu_1\tau_1\mu_2\tau_2,\mu_3\tau_3\mu_4\tau_4} \\ &\times f^\dagger_{j_1\mu_1\tau_1} f^\dagger_{j_2\mu_2\tau_2} f_{j_3\mu_3\tau_3} f_{j_4\mu_4\tau_4}, \end{aligned} \tag{1}$$

where $\varepsilon_{\boldsymbol{k}}$ is the dispersion of conduction electron with wave vector $\boldsymbol{k}$, $c_{\boldsymbol{k}\mu\tau}$ is the annihilation operator of a conduction electron, $f_{j\mu\tau}$ is the annihilation operator of a localized f electron in the bases of (j, μ, τ), j is the total angular momentum, $j = 5/2$ and $7/2$ are denoted by "a" and "b", respectively, μ distinguishes the cubic irreducible representation, Γ_8 states are distinguished by $\mu = \alpha$ and β, while the Γ_7 and Γ_6 states are labeled by $\mu = \gamma$ and δ, respectively, τ denotes the pseudo-spin, which distinguishes the degeneracy concerning the time-reversal symmetry, V denotes the hybridization between f electron in the μ orbital and conduction electron of the μ band, n is the local f-electron number at an impurity site, and E_f is the f-electron level to control n.

As for the spin-orbit term, we obtain $\lambda_a = -2\lambda$ and $\lambda_b = (3/2)\lambda$, where λ is the spin-orbit coupling of f electron and we set $\lambda = 0.265$ eV for the Ho ions. Concerning the CEF potential term for $j = 5/2$, we obtain $B_{a,\alpha} = B_{a,\beta} = 1320B^0_4/7$ and $B_{a,\gamma} = -2640B^0_4/7$, where B^0_4 denotes the fourth-order CEF parameter for the angular momentum $\ell = 3$. For $j = 7/2$, we obtain $B_{b,\alpha} = B_{b,\beta} = 360B^0_4/7 + 2880B^0_6$, $B_{b,\gamma} = -3240B^0_4/7 - 2160B^0_6$, and $B_{b,\delta} = 360B^0_4 - 3600B^0_6/7$. In the following calculations, we use the parametrization as $B^0_4 = Wx/15$ and $B^0_6 = W(1 - |x|)/180$ for $\ell = 3$, where x specifies the CEF scheme for the $O_{\rm h}$ point group, while W determines the energy scale of the CEF potentials. In this work, we set $W = 10^{-3}$ eV and treat x as the parameter to control the CEF ground state.

For the Coulomb interaction terms, we do not show the explicit forms of I here, but they are expressed by the four Slater-Condon parameters, F^0, F^2, F^4, and F^6. These values should be determined from experimental results, but here we simply set the ratio as $F^0/10 = F^2/5 = F^4/3 = F^6 = U$, where U indicates the Hund's rule interaction among the

f orbitals. In this work, we set $U = 1$ eV.

The model is analyzed with the use of a numerical renormalization group (NRG) method. We introduce a cut-off Λ for the logarithmic discretization of the conduction band. Due to the limitation of computer resources, we keep M low-energy states. Here we use $\Lambda = 8$ and $M = 5,000$. In the NRG calculation, the temperature T is defined as $T = D\Lambda^{-(N-1)/2}$, where D is half the conduction band width, which was set as 1 eV, and N is the number of renormalization steps.

From the NRG calculations, we have found a residual entropy $S_{\rm imp}$ of $\log\phi$ with the golden ratio $\phi = (1+\sqrt{5})/2$ for the local Γ_5 triplet ground state. For the multi-channel Kondo effect, the analytic value of the residual entropy $S_{\rm imp}$ has been found to be given by [2]

$$S_{\rm imp} = \log \frac{\sin[(2S+1)\pi/(n_{\rm c}+2)]}{\sin[\pi/(n_{\rm c}+2)]}, \qquad (2)$$

where S denotes the local impurity spin and $n_{\rm c}$ indicates the number of channels. In the present case with $n_{\rm c} = 3$, we obtain $S_{\rm imp} = \log\phi$ for both the cases of $S = 1/2$ and 1. Thus, in any case, the residual entropy $\log\phi$ is considered to be characteristic of the three-channel Kondo effect, but the value of S is not determined only from the residual entropy.

To confirm the value of S, we hit upon an idea to explore a quantum critical point (QCP) between the three-channel Kondo and Fermi-liquid phases. The QCP between the three-channel Kondo and Fermi-liquid phases is expected to be characterized by the residual entropy of the four-channel Kondo effect. From eq. (2), we obtain $S_{\rm imp} = 0.5\log 3$ and $\log 2$ for $S = 1/2$ and 1, respectively, for $n_{\rm c} = 4$.

In Fig. 3(a), we show the f-electron entropies for $W = 10^{-3}$ and $V = 0.7$ between $x = 0.65$ and 0.7. For $x = 0.65$, we observe the three-channel Kondo phase, while for $x = 0.7$, the local singlet phase appears. At $x = 0.6849$, the entropy plateaus with a value between $0.5\log 3$ and $\log 2$, and it eventually exits the plateau at around $T \sim 10^{-10}$. We deduce this as the signal of the QCP between the three-channel Kondo and Fermi-liquid phases. Note that this behavior has also been observed around at $x = -0.64$.

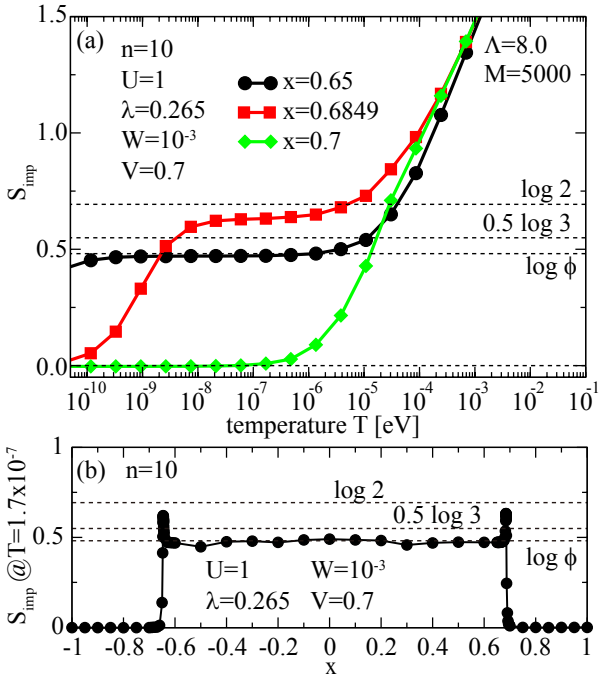

Figure 1: (a) Entropies vs. temperature for $x = 0.65$, 0.6849, and 0.7 with $W = 10^{-3}$ and $V = 0.7$. (b) Residual entropies at $T = 1.7\times 10^{-7}$ vs. x for $-1 \le x \le 1$.

In Fig. 3(b), we plot the value of the entropy at $T = 1.7\times 10^{-7}$ as a function of x for $-1 \le x \le 1$. We find sharp two peaks at around $x \approx -0.646$ and $x \approx 0.685$, and the peaks assume values between $0.5\log 3$ and $\log 2$. Since these values are apparently larger than $0.5\log 3$, we deduce that the peaks indicates the QCP characterized by the residual entropy of the four-channel Kondo effect with $S = 1$. This result is consistent with the local Γ_5 triplet ground state.

References

[1] T. Hotta, J. Phys. Soc. Jpn. **90**, 113701 (2021).

[2] I. Affleck and A. W. W. Ludwig, Nucl. Phys. B **360**, 641 (1991).

Magnetic field effect on excitonic phase in multi-orbital Hubbard model

Joji NASU
Department of Physics, Tohoku University
Sendai 980-8578

Excitonic insulators are insulating states where pairs of an electron in a conduction band and a hole in a valence band are condensed coherently. Although this state was proposed as a superconductivity analog about 50 years ago, recent discoveries of materials that could potentially exhibit excitonic insulators have renewed interest in studying this system. Among the candidates, cobalt oxides have received significant attention due to their multiple spin states, including low-spin, intermediate-spin, and high-spin states, which are affected by crystalline fields and Hund couplings. Recent research has suggested that excitonic condensation could occur through spontaneous hybridization between distinct spin states. The theoretical and experimental examinations of cobalt oxides in this perspective has revealed the emergence of a magnetic-field-induced excitonic phase and spin-splitting. The simplified two-orbital Hubbard model has been used in these studies to consider low-spin and high-spin states [1, 2, 3].

In this project, we have investigated magnetic field effects on the multi-orbital Hubbard model with the expressive ability of the three spin states, including the intermediate-spin state. We have derived a low-energy effective model and performed mean-field calculations, but due to the complexity of the model, finding solutions is computationally expensive. To reduce computation time, we have utilized the technique of parallel computation. Our findings show that increasing the applied magnetic field results in the appearance of two excitonic phases [4]. The low-field phase is not accompanied by spin-state alignments, while the excitonic phase appearing higher field is associated with a spin-state order and interpreted as a supersolid in terms of excitonic condensation. The magnetization curve should display signatures of these phases, which is consistent with a recent experiment measuring volume change up to 600T [4].

References

[1] T. Tatsuno, E. Mizoguchi, J. Nasu, M. Naka, S. Ishihara: J. Phys. Soc. Jpn. **85** (2016) 083706.

[2] J. Nasu, M. Naka, S. Ishihara: Phys. Rev. B **102** (2020) 045143.

[3] J. Nasu and M. Naka: Phys. Rev. B **103** (2021) L121104.

[4] A. Ikeda, Y. H. Matsuda, K. Sato, Y. Ishii, H. Sawabe, D. Nakamura, S. Takeyama, and J. Nasu: Nat. Commun. **14** (2023) 1744.

Correlation-induced phenomena in Kondo lattice systems

Robert PETERS

Department of Physics,

Kyoto University, Kyoto, 606-8502

Kondo insulators are strongly correlated insulators where the resistivity becomes large at low temperatures due to a gap in the single-particle spectrum [1]. Recently, quantum oscillations in strong magnetic fields have been observed in these materials while insulating. Furthermore, specific heat and thermal transport measurements on YbB_{12} and $YbIr_3Si_7$ have revealed low-lying excitations in these Kondo insulators that can transport heat but no electric current [2,3]. Thus, it has been argued that there are itinerant charge-neutral excitations that are responsible for thermal transport and lead to observable quantum oscillations in strong magnetic fields. However, a conclusion to these recent experiments is not yet found.

Using variational matrix product states, we analyzed the finite temperature behavior of a half-filled periodic Anderson model in one dimension, a prototypical model of a Kondo insulator. In our calculations [4], we confirmed the existence of energetically low-lying spin excitations [1] in this model and studied their energy-momentum dispersion and temperature dependence. We demonstrated that charge-charge correlations at the Fermi energy exhibit a different temperature dependence than spin-spin correlations. While energetically low-lying spin excitations emerge approximately at the Kondo temperature, which exponentially depends on the interaction strength, charge correlations vanish already at high temperatures.

Furthermore, we analyzed the charge and thermal conductivities at finite temperatures by calculating the time-dependent current-current correlation functions. While both charge and thermal conductivities can be fitted for all interaction strengths by gapped systems with a renormalized band gap, the gap in the system describing the thermal conductivity is generally smaller than the system describing the charge conductivity. Furthermore, the maximum of the charge conductivity over the temperature decreases monotonically with increasing interaction strength. On the other hand, the maximum of the thermal conductivity generally lies at smaller temperatures than the maximum of the charge conductivity and follows a nonmonotonic behavior , see Fig. 1. We thus found that charge and thermal conductivities are affected very differently by correlations and show a different temperature behavior.

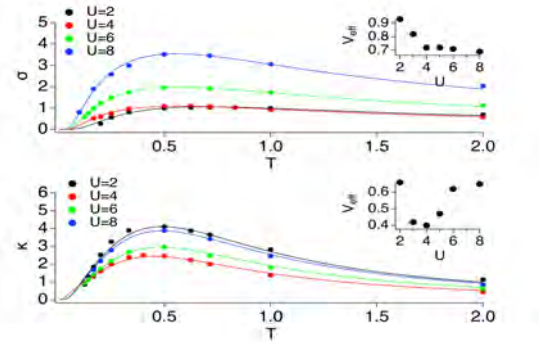

Figure 1: Charge conductivity and thermal conductivity for different interaction strengths. The insets show the effective gap in both conductivities.

In another work [5], we introduced a generalized quantum metric(GQM) on the Brillouin zone for correlated electron systems. This quantum metric is based on the optical conductivity that is written by single-particle Green's functions. We analytically proved that this definition is equivalent to the existing definition of the quantum metric in noninteracting systems and that it is positive semi-definite as necessary for a metric. Furthermore, we pointed out the relationship between the GQM and the Chern number in interacting systems. We then numerically confirmed these properties of the GQM in the Qi-Wu-Zhang model with and without interaction.

References

[1] H. Tsunetsugu, M. Sigrist, and K. Ueda
Rev. Mod. Phys. **69**, 809 (1997)

[2] Y. Sato, Z. Xiang, Y. Kasahara, T. Taniguchi, S. Kasahara, L. Chen, T. Asaba, C. Tinsman, H. Murayama, O. Tanaka, Y. Mizukami, T. Shibauchi, F. Iga, J. Singleton, Lu Li, and Y. Matsuda
Nature Physics **15**, 954 (2019)

[3] Y Sato, S Suetsugu, T Tominaga, Y Kasahara, S Kasahara, T Kobayashi, Shunsaku Kitagawa, K Ishida, R Peters, T Shibauchi, AH Nevidomskyy, L Qian, E Morosan, Y Matsuda, Nature comm. **13**, 394 (2022)

[4] R Peters and R Rausch, submitted to SciPost Physics

[5] T. Kashihara, Y. Michishita, and R. Peters
Phys. Rev. B **107**, 125116 (2023)

Electronic Structures of Nickel Dithiolene Complex-based Ambipolar Semiconductors

Tomoko FUJINO

Institute for Solid State Physics,

The University of Tokyo, Kashiwa-no-ha, Kashiwa, Chiba 277-8581

Air-stable single-component ambipolar organic semiconductors that conduct both holes and electrons are highly desired, but have been rarely realized. We synthesized neutral nickel bis(dithiolene) complexes (Fig. 1) that fulfill the stringent electronic requirements (i.e., shallow HOMO levels and deep LUMO levels) for air-stable ambipolar semiconductors [1]. The planar structures facilitated dense packing with effective intermolecular interactions. Remarkably, changing the methoxy substituents to ethoxy or propoxy groups led to a dramatic change in the packing mode from one-dimensional to herringbone-like, while maintaining effective intermolecular interactions, supported by the first-principles band calculation (OpenMX software). They are readily solution-processible to form active layers with well-defined and well-ordered structures in field-effect transistors. Devices based on these compounds exhibited efficient ambipolar characteristics, even after several months of exposure to air, whose carrier mobility are the top-class performances

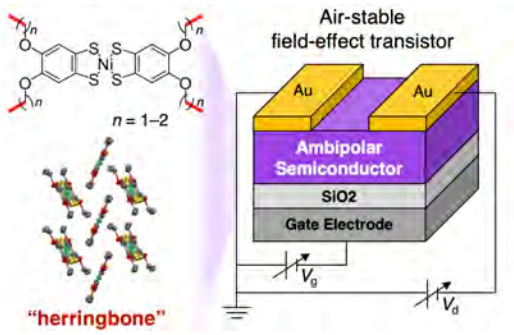

Fig. 1: Nickel dithiolene-based ambipolar semiconductors.

achieved for a single-component ambipolar semiconductor material driven in air.

References

[1] M. Ito, T. Fujino*, L. Zhang, S. Yokomori, T. Higashino, R. Makiura, K. J. Takeno, T. Ozaki, H. Mori*, J. Am. Chem. Soc. **145**, 2127 (2023), *Supplementary Cover*.

[2]. R. Kameyama, T. Fujino*, S. Dekura, S. Imajo, T. Miyamoto, H. Okamoto, H. Mori*, J. Mater. Chem. C **10**, 7531 (2022).

Inhomogeneous ground state due to kinetic energy effect in correlated electron systems

Takashi YANAGISAWA
National Institute of Advanced Industrial Science and Technology (AIST)
1-1-1 Umezono, Tsukuba 305-8568

1 Introduction

Our research is based on the optimized variational Monte Carlo method[1]. We use the optimized wave function improved by off-diagonal exponential operators such as $e^{-\lambda K}$ and $e^{-\alpha D}$ (K and D are the kinetic operator and the double occupancy operator, respectively), and the Gutzwiller-Jastrow wave function where the doublon-holon correlation is taken into account. We have investigated the ground-state phase diagram of the two-dimensional Hubbard model and the two-dimensional d-p model.

We performed parallel computation in Monte Carlo calculations. In order to reduce statistical errors, we carried out ~ 500 parallel calculations. Parallel computing is very important to reduce Monte Carlo statistical errors.

The many-body wave function is written in the form $\psi^{(1)} = \exp(-\lambda K)P_G\psi_0$, where K denotes the kinetic energy part (non-interacting part) of the Hamiltonian and $P_G = P_G(g)$ is the Gutzwiller operator to control the double occupancy with the variational parameter g. ψ_0 indicates a trial wave function which is usually taken as the Fermi sea, the BCS wave function or the state with some magnetic (or charge) orders. We can improve the wave function systematically by multiplying by operators P_G and $e^{-\lambda K}$ repeatedly. We can consider $\psi^{(2)} = \exp(-\lambda' K)P_G(g')\psi^{(1)}$ for different variational parameters λ' and g'. This wave function is a very good many-body wave function because the ground-state energy is lowered greatly and the ground-state energy is lower than those that are evaluated by any other wave functions. We also employ the Jastrow-type wave function which is written as $\psi_J = P_G P_Q P_J \psi_0$ where P_J indicates a nearest-neighbor number correlation operator and P_Q controls the nearest-neighbor doublon-holon correlation.

2 Ferromagnetic diagonal striped states in the Hubbard model

We have performed a variational Monte Carlo simulation to study the ground state of the two-dimensional Hubbard model on a square lattice. The energy gain of possible inhomogeneous electron states are computed as a function of U in the case where the hole density is $\delta = 1/8$ and next nearest-neighbor transfer $t'/t = -0.30$. The wave function is written as

$$\psi_{stripe} = P_{N_e} P_G P_J P_{DH} \psi_{MF}, \qquad (1)$$

where ψ_{MF} is the eigenstate of the following Hamiltonian

$$H_{MF} = -\sum_{ij\sigma} t_{ij} c^{\dagger}_{i\sigma} c_{j\sigma} + \frac{U}{2} \sum_{i\sigma} (\rho_i - \mathrm{sgn}(\sigma) m_i) n_{i\sigma}, \qquad (2)$$

with $\rho_i = \rho \cos(\mathbf{q}\cdot(\mathbf{r}_i - \mathbf{r}_0))$ and $m_i = m \sin(\mathbf{Q}\cdot(\mathbf{r}_i - \mathbf{r}_0))$. ρ and m are variational operators. Two incommensurate wave vectors $\mathbf{q}$ and $\mathbf{Q}$ characterize the charge and spin configurations, respectively. We set $\mathbf{q} = 2\mathbf{Q}$. $\mathbf{r}_0$ denotes the position of the domain boundary. P_{N_e} is the projection operator that extracts only the components with a fixed total number of electrons N_e. $P_{DH} = P_Q$ is the doublon-holon operator given by $P_{DH} = \prod_i (1 - (1-\eta)\prod_\tau d_i(1 - e_{i+\tau}))$ where $0 \le \eta 1$, $d_i = n_{i\uparrow} n_{i\downarrow}$, $e_i = (1 - n_{i\uparrow})(1 - n_{i\downarrow})$, and τ runs over all nearest-neighbor sites.

In Fig. 1, the energy difference per site between the normal and stripe states, $\Delta E = (E_{normal} - E_{stripe})/N_s$, of various stripe states at 1/8 doping, is shown as a function of U. The calculations were carried out on a 16×16 lattice. The results show that FM stripe states (open symbols) are more stable than AF stripe states (filled symbols) for $U/t \geq 16$.

The bond-centered ferromagnetic diagonal stripe state is stabilized in the strong coupling region with $U/t \geq 16$; this is due to the gain of both kinetic energy and on-site Coulomb interaction energy. The kinetic energy gain originates from the holon moving over the ferromagnetic domain and the gain of kinetic-exchange-interaction energy at the antiferromagnetic domain wall. For large U, the gain in the kinetic energy due to the transfer of holes on the ferromagnetic domain and that of the on-site Coulomb interaction energy exceed the loss of the kinetic exchange interaction energy, which leads to form an incommensurate electron state with the ferromagnetic domain.

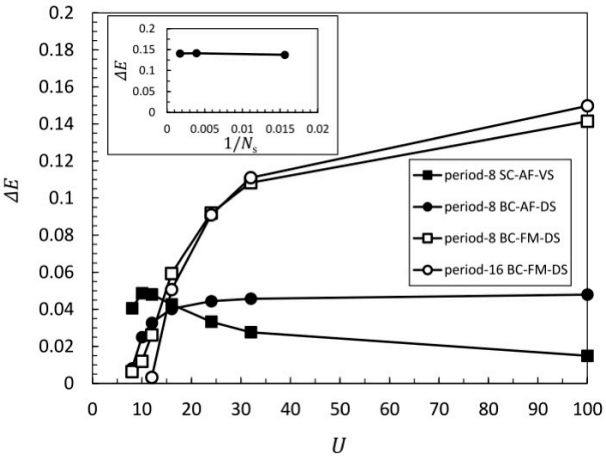

Figure 1: Optimized energy difference per site between the normal and striped states $\Delta E = (E_{normal} - E_{stripe})/N_s$ as a function of U. The data are from 16×16 lattices where electron number $N_e = 224$ (1/8 hole doping) and $t' = -0.30$. Filled squares indicate the period-8 bond-centered AF diagonal stripe state (8-period BC-FN-DS). Open squares (circles) denote the bond-centered FM diagonal stripe state (BC-FM-DS) with period-8 (period-16). Inset figure shows the system size dependence of the optimized energy difference per site for the period-8 BC-F-DS state with $U = 100$ at 1/8 hole doping. The error bars are smaller than the size of symbols.

3 Summary

We examined the ground state of the two-dimensional Hubbard model by using an advanced variational Monte Carlo method. In the strong coupling region where U is large, the kinetic energy gain is important in determining the ground state. In fact, the kinetic energy gain stabilizes superconducting state for the optimized BCS wave functions[3]. The kinetic term also plays an important role in striped states and the diagonal stripe becomes stable in this region due to the kinetic energy effect.

References

[1] T. Yanagisawa et al., J. Phys. Soc. Jpn. 67, 3867 (1998).
T. Yanagisawa, Phys. Rev. B75, 224503 (2007) (arXiv: 0707.1929).

[2] T. Yanagisawa, J. Phys. Soc. Jpn. 85, 114707 (2016).
T. Yanagisawa, J. Phys. Soc. Jpn. 88, 054702 (2019).
T. Yanagisawa, Condensed Matter 4, 57 (2019).

[3] T. Yanagisawa, Phys. Lett. A403, 127382 (2021).
T. Yanagisawa et al., EPL 134, 27004 (2021).

[4] M. Miyazaki, T. Yanagisawa, Phys. Lett. A448, 128276 (2022).

Unified description of cuprate high-temperature superconductors using multiband models

Hiroshi WATANABE
Research Organization of Science and Technology, Ritsumeikan University
1-1-1 Noji-Higashi, Kusatsu-shi, Shiga 525-8577

Understanding the various competing phases in cuprate high-temperature superconductors is a long-standing challenging problem. Although we have not yet reached a unified understanding of their properties, recent studies have shown that orbital degrees of freedom, both Cu e_g and O p orbitals, are key ingredient. Here we investigate the four-band *d-p* model that explicitly includes the $d_{x^2-y^2}$, d_{z^2}, p_x, and p_y orbitals [1, 2]. We construct the tight-binding energy bands for La_2CuO_4 and $HgBa_2CuO_4$ systems based on the first-principles calculation and examine the effect of Coulomb interactions with the variational Monte Carlo (VMC) method. The Gutzwiller-Jastrow type wave function is used for the VMC trial wave function. The system size for the calculation is N=24×24=576 unit cells (and thus 576×4=2304 orbitals in total) and the computation has been done mainly with the system B of the ISSP Supercomputer Center. We have compared the variational energies of various competing phases including superconductivity, ferro- and antiferromagnetic phases, and stripe phases with different periodicities to determine the ground state phase diagram for the hole doping rate x. We have also calculated physical quantities such as superconducting correlation functions, charge- and spin correlation functions, and local magnetic moments.

In Fig. 1, we show the hole density of the d_{z^2} orbital $n_{d_{z^2}}$ as a function of x for several values of Hund's coupling J/U_d at U_d/t_1=8, along with the superconducting correlation function P^{dd}. In La_2CuO_4, $n_{d_{z^2}}$ increases with x and is strongly enhanced by the Hund's coupling. This is because the system tends to increase $n_{d_{z^2}}$ to obtain the energy gain from the Hund's coupling. Since $n_{d_{z^2}}$ works destructively for superconductivity due to its localized character [1, 2], P^{dd} is suppressed by the Hund's coupling. On the other hand, in $HgBa_2CuO_4$, such an increase of $n_{d_{z^2}}$ and a suppression of P_{dd} are not so pronounced even for relatively large Hund's coupling. It results from the lower site energy $\varepsilon_{d_{z^2}}$ in the $HgBa_2CuO_4$ system that makes the d_{z^2} orbital almost inactive. The difference between two systems are well described in our four-band *d-p* model.

References

[1] H. Watanabe et al., Phys. Rev. Research **3**, 033157 (2021).

[2] H. Watanabe et al., J. Phys.: Condens. Matter **35**, 195601 (2023).

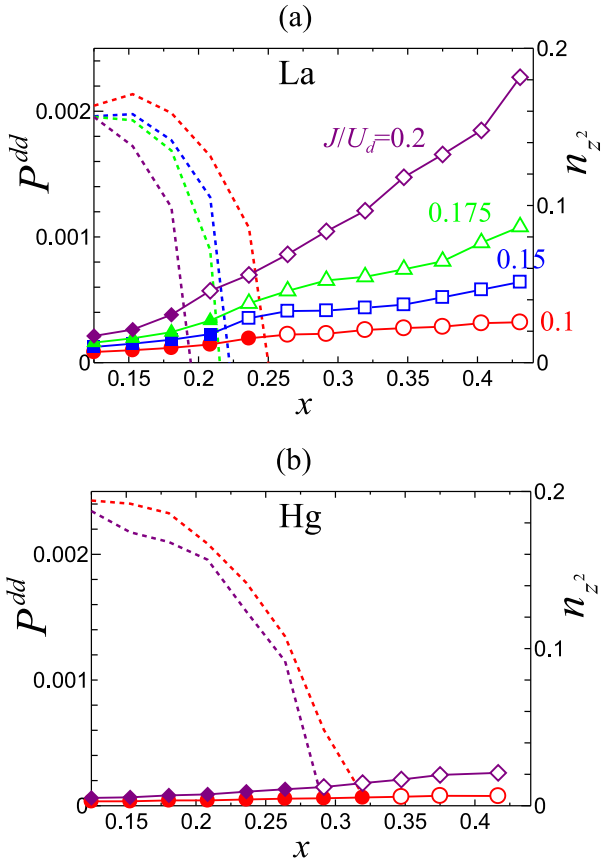

Figure 1: The hole doping rate x dependence of the hole density of the d_{z^2} orbital $n_{d_{z^2}}$ (solid lines with symbols) and superconducting correlation function P^{dd} (dotted lines) for (a) La_2CuO_4 and (b) $HgBa_2CuO_4$, respectively [2]. Solid (open) symbols correspond to the superconducting (paramagnetic) phase.

Gap opening mechanism for organic Dirac electron systems α-(BEDT-TTF)$_2$I$_3$ and α-(BEDT-TSeF)$_2$I$_3$

Akito Kobayashi[a], Daigo Ohki[a], Kazuyoshi Yoshimi[b] and Takahiro Misawa[b]
[a]*Department of Physics, Nagoya University, Nagoya 464-8602*
[b]Institute for Solid State Physics, University of Tokyo, Chiba 277-8581, Japan

In the Dirac electron system of organic conductors, phase transitions due to spontaneous symmetry breaking due to electron-electron interactions have been observed, and this has attracted interest as a research target for correlated Dirac electron systems. In α-(BEDT-TTF)$_2$I$_3$, it has been reported that the horizontal stripe charge order with inversion symmetry breaking induces a gap for massless Dirac electrons [1]. A related compound α-(BEDT-TSeF)$_2$I$_3$, on the other hand, has a distinctly different insulating state from α-(BEDT-TTF)$_2$I$_3$2 [2]. The gap opening mechanism has not yet been fully clarified.

To determine the origin of the differences in the gap opening mechanisms in α-(BEDT-TTF)$_2$I$_3$ and α-(BEDT-TSeF)$_2$I$_3$, we derive ab initio low-energy effective Hamiltonians and solve this using the many-variable variational Monte Carlo method (mVMC) [3]. It is found that an insulating state with the horizontal stripe charge order appears in α-(BEDT-TTF)$_2$I$_3$, which is consistent with experiments and previous studies as shown in Fig. 1(a). However, in α-(BEDT-TSeF)$_2$I$_3$, we find that an insulating state without any explicit symmetry breaking is realized. Because of the frustration in the inter-chain magnetic interactions, a dimensional reduction of the spin correlations occurs. As a result, one-dimensional spin correlations develop in α-(BEDT-TSeF)$_2$I$_3$ as shown in Fig. 1(b). This result suggests that the one-dimensional spin correlation induces the gap in α-(BEDT-TSeF)$_2$I$_3$, as in the one-dimensional Hubbard model [4]. Thus we found that α-(BEDT-TSeF)$_2$I$_3$ hosts massive Dirac electrons without symmetry breaking via dimensional reduction [5].

References

[1] H. Seo, J. Phys. Soc. Jpn. **69**, 805 (2000).

[2] S. Kitou et al., Phys. Rev. B **103**, 035135 (2021).

[3] T. Misawa et al., Phys. Commun. **235**, 447 (2019).

[4] E. H. Lieb and F. Y. Wu, Phys. Rev. Lett. **20**, 1445 (1968).

[5] D. Ohki et al., Phys. Rev. B **107**, L041108 (2023)

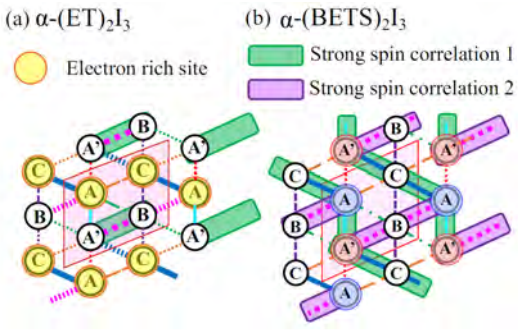

Figure 1: Schematic diagrams of α-type organic conductors for (a) α-(BEDT-TTF)$_2$I$_3$ and (b) α-(BEDT-TSeF)$_2$I$_3$.

Theoretical study of thermoelectric properties in Heusler compounds: A weak-coupling approach

Kazutaka NISHIGUCHI
Graduate School of System Informatics, Kobe University
Rokkodai-Cho, Nada-Ku, Kobe 657-8501

Heusler compound Fe_2VAl

Heusler compound Fe_2VAl is a promising thermoelectric material, which exhibits large power factor $P = \sigma S^2$ with σ and S being the electrical conductivity and Seebeck coefficient, respectively. On the other hand, the thermal the dimensionless figure of merit $ZT = \sigma S^2 T/\kappa$ is not so large yet reflecting its large thermal conductivity κ. Recently, it is experimentally observed in doped Fe_2VAl (i.e., $Fe_2V_{0.9}Cr_{0.1}Al_{0.9}Si_{0.1}$ and $Fe_{2.2}V_{0.8}Al_{1-y}Si_y$) as a weekly ferromagnetic material that ferromagnetic fluctuations enhance the thermoelectric properties such as S and P around the Curie temperature ($T_c = 285$ K). [1] It is not only a desirable property for practical use in realistic (room) temperatures, but also a fundamental and intriguing quantum phenomena where quantum fluctuations and thermoelectric effects are entangled by electron correlations.

Motivated above, we have studied electronic properties of Fe_2VAl using first-principles calculations based on the density functional theory (DFT) within the generalized gradient approximation (GGA). We performed DFT calculations with the Perdew–Burke–Ernzerhof (PBE) exchange-correlation functional and the projector augmented wave (PAW) method using The Vienna Ab Initio Simulation Package (VASP) [2] and Quantum ESPRESSO package. [3]

Using the maximally localized Wannier functions, we could construct a low-energy effective model from the first- principles bands around the Fermi level. The effective model is composed of the Fe-3d, V-3d, and Al-2sp3 Wannier orbitals, namely, 19 orbitals. The DFT b and structure and Wannier orbitals are shown in Fig. 1.

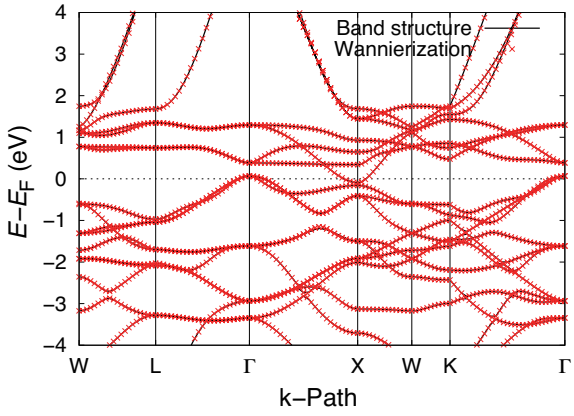

Figure 1: DFT band structure and Wannierization of Fe_2VAl.

Planar Defect in Layered Perovskite Photocatalyst $Y_2Ti_2O_5S_2$

Layered perovskite $Y_2Ti_2O_5S_2$ (YTOS) is a strong candidate for semiconductor photocatalysts suitable for overall water splitting under visible light. On the other hand, structural defects during synthesis should be controlled to improve photocatalytic performance similar to other photocatalysts [5]. Very recently, transmission electron microscopy (TEM) have revealed extremely large planar defects com-

posed of S–Mg–S layers in YTOS synthesized using the flux method.

We investigated the planar defect structure and electronic structure using first-principles calculations based on the density functional theory (DFT) [6]. The DFT calculations were performed within the PBE+U functional using PAW method, as implemented in VASP [2]. Here we set $U = 7.5$ eV for the $3d$ orbitals at the Ti sites to reproduce the experimental band gap, 1.9–2.0 eV [5].

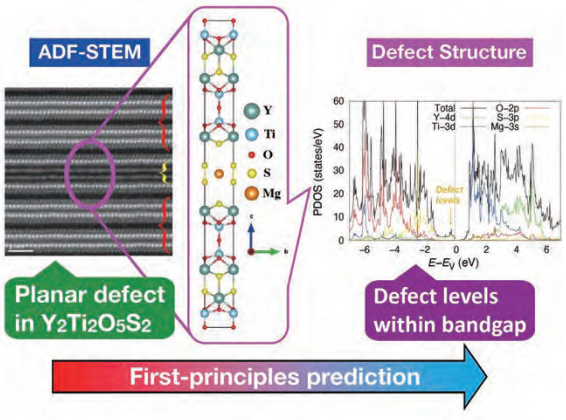

Figure 2: Planar defect in YTOS is investigated by electron microscopy and first-principles calculations.

We have microscopically determined the planar defect structure using the structural optimization, where a Mg atom is centered in the *ab*-square intersecting the defect S layers. The obtained defect structure is consistent with the ADF–STEM image. To understand the electronic structures, we have investigated the projected density of states (PDOS) and band structure, which shows that the defect bands appear within the original band gap. It is expected that such defect bands considerably increase the electron–hole recombination rate, enhancing the interband transitions of the defect valence and/or defect conduction bands via radiative or nonradiative transitions, which is an undesirable factor for the efficiency of the overall water splitting of YTOS. To consider the stability of the planar defect, we have finally evaluated the defect formation energy (E_{f}). The chemical potentials μ_i were determined by the phase diagram of the relevant compounds in the synthesis of YTOS. The evaluation of the formation energy suggests that E_{f} increases with decreasing μ_{S} and/or μ_{Mg}. Therefore, the optimum conditions for the S and Mg environments must be optimized for the synthesis of YTOS, which suppresses the formation of the planar defect.

References

[1] N. Tsujii, A. Nishide, J. Hayakawa, and T. Mori: Sci. Adv. **5**, eaat5935 (2019).

[2] G. Kresse *et. al.*: Phys. Rev. B **47**, 558 (1993); Phys. Rev. B **49**, 14251 (1994); Computational Materials Science **6** (1996) 15–50; Phys. Rev. B **54**, 11169 (1996).

[3] P. Giannozzi *et. al.*: J. Phys.: Condens. Matter **21**, 395502 (2009) ; J. Phys.: Condens. Matter **29**, 465901 (2017) ; J. Chem. Phys. **152**, 154105 (2020).

[4] I. Souza, N. Marzari, and D. Vanderbilt: Phys. Rev. B **65**, 035109 (2001) ; A. A. Mostofi *et. al.*: Comput. Phys. Commun. **178** (2008) 685–699; A. A. Mostofi *et. al.*: Comput. Phys. Commun. **185** (2014) 2309–2310; G. Pizzi *et. al.*: J. Phys.: Condens. Matter **32**, 165902 (2020).

[5] Q. Wang *et. al.*: Nat. Mater. **18**, 827 (2019) ; Z. Pan *et. al.*: Res. Chem. Intermed. **47**, 225 (2021).

[6] M. Nakabayashi, K. Nishiguchi, X. Liang, T. Hisatomi, T. Takata, T. Tsuchimochi, N. Shibata, K. Domen, and S. L. Tenno: J. Phys. Chem. C 2023, **127**, 7887–7893 (M.N. and K.N. contributed equally to this work).

Nonequilibrium dynamics induced by optical driving

Atsushi ONO
Department of Physics, Tohoku University,
Sendai 980-8578

The ultrafast dynamics of electrons in solids have been actively studied in recent years. For example, high-harmonic generation, which yields harmonics several tens of times higher than the incident light, has attracted interest as a phenomenon for generating broadband ultrashort pulses, while its mechanism involves nonperturbative and nonlinear processes, requiring accurate numerical calculations to understand such intriguing ultrafast phenomena.

This year, we focused mainly on the nonequilibrium dynamics of photocarriers excited by a resonant optical pulse and then driven by an optical electric-field pulse. We considered theoretical models of band insulators, Mott insulators, and charge-ordered insulators and calculated the real-time evolution using exact diagonalization and infinite time-evolving block decimation methods on the ISSP supercomputer system.

We found that in a band insulator, the optical driving pulse changes the relative velocity of photocarriers, resulting in carrier recombination and the generation of echoes of the excitation pulse. A detailed analysis revealed that the frequency of the echo pulses reflects the energy dispersion relation of the photocarriers. Furthermore, we performed numerical calculations for Mott insulators described by the Hubbard model and found that echo pulses can also be generated despite the breakdown of the single-electron picture, and their frequencies coincide with the energy of the doublon–holon pairs obtained from the Bethe ansatz, as shown in Fig. 1. We found that this echo phenomenon, termed an energy-band echo, can be observed in various insulators and reflects the dispersion relation of itinerant quasiparticles.

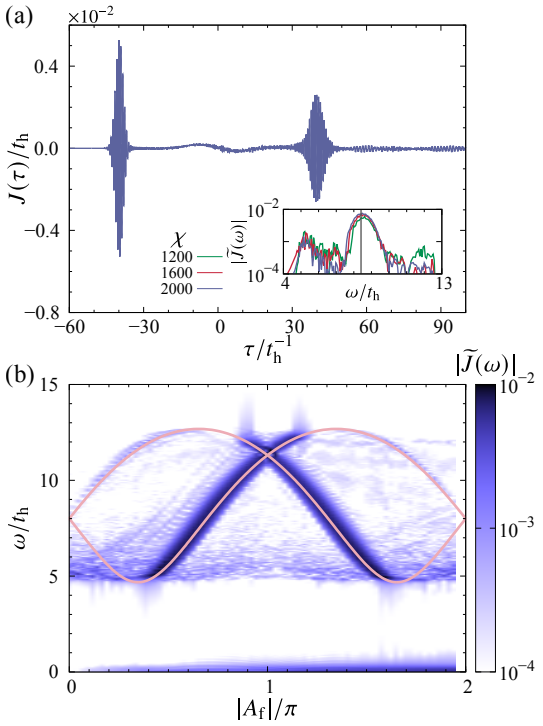

Figure 1: Echoes in a one-dimensional Mott insulator [1]. (a) Time profile of the electric current. The inset shows the Fourier spectrum. (b) Fourier spectral map of the electric current. The red curves show the dispersion relations of the doublon–holon pair. A_f is proportional to the amplitude of the optical driving pulse.

References

[1] S. Imai, A. Ono, and S. Ishihara, Phys. Rev. Research **4**, 043155 (2022).

3.4 Cooperative Phenomena in Complex Macroscopic Systems

Development of new tensor-network-based methods and study of critical phenomena in quantum/classical magnets

Naoki KAWASHIMA

Institute for Solid State Physics,

The University of Tokyo, Kashiwa-no-ha, Kashiwa, Chiba 277-8581

Tensor-network is now widely recognized as a new framework/language for developing numerical methods for otherwise intractable many-body problems and describing the structure of the problem from the information-scientific viewpoint. In SY2022, we developed a few new numerical methods for studying quantum spin system in two spatial dimensions and classical statistical-mechanical models based on tensor-network representation. We then applied them to some typical examples.

In [1], we studied the square-lattice S=2 Heisenberg model with cubic anisotropy. The magnetic anisotropy is quite ubiquitous --- it can be found in virtually every magnet though in many cases its effect is very weak. However, the true nature of critical phenomena can be dramatically altered by such a weak symmetry breaking field. In spite of the universal nature of the anisotropy, it is hard to incorporate in the numerical calculation in an accurate way. We studied the simplest lattice spin model for the two-dimensional quantum ferromagnet with cubic anisotropy by means of mean-field analysis and tensor network calculation. It turned out that while the mean-field approximation produces a qualitatively correct phase diagram, the 2D iPEPS calculation yielded a quantitatively accurate one. We also observed that iPEPS calculation became slower in pinning down the direction of the magnetic easy axes as one approaches the phase boundary --- an indication of the ``easy-axis softening". In fact, the low-energy effective theory in the reduced Hilbert space restricted in the lower atomic levels indicate the asymptotic U(1) symmetry on the phase boundary, which is consistent with the above-mentioned softening phenomena. From these results together with renormalization group considerations, we concluded that the emergence of the continuous symmetry becomes exact on the phase boundary. Therefore, this criticality belongs to the same universality class as the 3D classical XY model. The iPEPS calculation of the correlation functions and other quantities support this interpretation. Thus, our iPEPS calculation provided the first systematic and correct analysis, beyond the mean-field approximation, of the phase boundary and the critical phenomena of this simple quantum spin system.

In [2], we studied the phase transitions of the two-dimensional q-state Potts model. While the universality class of the model is well established, the scaling function of the Binder parameter had not been accurately obtained before. In particular, we focused on the non-monotonic behavior of the Binder parameter. We discovered that for q=3 its non-monotonic behavior as a function of the temperature is not the non-universal properties. Instead it reflects a bump in the scaling function. Therefore, the non-monotonicity is the universal property of the Potts model.

In [3], we developed an open source software called TeNeS. It is a program package for obtaining ground states of two-dimensional quantum lattice problems. It is based on the corner transfer matrix renormalization group (CTMRG) method. In principle, it is designed for an arbitrary two-body Hamiltonian and an arbitrary two-dimensional lattice can be dealt with by deforming it to a non-uniform square lattice, though the numerical efficiency of such a treatment strongly depends on the original problem.

References

[1] Wei-Lin Tu, Xinliang Lyu, S. R. Ghazanfari, Huan-Kuang Wu, Hyun-Yong Lee, Naoki Kawashima: arXiv:2204.01197.

[2] Hiroshi Watanabe, Yuichi Motoyama, Satoshi Morita, and Naoki Kawashima, Progress of theoretical and experimental physics 2023, 033A02 (1-19) (2023).

[3] Yuichi Motoyama, Tsuyoshi Okubo, Kazuyoshi Yoshimi, Satoshi Morita, Takeo Kato, Naoki Kawashima: Computational Physics Communications 279 108437 (1-15) (2022).

Large-scale Molecular Simulation of Soft Materials using All-Atom and Coarse-Grained Models

Wataru SHINODA

Research Institute for Interdisciplinary Science,

Okayama University, 3-1-1 Tsushima-naka, Okayama 700-8530

We illustrate here a simulation study on action of antimicrobial peptide (AMP), melittin, on lipid membranes as an example of our research works using massive parallel computer simulations. In this study, we conducted a series of coarse-grained molecular dynamics (CG-MD) simulations to investigate the complicated actions of melittin in lipid membrane systems. In a membrane system with a lower peptide/lipid (P/L) ratio than the threshold value for melittin pore formation, no pores were found during the simulation, although the peptides formed dimers on the membrane. At a higher P/L ratio than the threshold value, we successfully observed pore formation caused by the insertion of melittin peptides through their N-terminals. During the pore formation, it was found that membrane curvature was locally induced in the vicinity of the peptide aggregate. These findings were consistent with experimental observations and suggested melittin action. Additionally, we performed CG-MD simulations for large-scale membrane systems at high peptide concentrations twice. Interestingly, two different membrane pore formation processes were observed in the systems with the same number of peptides in different initial configurations. One system showed lipid extraction and pore formation by melittin peptides without inducing membrane curvature, while another showed large pores in a significantly curved membrane. (Figure 1) This result indicated that, depending on the melittin arrangements on the membrane at high melittin concentration, pores were formed either by relaxation of bending energy due to large curvature or by the peptide insertion into the thinned membrane due to lipid extraction.

Through this study, we have gained some insight into the behavior of melittin, an AMP, on lipid membranes. The membrane pore formation process of antimicrobial activity cannot be induced by a single melittin peptide, even at P/L ratios above the concentration required for pore formation. This was energetically evidenced by the free energy profile of a single melittin insertion into the membrane. These results were also supported by 5 μs CG-MD simulations. Pore formation is always induced by cooperative actions such as induction of melittin membrane curvature and extraction of lipids from the membrane. These two events are the key factors

that trigger pore formation. Cooperative action occurs when aggregates of melittin composed of at least four or more peptides are formed on the membrane. Although aggregation of cationic peptides appears to be disadvantageous, the screening effects of electrostatic interactions indicate that aggregation may occur on the membrane, as in the CG-MD simulations. However, spontaneous assembly of melittin peptides does not necessarily result in the formation of pores because the free energy barrier required for pore formation is small. The findings of this study will contribute to the development of antimicrobial agents that mimic AMP against viral and bacterial infection. We hope that the CG force field (pSPICA) developed in this research will help us to better understand the activities of AMP.

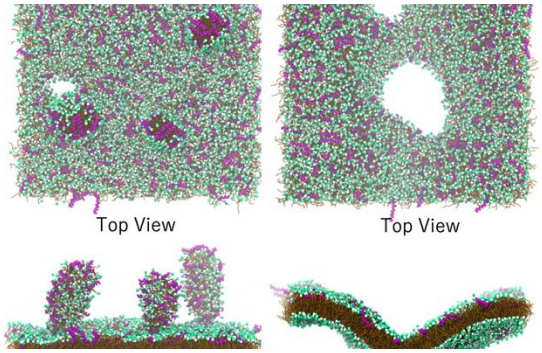

Figure 1: Observed membrane pore formation processes in a large membrane patch at P/L=5/128.

References

[1] Y. Miyazaki and W. Shinoda, Biochim. Biophys. Acta - Biomembranes, **1864**, 183955 (2022).

Crossover of fluctuating surfactant adsorbed interface

Shunta Kikuchi and Hiroshi WATANABE
Department of Applied Physics and Physico-Informatics, Keio University
Yokohama, Kanagawa 223-8522, Japan

We investigated the mechanical properties of a surfactant adsorbed at the interface between two liquids. The restoring force of the membrane is largely due to interfacial tension and elasticity. These are explained by the elastic energy model by Helfrich with the following equation [1].

$$|h(q)|^2 = \frac{k_B T}{\gamma q^2 + \kappa q^4},$$

where q is the wavenumber, $h(q)$ is the Fourier component of the fluctuation of the membrane, γ is the surface tension, and κ is the bending rigidity. The biomembrane is composed of a phospholipid bilayer, and its restoring force is thought to be either interfacial tension or elasticity, but the observed fluctuations are dominated by elasticity, with no effect of interfacial tension. We therefore investigated fluctuations in monolayer membranes to determine how the effects of interfacial tension and elasticity contribute to the resilience of the membranes.

We represented two kinds of liquids by preparing two kinds of atoms. The same type of atoms interacted with the Lennard-Jones potential, and the different type of atoms interacted with the WCA potential to reproduce a system in which the two liquids are phase-separated. We modeled the surfactant as a diatomic molecule and prepared an initial state in which the surfactant is adsorbed at the interface. Then, molecular dynamics was used for time evolution to observe the fluctuations at the surfactant-adsorbed interface. LAMMPS was used for time evolution.

Our investigation revealed a significant dependence of the interfacial tension within the system on the surfactant's natural length. Modifying the natural length could alter the interfacial tension from finite to nearly zero while maintaining the system's temperature constant. The findings demonstrate that the influence of q^2 is discernible in the film fluctuations when large values characterize interfacial tension. Conversely, a transition from q^2 to q^4 becomes evident in the Fourier spectrum when interfacial tension approaches near-zero values [2]. This crossover implies that when surfactant molecules are sufficiently adsorbed at the interface, and the interfacial tension is nearly zero, the bending stiffness dominates in the restoring force. In contrast, it plays the dominant role when the interfacial tension possesses finite values.

References

[1] W. Helfrich, Z. Natuforsch **C28**, 693 (1973).

[2] K. Shunta and H. Watanabe, J. Chem. Phys. **158**, 124901 (2023).

Correlation between the structure of charged phospholipid bilayer membrane and ion distribution

Yuji HIGUCHI
Research Institute for Information Technology, Kyushu University
Motooka Nishi-ku, Fukuoka 819-0395

We have studied soft matter by molecular simulations and revealed the self-assembly processes of amphiphilic molecules [1], water dynamics on lipid bulayer [2], and fracture processes of semicrystalline polymers [3]. This year, we studied the ion distribution on a charged surface as a model of biomembranes by coarse-grained molecular dynamics simulation using GROMACS [4] on systems B and C.

The electrostatics in soft matter systems is relevant to its self-assembly structures and dynamics, and therefore, essential to be understood. In particular, ion distributions on a charged surface as a model of biomembranes containing charged phospholipids have been extensively studied. Although theoretical studies have revealed the ion distributions perpendicular to the homogeneous charged surface, the ion distributions parallel to the heterogeneous charged surface and their dynamics are still unclear. Our coarse-grained molecular dynamics simulations show the dynamical changes of ion distribution profiles on the lipid membrane during phase separation. Figure 1 shows a typical snapshot of phase separation of neutral and negatively charged lipids with a NaCl concentration of 100 mM, and the cation distribution near the lipid membrane at 2.0 μs. The cations following negatively charged lipids in microsecond order indicate rapid redistribution of cations parallel to the membrane. We compare the simulation results with the modified Poisson–Boltzmann theory and reveal the importance of the ion-ion interactions in an aqueous solution. These results will contribute to the future development of the theory.

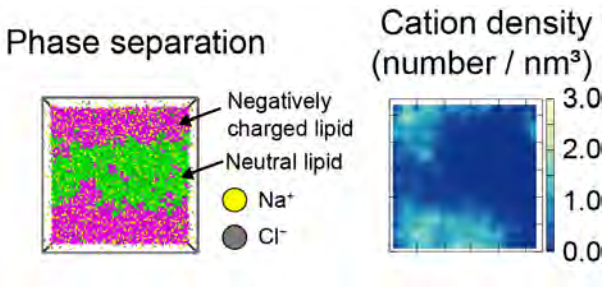

Figure 1: Phase separation and cation distribution of the charged and neutral lipids mixture at 2.0 μs with a NaCl concentration of 100 mM. The snapshot of the top view of the membrane and cation density (number/nm^3) near the surface.

References

[1] R. Wakabayashi, R. Imatani, M. Katsuya, Y. Higuchi, H. Noguchi, N. Kamiya, and M. Goto: Chem. Commun. **58** (2022) 585.

[2] Y. Higuchi, Y. Asano, T. Kuwahara, and M. Hishida: Langmuir **37** (2021) 5329.

[3] Y. Higuchi: Phys. Rev. E **103** (2021) 042502.

[4] M. J. Abraham, T. Murtola, R. Schulz, S. Páll, J. C. Smith, B. Hess, and E. Lindahl, SoftwareX **1-2** (2015) 19.

Constructing a Dataset of Thermal and Dielectric Properties of Polymers Using Molecular Dynamics Simulations

Yuta YOSHIMOTO

Department of Mechanical Engineering,

The University of Tokyo, 7-3-1 Hongo, Bunkyo-ku, Tokyo 113-8656

We have constructed a dataset of thermal and frequency-dependent dielectric properties of polymers using high-throughput molecular dynamics (MD) simulations. More than 500 polymers are constructed from the repeating units of previously synthesized polymers [1,2] and virtual polymers in the PI1M database [3] using RadonPy [4], an open-source Python library. As shown in Fig. 1(a), the MD-calculated values of coefficients of linear thermal expansion (CLTEs) show reasonable agreement with the available experimental values. Additionally, as shown in Fig. 1(b) and (c), the MD-calculated dielectric constants also exhibit reasonable agreement with the experimental counterparts at 10 MHz and 1 GHz, validating our MD simulation protocol. Currently, virtual polymers in the PI1M database have been screened using machine learning-aided prediction models of CLTEs and dielectric constants to further extend the dataset.

References

[1] L. Chen et al.: npj Comput. Mater. **6** (2020) 61.

[2] S. Otsuka et al.: Int. Conf. on Emerging Intelligent Data and Web Technologies (2011) 22.

[3] R. Ma and T. Luo: J. Chem. Inf. Model. **60** (2020) 4684.

[4] Y. Hayashi et al.: npj Comput. Mater. **8** (2022) 222.

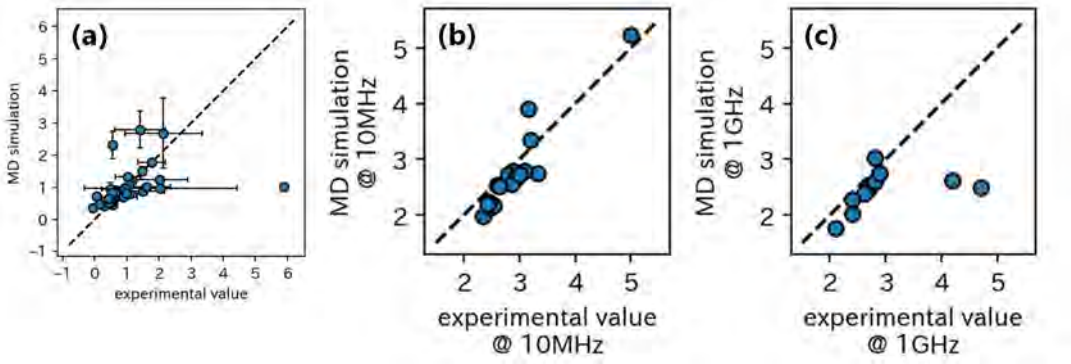

Fig. 1: Comparison of the MD-calculated values of coefficients of linear thermal expansion (a), dielectric constants at 10 MHz (b) and 1 GHz (c) with the experimental counterparts [1,2].

Critical Phenomena of Active Brownian Particles with Uniaxial Self-propulsion

Hiroyoshi Nakano
Institute for Solid State Physics, University of Tokyo
Kashiwa-no-ha, Kashiwa, Chiba 277-8581

Active matter is a distinct class of nonequilibrium many-body systems that show unique collective phenomena such as flocking, motility-induced phase separation, giant number fluctuations and active turbulence. Many experimental realizations have been reported, ranging from swimming bacteria to synthetic colloidal particles, which motivate extensive investigations of properties of active matter.

Active Brownian particles (ABPs) are one of the minimal model modeled on biologial motions [1]. The motion of the particles basically consists of three steps: (i) translational random walk, (ii) random rotation of the particle's orientation, and (iii) propelling movement along the particle's orientation. The ABPs undergo a phase separation even when the particles interact with each other via only excluded volume interactions. Its origin is sought for the self-propulsion. This type of phase separation is called motility-induced phase separation (MIPS) [2]. The speciality of the origin of the MIPS motivates the studies of whether the macroscopic behaviors of the MIPS are different from those of the phase separation induced by the intrinsic attractive force, such as the equilibrium liquid-gas transition.

Related to this problem, we focused on the ABPs with uniaxial self-propulsion [3]. This model is the ABPs that are refined so that the particles prefer to be oriented along a certain axis. We particularly examined the properties of critical phenomena by using the finite-size scaling method.

The result is summarized in Fig. 1. Figure 1 (a) presents typical snapshot of the phase-separated state, and Fig. 1 (b) presents the phase diagram. The phase-separated state appears at the large self-propulsion force F_0. The critical point is located at the triangle point in Fig. 1 (b). The binder ratios U for four system sizes are plotted in Fig. 1 (c), which shows that the binder ratios U cross at the unique point. It implies that this model undergoes the second-order phase transition. The critical exponent is estimated as

$$\beta = 0.35(4) \ , \ \nu_x = 0.65(6). \tag{1}$$

Surprisingly, this result is quite close to the critical exponent of the three-dimensional Ising model even though this model is in two-dimensions.

Our sophisticated simulations demonstrated that this result can be understood from the similarities between the ABPs with uniaxial self-propulsion and randomly driven lattice gas (RDLG). For the RDLG, the particles are subjected to the random driving forces along one axis. It is well known that the universality class of the RDLG is the same as that of the two-dimensional Ising model with the dipolar long-range interaction, which is close to that of the three-dimensional Ising model. Our simulations showed that the ABPs with uniaxial self-propulsion exhibits the same macroscopic behaviors as the RDLG in the homogeneous state and the phase-separated state. Based on this result, we consider that the critical point

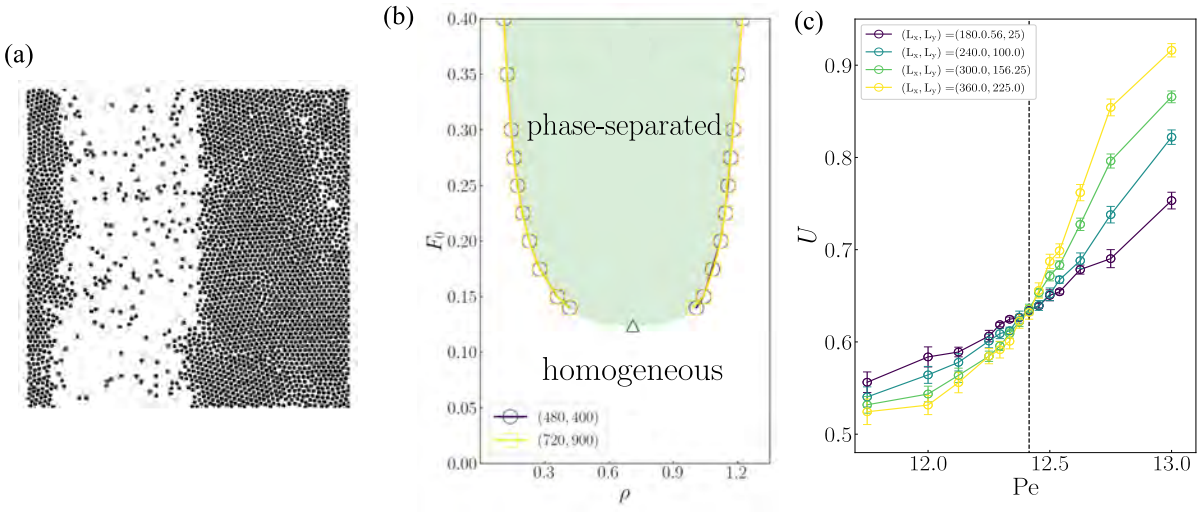

Figure 1: (a) Typical snapshot of phase-separated state. (b) Phase diagram of the ABPs with uniaxial self-propulsion. (c) Binder ratios for four system sizes.

of the ABPs with uniaxial self-propulsion belongs to the same universality class as that of the RDLG [4].

In summary, we performed the simulations of the two-dimensional ABPs with uniaxial self-propulsion. We showed that this model undergoes the MIPS and that the critical behaviors is quite close to the three-dimensional Ising model. Our result suggested that the critical points presumably belongs to the same universality class as that of the RDLG.

References

[1] Y. Fily and M. C. Marchetti: Phys. Rev. Let. **108**, 235702 (2012).

[2] M. E. Cates and J. Tailleur: Annu. Rev. Condens. Matter Phys. **6**, 219-244 (2015).

[3] H. Nakano, and K. Adach: in preparation.

[4] K. Adachi, K. Takasan, and K. Kawaguchi: Phys. Rev. Research **4** 013194 (2022).

Numerical Study on Novel Spin Nematic Phase

Tôru SAKAI[1,2], Hiroki NAKANO[1], Rito FURUCHI[1],
and Tokuro SHIMOKAWA[3]
[1]*Graduate School of Science, University of Hyogo,*
Kouto, Kamigori, Hyogo 678-1297, Japan
[2]*National Institute for Quantum Science and Technology,*
SPring-8, Kouto, Sayo, Hyogo 679-5148, Japan
[3]*Theory of Quantum Matter Unit,*
Okinawa Institute of Science and Technology Graduate University,
Onna-son, Okinawa 904-0495, Japan

1 Field-induced spin nematic Tomonaga-Luttinger liquid of the S=1/2 spin ladder system with anisotropic ferromagnetic rung interaction

The $S = 1/2$ quantum spin ladder system with the anisotropic ferromagnetic exchange interaction on the rung under magnetic field is investigated using the numerical diagonalization and the density matrix renormalization group (DMRG) analyses[1]. It is found that the nematic-spin-correlation-dominant Tomonaga-Luttinger liquid appears in some high magnetic field. It is included in the Tomonaga-Luttinger liquid phase where the two-magnon bound state is realized. For some suitable parameters, after the field-induced phase transition from this two-magnon Tomonaga-Luttinger liquid phase to the single-magnon Tomonaga-Luttinger liquid one, the re-entrant transition to the two-magnon phase would possibly occur, as the magnetization curves by DMRG indicate. Several phase diagrams with respect to the coupling anisotropy, the magnetization and the magnetic field are presented. The present result is a proposal of the candidate system which exhibits the spin nematic phase without the biquadratic interaction or the frustration. This mechanism also had been prposed for $S = 1$ antiferromagnetic chain with the single-ion anisotropy[2].

2 Spin Nematic Liquid of the S=1/2 Distorted Diamond Spin Chain in Magnetic Field

The spin nematic order has attracted a lot of interest in the field of magnetism. It is a kind of multipole order of spins. The previous theoretical and numerical studies[3] predicted that the spin nematic order would be induced by the frustration of the ferromagnetic and antiferromagnetic exchange interactions, or the biquadratic interaction. The spin nematic order is characterized by the long-range four spin correlation and the two-magnon bound state. The previous numerical diagonalization and the finite-size scaling study had indicated that a two-magnon bound state can occur in the S=1 antiferromagnetic chain with the single-ion anisotropy under magnetic field[4].The recent analysis of the critical exponents of the spin correlation functions[5] suggested that this two-magnon bound state includes the spin nematic liquid phase, as well as the spin density wave (SDW) liquid one. The phase di-

agrams with respect to the anisotropy and the magnetization were obtained by the numerical diagonalization of finite size clusters. In the present study[6], the S=1/2 distorted diamond spin chain is investigated using the numerical diagonalization of finite-size clusters. This system is a typical frustrated system. The recently discovered candidate material of this system, $K_3Cu_3AlO_2(SO_4)_4$ called alumoklyuchevskite[7], includes the ferromagnetic interactions. Thus we investigated the distorted diamond chain with the ferromagnetic interactions, as well as the coupling anisotropy. As a result we found that a two-magnon bound state appears in the magnetization process. We also discus about the spin nematic liquid behaviors.

References

[1] T. Sakai, R. Nakanishi, T. Yamada, R. Furuchi, H. Nakano, H. Kaneyasu, K. Okamoto and T. Tonegawa, Phys. Rev. B 106 (2022) 064433.

[2] T. Sakai, H. Nakano, R. Furuchi and K. Okamoto, J. Phys.: Conf. Ser. 2164 (2022) 012030.

[3] T. Hikihara et al., Phys. Rev. B 78 (2008) 144404.

[4] T. Sakai, Phys. Rev. B 58 (1998) 6268.

[5] T. Sakai, H. Nakano, K. Okamoto and R. Furuchi, J. Phys.: Conf. Ser. 2164 (2022) 012030.

[6] T. Sakai, H. Nakano, R. Fruchi and K. Okamoto, AIP Advances 13 (2023) 015313.

[7] M. Fujihara et al., Sci. Rep. 7 (2017) 16785.

Magnetization Plateau with Spontaneous Symmetry Breaking

Tôru SAKAI[1,2], Hiroki NAKANO[1], Rito FURUCHI[1],
and Tokuro SHIMOKAWA[3]
[1]*Graduate School of Science, University of Hyogo,*
Kouto, Kamigori, Hyogo 678-1297, Japan
[2]*National Institute for Quantum Science and Technology,*
SPring-8, Kouto, Sayo, Hyogo 679-5148, Japan
[3]*Theory of Quantum Matter Unit,*
Okinawa Institute of Science and Technology Graduate University,
Onna-son, Okinawa 904-0495, Japan

1 Translational Symmetry Broken Magnetization Plateau of the S=2 Antiferromagnetic Chain with Anisotropies

The magnetization plateau of the S=2 antiferromagnetic chain with interaction and single-ion anisotropies is investigated using the numerical diagonalization of finite-size clusters and some size scaling analyses[1]. The previous level spectroscopy analysis indicated that two different magnetization plateau phases appear at half of the saturation magnetization. One is due to the large-D mechanism and the other is due to the Haldane one. In the present study the phase diagram is extended to wider region of the anisotropies. As a result we find another half magnetization plateau phase, where the translational symmetry is spontaneously broken .

2 S=2 Quantum Spin Chain with the Biquadratic Exchange Interaction

The $S = 2$ quantum spin chain with the single-ion anisotropy D and the biquadratic exchange interaction is investigated using the numerical diagonalization of finite-size clusters and the level spectroscopy analysis. It is found that the intermediate-D phase corresponding to the symmetry protected topological (SPT) phase appears in a wide region of the ground state phase diagram. We also obtain the phase diagram at the half of the saturation magnetization which includes the SPT plateau phase[2].

References

[1] T. Yamada, R. Nakanishi, R. Furuchi, H. Nakano, H. Kaneyasu, K. Okamoto, T. Tonegawa and T. Sakai, arXiv:2208.10983; to appear in JPS Conf. Proc.

[2] T. Sakai, T. Yamada, R. Nakanishi, R. Furuchi, H. Nakano, H. Kaneyasu, K. Okamoto and T. Tonegawa, J. Phys. Soc. Jpn. 91 (2022) 074702.

Simulation of Quantum Many-Body Systems by Tensor Network and Sampling

Synge TODO
Department of Physics, University of Tokyo, Tokyo, 113-0033
Institute for Solid State Physics, University of Tokyo, Kashiwa, 277-8581

We developed novel numerical methods by combining quantum Monte Carlo, tensor network algorithms, and other optimization techniques. We investigated topological quantum phase transitions in strongly correlated many-body systems and optimization of quantum operations in quantum computing.

Tensor Renormalization Group and Markov Chain Monte Carlo Methods

The real-space renormalization group method using tensor networks has recently been widely used as a numerical method for many-body spin systems. The tensor renormalization group method can efficiently compute physical quantities for large classical/quantum systems. By extending the tensor network to a form in which tensors are placed not only on vertices but also on lines connecting vertices, we have increased the accuracy of the real-space renormalization method by about 100 times compared to existing numerical methods that require a similar amount of computation time. This method applies to general tensor networks. We are also working on a new sampling method that combines tensor network representation and Markov chain Monte Carlo methods.

Tensor Renormalization Group for Lattice Fermion Systems

Quantum many-body systems involving lattice fermions appear in various fields of physics. For example, lattice quantum chromodynamics is typical in particle physics, a many-body system describing the interaction between quarks via gluons. Strongly correlated electron systems in condensed matter physics are another example of a many-body system consisting of lattice fermions. We develop a method to calculate path integrals of lattice fermion systems. We represent the path integral of a lattice fermion system by a tensor network and perform approximate network contraction using the tensor renormalization group to compute the path integral in the infinite volume limit. We extended the bond-weighted tensor renormalization group (BTRG) to handle fermionic systems and performed empirical calculations using 2-dimensional Wilson fermions [1].

Worm Algorithm with Geometric Assignment Method

In Monte Carlo methods, there are cases where there are constraints on the "states" to be summed, and it is difficult to sample while satisfying the constraints (e.g., satisfiability problems). The worm algorithm is a method for efficient sampling by expanding the state space in such situations. A worm is a kink (point) that breaks a constraint, and the idea of the worm algorithm is that the constraint is violated once and then reconciled later. This Monte Carlo method introduces a constraint-breaking worm (kink), and sampling is performed by stochastically moving the worm. The conventional worm algorithm moves the worm almost wholly at random. We proposed a guideline for moving the worm for efficient computation—moving the

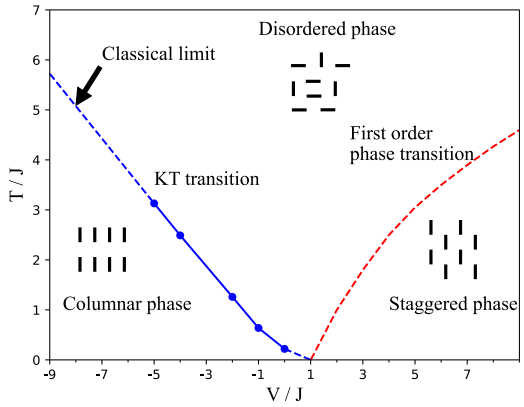

Figure 1: Finite-temperature phase diagram of square-lattice quantum dimer model.

worm straight ahead as much as possible—and confirmed a 25-fold improvement in computational efficiency compared to the conventional worm algorithm [2].

Finite-Temperature Phase Transition of the Quantum Dimer Model

The quantum dimer model was proposed by Rokhsar and Kivelson in 1988 as a low-energy effective model for frustrated magnetic materials. Although the Hamiltonian of the quantum dimer model has no negative sign problem, Monte Carlo simulations have been complicated because of the strong geometric restriction on the dimer configuration. We developed an efficient quantum Monte Carlo method that combines a cluster update method based on the stochastic series expansion (SSE) with a fast operator search method using priority queues. By choosing the appropriate order parameter and finite scaling, we obtained a finite-temperature phase diagram of the quantitative phase diagram of the quantum dimer model. The critical exponent at the critical point is consistent with the Kosterlitz-Thouless transition of the classical dimer model. The slope in the classical limit is also compatible with the critical temperature of the classical model. The slope of the phase boundary decreases as the quantum fluctuations increase, suggesting that the critical temperature becomes zero at the Rohksar-Kivelson (RK) point, i.e., the columnar dimer phase at absolute zero extends to the RK point without intermediate phases.

Continuous-Space Path-Integral Monte Carlo

The continuous-space path-integral Monte Carlo method is the only method that can numerically calculate physical quantities such as the superfluid density and condensation rate of interacting Bose particle systems. The worm algorithm allows for simulations in the grand canonical ensemble of superfluid helium in systems of several hundred particles. However, implementing the algorithm is complex, involving seven different update procedures. We developed more efficient and simpler update methods in the canonical ensemble. Advanced Markov-chain Monte Carlo methods, such as Hamiltonian Monte Carlo and event chain Monte Carlo, have been used to reduce the autocorrelation time of the simulation further. In addition, the Wang-Landau algorithm allows the hyperparameters to be automatically adjusted during the simulation, whereas the conventional worm algorithm has many hyperparameters that significantly affect the performance of the algorithm.

References

[1] Shinichiro Akiyama, Bond-weighting method for the Grassmann tensor renormalization group, J. High Energy Phys. **11**, 030 (2022).

[2] Hidemaro Suwa, Lifted directed-worm algorithm, Phys. Rev. E **106**, 055306 (2022).

Novel phenomena in frustrated magnets

Tsuyoshi OKUBO
Institute for Physics of Intelligence, The University of Tokyo
7-3-1 Hongo, Bunkyo-ku, Tokyo 133-0033

Frustrated interactions often induce novel phenomena in spin systems. One striking effect when we consider the quantum fluctuation may be the stabilization of quantum spin liquid without having long-range magnetic order [1, 2]. The ground state of the Kitaev model on the honeycomb lattice is one of the fundamental quantum spin liquids in the two-dimension[3, 4]. In the Kitaev model, the interactions are Ising type, $S_i^\gamma S_j^\gamma$, and the spin component $\gamma = x, y, z$ is determined from the direction to the neighboring site. Another example is the Kagome lattice Heisenberg model [1, 2]. It has been widely discussed on the possibility of the gapped Z_2 spin liquid or the gapless $U(1)$ spin liquid in the Kagome lattice Heisenberg antiferromagnets, e.g., see Ref. [5] and references therein.

In this year's project, we investigated finite temperature properties of frustrated spin models in the two-dimension, particularly concerning the thermal Hall conductivity. We mainly considered the Kagome lattice Heisenberg model with Dzyaloshinskii-Moriya (DM) interaction and compared its thermal Hall conductivity with the Kitaev model. To numerically calculate the thermal Hall conductivities at a finite temperature, we consider several finite-size clusters with open edges and represent their density matrix as a matrix product operator (MPO).

We calculate the MPO representing a density matrix at a given temperature by the exponential tensor renormalization grope (XTRG) algorithm [6]. In XTRG, we calculate the density matrix at an inverse temperature β, $\rho(\beta)$, through the relationship $\rho(\beta) = \rho(\beta/2)\rho(\beta/2)$ starting from the initial condition $\rho(\beta_0) = \exp(-\beta_0\mathcal{H}) \simeq 1-\beta_0\mathcal{H}$ for the sufficiently small β_0, where $\mathcal{H}$ is the Hamiltonian of the system. Once we have an MPO representation of a density matrix at $\beta/2$, we can approximate $\rho(\beta)$ through a standard tensor network compression algorithm to multiply two MPOs. When the bond dimension of the MPO is D, both the computation cost and the memory consumption of the XTRG algorithm scale $O(D^4)$. Although they are higher than the costs for the ground state, which scale $O(D^3)$, we can still calculate finite temperature properties by XTRG.

By the XTRG algorithm, we successfully calculated the temperature dependence of the energy current localized at the edge of the cylindrical system for the Kagome lattice Heisenberg model with the DM interaction under a magnetic field. We can calculate the thermal Hall conductivity by taking the temperature derivative of the energy current. In this system, the direction of the thermal Hall current depends on the sign of the DM interaction. Interestingly, in the XTRG calculation, its sign is opposite to the one calculated by Schwinger Boson mean-field theory [7]. We also found that similar sign inversion in the thermal Hall current is also observed in the case of the Kitaev model at high temperature: the sign is opposite to the expectation from the linear spin wave theory, although the sign at the low-temperature value is consistent with the expectation from the analysis of the Kitaev spin liquid. It will be a future problem to un-

derstand the origin of the difference in signs in high-temperature regions.

References

[1] L. Savary and L. Balents, Rep. Prog.Phys. **80** (2017) 016502.

[2] Y. Zhou, K. Kanoda, and T.K. Ng, Rev. Mod. Phys. **89** (2017) 025003.

[3] A. Kitaev, Ann. Phys. **321** (2006) 2.

[4] Y. Motome and J. Nasu, J. Phys. Soc.Jpn. **89** (2020) 012002.

[5] Y.C. He, M. P. Zaletel, M. Oshikawa, and F. Pollman, Phys. Rev. X, **7** (2017) 031020.

[6] H. Li, D.-W. Qu, H.-K. Zhang, *et al.* Phys. Rev. Research **2** (2020) 043015.

[7] H. Doki, M. Akazawa, H.-Y. Lee, J. H. Han, K. Sugii, M. Shimozawa, N. Kawashima, M. Oda, H. Yoshida, and M. Yamashita, Phys. Rev. Lett. **121** (2018) 097203.

Theoretical design of novel proteins for medical and industrial applications

Nao SATO[1], Hirotaro SHIMAMURA[2], Rina AOYAMA[1], Mizuki TERANISHI[1], Koji OOKA[3], Runjing LIU[1], Kaho KOTANI[1], Masataka YOSHIMURA[1], Yuuki HAYASHI[1,4], Shunji SUETAKA[1], and Munehito ARAI[1,2]

[1]Department of Life Sciences, Graduate School of Arts and Sciences, [2]Department of Physics, Graduate School of Science, [3]College of Arts and Sciences, and [4]Environmental Science Center, The University of Tokyo, Komaba, Meguro, Tokyo 153-8902

Proteins are widely used in medicine and industry as therapeutic agents for various diseases and as enzymes for industrial production. However, these proteins have been developed through extensive experiments, which require much time and cost. Therefore, there is an urgent need to develop efficient and theoretical methods for designing novel proteins. Here, we theoretically designed a variety of novel proteins using the Rosetta software suite [1] and experimentally verified the validity of our theoretical designs. In addition, we constructed a theory that can predict the folding mechanism of proteins, to elucidate the principles of protein design.

The KIX domain of CREB-binding protein is associated with leukemia, cancer and various viral diseases and has attracted considerable attention in drug discovery. We rationally designed a KIX inhibitor by performing theoretical saturation mutagenesis to search for the peptides expected to bind KIX more tightly than the original partner proteins. Among the 12 designed peptides, we experimentally found that a mutant of the MLL TAD peptide had the highest binding affinity for KIX among all previously reported inhibitors targeting the MLL site of KIX [2]. Thus, our approach may be useful for the rational design of helical peptides that inhibit protein-protein interactions involved in various diseases.

The programmed death-1 (PD-1) protein on the surface of T cells inhibits excessive inflammatory activity of T cells by binding to programmed death ligand-1 (PD-L1) expressed on antigen-presenting cells. However, reduced PD-1 function can cause abnormally activated T cells to damage normal cells, leading to autoimmune diseases. To prevent the T-cell activation by turning on the immune checkpoint, we theoretically designed PD-1 agonists that tightly bind the PD-L1 binding site of PD-1. Using Rosetta, we performed in silico saturation mutagenesis on the fragment of human PD-L1 and selected the mutants that are predicted to have high affinity for PD-1.

Experimental verification showed that we have successfully designed the PD-1 binders with higher affinity than the wild-type PD-L1, which may be useful as inhibitors of autoimmune diseases.

The novel coronavirus (SARS-CoV-2) infects human cells when its receptor-binding domain (RBD) binds to human ACE2. Antibodies that inhibit this binding have been used as antiviral drugs. However, existing drugs may become less effective as new variants of SARS-CoV-2 with mutations in the RBD emerge. Here, we theoretically modified existing antibody drugs to bind tightly to the RBD mutant of SARS-CoV-2 and experimentally showed that the modified antibodies were able to bind tightly to the RBD mutant. This approach is expected to be useful in the future as new viral variants emerge.

Formation of a ternary complex by interleukin 33, its receptor ST2, and IL-1 receptor accessory protein (IL-1RAcP) induces allergic diseases. To inhibit the complex formation, we have theoretically designed small proteins that tightly bind ST2 but inhibit the binding of IL-1RAcP. Experiments to verify the designs are ongoing.

Enzymes are widely used in the industrial production of useful substances. Therefore, it is necessary to develop efficient methods to improve enzymes. Using the Rosetta software, we are developing a universal method that can generally improve the activity of various enzymes. We have applied this method to enzymes such as dihydrofolate reductase and aldehyde deformylating oxygenase. Verification of this method is underway.

Elucidating the mechanisms by which proteins fold into specific three-dimensional structures is necessary to understand the design principles of proteins. To solve this problem, we are developing a statistical mechanics theory that can draw the folding free-energy landscapes of any proteins [3]. The program is written in C++ and Python. We have successfully calculated the free energy landscapes of folding reactions for all-α and all-β proteins in agreement with experiments. Our method can be used to draw the free energy landscapes of proteins associated with folding, binding, and catalysis, and to develop new protein design methods based on the prediction of protein dynamics.

References

[1] J. K. Leman, et al.: Nature Methods, **17**, 665 (2020).

[2] N. Sato, S. Suetaka, Y. Hayashi, and M. Arai: Scientific Reports, **13**, 6330 (2023).

[3] K. Ooka, R. Liu, and M. Arai: Molecules, **27**, 4460 (2022).

Multiscale Flow Simulations on Complex Fluids Undergoing Phase Transition

Yohei MORII and Toshihiro KAWAKATSU

Department of Physics, Tohoku University, Sendai, Miyagi 980-8578

The knowledge on the properties of complex flows, such as a viscoelastic polymer flow, around an obstacle plays a crucial role in designing flow channels in machines. In the present study, we analyze a flow of a dilute polymer solution passing through a moving wing using the multiscale simulation platform named MSSP, where smoothed particle hydrodynamics (SPH) method is coupled with microscopic particle simulations or phenomenological constitutive relations.

We modelled the wing using Joukowski wing as shown in Fig.1, and the polymer chains are modelled either by a Maxwellian constitutive relation (infinitely extensible) or FENE dumbbells (finite extensible). Simulations were performed at Ohtaka, where 2,560,000 SPH particles with 5,000,000,000 dumbbell particles embedded in these SPH particles were used. From the simulation data, we evaluated the rift coefficient C_{L} which is defined as the magnitude of the force exerted on the wing in the perpendicular direction to the inflow velocity divided by the inflow speed.

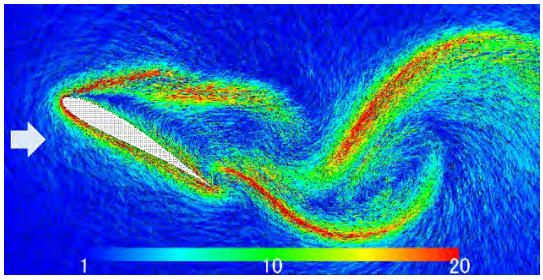

Fig.1 Flow pattern of a polymer solution around a Joukowski wing. Shown are the direction (bars) and the extension (colors) of polymers chains.

Figure 1 shows a snapshot of the molecular orientations and the bond stretching of the FENE dumbbells around a fixed Joukowski wing. When the wing starts to rotate slowly changing its angle to the inflow direction as $0° \rightarrow 45° \rightarrow 0°$, the value of C_{L} changes as shown in Fig.2, where the data are shown for Newtonian (red), Maxwellian(green) and FENE dumbbell(blue) models, respectively. We can confirm that the oscillation in C_{L} is suppressed by adding stretchable polymers(Maxwellian) while such a suppression is less obvious for FENE dumbbells.

References

[1] Y.Morii and T.Kawakatsu, Phys. Fluids, **33**, 093106 (2021).

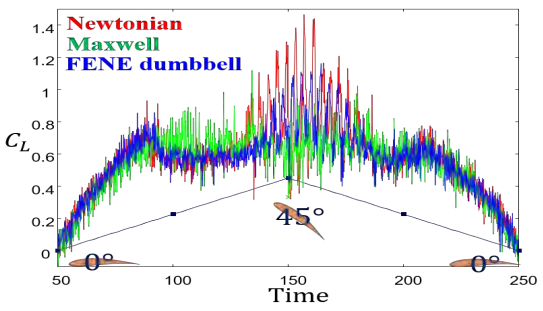

Fig.2 C_{L} as a function of the angle of the wing.

Simulations of quantum-classical-hybrid algorithms for sensor materials with considering noise

Wataru Mizukami

Center for Quantum Information and Quantum Biology, Osaka University, Osaka 560-0043, Japan

In the fiscal year, a domestically produced quantum computer was made publicly available in the cloud, and IBM announced a quantum computer with 443 quantum bits. Quantum computers with thousands of quantum bits are expected to appear in the near future, indicating significant progress in the development of quantum computing. A promising application for quantum computers is the simulation of quantum many-body systems. In the field of materials development, it is expected that simulations will become more accurate than current methods. Research into such simulation techniques is gaining momentum.

Our aim is to apply quantum computing to the development of materials for use in sensors. However, performing practical computations on realistic quantum chemistry problems with a large number of degrees of freedom using only quantum computers with limit number of qubits is not feasible. In addition, current quantum computers have short coherence times, making it difficult to perform useful computations using only quantum computers. As a result, the development of quantum-classical hybrid algorithms that utilise both quantum and classical computers has become crucial. In this study, we have performed the development and validation of quantum-classical hybrid algorithms using the ISSP's supercomputer and a quantum circuit simulator rather than an actual quantum computer.

This year, following up on last year's work, we focused on accelerating the simulation of the variational quantum eigensolver (VQE), a representative quantum-classical hybrid algorithm. We worked on speeding up VQE computations using GPUs and implemented VQE with multi-GPU support.

Moreover, we have been developing a method that combines the auxiliary-field quantum Monte Carlo (AFQMC) technique with VQE to compensate for degrees of freedom that cannot be handled by VQE alone. While a combination of AFQMC and quantum computation was proposed by Google in 2021, we have designed and implemented an algorithm that results in a more practical quantum circuit than their implementation. We tested this algorithm on simple systems, such as the OH molecule, and confirmed its satisfactory performance.

Tensor renormalization-group study of random spin systems

Koji HUKUSHIMA
Department of Basic Science, University of Tokyo
3-8-1 Komaba, Meguro-ku, Tokyo 153-8902

Statistical mechanical studies of spin glasses with both randomness and frustration have been conducted for a long time. It is an important issue whether the picture of phase transitions established in the mean-filed spin-glass model can be applied to finite-dimensional spin-glass models. It is quite difficult to study the finite-dimensional spin glass models using analytical methods. Therefore, the main results for these models have been obtained mainly by numerical studies, such as Markov-chain Monte Carlo (MCMC) methods. However, the long relaxation times of the MCMC methods for spin-glass systems are a serious barrier to studying large sizes. Recently, the tensor renormalization group (TRG) method, numerical calculation methods using tensor networks have attracted much attention.

In this project, we employ the higher-order tensor renormalization group (HOTRG) method, one of the TRG-type methods, to study the two-dimensional Ising spin-glass model. Previous studies have suggested that the spin-glass phase transition does not occur at finite temperatures in this system when the distribution of interactions is close to symmetric and highly disordered[1]. We investigate the phase transition of the system near the Nishimori line. Then, the stiffness of the system is calculated for sizes up to the linear dimension $L = 256$ using the HOTRG method, which calculates the free energy under different boundary conditions. In the calculations at higher temperatures than the Nishimori line, both boundary conditions lead to the same transition point and values close to the critical exponent of the pure Ising universality class, the latter of which is consistent with the picture dominated by the pure Ising fixed point there, as pointed out in many previous studies.

In contrast to the phase transitions above and on the Nishimori line, the transition points analyzed here have different values for the twist and replica boundary conditions. In other words, the paramagnetic/ferromagnetic and paramagnetic/non-paramagnetic transition points are different from each other, suggesting the existence of some non-paramagnetic phase between the paramagnetic and ferromagnetic phases at finite temperatures in the two-dimensional EA Ising model. This may correspond to the spin-glass phase or the previously proposed random antiphase state. The value of this transition point at low temperature is roughly consistent with the Nishimori fixed point, suggesting that the boundary between the paramagnetic and "spin-glass" phases descends almost vertically from the Nishimori fixed point toward lower temperatures. Meanwhile, the "spin-glass"/ferromagnetic phase boundary shows a re-entrant transition.

We also studied the critical phenomena of the J_1-J_2 Ising model by varying the parameter g using HOTRG[2]. This system involves a competition between the ferromagnetic interaction J_1 and antiferromagnetic interaction J_2. Furthermore, weak first-order and second-order transitions are observed near the ratio $g = J_2/|J_1| = 1/2$. Our results, based on HOTRG calculations for significantly larger sizes, indicate that the region of the first-order transition is marginally narrower than that in previous studies. Moreover, the universality class of the second-order transition connected to the transition line is not necessarily fully consistent with the Ashkin–Teller class considered earlier.

[1] K. Yoshiyama, K. Hukushima: in preparation.

[2] K. Yoshiyama, K. Hukushima: arXiv:2303.07733

Molecular dynamics study of phase separation induced by binding molecules

Koji HUKUSHIMA
Department of Basic Science, University of Tokyo
3-8-1 Komaba, Meguro-ku, Tokyo 153-8902

Chromatin is highly folded into a hierarchical structure in the nucleus while interacting with nuclear molecules. In addition, regions of active and repressed gene expression are formed on chromatin. These epigenetic regions are established and maintained by writer molecules that write and reader molecules that recognize chemical modifications on chromatin. The relationship between the one-dimensional epigenetic pattern on chromatin and the three-dimensional chromatin structure is an interesting question that has not yet been elusidated.

The SBS (Strings and Binders Switch) model[1] is a coarse-grained polymer model that takes into account the phase separation between chromatin and nuclear molecules that bind to chromatin, and to some extent recapitulates the experimental results such as HiC and FISH. In this model, chromatin forms clusters due to the effective attraction between chromatin segments via molecules that bind multivalently to chromatin[1,2].

In this project, we consider two types of binding molecules in the SBS model that promote or repress transcription as playing the roles of reader and writer of epigenetic modifications. When polymer segments are bound to these binding molecules, the state stochastically changes depending on the type of the binding molecule. The binding molecules switch between two states, one in which they can bind chromatin and one in which they cannot, at a constant rate, as in the previous study[3]. In this model, a one-dimensional pattern of epigenetic modification appears on the polymer, accompanied by a three-dimensional structure.

In this study, we performed coarse-grained molecular dynamics simulations on the SBS model with two types of biding molecules. From the time-series data of the coordination dynamics obtained by the molecular dynamics simulations, we devised a method to extract the time evolution of cluster formation, fission, coalescence, and annihilation. With the help of the method, it is revealed that the clusters move dynamically along the polymer, repeating coalescence and fission, and that there are no independent clusters. The evaluation of the lifetime of the clusters also suggested the existence of a phase that goes to infinity below a certain nonzero switching rate, despite a finite switching rate. This can be regarded as a dynamical percolation transition.

Our simulations also showed that the sequence of clusters of alternating types and the hierarchical structure of these clusters on the chromatin polymer emerge with the two types of binding molecules. When the binding molecules do not switch states, the polymer takes on a sausage-like shape with hierarchical structure, and as the switching rate increases, the structure becomes more dynamic and the clusters become more independent of each other. This provides insight into the mechanisms underlying the dynamics and stability of one-dimensional epigenetic patterns and three-dimensional cluster structures on chromatin in the SBS model.

The present work has been done in collaboration with Ryo Nakanishi.

[1] Mariano Barbieri et al., PNAS, 2012 109 (40) 16173-16178.
[2] Andrea M. Chiariello et al., Sci. Rep., 2016 29775(6).
[3] Chris A. Brackley et al., Biophys. J., 2017 112(6) 1085-1093.

Numerical simulations combined with machine learning to search for magnetic skyrmion in frustrated magnets

Satoru Hayami
Graduate School of Science, Hokkaido University, Sapporo 060-0810, Japan

A magnetic skyrmion, which is characterized by a topologically-nontrivial swirling spin texture, has attracted considerable attention, since it leads to unconventional transport phenomena, such as the topological Hall effect. In order to realize new electronic and spintronic devices based on the skyrmion, it is highly desired to understand when and how such topological spin textures are stabilized from the microscopic viewpoint. In the project with number 2022-Ca-0002, we have numerically investigated the possibility of magnetic skyrmions by focusing on magnetic frustration mechanisms in localized and itinerant systems. We have presented the main results this year below.

(i) Skyrmion crystals in trilayer systems: We have theoretically investigated a new stabilization mechanism of the skyrmion crystals in a trilayer system [1]. By focusing on the role of the layer-dependent Dzyaloshinskii-Moriya interaction and performing the simulated annealing for the spin model, we obtained various types of skyrmion crystal phases with different skyrmion number in a low-temperature phase diagram. We found the skyrmion crystal phases characteristics of the layered system: the twisted surface skyrmion crystal, anti-skyrmion crystal, and high-topological-number skyrmion crystal phases.

(ii) Rectangular and square skyrmion crystals in centrosymmetric tetragonal magnets: We considered the instability toward the rectangular skyrmion crystal without fourfold rotational symmetry on a centrosymmetric square lattice with magnetic anisotropy [2]. The model includes the effect of frustrated exchange interactions and the easy-axis single-ion anisotropy. We have shown that a competition of the interactions in momentum space triggers the formation of both rectangular and square skyrmion crystals. We have also shown that a phase transition between them occurs while varying the amplitude of the magnetic field.

(iii) Skyrmion crystals in a nonsymmorphic lattice structure: We have numerically investigated the stabilization mechanism of the skyrmion crystals in a nonsymmorphic lattice system with screw symmetry [3]. By performing unbiased numerical simulations based on the simulated annealing for a layered spin model to be characterized as a nonsymmorphic system with a threefold screw axis, we revealed that the skyrmion crystal is stabilized in both zero and nonzero magnetic fields by the interplay between the ferromagnetic interlayer exchange interaction and the layer- and momentum-dependent anisotropic exchange interactions. We also found two new types of skyrmion crystals characteristics of a threefold-screw system. Our result indicated a possibility to realize the skyrmion crystal in nonsymmorphic systems without a solely rotational symmetry within the same plane, which leads to extending the scope of the skyrmion crystal-hosting materials.

(iv) Skyrmion crystals in a ferromagnetic/antiferromagnetic bilayer: We proposed

a new stabilization mechanism of the skyrmion crystal in a bilayer system, which is composed of ferromagnetic and antiferromagnetic layers but free from the Dzyaloshinskii-Moriya interaction [4]. By performing the variational calculation and Monte Carlo simulation for the frustrated spin model, we found that the skyrmion crystal is robustly stabilized from zero to finite temperatures for the strong interlayer coupling. The results provided a new scenario to realize the skyrmion crystal in multi-layer systems including the domain structure and heterostructure by making use of the layer degree of freedom.

(v) Skyrmion crystal in the Hubbard model: We investigated a realization of the skyrmion crystal in the centrosymmetric triangular-lattice Hubbard model without localized spins [5]. On a basis of the self-consistent mean-field calculations, we found two types of skyrmion crystals with spatially nonuniform charge modulations in the ground state at a zero magnetic field. We have also shown that an unconventional triple-Q vortex phase without the net spin scalar chirality emerges. Furthermore, we found that the magnetic field induces the topological phase transition from the $3Q$ vortex phase to another skyrmion crystal phase. We clarified that the microscopic origin of these phases is the site-dependent moment reduction due to the kinetic motion of electrons in the Hubbard model, which is qualitatively different from the situation in the Kondo lattice model and other spin models.

(vi) Various topological spin textures in an itinerant honeycomb magnet: We have theoretically revealed new types of topological spin textures consisting of the magnetic skyrmion by focusing on the sublattice degree of freedom in the lattice structure [6]. We found five types of skyrmion crystals with different topological properties from the conventional one in an itinerant honeycomb magnet based on the simulated annealing. We have shown that the sublattice degree of freedom in the itinerant magnet enables us to realize the unobserved skyrmion crystals, such as the antiferro-type skyrmion crystal and ferri-type skyrmion crystal.

(vii) Magnetic field–temperature phase diagrams for centrosymmetric tetragonal magnets: We systematically constructed the magnetic field–temperature phase diagrams of the effective spin model for the itinerant electron model on a square lattice on the basis of an efficient steepest descent method with a small computational cost [7]. We found two distinct mechanisms to stabilize the square-type skyrmion crystal from zero to finite temperatures: One is the positive biquadratic interaction and the other is the high-harmonic wave-vector interaction. By showing the phase diagrams for different sets of model parameters, we discussed the stability tendency of the skyrmion crystal and other multiple-Q states.

References

[1] S. Hayami, Phys. Rev. B **105**, 184426 (2022)

[2] S. Hayami, Phys. Rev. B **105**, 174437 (2022).

[3] S. Hayami, Phys. Rev. B **105**, 224411 (2022).

[4] K. Okigami, R. Yambe, and S. Hayami, J. Phys. Soc. Jpn. **91**, 103701 (2022).

[5] K. Kobayashi and S. Hayami, Phys. Rev. B **106**, L140406 (2022).

[6] R. Yambe and S. Hayami, Phys. Rev. B **107**, 014417 (2023).

[7] S. Hayami and Y. Kato, J. Magn. Magn. Mater. **571**, 170547 (2023).

Universality classes of 3D $\pm J$ Ising model

Y. Ozeki and Y. Terasawa

Graduate School of Informatics and Engineering, The University of Electro-Communications

We investigate the universality classes of the $\pm J$ Ising model in three dimensions. Together with the ferromagnetic (FM) classes obtained previously [1], the spin glass (SG) transition is analyzed by the use of dynamical scaling analysis for nonequilibrium relaxation (NER) process [2]. the p-dependence of SG transition temperature $T_{\mathrm{SG(p)}}$ and critical exponents γ, ν, z are obtained.

To estimate the dynamical exponent z precisely, an extrapolation scheme is introduced for the asymptotic value of logarithmic derivative of the dynamical Binder parameter at the transition point. To do this, we performed Monte-Carlo simulation for multi-replica systems. Each replica system has the same bonds J_{ij}, while the initial configuration of relaxation is distinct. The replica overlap $q^{AB}(t)$ between two replicas A and B at time t, is defined by:

$$q^{AB}(t) = \frac{1}{N}\sum_i S_i^{(A)}(t) S_i^{(B)}(t), \qquad (1)$$

where $S_i^{(A)}$ is the i-th spin variable in replica A at time t. Te SG Binder parameter is obtained by

$$g_{\mathrm{SG}}(t,T) = \frac{1}{2}\left(3 - \frac{q^{(4)}(t)}{\{q^{(2)}(t)\}^2}\right), \qquad (2)$$

where

$$q^{(k)}(t) = \frac{2}{n(n-1)}\left[\sum_{A>B}\{q^{AB}(t)\}^k\right]_J. \qquad (3)$$

When $T = T_{\mathrm{SG}}$, this function is expected to diverge as

$$N \times g_{\mathrm{SG}}(t,T) \sim t^{d/z} \qquad (4)$$

where d is the spacial dimension. This relation allows us to estimate z independently.

The SG region in $0.5 \le p \le p_{\mathrm{mc}}$ is analyzed. To estimate T_{SG} and $z\nu$, we perform the dynamical scaling analysis for SG susceptibility $\chi_{\mathrm{SG}}(t)$ with the linear size $L = 61$, 512 independent samples and 64 replicas are used for averaging. To estimate z, we calculate $g_{\mathrm{SG}}(t)$ with the linear size $L = 31$, 460800 independent samples and 64 replicas are used for averaging.

In Figs. 1, the resulting p-dependence of SG critical exponent ν on the PM-SG boundary are shown

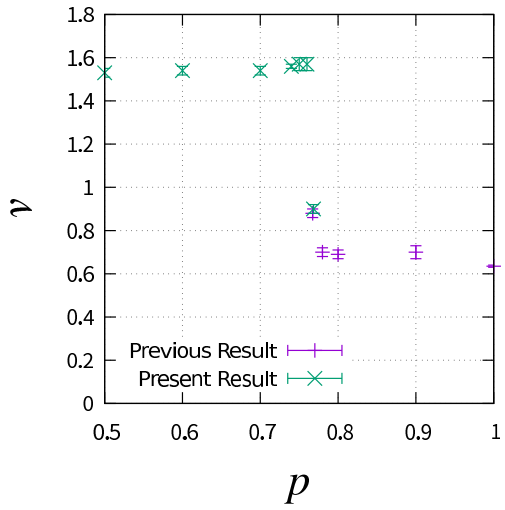

Figure 1: Result of estimated ν.

together with the previously obtained FM exponents on the PM-FM boundary [1]. Since both the FM and SG transitions occur at the multi-critical point (MCP), and FM and SG exponents become identical with each other [3], one may survey an exponent in whole region including SG and FM phases. As for the exponent ν, there exist three FM universality classes associated with the non-random FM fixed point ($p = 1$), the random fixed point ($p_{\mathrm{mc}} < p < 1$), and the MCP ($p = p_{\mathrm{mc}}$) [1]. On the other hand, the present result indicates a single universality class for PM-SG transition in $0.5 \le p < p_{\mathrm{mc}}$, and ν takes a value ~ 1.55.

References

[1] Y. Ozeki and N. Ito, *J. Phys.: Math. Theor.* **40** R149 (2007).

[2] Y. Echinaka and Y. Ozeki, *Phys. Rev.* E**94** 043312 (2016).

[3] Y. Ozeki and N. Ito, *J. Phys.A: Math. Gen.* **31** 5451 (1998).

Localization-delocalization transition in non-Hermitian random system

TOMI OHTSUKI[1]
TOHRU KAWARABAYASHI[2]
KEITH SLEVIN[3]
1) Dept. Phys., Sophia University, Chiyoda-ku, Tokyo 102-8554, Japan
2) Dept. Phys., Toho University, Miyama 2-2-1, Funabashi 274-8510, Japan
3) Dept. Phys., Osaka University, Toyonaka, Osaka 560-0043, Japan

Random quantum systems lack translational/rotational symmetries but can exhibit time reversal, spin rotation, chiral, and particle-hole symmetries. These symmetries classify random quantum systems into 10 distinct symmetry classes. The Wigner-Dyson classes discovered in the 1950s and 1960s have undergone significant research. Recent experimental findings regarding topological insulators and Weyl semimetals have inspired researchers to explore random systems outside of the Wigner-Dyson classes. These newly discovered 7 classes [3 chiral classes (Gade-Wegner classes) and 4 Bogoliubov-de Gennes classes] exhibit discrete chiral or particle-hole symmetries.

We have studied a series of Hamiltonians that pertain to the newly discovered quantum classes. We then introduced non-Hermiticity to the Hamiltonian, and we were able to extend the classification of systems to encompass 38 distinct classes. Through our research, we demonstrated that the inclusion of non-Hermitian elements alters the universality class [1] and that the widely utilized transfer matrix method employed in Anderson transitions also applies to non-Hermitian systems [2]. Additionally, our investigations revealed that the critical behaviors of the 38 non-Hermitian classes can be mapped to universality classes for the 10 Hermitian symmetry classes [3] (see Fig. 1).

Condensed matter physics has seen a significant increase in the utilization of machine learning techniques. Our research involves using convolutional neural networks (CNN) to analyze wave functions and study various quantum phase transitions. Specifically, we employ this method to classify wave functions in quasi-periodic systems[4]. Moreover, we utilize the neural network to interpret the quantum fingerprints in mesoscopic systems [5].

References

1. X. Luo, T. Ohtsuki, R. Shindou, Physical Review Letters **126**, 090402 (2021).
2. X. Luo, T. Ohtsuki, and R. Shindou, Physical Review B **104**, 104203 (2021).
3. X. Luo, Z. Xiao, K. Kawabata, T. Ohtsuki, and R. Shindou, Physical Review Research **4**, L022035 (2022).
4. X. Luo, T. Ohtsuki, Physical Review B **106**, 104205 (2022).
5. S. Daimon, K. Tsunekawa, S. Kawakami, T. Kikkawa, R. Ramos, K. Oyanagi, T. Ohtsuki, E. Saitoh, Nature Communications **13**, 3160 (2022).

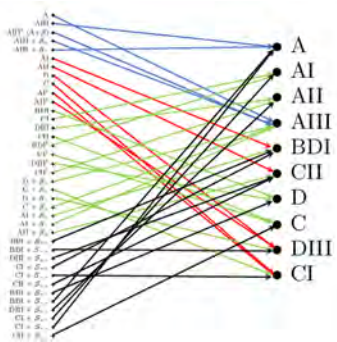

Figure 1: Correspondence of the Anderson transitions in non-Hermitian and Hermitian systems.

Slow spin dynamics near phase boundary between different ordered phases

Hidemaro SUWA
Department of Physics, University of Tokyo, Tokyo 113-0033

The metastable state is ubiquitous in our daily lives and in condensed matter physics. A typical example of the metastable state is diamond, a solid form of carbon. Graphite is the most stable phase at room temperature, but diamond is also stable as a metastable state, indicating that the time scale of relaxation is much longer than that of experiments. The metastable state is essential to not only statistical mechanics but also several functional materials. For example, the use of the metastable state enables higher-density storage and broader applications in phase-change memory. Recently, a skyrmion-lattice phase of MnSi has been stabilized by rapid cooling as a metastable state in a wider region of the phase diagram.

What is the condition for a metastable state to stay for a long time, or in what situation do the relaxation dynamics become significantly slow? We can find some answers in glass systems. Slow dynamics typically emerge near a eutectic point, a triple point between a liquid, a crystal, and another crystal phase. In the dynamics of particle systems, the particle number is usually conserved in time evolution. On the other hand, the dynamics of spin systems are typically non-conserved: magnetization is not conserved in time evolution. The question we answer through this project is where slow dynamics appear in the Ising model, a prototype model of statistical mechanics.

In analogy to the eutectic point, we derived one of the simplest Ising models showing a "Y-shape" first-order phase boundary (Fig. 1): the J_1-J_2-J_3 Ising model with a four-spin interaction. The four-spin interaction could be induced by integrating out other degrees of freedom, mimicking an effect of interactions with charge, phonons, etc. We studied the quench dynamics of the Ising model using the Monte Carlo method on ISSP System B in the class C project (ID: 2022-Ca-0100). The initial state is a random spin configuration, and the time evolution is simulated by Glauber dynamics. The relaxation time becomes significantly longer near the phase boundary. We also studied snapshot configurations and the structure factor as a function of time. Near the phase boundary, clusters of the metastable state remain for a quite long time and prevent vortices from recombining and annihilating. Our simulation is consistent with experimentally observed slow dynamics in vanadium oxides. The result of this project sheds new light on the stability of the metastable state and slow dynamics emerging near a phase boundary.

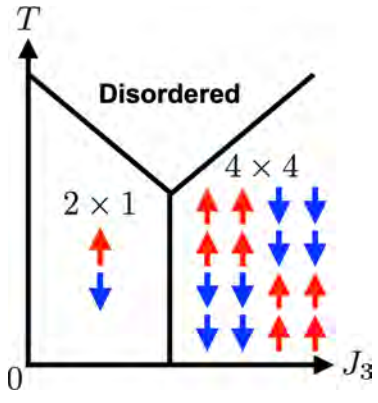

Figure 1: Schematic Y-shape phase diagram of the Ising model. The phase boundaries are of the first order.

Polymer Dynamics under Elongational Flow

Takahiro MURASHIMA

Department of Physics, Tohoku University,

Aramaki-aza-Aoba, Aoba-ku, Sendai, Miyagi 980-8578

Fundamental studies of polymer dynamics under elongational flows are important for a better understanding of complex flow in the molding process. We have developed a uniform elongational flow method [1] that can handle very large deformations under arbitrary (uniaxial, planar, and biaxial) elongational flows. This code works on LAMMPS [2], which brings the benefits of massive parallel computation at ISSP. Our previous work [3] was the first to discover the stress overshoot phenomena of ring/linear blends under biaxial elongational flow using this method. In this project, we investigated multicyclic/linear blend systems under biaxial elongational flows. We found sharper overshoot phenomena of multicyclic/linear blend than those of monocyclic/linear blend in our previous work [3]. The origin of overshoot in multicyclic/linear blend was the open-to-closed topological transition. This work [4] was selected as a supplementary journal cover of Macromolecules as shown in Fig. 1.

Fig. 1: Supplementary Journal Cover of Macromolecules, Volume 55, Issue 21 [4].

References

[1] T. Murashima, K. Hagita, T. Kawakatsu, Nihon Reoroji Gakkaishi, **46**, 207 (2018); https://github.com/t-murash/LAMMPS-UEFEX

[2] S. Plimpton, J. Comp. Phys. **117**, 1 (1995); A. P. Thompson et al., Comp. Phys. Comm., 271, 10817 (2022); https://www.lammps.org

[3] T. Murashima, K. Hagita, T. Kawakatsu, Macromolecules, **54**, 7210 (2021).

[4] T. Murashima, K. Hagita, T. Kawakatsu, Macromolecules, **55**, 9358 (2022).

Stability of quantum spin liquids in frustrated spin systems

Kota IDO

Institute for Solid State Physics,

The University of Tokyo, Kashiwa-no-ha, Kashiwa, Chiba 277-8581

The Kitaev spin liquid has attracted attention in order to realize topological quantum computing by Majorana fermions [1, 2]. However, because Kitaev candidate materials have additional magnetic interactions such as the Heisenberg term, the ground state becomes a magnetic ordered state. Applying a magnetic field is a promising way to suppress the magnetic order. In fact, it is reported that the half-integer quantization of the thermal Hall conductivity has been measured in a Kitaev candidate material under a magnetic field, which signals the realization of the Kitaev spin liquid by applying the magnetic field [3]. Therefore, it is desirable to accurately solve the extended Kitaev model under a magnetic field.

The variational Monte Carlo (VMC) method is a numerical method applicable to analysis of two-dimensional systems [4, 5]. Recently, by introducing the Jastrow-BCS wavefunction constructed from the Jordan-Wigner fermions, we succeeded in analyzing the magnetization process of the Kitaev honeycomb model with high accuracy [6]. However, the application of this approach is limited to only the Kitaev model with the magnetic field along z-direction. Thus, it is still challenging problem to solve the Kitaev model with other perturbative terms under the magnetic field along arbitrary direction.

In this project, we analyze the magnetization process of the Kitaev-Heisenberg model under the magnetic field along [001] or [111] direction by using the generalized spinon pair-product wavefunction, which has been already used for analysis of quantum spin liquids in strongly correlated systems [4]. We find that the VMC results by using this trial wavefunction can well reproduce the exact diagonalization results even when we impose a sublattice structure on the trial wavefunction. Applications to large size systems will be reported elsewhere.

References

[1] A. Kitaev, Ann. Phys. **321**, 2 (2006).

[2] H. Takagi et al., Nat. Rev. Phys. **1**, 264 (2019).

[3] Y. Kasahara et al., Nature **559**, 227 (2018).

[4] M. Kurita, Y. Yamaji, S. Morita, and M. Imada, Phys. Rev. B **92**, 035122 (2015).

[5] T. Misawa et al., Comput. Phys. Commun. **235**, 447 (2019).

[6] K. Ido and T. Misawa, Phys. Rev. B **101**, 045121 (2020).

Efficient Sampling Simulation of the Soft Modes Significantly Contribute to Protein Properties

D. P. TRAN, K. TAKEMURA, T.N. WIJAYA, R. OSAWA, M. YOSHIOKA, H. NAKAYA, S. IKIZAWA, T.Y. CHU, H. T. NGUYEN and A. KITAO

School of Life Science and Technology, Tokyo Institute of Technology

Ookayama, Meguro, Tokyo 152-8550

In this project, we employed Parallel Cascade Selection Moelcular Dynamics simulation (PaCS-MD) [1] as the enhanced sampling method to conduct efficient molecular simulation. Recently, we used the conmbination of the PaCS-MD together with Markov State Modeling (MSM) to unveil the energetic and kinetics of the interfacial activation of *Candida antarctica* Lipase B (CALB) [2].

We first constructed the well-relaxed structures of the CALB/W in water and the interface of water and tricaprylin (CALB/I). After that, we performed the PaCS-MD/MSM from open-to-close and close-to-open for both CALB/W and CALB/I with 30 replicas. Each trajectory length is 0.1ns. We monitored the the α5 helix (residues 142–146) and half of the α10 helix (residues 278–287) in all PaCS-MD simulations.

Then we constructed the free energy landscape (FEL) of both systems by using Markov State Modeling from the inter-Cα distances between Arg309 and Leu144 (Dist1) and Ala146 and Val286 (Dist2) and plot in Figure 1. We found that the FEL of CALB/W spans larger conformational space than that of the CALB/I, because of the flexibility of the lid region in water. The minima i1 and i2 in CALB/I FEL are stiffer comparing to that of w1-3 in CALB/W FEL. The free energy level of the closed conformation is much lower than that of the open conformation in water.

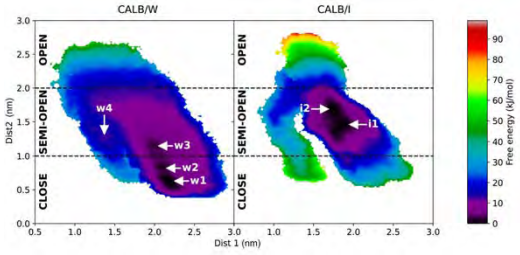

Figure 1. Free energy landscape (FEL) of CALB/W and /I obtained by PaCS-MD/MSM

After that, we performed the PCCA++ [3] to explore macroscopic view of the open-close transition of CALB. We employed the coarse graining the microstates into 6 microstates for both

cases. The CALB/W conformation can be split into three states: closed states (WC1, WC2, and WC3), one semi-open state (WS), and two open states (WO1 and WO2). In CALB/W, we found that the transition from semi-open state to the closed state is one-order of magnitude faster than that to the open state. In contrast, the CALB/I exhibits the timescale of semi-open to open states in nanosecond order. CALB prefers the transition to the closed state in water but moves to the open state in the interface.

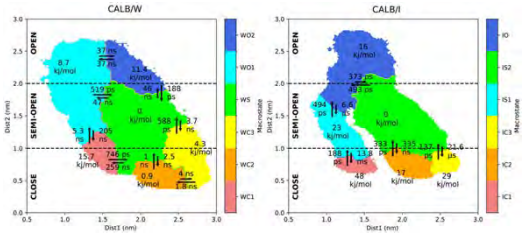

Figure 2. Microstates assignment using PCCA++ for both CALB/W and /I. PCCA++ results and MFPT between macrostates for CALB/W (left) and CALB/I (right). Transition time and free energy difference are also indicated.

Via analysis of PaCS/MSM, we found that the closed state is the most stable in the water system but the stable conformation in the interface system shifts to the semi-open state. In the interface system, the transition probability to the open state is higher than in the water system. We also suggest double mechanisms of substrate binding as followed: i) small and hydrophilic substrates bind without interfacial activation, ii) large and bulky substrates bind via interfacial activation. These findings could help expand CALB applications towards a wide variety of substrates.

References

[1] R. Harada and A. Kitao. J Chem Phys 139, 035103 (2013).

[2] T. N. Wijaya, A. Kitao (2023), ChemRxiv. doi: 10.26434/chemrxiv-2023-17v42

[3] S. Roeblitz, M. Weber, Adv Data Anal Classif 7, 147 (2013)

Thermal effects on quantum frustrated magnetisms

Tokuro Shimokawa

Theory of Quantum Matter Unit, Okinawa Institute of Science and Technology Graduate University, Onna 904-0495, Japan

Investigating the effects of thermal fluctuations in quantum frustrated magnets is crucial for developing our understanding of quantum spin liquids. $Ca_{10}Cr_7O_{28}$ (CCO) [1] is a quantum spin liquid candidate that can be described by the S=1/2 bilayer breathing kagome (BBK) Heisenberg model. Here, we examine the importance of thermal fluctuations by focusing on the J_1-J_2 classical honeycomb-lattice Heisenberg model corresponding to the classical system of this S=1/2 BBK model.

To do this, we employ classical Monte Carlo simulations, utilizing a hybrid parallelization approach combining the heat-bath method, over-relaxation method, and replica exchange method. We investigate the ordering behavior of the honeycomb lattice model in a finite-temperature magnetic field with a focus on the several J_2/J_1 parameter values. Physical quantities, including specific heat, magnetic susceptibility, equal-time structure factor, and chirality, are examined to identify the presence of a Skyrmion lattice state with sublattice structure and other additional multiple-q states [2].

We also report on the investigation of the static and dynamic properties of the S=1/2 J_A-J_B-J_C honeycomb-lattice Heisenberg model, which is believed to be important for understanding the quantum spin liquid behavior in different honeycomb-lattice material $Cu_2(pymca)_3(ClO_4)$ [3]. The investigations were carried out using quantum Monte Carlo simulations based on ALPS application [4] and exact diagonalization. Our results demonstrate the realization of a quantum paramagnetic state in this material, and suggest that focusing on dynamic properties is crucial for experimentally identifying this state [5].

References

[1] C. Balz, *et al.* Nat. Phys. **12** 942 (2016).

[2] T. S., *et al*, in preparation

[3] Z. Honda, *et al*, J. Phys. Soc. Jpn. **84**, 034601 (2015).

[4] A. Albuquerque, *et al*, J. Magn. Magn. Mater. **310**, 1187 (2007).

[5] T. S., Ken'ichi Takano, Zentaro Honda, Akira Okutani, and Masayuki Hagiwara, Phys. Rev. B **106**, 134410 (2022).

Matrix Product Renormalization Group

Masahiko G. YAMADA[AB]
Masahiro O. TAKAHASHI[B]
Takumi SANNO[B]
Yutaka AKAGI[C]
Hidemaro SUWA[C]
Satoshi FUJIMOTO[BD]
Masafumi UDAGAWA[A]
[A] *Department of Physics, Gakushuin University, Mejiro, Tokyo, 171-8588, Japan*
[B] *Department of Materials Engineering Science, Osaka University, Toyonaka 560-8531, Japan*
[C] *Department of Physics, The University of Tokyo, Hongo, Tokyo, 113-0033, Japan*
[D] *Center for Quantum Information and Quantum Biology, Osaka University, Toyonaka 560-8531, Japan*

In order to support and endorse the results found in [1], we have reproduced the matrix product renormalization group (MPRG) calculation done in [1] using the ISSP supercomputer. We newly find that by using the ISSP supercomputer the calculation with a larger bond dimension χ is possible. Indeed, the calculations with $\chi = 128$ are possible for both transverse-field Ising model and the spin-1/2 antiferromagnetic Heisenberg model.

The results agree well with an exact solution or a quantum Monte Carlo simulation. This means that MPRG has a potential to realize a large scale simulation up to $\chi = 128$ and a good scalability. The advantage over other methods will be discussed in the future, but it is likely that MPRG is superior to other conventional tensor network methods.

Currently, the algorithm of MPRG is not suitable for parallel computing, while it may be straightforward to support a graphics processing unit (GPU). We will persue this direction in the future study.

References

[1] M. G. Yamada, T. Sanno, M. O. Takahashi, Y. Akagi, H. Suwa, S. Fujimoto, M. Udagawa: arXiv:2212.13267 (2022).

Magnetism and superconductivity in ternary chromium chalcogenides

Harald JESCHKE
Research Institute for Interdisciplinary Science, Okayama University
3-1-1 Tsushima-naka, Kita-ku, Okayama 700-8530

We study $CrGeTe_3$ which is a van-der-Waals bound layered ferromagnet. Materials like $CrGeTe_3$ or CrI_3 have been intensely investigated in recent years because detached monolayers still order ferromagnetically and are discussed for various nanotechnological applications.

Recently, pressure experiments for $CrGeTe_3$ reported an interesting temperature-pressure phase diagram; importantly, at high pressures, an insulator to metal transition roughly coincides with increases of Curie-Weiss and magnetic ordering temperatures. Our aim is to understand the phase diagram and to investigate the nature of the strongly correlated metal at high pressures.

We perform calculations using density functional theory (DFT) in combination with dynamical mean field theory (DFMT), as implemented in DCore. Based on experimental crystal structures, we prepare tight binding representations of the DFT bands for pressures up to $P = 10\,\mathrm{GPa}$. Figure 1 shows the spectral function of a ferromagnetic insulating solution at ambient pressure [1]. The difficulty in this material is the fact that Te $6p$ bands are very important at the Fermi level. The insulator to metal transition involves pressure induced widening of Te $6p$ bands which then establish a Fermi surface at around 5 GPa. By analyzing the renormalization factor Z where $Z^{-1} = 1 - \partial \mathrm{Im}\Sigma(i\omega)/\partial\omega|_{\omega\to 0^+}$, we find that correlations of some Cr $3d$ orbitals are enhanced by increasing pressure.

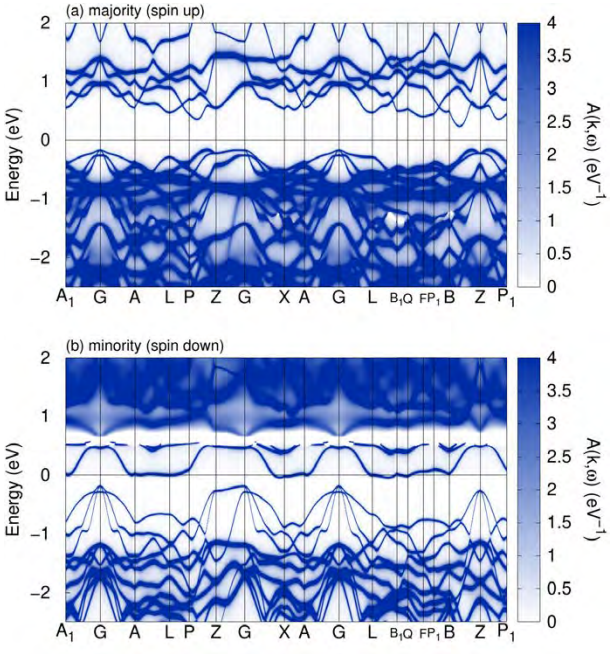

Figure 1: Spectral function for the ferromagnetic state of $CrGeTe_3$ at $P = 0\,\mathrm{GPa}$ and $T = 100\,\mathrm{K}$. Chromium magnetic moments are close to $3\,\mu_\mathrm{B}$.

References

[1] H.-X. Xu, M. Shimizu, J. Otsuki, H. O. Jeschke, in preparation.

Fluctuation exchange approximation calculations for the superconducting transition temperatures and pairing symmetries of organic charge transfer salts

Harald JESCHKE
Research Institute for Interdisciplinary Science, Okayama University
3-1-1 Tsushima-naka, Kita-ku, Okayama 700-8530

BEDT-TTF (bisethylene-dithio-tetrathiafulvalene) is a famous nearly flat molecule that forms hundreds of charge transfer (CT) salts, among them a number of famous superconductors. We study eight of the known ambient pressure superconductors in the κ phase where dimers of BEDT-TTF molecules form a triangular lattice which is doped with one hole per dimer. Our aim is to improve on earlier studies based on random phase approximation and two-particle selfconsistent approximation to predict the material dependence of superconducting transition temperature and order parameter. Our newly developed multi-orbital, multi-site fluctuation exchange approximation (flex) code was parallelized with OpenMP and MPI methods.

Figure 1 shows the leading solutions of the Eliashberg equation for one of the materials, together with the trend of the leading eigenvalues [1]. T_c trends are captured well by the dominant eigenvalue of the Eliashberg equation for five high-T_c materials. However, for three low-T_c materials, the present approach overestimates the strength of the s-wave solution. A possible reason for this discrepancy is the intra-dimer, inter-site interaction V that has been neglected so far and that is expected to play an important role in the κ-type CT salts.

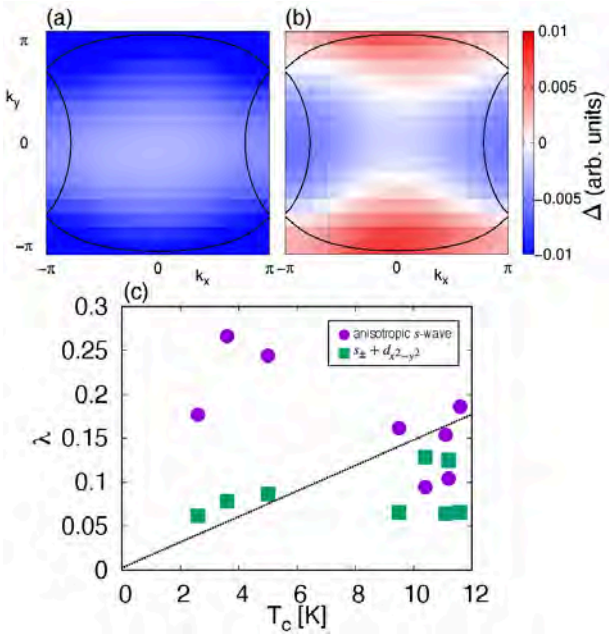

Figure 1: (a), (b) Imaginary part of an inter-dimer element of the anomalous self-energy for the two leading solutions for κ-$(ET)_2Cu[N(CN)_2]Br$. (c) Eigenvalues λ for anisotropic s-wave and for $s_\pm + d_{x^2-y^2}$-wave.

References

[1] M. Shimizu, D. Guterding, J. Otsuki, H. O. Jeschke, in preparation.

Numerical studies for science of bulk-edge correspondence and topological phases

Yasuhiro HATSUGAI

Department of Physics, University of Tsukuba

Tennodai 1-1-1, Tsukuba, Ibaraki 305-8571

The topological phases are independent of the symmetry breaking. It implies that there is no fundamental order parameter to characterize it. Most of them are gapped, and low-energy gapless excitation is absent. It implies that the bulk is hidden. However, with edges or boundaries, there exist low-energy gapless excitations that are localized only near the system boundaries and characterize the phase. This is the bulk-edge correspondence.

A topological pump (adiabatic pump) is another kind of topological phenomenon where the bulk-edge correspondence again governs the phenomena. Here the bulk-edge correspondence is special, that is, the edge states are hidden since the gapless nature of the edge states implies that the edge state cannot be observed by an experimental finite speed pump. Experimental observables for the topological pump are the center of mass (polarization) of the bulk, which is described by the Chern number integrated over the torus spanned by the time and gauge twist. In Fig. 1, we have shown numerical evaluation of the Chern numbers for the topological pump of SU(Q) interacting fermions [2]. The relation between the edge states spectrum and the Chern numbers are consistently discussed by using numerical studies.

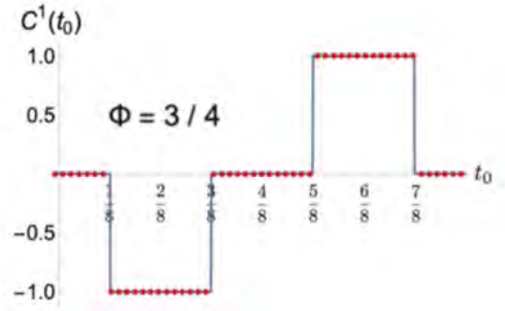

Fig. 1 Numerical results of the Chern number of SU(Q) topological pump (from ref. [2]).

References

[1] Y. Hatsugai, Phys. Rev. Lett. 71, 3697 (1993).).

[2] Y. Hatsugai, and Y. Kuno, arXiv:2210.11646

Effects of flux structures on Majorna excitations in Kitaev spin liquids

Akihisa Koga
Department of Physics, Tokyo Institute of Technology, Meguro, Tokyo 152-8551

Quantum spin liquids in the Kitaev model have been studied intensively in recent years. It is known that in the Kitaev model, spin degrees of freedom are split into itinerant Majorana fermions and localized fluxes due to the spin fractionalization. The ground state belongs to the flux-free state and low energy properties are described by itinerant Majorana fermions. In fact, the Majorana edge current has been observed in the half-quantized plateau in the thermal quantum Hall effect. Furthermore, the Majorana-mediated spin transport has been theoretically suggested, which should stimulate further investigation to realize quantum devices using Majorana fermions.

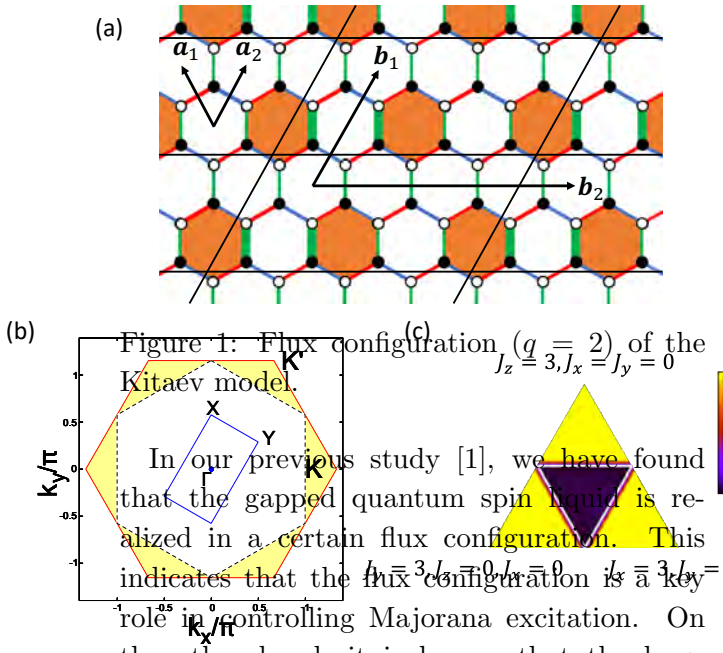

Figure 1: Flux configuration ($q = 2$) of the Kitaev model.

In our previous study [1], we have found that the gapped quantum spin liquid is realized in a certain flux configuration. This indicates that the flux configuration is a key role in controlling Majorana excitation. On the other hand, it is known that the large anisotropy in the exchange couplings stabilizes the gapped quantum spin liquid, which should be described by the toric code. Then a question arises. Are the above gapful states with distinct origins are adiabatically connected to each other? To answer this question, we consider several flux configurations to investigate how the anisotropy in the exchange couplings affects the Majorana excitations.

Motivated by this, we deal with the anisotropic Kitaev model with flux configurations. In particular, we focus on the triangular flux configurations, where the fluxes are periodically arranged in the honeycomb sheet, as shown in Fig. 1. Systematic numerical calculations demonstrate how the anisotropy of the exchange couplings and flux configuration induce the excitation gap. The induced gapped quantum spin liquid states are distinct from the gapped one realized in the large anisotropic limit. We then clarify the nature of gapped states in the Kitaev model, regarding the flux configuration as the superlattice potential for the flux-free state [2, 3].

References

[1] A. Koga, Y. Murakami, and J. Nasu, Phys. Rev. B **103**, 214421 (2021).
[2] A. Hashimoto, Y. Murakami, and A. Koga, J. Phys.: Conf. Ser. 2164, 012028 (2022).
[3] A. Hashimoto, Y. Murakami, and A. Koga, arXiv:2303.04295.

Molecular dynamics simulation of disease-related biomolecules

Hisashi Okumura

Exploratory Research Center on Life and Living Systems,

Institute for Molecular Science, Okazaki, Aichi 444-8585

Proteins maintain their functions with correctly folded structures. However, when their concentration increases due to, for example, aging, they aggregate to form oligomers, spherical aggregates, and amyloid fibrils, needle-like aggregates. These protein aggregates are associated with about 40 human neurodegenerative diseases. For instance, the amyloid-β (Aβ) peptide is related to Alzheimer's disease. We have performed several molecular dynamics (MD) simulations of Aβ aggregates. In this fiscal year, we performed MD simulations of the dimerization process of Aβ peptides and specified the key residue for aggregation of Aβ peptides.

Aβ has two isoforms: Aβ40 and Aβ42. Although the difference between Aβ40 and Aβ42 is only two residues in the C-terminus, Aβ42 aggregates much faster than Aβ40. It is not clear why the C-terminal two residues accelerate the aggregation. To investigate the dimerization process, we performed Hamiltonian replica-permutation molecular dynamics simulations of two Aβ40 peptides and those of two Aβ42 peptides using the supercomputer at the Supercomputer Center, the Institute for Solid State Physics, the University of Tokyo [1]. The replica-permutation method is an improved version of the replica-exchange method, in which the transition ratio of replicas in the temperature or parameter space is improved.

As a result, we identified the key residue, Arg5, for the Aβ42 dimerization. The two C-terminal residues in Aβ42 tend to form contact with Arg5 because of the electrostatic attraction between them, stabilizing the β-hairpin. This β-hairpin promotes dimerization through the intermolecular β-sheets.

Thus, we asked experimental collaborators to examine the effects of amino-acid substitutions of Arg5 to verify our theoretical prediction. We found that the mutations remarkably suppressed the aggregation of Aβ42. In this way, our prediction was approved by the experiments.

References

[1] S. G. Itoh, M. Yagi-Utsumi, K. Kato, and H. Okumura, ACS Chem. Neurosci. **13,** 3139 (2022).

Nontrivial properties of interface and finite size effects of free energies

Naoko NAKAGAWA
Department of Physics, Ibaraki University
2-1-1 Bunkyo, Mito, Ibaraki 310-8512

We investigate liquid-gas coexistence associated with first-order transitions via molecular dynamics simulations using LAMMPS. We managed two kinds of systems, one is a simple fluid of Lennard-Jones particles and the other is the two components fluid of argon and krypton.

In the former systems, we notice the configuration of the coexistence states and examine the thermodynamic quantities. Despite the finiteness of the system size, we find a sharp interface separating the two phases, whereas both the shape and the position of the interfaces largely fluctuate.

We set temperature and mean mass density as almost particles are in liquid, while a small number of particles be in gas. When the aspect ratio of the box confining the particles is close to unity, we observe typically a bubble with a round-shaped interface. Changing the aspect ratio, the shape of the interface transitioned into a flat shape, where the gas occupies a stripe region that may situate adjacent to the boundary. To characterize the transition, we calculate the virial pressure corresponding to the mean pressure over the system, which may provide the global thermodynamic properties in phase coexistence. With the transition for the shape of the interface, we find a significant change in the value of the virial pressure. It drops even to a negative value when the size of the bubble is too small. This indicates that the system behaves attractively, although the liquid or gas without coexistence,

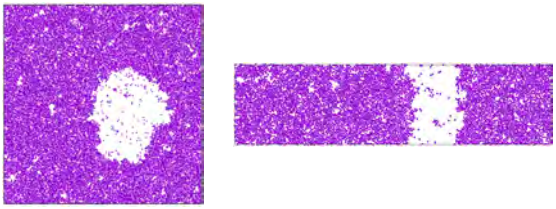

Figure 1: Phase coexistence of liquid and gas in the aspect ratio 1 and 4.

or the coexistence with a flat interface, shows positive pressure as is usual. Such anomaly of the virial pressure suggests that the system is not explained by thermodynamics in equilibrium, and may possess meta-stable or unstable characteristics. We will proceed calculations to characterize the local states for identifying the mechanism to maintain the metastability.

We also investigated the liquid-gas coexistence for the two components fluid of argon and krypton using the mixing free energy. The mixing free energy is numerically determined by applying the formula derived in [1]. We find that the finite size effects lead to the violation of the convexity in the free energy. To examine the stability of the coexistence states showing the violation of the convexity, we carefully examine the possibility of hysteresis. Up to now, we confirm that rather smaller systems do not show hysteresis in our setup. While we need further investigations with various system sizes, the result indicates that the finiteness of the system size may induce the violation of the

convexity in free energy in a different context from the metastability.

We have used the L4 CPU of System B with 4 nodes in 512 parallel computation using MPI for the calculation of 2×10^4 particles, the L16 CPU of System B with 16 nodes in 2048 parallel computation using MPI for the calculation of 8×10^4 particles, the L32 CPU of System B with 24 nodes in 3072 parallel computation using MPI for the calculations of 5×10^5 and 1×10^6 particles.

References

[1] A. Yoshida and N. Nakagawa: *Phys. Rev. Res.* **4**, 023119 (2022)

Nonequilibrium relaxation temperature scaling: Applications to quantum systems

Yoshihiko NONOMURA
MANA, National Institute for Materials Science
Namiki 1-1, Tsukuba, Ibaraki 305-0044

We numerically revealed that the critical nonequilibrium relaxation behaviors in cluster algorithms are described by the stretched-exponential simulation-time dependence of physical quantities in various classical spin systems [1, 2, 3] and in a quantum phase transition [4], and derived such a relaxation formula phenomenologically [5]. The nonequilibrium-to-equilibrium (NE-EQ) scaling used in these studies [1, 3, 4] were generalized to off-critical behaviors, and such a scaling was called as the "temperature scaling" [6].

Here we show that the temperature scaling also holds in quantum phase transitions. As an example, we consider the Néel-dimer quantum phase transition in the columnar-dimerized $S = 1/2$ antiferromagnetic Heisenberg model on a square lattice [4]. When the ratio of the strength of dimerized bonds to other bonds are taken as $(1 + \delta) : 1$, the staggered susceptibility in equilibrium diverges in the vicinity of the critical point δ_c as $\chi_{st}(t = \infty, \delta) \sim (\delta - \delta_c)^{-\gamma}$ with $\delta_c = 0.90947(6)$ [4]. Combining this formula with the initial-time stretched-exponential critical relaxation form $\chi_{st}(t; \delta_c) \sim \exp(ct^\sigma)$, we have $\chi_{st}(t, \delta)(\delta - \delta_c)^\gamma \sim \exp[ct^\sigma + \ln(\delta - \delta_c)^\gamma]$, or

$$\chi_{st}(t, \delta)(\delta - \delta_c)^\gamma \sim f_{sc}[ct^\sigma + \ln(\delta - \delta_c)^\gamma]. \quad (1)$$

Scaling results for the $L \times L$ periodic-boundary system with $L = 160$ and inverse temperature $\beta = L$ in the loop algorithm from dimer configurations are given in Figure 1. Using the estimate $\gamma = 1.400(3)$ obtained from this figure and the estimate $\gamma/\nu = 1.973(4)$ based on the NE-EQ scaling up to $L = 160$ [4], we have $\nu = 0.710(2)$ only with a diagonal quantity χ_{st}.

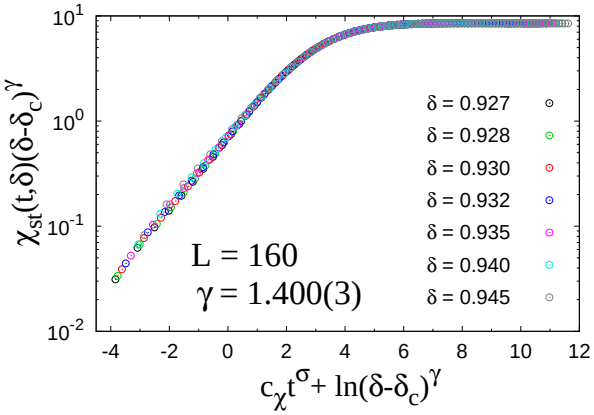

Figure 1: Temperature scaling of the staggered susceptibility in the 2D columnar-dimerized $S = 1/2$ antiferromagnetic Heisenberg model.

References

[1] Y. Nonomura, J. Phys. Soc. Jpn. **83**, 113001 (2014).

[2] Y. Nonomura and Y. Tomita, Phys. Rev. E **92**, 062121 (2015).

[3] Y. Nonomura and Y. Tomita, Phys. Rev. E **93**, 012101 (2016).

[4] Y. Nonomura and Y. Tomita, Phys. Rev. E **101**, 032105 (2020).

[5] Y. Tomita and Y. Nonomura, Phys. Rev. E **98**, 052110 (2018).

[6] Y. Nonomura and Y. Tomita, Phys. Rev. E **102**, 052118 (2020).

HPC-based fusion of quantum simulation, experiment analysis and data-driven science

Takeo Hoshi[1,2]

[1] *Department of Mechanical and Physical Engineering, Tottori University, 4-101 Koyama-Minami, Tottori 680-8550, Japan.*

[2]*Slow Positron Facility, Institute of Materials Structure Science, High Energy Accelerator Research Organization (KEK), Oho 1-1, Tsukuba, Ibaraki, 305-0801, Japan.*

We developed several new features on 2DMAT [1-6], an open-source data-analysis software for advanced experimental measurement techniques. 2DMAT was developed by the PASUMS project at FY2020, 2021[1]. A major achievement in the present project is the automated optimization of the massively parallel computation of the population annealing Monte Carlo (PAMC) method [7]. As results, we found an almost ideal parallel efficiency not only on the ISSP supercomputer (ohtaka) but also on the Fugaku supercomputer with upto 10^4 nodes [8] . As an application study, we used 2DMAT for the data analysis of total-reflection high-energy positron diffraction (TRHEPD)[9]. TRHEPD is an innovative measurement technology for the surface structure analysis and was realized at Slow Positron Facility, KEK [9]. The experimental setup of TRHEPD is similar to that of reflection high-energy electron diffraction (RHEED) but TRHEPD reveals the surface sensitivity and was used for the determination of surface structure. 2DMAT was applied to the analysis of Ge(001)-c4x2 surface structure as a test of the Bayesian inference by PAMC. [8] We analyzed the experiment diffraction data in the one-beam condition, in which only the z-coordinate of atom positions are measured. The Bayesian posterior probability distribution $P(X|D)$ was calculated for the data set of the atom positions X with the given experimental diffraction data set D and reproduced the correct atomic position of the $N_{\mathrm{a}} = 6$ atoms of the top-most and several subsurface layers. Moreover, the correct number of the atoms ($N_{\mathrm{a}} = 6$) was also reproduced from the calculated model evidence $P(D)$. In conclusion, the PAMC analysis, as a global search, determined the correct surface structure without any initial guess. Other application studies are ongoing.

References

[1] https://www.pasums.issp.utokyo.ac.jp/2DMAT

[2] K. Tanaka, *et al*. (T. Hoshi), Acta. Phys. Pol. A 137, 188 (2020).

[3] T. Hoshi, *et al*. (T. Hoshi), Comp. Phys. Commun. 271, 108186 (2022).

[4] T. Hanada, *et al*., Comp. Phys. Commun. 277 108371 (2022).

[5] Y. Motoyama, *et al*. (T. Hoshi), Comp. Phys. Commun. 280, 108465 (2022).

[6] K. Tanaka, *et al*. (T. Hoshi), JJAP Conf. Series 9, 011301 (2023).

[7] K. Hukushima, Y. Iba, AIP Conf. Proc. 690, 1604 (2003).

[8] N. Kinoshita, *et al*. (T. Hoshi), in JPS meeting, 22-25, Mar. 2023.

[9] https://www2.kek.jp/imss/spf/eng/

Chaotic dynamics in quantum many-body systems

Masaki TEZUKA

Department of Physics, Kyoto University, Kitashirakawa, Sakyo-ku, Kyoto 606-8502

The Sachdev-Ye-Kitaev (SYK) model is a model of fermions with independently random all-to-all four-point interactions obeying the Gaussian distribution. The model, both for Majorana and complex fermions, has an analytic solution in the limit of large number of fermions. The Lyapunov exponent, defined by the out-of-time ordered correlator, realizes the universal upper bound at low temperatures.

Previously, we studied the effect of a random hopping term, two-fermion interactions, added to the model [1]. The chaos bound behavior is lost and the eigenenergy spectrum becomes uncorrelated. The localization transition can be understood as a Fock-space localization, a type of many-body localization. We have obtained physical quantities related to this transition, such as the location of the transition point as well as the moments of the eigenstate wavefunctions and bipartite entanglement entropy close to the transition analytically and confirmed numerically [2].

A “sparse” version of the SYK model, in which the number of randomly chosen non-zero interaction terms is only on the order of the number of fermions, have been proposed a few years ago, and for Gaussian random couplings, the sparse model reproduces essential features of the original SYK model [3]. Using the ISSP Supercomputer, we analyzed the spectral statistics of a further simplification of the sparse SYK model, in which the magnitude of the nonzero couplings between Majorana fermions are set to be a constant [4]. In fact, this simplification is an improvement, as the spectral correlation is stronger and thus closer to the random-matrix universality for the same number of non-zero couplings, compared to the Gaussian random case.

We also studied the quantum error correction (QEC) capabilities of the unitary time evolution according to the SYK type Hamiltonians by the Hayden-Preskill protocol. This is a process in which one tries to decode an unknown quantum state thrown into a quantum many-body system with the knowledge of the initial state of the system and the time evolution, by accessing only a part of the system after the evolution. The error estimate for random unitary evolutions obeying the circular unitary (Haar) ensemble has been known. For the sparse SYK model, the QEC error estimate approaches the Haar value after a short time if the spectral statistics is random-matrix like. In the presence of two-fermion interactions, departure from the Haar value is observed before the Fock space localization [5].

References

[1] A. M. Garcia-Garcia, B. Loureiro, A. Romero-Bermudez, and M. Tezuka, Phys. Rev. Lett. **120** (2018), 241603.

[2] F. Monteiro, T. Micklitz, M. Tezuka, and A. Altland, Phys. Rev. Research **3** (2021), 013023; F. Monteiro, M. Tezuka, D. A. Huse, and T. Micklitz, Phys. Rev. Lett. **127** (2021), 030601.

[3] S. Su *et al.*, arXiv:2008.02303; A. M. Garcia-Garcia *et al.*, Phys. Rev. D **103**, 106002 (2021).

[4] M. Tezuka, O. Oktay, E. Rinaldi, M. Hanada, and F. Nori, Phys. Rev. B **107**, L081103 (2023).

[5] Y. Nakata and M. Tezuka, arXiv: 2303.02010.

Molecular Dynamics Simulation of Dissolution of Stretched PEG Crystal in Aqueous Solution

Koichi Mayumi, Kosuke Aomura, Haru Shinohara

The Institute for Solid State Physics,

The University of Tokyo, Kashiwa-no-ha, Kashiwa, Chiba 277-8581

Hydrogel is a material in which water is confined in a polymer network. Hydrogel has high biocompatibility and is expected to be applied to biomaterials, but its mechanical strength has been a problem. In our laboratory, we have developed a hydrogel with both toughness and resilience by using the self-reinforcing effect [1]. In this self-reinforcing gel, polyethylene glycol (PEG) is used as the main chain of the polymer network and water as the solvent. When the strain is removed, the PEG chains form hydration with the solvent water, and the crystals are quickly melted. Such solvation and dissolution processes are thought to play an important role in the strain-induced crystals that are reversible against elongation. In this study, we performed all-atom molecular dynamics simulations to understand extended PEG crystal dissolves in aqueous solution.

Based on the structures reported from X-ray diffraction results [2, 3], all-atom models of zigzag PEG chain crystals consisting of 24 PEG chains with 42 repeat units were created (Fig. 1). After energy minimization calculations, 4200 water molecules are added to the box so that the polymer fraction was 38 wt%. A stretching force was applied to both ends of each polymer chain for 400 ns. The applied force f was set at 6 points: 0, 10, 30, 70, 100, and 210 kJ/(mol nm). GROMACS 2016.5 was used as computational software. Simulations were performed on Ohtaka, ISSP supercomputer system B. The number of atoms in the

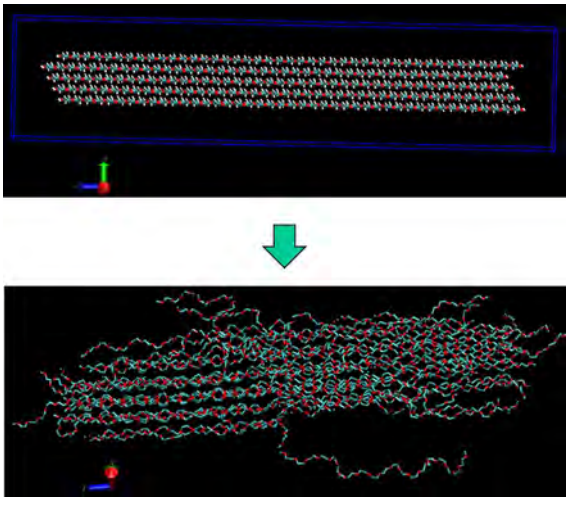

Fig. 1 Snap-shots of PEG zig-zag crystals stretched under f = 10 kJ/(mol nm) at time t = 0 and t = 400 ns.

simulation box was about 24,000, and the computation speed was about 200 ns/day with a parallel number of 512.

For f = 0 kJ/(mol nm), the zigzag chain crystals are dissolved within 200 ns, which is consistent with the rapid dissolution of stretched induced PEG crystals just after the applied stretching force is unloaded in our experiments. When f is 10 kJ/(mol nm), the zigzag chain crystal is dissolved and then the a helical PEG crystal is formed..

References

[1] C. Liu, N. Morimoto, L. Jiang, S. Kawahara, T. Noritomi, H. Yokoyama, K. Mayumi, K. Ito, *Science*, **372,** 1078-1081(2021).
[2] Takahashi, Y., Tadokoro, H. *Macromolecules,* **6**, 672-675 (1973).
[3] Takahashi, Y., Sumita, I., Tadokoro, H. *J. Polym. Sci., B, Polym. Phys.*, **11**, 2113-2122 (1973).

Molecular dynamics simulation for chemical reactions in multicomponent systems of thermosetting resins

Yutaka Oya

Department of Materials Science and Technology,

Tokyo University of Science, Niijuku, Katsushika-ku, Tokyo 125-8585

In this year, we have studied following two topics. The first is to establish the methodology for reproducing the crosslinked reactions of thermosetting polymers based on full-atomistic molecular dynamics simulation. We focused on multicomponent system including base resin with epoxy groups, curing agent with amine groups and lignin with hydroxyl groups, which is one of promising candidates for matrix of bio-based composites. The chemical reactions among these components were successfully realized for systems of several hundred thousand atoms by LAMMPS software. In the future study, we systematically investigate the thermal and mechanical characteristics, such as Young's modulus, strength, glass-transition temperature, for the crosslinked structures formed by these molecules.

The second is to investigate the stacking structure of organic photovoltaic materials. It is well known that electron transfer occurs through the π-π stacking structure of the donor and acceptor molecules. Such photoexcited reactions of conjugated polymers are expected to be applied to nondestructive inspection of mechanical damages of a composite. In this study, full atomic molecular dynamics simulations were performed for reproducing the equilibrium structure of the system including IT-4F (donor molecule) and PDTB (accepter molecule) as shown in Figure 1. Further, frequency distributions for each type of stacking structure in the system were analyzed. As a result, it was found that J-aggregation between IT4F and PDTB molecules is dominant in the system. In the future study,

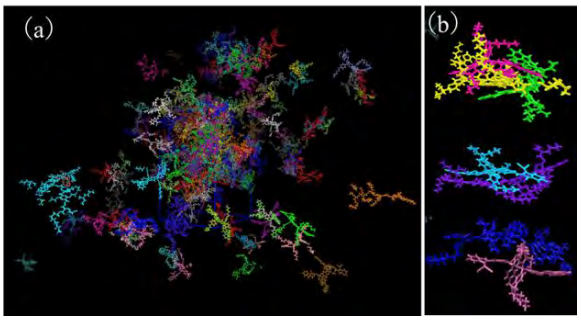

Figure 1. (a) Equilibrium structure of IT4F and PDTB molecules. (b) Snapshots of typical stacking structures obtained by molecular dynamics simulations.

Numerical study on low-energy states of quantum spin systems

Hiroki NAKANO
Graduate School of Science, University of Hyogo
Kouto, Kamigori, Hyogo 678-1297, Japan

Since researchers are often faced with many-body problems in the condensed matter physics, it is difficult to estimate physical quantities precisely. One of the typical issues is a quantum spin system. To study a quantum spin system, numerical approaches have widely and effectively been employed. Computational studies that were carried out have provided us with useful information of the target systems.

Within the field of quantum spin systems, three methods have been effectively used. The first and traditional one is the numerical diagonalization method. The second method is the quantum Monte Carlo (QMC) simulation. The third one is the density matrix renormalization group (DMRG) method. Each of these methods has advantages; however, it has also disadvantages at the same time. The QMC simulations can treat significantly large systems irrespective of the spatial dimensions of the systems; on the other hand, the negative sign problem with this approach prevents us with a difficulty in precise evaluation of physical quantities in frustrated systems. When the spatial dimension of a target system is one, however, the DMRG method is very useful irrespective of whether or not the target system includes frustration. Unfortunately, this method is still under development for the cases when the spatial dimension is larger than one. We can apply the numerical diagonalization method to various systems irrespective of the presence of frustrations and the spatial dimension. This method, on the other hand, has a severe weak point that it can treat only systems with very small sizes. To overcome this disadvantage of the numerical diagonalization method, we developed a hybrid-type parallelized code of Lanczos diagonalization[1]. This code enables us to treat various large systems that have not been treated yet within this method. We, therefore, study various quantum spin systems by this method as a primary approach in this project.

In the project in 2022, we tackled the $S = 1$ Heisenberg antiferromagnet in one dimension[2]. We successfully carried out Lanczos diagonalizations of this system up to 30 sites under the twisted boundary condition. The 30-site system was treated within Lanczos-diagonalization studies for the first time to the best of our knowledge. Note here that the largest treated matrix dimension is 18,252,025,766,941. Our results were analyzed via a convergence-acceleration technique; we finaly concluded

$$\Delta/J = 0.410479239 \pm 0.000000041$$

as the Haldane gap, namely, the spin excitation above the nondegenerate ground state. We confirmed that this result agrees with the result from the DMRG method[3]. We also studied the $S = 1/2$ Heisenberg antiferromagnet on the floret-pentagonal lattice[4]. Our calculations successfully clarified the behavior around the five-ninth of the saturation magnetization in its magnetization process. Our studies contribute much to our deeper understandings of

the quantum magnetism. Further investigations would clarify nontrivial quantum effects in these systems.

References

[1] H. Nakano and A. Terai: J. Phys. Soc. Jpn. **78**, 014003 (2009).

[2] H. Nakano, H. Tadano, N. Todoroki and T. Sakai: J. Phys. Soc. Jpn. **91**, 074701 (2022).

[3] H. Ueda and K. Kusakabe: Phys. Rev. B **84**, 054446 (2011).

[4] . R. Furuchi, H. Nakano, and T. Sakai: arXiv:2209.13887 to be published in JPS Conf. Proc.

Study of ground states and dynamics in frustrated quantum magnets using MPS-based simulations

Matthias GOHLKE
Theory of Quantum Matter Unit, Okinawa Institute of Science and Technology
1919-1 Tancha, Onna-son, Okinawa 904-0495

Competing interactions—or frustration—between the constituents of a many-body system have proven to be an origin of exotic phases of matter. A famous example in this context are quantum spin liquids (QSL), that do not exhibit conventional magnetic order of spin-dipolar moments, but rather are defined by emergent gauge fields, fractionalized excitations, and topological order. A topical example in this context are Kitaev-like frustrated magnets, that exhibit a bond-dependent spin-exchange resulting in exchange frustration and, for certain choices of parameters, can result in a QSL ground state. Part of the computational resources provided by ISSP has been used to study the related anisotropic Kitaev-Γ model [see (II)].

On the other hand, ordering of higher moments like spin-quadrupoles may occur as well. Unlike spin-dipolar order, spin-quadrupolar order is defined by a director—an arrow without a head—in close analogy to the rods of nematic order and liquid crystals. Thus, spin-quadrupolar order is also named quantum spin nematic (QSN). Part of the resources have been used to study the QSN phase stabilizing in a frustrated ferromagnet with external magnetic field [see (I)].

(I) QSN in a Spin-$\frac{1}{2}$ Frustrated Ferromagnet. Here, we focus on a quantum magnet with spin-$\frac{1}{2}$ degrees of freedom. Such magnets can only exhibit a QSN states if two spin-$\frac{1}{2}$ are combined into an effective spin-1 [1]. In fact, such QSN states on bonds has theoretically been observed in frustrated ferromagnets with ring-exchange on the square lattice [2].

Experimentally, the nature of such a ground state is intrinsically difficult to verify, due to the lack of probes that couple directly to the spin-quadrupole moments. Instead, it is necessary to examine the dynamics of a QSN: A continuous symmetry for the director of a spin-quadrupole remains, that give rise to a gapless Goldstone mode [3, 4].

Here, we study the square-lattice frustrated J_1-K model [1], with dominant ferromagnetic Heisenberg exchange J_1 between nearest neighbor spins, cyclic ring-exchange K around squares, and h_z the Zeeman coupling to a magnetic field along the z-axis. Using iDMRG and the matrix product states (MPS) framework as well as a recently developed exact diagonalization (ED) method near saturation [5], we confirm the existence of the QSN phase in an extended range of $K/|J_1|$. Overall we find a good agreement between high-field ED on symmetric clusters and iDMRG on cylindrical geometries with a circumference of $L_{\mathrm{circ}} = 6$ sites. The QSN phase is sandwiched between high-field polarized and 4-sublattice AF phase. Additional phases (Neél, vector-chiral) occur for large K.

Given the ground state as an MPS, we can then obtain dynamical properties via a time-evolution unitary $U(dt)$ represented as a matrix product operator. We confirm the condensation of two-magnon bound state at the corresponding wave vector of the QSN

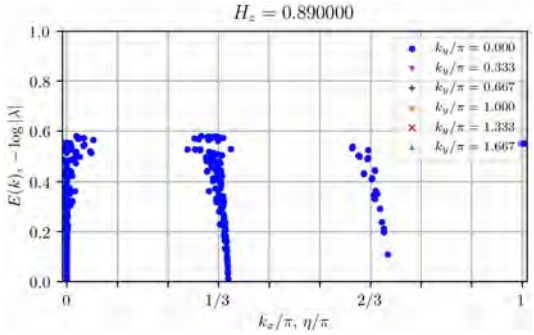

Figure 1: TM spectrum illustrating dominant correlations at $k_x = 0$ as well as incommensurate correlations near $k_x \approx 0.35\pi$.

state. Within the QSN phase, we observe (1) the magnon-like excitation that remains fully gapped, and (2) a gapless mode with its spectral weight in the dipolar structure factor vanishes as $\boldsymbol{q} \to 0$ & $\omega \to 0$ as predicted by prior mean-field studies. We do, however, observe relevant qualitative differences: an additional mode with a gapless node at an incommensurate, field-strength dependent wave vector occurs. Within this term, we have focused on identifying the incommensurate mode by means of the MPS transfer matrix (TM). The TM spectrum contains all the information on correlations. Momentum information is contained through the complex phase of the TM eigenvalues, and momentum along the circumference being a well defined quantum number as long as translation symmetry remains intact. Thus, the position in momentum space of the gapless modes can be extracted from the MPS, cf. Fig. 1.. Indeed, we find perfect agreement between the gapless mode in the dynamics and the TM, which will help us in further elucidating the nature of the incommensurate gapless mode accompanying the QSN phase.

All MPS-related simulations have been carried out using TenPy [8]. TenPy makes use of Cython and calls heavily optimized Lapack and Blas routines matrix operations, e.g. singular value decomposition.

(II) Extended QSL in an Anisotropic Kitaev-Γ Model. The characterization of quantum spin liquid phases in Kitaev materials has been a subject of intensive studies over the recent years. Most theoretical studies have focused on isotropic coupling strength in an attempt to simplify the problem. We, instead, have focused on an extended spin-1/2 Kitaev-Γ model on a honeycomb lattice with an additional tuning parameter that controls the coupling strength on one of the bonds [6], allowing us to connect the limit of isolated Kitaev-Γ chains, which is known to exhibit an emergent $SU(2)_1$ Tomonaga-Luttinger liquid (TLL) [7], to the two-dimensional model. We find that the critical properties of the TLL persist for finite inter-chain coupling, and a QSL develops in analogy to *sliding Luttinger liquids* that differs from the Kitaev spin liquid.

We have employed the TenPy package [8] to obtain the ground state in MPS form, study its scaling behavior via the MPS transfer matrix spectrum, and obtain dynamical properties.

References

[1] A. Andreev and I. Grishchuk, Sov. Phys. JETP **60** (1984) 267.

[2] N. Shannon, T. Momoi, and P. Sindzingre, Phys. Rev. Lett. **96** (2006) 027213.

[3] R. Shindou, S. Yunoki, and T. Momoi, Phys. Rev. B **87**, (2013) 054429.

[4] A. Smerald, H. T. Ueda, and N. Shannon, Phys. Rev. B **91** (2015) 174402.

[5] H. Ueda, S. Yunoki, and T. Shimokawa, Comp. Phys. Comm. **277** (2022) 108369.

[6] M. Gohlke, J. C. Pelayo, T. Suzuki, arXiv:2212.11000 (2022). *See also report by T. Suzuki.*

[7] Yang et al. Phys. Rev. Lett. **124**, 147205 (2020).

[8] J. Hauschild, and F. Pollmann, SciPost Phys. Lect. Notes 5 (2018).

Dynamical properties of the extended Kitaev-Γ model on a honeycomb lattice

Takafumi SUZUKI

Graduate School of Engineering,

University of Hyogo, Shosha, Himeji, Hyogo 670-2280

We have used ISSP supercomputer resources for the following two topics: (1) dynamical properties of the extended honeycomb-lattice Kitaev-Γ model and (2) supersolid states in two-dimensional hard-core bosonic Hubbard model with dipole interactions.

(1) Dynamical properties of the extended honeycomb-lattice Kitaev-Γ model

In this project, we have investigated ground states and dynamical properties of the S=1/2 Kitaev-Γ model [1] on a honeycomb lattice by the numerical exact diagonalization and density-matrix-renormalization-group approaches. The S=1/2 Kitaev-Γ model on a honeycomb lattice was proposed as the effective model of the honeycomb-lattice magnet, α-$RuCl_3$. So far, the ground-state phase diagram of this model with the isotropic coupling strength has been studied intensively. In recent experiments on the related compounds, RuX_3 (X=Br, I) [3], it has been reported that applying pressure can control the anisotropy of the coupling strength. The ground-state phase diagram of the S=1/2 Kitaev-Γ model with anisotropic interactions has not been fully understood yet. Note that the anisotropy means that by tuning the anisotropy, the model changes from the Kitaev-Γ spin chains to the isolated dimer model via the isotropically interacting model.

In the previous study, we focused on the ground phase diagram and the low-lying excitation in the case where the Kitaev interaction (K) and the Γ interaction (Γ) are negative and positive, respectively [4]. We clarified that the Tomonaga-Luttinger liquid (TLL) appearing in the spin chain limit (d=0) [5] persist for the finite interchain interactions and it becomes a proximate Tomonaga-Luttinger liquid (pTTL), which is analogous to sliding TLL [6]. In the pTTL phase, the dispersion curves for the low-lying excitation show a linear behavior around gapless wave-number points, which is similar to the characteristics observed in the S=1/2 antiferromagnetic Heisenberg chain. In this project, we have investigated the remaining part; the ground state and the excitations for $K \leqq 0$ and $\Gamma \geqq 0$. We have found that in the spin chain limit, an incommensurate phases exists between the TLL phase and D_4-symmetry-breaking phase [5]. In addition, we have found that the presence of the extended Kitaev spin liquid [5] is still controversial [7]. This implies that the extended Kitaev spin liquid phase is replaced by a different state from the D_3 ordered state [5]. These states we newly found in the chain limit changes two-dimensional long-range orders when the interchain interaction becomes finite [7].

(2) Supersolid states in two-dimensional hard-core bosonic Hubbard model with dipole interactions

In this project, we have studied the phase diagram of two-dimensional hard-core bosonic Hubbard model with dipole interactions. Many efforts have been made to realize supersolid states so far and ultracold-atomic gases trapped in optical lattices are candidate stages to study the supersolid states. In lattice Bose-Hubbard models, frustrated interactions play a key role to stabilize the supersolid states. In ref. [8], authors investigated the phase diagram of the two-dimensional bosonic hardcore Hubbard model with the dipole interactions by the mean-filed approach and the infinite entangled-pair-state. It was found that several supersolid states appear in between solid phases with different commensurate fillings by tilting the angle of the dipole axis from the direction perpendicular to the lattice plane. However, the range of the dipole interactions is restricted within a short

range in ref. [8]. Thus, when the farther neighbor interactions are included, whether those supersolid phases are stable or not is unclear.

We have investigated the phase diagram of the two-dimensional bosonic hardcore Hubbard model with the dipole interactions by quantum Monte Carlo computations and have applied two methods to discuss the details of each phase; finite-size-scaling analysis and machine-learning assisted approach. First, we have studied the phase diagram of the same model considered in ref. [8]. We have obtained consistent results with those by the iPEPS calculations. Next, we have investigated the phase diagram by changing the cut-off range of the dipole interactions. It has been found that two quarter solid states (ρ=1/4 and 3/4, where r is filling.) becomes unstable and diagonal-stripe solid states (ρ=1/3 and 2/3) becomes stable. The supersolid state related with the quarter solid disappears.

References

[1] J. G. Rau, E. Lee, and H. -Y. Kee, Phys. Rev. Lett. 112, 077204 (2014).
[2] T. Yamada, T. Suzuki, and S. Suga, Phys. Rev. B **102**, 024415 (2020).
[3] Y. Imai, et al., Phys. Rev. B **105**, L041112 (2022) and Y. Choi, et al., Phys. Rev. B **106**, 174430 (2022).
[4] M. Gohlke, J. C. Pelayo, and T. Suzuki, arXiv:2212.11000.
[5] W. Yang, et al., Phys. Rev. Lett. 124, 147205 (2020) and W. Yang, A. Nocera, and I. Affleck, Phys. Rev. Research 2, 033268 (2020).
[6] R. Mukhopadhyay, C. L. Kane, and T. C. Lubensky, Phys. Rev. B **64**. 045120 (2001).
[7] M. Gohlke, J. C. Pelayo, and T. Suzuki, in preparation.
[8] H.-K. Wu and W.-L. Tu, Phys. Rev. A **102**, 053306 (2020).

Systematic Searches for Grain Boundary Structures and Structure-based Prediction of Multiple Properties

Susumu FUJII
Division of Materials and Manufacturing Science, Osaka University
Yamadaoka, Suita, Osaka, 565-0871
Nanostructures Research Laboratory, Japan Fine Ceramics Center
Mutsuno, Atsuta, Nagoya 456-8587

Grain boundaries (GBs) are ubiquitus in inorganic solid materials except for glasses. At GBs, electronic and atomic structures that are different from its corresponding crystal structure are formed, providing unique properties that often determine macroscopic physical responces of materials. The GB structures vary significantly depending on the orientation between adjoined crystal grains, resulting in a variety of GB properties. Revealing GB structure-property relationship is important to improve the performance of structural and functional materials based on material microstructures.

To correlate GB structures with material properties, there are two technological difficulties. One is that a large-scale data for GB structures and their properties, with an accuracy comparable to first principles calculations, is necessary to provide a general and systematic understanding that is applicable to experimental design of microstructures. Another is that the computational and machine learning method to quantify GB structures and correlate them with properties is not well established. Regarding the latter, the authors reported that the use of structure descriptor and hierarchical clustering can clasify the local atomic environments composing GB structures, and multiple linear regression with the classified data provide an accurate prediction of GB thermal conductivities for MgO with physical interpretations [1].

The main drawback of our previous work is that we use an emprical potential to derive MgO GB structures and their thermal conductivities. In this study, we applied an accurate machine learing potential for silicon, distributed in MACHINE LEARNING POTENTIAL REPOSITORY [2], to our GB structure searches and property evaluations, to give more precise GB structure-property relationship [3]. Silicon is known as a typical semiconductor, and considered as a promising candidate for thermoelectric material. To reduce its high thermal conductivity, nanocrystalline silicon with high GB population has been extensively synthesized, leading to very low thermal conductivity less than 5 W/mK [4]. Revealing the impact of Si GBs on thermal conduction as well as electronic conduction is necessary for further improvement of its thermoelectric conversion efficiency.

We mainly performed GB structure searches with the methods of rigid body translations (RBTs) and structure optimization, and thermal conductivity calculations using perturbed molecular dynamics (MD). The necessary codes for RBTs and perturbed molecular dynamics were developed by the author, and the latter was implemented to the Large-scale Atomic/Molecular Massively Parallel Simula-

tor (LAMMPS) [5].

Using the code for RBTs and LAMMPS for structure optimization, we derived 45 silicon GB structures. Then, perturbed MD simulations were performed for calculating thermal conductivity of each GB structure. The perturbed MD simulations are highly computationally demanding, requiring large computational cells containing from three to thirteen thousands of atoms and with the time steps of more than one million. Repeating this simulation five times with different magnitude of perturbations for each GB yielded a set of statistically accurate thermal conductivities. As 230 separate perturbed MD simulations were necessary, all of them were performed in a single node rather than multiple nodes.

Compiling the GB structure data and thermal conductivity shows that bond angle strains at GBs significantly decreases their thermal conductivities. In addition, structural voids, formed at a few GBs, largely decreases GB thermal conductivities. These trends results from the features of covalent silicon, where one atom bonds strongly with four atoms to form a tetrahedron, and the strong directionality of the bonds tends to create voids at GBs.

In contrast to our results, a revious report using an empirical force field claims that GB energy is the dominant factor for determining GB thermal conductivity of silicon, rather than structural features of GBs [6]. A large scale calculations using supercomputers and the accurate machine learning potential indicate the importance of precisely estimating GB structures and their properties to reveal a robust GB structure-property relationship.

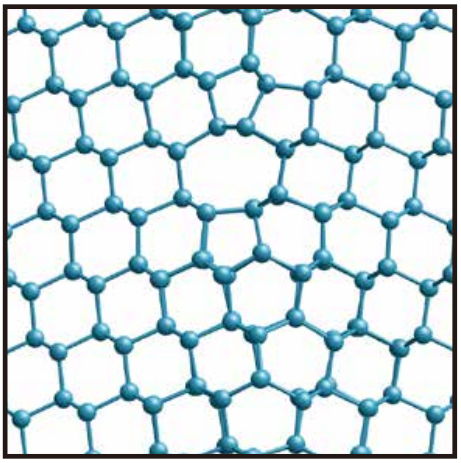

Figure 1: An example of silicon grain boundary structure derived using a machine learning potential.

References

[1] S. Fujii et al., Nature Commun. **11** (2020) 1854.

[2] A. Seko, arXiv:2007.14206.

[3] B. Jugdersuren et al., Phys. Rev. B. **96** (2017) 014206.

[4] S. Fujii and A. Seko, Comput. Mater. Sci. **204** (2022) 111137.

[5] S. Plimpton, J. Comput. Phys. **117** (1995) 1.

[6] J. Hickman and Y. Mishin, Phys. Rev. Mater. **4** (2020) 033405.

Kinetics of phase transition and polyamorphism

Kazuhiro Fuchizaki, Katsumi Nakamura, and Hiroki Naruta
Department of Physics, Ehime University, Matsuyama 790-8577

In FY2022, we continued to undertake the two tasks dealt with in FY2021: One was addressing the validity of the two-phase thermodynamic (2PT) model put forth by Goddard *et al.* [1], and the other was a new trial application of machine learning (ML) to judge the order of a phase transition.

One of our major issues is to explain a sign of the Clapeyron slope of a liquid-liquid transition (LLT) boundary. Liquid phosphorus [2] and sulfur [3] are known to undergo an LLT. However, the former (latter) LLT boundary has a negative (positive) slope, although both liquids are believed to be brought to high-density liquids via polymerization. Because a specific volume must be reduced upon an LLT, the entropy difference between high- and low-density liquids can determine the slope's sign. Therefore, a method to precisely evaluate a liquid entropy is required. The 2PT model has been widely used for this purpose. However, because the model was based on many assumptions, we must examine the validity before applying the model.

The second task is a brand-new research project that has not been tried thus far. We could finish the project in FY2022, and the submitted paper is now under review. Most of the computation time was exhausted in preparing the learning data.

The self-diffusion coefficient of a hard-sphere fluid

Our detailed examination ascertained that the 2PT model bears its validity in estimating the liquid fraction f, which is implicitly defined by

$$f = D(T,\rho)/D^{\mathrm{HS}}(T, f\rho;\sigma), \qquad (1)$$

where D and D^{HS} are the diffusion coefficients for the system in question and the corresponding hard-sphere fluid, respectively. ρ and T are the system's density and temperature. We explicitly include the dependence of D^{HS} on the hard-sphere diameter σ. The neat trick of Goddard *et al.* in deriving a closed equation to determine f was to replace the RHS of Eq. (1) with $D(\rho,T)/D_0^{\mathrm{HS}}(T,\rho;\sigma)$, thereby replacing the definition of f as $f = D(\rho,T)/D_0^{\mathrm{HS}}(T,\rho;\sigma)$. Enskog's theory then allows us to relate D^{HS} to the diffusion coefficient D_0^{HS} and the compressibility factor obtainable from the Carnahan–Starling equation of state. Furthermore, $D_0^{\mathrm{HS}}(T, f\rho) = D_0^{\mathrm{HS}}(T,\rho)/f$ is valid in the zero-pressure limit at which the Chapman–Enskog result is valid. These relations regarding the diffusion coefficients resulted in the cubic equation for f.

Here, we directly solved Eq. (1) instead of solving the cubic equation. We employed the modified Lennard-Jones (mLJ) system with 2048 particles for this judgment. We first evaluated the diffusion coefficient D, Eq. (1) numerator, for the mLJ system at the thermodynamic conditions reported in [4]. Next, we conducted molecular dynamics simulations for a hard-sphere fluid to find D^{HS}. We set $\rho = 0.05$, 0.331, and 0.6 and $\sigma = 1.0$, 1.1, 1.2, and 1.3, where ρ and σ are presented in the mLJ units.

On our way to evaluating the RHS of Eq. (1), we noticed that the empirical formula proposed by Speedy [5] could reproduce the simulated D^{HS} quite satisfactorily. This confirmation enabled us to interpolate the RHS with other fs without carrying out simulations. Finally, we numerically solved Eq. (1), whose RHS was

thus evaluated, to obtain the desired f, which was found to be relatively close to that obtainable from the cubic equation. Therefore, regarding estimating the molecular fraction, we concluded that the treatment of Goddard *et al.* was adequate.

Judging the (dis)continuity of phase transition using ML [6]

Our short-term memory often causes "memory hysteresis" against back-and-forth input of continuously varying input. For example, imagine a series composed of gradually varying pictures from A to B. Suppose that an A-like picture certainly changes to a B-like when we see picture C in the series when we see those pictures from A to B. When we see them in the reverse order, a picture in which we recognize a definite change from B-like to A-like will differ from C, thus inducing memory hysteresis. The size of hysteresis may increase with the smoothness of variation. Because an artificial neural network (ANN) is so constructed that it can reproduce the functionality of a biological neural network (BNN), an ANN would behave like a BNN when a set of continuously changing patterns is input in back-and-forth directions. We then expected that an ANN could distinguish a continuous or discontinuous phase transition from its hysteresis behavior when it sequentially learns a series of phase-transition patterns generated as a function of external parameters such as temperature or external field.

We implemented a convolutional neural network (CNN) to realize an ANN. To test the phase-transition order, we employed two-dimensional Ising and q-state Potts models with $q = 3$ through 6. For the Ising model, we generated spin configurations below and above the critical temperature T_c as a function of the external field h. For the Potts model, we obtained them around the phase-transition point as a function of temperature T. h or T constituted the labels. We let the CNN learn the difference between the configurations with adjacent labels in increasing (decreasing) order of the labels to assess the hysteresis size. The learning effects were stored in the CNN's weights, and we monitored the sum of the weights, W_{sum}, connected to the output layer. For the specifications of the CNN and the models, see [6].

We have already reported the results of the preliminary study [4]. For the Ising crossover transition, hysteresis appeared in W_{sum}'s behavior plotted as a label function, whereas no hysteresis was recognizable for the transition below T_c as expected. However, unlike the Ising case exhibiting an order-to-order transition, the Potts model did not allow the CNN to learn the configurations in reverse order, i.e., from the disordered to the ordered state. The CNN did not seem to capture the disordered state uniquely.

We could resolve this issue by "renormalizing" the q states into a single state to make the CNN facilitate capturing the Potts (dis)ordering aspect [6]. We confirmed that W_{sum}'s hysteresis arose for $q = 3$ and 4, whereas W_{sum} took maximum precisely at the transition point without hysteresis regardless of the learning direction. Interestingly, W_{sum} behaved marginally for the weak first-order transition realized when $q = 5$.

References

[1] S-T. Lin, M. Blanco, and W. A. Goddard: J. Chem. Phys. **119** (2003) 11792.

[2] Y. Katayama *et al.*: Nature **403** (2000) 170.

[3] L. Henry *et al.*: Nature **584** (2020) 382.

[4] K. Fuchizaki *et al.*: ISSP Supercomputer Center Activity Report (2021) 256.

[5] R. J. Speedy *et al.*: Mol. Phys. **66** (1989) 577.

[6] K. Nakamura and K. Fuchizaki: submitted to J. Phys. A.

Numerical Study of Magnetism in the Honeycomb-Lattice Spin Systems

Chitoshi YASUDA
Department of Physics and Earth Sciences, Faculty of Science, University of the Ryukyus, Okinawa 903-0213, Japan

Many low-dimensional antiferromagnets with excitation modes separated from the ground state by a finite energy gap have been synthesized, and effects of impurities on those materials in the gapped state have attracted our interest. In the previous work [1], the spin $S = 1/2$ and $S = 1$ two-dimensional quantum Heisenberg antiferromagnets on a square lattice, which is composed of bond-alternating chains and interchain interactions, have been investigated by the quantum Monte Carlo simulation with the continuous-imaginary-time loop algorithm, and ground-state phase diagrams parametrized by the strength of the bond alternation and that of the interchain coupling have been determined precisely. The phase diagrams reveal under what conditions spin-gapped states and magnetically ordered states are realized. Recently, various honeycomb-lattice systems are interested in relation to quantum spin liquid states. For example, the Kitaev model on the honeycomb lattice has the qunatum spin liquid state as the ground state.

In this project, we research the $S = 1/2$ and $S = 1$ quantum Heisenberg antiferromagnets on the anisotropic dimerized honeycomb lattice using the quantum Monte Carlo simulations with the continuous-imaginary-time loop algorithm [2], and compare the results with those of the square lattice. The honeycomb lattice is composed of bond-alternating chains and interchain interactions. Periodic boundary conditions are imposed in the x and y directions. For the simulation of the $S = 1$ system, the subspin-representation technique is applied [2, 3]. In this technique, the $S = 1$ system is represented by an $S = 1/2$ system with special boundary conditions in the imaginary-time directions. The phase-transition points of the ground state are estimated by the finite-size-scaling analyses of the correlation lengths evaluated by the second-moment method. For valid analyses, it was necessary to calculate up to a system of size $L_x \times L_y = 96 \times 48$, where the temperature is fixed to $T = 1/L_x$. The critical exponent for the correlation length ν is fixed at 0.71 consistent with the value for the three-dimensional classical Heisenberg model. In the $S = 1/2$ system, there are the dimerized state and the antiferromagnetic long-range ordered (AFLRO) state as the ground state. On the other hand, in the $S = 1$ system, there is the Haldane state in addition to the dimerized state and the AFLRO state. The phase diagram parametrized by the strength of the bond alternation and that of the interchain coupling show that the region of the dimerized state of the honeycomb-lattice system is narrower than that of the square-lattice system.

References

[1] M. Matsumoto, C. Yasuda, S. Todo, and H. Takayama, Phys. Rev. B **65**, 014407 (2001).

[2] S. Todo and K. Kato, Phys. Rev. Lett. **87**, 047203 (2001).

[3] K. Harada, M. Troyer, and N. Kawashima, J. Phys. Soc. Jpn. **67**, 1130 (1998).

Spin Dynamics Simulation of the Z_2-vortex Fluctuations

Hikaru KAWAMURA

Molecular Photoscience Research Center, Kobe University, Kobe 657-8501

Yo P. MIZUTA

Graduate School of Engineering Science, Osaka University, Toyonaka 560-8531

Kazushi AOYAMA

Graduate School of Science, Osaka University, Toyonaka, 560-0043

In as early as 1984, it was pointed out that the frustrated isotropic Heisenberg magnets in two dimensions (2D) could possess a novel vortex characterized by the parity-like two-valued topological number corresponding only to its presence/absence, a Z_2 vortex, which drove a topological transition at a finite temperature T_V associated with its binding-unbinding.[1] While the direct experimental observation of the Z_2 vortex has remained elusive for years, a very recent quasi-elastic neutron scattering (QENS) experiment performed on the powder sample of the quasi-two-dimensional (2D) triangular-lattice Heisenberg antiferromagnet $NaCrO_2$ has succeeded in directly probing the signature of the free Z_2 vortex via the observation of a sharp quasi-elastic (QE) scattering of its energy width as narrow as ~10 μeV corresponding to ~0:001J (J the exchange coupling).[2] The observed peak width was even narrower than that in the earlaier model simulation[3] by an order of magnitude. We then have performed further extensive spin-dynamics simulation on the frustrated 2D Heisenberg model by improving the energy resolution by an order of magnitude.[4] The dynamical spin structure factor computed at T slightly above T_V is shown in the figure below, which indeed exhibits a narrow central peak, in addition to the side peaks of spin-wave origin. Quantitative analysis of the data indicates that the width of the central peak indeed becomes as narrow as ~0.001J in the close vicinity of the K-

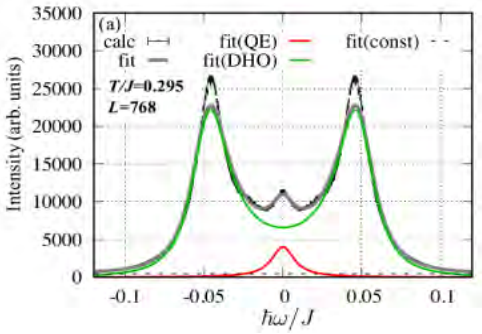

point slightly above T_V (=0.285J), consistently with the recent QENS experiment. [2]

References

[1] H. Kawamura and S. Miyashita, J. Phys. Soc. Jpn. **53**, 4138 (1984). [2] K. Tomiyasu et al, Phys. Rev. B **106,** 054407 (2022). [3] T. Okubo and H. Kawamura, J. Phys. Soc. Jpn. **79**, 084706 (2010). [4] Y.P. Mizuta et al, J. Phys. Soc. Jpn. **91**, 035001 (2022).

Finite temperature calculation of quantum manybody system using random phase product state and neural network wavefunction

Toshiaki IITAKA

Center for Computational Science,

RIKEN, 2-1 Hirosawa, Wako, Saitama, 351-0198 JAPAN

Calculation of thermal average of an observable A of a closed quantum many-body system in its thermal equilibrium at an inverse temperature is one of the most important problems in computational physics. It has, however, two major computational difficulties. The number of quantum states to be included and the dimension of each quantum state vector are both exponentially increases as the temperature and the system size increases, respectively. Each difficulty has been independently attacked using *random state method* [1, 2] and *variational wave function*, respectively.

In this project, we introduced random state method to general form of variational wave functions. Only few papers have investigated the application of random state method to variational wave functions [3-7].

Thermal average of observable A at inverse temperature β is calculated using *random state* $|\Phi\rangle$ as

$$\langle A\rangle = \frac{tr[e^{-\beta H}A]}{Z} = \frac{\langle\langle\langle\Phi|A|\Phi\rangle\rangle\rangle}{Z}$$

where

$$Z(\beta) = tr[e^{-\beta H}] = \langle\langle\langle\Phi|\Phi\rangle\rangle\rangle$$

is the *partition function* and the double bracket indicates statistical average over random states. The *thermal state* is defined by the imaginary time evolution of the random state.

$$|\Phi(\beta)\rangle = e^{-\beta H/2}|\Phi\rangle$$

Thermal energy E and specific heat C are expressed as

$$E(\beta) = \langle H\rangle$$

and

$$C(\beta) = k_B\beta^2\left[\langle E^2\rangle - \langle E\rangle^2\right].$$

Variational wave function is a point on a manifold embedded in the Hilbert space,

$$\left|\psi(w)\right\rangle = \sum_{\boldsymbol{\sigma}} c(w,\boldsymbol{\sigma})\left|\boldsymbol{\sigma}\right\rangle$$

which is parameterized with variational parameters, $w = \{w_i\}$, whose number is much less than the dimension of the Hilbert space.

Thermal state has been introduced in some variational wave functions such as MPS and PEPS as

$$\left|\Psi(\beta;w)\right\rangle = e^{-\beta H/2}\left|\Psi(w)\right\rangle$$

where $\left|\Psi(w)\right\rangle$ is random variational wavefunction.

In this project, the above formulation was extended to general form of variational wavefunction by calculating the imaginary time evolution with stochastic reconfiguration[3, 8]. It is noted that the trace is formally taken over the entire Hilbert space in our method while it was limited to its subspace in the previous method[3]. A numerical example for Restricted Boltzmann Machine is computed with NetKet [9] and the result is shown in Fig. 1.

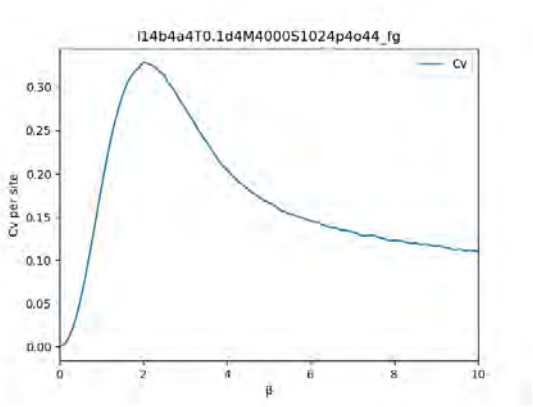

Fig.1 : Specific heat per site for 14 site spin-1/2 antiferromagnetic Heisenberg chain with PBC calculated with RBM($\alpha = 4$) and 1024 samples.

References

[1] T. Iitaka, and T. Ebisuzaki, Phys. Rev. Lett. **90**, 047203 (2003).

[2] T. Iitaka, and T. Ebisuzaki, Phys. Rev. E **69**, 057701 (2004).

[3] K. Takai *et al.*, J Phys Soc Jpn **85**, 034601 (2016).

[4] S. Garnerone, T. R. de Oliveira, and P. Zanardi, Phys. Rev. A **81**, 032336 (2010).

[5] T. Iitaka, arXiv:2006.14459 (2020).

[6] A. Iwaki, A. Shimizu, and C. Hotta, Physical Review Research **3**, L022015 (2021).

[7] S. Goto, R. Kaneko, and I. Danshita, Phys. Rev. B **104**, 045133 (2021).

[8] S. Sorella, Phys. Rev. Lett. **80**, 4558 (1998).

[9] G. Carleo *et al.*, SoftwareX **10**, 100311 (2019).

Tensor data analysis by tensor network

Kenji Harada
Graduate School of Informatics, Kyoto University
Kyoto 606-8501, Japan

Recently, data in various fields have been stored as a multi-dimensional array called a tensor. When the number of attributes (indexes) of a tensor increases, the size of the tensor becomes huge because it increases exponentially as the number of indexes increases. Therefore, we need the high-speed and high-quality use of tensor data of huge sizes.

A tensor network (TN) is an effective tool for representing a huge composite tensor and has been extensively developed in quantum information and statistical physics research. Since the tensor network can effectively represent such high-dimensional data, we may efficiently process the general tensor data.

Previous studies [1, 2] proposed using of a tree tensor network (TTN) for a multi-dimensional probability distribution. In this project, we try to improve the performance of a TTN algorithm for generative modeling to multi-dimensional data distribution.

Here, we consider a generative model based on a quantum state [1, 2]. Following the Born rule, we define $p(\mathbf{x})$ as the square of the amplitude of a wave function:

$$p(\mathbf{x}) = \frac{|\psi(\mathbf{x})|^2}{Z}, \tag{1}$$

where $\psi(\mathbf{x})$ is a wave function and Z is the normalization factor.

MPSs [1] and balance TTNs [2] have been proposed to define the wave function for generative modeling. The number of indexes of a tensor in the balance TTN is equal to that in the MPS. The only difference is the topology of the network; all physical indexes in the TTN, x_i, are connected, and the TTN network has no loop structure. Thus, an MPS is a specialized type of TTN. As shown in [2], the performance depends much on the network topology of TTNs.

We propose a new algorithm to change the network structure of a TTN for generative modeling. Several strategies can be used to select a better choice of local network structure[3]. Our network optimization improves the performance of generative modeling with a TTN.

References

[1] Zhao-Yu Han, Jun Wang, Heng Fan, Lei Wang, and Pan Zhang. Unsupervised Generative Modeling Using Matrix Product States. *Phys. Rev. X*, 8(3):031012, 2018.

[2] Song Cheng, Lei Wang, T. Xiang, and Pan Zhang. Tree tensor networks for generative modeling. *Phys. Rev. B*, 99(15):155131, 2019.

[3] Kenji Harada, Tsuyoshi Okubo, and Naoki Kawashima. Network optimization of tree generative models. in preparation.

Molecular dynamics simulation of $BaTiO_3$ nano structure II

T. Hashimoto
National Institute of Advanced Industrial Science and Technology (AIST), Tsukuba Central 2, 1-1-1 Umezono, Tsukuba, Ibaraki 305-8568, Japan

The ferroelectric domain wall (FDW) has dielectric, electrical, and mechanical properties that differ from those of bulk. It can even be considered a two-dimensional phase different from the bulk. In our previous study, we found that 71° and 109° Ising-like FDWs are observed in $BaTiO_3$ nanoclusters[1]. In this study, we focused on the FDW structures and energies of rhombohedral $BaTiO_3$.

We used a shell model proposed by Tinte et al.[2]. The calculations were performed with the code developed by us. We performed calculations for 71°, 109°, and 180°$\{1\bar{1}0\}$ FDWs in the rhombohedral phase. We used 10×6×6 5-atom unit cells for the 109° FDWs, and 8×6×6 and 10×6×6 10-atom building blocks for the 71° and 180°$\{1\bar{1}0\}$ FDWs, respectively. The initial Ising FDW configurations were made by shifting the Ti atoms in one direction in half of the supercell, and in the other direction in another half. The initial Bloch FDW configurations were made in the same way as the Ising case except that the local dielectric polarization vectors were rotated across the FDW. To mimic the isolated FDW between very thick domains in the supercell calculations, the in-plane lattice constants were set to be the same as those of the single domain phase, while the out-of-plane lattice constant was relaxed.

The domain widths and energies had been calculated with the Ginzburg–Landau–Devonshire (GLD) model and the GLD model with reduced gradient terms (GLD-r) [3]. The GLD and the GLD-r results predict that the 109° Bloch wall is more stable than the 109° Ising wall energy, which is not in accordance with the LDA results. The GLD-r model predicts narrower walls and lower wall energies compared to the GLD model, which improves the energy and width of the 71° Ising wall and the width of the 109° Ising wall, but overshoots the energy of the 109° Ising wall and the energy and width of the 109° Bloch wall. The GLD-r model predicts that the 180° Bloch wall is unstable compared to the 180° Ising wall, which is not in accordance with the LDA results.

The shell model results also have inconsistencies compared to the LDA results: The FDW energy of the 109° Ising wall is too low. The FDW energy of the 180°$\{1\bar{1}0\}$ Bloch wall is too high and the width of it is too narrow. However, it predicted that the 71° Ising wall has the lowest energy, followed by the 109° Ising wall and the 109° Bloch wall.

References

[1] T. Hashimoto and H. Moriwake, Physica B, **656**, 414768 (2023).

[2] S. Tinte, M. Stachiotti, S. Phillpot, M. Sepliarsky, D. Wolf, and R. Migoni: J. Phys.: Condens. Matter **16** (2004) 3495.

[3] M. Taherinejad, D. Vanderbilt, P. Marton, V. Stepkova, and J. Hlinka: Phys. Rev. B **86** (2012) 155138.

Numerical study of quantum many-body scars in bosonic systems

Ryui KANEKO
Department of Physics, Kindai University
Higashi-Osaka, Osaka 577-8502, Japan

Understanding how isolated quantum many-body systems thermalize is of great interest in physics. The eigenstate thermalization hypothesis (ETH) provides a sufficient condition for thermalization and is satisfied in many quantum systems in the presence of interactions [1, 2]. However, recent experiments of nonintegrable systems suggest ETH breaking. This phenomenon originates from the special eigenstates exhibiting extremely slow thermalization [3, 4]. Such quantum many-body scar (QMBS) states exist in various spin models [5–10]. It is desirable to search for the QMBS states in other quantum systems, which can be realized in experiments.

Here we focus on the Bose-Hubbard model suitable for experiments using ultracold atoms on optical lattices. The Hamiltonian is given as

$$\hat{H} = \hat{H}_0 + \hat{H}_{\rm int}, \tag{1}$$

$$\hat{H}_0 = -J\sum_i (\hat{a}_i^\dagger \hat{a}_{i+1} + \hat{a}_{i+1}^\dagger \hat{a}_i), \tag{2}$$

$$\hat{H}_{\rm int} = \frac{U}{2}\sum_i \hat{n}_i(\hat{n}_i - 1). \tag{3}$$

We specifically choose the model in a truncated Hilbert space with the maximum occupation number $n_{\rm max} = 2$. Note that three-body losses of atoms on optical lattices realize this constraint [11, 12].

We numerically diagonalize the Hamiltonian and find the eigenstates with a small entanglement entropy (see Fig. 1). We also analytically show that they are generated by applying the SU(2) ladder operator consisting of a linear combination of two-particle annihilation operators. The construction of the QMBS states is equivalent to the case of the $S = 1$ XY model [13, 14].

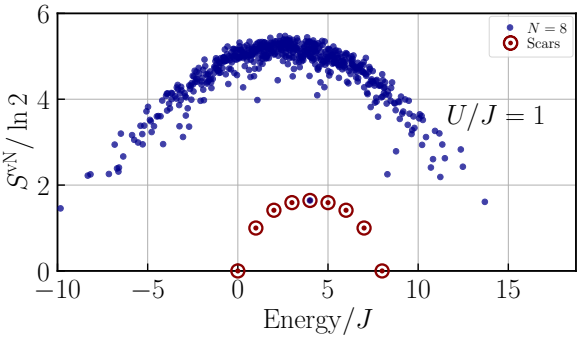

Figure 1: Entanglement entropy as a function of energy. The QMBS states are circled. We consider the system size $L = 8$ and the interaction strength $U/J = 1$ in Eq. (1). The quantum number sector with the particle number $N = L$ and the even parity $\mathcal{I} = +1$ is given by blue dots. Each QMBS state (a red circle with a dot) with the particle number N has the energy $UN/2$ and the expectation values $\langle\sum_{i=1}^L \hat{n}_i\rangle = N$ and $\langle\sum_{i=1}^L \hat{n}_i^2\rangle = 2N$. Its bipartite entanglement entropy at $N = L$, corresponding to a state $|S_{n=L/2}\rangle$, becomes $S_A^{\rm vN} \to [\ln(\pi L/8) + 1]/2$ for $L \to \infty$.

These findings will stimulate further research on the QMBS states in general Bose-Hubbard models without any constraints, which would be more suitable for experiments of ultracold atoms in optical lattices. The construction of the QMBS states in general spin

S systems has been discussed recently [15, 16], which could be extended to the Bose-Hubbard model by utilizing the improved Holstein-Primakoff transformation [17, 18].

References

[1] W. Beugeling *et al.*, Phys. Rev. E **89**, 042112 (2014).

[2] H. Kim *et al.*, Phys. Rev. E **90**, 052105 (2014).

[3] H. Bernien *et al.*, Nature **551**, 579 (2017).

[4] D. Bluvstein *et al.*, Science **371**, 1355 (2021).

[5] C. J. Turner *et al.*, Nat. Phys. **14**, 745 (2018).

[6] C. J. Turner *et al.*, Phys. Rev. B **98**, 155134 (2018).

[7] A. J. A. James *et al.*, Rev. Lett. **122**, 130603 (2019).

[8] N. Shibata *et al.*, Phys. Rev. Lett. **124**, 180604 (2020).

[9] M. Serbyn *et al.*, Nat. Phys. **17**, 675 (2021).

[10] S. Moudgalya *et al.*, Rep. Prog. Phys. **85**, 086501 (2022).

[11] A. J. Daley *et al.*, Phys. Rev. Lett. **102**, 040402 (2009).

[12] M. J. Mark *et al.*, Phys. Rev. Lett. **108**, 215302 (2012).

[13] M. Schecter and T. Iadecola, Phys. Rev. Lett. **123**, 147201 (2019).

[14] S. Chattopadhyay *et al.*, Phys. Rev. B **101**, 174308 (2020).

[15] N. O'Dea *et al.*, Phys. Rev. Research **2**, 043305 (2020).

[16] L.-H. Tang *et al.*, Phys. Rev. Research **4**, 043006 (2022).

[17] M. Vogl *et al.*, Phys. Rev. Research **2**, 043243 (2020).

[18] J. König and A. Hucht, SciPost Phys. **10**, 7 (2021).

Tensor-network study of the quench dynamics of the Kitaev honeycomb model

Ryui KANEKO
Department of Physics, Kindai University
Higashi-Osaka, Osaka 577-8502, Japan

The Kitaev honeycomb model [1] in the magnetic field displays a rich phase diagram of quantum phases [2,3]. These findings stimulate further research on the nonequilibrium dynamics of the model. One of the motivations for studying dynamics is an experimental interest; the Kitaev candidate materials may exhibit unconventional transport [4–6]. The other is an interest in statistical mechanics as to how the integrable Kitaev model, which is rare in quantum 2D systems, thermalizes in the presence of additional interaction [7,8]. These interests motivate us to study the dynamics of the simple Kitaev model with the magnetic field. As a benchmark, we specifically focus on the sudden quench of the ferromagnetic Kitaev model starting from the antiferromagnetic state without the magnetic field. Previous investigations are limited to mean-field calculations or numerical-diagonalization studies for small systems. We use the 2D tensor-network method using the infinite projected entangled state (iPEPS) [9,10], which can directly deal with inifinite systems accurately, to examine how far one can go for the quench dynamics of the Kitaev model.

We prepare the staggered antiferromagnetic state, whose spins are oriented along the z-axis, on a honeycomb lattice as the initial state $|\psi(0)\rangle$. The state can be prepared by the bond dimension $D = 1$, and is time evolved by the $S = 1/2$ Kitaev Hamiltonian

$$\hat{H} = -\sum_{\langle i,j\rangle_\gamma,\gamma\in\{x,y,z\}} J^\gamma \hat{S}_i^\gamma \hat{S}_j^\gamma, \qquad (1)$$

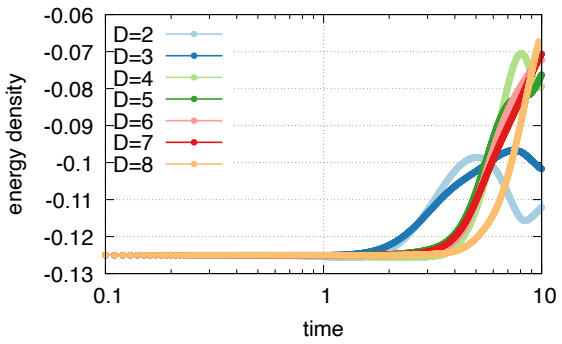

Figure 1: Time evolution of the energy density.

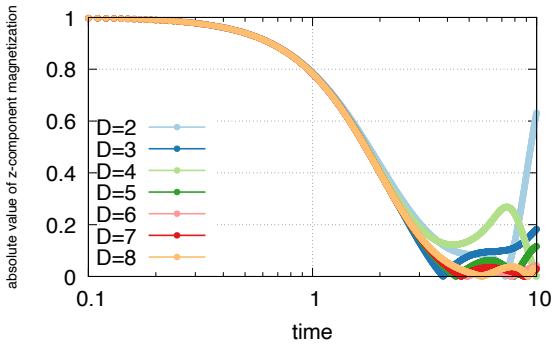

Figure 2: Time evolution of the absolute value of the z-component magnetization.

where γ corresponds to the bond direction and J^γ is the Kitaev interaction. Here we consider the isotropic and ferromagnetic interaction $J^\gamma = 1$. The wave function at each time $|\psi(t)\rangle = \exp(-it\hat{H})|\psi(0)\rangle$ is calculated by the simple update algorithm [11,12] using the tensor-network library TeNeS [13]. The wave function is optimized up to the bond dimension $D = 8$ to examine how physical quantities converge by improving the accuracy of the state

with increasing the bond dimension.

The energy should be conserved for the quench dynamics. We can estimate to what extent the simulation goes well by looking at the degree of conservation. In the present study, the energy is nearly conserved for $tJ^{\gamma} \lesssim 4$ when $D \gtrsim 4$ (see Fig. 1). Within this reliable time frame, the magnetization nearly vanishes at $tJ^{\gamma} \approx 4$. This observation is consistent with the previous study, where an emergent non-magnetic steady state has bee proposed [7].

Our study would serve as a reference for understanding the quench dynamics of the Kitaev model and relevant unconventional steady states, which can be identified by utilizing the 2D tensor-network method. It is left for future work to investigate the effect of the magnetic field in the model.

References

[1] A. Kitaev, Ann. Phys. (NY) **321**, 2 (2006).

[2] Z. Zhu *et al.*, Phys. Rev. B **97**, 241110(R) (2018).

[3] C. Hickey and S. Trebst, Nat. Commun. **10**, 530 (2019).

[4] J. Nasu and Y. Motome, Phys. Rev. Research **1**, 033007 (2019).

[5] T. Minakawa *et al.*, Phys. Rev. Lett. **125**, 047204 (2020).

[6] M. Udagawa *et al.*, Phys. Rev. Lett. **126**, 127201 (2021).

[7] L. Rademaker, SciPost Phys. **7**, 071 (2019).

[8] G.-Y. Zhu and M. Heyl, Phys. Rev. Research **3**, L032069 (2021).

[9] T. Nishino *et al.*, Prog. Theo. Phys. **105**, 409 (2001).

[10] F. Verstraete and J. I. Cirac, arXiv:cond-mat/0407066.

[11] J. Jordan *et al.*, Phys. Rev. Lett. **101**, 250602 (2008).

[12] H. C. Jiang *et al.*, Phys. Rev. Lett. **101**, 090603 (2008).

[13] Y. Motoyama *et al.*, Comp. Phys. Commun. **279**, 108437 (2022).

The Study on Superionic Conduction and Phase Transition by Disordering of Complex Hydride

Ryuhei Sato

Advanced Institute for Materials Research,

Tohoku University, 2-1-1 Katahira, Aoba-ku, Sendai 980-8577, Japan

The complex hydrides such as $LiCB_9H_{10}$ are promising candidates for electrolytes due to their high ionic conductivity and stability to metal anodes [1]. Although the development of such complex hydrides is progressing rapidly, the mechanism of superionic conductivity induced by the phase transition due to the disordering (≈ the change in rotational motion) of the complex anions is not clear. Therefore, the purpose of this study is to clarify the effect of the disordering on the ion conduction and the phase transition by using *ab initio* molecular dynamics (AIMD) and neural-net potential molecular dynamics (NNP-MD) simulations.

AIMD simulation at 1000K confirmed that $LiCB_9H_{10}$ exhibits concerted motion, in which multiple Li ions migrate simultaneously with the rotation of the complex anion. To clarify the effect of the $CB_9H_{10}^-$ rotation, we analyzed the change in diffusion coefficient with and without the rotation using NNP-MD simulations (Fig. 1). As shown in the figure, the activation energy increases when the anion rotation is stopped, and the conductivity decreases by nearly one order of magnitude at around room temperature [2].

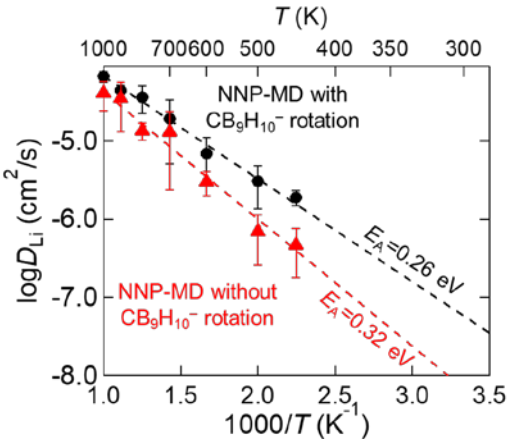

Figure 1 Arrhenius plot of Li self-diffusion coefficient during NNP-MD simulations of $LiCB_9H_{10}$ with and without $CB_9H_{10}^-$ rotation [2].

As shown in the discussion above, it is possible to quantitatively analyze the changes in ion transport caused by anion-rotation using NNP-MD simulations. However, it is difficult to obtain a specific relationship between the anion rotation and Li migration. Therefore, in order to visualize the ion transport mechanism in such a disordered system, we have developed an ion-migration-mechanism analysis method using topological data analysis based on persistent homology.

This year, we investigated the applicability of topological data analysis on ion migration mechanism [3]. Here, we choose α-AgI as a benchmark, because this system retains the ordered I bcc lattice while Ag ions are disordered in the system and shows complex concerted ion migration. MD simulations at various temperatures confirmed specific ring (one-dimensional hole in terms of homology) structures appear only when the system shows high ionic conductivity. Inverse analysis of these ring structures revealed that they were four-membered rings consisting of two Ag and I ions. By deforming these four-membered rings along the probability density distribution of the ring structure obtained by topological data analysis, we succeeded in visualizing the representative concerted ion migration of Ag ions in α-AgI[3]. In the future, we plan to apply this technique to complex hydride systems to clarify the relationship between anion rotation and ion migration.

Recently, complex hydrides are expected to be applied as multivalent-ion (ex. Zn^{2+} and Mg^{2+}) conductors [4]. Although the insertion of neutral molecules into complex hydrides is known to be effective to improve the ion conductivity for these multivalent-ion systems, there is no clear guideline to choose most effective neutral molecules for these complex hydrides. In addition, the specific mechanism of how the insertion of neutral molecules improves ionic conductivity is also unclear. Therefore, we created a workflow to analyze the effect of such neutral molecules on complex hydrides. Given a composition including neutral molecules, complex anions, and cations, a structure search method based on genetic algorithms (USPEX) can estimate the stable and reasonable structure including neutral molecules after several hundred DFT calculations. The activation energies of ion migration estimated from metadynamics simulations using the obtained structures are in good agreement with experimental values. The obtained trajectories of ion migration during the metadynamics simulation confirm that the coordination structure of the neutral molecule during ion migration has a significant effect on the activation energy. As a result of machine learning using the estimated activation energies, it was confirmed that the distance between anions and the electronegativity are important ones for the activation energy [5].

References

[1] W. Tang et al., *Adv. Eng. Mater.*, 6 (2016) 1502237.

[2] R. Sato et. al., to be submitted.

[3] R. Sato et al., *J. Chem. Phys.*, 158, (2023) 144116.

[4] K. Kisu et al., *J. Mater Chem. A*, 10 (2022) 24877.

[5] S. Egon, R. Sato et al. submitted to *NPJ. Comput. Mater.*

Theoretical studies on dynamics in biomolecular and liquid systems

Shinji Saito

Graduate University for Advanced Studies (Sokendai) / Institute for Molecular Science, 38 Nishigo-Naka, Myodaiji, Okazaki 444-8585, Japan

Fluctuations are inherent in condensed phase systems, such as liquid and biomolecular systems, and occur across diverse spatio-temporal scales. These fluctuations play a significant role in structural changes and reaction dynamics, thereby influencing various properties and functions. Consequently, an understanding of fluctuations is crucial for a comprehensive understanding of the relevant chemical/biological processes. In the second half of the fiscal year of 2022, our group utilized the supercomputer resources at ISSP for mainly two related projects, 1) the ion permeation process of potassium channel Kv1.2, and 2) the excitation energy transfer of light harvesting complex II (LHCII) in higher plants.

Kv1.2 is a mammalian voltage-controlled potassium channel from the Shaker K^+ channel family which regulates the cellular membrane potential by conditionally releasing the intracellular K^+ ions. Since its crystal structure was resolved about twenty years ago, it has become a typical and representative model for the study of ion channels. Here, we focus on the dynamical disorder revealed in the ion permeation processes under various ion concentrations and external voltages and attempt to understand the conformational origins of such dynamical disorder.

In the second half of the 2022 fiscal year, we constructed a Kv.12 model of about 140k atoms at the electrophysiological concentration of 0.15 M and performed roughly 100 μs molecular dynamics (MD) simulations at an external electric field of 500 mV using GROMACS. During the MD simulation, about 2300 potassium permeation events were observed. The time series analysis showed that these permeation events roughly followed the pattern of a Poisson process with a slight deviation from it. Further analyses and MD simulations at different ion concentrations and external electric field strength are to be performed for a complete picture of the dynamic disorder in the ion permeation process of Kv1.2.

LHCII, where the first step of the photosynthetic process occurs, has a complex structure which makes its excitation energy transfer (EET) difficult to be elucidated experimentally. In order to understand the EET dynamics of LHCII, we performed quantum mechanics (QM) calculation using the CAM-B3LYP functional and determined the optimal range separate parameters (between CAM and B3LYP) that reproduced the experimental

excitation energies of Chl *a* and *b* in three solvents [1]. With these optimized parameters, we refined the structures for 14 chlorophylls (Chl) in LHCII by using a modified version of GAMESS on the supercomputer at ISSP. In order to study the dynamical properties, we introduced a model called Molecular Mechanics Shepard interpolation Correction (MMSIC) that can give the approximate excitation energies during MD simulation based on the interpolation of optimized structures using the above-mentioned functional theory. The parallelized MMSIC-MD simulation sufficiently reproduced the QM/MM excitation energies on the fly and showed that the excitation energies of Chl *a* in LHCII varies wider than in solvents.

References

[1] Zhu, Zhe, Masahiro Higashi, Shinji Saito, Excited states of chlorophyll a and b in solution by time-dependent density functional theory, The Journal of Chemical Physics 156(12) (2022) 124111.

Structural formation of inverse patchy particles

Takamichi TERAO

Department of Electrical, Electronic and Computer Engineering,

Gifu University, Yanagido 1-1, Gifu, 501-1132

Inverse patchy colloids are those in which the anisotropy of interparticle interactions is due to inhomogeneous surface charges [1]. Previous studies of colloidal particle systems have largely dealt with the problem of aggregates, which are dominated by attractive interparticle interactions, and colloidal crystals, which are dominated by repulsive interactions. Conventional patchy particles are dominated by anisotropic attractive interactions. Inverse patchy particles, on the other hand, consist of heterogeneously charged units where the pair potentials between particles contain both attractive and repulsive properties. They are expected to exhibit novel properties and their properties with respect to structure formation are of interest.

In this study, we focused on the structural formation of inverse charged patchy particles. The surface of these particles is charged and the sign of the charge is reversed between the bipolar part and the other parts. The structure formation in these systems was studied by molecular dynamics simulations. The simulations were performed with the LAMMPS simulation package in the NVT ensemble. In thermal equilibrium, inverse patchy particles exhibit a variety of configurations by changing the ratio of positive and negative charges on the surface.

Figure 1 shows a snapshot of inverse patchy colloids when the motion of each sphere was confined between a pair of two-dimensional planes. From these results, we have revealed the dependence of the orientation order of the colloids on the charge coverage ratio, as well as the phase diagram of the system.

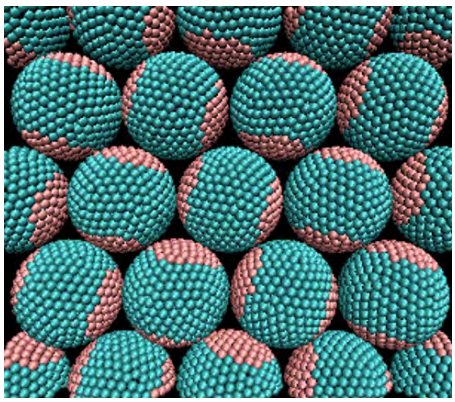

Fig. 1: Snapshot of inverse patchy colloids under geometrical confinement.

References

[1] P. D. J. van Oostrum, M. Hejazifar, C. Niedermayer, and E. Reimhult: J. Phys.: Condens. Matter 27 (2015) 2341.

Effect of chain crossing prohibition on phase-separated structure of block copolymers

Katsumi HAGITA,[1] and Takahiro MURASHIMA[2]

[1]*Department of Applied Physics, National Defense Academy, Yokosuka 239-8686*

[2]*Department of Physics, Tohoku University, Sendai 980-8578*

We have studied phase-separated structures of block copolymers in order to clarify topological effect of chain crossing prohibition. To achieve this aim, we firstly considered MP-SRP extensions [1,2] of dissipative particle dynamics (DPD) simulations [3]. We found that a slight change in the potential (force field) between original DPD [3] and MP-SRP extensions [1,2] affects weakly the lamellar domain spacing. The numerical precision is related to potential validity problems, and comparisons between different physics, Gaussian and excluded volume chains, may not be appropriate. Thus, we switched our approach to the development of force field parameters in order to treat directly with the phase separation phenomenon in the coarse-grained molecular dynamics (CGMD) simulations of the Kremer-Grest (KG) model [4]. Although implementations of the MP-SRP extensions [1,2] were developed using LAMMPS [5], the CGMD approach has the advantage of being free from the implementation and able to use HOOMD-blue [6] on the GPU. Notably, HOOMD-blue has a good performance for the standard DPD simulations [3].

To confirm fundamental behaviors using Gaussian chains, we performed large scale DPD simulations to estimate lamellar domain spacing of symmetric linear, ring, and four-arm-star block copolymer blends [7]. We also confirmed practical compatibility of lamellar domain spacing between self-consistent field theory and DPD simulations [8]. For fundamental understandings of topological effects by chain crossing prohibition, we performed CGMD simulations of polymers with rings. In [9], ring-filling effect on stress–strain curves of randomly end-linked tetra-arm prepolymers was studied. In [10], we discovered topological transition in multicyclic chains with structural symmetry inducing stress-overshoot phenomena in multicyclic/linear blends under biaxial elongational flow. In addition, we investigated topological barriers on the crystallization behavior of ring polyethylene melts with trefoil knots via united atom MD simulations [11].

Currently, we investigated interaction parameters of AB di-block copolymers for CGMD simulations. To consider a connection to Flory-Huggins χ parameter, we are studying

relationships among interaction parameters, lamellar domain spacing, and chain length (N). First, we performed CGMD simulations of AB di-BCP starting from the lamellar structures as shown in Fig. 1 (a). We confirmed the behaviors of domain spacing from weak to strong segregation conditions were consistent with theories, simulations, and experiments.

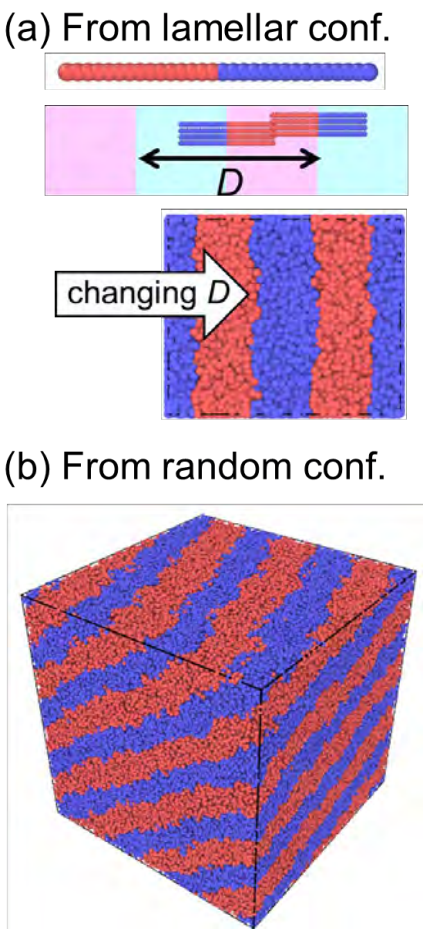

Fig. 1: Snapshots of CGMD models of AB di-BCP forming lamellar structures.

Second, we found that the AB-BCP in CGMD simulations spontaneously forms a lamellar structure as shown in Fig. 1 (b). We also confirmed that the lamellar domain spacing depends on the interaction parameters. After further studies on the interaction parameters, we will investigate topological constrain effect of polymers such as rings via CGMD simulations.

References

[1] R. D. Groot and P. B. Warren: J. Chem. Phys. **107** (1997) 4423.

[2] N. Iwaoka, K. Hagita and H. Takano: J. Chem. Phys. **149** (2018)114901.

[3] K. Hagita, T. Murashima, H. Shiba, N. Iwaoka, and T. Kawakatsu: Comput. Mater. Sci., **203** (2022) 111104.

[4] K. Kremer and G. S. Grest: J. Chem. Phys. **92** (1990) 5057.

[5] S. Plimpton: J. Comp. Phys. 117 (1995) 117.

[6] J. A. Anderson, J. Glaser, and S. C. Glotzer, Comput. Mat. Sci. **173**, 109363 (2020).

[7] K. Hagita, T. Murashima, and T. Kawakatsu, Macromolecules **55**, 8021 (2022).

[8] K. Hagita, and T. Murashima, Polymer **269**, 125733 (2023).

[9] K. Hagita, T. Murashima, T. Ohkuma, and H. Jinnai, Macromolecules **55**, 6547 (2022).

[10] T. Murashima, K. Hagita, and T. Kawakatsu, Macromolecules **55**, 9358 (2022).

[11] K. Hagita, T. Murashima, N. Sakata, K. Shimokawa, T. Deguchi, E. Uehara, and S. Fujiwara, Macromolecules **56**, 15 (2023).

Analysis of Various Crystal Forms of Glycine Nanocrystals by Large-Scale Metadynamics Simulations

Hiroki NADA

Faculty of Engineering, Tottori University, 4-101 Koyama-Minami, Tottori 680-8552

The control of structure and shape of glycine nanocrystals is important in connection with pharmaceutical engineering [1]. In this project, a classical molecular dynamics (MD) simulation combined with the metadynamics (MTD) method (hereafter, MTD simulation) was performed to elucidate stable structures and shapes of a glycine nanocrystal.

The MTD simulation was performed for a cubic system in which an α glycine nanocrystal consisting of 64 glycine molecules was placed at its center. The remainder of the system was filled with water molecules. AMBER force field was used for estimation of the intermolecular interaction energy and force acting between glycine molecules. The MTD simulation was carried out with DL_POLY 2.20 [2], in which PLUMED 1.3 [3] was implemented to permit combination with the MTD method, using System C of ISSP Supercomputer Center.

A free energy surface (FES) obtained using discrete C^{α}-C^{α} and N-N radial distribution functions represented by Gaussian window functions as collective variables indicated a few local minima. Each local minimum corresponded to a crystal-like structure with a different molecular arrangement of glycine molecules. Moreover, the shape of the nanocrystal was also different between those local minima. These results suggest that not only the structure of nanocrystals but also the shape of them can be analyzed using the MTD method.

In summary, the MTD method is a helpful tool to search for stable structures and shapes of nanocrystals consisting of complex molecules.

References

[1] X. Yang and A. S. Myerson: CrystEngComm. **17** (2015) 723.

[2] W. Smith and T. R. Forester: J. Mol. Graph. **14** (1996) 136.

[3] M. Bonomi et al.: Comput. Phys. Commun. **180** (2009) 1961.

Structural Analysis of Amorphous Silicon Monoxide by a Metadynamics Method with Unsupervised Machine Learning

Hiroki NADA

Faculty of Engineering, Tottori University, 4-101 Koyama-Minami, Tottori 680-8552

Amorphous SiO has been studied by many research groups because it can be functional materials [1]. However, molecular-scale structure of it remains elusive. The purpose of this project was elucidating molecular-scale structure of amorphous SiO using a classical molecular dynamics (MD) simulation combined with the metadynamics (MTD) method (hereafter, MTD simulation [2]).

MTD is an enhanced sampling method that increases the probability of reaching high free-energy states by adding a Gaussian bias potential to the Hamiltonian of a state. The MTD method affords a free energy surface (FES) in a space of collective variables (CVs) for a system of interest. This FES quantitatively represents the relative thermodynamic stabilities of many different states of the system.

The MTD simulation was carried out for each of amorphous Si, SiO and SiO_2 phases with DL_POLY 2.20 [3], in which PLUMED 1.3 [4] was implemented to permit combination with the MTD method, using System B of ISSP Supercomputer Center. In this project, we focused on the structural similarity between the examined amorphous phases. The structural similarity was analyzed by evaluating the geometrical similarity of Si-Si, Si-O, and Si-O pair-distribution functions. In this project, the geometrical similarity was evaluated using a method of unsupervised machine learning, dimensional reduction technique [5].

We confirmed that the present methodology is helpful to investigate detailed structures of multicomponent amorphous phases.

References

[1] A. Hirata et al.: Nat. Commun. **7** (2016) 11591.

[2] A. Laio and M. Parrinello: Proc. Natl. Acad. Sci. U. S. A. **99** (2002) 12562.

[3] W. Smith and T. R. Forester: J. Mol. Graph. **14** (1996) 136.

[4] M. Bonomi et al.: Comput. Phys. Commun. **180** (2009) 1961.

[5] H. Nada: ACS Omega **3** (2018) 5789.

Quantum algorithm for combinatorial optimization

Tatsuhiko SHIRAI
Department of Computer Science and Communications Engineering, Waseda University
Ookubo, Shinjuku-ku, Tokyo 169-8555

We have developed a quantum algorithm for QAOA (Quantum approximate optimization algorithm), which solves combinatorial optimization problems (COPs) in gate-based quantum computers. This year, we proposed a new method called spin-variable reduction method for formulating a constrained COP as an Ising model [1] and compared the performance with conventional methods in maximum glaph coloring problems.

QAOA is a hybrid quantum-classical algorithm designed to approximate the ground state of a Hamiltonian H. QAOA consists of calculations in a quantum computer and classical computer. The quantum computer calculates the expectation value of H over a variational state, which is given by

$$|\vec{\beta},\vec{\gamma}\rangle := e^{-i\beta_p H}e^{-i\gamma_p X}\cdots e^{-i\beta_1 H}e^{-i\gamma_1 X}|+\rangle\,, \tag{1}$$

where $\vec{\beta}=(\beta_1,\ldots,\beta_p)$ and $\vec{\gamma}=(\gamma_1,\ldots,\gamma_p)$. p denotes a circuit depth. X is called a mixer and adopted as $X=\sum_i \sigma_i^x$ where $\vec{\sigma}_i=(\sigma_i^x,\sigma_i^y,\sigma_i^z)$ is the Pauli operator acting on site i. $|+\rangle$ is defined as $\sigma_i^x|+\rangle=|+\rangle$ for all i. The classical computer optimizes $(\vec{\beta},\vec{\gamma})$ to minimize the value of $\langle\vec{\beta},\vec{\gamma}|\,H\,|\vec{\beta},\vec{\gamma}\rangle$. We solve the quantum dynamics on the super computer using openMP.

Maximum graph coloring problem colors each node of a given graph $G=(V,E)$ using n colors so that the number of edges connecting the nodes with different colors is maximized. This problem has a constraint that one color is assigned to each node. When solving a COP with constraints by QAOA, the Hamiltonian is given as $H=H_{\rm obj}+H_{\rm cst}$. Here, $H_{\rm obj}$ and $H_{\rm cst}$ denote the Hamiltonians for objective function and constraints of the COP, respectively. There are three methods to give the Hamiltonians: penalty method, domain-wall method, and spin-variable reduction method.

Figure 1 shows p dependences of success probability p_s. Here, we set $n=4$ and $|V|=6$, and generate 10 random graphs with edge density 0.75. We found that domain-wall method and spin-variable method outperforms penalty method.

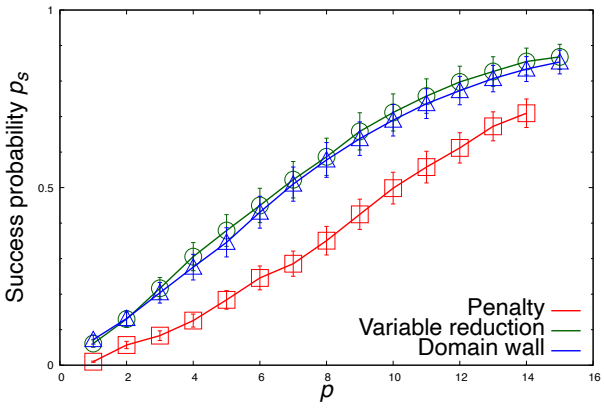

Figure 1: Performance comparison among penalty method (squares), spin-variable reduction method (circles), and domain-wall method (triangles).

References

[1] T. Shirai and N. Togawa: IEEE Transactions on Computers (Early Access).

Topological chirality order and its stability in breathing-kagome antiferromagnets

Kazushi AOYAMA
Department of Earth and Space Science, Graduate School of Science, Osaka University
Machikaneyama-cho, Toyonaka-shi, Osaka 560-0043

The quest for topological spin textures in solids is one of the central issues in condensed matter physics because of their possible applications to spin-electronic devices. A typical example of such topological spin textures is the so-called skyrmion crystal (SkX) where the total solid angle subtended by all the spin in the magnetic unit cell takes an integer topological in units of 4π. Noting that the scalar spin chirality $\chi_{ijk} = \mathbf{S}_i \cdot (\mathbf{S}_j \times \mathbf{S}_k)$ is related to the solid angle, the SkX could be regarded as a topological chiral order. Although the SkX is usually realized in the presence of a magnetic field being irrespective of whether the the Dzaloshinskii-Moriya interaction is active or not [1], a zero-field SkX is also possible in a specific metallic system [2]. Previously, we theoretically demonstrated that a breathing bond-alternation of the underlying lattice can induce a zero-field topological chiral order which can be viewed as a miniature version of the SkX [3]. In the work, we investigate effects of an additional single-ion magnetic anisotropy which more or less exists in real materials.

We consider the following classical J_1-J_3 model on the breathing kagome lattice with the single-ion magnetic anisotropy:

$$\mathcal{H} = J_1 \sum_{\langle i,j\rangle_S} \mathbf{S}_i \cdot \mathbf{S}_j + J_1' \sum_{\langle i,j\rangle_L} \mathbf{S}_i \cdot \mathbf{S}_j + J_3 \sum_{\langle\langle i,j\rangle\rangle} \mathbf{S}_i \cdot \mathbf{S}_j + D \sum_i (S_i^z)^2, \quad (1)$$

where $\mathbf{S}_i$ is a classical spin, the summation $\sum_{\langle\rangle_{S(L)}}$ runs over site pairs on small (large) triangles having the nearest neighbor (NN) interaction J_1 (J_1'), $J_3 > 0$ is the third NN antiferromagnetic interaction along the bond direction, and $D < 0$ ($D > 0$) represents an easy-axis (easy-plane) anisotropy. In the isotropic case of $D = 0$, a triple-$\mathbf{Q}$ state appearing for a relatively large J_3 takes the miniature SkX structure having a nonzero uniform total chirality [3]. By performing Monte Carlo simulations, we investigate the stability of this topological chiral order against the anisotropy D. In our simulations, 1×10^6 - 2×10^6 MC sweeps are carried out under the periodic boundary condition, and the first half is discarded for thermalization. $\mathbf{S}_i$ at each site is updated in a conventional random and a successive over-relaxation-like processes, where in the former (latter) process, we try to rotate a spin in a randomly proposed direction (by the angle π around the local mean field) by using the Metropolis algorithm. Observations are done at every MC sweep, and the statistical average is taken over 4 independent runs starting from different random initial configurations.

It is found that the zero-field topological chiral order with the miniature SkX structure is relatively robust against easy-axis ($D < 0$) and easy-plane ($D > 0$) anisotropies, although for strong easy-axis (easy-plane) anisotropy, a triple-$\mathbf{Q}$ collinear (coplanar) state is favored. Since the SkX and anti-SkX each having positive or negative chirality are energetically degenerate, the topological Hall effect of alternative sign is possible at zero field. For moderate

$D < 0$ ($D > 0$), the collinear (coplanar) phase preempts the SkX phase and in the chiral sector, it shows a random domain structure consisting of positive- and negative-chirality clusters [4]. It is also found that the miniature SkX is robust against the external magnetic field, but further analysis is necessary to clarify the in-field properties of the model.

References

[1] T. Okubo, S. Chung, and H. Kawamura, Phys. Rev. Lett. **108**, (2012) 017206.

[2] R. Ozawa, S. Hayami, and Y. Motome, Phys. Rev. Lett. **118**, 147205 (2017).

[3] K. Aoyama and H. Kawamura, Phys. Rev. B **105**, (2022) L100407.

[4] K. Aoyama and H. Kawamura, J. Phys. Soc. Jpn. **92**, (2023) 033701.

Molecular modeling of ferroelectric nematic phase

Takeaki ARAKI, and Matheus DE MELLO

Department of Physics,

Kyoto University, Kitashirakawa-Oiwake-cho, Sakyo, Kyoto 606-8502

Ferroelectric liquid crystals are partially ordered anisotropic fluids with ferroelectricity. Its experimental realization has not been reported for a long time. Recently, some experimental groups have succeeded in synthesizing molecules which possibly show ferroelectric nematic order [1-2].

Even though the molecular features required to stabilize the ferroelectric phase were systematically studied, the origins of the spontaneous polar ordering remain still unclear. In this work, we study a molecular liquid DIO, which were synthesized by Nishikawa *et al*., focusing on which of the dipole-dipole electrostactic interaction or the polar shape of the molecules is dominant for the polar ordering.

We performed all-atom molecular dynamics simulations of 1000-2000 DIO molecules with GROMACS. The partial charge on each atom is estimated by using Gaussian. In order to see the effect of the electrostatic interaction, we carried out the simulations of the DIO without the electric charges. We analyzed the nematic, polar order parameters, the spatial distribution, and the correlation between the molecular axes.

Our simulation results indicate the spontaneous polar ordering at a low temperature. The distribution function suggests the molecule shape can be regarded as a rod without the remarkable head-tail asymmetry. Owing to the electric charges, the local parallel-parallel alignment is favored than the parallel-anti parallel alignment, which is usually observed in the conventional nematic phase.

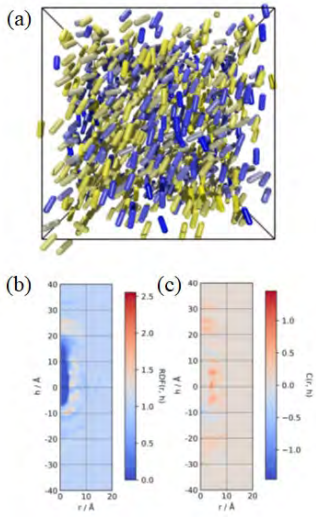

Fig. 1: (a) A snapshot of the liquid crystal phase of DIO at 330K. The molecule is represented with a rod whose color shows the orientation. (b) The distribution function. (c) The correlation function.

References

[1] H. Nishikawa, *et al.* Adv. Mater. 29, 1702354 (2017).

[2] R. J. Mandle, *et al.*, Chem. Eur. J. 23, 14554 (2017).

Aggregation of polyelectrolytes in mixed solvents

Takeaki ARAKI, and Dai Matsubara

Department of Physics,

Kyoto University, Kitashirakawa-Oiwake-cho, Sakyo, Kyoto 606-8502

Polymer systems often exhibit phase-separated structures with diverse patterns from microscopic to macroscopic length scales. In particular, diblock copolymer melts and polyelectrolyte in poor solvents are expected to be applied to nanostructures.

In this study, we consider mesoscopic pattern formation of weakly charged polyelectrolytes in binary mixture solvents by means of field theoretic polymer simulations in lattice space. The polymer is modeled as a continuous Gaussian chain, and is described by path integrals. The solvent-polyelectrolyte and solvent-solvent interactions are given by Flory Huggins parameters. The electrostatic interaction is obtained by solving Poisson-Boltzmann equation. The binary solvent itself is mixed. But the affinities of the solvents to the polyelectrolyte is different. One of the solvents prefers the polyelectrolyte more than the other.

Figure 1 shows the concentration field of the polyelectrolyte in the binary solvent mixtures. The composition of the more preferred solvent is increased from top to bottom with fixing the polyelectrolyte concentration. When the more preferred component is rich in the solvent (bottom), the polyelectrolyte is mixed homogeneously. As its composition is decreased (top), the system is phase-separated and a labyrinth pattern is formed. In the polymer-rich phase, a stripe concentration modulation pattern is observed.

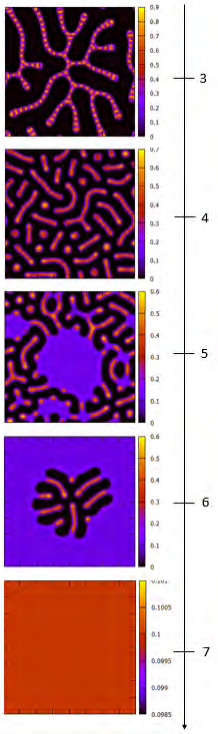

Fig. 1: Snapshots of the phase-separated pattern of the polyelectrolyte in binary mixture solvents. The concentration of the more preferred component is increased from top to bottom.

References

[1] G. H. Fredrickson, The Equilibrium Theory of Inhomogeneous Polymers, *Oxford University Press*, 2013.

Rheology Simulation of Dynamically Cross-linked Networks

Yusuke Yasuda

Research Center for Computational Design of Advanced Functional Materials.

National Institute for Advanced Industrial Science and Technology, Ibaraki 305-8568.

Recently a new type of dynamic bond elastomers called entropy-driven has gained attention for showing superior self-healing and toughness compared to conventional dynamic bond elastomers [1], but detailed understanding is not reached yet. Last year, we succeeded in fabricating a new coarse-grained model which can reproduce typical hysteresis and self-healing properties of conventional dynamic bond elastomer. This year, we introduced entropy-driven properties to the coarse-grained model.

In this work, we made coarse-grained model for dynamic bond elastomers based on Kremer-Grest model [1]. For cross-links between reactive bead, we introduced harmonic potential with associating and dissociating condition (Fig. 1). We tuned harmonic constant K and bond fracture energy ε_d. Under this condition we conducted equilibration simulation and mechanical tests. Calculation was conducted using molecular dynamics simulation software packages OCTA, and LAMMPS on ISSP Supercomputer System.

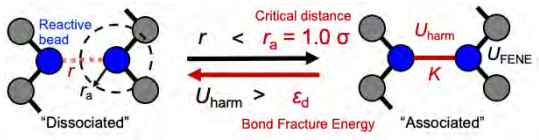

Fig.1, Schematic illustration of the coarse-grained model of dynamic bond elastomers.

From equilibration simulation, we found that equilibrium constant K_a has proportional dependence to 1/T, consistent to Gibbs equation. From the slopes and y-intercepts of the 1/T dependence of K_a, we defined ΔS_a and ΔU_a. From this analysis, we found that ΔU_a are influenced primarily by ε_d, and ΔS_a are predominantly influenced by on K. As K decreases, ΔS_a increases, confirming smaller K represents entropy-driven systems.

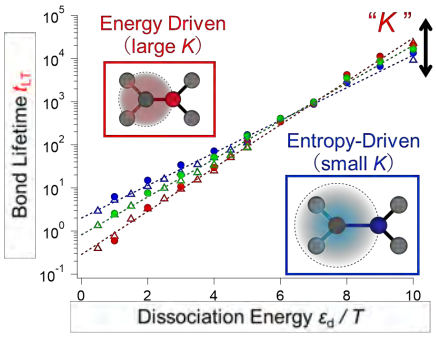

Fig. 2, the relationship among Bond lifetime, dissociation energy, and harmonic constant K

We also conducted lifetime analysis for different Ks. Then we found that average bond lifetime follows Arrhenius equation depending on K (Fig. 2), and dynamic bonds with smaller K shows shorter lifetime in high ε_d region, concluding that entropy-driven dynamic bond elastomers with high ε_d owing to smaller dissociation activation energy.

We also conducted mechanical and stress-recovery test. Both models show typical large hysteresis, and stress recovery at high temperature. Then we analyzed stress-relaxation behavior by analyzing relationship between stress and healing time, to find that stress-relaxation times are closely related to bond lifetime. Then we conclude that faster self-healing in entropy-driven dynamic bond elastomers originates from faster dissociation / association dynamics, which comes from lower activation energy for dissociation [3].

References [1] Kim et al. *Macromolecules* **2020**, *53*, 4121. [2] K, Kremer et al., *J. Chem. Phys.*, **1990**, *92*, 5057. [3] Y. Yasuda et al., *under review*.

Acknowledgement This work is partially supported by a project JPNP18016, commissioned by the New Energy and Industrial Technology Development Organization(NEDO)

Structural Analysis and Mechanical Properties Simulations of Polymer Networks with Various Network Structures

Yusuke Yasuda

Research Center for Computational Design of Advanced Functional Materials.

National Institute for Advanced Industrial Science and Technology, Ibaraki 305-8568.

Rubber elasticity theories proposed so far qualitatively reproduces the mechanical properties of vulcanized rubbers and cross-linked gels, but it is not quantitative. One reason of this is that the actual polymer networks contain inhomogeneity, and it is difficult to detect it by experiments. Then theoretically, homogeneous network is assumed.

In this work, we aimed to develop a methodology to handle network inhomogeneity, focusing on detecting structural defects in the network. We performed coarse-grained molecular dynamics simulations for networks with various inhomogeneity. Then we analyzed the structure during the crosslinking process and the mechanical properties under uniaxial deformation. We tried to extract substructures that contribute to the mechanical properties.

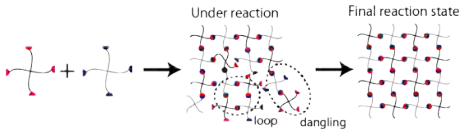

Fig, 1. Schematic illustration of the fabrication method of the system.

In this research, we fabricated coarse-grained model of star-shaped end-crosslinked elastomers which is known as a homogeneous network, was created based of the repulsive Kremer-Grest model. We prepared 3-arm and 4-arm systems referring to tetra-PEG, tri-PEG gel [1] tuning the arm length. Two terminal types A, B are prepared. Total number of beads in system are set approximately 1.0×10^5. τ density condition is set as $0.85\,\sigma^{-3}$Then system relaxation calculation and reaction calculations. For fabrication of networks with various inhomogeneity, we terminate the reaction calculation when reaction ratio reaches certain value in range of 0.24 – 0.96. Then we conducted uni-axial elongation test (λ=1-4) , and obtain stress-extension ratio curves. Then we calculated elastic modulus G_{sim} by fitting the initial shape of stress-extension ratio curves.

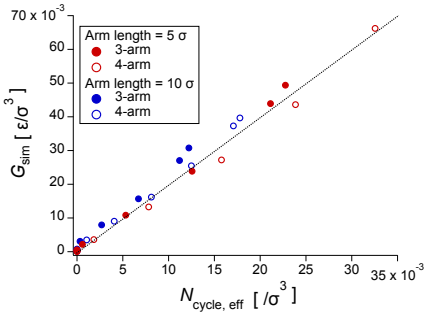

Fig. 2 Elastic moduli G_{sim} against the number of effective closed loops $N_{cycle,eff.}$

Then we tried to calculate the structure which contribute to elastic moduli. Based on the Scanlan-Case [2,3] criterion, we analyzed the network structure. We counted only effective chain s between branching points with three or more branches, excluding dangling, loop, super-dangling, super-loop structure and eliminate, including bridge and super-bridge structures. In the network constructed by effective chains, we counted the number of closed loops in network based on phantom network theory, finding that elastic moduli are proportional to $N_{cycle,eff}$ for all branch num and arm length.

References 1. 1. Fujiyabu et al., Sci Adv. 2022, 8(14), eabk0010 2. Scanlan, J. Polym. Sci., 1960, 43, 501, 3. Case, J. Polym. Sci., 1960, 45,

Acknowledgement This work is supported by a Grant-in-Aid for Young Scientists (22K14740)

Theory of microwave scattering in a dissipative superconducting circuit element

TSUYOSHI YAMAMOTO
Faculty of Pure and Applied Sciences, University of Tsukuba
Tsukuba, Ibaraki 305-8571

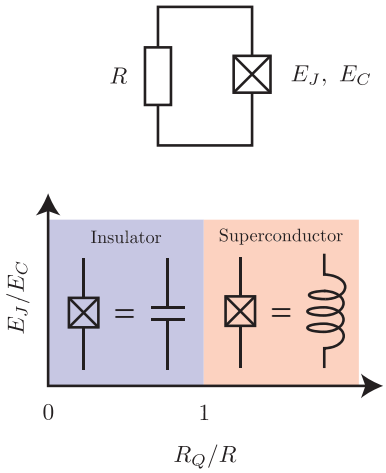

Figure 1: (top) A Josephson junction with the Josephson energy E_J and the charging energy E_C shunted by a resistor with the resistance R. (bottom) Illustration of the phase diagram of the Schmid-Buldagaev transition.

A Josephson junction is a building block of superconducting circuits. Thanks to its characteristic nonlinearity, we can develop a great variety of superconducting devices, such as a superconducting qubit and a parametric amplifier. Although the property of the isolated Josephson junction is understood well, it is little known, especially its many-body effects, when it contacts electromagnetic environments. The most notable phenomenon is a dissipation-induced quantum phase transition. Forty years ago, Schmid and Buldagaev theoretically found that a single Josephson junction shunted to a resistor, a resistively-shunted Josephson junction, undergoes a superconductor-insulator transition [1, 2]. When the resistance is larger than a resistance quantum ($R > R_Q = h/4e^2$), the Josephson junction becomes an insulator, while when $R < R_Q$, it becomes a superconductor, interestingly not being controlled by junction parameters (see Figure 1).

Although the theoretical works on the DC transport checked the Schmid-Bulgadaev transition [3, 4], there is no decisive evidence for the experimental observation [5], stirring up controversy. The recent development of superconducting circuits allows experimentalists to measure the AC-impedance of the resistively-shunted Josephson junction using microwave spectroscopy and then to obtain important properties, such as the excitation spectrum or the dynamical property. This endeavor would be a key to solving the ongoing debate problem.

In this project, we numerically investigated the AC-impedance of the resistively-shunted Josephson junction [6]. To obtain the AC-impedance, we calculated the phase-phase correlation function defined on the imaginary-time axis using the path-integral quantum Monte Carlo (PIQMC) simulation and then performed the analytical continuation for the PIQMC data using the Padé approximation. Since the Padè approximation needs highly-accurate calculations for the applying data, we performed the parallel computing for the Monte Carlo sampling mainly using “F2cpu”, succeeding in collecting a large enough Monte

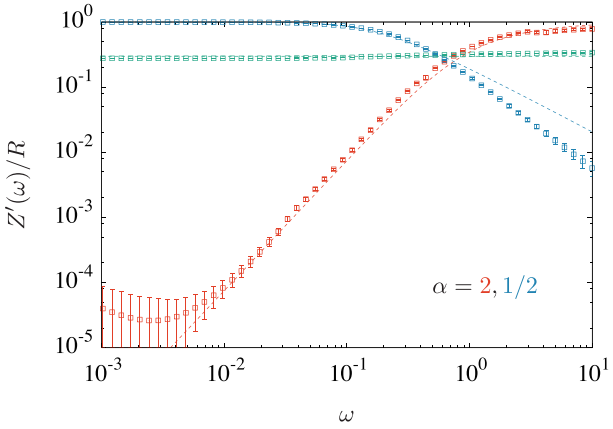

Figure 2: Frequency dependence of the real part of the AC-impedance $Z'(\omega)$ for various values of $\alpha = R_Q/R = 2$ (red), 1 (green), and 1/2 (blue), obtained by the PIQMC. At the DC limit ($\omega \to 0$), the AC-impedance goes to 0 and R for $\alpha > 1$ and $\alpha < 1$, respectively, which is a signature of the Schmid-Bulgadaev transition. The dashed lines represents the analytical formulas.

Carlo steps, typically $\sim 5 \times 10^7$, to provide the accurate calculations for the AC-impedance. Our numerical results for the AC-impedance as a function of frequency or Matsubara frequency (the Fourier space of the imaginary time) confirmed the superconductor-insulator transition, as originally predicted by Schmid and Bulgadaev and revealed the low- and high-energy physics and their crossover (see Figure 2) [7]. This work would give a deep understanding of the dissipative Josephson junction, which pushes further development for superconducting devices using Josephson junctions.

References

[1] A. Schmid, Phys. Rev. Lett. **51**, 1506 (1983).

[2] S. A. Bulgadaev, JETP Lett. **39**, 264 (1984).

[3] N. Kimura and T. Kato, Phys. Rev. B **69**, 012504 (2004).

[4] S. L. Lukyanov and P. Werner, J. Stat. Mech. P06002 (2007).

[5] A. Murani *et al.*, Phys. Rev. X **10**, 021003 (2020).

[6] P. Werner and M. Troyer, Phys. Rev. Lett. **95**, 060201 (2005).

[7] T. Yamamoto, T. Kato, L. I. Glazman, and M. Houzet, in preparation.

Grain boundary Li ion conductivity in NASICON-type Solid Electrolytes

Masanobu NAKAYAMA

Department of Advanced Ceramics,

Nagoya Institute of Technology, Gokiso, Showa-ku, Nagoya, Aichi 466-8555

$LiZr_2(PO_4)_3$ (LZP) related materials are promising solid electrolyte materials with high ionic conductivity and chemical stability.[1] Many material calculations have been applied to lithium ion-conducting NASICON-type solid electrolytes, but most of them are concerned with bulk conduction, and grain boundaries have rarely been investigated.[2], [3] In this study, the effect of dopant Ca on the ionic conductivity is discussed.

To calculate lithium ion diffusion in the grain boundary model of LZP, we used the Bond Valence Force Field (BVFF) proposed by Adams et al.[4] plus a Stillinger-Weber (SW) type force field representing three-body interactions. Parameters included in the force field were evaluated by a cuckoo search to match the results of first-principles calculations. The same was employed: force-field molecular dynamics (FFMD) calculations using the NVT ensemble were performed for 1 ns every 50 K from 400 K to 900 K. The results are presented in Table 1. The software package NAP[5], [6] was used for the above.

Figure 1 shows the grain boundary model used in this study. (a) and (b) have the same composition, but (a) with Ca ions randomly arranged and (b) with Ca ions segregated at the grain boundary, as experimentally confirmed. For these models, molecular dynamics was performed to evaluate the diffusion coefficient versus temperature, and the results are shown in Figure 2 as an Arrhenius plot. The obtained results show that the ionic conductivity (room temperature) of the segregated structure (b) is 5 x 10^{-4} cm^2 s^{-1}, which is about twice the diffusion coefficient of the random structure (a). On the other hand, no significant change in activation energy was observed. This suggests that the grain boundary conductivity can be controlled by controlling the arrangement of dopants.

A more detailed analysis of the obtained results shows that Li ions have a trapping effect near Ca ions. In previous studies, the grain boundary structure also has the effect of trapping Li ions. Therefore, it is suggested that Li ions become excessively concentrated near the grain boundary. We believe that such excess of lithium ions contributes to the enhancement of ionic conduction at the grain boundary.

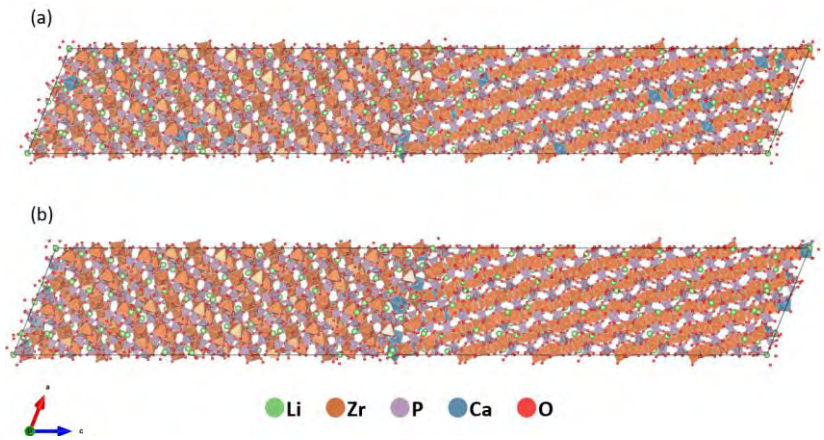

Figure 1 Grain boundary structure model for Ca-doped LZP. (a) Random substitution of Ca to Zr sites and (b) Ca segregation model near grain boundaries.

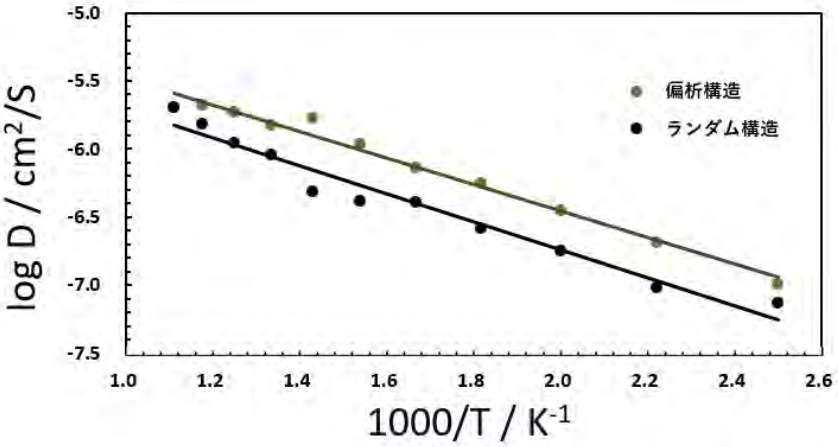

Figure 2 Comparison of diffusion coefficients of Li in two-types of grain boundary models of Ca-doped LZP. (Black symbol: random Ca arrangement model; Green symbol: Ca segregation model near to grain boundary.

References

[1] M. Nakayama et al., Chem. Commun., **58**, 9328–9340, (2022)

[2] K. Nakano et al., J. Phys. Chem. C, **125**, 23604–23612 (2021)

[3] R. Kobayashi et al., Acta Mater., **226**,117596 (2022)

[4] S. Adams et al., Phys. Stat. Sol. A, **208**, 1745-1753 (2011)

[5] R. Kobayashi, J. Open Source Softw.,**6**, 2768, (2020)

[6] R. Kobayashi et al., APL Mater., **8**, 081111, (2020)

Surface Tension Stabilizing Cell Motion Order

Katsuyoshi Matsushtia, Naoya Kamamoto, Maki Sudo, Taiko Arakaki
Depertment of Biological Science, Graduate School of Science, Osaka University
Machikaneyama, Toyonaka, Osaka 560-0043

Cells collectively move in particular scaffolds in various biological phenomena, including organ morphogenesis [1]. For example, neuronal cells move by interacting with surrounding glial tissue[2]. The collective motion reflects the interaction between the tissue and the surrounding scaffold. The ordering mechanism in this collective motion needs sufficient examination through the computer simulation based on statistical physics. In particular, the essential interaction in statistical physics is the surface tension between the cells and scaffolds, which should be incorporated into the simulation. To clarify the effect of the interface tension, we consider a collective motion of a cell cluster and its dependence on the surface tension.

We employed the cellular Potts model [3] and extended its cells with the polarity of cell-cell adhesion [4]. This model induces the spontaneous order of the cellular motion and successfully explains the collective migration of cells [5]. We changed the surface tension between the scaffold and the cells and observed the collective motion. In the case of low surface tension, the cells have an affinity with the scaffolds and individually exhibit a random walk. When the surface tension increases above the Graner-Glazier surface tension, the cells form a cluster and collectively move, In this case, the collective motion has a persistence time, in which the cluster almost straightly moves. As the surface tension increases, the switching from the straight motion to the rotational motion and inverse switching appears. In the case of large surface tension, the collective motion becomes the rotation, the center of which corresponds to the center of the cluster. Due to the rotational motion, the center of the cluster exhibits only diffusion.

This result explains the previous result of the cluster consisting of the two types of cells, which is reported in the previous project [6]. The cell cluster transitions from the rotational to straight motion as the differentiation of cells progresses. The present result implies that this motion transition originates from the surface tension decreases associated with the cell type changes in the differentiation.

We appreciate Prof. H. Kuwayama, Prof. S. Yabunaka, Dr. H. Hashimura, Prof. Sawamoto, Dr. Matsuda, Prof. H. Yoshino, and Prof. M. Kikuchi their various support on this work.

References

[1] P. Rørth, Ann. Rev. Cell Develop. Biol. **25**, 407 (2009).

[2] C. Nakajima, M. Sawada, K. Sawamoto, Curr. Opi. Neurobio. **66**, 1 (2021).

[3] F. Graner and J. Glazier, Phys. Rev. Lett. **69**, 2013 (1992).

[4] K Matsushita, Phys. Rev. E **95**, 032415 (2017).

[5] K Matsushita, Phys. Rev. E **97**, 042413 (2018).

[6] K. Matsushita, N. Kamamoto, M. Sudo, K. Fujimoto, Proc. Sympo. Traffic Flow Self-driven Parti. **27**, 23 (2021).

Calculation of ordered structures, dynamics and optical properties of soft materials

Jun-ichi FUKUDA

Department of Physics, Kyushu University, Motooka 744, Nishi-ku, Fukuoka 819-0395

We continued our study that started in the previous year on the structure of a cholesteric blue phase liquid crystal (BPLC) under an electric field. Our study was motivated by a recent experimental study [1] demonstrating the formation of various (meta)stable ordering with different periodicity in a reproducible manner by applying an electric field. Particularly, a tetragonal structure with $I4_122$ symmetry was shown to be (meta)stable even after the cessation of the electric field, which had not been reported.

Our numerical study focused on the role of planar surfaces that confine BPLC on its structure and stability, and was based on the Landau-de Gennes continuum theory that describes the orientational order by a second rank tensor. Calculations were carried out on a regular mesh, which facilitated the parallelization (in our case OpenMP was used). We also calculated the optical properties of the structures obtained (more specifically, how monochromatic incident light with a given wavevector is reflected and transmitted) by directly solving the Maxwell equations for the electromagnetic field of light. We employ plane-wave expansions in the directions normal to the thickness direction, and the Maxwell equations were discretized so that the matrix representing the Maxwell equation is of block tridiagonal form.

Our calculations [2] showed that structures with different and discretized periodicity are indeed (meta)stable. The free energy evaluation of these structures revealed that the periodicity of the most stable structure depends systematically on the electric field strength. We also calculated [2] the reflection spectra of the structures. We found strong selective reflection depending on the circular polarization of the incident light arising from the chirality of BPLC, and the variation of the reflection peak position in response to the electric field.

References

[1] D.-Y. Guo et al., Nature Mater. **19**, 94 (2020).

[2] J. Fukuda, Front. Soft Matter **2** 1011618 (2022).

Measurement-induced phase transitions in $U(1)$-symmetric monitored circuits

Yohei FUJI
Department of Applied Physics, University of Tokyo, Tokyo 113-8656

Many-body quantum systems evolved under repeated measurements have recently been shown to reveal a novel type of nonequilibrium phase transition called the measurement-induced phase transition [1, 2]. A paradigmatic example is the entanglement transition from a volume-law to an area-law entangled phase, which is induced by the competition between unitary dynamics and projective measurements. Surprisingly, the entanglement transition exhibits critical phenomena described by conformal field theory as in equilibrium phase transitions. It is then natural to ask whether universality classes due to symmetry or dimensionality also arise in measurement-induced phase transitions.

In this study, we considered one-dimensional random quantum circuits consisting of two-site unitary gates and projective measurements of single qubits, both of which are design to preserve a $U(1)$ charge corresponding to the total number of flipped qubits [3]. By employing parallel sampling implemented in Julia on Supercomputer System B at ISSP, we computed steady-state physical quantities averaged over many circuit realizations and measurement outcomes. In addition to the entanglement transition characterized by the logarithmic scaling of the entanglement entropy, we found a charge-fluctuation transition characterized by the logarithmic scaling of the bipartite charge fluctuation as shown in Fig. 1. The latter transition exhibits critical phenomena akin to the Tomonaga-Luttinger liquid theory, much like critical phenomena for the ground state of one-dimensional quantum systems preserving $U(1)$ symmetry. This result thus highlights the importance of symmetry for classifying and understanding the measurement-induced phase transitions.

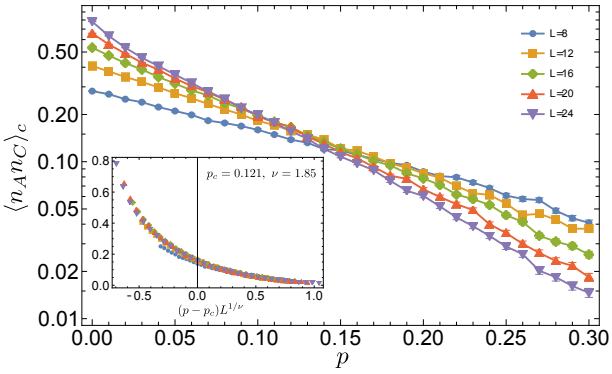

Figure 1: Subsystem charge correlation function $\langle n_A n_C \rangle_c$ between two disjoint subsystems A and C is plotted as a function of the measurement rate p. It is related to the bipartite charge fluctuation F_A by $\langle n_A n_C \rangle_c = F_A + F_C - F_{A \cup C}$.

References

[1] A. C. Potter and R. Vasseur, Entanglement Dynamics in Hybrid Quantum Circuits in *Entanglement in Spin Chains: From Theory to Quantum Technology Applications*, edited by A. Bayat, S. Bose, and H. Johannesson (Springer International Publishing, Cham, 2022) pp. 211–249.

[2] M. P. A. Fisher, V. Khemani, A. Nahum, and S. Vijay, Random Quantum Circuits, Annu. Rev. Condens. Matter Phys. **14**, 335 (2023).

[3] H. Oshima and Y. Fuji, Charge fluctuation and charge-resolved entanglement in a monitored quantum circuit with $U(1)$ symmetry, Phys. Rev. B **107**, 014308 (2023).

First principles studies of electronic structures in armchair-edged graphene nanoribbons

Junhuan LI, Kenta ARIMA

Graduate School of Engineering, Osaka University, Yamada-oka, Suita, Osaka 565-0871

Local electronic structures of graphene nanosheets have been intensively studied so far [1, 2]. However, the relationship between the electronic structure and atomic arrangement is still unclear. In this study, we simulated scanning tunneling microscopy (STM) images of armchair-edged graphene nanoribbons (AGNRs) by the first principles calculations.

Calculations were performed by STATE (Simulation Tool for Atom TEchnology) package. The AGNR we simulated was terminated by hydrogen atoms as shown in Figure 1. Periodic boundary conditions were applied to a supercell setup with length l_{cell}.

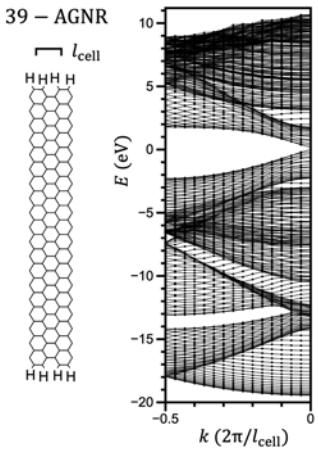

Fig. 1: The ribbon configuration and band structure of 39-AGNR.

The band structure of 39-AGNR (where 39 is the width measure by the number of rows of carbon atoms across the AGNR) is shown in the right panel of Figure 1. Based on the simulated band structure, the STM images were calculated using different sample biases. At a sample bias of -1 V, the simulated STM image exhibit hexagonal patterns as shown in Figure 2.

This work has been performed on System B of the Supercomputer Center, the Institute for Solid State Physics, the University of Tokyo.

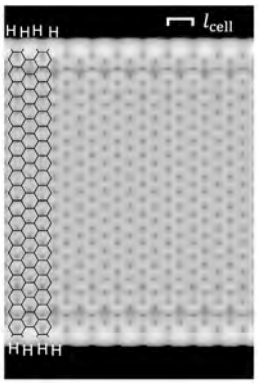

Fig. 2: The simulated STM image of 39-AGNR.

References

[1] T. Wassmann et al., J. Am. Chem. Soc. **132**, 3440 (2010).

[2] J. Li et al., Phys. Rev. B **103**, 245433 (2021).

Numerical studies on thermodynamics and excitation spectra in Heisenberg antiferromagnets on the triangular and kagome lattices

Yoshiyuki Fukumoto
Department of Physics, Faculty of Science and Technology, Tokyo University of Science
2641 Yamazaki, Noda, Chiba 278-8510

Neutron scattering experiments on two-dimensional frustrated spin systems with spontaneous magnetizations, such as a triangular-lattice system $Ba_3CoSb_2O_9$ [1] and a kagome-lattice system $Cs_2Cu_3SnF_{12}$ with the $\boldsymbol{q} = 0$ type ordering stabilized by Dzyaloshinskii-Moriya (DM) interactions [2,3], have revealed that the dynamic structure factors consist of not only collective magnon excitations but also spinon continuums.

As for the triangular-lattice system, Zhang and Li used the fermionic spinon operator to calculate dynamic structure factors within the RPA approximation [4]. They argued that the structure of the spinon continuum is closely related to the roton minimum of the magnon spectrum, and also found an amplitude mode composed from two spinons that cannot be captured by the spin wave approximation.

As for the kagome-lattice system, magnon dispersions obtained from a neutron scattering experiment on $Cs_2Cu_3SnF_{12}$ were analyzed based on the linear spin wave (LSW) approximation, and reported that the spin-wave interactions led to a large negative-renormalization, where the exchange parameter was found to be about 40% smaller than a reliable value, $J = 20.7$ meV, determined from magnetic susceptibility measurements [2]. Also, a recent neutron scattering experiment has observed a fourth collective excitation that is thought to be an amplitude mode [3].

In this article, we report our recent results of an Ising expansion (IEP) study on the large negative-renormalization observed in $Cs_2Cu_3SnF_{12}$. In order to stabilize the $\boldsymbol{q} = 0$ ordering, which is assumed in the xy plane, we incorporate the DM interaction with the D vector of $\boldsymbol{D} = (0, 0, D^{\parallel})$ and write a minimal Hamiltonian for this material as

$$H = J \sum_{\langle i,j \rangle} \boldsymbol{S}_i \cdot \boldsymbol{S}_j + \sum_{\langle i,j \rangle} \boldsymbol{D} \cdot (\boldsymbol{S}_i \times \boldsymbol{S}_j), \quad (1)$$

where $\boldsymbol{S}_i$ represents the $S = 1/2$ operator at site i. Introducing a perturbation parameter λ, we write $H_\lambda = H_0 + \lambda H_1$, where H_0 is an Ising model and we assume $\lambda \to 1$ recovers eq. (1). The perturbation calculation was performed using the connected cluster expansion method, including all clusters up to 9 links and 10 sites. Multi-block diagonalization was performed in the calculation of the effective Hamiltonian [5]. We also incorporated a local field term to improve convergence of the series [5]. The local field term is the form of staggered magnetic field stabilizing the $\boldsymbol{q} = 0$ ordering and its strength is defined as t. We include the local field term into H_0 and that with opposite sign into H_1, so as to cancel out with each other at $\lambda \to 1$. If we set $t = 0$, then we have unphysical results such as the magnon energies being negative in most of the wave vectors. When $t > 0$, the results change significantly at first, and the region of negative magnon energy decreases. When t increases to some extent, the region of negative magnon energy disappears and the result does not depend on t very much. As such value of t, we choose $t/J = 1$ in this study. As t is further increased, the resulting t dependence increases slowly, be-

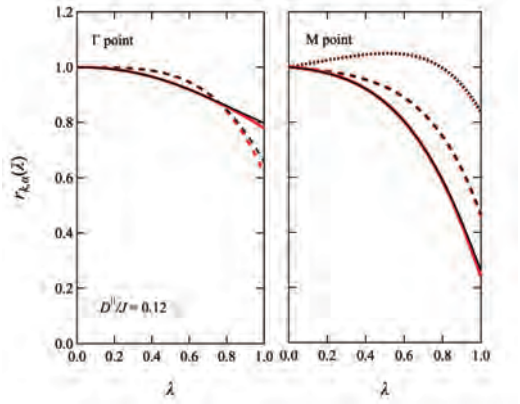

Figure 1: Renormalization factors $r_{\boldsymbol{k},\alpha}(\lambda)$. The black and red lines, respectively, represent the ninth and eighth order results.

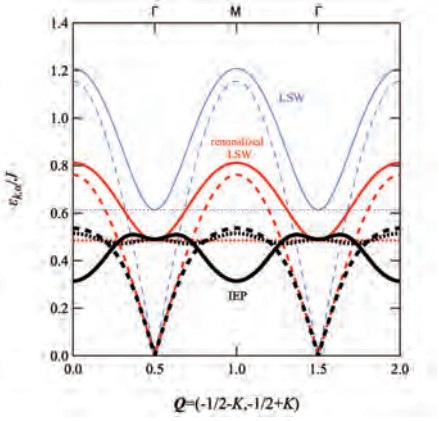

Figure 2: Comparison of magnon dispersions between the IEP and LSW. The choice of line type is the same as in Fig. 1.

cause it becomes harder to correctly handle the local field term included in the perturbation.

Let $\epsilon_{\boldsymbol{k},\alpha}$ be the magnon excitation energy to be obtained, where $\boldsymbol{k}$ is the wave vector and α is the identifier for three modes in the kagome lattice. We set $\epsilon_{\boldsymbol{k},\alpha} = r_{\boldsymbol{k},\alpha}(1) \times \epsilon^{\mathrm{LSW}}_{\boldsymbol{k},\alpha}$, where $\epsilon^{\mathrm{LSW}}_{\boldsymbol{k},\alpha}$ is the magnon excitation energy in the LSW and $r_{\boldsymbol{k},\alpha}(\lambda)$ is "renormalization factor". We calculate $r_{\boldsymbol{k},\alpha}(\lambda)$ by the IEP up to the ninth order, and evaluate value of $r_{\boldsymbol{k},\alpha}(1)$ by naive summation of the obtained series. In Fig. 1 we show the eighth and ninth order results of $r_{\boldsymbol{k},\alpha}(\lambda)$ at Γ and M points as a function of λ, and find a good convergence. In particular, for M point, the renormalization factor represented by the solid line amounts to 0.26 at $\lambda \to 1$, which demonstrates that large negative renormalization occurs in the kagome system.

Experimental results for $Cs_2Cu_3SnF_{12}$ show that the two high-energy modes are almost degenerate at the Γ point, and their energies are about 10 meV [2,3]. By fixing $J = 20.7$meV, which has been determined from magnetic susceptibility measurements [2], and searching the value of $D^{\parallel}$ so that the calculated energy of the high-energy modes at Γ point is 10 meV, we obtain $D^{\parallel}/J = 0.12$.

Figure 2 shows a comparison of the magnon dispersions between the IEP and the LSW. The path on the wave-vector plane, which connects Γ and M points, is chosen in the same way as in the experiment [3]. The black and blue lines are, respectively, the ninth-order IEP and LSW results, where $D^{\parallel}/J = 0.12$. On the other hand, the red lines are the results of the LSW with renormalized parameters where $D^{\parallel}/J = 0.18$ and the energy scale is modified by a factor 0.62 [2]. Figure 2 tells us that the dispersion relations calculated by the LSW undergo not only renormalization of the interaction parameters but also flattening of the high-energy part and the appearance of roton-like minimum around M point due to spin-wave interactions. As for the triangular lattice system, we had modification of high-energy part but no renormalization of interaction parameters [5].

In summary, we have used the IEP to investigate how spin-wave interactions modify the LSW predictions of magnon dispersions. We have successfully calculated the renormalization factor $r_{\boldsymbol{k},\alpha}(\lambda)$ by the IEP. As a result, in the kagome lattice system, in addition to the renormalization of the interaction parameter pointed out by Ono *et al.* [2], we have found that the high-energy part around M point undergoes strong deformation. In the near future, we plan to incorporate more realistic DM interactions to reproduce the detailed structure of experimental magnon spectrum data.

[1] S. Ito *et al.*, Nat. commn. 8, 235, 2017.
[2] T. Ono *et al.*, JPSJ 83, 043701, 2014.
[3] M. Saito *et al.*, PRB 105, 064424, 2022.
[4] C. Zhang *et al.*, PRB 102, 075108, 2020.
[5] W. Zheng *et al.*, PRB 74, 224420, 2006.

Numerical study of the effect of large bond randomness on the magnetization process and magnetic susceptibility in the spherical Kagome system $\{W_{72}V_{30}\}$

Yoshiyuki Fukumoto
Department of Physics, Faculty of Science and Technology, Tokyo University of Science
2641 Yamazaki, Noda, Chiba 278-8510

The spherical kagome system $\{W_{72}V_{30}\}$ is a frustrated cluster magnet consisting of thirty V^{4+} with $S = 1/2$ [1]. The exchange interaction has been estimated as $J = 115$K. In the experimental study of the low-temperature magnetization process, a step structure unique to cluster magnets has not been found [2]. To understand this result, the effects of bond randomness [2] and Dzyaloshinskii-Moriya (DM) interactions [3] were examined.

Subsequently, specific heat measurements were performed by Kihara *et al.* at temperatures $T < 11$K and magnetic fields up to 15T [4]. Although the magnitude of the specific heat is comparable to that expected in the Heisenberg model, the shape of the specific heat curve is completely different. In particular, in the Heisenberg-model calculation, a peak appeared near 2K, and it was found that even a magnetic field up to 15T affected the shape of the specific heat curve. However, in the experiment, the specific heat curve had no peak and was not affected by the magnetic field up to 15T. To resolve this problem, the specific heat calculation was performed considering bond randomness or DM interaction. Each strength is assumed to be about $0.1J$. However, it did not lead to an explanation of the experimental results.

In a previous study investigating the effect of bond randomness in a triangular lattice system [5], it was reported that when the randomness is large compared to the energy scale of the magnetic field, the magnetic field dependence of the specific heat disappears. Therefore, we decided to investigate the effect of strong bond randomness also in the spherical kagome system. As a result, it was clarified that the experimental results can be explained by assuming that the strength of the bond randomness is 40-50% of the exchange interaction. The results were published as a paper [6].

It is also interesting to study if the model Hamiltonian with the large bond randomness and a modest DM interaction reproduces experimental magnetic susceptibility. Magnetic susceptibility calculation in the presence of the both terms is a challenging problem in terms of computational complexity. If we have DM interactions, we need to work with vectors of dimension 2^{30}. In addition, when DM interaction exists, the magnetic susceptibility is obtained by applying a small magnetic field and calculating the expected value of magnetization by the cTPQ method. Then, it is necessary to average the direction of the magnetic field, the bond randomness, and the random vector of the cTPQ method. We will continue our research on efficient implementation of these averaging operations.

[1] A. M. Todae *et al.*, ChemComm, 3351 (2009).
[2] J. Schnack *et al.*, arXiv:1304.2603v1.
[2] Y. Fukumoto *et al.*, JPSJ 87, 124710 (2018).
[4] T. Kihara *et al.*, PRB 99, 064430 (2019).
[5] K. Watanabe *et al.*, JPSJ 83, 034714 (2014).
[6] M. Motohashi *et al.*, PTEP, 113I01 (2022).

Nematic Tomonaga-Luttinger Liquid Phase in an $S=1/2$ Ferromagnetic-Antiferromagnetic Bond-Alternating Chain with Next-Nearest-Neighbor Interactions

Takashi Tonegawa

Kobe University, University of Hyogo, and Osaka Metropolitan University

Recently, using mainly numerical methods, we [1] have investigated the ground-state phase diagram of an anisotropic $S=1/2$ two-leg ladder with different leg interactions. The xy and z components of the leg interactions between nearest-neighbor spins in the a (b) leg are denoted, respectively, by $J_{\mathrm{l},a}$ and $\Delta_{\mathrm{l}}J_{\mathrm{l},a}$ ($J_{\mathrm{l},b}$ and $\Delta_{\mathrm{l}}J_{\mathrm{l},b}$). On the other hand, the xy and z components of the uniform rung interactions are, respectively, denoted by $\Gamma_{\mathrm{r}}J_{\mathrm{r}}$ and J_{r}. In the above, Δ_{l} and Γ_{r} are the XXZ-type anisotropy parameters for the leg and rung interactions, respectively. This system has a frustration when $J_{\mathrm{l},a}J_{\mathrm{l},b}<0$ irrespective of the sign of J_{r}.

We [1] have numerically determined the phase diagram on the Δ_{l} ($0.0\le|\Delta_{\mathrm{l}}|\le1.0$) versus $J_{\mathrm{l},b}$ ($-2.0\le J_{\mathrm{l},b}\le3.0$) plane in the case where $J_{\mathrm{l},a}=0.2$, $J_{\mathrm{r}}=-1.0$, and $\Gamma_{\mathrm{r}}=0.5$. It is noted that the rung interaction is ferromagnetic and its anisotropy is of the Ising-type. Furthermore, the a leg interaction is antiferromagnetic, while the b leg interaction are either ferromagnetic or antiferromagnetic, the anisotropies of both leg interactions being of the XY-type. We have employed the physical consideration, and the level spectroscopy and phenomenological renormalization-group analyses of the numerical date obtained by the exact diagonalization method. Interestingly enough, we have found that two kinds of nematic Tomonaga-Luttinger Liquid (nTLL) phases appear; one of which appears in the unfrustrated and the other in the frustrated one. The nTLL state is characterized not only by the formation of two-magnon bound pairs but also by the dominant nematic four-spin correlation function. It should be emphasized that the asymptotic form of this correlation function in the unfrustrated region and that in the frustrated region show the power-law decay with the uniform character and the power-law decay with the staggered character, respectively. Thus, both nTLL phases are different phases, and the latter nTLL phase may be called the staggered nTLL phase.

According to the above result, it is reasonably expected that the nTLL state appears as the zero-field ground state in general $S=1/2$ unfrustrated one-dimensional systems in which pairs of $S=1/2$ spins coupled strongly with the Ising-type ferromagnetic interaction are connected by the weak XY-type antiferromagnetic interactions. Some examples of such systems are (A) the $S=1/2$ ferromagnetic-antiferromagnetic bond-alternating chain, (B) the $S=1/2$ two-leg ladder with ferromagnetic rung and antiferromagnetic leg interactions, (C) the $S=1/2$ Kondo necklace chain with ferromagnetic rung and antiferromagnetic leg interactions, and so on.

The purpose of this report is to discuss the system (A) with next-nearest-neighbor interactions, which is described by the Hamiltonian

$$\mathcal{H}=-J_{\mathrm{F}}\sum_{j=1}^{N/2}[\vec{S}_{2j-1},\vec{S}_{2j}]+J_{\mathrm{AF}}\sum_{j=1}^{N/2}[\vec{S}_{2j},\vec{S}_{2j+1}]+J_2\sum_{j=1}^{N}[\vec{S}_j,\vec{S}_{j+2}]$$

with

$$[\vec{S}_{2j-1},\vec{S}_{2j}]=\Gamma_{\mathrm{F}}\left(S^x_{2j-1}S^x_{2j}+S^y_{2j-1}S^y_{2j}\right)+S^z_{2j-1}S^z_{2j}\,,$$

$$[\vec{S}_{2j},\vec{S}_{2j+1}]=S^x_{2j}S^x_{2j+1}+S^y_{2j}S^y_{2j+1}+\Delta_{\mathrm{AF}}S^z_{2j}S^z_{2j+1}\,,$$

$$[\vec{S}_j,\vec{S}_{j+2}]=S^x_jS^x_{j+2}+S^y_jS^y_{j+2}+\Delta_{\mathrm{AF}}S^z_jS^z_{j+2}\,,$$

where $J_{\mathrm{F}}\gg J_{\mathrm{AF}}>0.0$, $1.0\ge\Gamma_{\mathrm{F}}\ge0.0$, $1.0\ge|\Delta_{\mathrm{AF}}|\ge0.0$, and N, being assumed to be a multiple of four, is the number of spins in the system. We note that the nearest-neighbor ferromagnetic interactions are stronger than the nearest-neighbor antiferromagnetic ones, and the anisotropies of the former and latter interactions are of the Ising-type and the XY-type, respectively. Furthermore, the anisptropies of the nearest-neighbor antiferromagnetic interactions and next-nearest-neighbor ones have the same form.

Using a variety of numerical methods based on the exact diagonalization calculation, we have determined the ground-state phase diagram on the J_2 versus Δ_{AF} plane in the case where $J_{\mathrm{F}}=-1.0$,

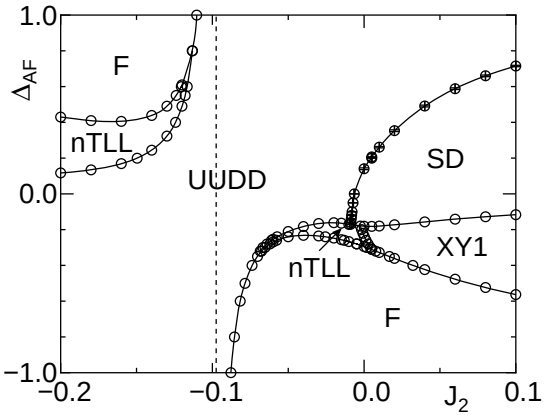

Figure 1: Ground-state phase diagram for $J_{\rm F}=-1.0$, $J_{\rm AF}=0.195$, and $\Gamma_{\rm F}=0.8$.

$J_{\rm AF}=0.195$, and $\Gamma_{\rm F}=0.8$. The obtained phase diagram, where the solid lines show the phase boundary lines, is depicted in Fig. 1. This phase diagram consists of the ferromagnetic (F), $XY1$, singlet-dimer (SD), and up-up-down-down (UUDD) phases as well as the nematic Tomonaga-Luttinger liquid (nTLL) phase. It should be emphasized that the one of the nTLL phases which appears in the frustrated region ($J_2<-1.0$) is the the staggered nTLL phase discussed above.

Finally, we discuss how to obtain the phase boundary lines in these phase diagrams. We denote, respectively, by $E_0^{\rm P}(N,M)$ and $E_1^{\rm P}(N,M)$, the lowest and second-lowest energy eigenvalues of the Hamiltonian $\mathcal{H}$ under the periodic boundary condition within the subspace of N and M, where $M(=0,\pm1,\cdots,\pm N/2)$ is the total magnetization. Furthermore, we denote by $E_0^{\rm T}(N,M,P)$ the lowest eigenvalue of $\mathcal{H}$ under the twisted boundary condition within the subspace of N, M, and P, where $P(=\pm1)$ is the eigenvalue of the space inversion operator with respect to the twisted bond. We have numerically calculated these energies for finite-size systems with up to $N=28$ spins by means of the exact-diagonalization method. The ground-state energy of the finite-N system is given by $E_0^{\rm P}(N,N/2)$ in the F region and by $E_0^{\rm P}(N,0)$ in the other regions. In the following way, we have estimated the finite-size critical values of the interaction parameters for each phase transition. Then, the phase boundary line for the transition has been obtained by connecting the results for the $N\to\infty$ extrapolation of the finite-size critical values.

First, the phase transitions between the $XY1$ and SD phases and between the nTLL and UUDD phases are the Berezinskii-Kosterlitz-Thouless transition [2]. In these transitions, the level spectroscopy method developed by Nomura and Kitazawa [3] is very powerful for calculating the finite-size critical values, which are estimated from $E_0^{\rm P}(N,0)=E_0^{\rm T}(N,M,-1)$. Secondly, the phase transition between the SD and UUDD phases is the 2D Ising-type transition. It is well known that the phase transition line is determined by the phenomenological renormalization-group (PRG) method [4]. Then, to estimate the finite-size critical values, we solve the PRG equation, $N\,\Delta_{00}(N)=(N+4)\,\Delta_{00}(N+4)$, where $\Delta_{00}(N)=E_1^{\rm P}(N,0)-E_0^{\rm P}(N,0)$. Thirdly, the nTLL state accompanies two-magnon bound-states, while the $XY1$ state does not. Then, in the ground-state magnetization curve for the finite-size system, the magnetization increases from $M=0$ to $M=2$ in the former state and from $M=0$ to $M=1$ in the latter state. Thus, the finite-size critical values are estimated from $\Delta_{10}(N)=\Delta_{20}(N)/2$, where $\Delta_{M0}(N)=E_0^{\rm P}(N,M)-E_0^{\rm P}(N,0)$. Lastly, it is apparent that the finite-size critical values for the phase transitions between the F phase and one of the nTLL, $XY1$, and UUDD phases are estimated from $E_0^{\rm P}(N,N/2)=E_0^{\rm P}(N,0)$.

In conclusion, we remark that the phase diagram shown in Fig. 1 is nearly point-symmetric around the point $(J_2,\,\Delta_{\rm AF})=(-J_{\rm AF}/2.0=-0.0975,\,0.0)$ (see the dotted line) and the F and nTLL phases appear in two places. This characteristic feature of the phase diagram can be well explained by the perturbation calculation from the strong ferromagnetic coupling limit [5]. The key point is the fact that the anisptropies of the nearest-neighbor antiferromagnetic interactions and next-nearest-neighbor ones have the same form.

The present work has been done in collaboration with Kiyomi Okamoto, Kiyohide Nomura, and Tôru Sakai.

[1] T. Tonegawa, T. Hikihara, K. Okamoto, S. C. Furuya, and T. Sakai, J. Phys. Soc. Jpn. **87**, 104002 (2018).
[2] Z. L. Berezinskii, Sov. Phys. JETP **34**, 610 (1971); J. M. Kosterlitz and D. J. Thouless, J. Phys. C **6**, 1181 (1973).
[3] K. Nomura and A. Kitazawa, J. Phys. A **31**, 7341 (1998).
[4] M. P. Nightingale, Physica A **83**, 561 (1976).
[5] K. Okamoto, T. Tonegawa, K. Nomura, and T. Sakai, Presentation at the Autumn Meeting of the Physical Society of Japan, September 12∼15, 2022.

Phase separation dynamics in hydrodynamic models

Kyosuke ADACHI

Nonequilibrium Physics of Living Matter RIKEN Hakubi Research Team, RIKEN Center for Biosystems Dynamics Research (BDR), 2-2-3 Minatojima-minamimachi, Chuo-ku, Kobe 650-0047, Japan

RIKEN Interdisciplinary Theoretical and Mathematical Sciences Program (iTHEMS), 2-1 Hirosawa, Wako 351-0198, Japan

Liquid-liquid phase separation (LLPS), which is widely recognized in condensed matter and soft matter physics, has gained renewed attention in cell biology. Several kinds of protein condensates have been found in a cell, and LLPS is discussed as a possible mechanism of the formation and dynamics of condensates [1]. To understand how the amino acid sequence of proteins and intracellular nonequilibrium environments can affect the phase separation dynamics, numerical simulations of polymer models and hydrodynamic models should be useful.

This year, as a preliminary study, we performed several numerical simulations of hydrodynamic models, which are PDE models of the particle density field. We first tested the Model B dynamics [2] by the Euler-Maruyama method with discretization of time and space. Using parallel computing to collect many samples with different initial conditions and noise realizations, we confirmed the Lifshitz-Slyozov-Wagner (LSW) scaling for the growth of the cluster size. Then, as a simple extension to nonequilibrium conditions that can be relevant to intracellular situations, we considered a model that breaks the fluctuation-dissipation relation. This model is similar to Active Model B+ [3], which have been originally proposed as a model of active matter. Performing numerical simulations with small additional terms to improve numerical stability, we found that the cluster growth is slower than that in Model B, suggesting the suppression of the phase separation dynamics due to the nonequilibrium conditions.

References

[1] S. F. Banani *et al*., Nat. Rev. Mol. Cell Biol. **18**, 285 (2017).

[2] P. C. Hohenberg and B. I. Halperin, Rev. Mod. Phys. **49**, 435 (1977).

[3] C. Nardini *et al*., Phys. Rev. X **7**, 021007 (2017).

Solution of the Eliashberg equation with the electron-electron Coulomb interaction

Ryosuke AKASHI
National Institutes for Quantum Science and Technology

The Eliashberg theory[1] with the Migdal approximation [2] is the state-of-the-art framework for the first-principles calculations of phonon-mediated superconductors. In principle, the competition between the phonon-mediated pairing attraction and screened Coulomb repulsion is accurately treated there for weakly correlated metals, which is crucial for reliable estimation of the superconducting transition temperature $T_{\rm c}$. However, the latter part has been mostly treated as a single empirical parameter μ^*[3], with which one cannot apply the theory to undiscovered systems where the $T_{\rm c}$ measurement does not exist. It is only recent that the effect of the screened Coulomb interaction on the pairing has been explored non-empirically.

The author has recently studied the effect of frequency dependent screened Coulomb interaction within the random -phase approximation. He has revealed the cooperative mechanism of the plasmonic and phononic pairing attractions from first principles, by analysing the non-diagonal (pairing) part of the self energy [4, 5]. On the other hand, a part of diagonal self energy due to the plasmons were shown to have negative effect, partially cancelling the former pairing [6]. However, the full treatment of all the components of the screened Coulomb-induced frequency dependent self energy was missing. In this project, we calculated the Eliashberg equations with all the screened Coulomb self energy parts included for uniform electron gas [7].

The Eliashberg equations with the Migdal approximation are written as follows:

$$Z_i(i\omega_j) = 1 - T\sum_{i'j'} \frac{\omega_{j'}}{\omega_j} \frac{Z_{i'}(\omega_{j'})}{\Theta_{j'}(i\omega_{j'})} W_{ii'}(\omega_j - \omega_{j'}), \quad (1)$$

$$\chi_i(i\omega_j) = T\sum_{i'j'} \frac{\xi_{i'} + \chi_{i'}(\omega_{j'})}{\Theta_{j'}(i\omega_{j'})} W_{ii'}(\omega_j - \omega_{j'}), \quad (2)$$

$$\phi_i(i\omega_j) = -T\sum_{i'j'} \frac{\phi_{i'}(\omega_{j'})}{\Theta_{j'}(i\omega_{j'})} W_{ii'}(\omega_j - \omega_{j'}), \quad (3)$$

$$\Theta_i(i\omega_j) = [\omega_j Z_i(i\omega_j)]^2 + [\xi_i + \chi_i(i\omega_j)]^2 + [\phi_i(i\omega_j)]^2 . \quad (4)$$

Indices i (i') and j (j') denote the basis state and Matsubara frequency, respectively. ξ_i is the energy eigenvalue of the state i measured from the chemical potential. $W_{ii'}(\nu_j)$ is the matrix element of the interaction between the Cooper pair states labeled by i and $i*$ with the Bosonic Matsubara frequency ν_j.

For homogeneous electron gas the basis i corresponds to the plane-wave state. We have implemented a code package that solves the above equations with an approximate manner. The interaction $W_{ii'}(\nu_j)$ was set to the screened Coulomb interaction $W_{\rm el}$ within the random phase approximation plus the attraction mediated by the Einstein phonon with definite frequency and electron-phonon coupling $W_{\rm ph}$. The diagonal terms Z and χ were evaluated at $T = 0$ noniteratively with initial value $Z = 1$ and $\chi = 0$ and without $W_{\rm ph}$, which corresponds to the G_0W_0 approximation. The equation for the nondiagonal term ϕ was later linearized with $W_{\rm ph}$ and its largest eigenvalue, which becomes unity at the transition temperature, was calculated. The iterative method

was used, which required only no more than a few hours in a serial run at *system B* at $T \sim 100K$.

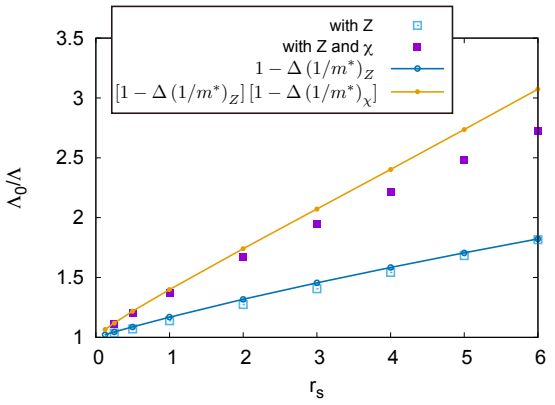

Figure 1: Ratio of the largest eigenvalues of the linearized Eliashberg equation with and without the self-energy corrections. Lines indicate approximate formulas. Taken from Ref. [7]

We show the results of the corrections to the pairing strength in Fig. 1. The blue open (purple closed) squares denote the inverse ratio of the largest eigenvalues with Z (Z and χ) to the non-interacting value. The values larger than unity indicate suppression of the pairing by the Coulomb self energy. The χ term has been known to cancel the effect of Z for the effective mass. In contrast, our result shows that χ cooperate with Z for the pairing suppression. This result highlight the importance of χ for superconducting calculations, which is computationally demanding and has mostly been ignored in the previous studies.

We also analyzed the band structure of a compound HgCr2Se4 [8]. The calculations were performed using Quantum Espresso [9] with norm conserving pseudopotentials from *Pseudo dojo* [10]. Self consistent calculations using the HSE06 exchange-correlation functional [11] and spin-orbit coupling required half a day per run with 2 nodes in *fat* group in *Ohtaka*. For the memory requirement the jobs could not run in *cpu* queue group. The band structure was interpolated using Wannier90 [12].

References

[1] G. M. Eliashberg, Zh. Eksp. Teor. Fiz. **38**, (1960) 966.

[2] A. B. Migdal, Zh. Eksp. Teor. Fiz. **34**, (1958) 1438.

[3] P. Morel and P. W. Anderson, Phys. Rev. **125**, (1962) 1263.

[4] Y. Takada, J. Phys. Soc. Jpn. **45** (1978) 786.

[5] R. Akashi and R. Arita, Phys. Rev. Lett. **111** (2013) 057006.

[6] A. Davydov, A. Sanna, C. Pellegrini, J. K. Dewhurst, S. Sharma, and E. K. U. Gross, Phys. Rev. B **102**, (2020) 214508.

[7] R. Akashi, Phys. Rev. B **105** (2022) 104510.

[8] H. Tanaka *et al.*, Phys. Rev. Lett. accepted.

[9] P. Giannozzi *et al.*, J. Phys. Condens. Matter **29**, (2017) 465901.

[10] G. Pizzi *et al.*, J. Phys. Condens. Matter **32**, (2020) 165902.

[11] J. Heyd, G. E. Scuseria, and M. Ernzerhof, J. Chem. Phys. 436 124, (2006) 219906.

[12] N. Marzari and D. Vanderbilt, Phys. Rev. B **56** (1997) 12847.

Gapless symmetry-protected topological phase of quantum antiferromagnets on anisotropic triangular strip

Yuichiro HIDAKA[1], Shunsuke C. FURUYA[2], Atsushi UEDA[1], and Yasuhiro TADA[3]
[1]*Institute for Solid State Physics, University of Tokyo*
Kashiwa-no-ha, Kashiwa, Chiba 277-8581
[2]*Department of Basic Science, University of Tokyo*
Meguro, Tokyo 153-8902
[3]*Quantum Matter Program, Graduate School of Advanced Science and Engineering, Hiroshima University, Higashihiroshima, Hiroshima 739-8530*

Classifying phases of matter is one of the paramount issues in condensed matter physics. One of the important classes of the quantum phase of matter is a symmetry-protected topological (SPT) phase. An SPT phase is a gapped phase that preserves some given symmetries but is not adiabatically connected to a trivial phase without breaking the symmetries [1]. Recently many researchers attempt to extend the concept of the SPT phase into gapless systems [2, 3].

One of the gapless SPT phases we study is the anisotropic triangular strip (ATS) model, which is the three-leg XXZ spin ladder with the frustrated XXZ rung interaction. The lattice is shown in Fig.1. According to the field-theoretic analysis, if the rung coupling is sufficiently small, the ground state of the ATS model is the gapless SPT state, in that the ground state has simultaneously the properties of the Haldane state and the Tomonaga-Luttinger liquid. This property is also supported by the numerical calculation [4].

In the present study, we investigate the ground state of the ATS model, where we expand the region of the parameters. We used the ITensor and TeNPy libraries [5, 6]. We found that the entanglement spectrum of the ATS model is doubly degenerate, which is the important feature of the Haldane state if the rung coupling $J_\times$ is sufficiently small (Fig.2). Moreover, from the calculation of the entanglement entropy, we found that the ground state has the central charge $c = 1$. On the other hand, if the rung coupling $J_\times$ is sufficiently larger than the ladder coupling J, the ground state becomes the ferrimagnetic state. This is checked by the calculation of magnetization. Finally, if the rung coupling $J_\times$ is of the same order as the ladder coupling, the ground state is in the trivial phase, in which we cannot see the even-fold degeneracy of the entanglement spectrum, and is in a gapless phase. The phase diagram of the ATS model is determined as shown in Fig.3 [7].

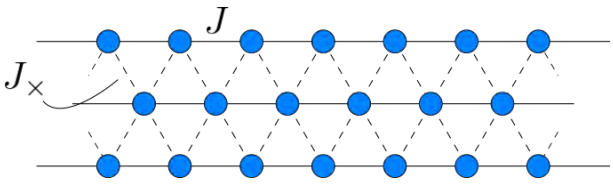

Figure 1: The anisotropic triangular strip (ATS) XXZ model. J denotes the ladder coupling and $J_\times$ denotes the frustrated rung coupling. All coupling is the XXZ interaction: $S_i^x S_j^x + S_i^y S_j^y + \Delta S_i^z S_j^z$.

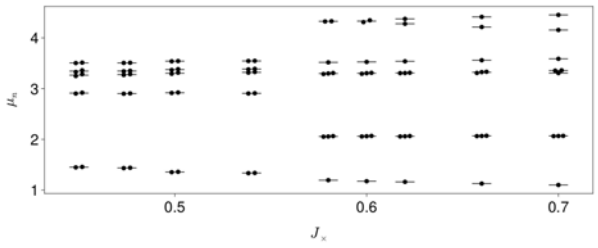

Figure 2: The entanglement spectrum of the ATS model with $\Delta = 0.8$. When $J_\times < 0.54$ we can see the even-fold degeneracy of the entanglement spectrum, which implies the Haldane state.

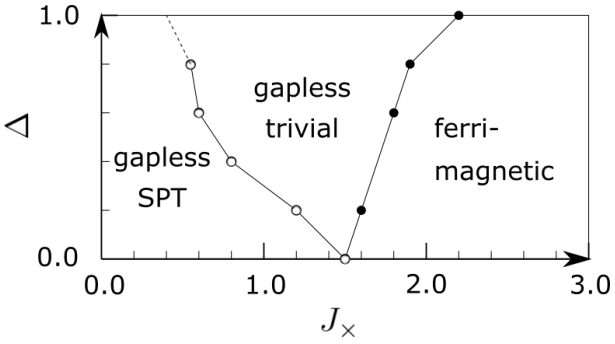

Figure 3: The phase diagram of the ATS model.

References

[1] X. Chen, Z.-C. Gu, and X.-G. Wen, Phys. Rev. B 83, 035107 (2011).

[2] T. Scaffidi, D. E. Parker, and R. Vasseur, Phys. Rev. X 7, 041048 (2017).

[3] S. C. Furuya and M. Oshikawa, Phys. Rev. Lett. 118, 021601(2017).

[4] Y. Hidaka, S. C. Furuya, A. Ueda, and Y. Tada, Phys. Rev. B 106, 144436(2022).

[5] M. Fishman, S. R. White, and E. M. Stoudenmire, arXiv:2007.14 (2020).

[6] J. Hauschild and F. Pollmann, SciPost Phys. Lect. Notes , 5 (2018).

[7] Y. Hidaka, S. C. Furuya, A. Ueda, and Y. Tada, in preparation.

Finite temperature calculations of frustrated quantum spin systems

Katsuhiro MORITA
Department of Physics and Astronomy, Faculty of Science and Technology, Tokyo University of Science, Noda, Chiba 278-8510

The $S = 1/2$ kagome antiferromagnets are known to have exotic properties even at finite temperatures. The specific heat has a multiple-peak structure [1], and the 1/3 magnetization plateau is expected to melt asymmetrically at finite temperatures [2, 3]. These properties do not appear in the triangular lattice model, for example. Therefore, these properties are considered to be unique to the kagome lattice model.

In this study, we have calculated the magnetic specific heat, entropy, magnetic susceptibility, and finite temperature magnetization curves for the $S = 1/2$ $J_1 - J_2$ kagome lattice Heisenberg model using the orthogonalized finite temperature Lanczos method [4, 5] on Supercomputer System B at the ISSP. J_1 represents the nearest-neighbor interaction and J_2 represents the next nearest-neighbor interaction. Here we set $J_1 = 1$ as the energy unit. In this study, the calculations were performed with a 36-site kagome cluster.

We have found that the entropy remains at low for $-0.06 < J_2 < 0.02$, and outside this range, the entropy decreases rapidly. At $J_2 \simeq 0$, the magnetic specific heat has a triple-peak structure, but as $|J_2|$ increases, the specific heat tends to have a double-peak structure. In the finite temperature magnetization curves, there is asymmetric melting of the 1/3 magnetization plateau around $J_2 = 0$, but the 1/3 plateau becomes clearly visible as $|J_2|$ increases. This is because the $\mathbf{q} = \mathbf{0}$, up-up-down state stabilizes for $J_2 > 0$, the $\sqrt{3} \times \sqrt{3}$ up-up-down state stabilizes for $J_2 < 0$, and the plateau becomes unstable around the boundary.

These results will be compared with experimental results in the future to clarify the magnetic properties of the compounds.

References

[1] T. Shimokawa and H. Kawamura, J. Phys. Soc. Jpn. **85**, 113702 (2016).

[2] J. Schnack, J. Schulenburg, and J. Richter: Phys. Rev. B **98**, 094423 (2018).

[3] T. Misawa, Y. Motoyama, and Y. Yamaji: Phys. Rev. B **102**, 094419 (2020).

[4] K. Morita and T. Tohyama: Phys. Rev. Research **2**, 013205 (2020).

[5] K. Morita: Phys. Rev. B **105**, 064428 (2022).

Machine learning molecular dynamics studies of complex structural materials

Masahiko OKUMURA[1], Hayato SHIBA[2], Masatoshi HANAI[3], Yasunobu ANDO[4], Akiko YAMAGUCHI[1], Keita KOBAYASHI[1], and Hiroki NAKAMURA[1]

[1]*Center for Computational Science and e-Systems, Japan Atomic Energy Agency, Wakashiba, Kashiwa, Chiba 277-0871*

[2]*Information Technology Center, University of Tokyo, Chiba 277-0882*

[3]*Graduate School of Information Science and Technology, University of Tokyo, Tokyo 133-8658*

[4]*Research Center for Computational Design of Advanced Functional Materials, National Institute of Advanced Industrial Science and Technology, Tsukuba, Ibaraki 305-8568*

Machine learning molecular dynamics (MLMD) is a promising simulation method with high accuracy and low computational costs [1]. Artificial neural networks (ANNs) are used to reproduce the results of first-principles calculations (FPCs). The ANNs are trained using datasets that consist of a lot of the results of FPCs. For this method, supercomputers are used for 1) making huge amounts of the FPC results, 2) training the ANNs, and 3) conducting molecular dynamics (MD) simulations with the ANN potentials. Density functional calculations are popular for making the training data. Several methods are used to train the ANNs, e.g., stochastic gradient descent, adaptive momentum estimation, extended Kalman filter (EKF), etc. The EKF method is known as one of the best optimizers for the ANN potential. However, the calculation speed for an epoch is slower than the other methods. To overcome this weak point, the multi-stream EKF method is often used with parallel computers [2]. The MD simulations with the ANN potentials for large systems are usually conducted on a supercomputer.

Preparing the training dataset and training the ANNs are the time-consuming steps of MLMD. Notably, the ANNs for complex materials require a large dataset, because many atom configurations are realized, where the complex materials are, in this report, defined as those with large unit cells with periodic boundary conditions. For making a dataset of complex materials, a large number of FPCs with many atom configurations in large unit cells are required. With the large dataset, heavy ANN training is needed. Density functional calculations are popular to make the data, which are popular calculations on the ISSP

supercomputer. But the ANN training calculations may not be popular. Therefore, we evaluated the scaling of the ANN training on System B, and the results are compared with those given by Oakbridge-cx operated by the Information Technology Center, The University of Tokyo. We prepared 7,007 data of ThO_2, which shows superionic transition below its melting point [3]. Therefore, large unit cells are needed to reproduce the superionic transition and melt, i.e., ThO_2 can be considered a complex material although the structure of its solid state is simple. The dataset contains the configurations of solid, super-ionic, and liquid states of ThO_2. The n2p2 open-source software for MLMD [4] was used, which provides the multistream EKF method using MPI.

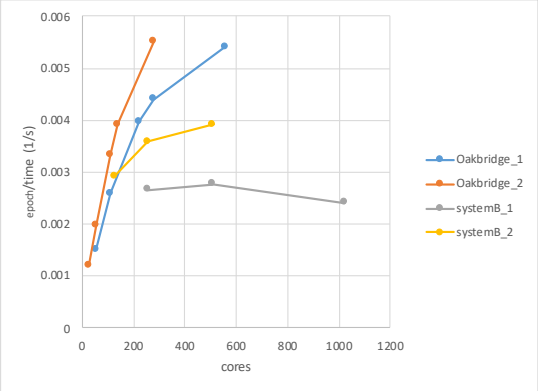

Fig. 1 The relation between the number of cores and the number of steps per second is shown. The blue and orange plots represent full- and half-core calculations on Oakbridge-cs, respectively. The gray and yellow pots represent full- and half-core calculations on Oakbridge-cs, respectively.

Figure 1 shows the relation between the number of cores and epoch/time (1/s) for System B and Oakbridge-cs. The blue and orange plots show the results of Oakbridge-cx, where the former and the latter are the results of calculations using all and half of the cores on a CPU, respectively. We found that the reduction of the active cores improves the performance. This may be because the relative memory size was increased by the reduction of the active cores. The gray and yellow plots represent the results of System B, where the former and the latter are the results of calculations using all and half of the cores on a CPU, respectively. For System B, the same tendency was obtained, i.e., the reduction of the active cores accelerates the learning speed.

We investigated the relation between the number of cores and the number of epochs per second. We found that the reduction of active cores improves the calculation speed both for System B and Oakbridge-cx.

References

[1] J. Behler and M. Parrinello, Phys. Rev. Lett. **98**, 146401 (2007).

[2] A. Singraber *et al.*, J. Chem. Theo. Comp. **15**, 3075 (2019).

[3] K. Kobayashi *et al.*, Sci. Rep. **12**, 9808 (2022).

[4] A. Singraber *et al.*, J. Chem. Theo. Comp. **15**, 1827 (2019).

Multi-impurity method for bond-weighted tensor renormalization group

Satoshi MORITA
Graduate School of Science and Technology, Keio University
Kohoku-ku, Yokohama, Kanagawa 223-8522

Tensor network (TN) methods are attracting much attention as powerful tools for computing strongly correlated many-body problems. The partition function of classical statistical systems can be represented by the TN form. However, the contraction of a large TN still requires an exponentially large computational effort. The concept of the real-space renormalization group resolves this problem. The tensor renormalization group (TRG) method and its variants calculate a coarse-grained tensor by information compression using the singular value decomposition [1, 2]. These methods can calculate the partition function approximately in logarithmic time for the system size. Recently, Adachi, et al. have proposed the bond-weighted TRG (BWTRG) method, which improves the accuracy of TRG by introducing a bond weight and distributing it appropriately [3].

In this study, we propose an algorithm to calculate higher-order moments of physical quantities based on BWTRG. We introduce a bond-weight impurity which represents a physical quantity. With the appropriate update rules, coarse-grained bond-weights containing multiple impurities can be generated to calculate the higher-order moments of the physical quantity. Our proposed method is compared with conventional methods on the two-dimensional classical spin model. The proposed method achieves higher accuracy at lower computational cost than the higher-order TRG algorithm [4]. We also show that the finite-size scaling analysis of the squared magnetization provides critical exponents and distinguishes the weakly first-order and continuous phase transitions.

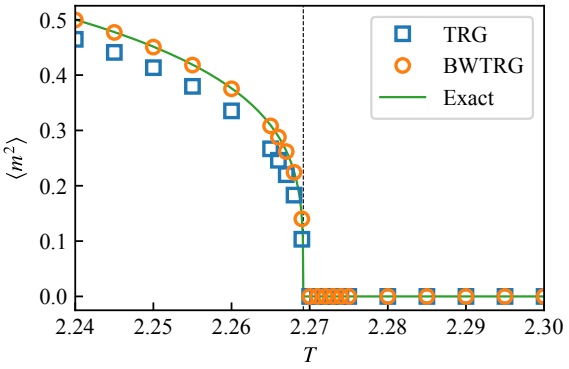

Figure 1: The squared magnetization of the Ising model on the square lattice calculated by TRG and BWTRG with the bond dimension $\chi = 128$ and the system size $L = 2^{25}$. The green solid curve shows the exact solution in the thermodynamic limit.

References

[1] M. Levin and C. P. Nave, Phys. Rev. Lett. **99**, 120601 (2007).

[2] Z. Y. Xie, J. Chen, M. P. Qin, J. W. Zhu, L. P. Yang, and T. Xiang, Phys. Rev. B **86**, 1 (2012).

[3] D. Adachi, T. Okubo, and S. Todo, Phys. Rev. B **105**, L060402 (2022).

[4] S. Morita and N. Kawashima, Comput. Phys. Commun. **236**, 65 (2019).

Majorana Kramers Qubits and Yang-Lee Anyons in Topological Superconductors

Takeshi MIZUSHIMA
Department of Materials Engineering Science, Osaka University
Toyonaka, Osaka 560-8531

We have investigated non-Abelian statistics of Majorana Kramers pairs (MKPs) in time-reversal invariant topological superconductors (TRITSCs) [1]. Numerically solving the time-dependent Bogoliubov-de Gennes equation, we have simulated the braiding dynamics of MKPs in a network of one-dimensional TRITSCs. We have first considered the tolerance of MKPs against a perturbation with broken time-reversal symmetry such as a magnetic field and demonstrated the robustness of the non-Abelian braiding of MKPs when the initial and final states of a braiding process maintain the combined symmetry of time reversal and mirror reflection symmetries. The Majorana Kramers qubit is tolerant even when intermediate states break the combined symmetry. We have also discussed the effect of gate-induced inhomogeneous potentials at junctions between superconducting nanowires. Such a potential generally induces a non-Majorana nearly zero-energy Andreev bound state at the junctions. Our numerical simulation shows that the dynamics of MKPs accumulate significant errors when such non-Majorana states exist and interfere with MKPs. Although we concentrated on Majorana particles in a TRITSC in this work, it is expected that effects of non-Majorana states generated by inhomogeneous gate potentials on the non-Abelian braiding are ubiquitous for any topological superconductors with broken time-reversal symmetry.

We have also demonstrated that a Yang-Lee anyon system is constructed from collective Majorana bound states in a network of topological superconducting nanowires [2]. Yang-Lee anyons are nonunitary counterparts of Fibonacci anyons, obeying the same fusion rule. Because of nonunitarity, the central charge and the scaling dimension for the one nontrivial primary field are negative, $c = -22/5$ and $\Delta = -2/5$, respectively. The nonunitary conformal field theory with $c = -22/5$ describes the nonunitary critical phenomenon known as the Yang-Lee edge singularity. In Ref. [2], we consider a topological superconductor junction system coupled with dissipative electron baths as a non-hermitian platform for interacting Majorana quasiparticles. Numerically calculating the central charge and scaling dimension, we find the condition that the non-Hermitian Majorana system can simulate the Ising spin model of the Yang-Lee edge singularity and confirmed that, by controlling model parameters in a feasible way, the Yang-Lee edge criticality is realized. We also discuss the scheme for the measurement and the braiding of Yang-Lee anyons, aiming at the application to universal quantum computation.

References

[1] Y. Tanaka, T. Sanno, T. Mizushima, and S. Fujimoto: Phys. Rev. B **106**, 014522 (2022).

[2] T. Sanno, M. G. Yamada, T. Mizushima, and S. Fujimoto: Phys. Rev. B **106**, 174517 (2022).

Quantum Monte Carlo simulations of Spin Hall magnetoresistance in quasi-two-dimensional antiferromagnetic insulator/metal bilayer systems

Takeo Kato

Institute for Solid State Physics,

The University of Tokyo, Kashiwa-no-ha, Kashiwa, Chiba 277-8581

Spin Hall magnetoresistance (SMR) is a novel type of magnetoresistance caused by spin current. SMR was firstly observed in 2013 by Nakayama in a bilayer system composed of a metal and a magnetic insulator [1]. The phenomenological theory for SMR [2] is widely used for analysis of SMR, but it can't describe the temperature dependence of SMR in a bilayer system composed of a metal and an antiferromagnetic-insulator [3] .

In this study, we discuss the SMR dependence of temperature, thickness of AFI, and randomness of exchange interaction. To discuss about these features, we expand the microscopic theory of SMR based on Keldysh Greens function [4]. In this theory the spin current is expressed in terms of the spin susceptibility of the antiferromagnetic insulator, but analytical calculation based on spin-wave theory are available for only low temperature. Due to calculate widely temperature dependence of SMR by the quantum Monte Carlo method, we obtained the spin conductance formulation by Matsubara Greens function [5].

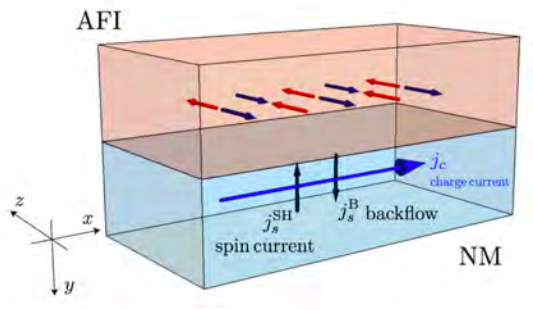

Fig. 1:Setup for SMR calculation cited from[5].

We used DSQSS for the quantum Monte Carlo method, and we adjustment some code to be able to calculate the local spin susceptibility. The accuracy for the calculation is proportional to the number of Monte Carlo steps, so We performed parallelization calculations with MPI, which is included in DSQSS, to achieve a high degree of accuracy.

We show the result of this calculations based on the paper [5]. The temperature and thickness dependence of SMR is shown in Fig. 2. The black points indicate the total SMR signal, whereas the red and blue plots are contribution from *z*-component and *xy*-components of spin susceptibility. Green arrows indicate the ordering temperature.

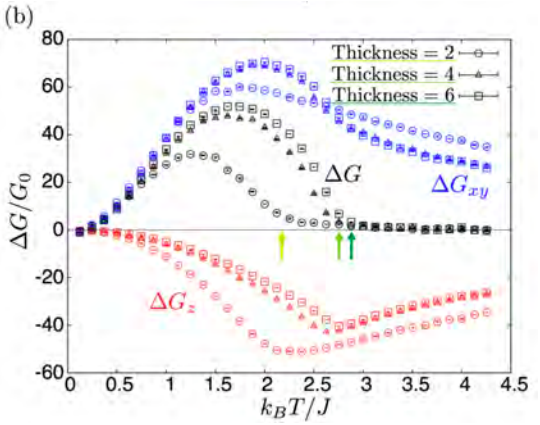

Fig. 2: S=1 result for SMR cited from [5].

It shows that at high temperature SMR signals vanish in consistent with the analytical calculation by the high temperature expansion. SMR has a peak less than the ordering temperature and the thickness dependence becomes weaker for four or more layers.

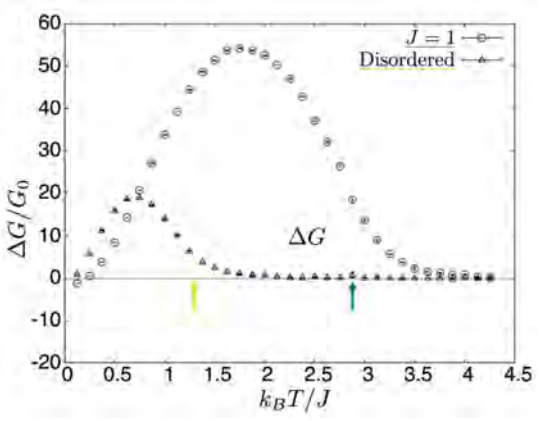

Fig. 3: Disordered case of result cited from [5].

The effect of randomness by disordered exchange interactions is shown in Fig. 3. It shows that the ordering temperature is suppressed and the SMR signal becomes small in the disordered case.

We calculated SMR in AFI by quantum Monte Carlo simulations, and we discussed about the SMR dependence of temperature, thickness of AFI, and randomness of exchange interaction.

References

[1] H. Nakayama, et al., Phys. Rev. Lett. **110**, 206601 (2013).

[2] Y. T. Chen, et al., Phys. Rev. B **87**, 144411 (2013).

[3] D. Hou, et al., Phys. Rev. Lett. **118**, 147202 (2017).

[4] T. Kato, Y. Ohnuma, and M. Matsuo, Phys. Rev. B **102**, 094437 (2020).

[5] T. Ishikawa, M. Matsuo, and T. Kato, Phys. Rev. B **107**, 054426 (2023).

Precise structural analysis of atomic arrangement of hydrogen-adsorbed ceria surfaces by using 2DMAT

Izumi MOCHIZUKI

Slow Positron Facility, Institute of Materials Structure Science, High Energy Accelerator Research Organization (KEK), Oho 1-1, Tsukuba, Ibaraki, 305-0801, Japan

We used 2DMAT [1-7], an open-source data-analysis software that is preinstalled on the ISSP supercomputers, developed by the PASUMS project at FY2020 and 2021 for data analyses of total-reflection high-energy positron diffraction (TRHEPD). TRHEPD is an innovative method for the precise determination of atomic arrangement of crystal surfaces due to its exceeding surface sensitivity. It is realized at Slow Positron Facility, IMSS, KEK [8].

We applied 2DMAT to the structural analysis of a Ge(001)-c(4×2) surface as a test of the analysis method by an optimization procedure, Nelder-Method method [5, 7].

We also investigated a hydrogen (H) adsorbed CeO_2(111)-(1×1) surface [9]. It was a challenge for the detection of surface hydrogen since it is quite difficult for other experimental measurements. In this study, we first calculated the structure of the bare CeO_2(111)-(1×1) surface and that of the H-adsorbed one by using Quantum ESPRESSO in the DFT+U method. The results were then compared with those obtained by the TRHEPD experiment. We found that the TRHEPD can detect the surface hydrogen properly with the data-driven analysis, as an innovative feature of TRHEPD. More detailed analysis is ongoing.

References

[1] https://www.pasums.issp.utokyo.ac.jp/2DMAT

[2] K. Tanaka, *et al*. (I. Mochizuki), Acta. Phys. Pol. A 137, 188 (2020).

[3] T. Hoshi, *et al*. (I. Mochizuki), Comp. Phys. Commun. 271, 108186 (2022).

[4] T. Hanada, *et al*., Comp. Phys. Commun. 277 108371 (2022).

[5] Y. Motoyama, *et al*. (I. Mochizuki), Comp. Phys. Commun. 280, 108465 (2022).

[6] K. Tanaka, *et al*. (I. Mochizuki), JJAP Conf. Series 9, 011301 (2023).

[7] N. Kinoshita, *et al*. (I. Mochizuki), in JPS meeting, 22-25, Mar. 2023.

[8] https://www2.kek.jp/imss/spf/eng/

[9] I. Mochizuki, in *Innovation catalysis science through the integration of high-performance data-driven science and advanced measurement technology*, online mini-symposium, Joint Usage/Research Center for Catalysis (JURCC), 30. Mar. 2023, https://sites.google.com/view/hpc-catal2023

Equilibration and glass transition in the dense hard sphere systems

Masaharu ISOBE
Nagoya Institute of Technology
Gokiso-cho, Showa-ku, Nagoya, 466-8555

As the simplest models, the hard disk/sphere systems have been investigated via molecular simulation in both equilibrium and non-equilibrium phenomena [1]. In this project, we focus on the equilibration and the non-equilibrium phase transition in the hard disk/sphere model system with modern algorithms, *i.e.*, Event-Chain Monte Carlo (ECMC) [2, 3], Newtonian ECMC (NEC) [4] and Event-Driven Molecular Dynamics(EDMD) [5].

Efficiency of Newtonian Event-Chain Monte Carlo in dense hard disk systems

In the statistical mechanics of many body systems, the physical properties at the true equilibrium state are crucial. To invent efficient method of equilibration in the molecular simulation is one of fascinating topics where the simple model systems such as hard-spheres and Ising spins have been investigated actively and made important contribution. In 2009, Event-Chain Monte Carlo (ECMC) [2] was invented in hard disk systems that updates the particle position with sequential collisions (i.e., event-chain) and has been applied to the many typical models studied in statistical physics [3]. ECMC has several variants depending on how the direction of movement of the particles after the collision is determined. Recently, Newtonian-ECMC (NEC) [4] was invented by applying the velocity collision rule to each collision event to dictate the direction of particle movement; this is often used in the Event-Driven Molecular Dynamics (EDMD) of hard-sphere systems. NEC outperformed not only other variants of ECMC but EDMD in the diffusion coefficient and melting process in hard sphere systems. However, the optimal performance strongly depends on the physical properties and chain length (or duration) of ECMC (and its variants). Previously, we found the high efficiency of NEC in diffusion coefficient of liquid state in hard disk systems for all chain lengths and various system sizes, which is caused by the spatially homogeneous sampling of the displacement (i.e., collision) [7]. To figure out the mechanism of equilibration of NEC in dense systems, we focus on the equilibrium state of dense hard disk systems above the fluid-to-solid transition point, which show the relaxation via hopping motion even in the packing fraction at the solid phase in hard disk systems for each methods. We also found profoundly efficient diffusion coefficient by NEC even when the relaxation becomes only successive hopping motion in highly dense systems.

Free volume estimator (NELF-A) in dense poly-disperse hard disk systems — local structure analysis on pressure and inherent structure

In many-particle systems, the free volume of a tagged particle constructed from excluded volume by surrounding particles made a crucial contribution to describing the macroscopic properties in the history of liquid state theory. Several numerical algorithms for calculating the free volume (FV) have been invented, such

as Monte Carlo (MC) sampling and Voronoi tessellation. However, MC is an approximate calculation, and the Voronoi tessellation requires high computational costs (especially for poly-disperse systems). As an alternative algorithm, we propose the simple, efficient, and precise method, Neighbors for Enclosing Local Free Area (called NELF-A), which is easily applied to dense poly-disperse hard disk systems often used in glassy model systems [8].

As an application of the NELF-A, we implement an alternative method to obtain the inherent structure instead of short-time averaged coarse-graining trajectories. The summary of the algorithm is as follows: (i) The displacement vectors from a particle position to a geometric center of FV estimated by NELF-A for each particle are drawn. (ii) The positions in a whole system are updated with the displacement vectors multiplied by a scaling parameter β less than unity. (iii) Repeat (ii) until the positions converge toward an inherent structure. The FV in equilibrium state eventually converging positions after (i)-(iii) procedure and the isotropic shape of FV located on a triangular lattice could be observed (i.e., inherent structure). Even in a typical non-equimolar binary mixture hard disk system, the probability density distribution obtained by (i)-(iii) procedure is fairly consistent with the conventional method based on the short-time averaged coarse-graining trajectories. We also confirmed the accuracy of this method by estimating pressure based on FV-based as compared with the other conventional methods.

Anomalous phase transition in self-propelled hard disk systems

In this study, we investigate the phase behavior of the self-propelled hard disk systems with the Vecsek-type interaction via EDMD simulation systematically. In addition to the ordinal order-disorder transition of the collective velocity field known in the original point particle of the Vicsek model, we observed the novel competition driven by the global positional order (so-called Alder transition) due to the exclusive effect of hard disk, which causes anomalous fluctuations around phase transition and transition shifts [9].

References

[1] M. Isobe: Mol. Sim. **42** (2016) 1317.

[2] E. P. Bernard, W. Krauth, and D. B. Wilson: Phys. Rev. E **80** (2009) 056704.

[3] W. Krauth: Front. Phys. **9** (2021) 229.

[4] M. Klement and M. Engel: J. Chem. Phys. **150** (2019) 174108.

[5] M. Isobe: Int. J. Mod. Phys. C **10** (1999) 1281.

[6] M. Klement, S. Lee, J. A. Anderson and M. Engel: J. Chem. Theor. and Comp. **17** (2021) 4686.

[7] H. Banno, D. Mugita, and M. Isobe: J. of Phys.: Conf. Ser. **2207** (2022) 012011.

[8] K. Souno, H. Koyama, D. Mugita, and M. Isobe: *in preparation.*

[9] N. Murase and M. Isobe: Proceedings of the 28th Symposium on Traffic Flow and Self-driven Particles, **28** (2023) 9. (in Japanese)

Molecular dynamics analyses of ion migration at electrode-electrolyte interfaces and grain boundaries in electrolytes

Ryo KOBAYASHI

Department of Applied Physics, Nagoya Institute of Technology,

Gokiso-cho, Showa-ku, Nagoya, Aichi 466-8555

All-solid-state batteries (ASSBs) are considered as a promising candidate for next-generation lithium-ion batteries. They use a solid-state electrolyte instead of the liquid-state electrolyte used in conventional lithium-ion batteries. The key to achieving high performance in ASSBs is to reduce or control the resistivity at interfaces such as the electrode/electrolyte interface and grain boundaries (GBs) within the electrolyte. To achieve this, we need a deeper understanding of the atomic structure and precise mechanisms of ion migration at GBs. The goal of this project is to obtain new insights into these processes by using large-scale molecular dynamics (MD) simulations.

In order to obtain atomistic insights on Li-ion migration mechanism at GBs, we performed non-equilibrium MD simulation of large-scale poly-crystalline Li2Zr(PO4)3 (LZP) system containing half a million atoms using a interatomic potential generated using a meta-heuristic approach [1,2,3] and extracted local ion flux information around GBs [4]. From the simulation and local ion-flux analyses, we showed that, in poly-crystalline materials, the ions migrate towards the lower reaches of grain and go through spots at GBs, and the high-flux spots contain migration paths as low energy as the bulk ones.

This methodology can be applicable to a wide variety of systems for electrolytes and interfaces between electrode and electrolyte.

References

[1] R. Kobayashi, Y. Miyaji, Nakano, K. M. Nakayama, *APL Materials* **8**, 081111 (2020)

[2] Nagoya Atomistic-simulation Package (nap) http://github.com/ryokbys/nap

[3] Optzer, http://github.com/ryokbys/optzer

[4] R. Kobayashi, K. Nakano, M. Nakayama, Acta Materialia, 226 (2022) 117596.

[5] M. Nakayama, K. Nakano, M. Harada, N. Tanibata, H. Takeda, Y. Noda, R. Kobayashi, M. Karasuyama, I. Takeuchi, M. Kotobuki, *Chem. Commun.* **58**, 9328–9340 (2022)

Theoretical study for firefly bioluminescence substrate analogs and related molecules

Miyabi HIYAMA
Graduate School of Science and Technology, Gunma University
Tenjin-cho, Kiryu, Gunma 376-8515

In this year, we studied the stable structures of adenosine triphosphate (ATP)-metal complexes in aqueous solutions and the theoretical absorption spectra for the firefly luciferin analog named "seMpai".

It is believed that the cofactor ATP and Mg^{2+} form a complex and react with the substrate luciferin in firefly bioluminescence. Wang et al. [1] reported that the bioluminescence quantum yields decreased with increasing cadmium or zinc concentration when these metal ions were used instead of magnesium one. The effects of metals on luciferin, on ATP, and on proteins may be responsible for this feature. We expected that the effect of metals on ATP was most significant than the others because the ATP is directly related to the bioluminescence reaction. Thus, the optimized structures of ATP-Mg^{2+}, ATP-Zn^{2+}, and ATP-Cd^{2+} in aqueous solutions were obtained using the density functional theory (DFT). For the initial structures for these calculations, the results from Global Reaction Mapping (GRRM11) calculations [2] were used because there were many local minimum structures of these complexes. We found that there was no clear difference in the structure of these metal ion coordination to ATP. It also found that ATP-Zn^{2+} and ATP-Cd^{2+} were unstable in aqueous solutions, unlike ATP-Mg^{2+} .

In these days, one of the firefly luciferin analogs named "seMpai", which is prepared with the aim of improving water solubility and produces red luminescence with firefly luciferase, was reported [3]. To elucidate the absorption characteristics of this analog, the optimization structure of its ground state for its conjugate acids and bases expected to be main component in the aqueous solutions were obtained from DFT calculations. The time dependent DFT (TDDFT) calculations were carried out to estimate the theoretical absorption spectra for these structures.

The computational chemistry software package, Gaussian09 [4], was used for DFT and TDDFT calculations. All calculations using Gaussian09 and GRRM11 were performed on system B of Super Computer Center in ISSP.

References

[1] Y. Wang, H. Kubota, N. Yamada, T. Irie, H. Akiyama: Photochem. Photobiol. **87**, 846 (2011).

[2] K. Ohno, S. Maeda: Chem. Phys. Lett. **384**, 277 (2023). S. Maeda, K. Ohno,: J. Phys. Chem. A, **109** 5742 (2005). K. Ohno, S. Maeda, J. Phys. Chem. A, **110** 8933 (2006).

[3] R. Saito, T. Kuchimaru, S. Higashi, S. W. Lu,M. Kiyama, S. Iwano, R. Obata, T. Hirano, S. Kizaka-Kondoh, S. A. Maki: Bull. Chem. Soc. Jpn. **92**, 608 (2019).

[4] Gaussian09 Revision D.01, M. J. Frisch et al.

Analysis of Ising model in statistical-mechanical informatics

Yuya SEKI

Graduate School of Science and Technology, Keio University, Kanagawa 223-8522

We have developed an optimization method for discrete black-box optimization problems by combining machine learning, simulated annealing, and integer encoding methods [1]. Our approach is based on factorization machine with annealing (FMA) [2] that uses factorization machines as machine learning model. Factorization machine with annealing approximates an objective function of a black-box optimization problem by training a factorization machine. Instead of minimizing the objective function that requires high cost to evaluate it, FMA minimizes a model equation of FM. Here, simulated annealing can be used for the minimization because the model equation of FM has a QUBO form that is equivalent to Ising model. Since FM is an important factor in performance of FMA, we analyze properties of model equations of FM, which are Ising models, by using numerical simulations on the supercomputer.

Tuning parameters in the FMA method is required to achive a high performance. To this end, we performed the calculation in parallel by changing the parameters with multiple processes on the supercomputer. In addition to the parallel computing mentioned above, we use multithreading to reduce computational time for the Monte Carlo simulation to minimizes the model equation of the trained FM. By using the parallel computing on the supercomputer, we obtained numerical results efficiently.

This year we investigated the performance of FMA for integer-variable black-box optimization problems in detail [1]. Integer variables can be represented as binary variables through integer encoding methods such as binary encoding, one-hot encoding, and domain-wall encoding. Since the encoded bit strings differ depending on the encoding methods, the performance of FMA is determined by the choice of the encoding method. Through a numerical simulation, we found that the FMA with one-hot encoding method has higher performance than FMA with other encoding methods. By using simulation on the supercomputer, we revealed the relationship between sparsity of bit string and the performance of FMA.

References

[1] Y. Seki *et al.*: arXiv:2209.01016 (2022).

[2] K. Kitai *et al.*: Phys. Rev. Research **2** (2020) 013319.

Quantum Pyrochrole Magnet

H. Kadowaki
Department of Physics, Tokyo Metropolitan University
Hachioji, Tokyo 192-0397, Japan

We are investigating static correlations $\langle \sigma^z_{\boldsymbol{Q}} \sigma^z_{-\boldsymbol{Q}} \rangle$ and dynamic correlations $\langle \sigma^z_{\boldsymbol{Q}}(0) \sigma^z_{-\boldsymbol{Q}}(t) \rangle$ characterized by the modulation wave vector $\boldsymbol{k} \sim (\frac{1}{2}, \frac{1}{2}, \frac{1}{2})$, which were observed by neutron scattering experiments, e.g. Ref. [1, 2], in the frustrated pyrochlore magnet $Tb_{2+x}Ti_{2-x}O_{7+y}$ (TTO). TTO with $x < x_c \simeq -0.0025$ is very interesting because of their quantum spin liquid (QSL) ground state. A simple question "why TTO shows the static short-range order with $\boldsymbol{k} \sim (\frac{1}{2}, \frac{1}{2}, \frac{1}{2})$?" has been a difficult problem for many years [3]. Recently we have solved this problem using quantum simulation based on thermal pure quantum (TPQ) states, and proposed that small three-spin interaction terms of a form $\sigma^{\pm}_{\boldsymbol{r}} \sigma^z_{\boldsymbol{r}'} \sigma^z_{\boldsymbol{r}''}$ are a key ingredient of both $\boldsymbol{k} \sim (\frac{1}{2}, \frac{1}{2}, \frac{1}{2})$ and the QSL state of TTO at low temperatures [4].

We are now extending the quantum simulation for $\langle \sigma^z_{\boldsymbol{Q}} \sigma^z_{-\boldsymbol{Q}} \rangle$ to inelastic neutron spectra, i.e., simulating $\langle \sigma^z_{\boldsymbol{Q}}(0) \sigma^z_{-\boldsymbol{Q}}(t) \rangle$ using a TPQ method [5]. We have written a simulation program, which now works very well, and are performing time-consuming calculations, which we would like to continue in 2023.

References

[1] H. Takatsu et al. Phys. Rev. Lett. **116**, (2016) 217201.

[2] H. Kadowaki et al. J. Phys. Soc. Jpn. **87** (2018) 064704.

[3] H. Kadowaki et al. Phys. Rev. B **99** (2019) 014406.

[4] H. Kadowaki, M. Wakita, B. Fåk, J. Ollivier, and S. Ohira-Kawamura, Phys. Rev. B **105** (2022) 014439.

[5] H. Endo et al. Phys. Rev. Lett. **121** (2018) 220601.

Atomistic model study on the coercivity mechanism of permanent magnets

Hiroshi Hayasaka[1], Masamichi Nishino[2, 1], and Seiji Miyashita[3,4,1]

[1]*Elements Strategy Initiative Center for Magnetic Materials, National Institute for Materials Science, 1-2-1 Sengen, Tsukuba, Ibaraki 305-0047, Japan*

[2]*Research Center for Advanced Measurement and Characterization, National Institute for Materials Science, 1-2-1 Sengen, Tsukuba, Ibaraki 305-0047, Japan*

[3]*Institute for Solid State Physics, The University of Tokyo, 5-1-5 Kashiwanoha, Kashiwa 277-8581, Japan*

[4]*The Physical Society of Japan, 2-31-22 Yushima, Tokyo 113-0033, Japan*

1. Angular dependence of coercivity

We investigated angular dependences of nucleation and pinning fields in anisotropic Heisenberg model. Unlike a deterministic process in magnetization reversal at zero temperature, reversal is a stochastic process for barrier crossing at finite temperatures. We studied the thermal fluctuation effect using the stochastic LLG equation method [1].

At zero temperature, the normalized nucleation field shows an asymmetric bowl-like angular dependence, and the value at large angles rapidly increases. On the other hand, the pining field shows almost constant dependence at $\theta < 40^\circ$ and increases at larger θ. The thermal fluctuation effect reduces the nucleation and pinning fields. At higher temperatures, the thermal effect makes both fields closer, in which the surface nucleation at the hard magnet plays an important role [2].

2. Coercivity enhancement by dysprosium substitution into neodymium permanent magnets

We investigated the features and mechanisms of the enhancement of the threshold field for magnetization reversal in atomistic Nd-Fe-B model with Dy substitution. The results showed that a change from surface to bulk nucleation occurs when the number of substituted layers increases and the anisotropy energy of Dy is resistant to temperature increase, which significantly enhances coercivity, especially at high temperatures [3].

References

[1] M. Nishino, and S. Miyashita, Phys. Rev. B **91**, 134411 (2015)

[2] H. Hayasaka, M. Nishino, and S. Miyashita, Phys. Rev. B **105**, 224414 (2022)

[3] M. Nishino, H. Hayasaka, and S. Miyashita, Phys. Rev. B **106**, 054422 (2022)

Large-scale molecular-dynamics simulation of pressure-induced coordination change in silica glass with ANN potentials

Daisuke WAKABAYASHI

Photon Factory, Institute of Materials Structure Science,

High Energy Accelerator Research Organization (KEK), Tsukuba 305-0801

Silica is well known as an archetypal oxide and the compression behavior of silica glass and melt has attracted considerable attention in various research fields. Theoretical studies using molecular-dynamics simulations have been actively conducted to obtain information on the atomic arrangements and bonding states of silica glass under high pressure. Since there is no long-range order in amorphous materials as exists in crystals, calculations on a large number of atoms are required to reproduce the structural changes. There is a limit to the size of the system which can be calculated by ab-initio methods.

In this study, we have fitted the potential with a machine-learning technique (ANN potential) on the basis of the results of ab-initio calculations, and have applied it for the calculations with an extended system. However, in our previous projects, it has been observed that the large-scale calculations of melt were difficult to stabilize and quickly diverged, making them impossible to continue. In this project, potential averaging and active learning are employed in combination to avoid computational instability efficiently [1].

The test calculations were performed for the solidification process of silica melt under high pressure. The ANN potential was determined with the total potential energy, atomic force, and pressure data obtained by ab-initio calculations for a temperature range of 300-5,000 K at 60 GPa with 144 atoms. Using the potential, we made molecular-dynamics calculations on silica melt at 60 GPa and 4,000 K for a system of about 30,000 atoms.

The use of multiple interatomic potentials averaged together stabilizes the calculations. The initial parameter sets for the fitting were randomly generated, and five ANN potentials were determined from the five parameter sets, respectively. In order to avoid extreme results, molecular-dynamics simulations were performed in an extended system using the average value of the atomic forces calculated by the five ANN potentials.

In addition, active learning was carried out to efficiently compensate for the lack of data. First, molecular-dynamics simulations were performed at 60 GPa and 4,000 K with the averaged ANN potentials in a system of the same size as in the ab initio calculations. The atomic

forces calculated from each ANN potential should agree, and therefore it is likely that atomic configurations at steps having a large variation in atomic force among the five potentials have not been well learned. Then, the standard deviation of the atomic forces was estimated for all atoms at each step, and the atomic configurations for which the maximum value was larger than 0.25 eV/Å were extracted [2]. The total potential energies, atomic forces, and pressure in the extracted configurations were calculated by an ab initio method and added to the initial dataset. Active learning was carried out twice in total.

The averaged ANN potential obtained after two active-learning cycles did not cause any computational instability during the simulations at 60 GPa and 4,000 K and in the subsequent simulations of the cooling process down to 300 K. Without active learning, the calculation becomes unstable before 2,000 steps and cannot reproduce the results of the ab initio calculations. The time at which the destabilization occurs is significantly delayed with each active-learning cycle.

The calculations on silica glass at 60 GPa and 300 K have not only reproduced ab initio calculations, but have also been found to significantly improve the precision of the intermediate-range structure and reproduce the experimental data in the literature [3]. This suggests that the experimentally observed structural transformation of silica glass, in which the coordination number of Si changes from 4 to 6 with increasing pressure [4], can be simulated in more detail. In fact, the calculations of the depressurization process down to 0 GPa were successful with the ANN potentials determined in the same method as for the cooling process and reproduced the change in coordination number from 6 to 4.

References

[1] D. Wakabayashi, K. Shimamura, A. Koura, and F. Shimojo, submitted to J. Phys. Soc. Jpn.

[2] Y. Zhang, H. Wang, W. Chen, J. Zeng, L. Zhang, H. Wang, and W. E, Comput. Phys. Comm. **253**, 107206 (2020).

[3] D. Wakabayashi, N. Funamori, T. Sato, and T. Taniguchi, Phys. Rev. B **84**, 144103 (2011).

[4] T. Sato and N. Funamori, Phys. Rev. B **82**, 184102 (2010).

First-principles investigation of ductile deformation mechanism in silver sulfide

Masaaki MISAWA
Department of Intelligent Mechanical Engineering, Fukuoka Institute of Technology
Wajiro-higashi, Higashi-ku, Fukuoka 811-0295

β-Ag_2S, a low-temperature phase of silver sulfide, exhibits metal-like ductility at room temperature even though it is an inorganic semiconductor[1]. Elucidating the origin of this ductility will be extremely useful for designing materials for flexible next-generation semiconductor devices. Although several theoretical investigations have been done to elucidate the mechanism of ductile deformation of β-Ag_2S from the viewpoint of bonding states in crystals [1, 2], theoretical verification considering dynamics under finite temperatures has not yet been performed. Therefore we have investigated the behavior of β-Ag_2S under shear stress based on first-principles molecular dynamics method [3].

In this study, we have performed first-principles molecular dynamics simulations for the six types of deformations of β-Ag_2S crystals: the (100)[010], (100)[001], (010)[100], (010)[001], (001)[100], and (001)[010] shear, where $(KLM)[klm]$ shear means that simple shear deformation in which the crystal's (KLM) plane slides toward the $[klm]$ direction. The shear rate in the simulations was equivalent to $d\gamma/dt = 0.05$ ps^{-1}, and shear deformations up to $\gamma = 0.50$ were performed under room temperature (300 K). The radial distribution function of the sulfur ion sublattice during the deformation process was analyzed to elucidate atomistic behaviors of β-Ag_2S under shear stress, and it was observed that peaks that once disappeared during deformation were restored in the four systems: (100)[001], (010)[100], (001)[100], and (001)[010] shear. In addition, we performed a more detailed study for the (100)[010] and (010)[001] shear systems, in which structural recovery did not occur, by slowing the shear rate, and observed structural recovery in these systems as well. A common feature of these structural recovery mechanisms is that the fracture is repaired by the mass movement of sulfur atoms in a particular crystal plane.

We also pointed out that the BCC-like structure of the sulfur sublattice in β-Ag_2S may be responsible for this atomistic behavior. Ag_2Se, which is not ductile, does not have such a highly symmetric anion-sublattice and thus cannot undergo the mass movement of atoms in response to shear stress, resulting in difficulty in structural recovery. Such atomistic understanding is expected to accelerate research and open a possibility in designing a wide variety of inorganic ductile semiconductors for future flexible electronics based on silver chalcogenides.

References

[1] X. Shi *et al.*: Nat. Mater. **17**, 421 (2018).

[2] G. Li *et al.*: npj Comput. Mater. **4**, 44 (2018).

[3] M. Misawa *et al.*: Sci. Rep. **12**, 19458 (2022).

Development of machine-learning-based phase diagram construction method for high-throughput batch experiments

Ryo TAMURA
International Center for Materials Nanoarchitectonics,
National Institute for Materials Science,
1-1 Namiki, Tsukuba, Ibaraki, 305-0044

Phase diagrams are valuable guidelines for the development of new materials. Through experiments, phase diagrams have been determined in various spaces, such as between processes, between external fields, and between compositions. In the field of materials informatics, tools focusing on phase diagrams have been developed using machine learning (ML). Among these tools, we have developed an ML method based on uncertainty sampling (US)[1] to efficiently construct phase diagrams, which we call the Phase Diagram Construction (PDC) package[2]. This method evaluates the uncertainty based on the ML model learned under the conditions that the phase domain is specified. Using evaluated uncertainty, the experimental condition with most uncertainty in the phase diagram is selected as the next experimental condition. Based on this suggestion, an experiment will be conducted and the corresponding phase domain is identified. The number of known points is then increased and the next experimental condition is proposed using the updated ML model. By applying the PDC to the known phase diagram, it was demonstrated that this iterative process can rapidly construct an accurate phase diagram and discover new phase domains[1]. For further validation, PDC was applied to construct a new diagram for obtaining Zn-Sn-P films by molecular beam epitaxy[3]. The PDC experiments detected new phases that were not observed in the initial stage, and detailed phase boundaries were quickly determined. Thus, the PDC proved to be useful in the case where one condition is proposed in ML and one experiment is performed in each iteration. Further speed-up can be achieved by incorporating the knowledges of materials science[4].

In addition, we developed PDC for high-throughput batch experiments[6]. To address the performance of the method, the target was a Cu-Mg-Zn ternary alloy. Both isothermal sections of this system (two-dimensional) and its temperature-dependent phase diagram as a whole (three-dimensional) were considered. We showed that PDC is suitable for high-throughput batch experiments to efficiently construct phase diagrams. Using this version, a temperature-composition phase diagram of a crosslinked polymer was constructed, and its usefulness was confirmed[5].

References

[1] K. Terayama, R. Tamura, Y. Nose, H. Hiramatsu, H. Hosono, Y. Okuno, and K. Tsuda, Physical Review Materials **3**, 033802 (2019).

[2] https://github.com/tsudalab/PDC

[3] R. Katsube, K. Terayama, R. Tamura, and Y. Nose, ACS Materials Letters **2**, 571-575 (2020).

[4] K. Terayama, K. Han, R. Katsube, I. Ohnuma, T. Abe, Y. Nose, and R. Tamura, Scripta Materialia **208**, 114335 (2022).

[5] W. Hu, T. Chen, R. Tamura, K. Terayama, S. Wang, I. Watanabe, and M. Naito, Science and Technology of Advanced Materials **23**, 66-75 (2022).

[6] R. Tamura, G. Deffrennes, K. Han, T. Abe, H. Morito, Y. Nakamura, M. Naito, R. Katsube, Y. Nose, and K. Terayama, Science and Technology of Advanced Materials: Methods **2**, 153-161 (2022).

Study on Novel Algorithm for Ising Machines

Shu Tanaka

Department of Applied Physics and Physico-Informatics, Keio University

Hiyoshi, Yokohama, Kanagawa, 223-8522

Ising machines are special computers for combinatorial optimization problems. The Ising machine expresses the objective function and constraints of a combinatorial optimization problem in terms of an Ising model, and searches for low-energy states of the Ising model. Since the Ising machine operates on the basis of stochastic behavior, it is necessary to develop various internal algorithms to improve the solution accuracy. In this research project, we investigated algorithms to improve the performance of the Ising machine from the viewpoint of statistical mechanics.

(I) Dynamical properties of bit-width reduction algorithms for simulated-annealing-based Ising machine

Ising machines have several hardware limitations. We have focused on cases where the possible values of the interaction coefficients and local field coefficients in the Ising model are limited and have proposed a method to make Ising machines work properly even in the presence of such limitations [1]. Reference [1] confirms the validity of the proposed method by comparing the ground states. On the other hand, the dynamic properties of the proposed method were not clarified. We have used the method of a previous study [2,3] to study the slow relaxation due to entropy effects, temperature-dependent effective interactions, and local magnetic fields. As a result, it was confirmed that there is a change in the time scale depending on the bit-width to be reduced [4].

(II) Black-box optimization using Ising machines

An Ising machine is a piece of hardware that takes an Ising model or equivalent Quadratic Unconstrained Binary Optimization (QUBO) representation as an input format and operates to find its ground state. Ising machines have been applied in various situations to combinatorial optimization problems that can be represented by Ising models or QUBOs. On the other hand, a method to use Ising machines for black-box discrete optimization, i.e., discrete optimization problems where the objective function is not explicitly given, was proposed by us in 2020 [5]. We extended it and proposed a method to perform integer-valued black-box optimization with Ising machines [6].

References

[1] D. Oku, M. Tawada, S. Tanaka, and N. Togawa, IEEE Trans. Comp. **71**, 223 (2020).

[2] S. Miyashita, S. Tanaka, M. Hirano, J. Phys. Soc. Jpn. **76**, 083001 (2007).

[3] S. Tanaka and S. Miyashita, J. Phys. Soc. Jpn. **78**, 084002 (2009).

[4] S. Kikuchi, N. Togawa, and S. Tanaka, arXiv:2304.12796 (2023).

[5] K. Kitai, J. Guo, S. Ju, S. Tanaka, K. Tsuda, J. Shiomi, and R. Tamura, Phys. Rev. Res. **2** (2020) 013319.

[6] Y. Seki, R. Tamura, and S. Tanaka, arXiv:2209.01016 (2022).

Charge distribution in metallic and charge order phase in organic crystals

Masatoshi SAKAI, Hiroki WATANABE, Ryosuke ANDO, Ryo WATANUKI

Department of Electrical and Electronic Engineering,

Chiba University, 1-33 Yayoi-cho Inage, Chiba 263-8522

Our research group conducts developments of novel electronic devices using organic charge order materials. In our previous work, we observed obvious field effect transistor (FET) characteristics of α-(BEDT-TTF)$_2$I$_3$[1] with 4-probe electrical measurement and small FET modulation of β-(BEDT-TTF)$_2$PF$_6$ [2] with 2-terminal electrical measurement. To analyze these experimental results, we are trying to calculate the electronic state of α-(BEDT-TTF)$_2$I$_3$ and β-(BEDT-TTF)$_2$PF$_6$. This report is a interim report of this research work in progress.

At first, about the electronic state of α-(BEDT-TTF)$_2$I$_3$ crystal, we adopted new parameter sets[3] of t, U, V because the previous parameter set could not reproduce the experimentally observed charge order structure. This time we adopted the parameter set considering the breaking of inversion symmetry. By adopting these novel parameters, we obtained calculated charge distribution of which the charge distribution trend agrees with that of the experimentally obtained one. And we could marshal the trend of the parameter set, which can obtain the charge order phase and metallic phase. Next, we are planning to try calculating real-time evolution from the insulator to the metallic phase and vice versa..

Furthermore, we also proceeded the calculation of the charge order phase of β-(BEDT-TTF)$_2$PF$_6$ crystal. This calculation started from the first-principle calculation (Quantum Espresso), and we obtained parameters using RESPACK. By using the obtained parameters, we tried to represent the charge distribution of the experimentally observed charge order. At present, we are making a superlattice structure to represent the real charge order. We are also trying to calculate the process and probability between the insulator and metallic phase of β-(BEDT-TTF)$_2$PF$_6$ to analyze our phase transition device characteristics.

---

[1] under preparation

[2] M. Sakai et al., Nanosci. and Nanotechnol. 16, 3267 (2016).

[3] D. Ohki et al., Phys. Rev. B 107, L041108 (2023).

Magnetic structures on the thin films made by the dipolar interaction and the frictional force stemming from these structures

Hisato Komatsu

Kyushu University, Kasuga, Fukuoka 816-8580 *

Masamichi Nishino and Yoshihiko Nonomura

National Institute for Materials Science, Tsukuba, Ibaraki 305-0044

We applied for the usage of the ISSP Supercomputer planning to investigate the magnetic structures of the dipolar system. However, we have not got notable results on this subject. Instead, we studied a theoretical model of the magnetic friction.

Magnetic friction, the frictional force generated from the magnetic interaction between spin variables, has been extensively studied in recent years. These studies aimed not only to investigate the behavior of the magnetic systems, but also to reveal the microscopic mechanisms of the friction. For this purpose, many types of theoretical models have been proposed and investigated[1, 2].

In the case of the normal solid surfaces, there is a well-known empirical law called the Dieterich-Ruina law[3, 4]. In our previous studies, we proposed models of magnetic friction that seemed to obey this law, at least in the steady state[5, 6]. These studies revealed that magnetic structures can behave as a kind of potential barrier that prevent the lattice motion. In the study of this academic year, we investigated a simplified model of the magnetic friction to consider the finite-size effect, which cannot be discussed in our previous studies. Specifically, we introduced a model composed of N Ising spin variables $\{\sigma_i\}$ interacting with each other by the following Hamiltonian:

$$H = -\frac{J(x)}{N}\sum_{i,j}\sigma_i\sigma_j = -NJ(x)m^2. \qquad (1)$$

Here, x is a real value representing the shift of the lattice, m is the magnetization per spin: $m \equiv \sum_i \sigma_i/N$, and $J(x)$ is the periodic function of x. For simplicity, we impose a periodic boundary condition on x. As a concrete form of $J(x)$, two types, A and B, are considered. Type-A is a piecewise linear function, and type-B is a sinusoidal function.

We introduce the time development of spin variables by the Glauber dynamics, and define one Monte Carlo step (MCS) as the unit time. In addition, the time development of x under this Hamiltonian and external force $F_{\rm ex}$ are introduced as the following overdamped Langevin equation:

$$\gamma N\frac{dx}{dt} = F_{\rm ex} - \frac{\partial H}{\partial x} + \sqrt{2\gamma NT}R(t), \qquad (2)$$

where $R(t)$ is the white Gaussian noise, $\langle R(t)R(t')\rangle = \delta(t-t')$. Here, we introduce coefficient N, considering the situation that N spins move simultaneously.

*Present address : Shiga-university, Hikone, Shiga 522-0069

We investigated this system by numerical simulation using ISSP Supercomputer, and found that this system shows two different behaviors depending on the damping constant γ. When γ is small, the stick and slip states are separated as the metastable states, and the probability that each state appears determines the relation between F_{ex} and the lattice velocity v. When γ is large, on the other hand, such separation does not appear and v is determined by the thermal activation process. We calculated the histogram of m and x like Fig. 1 and the F_{ex}-v relation, by the simulation. Furthurmore, we also estimated these quantities under sufficiently large or small γ theoretically using approximations, and compared it with the result of the simulation.

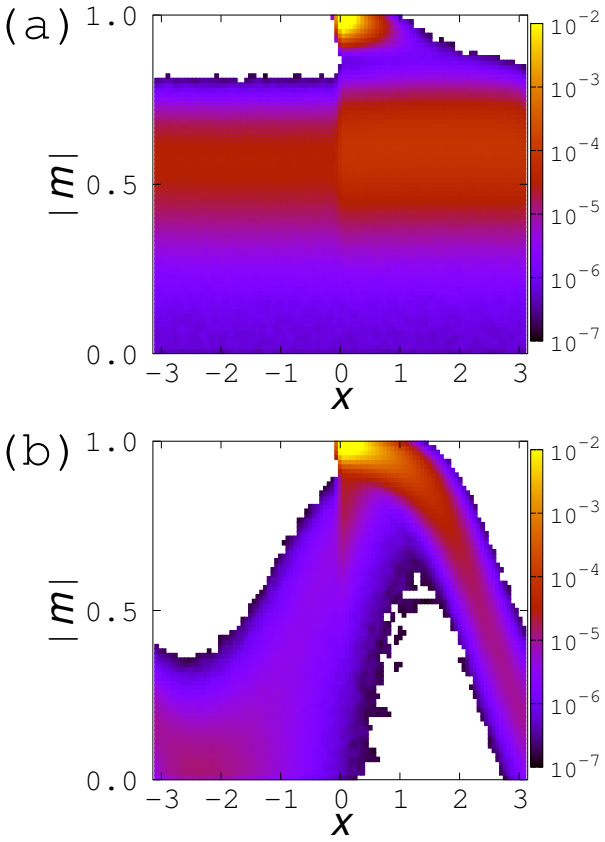

Figure 1: Examples of the histogram of the magnetization m and shift of the lattice x under (a)small γ and (b)large γ. In the case that γ is small, stick and slip states are separated as the metastable states like graph (a). These graphs are the results of the type-A model, type-B model also shows the similar result.

References

[1] D. Kadau, A. Hucht, and D. E. Wolf, Phys. Rev. Lett. **101**, 137205 (2008).

[2] M. P. Magiera, L. Brendel, D. E. Wolf, and U. Nowak, Europhys. Lett. **87**, 26002 (2009).

[3] A. Ruina, J. Geophys. Res. **88**, 10359 (1983)

[4] J. H. Dieterich, Tectonophysics **144**, 127 (1987)

[5] H. Komatsu, Phys. Rev. E. **100**, 052130 (2019)

[6] H. Komatsu, Phys. Rev. E. **102**, 062131 (2020)

[7] B. N. J. Persson, O. Albohr, F. Mancosu, V. Peveri, V. N. Samoilov, and I. M. Sivebaek, Wear **254** 835 (2003).

Numerical Study of One Dimensional Frustrated Quantum Spin Systems

Kazuo HIDA
Professor Emeritus, Division of Material Science,
Graduate School of Science and Engineering,
Saitama University, Saitama, Saitama 338-8570

1 Model

We investigate the ground-state phases of mixed diamond chains described by the following Hamiltonian:

$$\mathcal{H} = \sum_{l=1}^{L} \Big[(1+\delta)\boldsymbol{S}_l(\boldsymbol{\tau}_l^{(1)} + \boldsymbol{\tau}_{l-1}^{(1)}) + (1-\delta)\boldsymbol{S}_l(\boldsymbol{\tau}_l^{(2)} + \boldsymbol{\tau}_{l-1}^{(2)}) + \lambda \boldsymbol{\tau}_l^{(1)}\boldsymbol{\tau}_l^{(2)} \Big], \quad (1)$$

where $\boldsymbol{S}_l, \boldsymbol{\tau}_l^{(1)}$ and $\boldsymbol{\tau}_l^{(2)}$ are spin operators with magnitudes $S_l = \tau_l^{(1)} = 1/2$ and $\tau_l^{(2)} = 1$, respectively. The number of unit cells is denoted by L, and the total number of sites is $3L$. The lattice structure is depicted in Fig. 1. We consider the region $\lambda \geq 0$ and

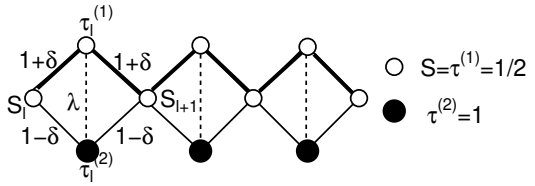

Figure 1: Structure of the diamond chain investigated in this work.

$1 \geq \delta \geq -1$. For $\delta = 0$, $\boldsymbol{\tau}_l^{(1)} + \boldsymbol{\tau}_l^{(2)}$ commutes with the Hamiltonian (1) for all l. In [1], we made use of this property to determine the ground-state phase diagram. In addition to the Lieb-Mattis(LM) type ferrimagnetic phase and the nonmagnetic Tomonaga-Luttinger liquid (TLL) phase, an infinite series of ferrimagnetic phases with spontaneous magnetizations $m_{\rm sp} = 1/p$, where $p(= 1, 2, ..., \infty)$ is the spatial periodicity of the ground state. Since the spin operators $\boldsymbol{\tau}^{(1)}$ and $\boldsymbol{\tau}^{(2)}$ have different magnitudes, however, it is not natural to assume $\delta = 0$ in a realistic situation. Hence, we examine more general cases with $\delta \neq 0$ in the present work.

2 Analytical Results

Let us start with the analytic consideration of several limiting cases.

1. $\lambda \gg 1+\delta, 1-\delta$: All pairs of $\boldsymbol{\tau}_l^{(1)}$ and $\boldsymbol{\tau}_l^{(2)}$ form spin-1/2 states. If the effective interaction between them is antiferromagnetic, the ground state is a TTL state. If it is ferromagnetic, the ground state is the LM-type ferrimagnetic state with $m_{\rm sp} = 1$. Using the perturbation calculation with respect to $(1 \pm \delta)/\lambda$, we find the phase boundary between these two phases is given by $\delta = 0.6$.

2. $\lambda \leq 0$、$1 \pm \delta > 0$: The system is unfrustrated and the ground state is the LM-type ferrimagnetic state with $m_{\rm sp} = 1$. A similar ground state is expected for $0 < \lambda \ll 1 \pm \delta$.

3. $1 + \delta \simeq 0$ and $\lambda \simeq 0$: For $1 + \delta = \lambda = 0$, $\boldsymbol{S_l}$ snd $\boldsymbol{\tau}_l^{(2)}$ form a ferrimagnetic chain with $m_{\rm sp} = 1/2$ and $\boldsymbol{\tau}_l^{(1)}$ are free spins with magnitude 1/2. For small $1 + \delta$ and λ, we can determine the phase boundary between the LM-type ferrimagnetic

phase with $m_{\rm sp} = 1$ and the nonmagnetic phase as $\lambda/(1+\delta) \simeq 0.738$ by the perturbation calculation with respect to these small parameters $1+\delta$ and λ combined with the numerical exact diagonalization (NED) calculation of the ferrimagnetic chain.

4. $1-\delta = 0$ or $\lambda = 0$: If $1-\delta = \lambda = 0$, $\boldsymbol{S}_l$ and $\boldsymbol{\tau}_l^{(1)}$ form a spin-1/2 antiferromagnetic Heisenberg chain aand $\boldsymbol{\tau}_l^{(2)}$ are free spins. If $\lambda > 0$ and $\delta = 1$, the ground state is the LM-type ferrimagnetic phase with $m_{\rm sp} = 1$. The same is true if $\delta < 1$ and $\lambda = 0$. However, if $\lambda > 0$ and $\delta < 1$, these two interactions frustrate, and a nontrivial ground state is realized.

3 Numerical Results

We have carried out the NED calculation for $L = 4, 6$ and 8 and the DMRG calculation for $L = 24$ and 48. The magnetization curves and spontaneous magnetization are calculated to obtain the ground-state phase diagram of Fig. 2. It should be remarked that the two ferrimagnetic phases with $m_{\rm sp} = 1$ are not a single phase, but are separated by the partial ferrimagnetic phase and nonmagnetic phase. The nonmagnetic phase continues to the TLL phase for large δ. Hence, the whole nonmagnetic phase is likely to be a TLL phase. However, since the sum of the spin magnitudes in a unit cell is an integer, the Lieb-Schultz-Mattis theorem does not exclude the gapped phase.

The fate of the infinite series of ferrimagnetic phases found for $\delta = 0$ in [1] is also investigated. The λ-dependence of the spontaneous magnetization for $\delta = 0.1$ is shown in Fig. 3. It seems that the width of the ferrimagnetic phase with $m_{\rm sp} = 1/2$ ($p = 2$) remains finite, while those with $p \geq 3$ are smeared out and the corresponding region turns into the partial ferrimagnetic phase suggesting the fragility of the ferrimagnetic phases with large p.

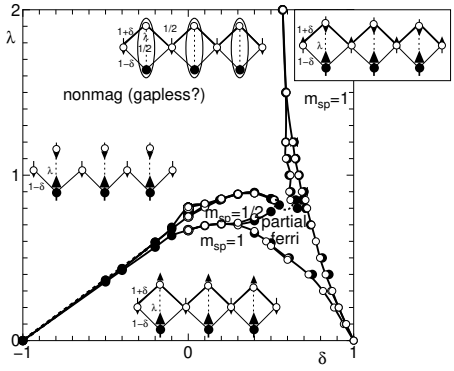

Figure 2: Ground-state phase diagram. The open circles are the phase boundaries estimated from the NED data extrapolated to the thermodynamic limit. The filled circles are the phase boundaries estimated from the DMRG data for $L = 24$ and 48. The curves are guides for the eye. The insets are schematical spin structures in different phases.

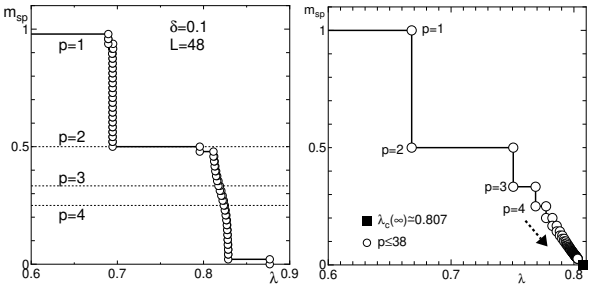

Figure 3: Left panel : λ-dependence of the spontaneous magnetization in the ground state for $\delta = 0.1$ calculated by the DMRG method for open chains with $L = 48$. Right panel: The corresponding figure for $\delta = 0$ taken from ref. [1].

References

[1] K. Hida, J. Phys. Soc. Jpn. **90**, 054701 (2021).

Novel phenomena in mismatched multilayer systems: Search for new candidate materials and analysis of electronic structures

Toshikaze KARIYADO

Research Center for Materials Nanoarchitectonics,

National Institute for Materials Science, Namiki, Tsukuba, Ibaraki 305-0044

Recently, artificially stacked 2D systems attract much attention as a playground for electronic structure manipulations. In particular, systems with nanoscale moiré pattern induced by slight mismatch between layers are interesting, since the nanoscale patterns tend to have striking effects on low energy band structures.

In this project, we propose twisted bilayer BC_3 as a system for realizing interesting valley related physics [1]. BC_3 is a graphene derivative with a honeycomb network of atoms [2]. The monolayer BC_3 is a three-valley semiconductor with its conduction minima at three M-points in the hexagonal Brillouin zone. Each of the valleys shows a 2D parabolic dispersion around the conduction minima, though there is anisotropy. It is found that upon making twisted bilayers, the 2D dispersion is squeezed into quasi-1D one. Interestingly, the quasi-1D directionality depends on the valley degrees of freedom. That is, twistronics applied on bilayer BC_3 leads to valley dependent band structure manipulation, which potentially paves a way to valleytronics applications.

In the analysis of monolayer and bilayer BC_3, we make full use of the ab initio method, using mainly Quantum Espresso and sometimes OpenMX. A characteristic feature of moiré bilayer systems is that the relation between two layers depends on position, and it is important to know the *local* crystalline and electronic structures to build a model to handle the nanoscale moiré pattern. This means that we need to work out computations on various local structures corresponding to the various positions in the nanoscale moiré unit cell. Then, large computational resources are required, and the numerical efficiency is important. For the numerical efficiency, the Quantum Espresso package offers an efficient parallelized version.

References

[1] T. Kariyado, Phys. Rev. B **107**, 085127 (2023).

[2] H. Tanaka *et al.*, Solid State Commun. **136**, 22 (2005).

Structure analysis of borophene by using 2DMAT

Akari TAKAYAMA

Department of Physics,

Waseda University, Ohkubo, Shinjuku-ku, Tokyo 169-8555

Introduction

Atomic-layer sheet composed of group XIV elements such as graphene and silicene have been actively studied. These atomic-layer sheets form a honeycomb structure and are expected to be applicable to various technologies because of their excellent electron mobility due to their peculiar band dispersion following the Dirac equation. Recently, an atomic-layer sheet material of boron (the group XIII element), called "borophene" is attracting attention, especially after the success of its fabrication on metal substrates. Unlike atomic-layer sheets of group XIV elements that form a honeycomb lattice, flat layers of boron are theoretically stable when composed of a triangular lattice and hexagonal hollows. Experimental observations of epitaxial borophene on Ag(111) have been consistent with the theoretical structural models [1, 2], but the atomic structure has not been examined directly. More interestingly, scanning tunneling microscopy (STM) observations of a honeycomb structure on an Al(111) substrate were reported [3], but the detailed atomic structure of this honeycomb lattice is unclear. Thus, there is a strong need to conduct structural analysis by an appropriate diffraction experiment on the surface.

In our research, we studied the atomic structure of borophene on Ag(111) and on Al(111) by means of total-reflection high-energy positron diffraction (TRHEPD). For structure analysis, calculations of the rocking curves for TRHEPD were performed by the structure-analysis program, "2DMAT" [4], which is included as standard software in ISSP's supercomputer. Using massive parallel computer simulations on supercomputer is very useful for structure analysis of large periodic structure and surface superstructure with lattice reconstruction because they require many variables for analysis.

Results and discussion

The TRHEPD experiment consists of measuring a series of the diffraction patterns for a fixed incident azimuthal direction at various glancing angles (θ). Here, the rocking curve is defined as the diffraction intensity of the (00) spot plotted as a function of θ. In the structural analysis, the experimental rocking curves are compared with those calculated for various structural models. Figure 1 shows the rocking curves of (a) a pristine Ag(111) surface and (b) the borophene grown on it, measured under the

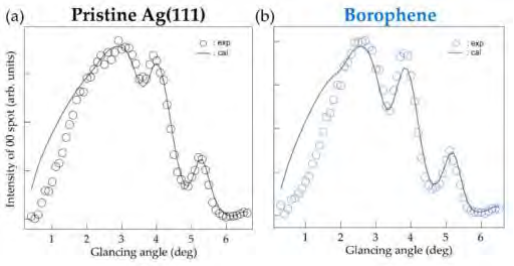

Fig. 1: Rocking curves under one-beam condition with calculated curves for (a) Ag(111) and (b) borophene on Ag(111).

one-beam condition. In the one-beam condition, the beam is incident along an off-symmetric direction, thus the rocking curve in the one-beam condition essentially gives the information on the atomic positions in the out-of-plane direction. The experimental profile was reproduced by the proposed model [2]; layer distance between Ag and borophene is 2.4 Å and the magnitude of bucking for borophene 0.04 Å. This indicates that there is no buckling, and we have directly confirmed that the borophene is a flat sheet [5].

Figure 2 shows the rocking curves of (a) a pristine Al(111) surface and (b) the borophene grown on it under the one-beam condition obtained from the experiment and from calculation of Al(111). After boron deposition, the peak position shifted slightly, but the whole shape of the rocking curve did not change much. According to angle-resolved photoemission spectroscopy (ARPES) measurements and band calculations for borophene on Al(111) substrates, it is predicted that the borophene forms AlB_2 at the top surface [6]. However, the rocking curve of the AlB_2 model differs significantly from our experimental results, which is inconsistent with the results of this study. One possible reason for the difference between our experiment and previous studies is the effect of ripple structure [3]. Since the ripple structure was not considered in this analysis, it is possible that the model used in the analysis did not correctly reproduce the experimental results. It has also been pointed out that borophene on Al substrate forms long-period moiré structures due to lattice mismatch with the substrate [7]. To determine the structure of honeycomb borophene on Al substrate, we will analyze the giant lattice system utilizing parallel computation on a supercomputer.

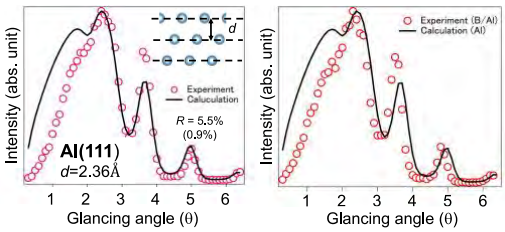

Fig. 2: Rocking curves under one-beam condition for (a) before and (b) after boron deposited on Al(111).

References

[1] R. Wu, *et al*., Nature Nanotechnology, **14** (2019) 44.

[2] G. P. Campbell, *et al.*, Nano Letters, **18** (2018) 2816.

[3] W. Li, *et al.*, Science, **63**, (2018) 282.

[4] Y. Motoyama, *et al*., Computer Physics Communications, **280** (2022) 108465.

[5] Y. Tsujikawa, AT *et al.*, Molecules. **27** (2022) 4219.

[6] D. Geng, *et al*., Physical Review B **101** (2020) 161407(R).

[7] A. B. Preobrajenski, *et al*., ACS Nano, **15**, (2021) 15153.

Magnetic structures of multiple-Q orders in inversion-symmetric Hubbard Models

Takashi UCHIDA
Hokkaido University of Science
4-1, 7-15, Maeda, Teine-ku, Sapporo 006-8585

In the last decade, multiple-Q orders in magnetic systems have attracted attention because they sometimes reveal topologically protected magnetic structures such as magnetic skyrmions. Typically, these structures are realized in the Dzyaloshinskii-Moriya (DM) interaction driven systems under magnetic field. The multiple-Q orders can also be realized in inversion-symmetric systems where the DM interaction is absent [1, 2].

In order to investigate the nature of the multiple-Q orders in inversion-symmetric itinerant systems, we have explored the magnetic structures of the triangular-lattice single-band Hubbard model by means of the molecular spin dynamics (MSD) method [3]. The present formulation of the MSD adopts the static approximation to the functional integral method and the isothermal molecular dynamics technique, and reduces to the generalized Hartree-Fock approximation at the ground state.

In the present work, we have performed the MSD calculation with use of the global charge neutrality condition instead of using the local charge neutrality condition [3]. This has the advantage that the charge transfer among the atoms is allowed in the magnetic structure formation. In the numerical calculations the most time-consuming process is the magnetic force calculation at each time step, where the local electronic structures are calculated in real space by means of the recursion method. We have adopted the MPI parallel calculation scheme and found it effective in saving both computing time and CPU resources.

We have performed magnetic structure calculations on a hexagonal supercell with 972 lattice points, which is embedded in a large cluster consisting of 6 such supercells, each of which are connected by the periodic boundary condition. Under zero magnetic field and the fixed value of the temperature $T/t = 0.0005$, we have explored the magnetic structures changing the Coulomb interaction strength U/t and the electron number n along the antiferromagnetic-ferromagnetic boundary. We have found that the stable states for $U/t < 4.0$ and $n = 1.45 \sim 1.53$ are the 3Q magnetic orders with the Q vectors pointing in the direction of three axes of the triangular lattice and that they are accompanied by 3Q charge density waves (CDW) with the same Q vectors as the magnetic ones. The present results with use of the global charge neutrality condition reveal the enhancement of the amplitude of the main 3Q magnetic order as compared to those with use of the local charge neutrality condition, showing that the CDW contributes to stabilize the magnetic 3Q order.

References

[1] T. Okubo, S. Chung, and H. Kawamura: Phys. Rev. Lett. **108** (2012) 017206

[2] Y. Kakehashi: J. Phys. Soc. Jpn. **89** (2020) 094710.

[3] Y. Kakehashi, S. Akbar, and N. Kimura: Phys. Rev. B**57** (1998) 8354.

Development of integrated interface of eigensolvers Rokko and application to quantum spin systems

Tatsuya Sakashita
Center for Quantum Information and Quantum Biology, Osaka University
1-2 Machikaneyamachō, Toyonaka, Osaka 560-0043

To establish universal exact diagonalization package for quantum lattice models including the Heisenberg-Kitaev model, we focused on developing integrated interfaces for eigensolvers, "Rokko"[1].

In Rokko, we implemented the integrated interfaces for the following types:

- Serial solvers for dense matrices (Eigen3, LAPACK)
- MPI parallelized solvers for dense matrices (EigenExa[2], ELPA[3], Elemental[4], ScaLAPACK)
- MPI parallelized solvers for sparse matrices (Anasazi in Trilinos[5], SLEPc[6]) to cover matrix representations below:
  - CRS (Compressed Row Storage)
  - Matrix-free method (the method to give matrix-vector product routines to solvers)

Rokko has the following features:

- Integrated interfaces for eigensolvers and matrices, independent of individual eigensolver libraries
- Rokko's interfaces are implemented by utilizing factory. It enables the user to dynamically select a solver.
- C, Fortran, and Python bindings of Rokko
- Automatically detecting libraries by using CMake in building Rokko
- Unit and integrated test programs by GoogleTest
- Install scripts of eigensolvers for various architectures

We prepare a paper to report design policy, software structure, and usage examples of Rokko.

References

[1] T. Sakashita, R. Igarashi, Y. Motoyama, T. Okubo, and S. Todo. Repository of Rokko. `https://github.com/t-sakashita/rokko.git`, 2012.

[2] T. Imamura, T. Hirota, and T. Fukaya. EigenExa web page. `https://www.r-ccs.riken.jp/labs/lpnctrt/projects/eigenexa/`, 2021.

[3] ELPA Consortium. ELPA (Eigenvalue soLvers for Petaflop Applications web page). `http://elpa.rzg.mpg.de`, 2013.

[4] J. Poulson. Distributed-memory dense linear algebra Elemental web page. `https://github.com/elemental/Elemental`, 2013.

[5] M. A. Heroux, R. A. Bartlett, and V. E. Howle. Trilinos Project web page. `https://trilinos.github.io`, 2003.

[6] V. Hernandez, J. E. Roman, and V. Vidal. SLEPc web page. `http://slepc.upv.es`, 2002.

Systematic understanding of the slip behaviors of slow and fast earthquakes and the effect of the upper value of porosity

Takehito SUZUKI
Department of Physical Sciences, Aoyama Gakuin University
5-10-1, Fuchinobe, Chuo-ku, Sagamihara, Kanagawa 252-5258

Two qualitatively different behaviors of earthquakes have been known. One is the fast earthquakes, which we feel naturally. The other one is slow earthquakes, which generate negligible seismic waves. Although the slow earthquakes are not disastrous, they are considered to sometimes change to the fast earthquakes after several repetitions. Whether this transition occurs or not is a fatal problem to the human society. Systematic understanding for the slip behaviors of the slow and fast earthquakes is aimed in this study.

The fault rocks can be considered as porous media, and the pores within the media are usually considered to be filled with water. If the dynamic earthquake slip (frictional slip) occurs, we can consider the interaction among heat, fluid pressure, and porosity [1, 2]. The slip is interpreted as the deformation around the contact area, called slip zone, which has a finite width w_h. During the dynamic slip, the generation of pores [frictional heating] reduces [raises] the fluid pressure in the slip zone, inducing the increase [reduction] in the friction stress and the reduction [increase] in the slip velocity [1, 2]. The fluid-pressure increase due to frictional heating will be called FH effect, whereas the fluid-pressure decrease due to the pore generation is referred to as PG effect. The slow and ordinary earthquakes are dominated by the PG and FH effects, respectively.

The spring-block model and the interaction between three quantities are employed to investigate both the slow and fast earthquakes. This system repeats the dynamic slip and cessation. The healing of pores in the cessation time is also taken into account.

With this system, we found an important function determining the system behavior [3]. For the derivation of the function, we employed three important assumptions: (i) we consider a single block, (ii) the diffusions of heat and fluid are neglected, and (iii) the change in the bulk modulus of the medium, M_0', due to porosity change is neglected; i.e., $M_0'(\phi) = M_0'(\phi_0)$, where ϕ_0 is the porosity at the onset of the slip. With these assumptions, we found a function of the slip u_f,

$$F(u_f) = \frac{1}{2}k_p u_f^2 + \mu_{\rm stat}(\sigma_n^0 + p_0)u_f - \mu_{\rm slid}\left[\frac{1}{\gamma}\left(\sigma_n^0 + p_0 - \frac{M_0'\alpha_0}{\frac{\alpha_0}{\phi_\infty} - \gamma}\right)(1 - e^{-\gamma u_f}) + \frac{M_0'\phi_\infty}{\frac{\alpha_0}{\phi_\infty} - \gamma}(1 - e^{-\alpha_0 u_f/\phi_\infty})\right], \quad (1)$$

where k_p is the spring constant, $\mu_{\rm slid}$ and $\mu_{\rm stat}$ are the sliding and maximum static friction coefficients, respectively, σ_n^0 is the normal stress acting on the interface, p_0 is the fluid pressure at the onset of the slip, γ is the positive constant, and α_0 and ϕ_∞ are the positive constants appearing in the porosity evolution law

$$\frac{\partial \phi}{\partial t} = \alpha_0 v\left(1 - \frac{\phi}{\phi_\infty}\right)[H(y + \frac{w_h}{2}) - H(y - \frac{w_h}{2})]. \quad (2)$$

Two solutions whose magnitudes are different in two orders emerge for the equation $F(u_f) = 0$, and the small and large ones correspond to the slow and fast earthquakes, respectively. Detailed analysis shows that this behavior of the solution can be interpreted as the phase transition of the first order [3].

We should now remove above-mentioned three assumptions to treat more realistic situation. We performed numerical calculations with ISSP supercomputer. The number of blocks is 40, and the diffusions of heat and fluid are included. Moreover, from Eq. (2), the assumption (iii) should be valid if the value of ϕ_∞ is negligibly small. We consider three values for ϕ_∞, and the condition where we can apply the analytical treatment will be clarified.

If we assume $\phi_\infty = 0.01$, only the fast earthquakes occur, and the slow earthquakes do not occur (Fig. 1a). This is because the porosity change is negligible, and the fluid pressure change due to the PG effect is negligibly small. If we assume $\phi_\infty = 0.1$, both the fast and slow earthquakes occur (Fig. 1b) because both the FH and PG effects work in this case. If we assume $\phi_\infty = 0.9$, the fast and slow earthquakes occur (Fig. 1c). The FH and PG effects work also in this case.

Additionally, the analytical treatment using $F(u_f)$ was found to be effective for $\phi_\infty = 0.01$ and 0.1, whereas it was not effective for the slow earthquake observed for $\phi_\infty = 0.9$. The value 0.9 may be too large to employ the above-mentioned assumption (iii). The function $F(u_f)$ is useful for predicting the dynamic slip behaviors of the natural fault zones if ϕ_∞ is much smaller than unity.

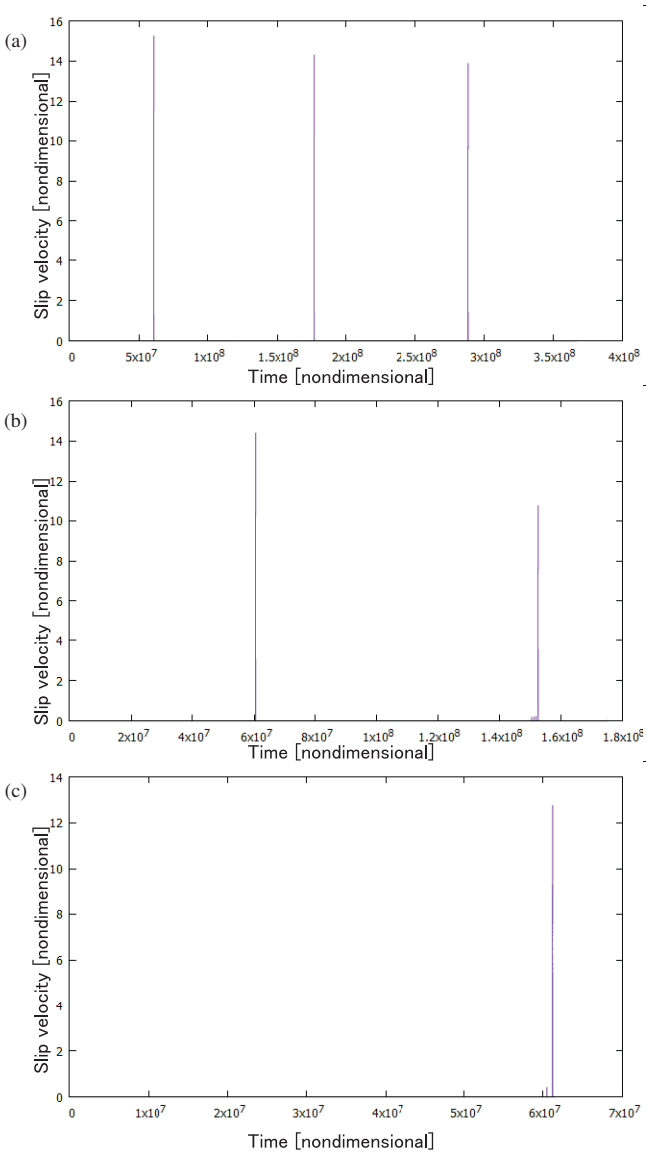

Figure 1: The slip velocity of the 20th block with (a) $\phi_\infty = 0.01$, (b) 0.1, and (c) 0.9.

References

[1] T. Suzuki, and T. Yamashita: J. Geophys. Res. **119** (2014)

[2] T. Suzuki: Phys. Rev. E **96** (2017)

[3] T. Suzuki, and H. Matsukawa, in prep.

Shape dependence of macroscopic friction between solids

Michio OTSUKI

Graduate School of Engineering Science,

Osaka University, Machikaneyama, Toyonaka, Osaka 560-8531

Amonton's law states that the static friction coefficient does not depend on the external pressure or the shape of the object. Recent studies have shown that Amonton's law systematically breaks down for macroscopic objects due to precursor slip before the onset of bulk sliding [1, 2]. However, it is unclear whether the results apply to more realistic 3D systems since the analysis in previous works is restricted to 2D systems.

First, we have numerically investigated the sliding motion of a 3D viscoelastic block on a rigid substrate using finite element simulation as shown in Fig. 1. The maximum computational size requires 500,000 nodes and 10 billion time steps, which takes 100 hours using our code compiled with the Intel Fortran compiler and a parallel computation of 2,000 MPI processes on the CPU server. The block exhibits stick-slip motion characterized by the static friction coefficient. The static friction coefficient decreases with increasing external pressure, length, or width of the block, which contradicts Amonton's law. The precursor slip occurs in the 2D interface between the block and substrate before bulk sliding. The instability analysis of a simplified model explains the decrease in the static friction coefficient and the behavior of precursor slip [3].

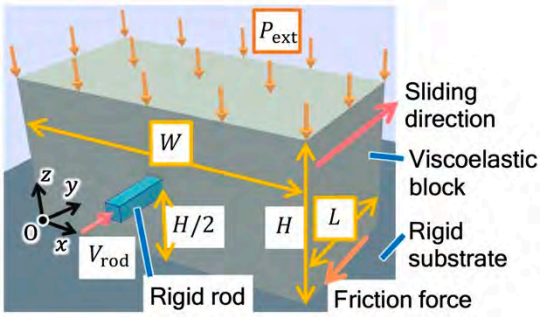

Fig. 1 Schematic of a 3D viscoelastic block on a fixed rigid substrate.

In addition, we have studied the effect of the shape of the frictional interface. Frictional interfaces of some industrial products, such as shoe soles and tires, are often grooved. However, there is a need to understand how grooves affect the frictional properties. Therefore, we have numerically investigated the slip of objects that are longitudinally grooved as shown in Fig. 2. The static friction coefficient is a decreasing function of groove width and depth. Furthermore, our theoretical analysis shows that the decrease is caused by a reduction in the effective viscosity due to the groove. These results provide new insight into the design of grooves for friction control.

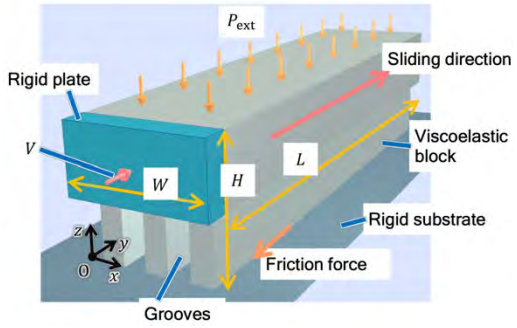

Fig. 2 Schematic of a 3D viscoelastic block with grooves block on a fixed rigid substrate.

References

[1] M. Otsuki and H. Matsukawa, Sci. Rep. **3**, 1586 (2013).

[2] Y. Katano, K. Nakano, M. Otsuki, and H. Matsukawa, Sci. Rep. **4**, 6324 (2014).

[3] W. Iwashita, H. Matsukawa, and M. Otsuki, Sci. Rep. **13**, 2511 (2023).

3.5 SCCMS Projects

Developing graph neural networks that helps predicting the molecular dynamics of glassy liquids

Hayato SHIBA
Information Technology Center, University of Tokyo
Kashiwa-no-ha, Kashiwa, Chiba 277-0882

In the past two decades, structure–dynamics correspondence in glass-forming liquids have been hot topic. Along with the drastic slowdown of atomic motion accompanying the glass transition, localized domains of les that rearrange more preferentially than others grow up. Structural analyses of local geometric orders and of real-space normal modes of vibrations have clarified the existence of correlations between the structure and the dynamics. It has remained, however, unclear to what extent the dynamics can be dictated by the structure. Recently, machine learning methodologies, in particular, graph neural networks (GNNs), enabled us to predict the slow dynamics far better than these methodologies. The GNNs have turned out to be a good fit for making predictions more accurately than ever, and thus, open a new paths to further reveal the structure-dynamics relationship.

In FY2022, we have engaged in improving our model, BOTAN (BOnd TArgeting Network), which we have proposed in FY2021. In BOTAN, a decoder for edge features is additionally implemented to the previous GNN model to enable itself to learn relative motion between neighbor pairs (edge target) in addition to self-motion of particles (node target). This model has tens of thousands of weight parameters in it, which is the reason why it can capture the complex relation between the structure and the dynamics. However, in the meawhile, it is difficult to train such a large model, especially when edge features come in

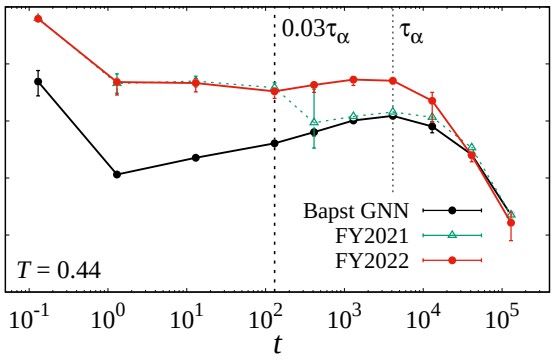

Figure 1: Comparison of pearson correlation coefficients between different GNN models: the original GNN model and of BOTAN (in FY2021 and FY2022).

as the training target. In order to fix such shortcomings, we have introduced a set of pretrained weight parameters that reflect the fact that closer pairs are more likely to separate in a short-time range. This improvement has updated the best predictive performance even on the time-scale of glassy structural relaxation, see Fig. 1 in which the Pearson correlation coefficients representing the predictive accuracy (τ_α denotes the structural relaxation time). BOTAN is now one of the state-of-the-art models for glassy dynamics relaxation, as well as other models that have also appeared in FY2022. The full article introducing his state-of-the-art model of BOTAN has been published [1], together with training code implemented on PyTorch Geometric [2].

In FY2022, we have started our next trial to

develop a new application of BOTAN: learning the dynamics of a glassy liquid under quasi-static shear at zero temperature. We have simulated using so-called the Kob-Andersen binary glass-forming mixture and computed the dataset for training by using System B at ISSP, and now we are trying to apply BOTAN for the prediction of rearranging hotspot from the initial structure.

References

[1] H. Shiba, M. Hanai, T. Suzumura, and T. Shimokawabe: J. Chem. Phys. **158**, 084503 (2023).

[2] `https://github.com/h3-Open-BDEC/pyg_botan`

A systematic *ab initio* study of quasi-one-dimensional molecular conductors TM salts

Kazuyoshi Yoshimi[a], Takahiro Misawa[a,b], Takao Tsumuraya[c], and Hitoshi Seo[d,e]
[a] *Institute for Solid State Physics, University of Tokyo, Kashiwa-no-ha, Kashiwa, Chiba 277-8581*
[b] *Beijing Academy of Quantum Information Sciences, Haidian District, Beijing 100193, China*
[c] *POIE, Kumamoto University, 2-39-1 Kurokami, Kumamoto 860-8555, Japan*
[d] *Condensed Matter Theory Laboratory, RIKEN, Wako, Saitama 351-0198, Japan*
[e] *Center for Emergent Matter Science (CEMS), RIKEN, Wako, Saitama 351-0198, Japan*

The quasi-one-dimensional organic conductor TM_2X (TM=TMTSF, TMTTF, X: monovalent anion) has been extensively studied experimentally and theoretically due to its diverse ground states induced by changes in pressure and molecular substitution[1, 2]. While the importance of electronic correlation effects has been pointed out in these studies, a systematic evaluation of electronic correlation effects has not been carried out due to the difficulty of quantitatively estimating electronic interactions in molecular systems.

In this study, we derive effective models using first-principles calculations as a starting point and the constrained random phase approximation method. The analysis of organic conductors involves molecules with many atoms as a unit, which requires significant computational effort and memory to derive effective models. We addressed this problem by using the recently developed software RESPACK[3] and exploiting its parallelization feature to take advantage of large computing resources. Using the first-principles software Quantum ESPRESSO[4] and RESPACK, we systematically derived effective models for TM_2X and analyzed the electronic states using a many-variable variational Monte Carlo solver, mVMC [5].

Based on the obtained results, we discuss the material dependence of the electronic correlation effects in the TM molecular system and clarify the relationship between the different ground states observed in the experiment and the electronic correlation effects. We show that the correlation effect in this system can be characterized by the screened on-site Coulomb interaction U relative to the intrachain transfer integrals. This parameter is material dependent and we show that it plays a key role in understanding the spin and charge ordering phenomena in the system[6].

We thank R. Kato, S. Kitou, and T. Nakamura for fruitful discussions. This work was supported by MEXT/JSPJ KAKENHI under grant numbers 19K03723, 19K21860, 20H04463, 21H01041 and 22K03526. KY and TM were supported by Building of Consortia for the Development of Human Resources in Science and Technology, MEXT, Japan. The input and output files for RESPACK and mVMC are uploaded to ISSP data repository[7].

References

[1] D. Jerome, Chem. Rev. 104, 5565 (2004).

[2] K. Yoshimi, H. Seo, S. Ishibashi, and S. E. Brown, Phys. Rev. Lett. 108, 096402 (2012), and references therein.

[3] K. Nakamura, Y. Yoshimoto, Y. Nomura et al., Comp. Phys. Commun. 261, 100781 (2021).

[4] P. Giannozzi, O. Andreussi, T. Brumme et al., J. Phys.: Condens. Matter 29, 465901 (2017).

[5] T. Misawa, S. Morita, K. Yoshimi et al., Comp. Phys. Commun. 235, 447 (2019).

[6] K. Yoshimi, T. Misawa, T. Tsumuraya, and H. Seo, arXiv:2210.13726.

[7] https://isspns-gitlab.issp.u-tokyo.ac.jp/k-yoshimi/tm-salts

Development of an effective model estimation tool by Bayesian optimization

Kazuyoshi Yoshimi
Institute for Solid State Physics, University of Tokyo
Kashiwa-no-ha, Kashiwa, Chiba 277-8581

Analysis based on effective models is useful to understand properties of materials. The reliability of an effective model is often evaluated by comparing it with experimental data, but this requires trial and error due to the existence of the large number of model parameters. We have developed a tool called Bayesian optimization tool of Effective Models (BEEMs) [1] to estimate effective models as an inverse problem using experimental data and Bayesian optimization with Gaussian processes [2].

In BEEMs, the quantum lattice model solver HΦ[3] is used as the forward solver and the magnetization curves are calculated based on the given Hamiltonian. The cost function is the difference between the obtained magnetization curve and the target magnetization curve. We use the Bayesian optimization library PHYSBO[4] to find the next candidate point of the Hamiltonian that may have a smaller cost function.

BEEMs is available from the GitHub page and can be installed by the following procedures:

```
$ git clone
  https://github.com/k-yoshimi/BEEMs.git
$ cd BEEMs
$ pip3 install .
```

Then, you can use `beems` as a python package. Post tools `gauss_fit`, `mag_plt`, and `output_score` are also available. `gauss_fit` is a tool for constructing a score function using a Gaussian process based on the results obtained by Bayesian optimization. `mag_plot` is a tool for plotting magnetization at specified candidate points. `output_score` is a tool for displaying the score and the candidate point parameters up to the specified rank.

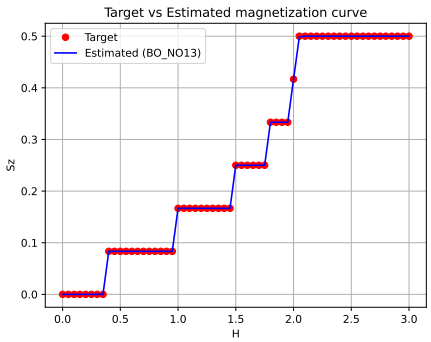

Figure 1: The magnetization curve at $(J_2, J_3) = (0.1, 0.02)$ (represented by red symbols).The proposed magnetization curve using BEEMs (represented by the blue line).

As a demonstration, we performed model parameter fitting for $S = 1/2$ Heisenberg spin chain with 12 sites under periodic boundary condition. The Hamiltonian is given by $\mathcal{H} = \sum_{i=1}^{12} [J_1 \mathbf{S}_i \cdot \mathbf{S}_{i+1} + J_2 \mathbf{S}_i \cdot \mathbf{S}_{i+2} + J_3 \mathbf{S}_i \cdot \mathbf{S}_{i+3}]$. For simplicity, we set $J_1 = 1$ and calculated the magnetization curve at $J_2 = 0.1$ and $J_3 = 0.02$ as the reference data as shown in Fig. 1. Figure 2 shows the mean squared error (MSE) between the reference data and the calculated data. Up to the fifth step, random sampling is performed even if Bayesian optimization is selected. It is seen that after performing Bayesian optimization, the cost function reaches almost zero in the 13th step,

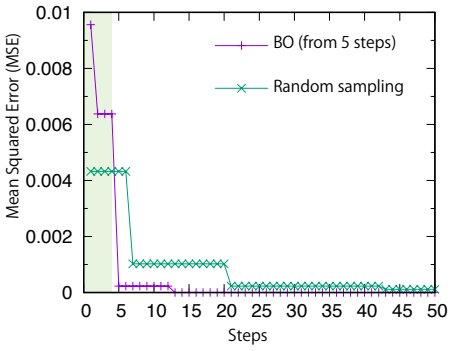

Figure 2: Mean squared error(MSE) between the reference data and the calculated data obtained by the Bayesian optimization (BO) and random sampling, respectively. The green shaded area indicates the region where the random sampling is performed.

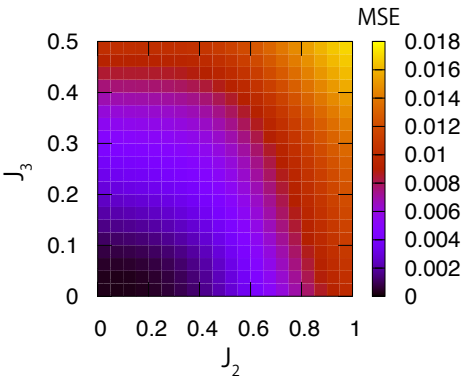

Figure 3: The color map of MSE estimated by the trained model using gaussian process.

while random sampling is underperformed comparing to Bayesian optimization even after 50 steps. The optimal parameters found by Bayesian optimization for the best score are $J_1 = 1.0, J_2 = 0.1$, and $J_3 = 0.025$. We created a trained model using `gauss_fit.py` to estimate MSE obtained with the Gaussian process after 50 trials. As a result, we found that the region where (J_2, J_3) is relatively small has a lower score as shown in Fig. 3. Using such a map, it is possible to check the accuracy of the estimated parameters. For example, we could explore approaches such as refining the grid size in the low score region.

In summary, we have developed BEEMs: an effective model estimation tool by combining HΦ and PHYSBO. In version 1.0, it is possible to estimate the effective model based on the magnetization curve. In the future, we aim to improve the calculation speed, as currently all magnetic fields have to be calculated. We plan to add a mode that can calculate the magnetization curve by splitting the calculation by S_z when S_z is conserved. We also plan to extend the tool to estimate other physical quantities if there is demand. We also plan to provide an expert level manual and allow users to define their own classes for use.

We would like to acknowledge T. Misawa, R. Tamura, and Y. Yamaji for their contribution to code development and useful discussion. KY was supported by JSPS KAKENHI Grant Number 21H01041.

References

[1] https://github.com/k-yoshimi/BEEMs

[2] C.E. Rasmussen and C.K.I. Williams, Gaussian Processes for Machine Learning, The MIT Press (2005).

[3] M. Kawamura, K. Yoshimi, T. Misawa et al., Comp. Phys. Commun. 217, 180 (2017).

[4] Y. Motoyama, R. Tamura, K. Yoshimi et al., Comp. Phys. Commun. 235, 447 (2019).

Exciton Properties in Organic Optoelectronic Devices from Large-Scale Electronic Structure Calculations

Takatoshi Fujita
National Institutes for Quantum Science and Technology
Anagawa, Inage-ku, Chiba 263-8555

Accurate calculations of electronic states are essential for computational studies of organic materials which are directed toward understanding of fundamental processes in organic electronic devices. We have developed the novel large-scale excited-state methods [1] based on the fragment molecular orbital (FMO) method, exicton model, and GW and Bethe-Salpeter equation (BSE) method with Tamm-Dancoff approximation (TDA). In this method, the excited-state Hamiltonian matrix elements at the GW/TDA-BSE level is calculated in the basis of fragment configuration state functions which describe intrafragment excitations or interfragment charge-transfer excitations. The excited-state Hamiltonian is then diagonalized to approximate the adiabatic excited states of an entire system. The novel fragment-based GW/BSE method allows for the efficient calculation of delocalized excited-states in realistic molecular aggregates. In addition, the excited-state Hamiltonian derived this method can be used for real-time simulations in combinations with the wavepacket prorogation method.

We have developed a computational method for excited-state dynamics and time-resolved spectroscopy signals in molecular aggregates [2], on the basis of ab initio excited-state calculations. As an application, we consider the charge separation dynamics and pump–probe spectroscopy in the amorphous P3HT/PCBM blend. To simulate quantum dynamics and time-resolved spectroscopy, the model Hamiltonian for single-excitation and double-excitation manifolds was derived on the basis of fragment-based excited-state calculations within the GW approximation and the BSE. After elucidating the energetics of the electron–hole separation and examining linear absorption spectrum, we investigated the quantum dynamics of exciton and charge carriers in comparison with the pump–probe transient absorption spectra. In particular, we introduced the pump–probe excited-state absorption (ESA) anisotropy as a spectroscopic signature of charge carrier dynamics after exciton dissociation. We found that the charge separation dynamics can be probed by the pump–probe ESA anisotropy dynamics after charge-transfer excitations. The present study provides the fundamental information for understanding the experimental spectroscopy signals, by elucidating the relationship between the excited states, the exciton and charge carrier dynamics, and the time-resolved spectroscopy.

References

[1] T. Fujita, Y. Noguchi, J. Phys. Chem. A **125** (2021) 10580.

[2] T. Fujita, T. Hoshi, https://doi.org/10.26434/chemrxiv-2023-773xs.

Development of an efficient method for calculating miscibility of long-chain polymer blends using molecular dynamics simulations

Kazuo Yamada and Nobuyuki Matubayasi

Division of Chemical Engineering, Graduate School of Engineering Science, Osaka University, Toyonaka, Osaka 560-8531

We have studied the mutual miscibility of polymer species in polymer mixtures using all-atom molecular dynamics simulations. The mutual miscibility of polymers is determined by the free energy of mixing given by the difference between the chemical potentials of the pure and mixed states of the constituent species. Since the chemical potential is sensitive to intra- and intermolecular interactions, an atomistic treatment of polymer mixture systems is desired to evaluate free energy of mixing. However, atomistic calculation of the chemical potential of an entire polymer chain is a difficult task with current computer capabilities because of the enormous number of intramolecular degrees of freedom in polymer chain. To solve this problem, we developed a chain increment method that approaches the chemical potential of polymers using an all-atom model [1]. The intermolecular interaction of a polymer of interest with the surrounding molecules is introduced sequentially for the monomers (segments), and the free energy for turning on the interaction is treated within the framework of a theory of solutions (energy-representation method). In our method, we compute the monomer-wise chemical potential $\Delta\mu_i^{\mathrm{incr}}$ for the incremented monomers in the tagged polymer and the total free-energy of solvation $\Delta\mu$ of the polymer is the sum of $\Delta\mu_i^{\mathrm{incr}}$. This year, we focused on the computation of the free energy of solvation in polymer mixture systems.

Results

The free energy was computed for the mixing of polyethylene (PE) and polyvinylidene difluoride (PVDF) mixture systems with the molar ratio 1:0, 3:1, 1:1, 1:3, and 0:1. The number of the monomer unit n and polymer n_{mol} are fixed 100 and 200, respectively. All-atom molecular dynamics simulation and free-energy calculation has been computed by supercomputer system at ISSP. Figure 1 shows the monomer-wise chemical potential $\Delta\mu_i^{\mathrm{incr}}$ and averaged interaction energy $\langle u\rangle_i$ for each monomer i = 20, …, and 80 by using our scheme [1]. It was seen that both $\Delta\mu_i^{\mathrm{incr}}$ and $\langle u\rangle_i$ are insensitive to the location of the monomer in the inner part of the polymer chain

and depends on the mixing ratio of the polymer systems. The standard error of $\Delta\mu_i^{\mathrm{incr}}$ at i each of i = 20, ... , and 80 is less than ~0.1 kcal/mol for both PE and PVDF at all the molar ratios in Figure 1.

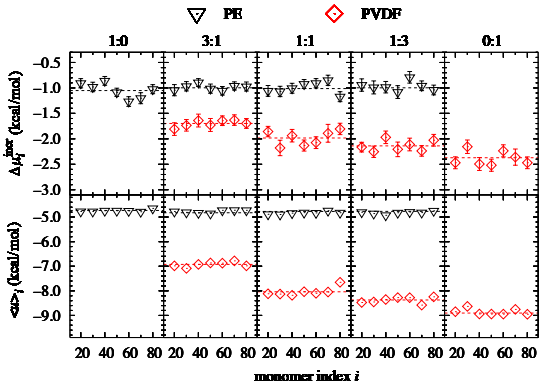

Figure 1: Incremental free energy $\Delta\mu_i^{\mathrm{incr}}$ and the average interaction energy $\langle u\rangle_i$ against the indices i of the incremented PE and PVDF monomers in the PE/PVDF mixture systems.

Figure 2 shows the mixing free energy per monomer $\Delta_{\mathrm{mix}}G/N$ of the PE/PVDF mixture versus the molar fraction of PVDF. According to Figure 1, $\Delta\mu_i^{\mathrm{incr}}$ of PE is within 0.1 kcal/mol over the entire range of mixing ratios, and the mole fraction dependence of $\Delta_{\mathrm{mix}}G/N$ is dominated by that of PVDF. Also, the sign of $\Delta_{\mathrm{mix}}G/N$ is positive for each mixing ratio examined since $\Delta\mu_i^{\mathrm{incr}}$ of PVDF becomes negative for larger mole fractions of PVDF. Figure 2 thus shows that PE and PVDF are immiscible with each other, which is consistent with experimental reports.

Conclusion

When solute degrees of freedom are large, as in polymeric systems, atomistic calculations of solvation free energies are extremely computationally expensive. The chain increment method we have developed approaches free energy of mixing by focusing on the solvation free energy as repeated monomers turn on their interactions with surrounding molecules. Combined with energy-representation method, the pair-wise solvation free energy can be calculated in computational time that is feasible for all-atom MD simulations. Extending this approach to polymer mixtures and applying it to the PE/PVDF system demonstrates that polymer mutual miscibility evaluations can be computed in an all-atom model.

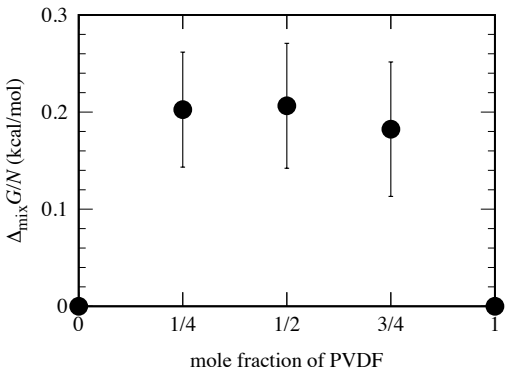

Figure 2: Free energy of mixing per monomer $\Delta_{\mathrm{mix}}G/N$ for the PE/PVDF system at mole fractions of 0, 1/4, 1/2, 3/4, and 1 for PVDF. Since the total number of polymer chains in the system is 200 and the degree of polymerization n is 100 for PE and PVDF, the total number of monomers N is equal to 20000.

References

[1] K. Yamada and N. Matubayasi: Macromol. **53** (2020) 775-788.

Fugaku Battery and Fuel Cell Project

Osamu Sugino

Institute for Solid State Physics,

The University of Tokyo, Kashiwa-no-ha, Kashiwa, Chiba 277-8581

Fiscal 2022 was the final year of the Fugaku-denchi Project [1], in which we participated in the study of the oxygen reduction reaction (ORR) occurring on an oxide electrocatalyst, i.e., zirconium oxynitride. This defective zirconia is known to produce high voltage comparable to platinum under open circuit conditions, but the reaction mechanism is still unknown. Due to the lack of detailed experimental information, we have performed a thought experiment based on reliable first-principles simulations. We first performed a first-principles Monte Carlo simulation with abICS [2] to find a distribution of nitrogen impurities (N_O) and oxygen vacancies (V_O). The results were used to create a model where N_Os and V_Os are located at a subsurface and surface site, respectively. We then investigated the free-energy profile for ORR occurring on the model [3].

Since there are many possible reaction sites for oxide surfaces, we examined all possible adsorption structures of the ORR intermediates and then used a quick and easy method to determine the reaction pathways based on the structural similarity of the intermediates. Among the resulting free energy profiles, we chose those containing relatively small endothermic elementary reactions only. The hydration of OH* was suggested to be the rate determining step under the assumption of minor contribution of the details of activation barrier. The corresponding reaction heat is about 0.4 eV, which is comparable to that on the platinum surface. Importantly, a similar value was obtained for the surface without defects, suggesting that the defects play a minor role in determining the activity of ORR. Experimentally, however, the defects were reported to enhance the reaction current density. A possible explanation for the apparent discrepancy is that defects contribute to increasing the carrier density without changing the activity as much. We are now examining other possibilities as well by using advanced exchange-correlation functionals, increasing the number of possible structures, and considering the activation energies. Making a reliable machine learning potential will be an important step for that purpose.

We are grateful for the opportunity provided by the ISSP supercomputer systems to study the ORR intermediates in detail, which would otherwise be too challenging.

References

[1] https://www.nims.go.jp/fugaku-denchi/en/index.html

[2] https://www.pasums.issp.u-tokyo.ac.jp/abics/

[3] “Effect of Nitrogen Doping and Oxygen Vacancy on the Oxygen Reduction Reaction on the Tetragonal Zirconia (101) Surface”, S. Muhammady, J. Haruyama, S. Kasamatsu, and O. Sugino, J. Phys. Chem. **C126**, 15662–15670 (2022).

Materials design of high performance magnetic materials

Tetsuya FUKUSHIMA
Institute for Solid State Physics, University of Tokyo
Kashiwa-no-ha, Kashiwa, Chiba 277-8581

In this year, we have developed an all electron first-principle calculation code, where a full-potential Korringa-Kohn-Rostoker (KKR) Green's function method is implemented, for the design of permanent magnets and spintronics materials.

It is well known that the local density approximation (LDA) and generalized gradient method (GGA) are poor approaches for strongly correlated materials. In particular, LDA and GGA give unrealistic results for localized f-electron systems. When the electron configurations are not f^7 or f^{14}, the occupied and unoccupied orbitals split off due to the correlation energy. However, in the LDA and GGA calculations, the f orbitals do not split and are pinned on the Fermi energy, leading to significantly overestimated cohesive energy. One of the origin of this problem is the error for self-interaction energy. The Coulomb and exchange terms in a same orbital should be canceled out, because the energy of electron interacts with itself (self-interaction energy) is zero. This is satisfied in Hartree-Fokc approximation; however, LDA and GGA lead to finite self-interaction energy.

We implemented the self-interaction correction (SIC) method to our full-potenital KKR Green' function code and applied it rare earth compounds. In our code, the spherical electron densities of the $4f$ orbitals are extracted from the Green's function, and then the spherical components of the SIC potential are calculated. This means that the our SIC potential is not full-potential. The full-potential SIC is needed to accurately describe the orbital splittings reflecting from the geometric shape of the f orbitals. The SIC potential is constructed by using the exchange correlation potential parameterized by Moruzzi, Janak, and Williams.

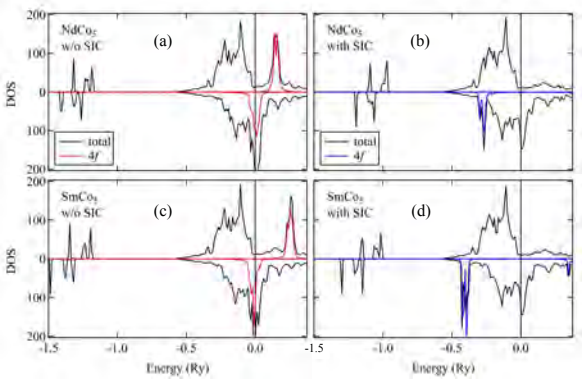

Figure 1: Calculated density of states of $NdCo_5$ and $SmCo_5$. (a,c) and (b,d) correspond to LDA and SIC results, respectively.

In order to investigate the effect of SIC on the electronic structure, we compared the density of states of $NaCo_5$ and $SmCo_5$ calculated by LDA and SIC (see figure 1). We used the experimental lattice constants in these calculations. The space group is $P6/mmm$. As shown in Fig. 1(a,c), in the LDA calculation, the partially occupied f states are located on the Fermi level. On the other hand, SIC lead to the splitting unoccupied and occupied f states. Note that the LDA+U method is often used to correct for such LDA errors, but the value of on-site Coulomb interaction (U) is an empirical parameter and is not suitable for materials screening and design.

Figure 2 shows the density of states of Ce_2O_3

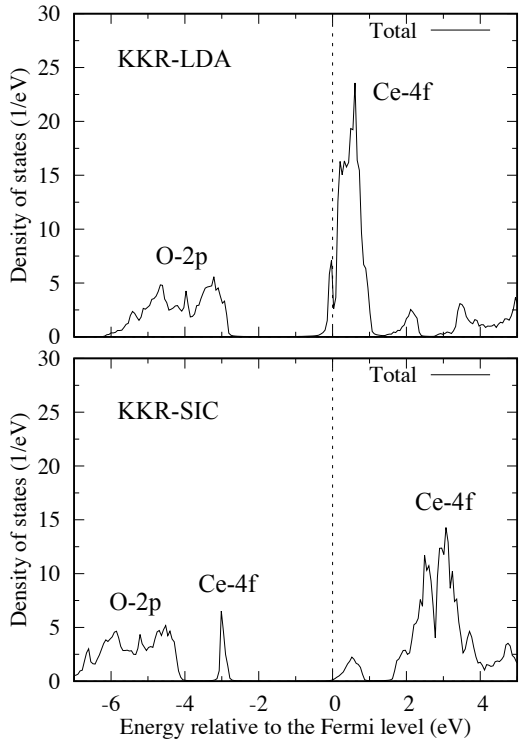

Figure 2: Density of states of Ce_2O_3 calculated by LDA and SIC.

calculated by LDA and SIC. The space group is $P\bar{3}m1$ and the antiferromagnetic state is assumed in the calculations. It is thought that the valence of the Ce ion in Ce_2O_3 is 3+ and the electron configuration f^1 is realized. In the SIC calculation, the occupied f states containing one electron are pushed down to energetically lower region, and are located around -3.0 eV. The unoccupied f states lie around 1.0 eV to 3.0 eV. Pourovskii et al. performed the electronic structure calculations for Ce_2O_3 on the basis of Linear Muffin-Tin Orbital Method with dynamical mean field approximation (DMFT) [1]. Our results obtained from the SIC calculations are quite consistent with their DMFT calculations.

References

[1] L. V. Pourovskii, B. Amadon, S. Biermann, and A. Georges, Phys. Rev. B **76**, 235101 (2007)

Development of high-performance permanent magnets by large-scale simulation and data-driven approach

Takashi MIYAKE
CD-FMat, National Institute of Advanced Industrial Science and Technology
Umezono, Tsukuba, Ibaraki 305-8568

RFe$_{12}$-type compounds with the ThMn$_{12}$ structure are potential main phase for rare-earth magnets. Because of high Fe content, high magnetization and high Curie temperature can be expected. However, RFe$_{12}$ is known to be unstable, and there have been many trials for stabilizing the ThMn$_{12}$ structure by chemical doping. In this study, we investigate the stability of (R,Zr)(Fe,Co,Ti)$_{12}$ (R=Y, Nd, Sm) against the 2-17 and unary phases by first-principles calculation [1].

The calculation is based on density functional theory in the local density approximation. We use AkaiKKR which is based on the Korringa-Kohn-Rostoker Green function method. The open-core approximation is used for the f electrons in Nd and Sm. Randomness caused by doping is treated by coherent potential approximation.

In order to investigate the stability, we consider $R_{1-\zeta_1-\zeta_2-\zeta_3-\zeta_4}\mathrm{Zr}_{\zeta_1}\mathrm{Fe}_{\zeta_2}\mathrm{Co}_{\zeta_3}\mathrm{Ti}_{\zeta_4}$. In the four-dimensional space $(\zeta_1, \zeta_2, \zeta_3, \zeta_4)$, we compare the total energy for the 1-12, 2-17, and unary phases, and identified stable phases. Figure 1 shows the phase diagram of the Sm system on the (Sm,Zr)(Fe,Co)$_{12}$ plane. We then compare the total energy difference between $(R_{1-\alpha}\mathrm{Zr}_\alpha)(\mathrm{Fe}_{1-\beta}\ \mathrm{Co}_\beta\ )_{12-\gamma}$ Ti_γ and stable phases, and calculate the hull distance. Figure 2 shows the result for $(\mathrm{Sm}_{1-\alpha}\mathrm{Zr}_\alpha)(\mathrm{Fe}_{1-\beta}\mathrm{Co}_\beta)_{12}$. We see that the hull distance is not monotonic as a function of α and β. We also see that the hull distance is small for high Zr concentration.

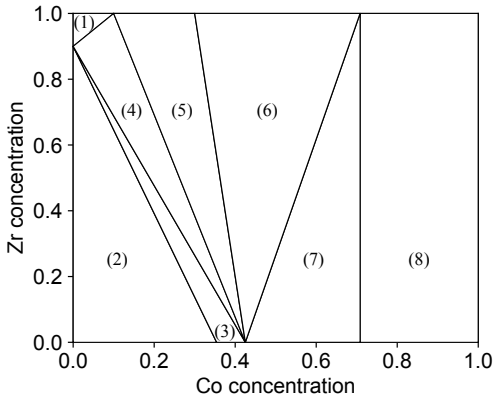

Figure 1: Phase diagram on the (Sm,Zr)(Fe,Co)$_{12}$ plane. (1) (S,Zr)Fe$_{12}$, Zr(Fe,Co)$_{12}$, Zr$_2$Fe$_{17}$ and unary Fe; (2) (Sm,Zr)Fe$_{12}$, Sm$_2$(Fe,Co)$_{17}$, and unary Sm and Fe; (3) (Sm,Zr)Fe$_{12}$, Sm$_2$(Fe,Co)$_{17}$, and unary Fe; (4) (Sm,Zr)Fe$_{12}$, Zr(Fe,Co)$_{12}$, Sm$_2$(Fe,Co)$_{17}$, and unary Fe; (5) Zr(Fe,Co)$_{12}$, Sm$_2$(Fe,Co)$_{17}$, and unary Fe; (6) Zr(Fe,Co)$_{12}$, Sm$_2$(Fe,Co)$_{17}$, Zr$_2$Co$_{17}$, and unary Fe; (7) Sm$_2$(Fe,Co)$_{17}$, Zr$_2$Co$_{17}$, and unary Fe; (8) Sm$_2$Co$_{17}$, Zr$_2$Co$_{17}$, and unary Fe and Co.

References

[1] Taro Fukazawa, Yosuke Harashima, Hisazumi Akai and Takashi Miyake: Phys. Rev. Mater. **6**, 054404 (2022).

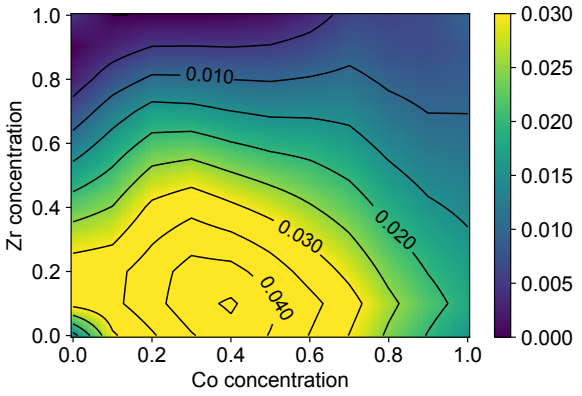

Figure 2: Hull distance in eV for $(Sm_{1-\alpha}Zr_{\alpha})(Fe_{1-\beta}Co_{\beta})_{12}$ with the $ThMn_{12}$ structure.

Data driven analysis for impurity effects on photocatalysts

Mikiya FUJII and Yosuke HARASHIMA
Division of Materials Science, Nara Institute of Science and Technology
Takayama-cho, Ikoma, Nara 630-0192

Photocatalytic generation of hydrogen from solar energy (green hydrogen) is one of the key elements for solving resource, energy, and environmental problems. The purpose of this study is to obtain guidelines for controlling the properties of new photocatalytic compounds and impurities to improve the yield of hydrogen production in response to visible light, which is still not sufficient. For this purpose, a combined analysis of first-principles calculations and informatics will be performed. While materials development has been conducted within a limited search space based on experience, this study will develop a new research in photocatalytic materials development by utilizing information science to predict and develop new materials with a greatly expanded search space. [1, 2] In addition to solving energy problems through hydrogen-producing photocatalysts, this research will have a spillover effect on the synthesis of carbon-neutral petrochemical feedstocks from CO_2 and green hydrogen.

Process informatics for calcination process with dynamical Monte Carlo simulations:

The hydrogen evolution rate (HER) of photocatalytic materials depends strongly on their calcination processes. The calcination process will determine an amount of product compound, defect, and surface area. The HER is considered to be highly dependent on those features, however, experimental analysis to detect the features is time-consuming. We developed a dynamical Monte Carlo (DMC) simulation code to predict the features, and constructed an HER prediction model using the calculated features. The DMC code is written in C++ and the HER prediction code is in Python. The DMC code is based on formation energies of product compounds, defect energies, and surface energies. We will use the first-principles calculation code, Vienna Ab initio Simulation Package (VASP), to calculate these quantities. In Ref. [3], quantum chemical calculations were used as explanatory variables in the model to predict experimental values in flow copolymerization [4]. It was found that information on the so-called transition states of intermediates is important in predicting the products of chemical reactions. This is a kind of data assimilation [5], which we will incorporate into our future method of calculating intermediates in crystal formation by process simulation.

Highthroughput search of high entropy catalyst:

Platinum is known for its high catalytic performance, but it is very rare, so there is a need to develop alternatives. We performed a systematic search for high-entropy alloys that would mimic platinum. The electronic structures were calculated by using first-principles code, AkaiKKR, which is based on the KKR-Green's function method. It enables us to consider nonstoichiometric chemical compositions by the coherent potential approximation. We considered up to a quaternary system which consist of transition metal elements and performed first-principles calculations on more

than 100,000 samples.

References

[1] M. Fujii: JSAP Review, **2022**, 220416 (2022).

[2] 藤井幹也: 応用物理, **91**, 688 (2022).

[3] S. Takasuka, *et al.*: Digital Discovery, accepted.

[4] A. Wakiuchi, *et al.*: Macromol. Mater. Eng. 2200626 (2022).

[5] Y. Harashima: (invited talk) The 24th Annual Meeting of Japan Society of Theoretical Chemistry, May 18th 2023.

Computational and Data Materials Science Study for ET Revolution by Developing Next-Generation Battery and Fuel Cell

Yoshitaka TATEYAMA

National Institute for Materials Science,

Namiki 1-1, Tsukuba, Ibaraki 305-0044

We clarified a long-standing problem of atomistic insight of the dopant effect on the ionic conduction around grain boundary, by extensive first-principles MD calculations of diffusion coefficients[1].

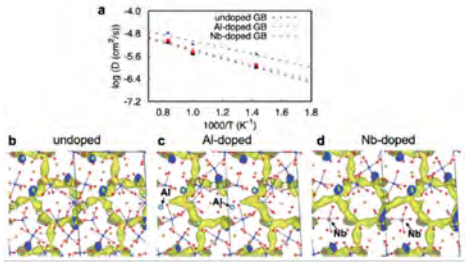

Fig. 1: Calculated self-diffusion coefficients of $Li_7La_3Zr_2O_{12}$ solid electrolyte.

We also developed a high-throughput first-principles MD sampling flow for the ionic conductivity calculations, and proposed potential solid electrolytes with higher ionic conducitivy by applying the flow to Na-ion sulfide solid electrolytes[2].

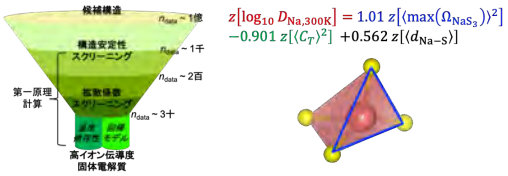

Fig. 2: Schematic picture of the high-throughput screening flow for the search for solid electrolyte materials with the higher ionic conductivities.

We further addressed the speed-up of the conductivity calculations by developing a new method of chemical charge diffusion non-equilibrium MD (CCD-NEMD), and demonstrated that this new method surely accelerates the sampling of mean-square-displacement[3].

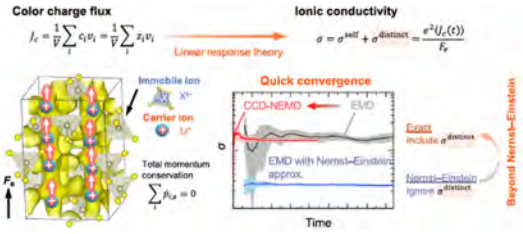

Fig. 3: (left) Definition of flux and color charges to the Li ions and anion units in the $Li_{10}GeP_2S_{12}$ model system. (right) Schematic picture about the speed-up of the evaluation of correlated ionic conductivity.

References

[1] B. Gao, R. Jalem, and Y. Tateyama, J. Mater. Chem. A, **10**, 10083-10091 (2022).

[2] S.-H. Jang, Y. Tateyama, and R. Jalem, Adv. Funct. Mater. **32**, 2206036 (2022).

[3] R. Sasaki, B. Gao, T. Hitosugi, and Y. Tateyama, npj Comput. Mater. **9**, 48 (2023).

Theoretical study of hydrogen-evolution semiconductor photocatalysts using first-principles calculations

Seiichiro L. TEN-NO
Graduate School of System Informatics, Kobe University
Rokkodai-Cho, Nada-Ku, Kobe 657-8501

Planar Defect in Layered Perovskite Photocatalyst $Y_2Ti_2O_5S_2$

Layered perovskite $Y_2Ti_2O_5S_2$ (YTOS) is a promising semiconductor photocatalyst with an electronic structure suitable for overall water splitting under visible light. Similar to other photocatalysts, structural defects during synthesis should be controlled to promote photocatalytic performance [1, 2]. Very recently, transmission electron microscopy (TEM) have revealed extremely large planar defects composed of S–Mg–S layers in YTOS synthesized using the flux method. It is not clear how such a characteristic planar defect makes an effect on photocatalytic activities in YTOS.

Motivated by this observation, we investigated the planar defect structure and electronic structure using first-principles calculations based on the density functional theory (DFT) [3]. The DFT calculations were performed within the PBE+U (Perdew–Burke–Ernzerhof functional with Hubbard U correction) exchange-correlation functional using the projector augmented wave (PAW) method, as implemented in the Vienna ab initio simulation package (VASP). Here we set $U = 7.5$ eV for the $3d$ orbitals at the Ti sites to reproduce the experimental band gap, 1.9–2.0 eV [1].

We have microscopically determined the planar defect structure using the structural optimization, where a Mg atom is centered in the ab-square intersecting the defect S layers (Fig. 1). The obtained defect structure is consistent with the ADF–STEM image: for example, the distance between the Y layers of the defect model, 9.93 Å, is in quantitative agreement with the experimental value, ca. 10.00 Å.

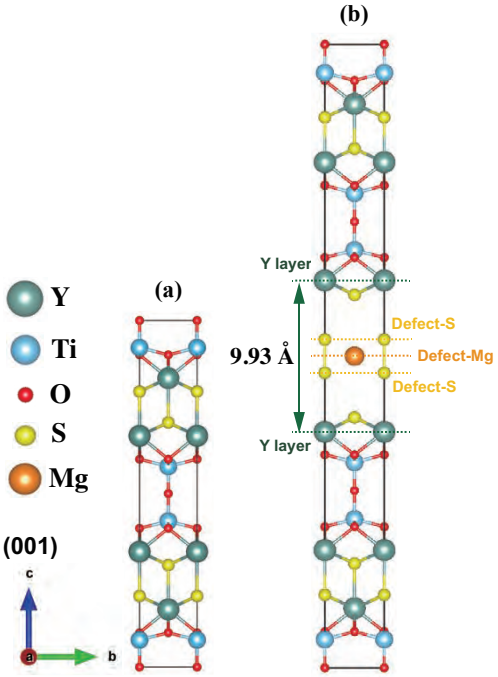

Figure 1: The optimized structure of (a) the conventional unit cell and (b) supercell with the MgS_2 planar defect.

To understand the electronic structures, we have investigated the projected density of states (PDOS) and band structure shown in Fig. 2. The electronic structure shows that the

defect bands appear within the original band gap. The large dispersion of the bands reflects the planar (two-dimensional) nature of the defect in S and Mg with a high state density, in contrast to point defects. It is expected that such defect bands considerably increase the electron–hole recombination rate, enhancing the interband transitions of the defect valence and/or defect conduction bands via radiative or nonradiative transitions, which is an undesirable factor for the efficiency of the overall water splitting of YTOS.

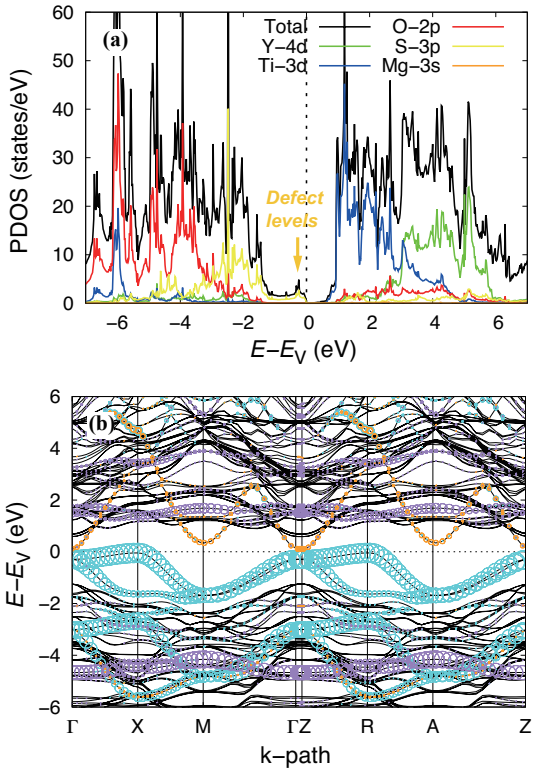

Figure 2: (a) PDOS for YTOS with the planar defect. (b) Band structure with the planar defect. The defect S-3$p_{x,y}$, S-3p_z, and Mg-3s weights are colored in cyan, purple, and orange, respectively. The energy (E) for each case is measured from the valence band maximum (E_{V}).

To consider the stability of the planar defect, we have finally evaluated the defect formation energy (E_{f}). The chemical potentials μ_i were determined by the phase diagram of the relevant compounds in the synthesis of YTOS. Fig. 3 shows E_{f} as a function of the chemical potential of S relative to bulk precipitate ($\Delta\mu_{\mathrm{S}}$), where A, B, and C denote the representive points of the phase diagram. The evaluation of the formation energy suggests that E_{f} increases with decreasing $\Delta\mu_{\mathrm{S}}$ and/or $\Delta\mu_{\mathrm{Mg}}$. Therefore, the optimum conditions for the S and Mg environments must be optimized for the synthesis of YTOS,which suppresses the formation of the planar defect.

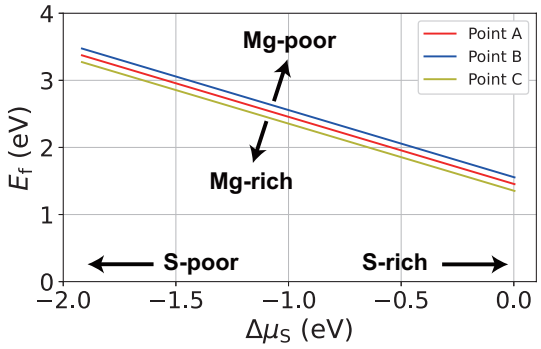

Figure 3: Formation energy of the MgS_2 planar defect E_{f} against $\Delta\mu_{\mathrm{S}}$. The red, blue, and yellow lines represent E_{f} at points A, B, and C of the phase diagram, respectively.

References

[1] Q. Wang *et. al.*: Nat. Mater. **18**, 827 (2019).

[2] Z. Pan *et. al.*: Res. Chem. Intermed. **47**, 225 (2021).

[3] M. Nakabayashi, K. Nishiguchi, X. Liang, T. Hisatomi, T. Takata, T. Tsuchimochi, N. Shibata, K. Domen, and S. L. Ten-no: J. Phys. Chem. C (in press: https://doi.org/10.1021/acs.jpcc.3c00820).

3.6 Software Advancement Projects and Workshop Support

Acceleration of first-principles statistical thermodynamics framework abICS using an on-lattice neural network model and active learning

Shusuke KASAMATSU[1], Tatsumi AOYAMA[2], Yuichi MOTOYAMA[2],
Kazuyoshi YOSHIMI[2], and Osamu SUGINO[2]
[1]*Faculty of Science, Academic Assembly, Yamagata University, Yamagata 990-8560*
[2]*Institute for Solid State Physics, University of Tokyo, Kashiwa 277-8581*

In 2019, ab Initio Configuration Sampling toolkit, or abICS for short, was developed as an ISSP Software Advancement Project for directly combining first-principles relaxation and total energy calculations with replica exchange Monte Carlo (RXMC) sampling [1]. The motivation was that effective models such as cluster expansion, which are used to speed up the usual Metropolis Monte Carlo sampling for analyzing order/disorder in alloy systems, are limited in describing complex many-component systems with sufficient accuracy. Our aim at that time was to enable direct sampling on first-principles energies by employing highly parallel sampling methods such as RXMC in combination with massively parallel supercomputing resources. A few years later, some of the authors found that an on-lattice neural network model overcomes many issues found in previous effective models if sufficient training data is provided in an active learning setting [2,3]. This led to the proposal of last year's Software Advancement Project, which we outline in this report.

The abICS framework developed in this project uses Python as a glue language to piece together the necessary components (Fig. 1). It is registered on PyPI (Python Package Index; pypi.org) and can be installed easily in most environments through the command "`pip install --user abics`". A typical use case is outlined as follows:

1. Random configurations on a lattice are relaxed and their total energies are calculated using the first-principles code of choice. We support VASP, Quantum Espresso, and OpenMX.
2. A neural network model is trained on data from step 1 to predict relaxed energies from configurations on the non-relaxed lattice. We currently use aenet code [4] for the neural network training.
3. RXMC or population annealing MC (PAMC) calculation is performed using the neural network model from step 2. Two sampling modes are available:

canonical sampling with a fixed number of atoms or grand canonical sampling which allows for changes in the composition. For the neural network evaluation, we provide a file IO-based interface to aenet, and we also provide an interface to aenet-lammps [5] python interface which does not rely on file IO and is thus usually faster.

4. A subset of samples from step 3 are relaxed and their total energies are calculated using first-principles calculation. If the results deviate considerably from the neural network prediction, the data is added to the training data set and the procedure is repeated from step 2.

The overall procedure is controlled by an input file in TOML format, which is an easy-to-read software configuration format that is being used in many projects [6]. The parameters for the first-principles calculations and neural network training/evaluation are controlled by separate files following formats of the specified solver.

We believe that abICS will be a game-changer in modeling order/disorder in many-component crystalline systems as we have already demonstrated for partially hydrated Sc-doped $BaZrO_3$ [3]. Please do not refrain from contacting us if you find any difficulties in using or extending this software.

References

[1] S. Kasamatsu and O. Sugino, J. Phys.: Condens. Matter **31**, 085901 (2019).

[2] S. Kasamatsu et al., J. Chem. Phys. **157**, 104114 (2022).

[3] K. Hoshino, S. Kasamatsu, et al., Chem. Mater. **35**, 2289-2301 (2023).

[4] N. Artrith et al., Phys. Rev. B **96**, 014112 (2017). http://ann.atomistic.net/

[5] M. S. Chen et al., J. Chem. Phys. **155**, 074801 (2021). https://github.com/HidekiMori-CIT/aenet-lammps

[6] https://github.com/toml-lang/toml

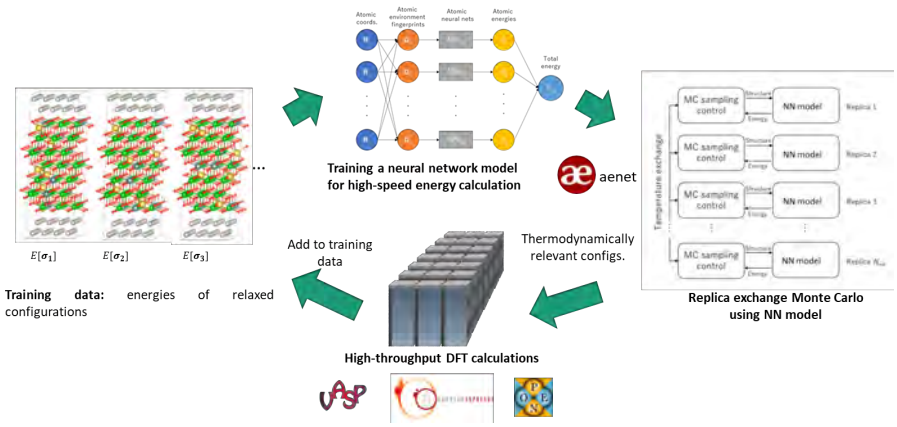

Fig. 1: Overview of the active learning procedure using abICS.

H-wave: A quantum lattice solver using Wavenumber-Space Mean Field Approximation and Random Phase Approximation

Akito Kobayashi[a], Tatsumi Aoyama[b], Yuichi Motoyama[b], Takeo Kato[b], and Kazuyoshi Yoshimi[b]
[a]*Department of Physics, Nagoya University, Nagoya 464-8602*
[b]*Institute for Solid State Physics, University of Tokyo, Kashiwa-no-ha, Kashiwa, Chiba 277-8581*

In a project for Advancement of Software Usability in Materials Science (PASUMS) [1] in FY2022, `H-wave` [2] has been developed to perform unrestricted Hartree-Fock (UHF) approximation in wavenumber space and random phase approximation (RPA) for itinerant electron systems. UHF and RPA correspond to simple approximations that deal with fluctuations up to first order and enable analyses of electron correlation effects in materials at a low computational cost. The input files describing the one-body and two-body interactions are based on the `Wannier90` [3] format. This allows smooth connection for the software packages that derive the effective models from first principles calculations, such as `RESPACK` [4], to the analyses of the effective model with `H-wave`.

`H-wave` is implemented in Python3 and is available from PyPI package repository. The source archive can be obtained from the GitHub site[1]. To use `H-wave`, we must prepare an input parameter file written in the TOML format which specifies calculation conditions and file names of the definition files for the geometry and Hamiltonian. The Hamiltonian is defined through the input files of the transfer integrals and the interactions denoted by CoulombIntra, CoulombInter, Hund, Ising, Exchange, and PairLift. In UHF mode, a PairHop term can also be specified. To learn

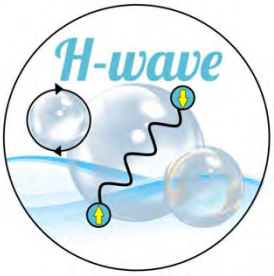

Figure 1: A logo of H-wave designed by T. Kawamura.

details of the input files, the readers may refer to the manual [2]. Once these input files are prepared, the calculation will be performed by typing the following command:

```
$ hwave input.toml
```

where `hwave` is the executable file of `H-wave` and `input.toml` is the name of the input file. After the calculations are completed, the following physical quantities are obtained:

in `UHF` mode: energy, eigen values and vectors, and one-body Green's functions.

in `RPA` mode: irreducible susceptibilities

A brief tutorial is included in the manual, and several application examples have been uploaded to the ISSP data repository [5]. For the UHF calculations, we provide examples such as the band and density of state plots, and the finite temperature calculations. In addition, a more applied example analysis of the

[1] https://github.com/issp-center-dev/h-wave

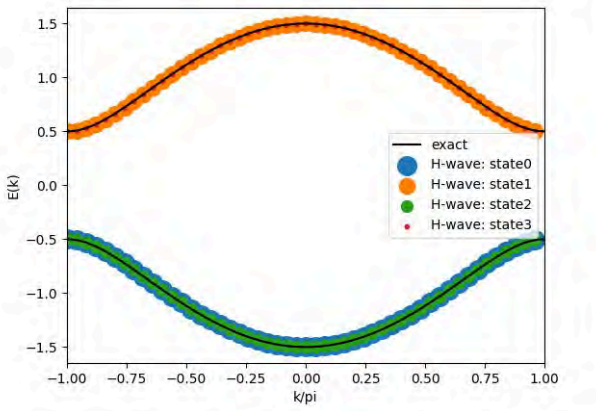

Figure 2: The band dispersion of SSH model.

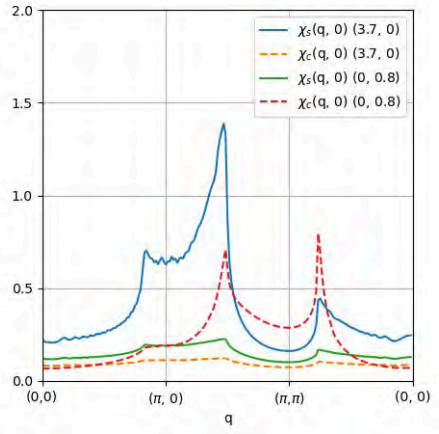

Figure 3: The charge and spin susceptibilities at $(U, V) = (3.7, 0)$ and $(0, 0.8)$ in Ref. [8].

Su–Schrieffer-Heeger (SSH) model [6] which is one of the well-known platforms for the emergence of the topological insulator is also provided. In this sample, the scripts to obtain the band dispersion (shown in Fig.2) and the Zak phase [7] of the lowest band, which corresponds to the topological number, are also provided. For RPA calculations, we provide examples for calculating charge and spin susceptibility that reproduce the results of Refs. [8, 9]. Figure 3 shows the static charge and spin susceptibilities ($\chi_s(q, 0)$ and $\chi_c(q, 0)$) for one-orbit two-dimensional extended Hubbard model on the square lattice at $(U, V) = (3.7, 0)$ and $(0, 0.8)$ examined in Ref. [8].

In this report, we introduced the features and examples of `H-wave` developed through PASUMS. In the future, we would like to develop functions such as follows; (a) providing calculation scripts for quantities corresponding to dynamic susceptibility measured in experiments, (b) evaluating the instability of superconducting transition by solving the linear Eliashberg equation considering charge and spin fluctuations as pairing interactions, and (c) adding more samples such as the calculation with spin-orbit interactions. We believe that `H-wave` is useful for a wide range of materials scientists and can contribute to the promotion of the computational materials design.

We would like to acknowledge K. Ido, T. Misawa, and T. Kawamura for their contribution to code development and useful discussion. AK and KY were supported by JSPS KAKENHI Grant Number 22K03526. KY was supported by JSPS KAKENHI Grant Number 21H01041.

References

[1] https://www.pasums.issp.u-tokyo.ac.jp

[2] https://www.pasums.issp.u-tokyo.ac.jp/h-wave

[3] G. Pizzi *et al*, J. Phys.: Condens. Matter **32** 165902 (2020).

[4] K. Nakmura, Y. Yoshimoto, Y. Nomura *et al.*, Comp. Phys. Commun. **261**, 107781 (2021).

[5] https://isspns-gitlab.issp.u-tokyo.ac.jp/hwave-dev/hwave-gallery

[6] W. P. Su, J. R. Schrieffer, and A. J. Heeger, Phys. Rev. Lett. **42**, 1698 (1979).

[7] J. Zak, Phys. Rev. Lett. **62**, 2747 (1989).

[8] A. Kobayashi, Y. Tanaka, M. Ogata, and Y. Suzumura, J. Phys. Soc. Jpn. **73**, 3135 (2004).

[9] K. Yoshimi, M. Nakamura, and H. Mori, J. Phys. Soc. Jpn. **76**, 024706 (2007).

Report of CCMS hands-on sessions in the 2022 fiscal year

Kota IDO

Institute for Solid State Physics,

The University of Tokyo, Kashiwa-no-ha, Kashiwa, Chiba 277-8581

In the 2022 fiscal year, Center for Computational Materials Science (CCMS) in the Institute for Solid State Physics (ISSP) held 8 hands-on sessions where the ISSP supercomputer was used [1-8]. In this report, we briefly summarize them.

Table 1 shows the list of the hands-on sessions in the 2022 fiscal year. There are 8 software used in the hands-on sessions: 2DMAT, abICS, PHYSBO, TeNeS, HΦ, mVMC, DSQSS, and ESM-RISM. Development of the software mentioned above was supported by "Project for advancement of software usability in materials science" (PASUMS) [9].

Table 1: List of CCMS hands-on sessions where the ISSP supercomputer was used in the 2022 fiscal year.

Date	Lecturer	Software
Apr. 26	K. Yoshimi et al.	2DMAT[10]
June 27	S. Kasamatsu et al.	abICS[11]
June 20	K. Tsuda et al.	PHYSBO[12]
Oct. 25	T. Okubo et al.	TeNeS[13]
Nov. 21	Y. Yamaji et al.	HΦ[14]
Nov. 28	T. Misawa et al.	mVMC[15]
Dec. 14	Y. Motoyama et al.	DSQSS[16]
Dec. 22	M. Ohtani et al.	ESM-RISM[17]

Features of each software are as follows. 2DMAT is a Python package to search an optimal result by applying a search algorithm to a direct-problem solver [10]. abICS is an *ab initio* software framework to perform configuration samplings in disordered systems [11]. PHYSBO is a Python library to perform a fast and scalable Bayesian optimization [12]. TeNeS is a software package for performing simulations in quantum many-body systems based on tensor network methods [13]. HΦ is a package of solvers for quantum many-body systems based on exact diagonalization methods [14]. mVMC is a low-energy solver based on the variational Monte Carlo method for a wide range of quantum lattice models [15]. DSQSS is a software package of the quantum Monte Carlo method based on Feynman's path integral representation for quantum lattice systems [16]. ESM-RISM is an *ab initio* method for electrode/electrolyte interfaces, which has been implemented in open-source software Quantum ESPRESSO [17, 18].

In all of the hands-on sessions, lecturers explained the basics of each software and gave its tutorial. Materials of some hands-on sessions are available on each official page.

References

[1] https://ccms.issp.u-tokyo.ac.jp/event/5274

[2] https://ccms.issp.u-tokyo.ac.jp/event/5099

[3] https://ccms.issp.u-tokyo.ac.jp/event/5456

[4] https://ccms.issp.u-tokyo.ac.jp/event/5631

[5] https://ccms.issp.u-tokyo.ac.jp/event/5659

[6] https://ccms.issp.u-tokyo.ac.jp/event/5665

[7] https://ccms.issp.u-tokyo.ac.jp/event/5685

[8] https://ccms.issp.u-tokyo.ac.jp/event/5698

[9] https://www.pasums.issp.u-tokyo.ac.jp

[10] https://www.pasums.issp.u-tokyo.ac.jp/2dmat/en/

[11] https://www.pasums.issp.u-tokyo.ac.jp/abics/en/

[12] https://www.pasums.issp.u-tokyo.ac.jp/physbo/en/

[13] https://www.pasums.issp.u-tokyo.ac.jp/tenes/en

[14] https://www.pasums.issp.u-tokyo.ac.jp/hphi/en/

[15] https://www.pasums.issp.u-tokyo.ac.jp/mvmc/en/

[16] https://www.pasums.issp.u-tokyo.ac.jp/dsqss/en/

[17] https://www2.ccs.tsukuba.ac.jp/public/otani/programs.html

[18] https://www.quantum-espresso.org

Supercomputer course of Computational Materials Design (CMD®) workshop

Masaaki GESHI[1], Yoshitada MORIKAWA[2], Tomoya ONO[3]

[1]*R^3 Institute for Newly-Emerging Science Design,*
Osaka University, Machikaneyama, Toyonaka, Osaka 560-0043

[2] *Department of Precision Engineering,*
Osaka University, Yamada-oka, Suita, Osaka 565-0871

[3]*Graduate School of Engineering,*
Kobe University, Rokkodai-cho, Nada, Kobe 657-8501

The 41st Computational Materials Design (CMD®) workshop (CMD41) has been held from September 5th to September 9th and the 42nd CMD® workshop (CMD42) has been done from February 20th to February 24th. Both were held online. In this workshop we have the supercomputer course to train up human resources to advance research by using system B supercomputer of ISSP, the University of Tokyo.

In CMD41, nine participants took the supercomputer course and followed a tutorial on STATE-Senri developed by Y. Morikawa. After an introductory lecture on large-scale computing and an explanation of how to use the supercomputer of ISSP by M. Geshi, the participants started constructing computational models for their own research subjects with the help of the lecturers. Then they carried out calculations using supercomputers. Specific themes included molecular adsorption on solid surfaces, chemical reactions of molecules in solutions, chemical reactions of molecules on catalytic surfaces, reactions at solid-solid interfaces, and so on. The participants performed calculations and examined their results.

In CMD42 three participants took the supercomputer course and used the supercomputer of ISSP. They got a tutorial on RSPACE developed by T. Ono. After giving the introductory lecture of large-scale computing by M. Geshi and introducing the calculation method of electronic structures and electron conduction property using RSPACE, exercises instructed in the textbook were carried out. Then, electronic structure calculations were carried out for various molecules, and the electronic density distribution was visualized. The attendees also performed massively parallel calculations to confirm the efficiency for parallel computing. Finally, the electron conduction properties of two-dimensional materials and dialectic materials sandwiched between metallic electrodes were investigated.

4 PUBLICATION LIST

Example:

LASTNAME, Firstname [project class; # points (B), # points (C)] (Page #)
— *Project title*
1. First paper
   Names of Authors, etc.
2. Second paper
   ...

□ ISSP Joint Research Projects

○ B–E classes

ADACHI, Kyosuke [B class; 700 (B), 100 (C)] (311)
— *Multi-component phase separation dynamics of proteins*

AKASHI, Ryosuke [B class; 600 (B), 100 (C)] (312)
— *Solution of the Eliashberg equation with the electron-electron Coulomb interaction*
1. Revisiting homogeneous electron gas in pursuit of properly normed ab initio Eliashberg theory
   R. Akashi Physical Review B **105**, 104510 (2022).
   DOI:10.1103/PhysRevB.105.104510

AOYAMA, Kazushi [B class; 900 (B), 180 (C)] (291)
— *Magnetic field effect on a topological chiral order in breathing-kagome antiferromagnets*
— *Topological chirality order and its stability in breathing-kagome antiferromagnets*
1. Zero-Field Miniature Skyrmion Crystal and Chiral Domain State in Breathing-Kagome Antiferromagnets
   K. Aoyama and H. Kawamura, J. Phys. Soc. Jpn. **92**, (2023) 033701.
   DOI:10.7566/JPSJ.92.033701

2. Spin and thermal transport and critical phenomena in three-dimensional antiferromagnets
   K. Aoyama, Phys. Rev. B **106**, (2022) 224407.
   DOI:10.1103/PhysRevB.106.224407

3. Hedgehog lattice and field-induced chirality in breathing-pyrochlore Heisenberg antiferromagnets
   K. Aoyama and H. Kawamura, Phys. Rev. B **106**, (2022) 064412.
   DOI:10.1103/PhysRevB.106.064412

ARAI, Munehito [C class; 6600 (B), 0 (C)] (230)
— *Theoretical design of novel antibodies that inhibit disease-related protein-protein interactions*
— *Theoretical design of novel proteins for medical and industrial applications*

ARAI, Toyoko [B class; 500 (B), 80 (C)] (170)
— *RSDFT calculation of the force acting between a tip and a sample detected by noncontact atomic force microscope*

ARAKI, Takeaki [B class; 900 (B), 170 (C)] (293, 294)
— *Aggregation of polyelectrolytes in mixed solvents*
— *Molecular modeling of ferroelectric nematic phase*

ARIMA, Kenta [B class; 700 (B), 170 (C)] (305)
— *Calculation of electronic structures of graphene nanoribbons with wrinkles*
— *Understanding electronic structures and reactivity of functional graphene sheets toward machining catalyst*

ARUGA, Tetsuya [B class; 500 (B), 160 (C)] (160, 162)
— *In-plane interaction of conjugated molecules*
— *Interaction of magnetic metal phthalocyanines with metal surfaces*

BIN, Xu [C class; 3400 (B), 400 (C)] (108)
— *Machine learning based optimized polymer for thermal function materials*

BUERKLE, Marius [B,C class; 5600 (B), 550 (C)] ()
— *Combining first-principles quantum transport and deep learning to create a virtual experimental environment*
— *First-principles computational study of nanocrystals for photovoltaic applications*

BUI, VANPHO [C class; 1400 (B), 0 (C)] (130)
— *Study on the catalytic mechanism of RuTi alloy in catalyst referred etching method*

DEKURA, Shun [C,D class; 5200 (B), 640 (C)] (79, 80, 81)
— *Elucidation of the mechanism of fast proton conduction based on proton tautomerism in molecular crystals by using first-principles calculations*
— *First-principles calculations of electron correlation parameters to elucidate pi-electron-proton coupled physical properties of the unconventional molecular conductors Cat-TTF analogues*
— *Systematic elucidation of structure and electronic state of pi-electron-proton coupled molecular conductors under pressure*

1. Conjugation Length Effect on the Conducting Behavior of Single-crystalline Oligo(3,4-ethylenedioxythiophene) (nEDOT) Radical Cation Salts
   R. Kameyama, T. Fujino, S. Dekura, H. Mori, Phys. Chem. Chem. Phys. **24**, 9130 (2022).
   DOI:10.1039/D2CP00250G

2. Band-filling effects in single-crystalline oligomer models for doped PEDOT: 3,4-ethylenedioxythiophene (EDOT) dimer salt with hydrogen-bonded infinite sulfate anion chains
   R. Kameyama, T. Fujino, S. Dekura, S. Imajo, T. Miyamoto, H. Okamoto, H. Mori, J. Mater. Chem. C **10**, 7543 (2022).
   DOI:10.1039/D2TC01216B

3. Molecular Arrangement Control of [1]Benzothieno[3,2-b][1]benzothiophene (BTBT) via Charge-Assisted Hydrogen Bond
   R. Akai, K. Oka, S. Dekura, H. Mori, N. Tohnai, Bull. Chem. Soc. Jpn. **95**, 1178 (2022).
   DOI:10.1246/bcsj.20220134

4. Neutral Radical Molecular Conductors Based on a Gold Dimethoxybenzenedithiolene Complex with and without Crystal Solvent
   S. Yokomori, S. Dekura, A. Ueda, T. Higashino, H. Mori, Chem. Lett. **52**, 25 (2023).
   DOI:10.1246/cl.220446

EGAMI, Yoshiyuki [C class; 11400 (B), 950 (C)] (55)
— *First-principles electron-transport study on 2D layered material-based heterostructures*
— *First-principles study on electron-transport properties of large scale atomic layered materials*

1. Unique Electrical Signature of Phosphate for Specific Single-Molecule Detection of Peptide Phosphorylation
   T. Harashima, Y. Egami, K. Homma, Y. Jono, S. Kaneko, S. Fujii, T. Ono, and T. Nishino, J. Am. Chem. Soc. **144**, 17449 (2022).
   DOI:10.1021/jacs.2c05787

FUCHIZAKI, Kazuhiro [C class; 2600 (B), 0 (C)] (269)
— *Kinetics of phase transition and polyamorphism*

1. Can weight hysteresis in a neural network judge the continuity/discontinuity of a phase transition?
   K. Nakamura and K. Fuchizaki, submitted to J. Phys. A.

FUJI, Yohei [B class; 700 (B), 180 (C)] (303)
— *Numerical investigation of universality classes in measurement-induced phase transitions*

1. Charge fluctuation and charge-resolved entanglement in a monitored quantum circuit with $U(1)$ symmetry
   H. Oshima and Y. Fuji, Phys. Rev. B **107**, 014308 (2023).
   DOI:10.1103/PhysRevB.107.014308

FUJII, Susumu [C class; 2800 (B), 0 (C)] (267)
— *Systematic searches for grain boundary structures and structure-based prediction of multiple properties*

FUJIMOTO, Yoshitaka [C class; 600 (B), 0 (C)] (164)
— *Atomic structures and electronic properties of nanocarbon-based materials*

1. Theoretical study on quantum transport of carbon nanotubes for detecting toxic molecules: The role of dopants
   Y. Fujimoto, Journal of Electrochemical Science and Engineering **12**, 431 (2022).

2. First-Principles Theoretical Design of Graphene-Based Field Effect Transistors
   Y. Fujimoto, Advanced Nanoscale MOSFET architectures: Current Trends and Future Perspectives, Accepted.

FUJINO, Tomoko [C class; 1200 (B), 0 (C)] (204)
— *Electronic structures of EDXT oligomers in charge transfer salts: estimation of intramolecular and intermolecular Coulomb repulsion energy*

1. Ambipolar Nickel Dithiolene Complex Semiconductors: from One- to Two-dimensional Electronic Structures based upon Alkoxy Chain Lengths
   M. Ito, T. Fujino*, L. Zhang, S. Yokomori, T. Higashino, R. Makiura, K. J. Takeno, T. Ozaki, H. Mori*, J. Am. Chem. Soc. 145, 2127 (2023).
   DOI:10.1021/jacs.2c08015

2. Band-filling Effects in Single-crystalline Oligomer Models for Doped PEDOT: 3,4-Ethylenedioxythiophene (EDOT) Dimer Salt with Hydrogen-bonded Infinite Sulfate Anion Chains
   R. Kameyama, T. Fujino*, S. Dekura, S. Imajo, T. Miyamoto, H. Okamoto, H. Mori*, J. Mater. Chem. C 10, 7543 (2022).
   DOI:10.1039/D2TC01216B

FUJISHIRO, Hiroki [C class; 2800 (B), 0 (C)] ()
— *Strained Band-Structure Engineering for Antimonide-Based Terahertz Transistors*

FUKUDA, Jun-ichi [B class; 800 (B), 80 (C)] (302)
— *Calculation of ordered structures dynamics and optical properties of soft materials*

1. Simulation of a cholesteric blue phase cell with large but finite thickness
   J. Fukuda, Front. Soft Matter **2**, 1011618 (2022).
   DOI:10.3389/frsfm.2022.1011618

FUKUDA, Masahiro [B class; 400 (B), 80 (C)] (176)
— *AB type 2D materials database construction by DFT*

1. Prediction of quaternary hydrides based on densest ternary sphere packings
   Ryotaro Koshoji, Masahiro Fukuda, Mitsuaki Kawamura, and Taisuke Ozaki, Phys. Rev. Materials **6**, 114802 (2022).
   DOI:10.1103/PhysRevMaterials.6.114802

2. Atomic arrangement of Si adatom on the Silicene/Ag(111) surface
   Yuuki Adachi, Zhang Runnan, Wang Xinbo, Masahiro Fukuda, Taisuke Ozaki, Yoshiaki Sugimoto, Applied Surface Science, 157336 (2023).
   DOI:10.1016/j.apsusc.2023.157336

Data Repository
OpenMX database of Atoms using standard basis sets
https://isspns-gitlab.issp.u-tokyo.ac.jp/masahiro.fukuda/openmx-database-of-atoms-using-standard-basis-sets

OpenMX database of bulks using standard basis set
https://isspns-gitlab.issp.u-tokyo.ac.jp/masahiro.fukuda/openmx-database-of-bulks-using-standard-basis-set

Structure map of AB2 type 2D materials by high-throughput DFT calculations
https://isspns-gitlab.issp.u-tokyo.ac.jp/masahiro.fukuda/structure-map-of-ab2-type-2d-materials-by-high-throughput-dft-calculations
DOI:10.1039/D0MA00999G

FUKUDA, Tuneo [C class; 400 (B), 0 (C)] (184)
— *First-principles study of stability of Cu-Ni two-dimensional alloy*

FUKUMOTO, Yoshiyuki [B class; 800 (B), 0 (C)] (306, 308)
— *Numerical studies on thermodynamics and excitation spectra in Heisenberg antiferromagnets on the triangular and kagome lattices*
— *Numerical study of the effect of large bond randomness on the magnetization process and magnetic susceptibility in the spherical Kagome system {W72V30}*

1. Effects of bond-randomness and Dzyaloshinskii-Moriya interactions on the specific heat at low temperatures of a spherical kagome cluster in $\{W_{72}V_{30}\}$
   M. Motohashi, K. Inoue, K. Morita, Y. Fukumoto, and H. Nakano, Prog. Theor. Exp. Phys. 2022, 113I01, (2022).

GOHDA, Yoshihiro [C class; 6000 (B), 450 (C)] (74)
— *Control of magnetic anisotropy by strain and electric polarization at interfaces*

1. Giant converse magnetoelectric effect in a multiferroic heterostructure with polycrystalline Co_2FeSi
   S. Fujii, T. Usami, Y. Shiratsuchi, A.M. Kerrigan, A.M. Yatmeidhy, S. Yamada, T. Kanashima,

R. Nakatani, V.K. Lazarov, T. Oguchi, Y. Gohda, and K. Hamaya, NPG Asia Mater. **14**, 43 (2022).
DOI:10.1038/s41427-022-00389-1

2. Superconductivity in a two monolayer thick indium film on Si(111)$\sqrt{3} \times \sqrt{3}$-B
T. Ogino, I. Seo, H. Tajiri, M. Nakatake, S. Takakura, Y. Sato, Y. Hasegawa, Y. Gohda, K. Nakatsuji, and H. Hirayama, Phys. Rev. B **106**, 045423 (2022).
DOI:10.1103/PhysRevB.106.045423

3. Origin of anisotropic magnetoresistance tunable with electric field in $Co_2FeSi/BaTiO_3$ multiferroic inetrfaces
S. Tsuna, R. Costa-Amaral, and Y. Gohda, J. Appl. Phys. **132**, 234101 (2022).
DOI:10.1063/5.0128149

4. First-principles phonon calculations of neodymium-magnet compounds
S. Tsuna and Y. Gohda, J. Appl. Phys. **133**, 115103 (2023).
DOI:10.1063/5.0142945

5. Structures of Sm-Cu intermetallics with Fe as subphase candidates in $SmFe_{12}$-based permanent magnets studied by first-principles thermodynamics
S. Nishino and Y. Gohda, Jpn. J. Appl. Phys. **62**, 030902 (2023).
DOI:10.35848/1347-4065/acc0b8

GOHLKE, Matthias [C class; 3000 (B), 150 (C)] (263)
— *Ground state and dynamical properties of the J_1J_2K-Heisenberg model on the square lattice*

GONOME, Hiroki [C class; 3800 (B), 550 (C)] (104)
— *Study of the principle of photothermal conversion by ab initio calculations*

HAGITA, Katsumi [C class; 1000 (B), 150 (C)] (286)
— *Effect of chain crossing prohibition on phase-separated structure of block copolymers*

1. Ring-Filling Effect on StressStrain Curves of Randomly End-Linked Tetra-Arm Prepolymers
K. Hagita, T. Murashima, T. Ohkuma, H. Jinnai, Macromolecules **55**, 6547 (2022).
DOI:10.1021/acs.macromol.2c00451

2. Topological transition in multicyclic chains with structural symmetry inducing stress-overshoot phenomena in multicyclic/linear blends under biaxial elongational flow
T. Murashima, K. Hagita, T. Kawakatsu, Macromolecules **55**, 9358 (2022).
DOI:10.1021/acs.macromol.2c01579

3. Practical compatibility between self-consistent field theory and dissipative particle dynamics
K. Hagita, T. Murashima, Polymer **269**, 125733 (2023).
DOI:10.1016/j.polymer.2023.125733

4. Lamellar Domain Spacing of Symmetric Linear, Ring, and Four-Arm-Star Block Copolymer Blends
K. Hagita, T. Murashima, and T. Kawakatsu Macromolecules **55**, 8021 (2022).
DOI:10.1021/acs.macromol.2c00500

5. 分子シミュレーションを用いたフェノール樹脂の構造-物性相関解析
首藤靖幸, 和泉篤士, 萩田克美, 柴山充弘ネットワークポリマー **43**, 246 (2022).
DOI:10.11364/networkedpolymer.43.6_246

6. Molecular Dynamics of Topological Barriers on the Crystallization Behavior of Ring Polyethylene

Melts with Trefoil Knots
K. Hagita, T. Murashima, N. Sakata, K. Shimokawa, T. Deguchi, E. Uehara, and S. Fujiwara Macromolecules **56**, 15 (2023).
DOI:10.1021/acs.macromol.2c01843

HAMADA, Ikutaro [C class; 8200 (B), 0 (C)] (67)
— *Density functional theory study of adsorption and reaction of molecules on metal surfaces*
— *Density functional theory study of molecule/metal interfaces*

1. Interaction of water with nitrogen-doped graphene
   A. F. Z. Abidin and I. Hamada, Phys. Rev. B **105**, 075416 (2022).
   DOI:10.1103/PhysRevB.105.075416

2. Comparative density functional theory study for predicting oxygen reduction activity of single-atom catalyst
   A. F. Z. Abidin and I. Hamada, Surf. Sci. **724**, 122144 (2022).
   DOI:10.1016/j.susc.2022.122144

3. Phonon dispersion of the organic semiconductor rubrene
   K. Takada, K. Yoshimi, S. Tsutsui, K. Kimura, K. Hayashi, I. Hamada, S. Yanagisawa, N. Kasuya, S. Watanabe, J. Takeya, and Y. Wakabayashi, Phys. Rev. B **105**, 205205 (2022).
   DOI:10.1103/PhysRevB.105.205205

Data Repository
Interaction of water with nitrogen-doped graphene
DOI:10.24435/materialscloud:6b-bc

Comparative density functional theory study for predicting oxygen reduction activity of single-atom catalyst
DOI:10.24435/materialscloud:hv-yd

HAMAGUCHI, Satoshi [C class; 8600 (B), 800 (C)] ()
— *Study on plasma resistance of metal oxides*

HAMAMOTO, Yuji [C,D class; 4400 (B), 0 (C)] (99, 100)
— *First principles study of the adsorption structure of helicene on the Ag(111) surface*
— *Global search for metastable structures of silicene on the Ag(111) surface by Gaussian process regression*

1. Hybridization-Induced Image Potential States with Large Effective Mass in Lead Phthalocyanine Overlayers on Graphene
   Y. Hamamoto, H. Sawada, S. A. Wella, K. Inagaki, I. Hamada, and Y. Morikawa, J. Phys. Chem. C **126**, 10855 (2022).
   DOI:10.1021/acs.jpcc.2c01652

HARADA, KENJI [C class; 1200 (B), 600 (C)] (275)
— *Tensor data analysis by tensor network*

HARASHIMA, Yosuke [C class; 1000 (B), 0 (C)] (150)
— *Exponent puzzle for metal-insulator transition in doped semiconductors*

1. Systematic search for stabilizing dopants in ZrO_2 and HfO_2 using first-principles calculations
   Y. Harashima, H. Koga, Z. Ni, T. Yonehara, M. Katouda, A. Notake, H. Matsui, T. Moriya, M. K. Si, R. Hasunuma, A. Uedono, and Y. Shigeta, IEEE Trans. Semicon. Man., accepted.
   DOI:10.1109/TSM.2023.3265658

HARUYAMA, Jun [C class; 3200 (B), 400 (C)] (110)

— *Electrochemical reaction analysis using density functional calculation + implicit solvation model 4*

1. First-Principles Study for Water Adsorption Layers on Platinum Surface
   J. Haruyama, T. Sugimoto, and O. Sugino Vacuum and Surface Science **65**, 355 (2022).
   DOI:10.1380/vss.65.1

2. Effect of Nitrogen Doping and Oxygen Vacancy on the Oxygen Reduction Reaction on the Tetragonal Zirconia(101) Surface
   S. Muhammady, J. Haruyama, S. Kasamatsu, and O. Sugino, Vacuum and Surface Science **126**, 15662 (2022).
   DOI:10.1021/acs.jpcc.2c04132

3. First-principles study of water adsorption monolayer on Pt(111): adsorption energy and second-order nonlinear susceptibility
   J. Haruyama, T. Sugimoto, and O. Sugino, submitted to Phys. Rev. Mater.

Data Repository
QE input for H20 adsorption monolayer system on Pt(111)
https://isspns-gitlab.issp.u-tokyo.ac.jp/j-haruyama/Pt111_H2O-monolayer

HASHIMOTO, Tamotsu [C class; 1200 (B), 200 (C)] (276)

— *Molecular dynamics simulation of $BaTiO_3$ nano structure II*

1. Domain structures in dielectric polarization vortex of $BaTiO_3$ nanoclusters: A shell model molecular dynamics study
   T. Hashimoto and H. Moriwake, Physica B, **656**, 414768 (2023).
   DOI:10.1016/j.physb.2023.414768

2. Domain structures of rhombohedral $BaTiO_3$ by a shell model
   T. Hashimoto and H. Moriwake, submitted

HATSUGAI, Yasuhiro [C class; 4400 (B), 350 (C)] (249)

— *Numerical studies for science of bulk-edge correspondence and topological phases*

1. Machine Learning Study on the Flat-Band States Constructed by Molecular-Orbital Representation with Randomness
   T. Kuroda, T. Mizoguchi, H. Araki, and Y. Hatsugai J. Phys. Soc. Jpn. 91, 044703 (2022).
   DOI:10.7566/JPSJ.91.044703

2. Adiabatic continuity of the spinful quantum Hall states
   K. Kudo and Y. Hatsugai Phys. Rev. B 106, 075120 (2022).
   DOI:10.1103/PhysRevB.106.075120

3. Observation of bulk-edge correspondence in topological pumping based on a tunable electric circuit
   K. Yatsugi, T. Yoshida, T. Mizoguchi, Y. Kuno, H. Iizuka, Y. Tadokoro, and Y. Hatsugai Commun. Phys. 5, 180 (2022).
   DOI:10.1038/s42005-022-00957-5

4. Higher-Order Topological Insulator on a Martini Lattice and Its Square Root Descendant
   D. Matsumoto, T. Mizoguchi, and Y. Hatsugai J. Phys. Soc. Jpn. 92, 034705 (2023).
   DOI:10.7566/JPSJ.92.034705

5. Molecular-orbital representation with random U(1) variables

T. Mizoguchi and Y. Hatsugai Phys. Rev. B 107, 094201 (2023).
DOI:10.1103/PhysRevB.107.094201

6. Reduction of one-dimensional non-Hermitian point-gap topology by interactions
T. Yoshida and Y. Hatsugai Phys. Rev. B 106, 205147 (2022).
DOI:10.1103/PhysRevB.106.205147

7. Discriminant indicator with generalized rotational symmetry
H. Wakao, T. Yoshida, and Y. Hatsugai Phys. Rev. B 105, 214103 (2022).
DOI:10.1103/PhysRevB.105.214103

8. Unconventional gapless semiconductor in an extended martini lattice in covalent honeycomb materials
T. Mizoguchi, Y. Gao, M. Maruyama, Y. Hatsugai, and S. Okada Phys. Rev. B 107, L121301 (2023).
DOI:10.1103/PhysRevB.107.L121301

9. Fate of exceptional points under interactions: Reduction of topological classifications
T. Yoshida and Y. Hatsugai Phys. Rev. B 107, 075118 (2023).
DOI:10.1103/PhysRevB.107.075118

10. A symmetry-protected exceptional ring in a photonic crystal with negative index media
T. Isobe, T. Yoshida, and Y. Hatsugai arXiv:2212.11090

11. Topological pump of SU(Q) quantum chain and Diophantine equation
Y. Hatsugai and Y. Kuno, arXiv:2210.11646

HAYAMI, Satoru [C class; 5600 (B), 450 (C)] (236)
— Numerical simulations combined with machine learning to search for magnetic skyrmion in frustrated magnets

1. Spin Conductivity Based on Magnetic Toroidal Quadrupole Hidden in Antiferromagnets
S. Hayamia and M. Yatsushiro, J. Phys. Soc. Jpn. **91**, 063702 (2022).
DOI:10.1103/PhysRevB.105.155157

2. Multifarious skyrmion phases in centrosymmetric trilayer magnets
S. Hayami, Phys. Rev. B **105**, 184426 (2022).
DOI:10.1103/PhysRevB.105.184426

3. Rectangular and square skyrmion crystals on a centrosymmetric square lattice with easy-axis anisotropy
S. Hayami, Phys. Rev. B **105**, 174437 (2022).
DOI:10.1103/PhysRevB.105.174437

4. Antisymmetric thermopolarization by electric toroidicity
J. Nasu and S. Hayami, Phys. Rev. B **105**, 245125 (2022).
DOI:10.1103/PhysRevB.105.245125

5. Skyrmion crystal with integer and fractional skyrmion numbers in a nonsymmorphic lattice structure with the screw axis
S. Hayami, Phys. Rev. B **105**, 224411 (2022).
DOI:10.1103/PhysRevB.105.224411

6. Skyrmion crystal under D3h point group: Role of out-of-plane Dzyaloshinskii-Moriya interaction
S. Hayami and R. Yambe, Phys. Rev. B **105**, 224423 (2022).

DOI:10.1103/PhysRevB.105.224423

7. Square skyrmion crystal in centrosymmetric systems with locally inversion-asymmetric layers
S. Hayami, J. Phys.: Condens. Matter **34**, 365802 (2022).
DOI:10.1088/1361-648X/ac7bcb

8. Nonlinear spin Hall effect in PT-symmetric collinear mag- nets
S. Hayami, M. Yatsushiro, and H. Kusunose, Phys. Rev. B **106**, 024405 (2022).
DOI:10.1103/PhysRevB.106.024405

9. Nonlinear nonreciprocal transport in antiferromagnets free from spin-orbit coupling
S. Hayami and M. Yatsushiro, Phys. Rev. B **106**, 014420 (2022).
DOI:10.1103/PhysRevB.106.014420

10. Stability of Skyrmion Crystal Phase in Centrosymmetric Distorted Triangular-Lattice Antiferromagnets
S. Hayami, J. Phys. Soc. Jpn. **91**, 093701 (2022).
DOI:10.7566/JPSJ.91.093701

11. Magnetic Hedgehog Lattice in a Centrosymmetric Cubic Metal
S. Okumura, S. Hayami, Y. Kato, and Y. Motome, J. Phys. Soc. Jpn. **91**, 093702 (2022).
DOI:10.7566/JPSJ.91.093702

12. Nonreciprocal Transport in Noncoplanar Magnetic Systems without Spin-Orbit Coupling, Net Scalar Chirality, or Magnetization
S. Hayami and M. Yatsushiro, J. Phys. Soc. Jpn. **91**, 094704 (2022).
DOI:10.7566/JPSJ.91.094704

13. Engineering a skyrmion crystal in ferromagnetic/antiferromagnetic bilayers based on magnetic frustration mechanism
K. Okigami, R. Yambe, and, S. Hayami, J. Phys. Soc. Jpn. **91**, 103701 (2022).
DOI:10.7566/JPSJ.91.103701

14. Ferroaxial moment induced by vortex spin texture
S. Hayami, Phys. Rev. B **106**, 144402 (2022).
DOI:10.1103/PhysRevB.106.144402

15. Electric Ferro-Axial Moment as Nanometric Rotator and Source of Longitudinal Spin Current
S. Hayami, R. Oiwa, and H. Kusunose, J. Phys. Soc. Jpn. **91**, 113702 (2022).
DOI:10.7566/JPSJ.91.113702

16. Skyrmion and vortex crystals in the Hubbard model
K. Kobayashi and S. Hayami, Phys. Rev. B **106**, L140406 (2022).
DOI:10.1103/PhysRevB.106.L140406

17. Zero-field skyrmion, meron, and vortex crystals in centrosymmetric hexagonal magnets
S. Hayami, J. Magn. Magn. Mater. **564**, 170036 (2022).
DOI:10.1016/j.jmmm.2022.170036

18. Magnetic Toroidal Moment under Partial Magnetic Order in Hexagonal Zigzag-Chain Compound Ce_3TiBi_5
S. Hayami and H. Kusunose, J. Phys. Soc. Jpn. **91**, 123701 (2022).
DOI:10.7566/JPSJ.91.123701

19. Effective spin model in momentum space: Toward a systematic understanding of multiple-Q

instability by momentum-resolved anisotropic exchange interactions
R. Yambe and S. Hayami, Phys. Rev. B **106**, 174437 (2022).
DOI:10.1103/PhysRevB.106.174437

20. Orthorhombic distortion and rectangular skyrmion crystal in a centrosymmetric tetragonal host
S. Hayami, J. Phys.: Mater. **6**, 014006 (2023).
DOI:10.1088/2515-7639/acab89

21. Stacking-dependent nonreciprocal transport in magnetic skyrmions
S. Hayami, J. Magn. Magn. Mater. **568**, 170420 (2023).
DOI:10.1016/j.jmmm.2023.170420

22. Ferrochiral, antiferrochiral, and ferrichiral skyrmion crystals in an itinerant honeycomb magnet
R. Yambe and S. Hayami, Phys. Rev. B **107**, 014417 (2023).
DOI:PhysRevB.107.014417

23. Multiple-Q instability under fourth-order inplane single-ion anisotropy
S. Hayami, J. Magn. Magn. Mater. **570**, 170507 (2023).
DOI:10.1016/j.jmmm.2023.170507

24. Widely-sweeping magnetic fieldtemperature phase diagrams for skyrmion-hosting centrosymmetric tetragonal magnets
S. Hayami and Y. Kato, J. Magn. Magn. Mater. **571**, 170547 (2023).
DOI:10.1016/j.jmmm.2023.170547

25. Cluster Toroidal Multipoles formed by Electric-Quadrupole and Magnetic-Octupole Trimers: A Possible Scenario for Hidden Orders in $Ca_5Ir_3O_{12}$
S. Hayami and H. Kusunose, J. Phys. Soc. Jpn. **92**, 033702 (2023).
DOI:10.7566/JPSJ.92.033702

HAYASAKA, Hiroshi [B class; 400 (B), 70 (C)] (330)
— *Atomistic model study on the coercivity mechanism of permanent magnets*

1. Microscopic study on the angular dependence of coercivity at zero and finite temperatures
H. Hayasaka, M. Nishino, and S. Miyashita Phys. Rev. B 105, 224414 (2022).
DOI:10.1103/PhysRevB.105.224414

2. Microscopic origin of coercivity enhancement by dysprosium substitution into neodymium permanent magnets
M. Nishino, H. Hayasaka, and S. Miyashita Phys. Rev. B 106, 054422 (2022).
DOI:10.1103/PhysRevB.106.054422

HIDA, Kazuo [B class; 300 (B), 60 (C)] (341)
— *Numerical Study of One Dimensional Frustrated Quantum Spin Systems*

HIGUCHI, Yuji [C class; 10200 (B), 900 (C)] (219)
— *Correlation between the structure of charged phospholipid bilayer membrane and ion distribution by multi-scale simulation*
— *Structure and dynamics of charged phospholipid bilayer membrane and water molecules*

HINUMA, Yoyo [B class; 400 (B), 0 (C)] (183)
— *Evaluating surface oxygen vacancy stability in complicated oxides for catalyst informatics*

1. Trends in Surface Oxygen Formation Energy in Perovskite Oxides
Y. Hinuma, S. Mine, T. Toyao and K. Shimizu, ACS Omega 2022, 7, 18427

DOI:10.1021/acsomega.2c00702

HIRATSUKA, Masaki [B class; 500 (B), 80 (C)] ()
— *Validation of a Machine Learning Method for Predicting Vibration Spectra*

HIYAMA, Miyabi [B class; 400 (B), 80 (C)] (327)
— *Theoretical study for firefly bioluminescence substrate analogs and related molecules*

HOSHI, Takeo [C class; 3600 (B), 350 (C)] (255)
— *HPC-based fusion of experiment analysis simulation and data-driven science*

1. Two-stage data-analysis method for total-reflection high-energy positron diffraction (TRHEPD)
   K. Tanaka, I. Mochizuki, T. Hanada, A. Ichimiya, T. Hyodo, and T. Hoshi, JJAP Conf. Series **9**, 011301 (2023).
   DOI:10.56646/jjapcp.9.0_011301

2. Data-analysis software framework 2DMAT and its application to experimental measurements for two-dimensional material structures
   Y. Motoyama, K. Yoshimi, I. Mochizuki, H. Iwamoto, H. Ichinose, and T. Hoshi, Comp. Phys. Commun. **280**, 108465 (2022).
   DOI:10.1016/j.cpc.2022.108465

3. sim-trhepd-rheed Open-source simulator of total-reflection high-energy positron diffraction (TRHEPD) and reflection high-energy electron diffraction (RHEED)
   T. Hanada, Y. Motoyama, K. Yoshimi, and T. Hoshi, Comp. Phys. Commun. **277**, 108371 (2022).
   DOI:10.1016/j.cpc.2022.108465

4. Data-driven Sensitivity Analysis in Surface Structure Determination by Total-Reflection High-Energy Positron Diffraction (TRHEPD)
   T. Hoshi, I. Mochizuki, S. Tanaka, T. Hyodo, and K. Hukushima Photon Factory Highlights 2021, 46 (2022).

Data Repository
2DMAT Gallery
https://isspns-gitlab.issp.u-tokyo.ac.jp/2dmat-dev/2dmat-gallery

HOTTA, Takashi [C class; 4200 (B), 0 (C)] (199)
— *Research of Three-Channel Kondo Effect Emerging from Holmium Ions*

1. Effect of Local Jahn-Teller Phonons on Quantum Critical Point in a Two-Orbital Anderson Model
   Y. Matsumoto and T. Hotta, J. Phys. Soc. Jpn. **91**, 124712 (2022).
   DOI:10.7566/JPSJ.91.124712

HUKUSHIMA, Koji [C class; 5800 (B), 300 (C)] (234, 235)
— *Molecular dynamics study of phase separation induced by binding molecules*
— *Tensor renormalization-group study of random spin systems*

1. Estimating Distributions of Parameters in Nonlinear State Space Models with Replica Exchange Particle Marginal MetropolisHastings Method
   H. Inoue, K. Hukushima, and T. Omori Entropy **24**, 115 (2022).

2. Phase transition in compressed sensing with horseshoe prior
   Y. Nagano and K. Hukushima Phys. Rev. E **107**, 034126 (2023).

3. Statistical-mechanical Study of Deep Boltzmann Machine Given Weight Parameters after Training by Singular Value Decomposition
Y. Ichikawa and K. Hukushima J. Phys. Soc. Jpn. **91**, 114001 (2022).

4. Absence of Phase Transition in Random Language Model
K. Nakaishi and K. Hukushima Phys. Rev. Res. **4**, 023156 (2022).

IDO, Kota [C class; 4600 (B), 450 (C)] (242)
— *Stability of quantum spin liquids in frustrated quantum spin systems*

IITAKA, Toshiaki [C class; 1600 (B), 250 (C)] (273)
— *Finite temperature calculation of quantum manybody system using random phase product state and neural network wavefunction*

IKEDA, Hiroaki [B class; 400 (B), 80 (C)] ()
— *first principles calculations in quantum liquid crystals*

IKUHARA, Yuichi [C class; 5800 (B), 0 (C)] (82)
— *Exploring singular atomic arrangements via first-principles calculations*
— *Molecular dynamics simulation of grain boundaries in perovskite oxide*

IMADA, Masatoshi [E class; 32000 (B), 2550 (C)] (23)
— *Integrated spectroscopic studies by combining experimental data and high precision large-scale computation for strongly correlated electrons*
— *Systematic ab initio studies on high temperature superconductivity of transition metal oxides*

1. Unconventional exciton evolution from the pseudogap to superconducting phases in cuprates
A. Singh, H. Y. Huang, J. D. Xie, J. Okamoto, C. T. Chen, T. Watanabe, A. Fujimori, M. Imada, and D. J. Huang, Nat. Commun. **13**, 7906 (2022).
DOI:10.1038/s41467-022-35210-8

2. *Ab initio*low-energy effective Hamiltonians for the high-temperature superconducting cuprates $Bi_2Sr_2CuO_6$, $Bi_2Sr_2CaCu_2O_8$, $HgBa_2CuO_4$, and $CaCuO_2$
Jean-Baptiste Morée, M. Hirayama, M. T. Schmid, Y. Yamaji, and M. Imada, Phys. Rev. B **106**, 235150 (2022).
DOI:10.1103/PhysRevB.106.235150

3. Unconventional dual 1D-2D quantum spin liquid revealed by *ab initio* studies on organic solids family
K. Ido, K. Yoshimi, T. Misawa, and M. Imada, npj Quantum Mater. **7**, 48 (2022).
DOI:0.1038/s41535-022-00452-8

4. Optimized implementation for calculation and fast-update of Pfaffians installed to the open-source fermionic variational solver mVMC
R.-Q. G. Xu, T. Okubo, S. Todo, and M. Imada, Compt. Phys. Commun., **277**, 108375 (2022).
DOI:10.1016/j.cpc.2022.108375

INAGAKI, Kouji [B class; 400 (B), 80 (C)] (175)
— *First-principles calculation of graphitization of diamond surface and its exfoliation process*

INAOKA, Takeshi [B class; 300 (B), 60 (C)] (185)
— *Search and realization of novel electronic properties of surfaces and interfaces and of nanostructures*

1. Formation of an iodine metallic band in the x-form phthalocyanine crystal
T. Inaoka, to be submitted.

ISHIBASHI, Shoji [C class; 2400 (B), 0 (C)] (121)
— *Prediction of properties of organic ferroelectrics and piezoelectrics by first-principles calculation*

1. Competition of Polar and Antipolar States Hidden Behind a Variety of Polarization Switching Modes in Hydrogen-Bonded Molecular Chains
   S. Horiuchi, H. Minemawari, and S. Ishibashi, Mater. Horizons, Advance Article (2023).
   DOI:10.1039/d2mh01530g

ISHIDA, Kunio [C class; 2400 (B), 400 (C)] ()
— *Initial dynamics of photoinduced cooperativity by quantized light*

ISHII, Fumiyuki [C class; 9800 (B), 450 (C)] (60)
— *Development of an accurate and efficient method for calculating the anomalous Hall effect*
— *First-principles calculation of thermoelectric properties in atomic-layer and topological materials*

1. First-principles LCPAO Approach to Insulators Under Finite Electric Fields with Forces
   N. Yamaguchi and F. Ishii, Comput. Phys. Commun. **280** (2022) 108487.

2. First-principles calculation of anomalous Hall and Nernst conductivity by local Berry phase
   H. Sawahata, N. Yamaguchi, S. Minami, and F. Ishii, Phys. Rev. B, **107**, (2023) 024404.

3. First-principles study of anomalous Hall effect and anomalous Nernst effect in Fe_2Si
   T. Tominaga N. Yamaguchi, H. Sawahata, and F. Ishii, Jpn. J. Appl. Phys. **62**, (2023) SD1019.

4. Persistent spin helix on a diamond surface
   H. P. Kadarisman, N. Yamaguchi, and F. Ishii, Appl. Phys. Express, **16** (2023) 023001.

ISOBE, Masaharu [B class; 500 (B), 0 (C)] (324)
— *Equilibration and glass transition in the dense hard sphere systems*

1. Anomalous phase transition in self-propelled hard disk systems
   N. Murase and M. Isobe, Proceedings of the 28th Symposium on Traffic Flow and Self-driven Particles, **28**, 9 (2021).

JESCHKE, Harald [C class; 4800 (B), 0 (C)] (247, 248)
— *Fluctuation exchange approximation calculations for the superconducting transition temperatures and pairing symmetries of organic charge transfer salts*

JOUTSUKA, Tatsuya [C class; 1200 (B), 0 (C)] (134)
— *Analyzing Reaction Mechanism of Charge Transfer in Catalysis by Electronic Structure Calcutions*

1. Understanding the structure of Cu-doped $MgAl_2O_4$ for CO_2 hydrogenation catalyst precursor using experimental and computational approaches
   T. Joutsuka,* R. Hamamura, K. Fujiwara, T. Honma, M. Nishijima, and S. Tada, Int. J. Hydrog. Energy 47, 21369 (2022).
   DOI:10.1016/j.ijhydene.2022.04.295

2. Active sites on $Zn_xZr_{1-x}O_{2-x}$ solid solution catalysts for CO_2-to-methanol hydrogenation
   S. Tada, N. Ochiai, H. Kinoshita, M. Yoshida, N. Shimada, T. Joutsuka, M. Nishijima, T. Honma, N. Yamauchi, Y. Kobayashi, and K. Iyoki, ACS Catal. 12, 7748 (2022).
   DOI:10.1021/acscatal.2c01996

3. Molecular Mechanism of Autodissociation in Liquid Water: Ab Initio Molecular Dynamics Simulations

T. Joutsuka, J. Phys. Chem. B 126, 24, 4565 (2022).
DOI:10.1021/acscatal.2c01996

4. Catalysis of Surface Dispersed Cu^{2+} Species on t-ZrO_2: Square-Planar Cu Catalyzed Cross-Coupling of Arylboronic Acid and Imidazole
M. Kondo, T. Joutsuka, K. Fujiwara, T. Honma, and S. Tada, Catal. Sci. Technol. 13, 2247 (2023).
DOI:10.1039/D3CY00024A

5. Study of Cu-growth feature by selective low-pressure chemical vapor deposition using a CuI precursor
G. Toyoda, H. Kikuchi, S. Yamauchi, T. Joutsuka, T. Fuse, and Y. Kubota, Jpn. J. Appl. Phys. 62, SH1002 (2023).
DOI:10.35848/1347-4065/acc257

6. Adsorption of CO_2 on Amorphous and Crystalline Zirconia: A DFT and Experimental Study
T. Joutsuka and S. Tada, J. Phys. Chem. C 127, 6998 (2023).
DOI:10.1021/acs.jpcc.3c01185

KADOWAKI, Hiroaki [B class; 400 (B), 70 (C)] (329)
— *quantum pyrochrole magnet*

KAGESHIMA, Hiroyuki [C class; 1000 (B), 0 (C)] (148)
— *Study on structural elementary excitations at solid surfaces and interfaces*

1. First-principles study on silicon emission from interface into oxide during silicon thermal oxidation
H. Kageshima, T. Akiyama, and K. Shiraishi, Materials Science in Semiconductor Processing 162, 107527 (2023).
DOI:10.1016/j.mssp.2023.107527

KANEKO, Ryui [B class; 1200 (B), 180 (C)] (277, 279)
— *Numerical study of quantum many-body scars in bosonic systems*
— *Tensor-network study of the quench dynamics of the Kitaev model*

1. Ground-state phase diagram of a spin-1/2 frustrated XXZ ladder
T. Ogino, R. Kaneko, S. Morita, and S. Furukawa, Phys. Rev. B **106**, 155106 (2022).
DOI:10.1103/PhysRevB.106.155106

2. Rényi entanglement entropy after a quantum quench starting from insulating states in a free boson system
D. Kagamihara, R. Kaneko, S. Yamashika, K. Sugiyama, R. Yoshii, S. Tsuchiya, and I. Danshita, Phys. Rev. A **107**, 033305 (2023).
DOI:10.1103/PhysRevA.107.033305

3. Dynamics of correlation spreading in low-dimensional transverse-field Ising models
R. Kaneko, I. Danshita, arXiv:2301.01407.
DOI:10.48550/arXiv.2301.01407

KARIYADO, Toshikaze [B class; 300 (B), 50 (C)] (343)
— *Novel phenomena in mismatched multilayer systems: Search for new candidate materials and analysis of electronic structures*

1. Twisted bilayer BC_3: Valley interlocked anisotropic flat bands
T. Kariyado, Phys. Rev. B **107**, 085127 (2023).
DOI:10.1103/PhysRevB.107.085127

KASAMATSU, Shusuke [E class; 14000 (B), 1100 (C)] (51, 374)
— *Understanding structure-property relationships of disordered materials using first-principles based high-throughput simulation framework*

1. Facilitating ab initio configurational sampling of multicomponent solids using an on-lattice neural network model and active learning
   S. Kasamatsu, Y. Motoyama, K. Yoshimi, U. Matsumoto, A. Kuwabara, and T. Ogawa, J. Chem. Phys. **157**, 104114 (2022).
   DOI:10.1063/5.0096645

2. Structural Analysis of Amorphous GeO_2 under High Pressure Using Reverse Monte Carlo Simulations
   K. Matsutani, A. Yamauchi, S. Kasamatsu, and T. Usuki J. Phys. Soc. Jpn. **91**, 124601 (2022).
   DOI:10.7566/JPSJ.91.124601

3. Probing Local Environments of Oxygen Vacancies Responsible for Hydration in Sc-Doped Barium Zirconates at Elevated Temperatures: In SituXray Absorption Spectroscopy, Thermogravimetry, and Active Learning Ab Initio Replica Exchange Monte Carlo Simulations
   K. Hoshino, S. Kasamatsu, J. Hyodo, K. Yamamoto, H. Setoyama, T. Okajima, and Y. Yamazaki, Chem. Mater. **35**, 2289 (2023).
   DOI:10.1021/acs.chemmater.2c02116

KATO, Takeo [B class; 500 (B), 80 (C)] (321)
— *Numerical Study of Spin Transport in Magnetic Junctions*

1. Spin Hall magnetoresistance in quasi-two-dimensional antiferromagnetic-insulator/metal bilayer systems
   T. Ishikawa, M. Matsuo, and T. Kato, Phys. Rev. B **107**, 054426 (2023).
   DOI:10.1103/PhysRevB.107.054426

KATOW, Hiroki [C class; 1000 (B), 0 (C)] (146)
— *Development of First Principles methods for Light-Matter Interaction*

1. First-Principles Study of the Optical Dipole Trap for Two-Dimensional Excitons in Graphane
   H. Katow, R. Akashi, Y. Miyamoto, and S. Tsuneyuki, Phys. Rev. Lett. **129**, 047401 (2022).
   DOI:10.1103/PhysRevLett.129.047401

KAWAKATSU, Toshihiro [C class; 6200 (B), 0 (C)] (232)
— *Multiscale Flow Simulations on Complex Fluids Undergoing Phase Transition*

KAWAMURA, Hikaru [C class; 2400 (B), 0 (C)] (272)
— *Novel order in frustrated magnets*
— *Novelorderinfrustratedmagnets*

1. Skyrmion crystal in the RKKY system on the two-dimensional triangular lattice
   K. Mitsumoto and H. Kawamura, Phys. Rev. B **105**, 094427(2022).
   DOI:10.1103 /PhysRevB.105.094427

2. Emergent skyrmion-based chiral order in zero-field Heisenberg antiferromagnets on the breathing kagome lattice
   K. Aoyama and H. Kawamura, Phys. Rev. B **105**, L100407 (2022).
   DOI:10.1103/PhysRevB.105.L100407

3. Spin Dynamics Simulation of the Z_2-vortex Fluctuations

Y.P. Mizuta, K. Aoyama, K. Tomiyasu, M. Matsuura, and H. Kawamura, J. Phys. Soc. Jpn. **91**, 035001 (2022).
DOI:10.7566/JPSJ.91.035001

4. Hedgehog lattice and field-induced chirality in breathing-pyrochlore Heisenberg antiferromagnets
K. Aoyama and H. Kawamura, Phys. Rev. B 106, 064412 (2022).
DOI:10.1103/PhysRevB.106.064412

5. Zero-field miniature skyrmion crystal and chiral domain state in breathing-kagome antiferromagnet
K. Aoyama and H. Kawamura, J. Phys. Soc. Jpn. 92, 033701 (2023).
DOI:10.7566/JPSJ.92.033701

KAWANO, Shoya [B,D class; 1150 (B), 0 (C)] (136, 138)
— *First-principles calculation of oxygen defects on the surface of titanium dioxide TiO_2*
— *Thermal conductivity calculation for high thermal conductive insulator*

KAWASHIMA, Naoki [E class; 35500 (B), 2750 (C)] (214)
— *Loop-gas representation of classical and quantum statistical-mechanical models and its tensor-network calculation*

1. Non-monotonic behavior of the Binder parameter in discrete spin systems
H. Watanabe, Y. Motoyama, S. Morita, and N. Kawashima, Prog. Theor. Exp. Phys. 033A02 (2023).
DOI:10.1093/ptep/ptad022

2. TeNeS: Tensor Network Solver for Quantum Lattice Systems
Y. Motoyama, T. Okubo, K. Yoshimi, S. Morita, T. Kato, and N. Kawashima, Comput. Phys. Commun. 279, 108437 (2022).
DOI:10.1016/j.cpc.2022.108437

3. Reply to Comments on "Universal and Non-Universal Correction Terms of Bose Gases in Dilute Region: A Quantum Monte Carlo Study"
A. Masaki-Kato, Y. Motoyama, and N. Kawashima, J. Phys. Soc. Jpn. 91, 066002 (2022).

KITAO, Akio [C class; 4600 (B), 400 (C)] (243)
— *Efficient sampling simulation of the soft modes significantly contribute to protein properties*

1. Inhibition of the hexamerization of SARS - CoV - 2 endoribonuclease and modeling of RNA structures bound to the hexamer
D. P. Tran, Y. Taira, T. Ogawa, R. Misu, Y. Miyazawa, A. Kitao, Sci. Rep. **12** (2022) 3860.
DOI:10.1038/s41598-022-07792-2

2. Structure of MotA, a flagellar stator protein, from hyperthermophile
T. Nishikino, N. Takekawa, D. P. Tran, J. Kishikawa, M. Hirose, S. Onoe, S. Kojima, M. Homma, A. Kitao, T. Kato, and K. Imada, Biochem. Biophys. Res. Commun. **631** (2022) 78.
DOI:10.1016/j.bbrc.2022.09.072

KOBAYASHI, Akito [B class; 400 (B), 80 (C)] (209, 376)
— *Systematic elucidation of ordered states in organic Dirac electron systems*

1. Gap opening mechanism for correlated Dirac electrons in organic compounds α-(BEDT-TTF)2I3 and α-(BEDT-TSeF)2I3
D. Ohki, K. Yoshimi, A. Kobayashi, and T. Misawa Phys. Rev. B 107, L041108 (2022).
DOI:10.1103/PhysRevB.107.L041108

2. Fragment-orbital-dependent spin fluctuations in the single-component molecular conductor [Ni(dmdt)2]
T. Kawamura and A. Kobayashi Phys. Rev. B 105, 205145 (2022).
DOI:10.1103/PhysRevB.105.205145

3. Interaction-induced quantum spin Hall insulator in the organic Dirac electron system alpha-(BEDT-TSeF)2I3
D. Ohki, K. Yoshimi, and A. Kobayashi Phys. Rev. B 105, 205123 (2022).
DOI:10.1103/PhysRevB.105.205123

Data Repository
H-wave Gallery
https://isspns-gitlab.issp.u-tokyo.ac.jp/hwave-dev/hwave-gallery

KOBAYASHI, Katsuyoshi [B class; 600 (B), 90 (C)] (159)
— *Theoretical study on electronic properties of new nanoscale surfaces and interfaces*

1. Formation of monolayer V_5Se_8 from multilayer VSe_2 films via V- and Se-desorption
K. Sumida, S. Kusaka, Y. Takeda, K. Kobayashi, and T. Hirahara Phys. Rev. B **106**, 195421 (2022).
DOI:10.1103/PhysRevB.106.195421

KOBAYASHI, Nobuhiko [C class; 4800 (B), 400 (C)] (86)
— *Quantum transport theory by large scale first-principles electron transport calculations*

1. Electronic and magnetic properties of $CoSb_3$, Cr-doped $CoSb_3$, and related compound thin films
K. Kobayashi, H. Takaki, M. Shimono, H. Ishii, N. Kobayashi, K. Hirose, and T. Mori Jpn. J. Appl. Phys. 62 SC1046 (2023).

2. Single-molecule detection with enhanced Raman scattering of tungsten oxide nanostructure
Y. Shingaya, H. Takaki, N. Kobayashi, M. Aono; T. Nakayama Nanoscale, 14 14552 (2022).

3. First-principles study of Fe_2VAl and Fe_2VAl/Si thin films and their magnetic properties
K. Kobayashi, H. Takaki, M. Shimono, H. Ishii, N. Kobayashi, K. Hirose, and T. Mori Jpn. J. Appl. Phys. 61 SL1013 (2022).

4. π - Extended Zigzag - Shaped Diphenanthrene - Based p-Type Semiconductors Exhibiting Small Effective Masses
M. Mitani, S. Kumagai, CP. Yu, A. Oi, M. Yamagishi, S. Nishinaga, H. Mori, Y. Nishihara, D. Hashizume, T. Kurosawa, H. Ishii, N. Kobayashi, J. Takeya, and T. Okamoto Adv. Electron. Mater. 8, 2200452 (2022).

KOBAYASHI, Ryo [B class; 400 (B), 80 (C)] (326)
— *Molecular dynamics analyses of ion migration at electrode-electrolyte interfaces and grain boundaries in electrolytes*

1. Na superionic conductor-type $LiZr_2(PO_4)_3$ as a promising solid electrolyte for use in all-solid-state Li metal batteries
M. Nakayama, K. Nakano, M. Harada, N. Tanibata, H. Takeda, Y. Noda, R. Kobayashi, M. Karasuyama, I. Takeuchi, and M. Kotobuki, Chem. Commun. 58, 9328 (2022).
DOI:10.1039/D2CC01526A

2. Screening chloride Li - ion conductors using high - throughput force - field molecular dynamics
S. Aizu, S. Takimoto, N. Tanibata, H. Takeda, M. Nakayama, and R. Kobayashi, J. Am. Ceram. Soc. 106, 3035 (2023).

DOI:10.1111/jace.18991

KOGA, Akihisa [C class; 4200 (B), 400 (C)] (250)
— *Effects of flux structures on Majorna excitations in Kitaev spin liquids*

1. Scattering phenomena for spin transport in Kitaev spin liquid
   J. Nasu, Y. Murakami, and A. Koga, Phys. Rev. B **106**, 024411 (2022).

2. Optical response of the tightbinding model on the Fibonacci chain
   H. Iijima, Y. Murakami, and A. Koga J. Phys. Soc. Jpn. **91**, 124702 (2022).

KOMATSU, Hisato [B class; 300 (B), 60 (C)] (339)
— *Magnetic structures on the thin films made by the dipolar interaction and the frictional force stemming from these structures*

1. Transition between the stick and slip states in a simplified model of magnetic friction
   H. Komatsu, Submitted to Phys. Rev. E

KOURA, Akihide [C class; 5000 (B), 0 (C)] ()
— *Machine learning study on static structure of glass materials based on it ab initio molecular dynamics*

KUNISADA, Yuji [C class; 7800 (B), 0 (C)] (71)
— *Development of Efficient Oxygen Storage Materials and Hydrogen Permeation Barrier Materials*

KUROKI, Kazuhiko [C class; 5400 (B), 0 (C)] (194)
— *Theoretical studies on cuprate superconductors with quasi-one-dimensional electronic structure*

1. Possibility of N-type Doping in $CaAl_2Si_2$-type Zintl Phase Compound $CaZn_2X_2$ (X = As, P)
   K. Nishiguchi, M. Ochi, C.H. Lee, and K. Kuroki, J. Phys. Soc. Jpn. **91**, 064707 (2022).
   DOI:10.7566/JPSJ.91.064707

KUSAKABE, Koichi [C class; 3400 (B), 350 (C)] (109)
— *Theoretical study of quantum effects in nanographene devices*

1. Spin-topological electronic valve in Ni/hBN-Graphene-hBN/Ni Magnetic Junction
   Y. Wicaksono, H. Harfah, G. K. Sunnardianto, M. A. Majidi, and K. Kusakabe, Magnetochem. **9**, 113 (2023).
   DOI:10.3390/magnetochemistry9050113

2. Colossal In-plane Magnetoresistance Ratio of Graphene Sandwiched with Ni Nanostructures
   Y. Wicaksono, H. Harfah, G. K. Sunnardianto, M. A. Majidi, and K. Kusakabe, RSC Adv. **12**, 13985 (2022).
   DOI:10.1039/D2RA00957A

3. Theoretical Analysis on the Stability of 1-Pyrenebutanoic Acid Succinimidyl Ester Adsorbed on Graphene
   Y. Oishi, H. Ogi, S. Hagiwara, M. Otani, and K. Kusakabe, ACS Omega **7**, 35, 31120 (2022).
   DOI:10.1021/acsomega.2c03257

4. Search for the decomposition process of 2,4,6-trinitrotoluene by an evolutionary algorithm
   T. Ishikawa, K. Kusakabe, Y. Makino, S. Sakamoto, N. Okuyama, J. Phys. Chem. A **126**, 8082 (2022).
   DOI:10.1021/acs.jpca.2c04913

5. Terahertz-induced martensitic transformation in partially stabilized zirconia
M. Nagai, Y. Higashitani, M. Ashida, K. Kusakabe, H. Niioka, A. Hattori, H. Tanaka, G. Isoyama, N. Ozaki, Commun. Phys. in press (2023)

LEE, Minhyeok [C class; 1400 (B), 0 (C)] (128)
— Development of the Low-Temperature Oxidation Model for Alternative Fuels Using Machine Learning
— Modeling of the Ammonia Decomposition Reaction on Iron-based Material Surfaces

LI, Hao [C class; 4400 (B), 0 (C)] (97)
— Design of CO2 Reduction Catalysts by pH-Field Dependent Simulation and New Machine Learning-Based Methodology

1. The Surface States of Transition Metal X-ides under Electrocatalytic Conditions
H. Liu, X. Jia, W. Li, C. D'agostino, and H. Li, J. Chem. Phys. 158, 124705 (2023).
DOI:10.1063/5.0147123

2. Spin-Selective Coupling in Mott–Schottky Er_2O_3-Co Boosts Electrocatalytic Oxygen Reduction
X. Wang, M. Li, P. Wang, D. Sun, L. Ding, H. Li, Y. Tang, and G. Fu, Small Methods (2023).
DOI:10.1002/smtd.202300100

3. Design of Molecular M-N-C Dual-atom Catalysts for Nitrogen Reduction Starting from surface state analysis
Y. Zhang, Z. Yu, F. She, L. Wei, Z. Zeng, and H. Li, J. Colloid Interface Sci. 640, 983 (2023).
DOI:10.1016/j.jcis.2023.03.033

4. Efficient Asymmetrical Silicon-Metal Dimer Electrocatalysts for Nitrogen Reduction Reaction
C. Liu, H. Zheng, T. Wang, X. Zhang, Z. Guo, and H. Li, Phys. Chem. Chem. Phys. 25, 13126 (2023).
DOI:10.1039/D2CP05959B

5. The Role of Single-Boron of N-doped Graphene for Effective Nitrogen Reduction
C. Liu, T. Wang, Z. Guo, F. Zhu, G. Qin, H. Li, and S. Li, J. Mater. Sci. Technol. 159, 244 (2023).
DOI:10.1016/j.jmst.2023.03.033

6. Heterogeneous Molecular Co–N–C Catalysts for Efficient Electrochemical H_2O_2 Synthesis
C. Liu, Z. Yu, F. She, J. Chen, F. Liu, J. Qu, J. M. Cairney, C. Wu, K. Liu, W. Yang, H. Zheng, Y. Chen, H. Li, and L. Wei, Energy Environ. Sci.16, 446 (2023).
DOI:10.1039/d2ee02734h

7. Improving the Oxygen Evolution Activity of Layered Double-Hydroxide via Erbium-Induced Electronic Engineering
Y. Zhu, X. Wang, X. Zhu, Z. Wu, D. Zhao, F. Wang, D. Sun, Y. Tang, H. Li, Hao and G. Fu, Small 19, 2206531 (2023).
DOI:10.1002/smll.202206531

8. N-doped $LaPO_4$: An effective Pt-free catalyst for electrocatalytic oxygen reduction
R. Zhao, Z. Chen, Q. Li, X. Wang, Y. Tang, F. Fu, H. Li, J.-M. Lee, and S. Huang, Chem Catalysis 2, 3590 (2022).
DOI:10.1016/j.checat.2022.11.008

9. Design of Single-Atom Catalysts for Hg0 Oxidation Using H_2O_2
W. Yang, X. Chen, L. Chen, Y. Feng, C. Wu, X. Ding, Z. Gao, Y. Liu, and H. Li, J. Phys. Chem. C 126, 21234 (2022).
DOI:10.1021/acs.jpcc.2c06266

10. Surface States of Dual-atom Catalysts Should be Considered for Analysis of Electrocatalytic Activity
W. Yang, Z. Jia, B. Zhou, L. Wei, Z. Gao, and H. Li, Commun. Chem. 6, 6 (2023).
DOI:10.1038/s42004-022-00810-4

LIAO, YUXUAN [C class; 4000 (B), 300 (C)] ()
— *Ultimate Suppression of Nanoheat Transport with Quasi-phononic Crystal*

MAEHIRA, Takahiro [B class; 400 (B), 30 (C)] (180)
— *Electronic Structure and Fermiology of d- and f-electron compounds*

MAKINO, Takayuki [B class; 400 (B), 70 (C)] (178)
— *Ab-inition calculations for vibrational and magnetic properties of rare-earth monooxides with insulating ground states*

MAO, WEI [C class; 400 (B), 250 (C)] ()
— *First-principles calculation of microscopic behaviors of hydrogen and Li in metal oxides*

MATSUKAWA, Hiroshi [C class; 3600 (B), 350 (C)] ()
— *Physics of Friction*

MATSUSHITA, Katsuyoshi [C class; 1000 (B), 0 (C)] (301)
— *Numerical Study of Collective Cell Migration in Tissue Interface*
— *Tissue-Interface Adhesion Stabilizing Cell Motion Order*

1. Collective Cell Movement under Cell-Scale Tension Gradient at Tissue Interface
K. Matsushita, H. Hashimura, H. Kuwayama, and K. Fujimoto, J. Phys. Soc. Jpn. **91**, 054802 (2022).
DOI:10.7566/JPSJ.91.054802

2. Collective Cell Movement through Cell Sensing in Crossover from Suspended to Aggregated States
K. Matsushita, T. Arakaki, N. Kamamoto, M. Sudo, and K. Fujimoto, The Symposium on Traffic Flow and Self-driven Particles **28**, 5 (2023).

MATSUSHITA, Yu-ichiro [E class; 7900 (B), 1250 (C)] (65)
— *Proposal for Green Devices Based on First-Principles Calculations: From Material Exploration to Device Fabrication*

1. DzyaloshinskiiMoriya interactions in $Nd_2Fe_{14}B$ as the origin of spin reorientation and the rotating magnetocaloric effect
H. B. Tran and Y.-i. Matsushita, Applied Materials Today **32**, 101825 (2023).
DOI:10.1016/j.apmt.2023.101825

2. Spin property improvement of boron vacancy defect in hexagonal boron nitride by thermal treatment
T. Suzuki, Y. Yamazaki, T. Taniguchi, K. Watanabe, Y. Nishiya, Y.-i. Matsushita, K. Harii, Y. Masuyama, Y. Hijikata, and T. Ohshima, Applied Physics Express **16**, 032006 (2023).
DOI:10.35848/1882-0786/acc442

3. Effect of nitrogen introduced at the SiC/SiO_2 interface and SiC side on the electronic states by first-principles calculation
K. Tachiki, Y. Nishiya, J.-I. Iwata, and Y.-i. Matsushita, arXiv:2303.08527 (2023).
DOI:10.48550/arXiv.2303.08527

4. Atomic scale localization of Kohn-Sham wavefunction at SiO_2/4H-SiC interface under electric field, deviating from envelope function by effective mass approximation
H. Yoshioka, J-I. Iwata, and Y-i. Matsushita, arXiv:2303.05085 (2023).
DOI:10.48550/arXiv.2303.05085

5. First-quantized eigensolver for ground and excited states of electrons under a uniform magnetic field
T. Kosugi, H. Nishi, and Y-i. Matsushita, arXiv:2212.13800 (2022).
DOI:10.48550/arXiv.2212.13800

6. Acceleration of probabilistic imaginary-time evolution method combined with quantum amplitude amplification
H. Nishi, T. Kosugi, Y. Nishiya, and Y-i. Matsushita, arXiv:2212.13816 (2022).
DOI:10.48550/arXiv.2212.13816

7. Atomic and electronic structures of nitrogen vacancies in silicon nitride: Emergence of floating gap states
F. Nanataki, K. Shiraishi, J-I. Iwata, Y-i. Matsushita, and A. Oshiyama, Phys. Rev. B **106**, 155201 (2022).
DOI:10.1103/PhysRevB.106.155201

8. Exhaustive search for optimal molecular geometries using imaginary-time evolution on a quantum computer
T. Kosugi, H. Nishi, and Y. Matsushita, arXiv:2210.09883 (2022).
DOI:10.48550/arXiv.2210.09883

9. Systematic study on the dependence of the warm-start quantum approximate optimization algorithm on approximate solutions
K. N. Okada, H. Nishi, T. Kosugi, and Y.-i. Matsushita, arXiv:2209.02942 (2022).
DOI:10.48550/arXiv.2209.02942

10. Skyrmions in van der Waals centrosymmetric materials with Dzyaloshinskii-Moriya interactions
H. B. Tran and Y.-i. Matsushita, arXiv:2209.02333 (2022).
DOI:10.48550/arXiv.2209.02333

11. Imaginary-time evolution using forward and backward real-time evolution with a single ancilla: First-quantized eigensolver algorithm for quantum chemistry
T. Kosugi, Y. Nishiya, H. Nishi, and Y.-i. Matsushita, Phys. Rev. Research **4**, 033121 (2022).
DOI:10.1103/PhysRevResearch.4.033121

MAYUMI, Koichi [C class; 3800 (B), 0 (C)] (258)
— *Mechanism of Strain-Induced Crystallization in Polymer Gels*

MINAMI, Susumu [B class; 500 (B), 90 (C)] (169)
— *First-principles study of magnetic tunnel conductance and interfacial structure in topological magnets*

MISAWA, Masaaki [B class; 400 (B), 0 (C)] (333)
— *Molecular dynamics study on destruction phenomena under extreme conditions*

1. Surface Diffusion-Limited Growth of Large and High-Quality Monolayer Transition Metal Dichalcogenides in Confined Space of Microreactor
H. Suzuki, R. Hashimoto, M. Misawa, Y. Liu, M. Kishibuchi, K. Ishimura, K. Tsuruta, Y. Miyata, and Y. Hayashi, ACS Nano **16**, 11360 (2022).
DOI:10.1021/acsnano.2c05076

2. First-principles analysis of stearic acid adsorption on calcite (104) surface
N. Machida, M. Misawa, Y. Kezuka, and K. Tsuruta, e-Journal of Surface Science and Nanotechnology **20**, 261 (2022).
DOI:10.1380/ejssnt.2022-041

3. Defect-free and crystallinity-preserving ductile deformation in semiconducting Ag_2S
M. Misawa, H. Hokyo, S. Fukushima, K. Shimamura, A. Koura, F. Shimojo, R. K. Kalia, A. Nakano, and P. Vashishta, Sci. Rep. **12**, 19458 (2022).
DOI:10.1038/s41598-022-24004-z

MITARAI, Yoko [B class; 900 (B), 80 (C)] (152)
— *Phase stability and mechanical properties of high-entropy alloys*
— *Phase transformation of high-entropy alloys*

MIZUKAMI, Wataru [C class; 5600 (B), 500 (C)] (233)
— *Simulations of stochastic quantum-classical-hybrid calculations for sensor materials with considering noise*

1. Solvent distribution effects on quantum chemical calculations with quantum computers
Y. Yoshida, W. Mizukami, and N. Yoshida, arXiv.2208.12487
DOI:10.48550/arXiv.2208.12487

2. Hunting for quantum-classical crossover in condensed matter problems
N. Yoshioka, T. Okubo, Y. Suzuki, Y. Koizumi, and W. Mizukami, arXiv.2210.14109
DOI:10.48550/arXiv.2210.14109

MIZUSHIMA, Takeshi [B class; 500 (B), 80 (C)] (320)
— *Nonlinear dynamics of superconducting liquid crystal order*

1. Manipulation of Majorana Kramers Qubit and its Tolerance in Time-Reversal-Invariant Topological Superconductor
T. Sanno, M. G. Yamada, T. Mizushima, and S. Fujimoto, Phys. Rev. B **106**, 014522 (2022).
DOI:10.1103/PhysRevB.106.014522

2. Engineering Yang-Lee anyons via Majorana bound states
Y. Tanaka, T. Sanno, T. Mizushima, and S. Fujimoto, Phys. Rev. B **106**, 174517 (2022).
DOI:10.1103/PhysRevB.106.174517

MOCHIZUKI, Izumi [B class; 500 (B), 0 (C)] (323)
— *Precise structural analysis of atomic arrangement of hydrogen-adsorbed ceria surfaces by using 2DMAT*

1. Two-stage data-analysis method for total-reflection high-energy positron diffraction (TRHEPD)
K. Tanaka, I. Mochizuki, T. Hanada, A. Ichimiya, T. Hyodo, and T. Hoshi, JJAP Conf. Series **9**, 011301 (2023).
DOI:10.56646/jjapcp.9.0_011301

2. Data-analysis software framework 2DMAT and its application to experimental measurements for two-dimensional material structures
Y. Motoyama, K. Yoshimi, I. Mochizuki, H. Iwamoto, H. Ichinose, and T. Hoshi, Comp. Phys. Commun. **280**, 108465 (2022).
DOI:10.1016/j.cpc.2022.108465

3. Data-driven Sensitivity Analysis in Surface Structure Determination by Total-Reflection High-Energy Positron Diffraction (TRHEPD)
T. Hoshi, I. Mochizuki, S. Tanaka, T. Hyodo, and K. Hukushima Photon Factory Highlights 2021,

46 (2022).

Data Repository
2DMAT Gallery
https://isspns-gitlab.issp.u-tokyo.ac.jp/2dmat-dev/2dmat-gallery

MOCHIZUKI, Masahito [C class; 6200 (B), 50 (C)] (192)
— *Research for photoinduced phenomena in topological magnets*
— *Research on photoinduced topological electronic states in metallic magnets*

1. Low-Energy Excitations of Skyrmion Crystals in a Centrosymmetric Kondo-Lattice Magnet: Decoupled Spin-Charge Excitations and Nonreciprocity
R. Eto, R. Pohle, and M. Mochizuki, Phys. Rev. Lett. bf 129, 017201 (2022).
DOI:10.1103/PhysRevLett.129.017201

2. Dynamical Phase Transitions in the Photodriven Charge-Ordered Dirac-Electron System
Y. Tanaka and M. Mochizuki, Phys. Rev. Lett. bf 129, 047402 (2022).
DOI:10.1103/PhysRevLett.129.047402

MOCHIZUKI, Yasuhide [C class; 5000 (B), 400 (C)] (83)
— *Elucidation and design principle of negative thermal expansion originating from lattice vibration*

1. Chemical Aspect of Displacive-Type Ferroaxial Phase Transition from Perspective of Second-Order Jahn-Teller Effect: NASICON Systems as an Example
T. Nagai, Y. Mochizuki, S. Yoshida, and T. Kimura, J. Am. Chem. Soc. **145**, 8090 (2023).
DOI:10.1021/jacs.3c00797

MORIKAWA, Yoshitada [E class; 18000 (B), 1300 (C)] (45)
— *Theoretical study on dynamical processes in heterogeneous catalysis using density functional theory and machine learning methods*

1. The Elucidation of Cu-Zn Surface Alloying on Cu(997) by Machine-Learning Molecular Dynamics
Harry Handoko Halim and Yoshitada Morikawa, ACS Physical Chemistry Au **2**, 430 (2022).
DOI:10.1021/acsphyschemau.2c00017

2. Hydrogenation of formate species using atomic hydrogen on a Cu(111) model catalyst
K. Takeyasu, Y. Sawaki, T. Imabayashi, S. E. M. Putra, H. H. Halim, J. Quan, Y. Hamamoto, I. Hamada, Y. Morikawa, T. Kondo, T. Fujitani, and J. Nakamura J. Am. Chem. Soc. **144**, 12158 (2022).
DOI:10.1021/jacs.2c02797

3. Density functional theory study of NO-H_2O co-adsorption on Cu(111)
T. N. Pham, Y. Hamamoto, K. Inagaki, I. Hamada, and Y. Morikawa, Phys. Rev. Materials **6**, 075801 (2022).
DOI:10.1103/PhysRevMaterials.6.075801

4. Activity and selectivity of N_2 fixation on B doped g-C_9N_{10}: A density functional theory study
Y.-L. Wang, T. N. Pham, L.-K. Yan, and Y. Morikawa, J. Mater. Chem. C **10**, 11791-11800 (2022).
DOI:10.1039/D2TC02041F

MORITA, Katsuhiro [B class; 600 (B), 0 (C)] (316)
— *Finite temperature calculations of frustrated quantum spin systems*

MORITA, Satoshi [B class; 500 (B), 80 (C)] (319)
— *Identification of universality classes by tensor network methods*

1. Non-monotonic behavior of the Binder Parameter in the systems with the Potts symmetry
   H. Watanabe, Y. Motoyama, S. Morita, and N. Kawashima, Prog. Theor. Exp. Phys. **2023**, 033A02 (2023).
   DOI:10.1093/ptep/ptad022

2. Ground-state phase diagram of a spin-1/2 frustrated XXZ ladder
   T. Ogino, R. Kaneko, S. Morita, and S. Furukawa, Phys. Rev. B **106**, 155106 (2022).
   DOI:10.1103/PhysRevB.106.155106

3. TeNeS: Tensor Network Solver for Quantum Lattice Systems
   Y. Motoyama, T. Okubo, K. Yoshimi, S. Morita, T. Kato, and N. Kawashima, Comput. Phys. Commun. **279**, 108437 (2022).
   DOI:10.1016/j.cpc.2022.108437

MOTOME, Yukitoshi [C class; 12800 (B), 950 (C)] (190)
— *Theoretical study of strongly-correlated topological phenomena by exploiting first-principles calculations and machine learning*

1. Inter-edge spin resonance in the Kitaev quantum spin liquid
   T. Misawa, J. Nasu, and Y. Motome submitted to Phys. Rev. B

2. Ground-State Phase Diagram of the Kitaev-Heisenberg Model on a Three-dimensional Hyperhoneycomb Lattice
   K. Fukui, Y. Kato, and Y. Motome, submitted to J. Phys. Soc. Jpn.

3. Thermally-robust spatiotemporal parallel reservoir computing by frequency filtering in frustrated magnets
   K. Kobayashi and Y. Motome, submitted to Nature Commun.

4. One, two, three, ⋯ infinity: topological properties of thin films of Co-based shandite
   K. Nakazawa, Y. Kato, and Y. Motome submitted to Commun. Phys.

5. Spin nematics meet spin liquids: Exotic quantum phases in the spin-1 bilinear-biquadratic model with Kitaev interactions
   R. Pohle, N. Shannon, and Y. Motome, Phys. Rev. B. **107**, L140403 (2023).
   DOI:10.1103/PhysRevB.107.L140403

6. Hidden topological transitions in emergent magnetic monopole lattices
   Y. Kato and Y. Motome, Phys. Rev. B. **107**, 094437 (2023).
   DOI:10.1103/PhysRevB.107.094437

7. Inverse Hamiltonian design by automatic differentiation
   K. Inui and Y. Motome Commun. Phys. **6**, 37 (2023).
   DOI:10.1038/s42005-023-01132-0

8. Anomalous Hall effect in antiferromagnetic perovskites
   M. Naka, Y. Motome, and H. Seo Phys. Rev. B. **106**, 195149 (2022).
   DOI:10.1103/PhysRevB.106.195149

9. Ground-state phase diagram of spin-S Kitaev-Heisenberg models
   K. Fukui, Y. Kato, J. Nasu, and Y. Motome, Phys. Rev. B. **106**, 174416 (2022).
   DOI:10.1103/PhysRevB.106.174416

10. Magnetic Hedgehog Lattice in a Centrosymmetric Cubic Metal
S. Okumura, S. Hayami, Y. Kato, and Y. Motome, J. Phys. Soc. Jpn. **91**, 093702 (2022).
DOI:10.7566/JPSJ.91.093702

11. Feasibility of Kitaev quantum spin liquids in ultracold polar molecules
K. Fukui, Y. Kato, J. Nasu, and Y. Motome, Phys. Rev. B **106**, 014419 (2022).
DOI:10.1103/PhysRevB.106.014419

12. Phase degree of freedom and topology in multiple-Q spin textures
K. Shimizu, S. Okumura, Y. Kato, and Y. Motome, Phys. Rev. B **105**, 224405 (2022).
DOI:10.1103/PhysRevB.105.224405

13. Magnetic fieldtemperature phase diagrams for multiple-Q magnetic ordering: Exact steepest descent approach to long-range interacting spin systems
Y. Kato and Y. Motome Phys. Rev. B **105**, 174413 (2022).
DOI:10.1103/PhysRevB.105.174413

14. Asymmetric modulation of Majorana excitation spectra and nonreciprocal thermal transport in the Kitaev spin liquid under a staggered magnetic field
K. Nakazawa, Y. Kato, and Y. Motome Phys. Rev. B **105**, 165152 (2022).
DOI:10.1103/PhysRevB.105.165152

MURASHIMA, Takahiro [C class; 4800 (B), 400 (C)] (241)
— *Polymer Dynamics under Elongational Flow*

1. Topological transition in multicyclic chains with structural symmetry inducing stress-overshoot phenomena in multicyclic/linear blends under biaxial elongational flow
T. Murashima, K. Hagita, and T. Kawakatsu, Macromolecules **55**, 9358 (2022).
DOI:10.1021/acs.macromol.2c01579

NADA, Hiroki [B,C class; 700 (B), 400 (C)] (288, 289)
— *Analysis of Various Crystal Forms of Glycine Nanocrystals by Large-Scale Metadynamics Simulations*
— *Structural Analysis of Amorphous Silicon Monoxide by a Metadynamics Method with Unsupervised Machine Learning*

1. Stable Binding Conformations of Polymaleic and Polyacrylic Acids at a Calcite Surface in the Presence of Countercations: A Metadynamics Study
H. Nada, Langmuir **38** (2022) 7046.
DOI:10.1021/acs.langmuir.2c00750

2. Effect of nitrogen molecules on the growth kinetics at the interface between a (111) plane of cubic ice and water
H. Nada, J. Chem. Phys. **157** (2022) 124701.
DOI:10.1063/5.0106842

3. Cinematographic recording of metastable floating island in 2-D and 3-D crystal growth
M. Sakakibara, H. Nada, T. Nakamuro, E. Nakamura ACS Central Science **8** (2022) 1704.
DOI:10.1021/acscentsci.2c01093

4. Formation of Hydrogen-Ordered Cubic Ice Polymorphs via Annealing of Ice Ic at 100-130 K
A. Kouchi1, T. Yamazaki, H. Katsuno, H. Nada, T. Hama, Y. Kimura Submitted to Chem. Phys.

NAKAGAWA, Naoko [C class; 3800 (B), 350 (C)] (252)
— *Nontrivial properties of interface and finite size effects of free energies*

1. Work relation for determining the mixing free energy of small-scale mixtures
A. Yoshida and N. Nakagawa, Phys. Rev. Res. 4, 023119 (2022).
DOI:10.1103/PhysRevResearch.4.023119

2. 微小溶液の混合自由エネルギーを決定する仕事関係式 – ジャルジンスキー等式・錬金術的操作・分子の識別可能性
吉田旭、中川尚子、日本物理学会誌 78, 140 (2023).

NAKAMURA, Kazuma [C class; 2000 (B), 0 (C)] (122)
— *Ab initio calculations for stability of multilayer sysmte*
— *Ab initio calculations for structural stability and property of multilayer system*

1. Hidden Markov model analysis for fluorescent time series of quantum dots
T. Furuta, K. Hamada, M. Oda, K. Nakamura, Phys. Rev. B. **106**, (2022) 104305.

NAKANO, Hiroki [C class; 3000 (B), 250 (C)] (261)
— *Numerical study on low-energy states of quantum spin systems*

1. The Haldane Gap of the $S = 1$ Heisenberg Antiferromagnetic Chain
H. Nakano, H. Tadano, N. Todoroki, and T. Sakai, J. Phys. Soc. Jpn. 91, 074701 (2022).
DOI:10.7566/JPSJ.91.074701

NAKANO, Hiroyoshi [C class; 7800 (B), 350 (C)] (221)
— *Nonequilibrium long-range correlation in heat conduction systems*
— *Numerical analysis of motility-induced phase transition in active Brownian particle system*

NAKAYAMA, Akira [C class; 2400 (B), 0 (C)] (119)
— *First-principles molecular dynamics study for metal-oxide catalysis*

NAKAYAMA, Masanobu [C class; 1000 (B), 0 (C)] (299)
— *Unveiling grain boundary alkaline ion conductivity by using materials simulation and*

1. Materials Simulation for the Modulated Arrangement in A-Site Deficient Perovskite-Type Lithium Doped Lanthanum Niobate as Solid Electrolytes for All Solid-State Li Ion Batteries
Z. Yang and M. Nakayama, J. Phys. Soc. Jpn. 91, 091010 (2022).
DOI:10.7566/JPSJ.91.091010

2. Na superionic conductor-type $LiZr_2(PO_4)_3$ as a promising solid electrolyte for use in all-solid-state Li metal batteries
M. Nakayama, K. Nakano, M. Harada, N. Tanibata, H. Takeda, Y. Noda, R. Kobayashi, M. Karasuyama, I. Takeuchi, and M. Kotobukii , Chem. Commun. 58, 9328 (2022).
DOI:10.1039/D2CC01526A

3. Bayesian optimisation with transfer learning for NASICON-type solid electrolytes for all-solid-state Li-metal batteries
H. Fukuda, S. Kusakawa, K. Nakano, N. Tanibata, H. Takeda, M. Nakayama, M. Karasuyama, I. Takeuchi, T. Natori, Y. Ono, and T. Natori, RSC Adv. 12, 30696 (2022).
DOI:10.1039/D2RA04539G

4. Screening chloride Li-ion conductors using high-throughput force-field molecular dynamics
S. Aizu, S. Takimoto, N. Tanibata, H. Takeda, M. Nakayama, and R. Kobayashi , J. Am. Ceram. Soc., 106, 4045 (2023).
DOI:10.1111/jace.18991

5. Reaction Kinetics of Carbonation at the Surface of Garnet-Type $Li_7La_3Zr_2O_{12}$ as Solid Elec-

trolytes for All-Solid-State Li Ion Batteries
M. Nakayama, T. Horie, R. Natsume, S. Hashimura, N. Tanibata, H. Takeda, H. Maeda, and M. Kotobuki, J. Phys. Chem. C 127, 7595 (2023).
DOI:10.1021/acs.jpcc.2c08588

6. Bayesian optimisation with transfer learning for NASICON-type solid electrolytes for all-solid-state Li-metal batteries
H. Fukuda, S. Kusakawa, K. Nakano, N. Tanibata, H. Takeda, M. Nakayama, M. Karasuyama, I. Takeuchi, T. Natori, Y. Ono, and T. Natori, RSC Adv. 12, 30696 (2022).
DOI:10.1039/D2RA04539G

NAKAYAMA, Takashi [C class; 4600 (B), 400 (C)] (89)
— *Theory of tunneling currents at semiconductor pn junctions in electric fields based on first-principles calculation*

1. Enhancement of tunneling currents by isoelectronic nitrogen-atom doping at semiconductor pn junctions; comparison of indirect and direct band-gap systems
S. Cho and T. Nakayama, Jpn. J. Appl. Phys. **61**, 124002 (2022).
DOI:10.35848/1347-4065/ac9fb0

2. Photo-carrier induced composition separation in mixed-halide $CsPb(I_xBr_{1-x})_3$ perovskite semiconductors; first-principles calculation
A. Tomita and T. Nakayama, Appl. Phys. Express,**16**, 041002 (2023).
DOI:10.35848/1882-0786/acc6b3

NASU, Joji [C class; 3200 (B), 250 (C)] (201)
— *Magnetic field effect on excitonic phase in multi-orbital Hubbard model*

1. Antisymmetric Thermopolarization by Electric Toroidicity
J. Nasu and S. Hayami, Phys. Rev. B **105**, 245125 (2022).
DOI:10.1103/PhysRevB.105.245125

2. Scattering phenomena for spin transport in Kitaev spin liquid
J. Nasu Y. Murakami, and A. Koga, Phys. Rev. B **106**, 024411 (2022).
DOI:10.1103/PhysRevB.106.024411

3. Feasibility of Kitaev quantum spin liquids in ultracold polar molecules
K. Fukui, Y. Kato, J. Nasu and Y. Motome, Phys. Rev. B **106**, 014419 (2022).
DOI:10.1103/PhysRevB.106.014419

4. Ground-state phase diagram of spin-S Kitaev-Heisenberg models
K. Fukui, Y. Kato, J. Nasu, and Y. Motome, Phys. Rev. B **106**, 174416 (2022).
DOI:10.1103/PhysRevB.106.174416

NIKI, Kaori [C class; 1000 (B), 0 (C)] (144)
— *Analysis of wavenumber space-resolved photoelectron spectrum of molecules adsorbed on surface*

1. Adsorbed CO_2Mediated CO_2 Photoconversion Cycle into Solar Fuel at the O Vacancy Site of Zirconium Oxide
K. Hara, M. Nozaki, R. Hirayama, R. Ishii, K. Niki, and Y. Izumi, J. Phys. Chem. C 127, 1776 (2023).
DOI:10.1021/acs.jpcc.2c06048

NISHIDATE, Kazume [C class; 800 (B), 0 (C)] (158)
— *Electronic structure investigation of the Ba_2PrBiO_6 photocatalyst*

1. Enhanced photocatalytic activities under visible light of double-perovskite oxide semiconductor $Ba_2Tb(Bi, Sb)O_6$ with mixed-valence
   D. C. Roy, M. Matsukawa, T. Yonai, M. Arakida, H. Taniguchi, K. Nishidate, S. Aisawa, A. Matsushita, and L. Shiqi, J. Mater. Sci. Mater. Electron. **34** (2023) 281.
   DOI:10.1007/s10854-022-09542-6

2. Gap opening at the Dirac point of graphene on Cu(111): Hybridization versus sublattice symmetry breaking
   K. Nishidate, M. Matsukawa, and M. Hasegawa, Surface Science, 728, 122196 (2023).
   DOI:10.1016/j.susc.2022.122196

NISHIGUCHI, Kazutaka [B class; 400 (B), 70 (C)] (210)
— *Theoretical study of thermoelectric properties in Heusler compounds: A weak-coupling approach*

1. Characterization of Planar Defect in Layered Perovskite Photocatalyst $Y_2Ti_2O_5S_2$ by Electron Microscopy and First-Principles Calculations
   M. Nakabayashi, K. Nishiguchi, X. Liang, T. Hisatomi, T. Takata, T. Tsuchimochi, N. Shibata, K. Domen, and S. L. Ten-no, J. Phys. Chem. C (in press).
   DOI:10.1021/acs.jpcc.3c00820

NISHIKAWA, Yoshihiko [C class; 6800 (B), 500 (C)] ()
— *Numerical study of thermodynamic properties of a lattice glass model*

NOGUCHI, Hiroshi [C class; 6200 (B), 500 (C)] (35)
— *structure formation of biomembrane*

1. Conformations of three types of ultra-long-chain fatty acids in multi-component lipid bilayers
   K. Kawaguchi, H. Nagao, H. Shindou, and H. Noguchi J. Phys. Chem. B 126, 9316-9324 (2022).
   DOI:10.1021/acs.jpcb.2c06189

2. Effects of gas-liquid phase transitions on soundwave propagation: A molecular dynamics study
   Y. Asano, H. Watanabe, and H. Noguchi Phys. Rev. Fluids 7, 064302 (2022).
   DOI:10.1103/PhysRevFluids.7.064302

NOGUCHI, Yoshifumi [C class; 3800 (B), 350 (C)] (106)
— *Investigation on optical properties of TADF molecules*

1. Development of the Bethe-Salpeter method considering second-order corrections for a *GW* electron-hole interaction kernel
   S. Yamada, Y. Noguchi, K. Ishii , D. Hirose, O. Sugino, and K. Ohno, Phys. Rev. B. **106**, 045113 (2022).
   DOI:10.1103/PhysRevB.106.045113

NOMURA, Yusuke [C class; 4200 (B), 400 (C)] (196)
— *Study on nonlocal correlations in multi-orbital strongly-correlated materials*

1. Ab initio materials design of superconductivity in d^9 nickelates
   M. Kitatani, Y. Nomura, M. Hirayama, and R. Arita APL Materials **11**, 030701 (2023).

2. Doping Asymmetry and Layer-Selective Metal-Insulator Transition in Trilayer $K_{3+x}C_60$
   C. Yue, Y. Nomura, and P. Werner Phys. Rev. Lett. **129**, 066403 (2022).

3. Fermi Surface Expansion above Critical Temperature in a Hund Ferromagnet

Y. Nomura, S. Sakai, and R. Arita Phys. Rev. Lett. **128**, 206401 (2022).

4. Investigating Network Parameters in Neural-Network Quantum States
   Y. Nomura J. Phys. Soc. Jpn. **91**, 054709 (2022).

NONOMURA, Yoshihiko [C class; 3600 (B), 350 (C)] (254)
— *Nonequilibrium relaxation temperature scaling: Applications to quantum systems*

NOZAWA, Kazuki [C class; 1400 (B), 200 (C)] (126)
— *First-principles study of surface atomic structure and chemical properties of intermetallic compounds*

1. First-principles study of the initial stage of Pentacene adsorption on the twofold surface of the Ag-In-Yb quasicrystal
   M. Sato, T. Hiroto, Y. Matsushita, and K. Nozawa, J. Phys.: Conf. Ser. 2461 012016 (2023).
   DOI:10.1088/1742-6596/2461/1/012016

OBATA, Masao [B class; 800 (B), 140 (C)] (153)
— *Analysis of magnetic material with an anisotropic crystal structure*
— *Analysis of magnetic materials with anisotropic crystal structures*

1. Intrinsic instability to martensite phases in ferromagnetic shape memory alloy Ni_2MnGa: Quasiparticle self-consistent *GW* investigation
   M. Obata, T. Kotani, and T. Oda, Phys. Rev. Materials **7**, 024413 (2023).
   DOI:10.1103/PhysRevMaterials.7.024413

OCHI, Masayuki [C class; 4600 (B), 0 (C)] (94)
— *Development of a first-principles calculation method using many-body wave functions*

1. Chemical Pressure Effect on Structural and Physical Properties of 15R-$SrVO_{2.2}N_{0.6}$ with Anion-Vacancy Order
   K. Murayama, H. Takatsu, M. Ochi, M. Namba, K. Kuroki, and H. Kageyama J. Phys. Soc. Jpn. **91**, 064805 (2022).
   DOI:10.7566/JPSJ.91.064805

2. Topochemical Synthesis of Ca_3CrN_3H Involving a Rotational Structural Transformation for Catalytic Ammonia Synthesis
   Y. Cao, M. A. Kirsanova, M. Ochi, W. A. Maksoud, T. Zhu, R. Rai, S. Gao, T. Tsumori, S. Kobayashi, S. Kawaguchi, E. Abou-Hamad, K. Kuroki, C. Tassel, A. M. Abakumov, Y. Kobayashi, and H. Kageyama Angew. Chem. Int. Ed. **61**, e202209187 (2022).
   DOI:10.1002/anie.20220918

3. Superconductivity in a Magnetic Rashba Semimetal EuAuBi
   H. Takahashi, K. Akiba, M. Takahashi, A. H. Mayo, M. Ochi, T. C. Kobayashi, and S. Ishiwata J. Phys. Soc. Jpn. **92**, 013701 (2023).
   DOI:10.7566/JPSJ.92.013701

4. Field-tunable Weyl points and large anomalous Hall effect in the degenerate magnetic semiconductor $EuMg_2Bi_2$
   M. Kondo, M. Ochi, R. Kurihara, A. Miyake, Y. Yamasaki, M. Tokunaga, H. Nakao, K. Kuroki, T. Kida, M. Hagiwara, H. Murakawa, N. Hanasaki, and H. Sakai Phys. Rev. B **107**, L121112 (2023).
   DOI:10.1103/PhysRevB.107.L121112

5. TC++: First-principles calculation code for solids using the transcorrelated method
   M. Ochi Comput. Phys. Commun. **287**, 108687 (2023).

DOI:10.1016/j.cpc.2023.108687

ODA, Tatsuki [C class; 5200 (B), 800 (C)] (77)
— *Analyses on electronic and magnetic structure and parallelization development in quasi-particle self-consistent GW code*

1. Intrinsic instability to martensite phases in ferromagnetic shape memory alloy Ni_2MnGa: Quasi-particle self-consistent GW investigation
   M. Obata, T. Kotani, and T. Oda, Phys. Rev. Mater. **7** (2023) 024413.

OHKUBO, Yuji [B class; 900 (B), 0 (C)] (154)
— *Clarification of atomistic mechanism application of process design for adhesion interface between metal and plasma-treated fluoropolymers using first principles calculation*

OHMURA, Satoshi [C class; 1000 (B), 0 (C)] (143)
— *Ab initio molecular-dynamics study of structural and transport properties of liquid mixtures containing hydrocarbon under ultra-high pressure*

1. Ab Initio Molecular-Dynamics Study of Structural and Bonding Properties of Liquid Fe–Light–Element–O Systems Under High Pressure
   S. Ohmura, F. Shimojo, and T. Tsuchiya, Front. Earth Sci. **10**, 873088 (2022)
   DOI:10.3389/feart.2022.873088

2. Development of a Multitimescale Time-Resolved Electron Diffraction Setup: Photoinduced Dynamics of Oxygen Radicals on Graphene Oxide
   Y. Saida, R. Shikata, K. En-ya, S. Ohmura, Y. Nishina, and M. Hada J. Phys. Chem. A **126**, 6301 (2022).
   DOI:10.1021/acs.jpca.2c04075

OHNISHI, Masato [C class; 4400 (B), 500 (C)] (91)
— *Development of Thermal Materials Using Phonon Database*

1. Anharmonic phonon renormalization and thermal transport in the type-I Ba8Ga16Sn30 clathrate from first principles
   M. Ohnishi, T. Tadano, S. Tsuneyuki, and J. Shiomi, Phys. Rev. B **106**, 24303 (2022).
   DOI:10.1103/PhysRevB.106.024303

OHNO, Kaoru [C class; 4200 (B), 400 (C)] (93)
— *Improvement and application of all-electron mixed basis program*

1. Electronic structure of $Li^+@C_{60}$ adsorbed on methyl-ammonium lead iodide perovskite $CH_3NH_3PbI_3$ surfaces
   K.-H. Chew, R. Kuwahara, and K. Ohno, Mater. Adv. **3**, 290-299 (2022).
   DOI:10.1039/D1MA00741F

2. Electronic Structures of Group IIIV Element Haeckelite Compounds: A Novel Family of Semiconductors, Dirac Semimetals, and Topological Insulators
   M. Khazaei, A. Ranjbar, Y.-G. Kang, Y. Liang, R. Khaledialidusti, S. Bae, H. Raebiger, V. Wang, M. J. Han, H. Mizoguchi, M. S. Bahramy, T. D. Kühne, R. V. Belosludov, K. Ohno, and H. Hosono, Adv. Functional Mater. **32**, 2110930 (2022).
   DOI:10.1002/adfm.202110930

3. Allproportional solid solution versus twophase coexistence in the TiV alloy by firstprinciples phase field and SQS methods
   K. Ohno, R. Kuwahara, T. N. Pham, S. Bhattacharyya, and R. Sahara, Sci. Rep. **12**, 10070

(2022).
DOI:10.1038/s41598-022-13906-7

4. Extended quasiparticle approach to non-resonant and resonant X-ray emission spectroscopy
K. Ohno and T. Aoki, Phys. Chem. Chem. Phys. **24**, 16586 (2022).
DOI:10.1039/D2CP00988A

5. Development of the Bethe-Salpeter method considering second-order corrections for a *GW* electron-hole interaction kernel
S. Yamada, Y. Noguchi, K. Ishii, D. Hirose, O. Sugino, and K. Ohno, Phys. Rev. B **106**, 045113 (2022).
DOI:10.1103/PhysRevB.106.045113

6. Position dependent dielectric function near the Cu surface
Y. Sakamoto, K. Fujii, S. Nakamura, and K. Ohno, J. Phys. Soc. Jpn. (Lett.) **91**, 113703 (2022).
DOI:10.7566/JPSJ.91.113703

7. Electronic structure analysis of light element-doped anatase TiO_2 using all-electron *GW* approach
T. Ishikawa, R. Sahara, K. Ohno, K. Ueda, and T. Narushima, Comp. Mat. Sci. **220**, 112059 (2023).
DOI:10.1016/j.commatsci.2023.112059

8. Microstructures in iron-rich FeSi alloys by first-principles phase field and special quasirandom structure methods
K. Ohno, R. Kuwahara, R. Sahara, T. N. Pham, S. Bhattacharyya, Y. Kawaoze, and K. Fujisaki, ISIJ International **63**, 553 (2023).
DOI:10.2355/isijinternational.ISIJINT-2022-465

OHSAWA, Kazuhito [C class; 1000 (B), 0 (C)] (141)
— *Study of interaction between radiation damage and interstitial atom*

OHTO, Tatsuhiko [C class; 3000 (B), 0 (C)] (114)
— *First-principles study on the structure of water/graphene interfaces depending on the number of graphene layers*

1. Controlling the Emissive, Chiroptical, and Electrochemical Properties of Double [7] Helicenes through Embedded Aromatic Rings
J. Hong, X. Xiao, H. Liu, E. Dmitrieva, A. A. Popov, Z. Yu, M.-D. Li, T. Ohto, J. Liu, A. Narita, P. Liu, H. Tada, X.-Y. Cao, X.-Y. Wang, Y. Zou, K. Mullen, and Y. Hu Chem. Eur. J. 28, e202202243 (2022).

2. The dielectric function profile across the water interface through surface-specific vibrational spectroscopy and simulations
K.-Y. Chiang, T. Seki, C.-C. Yu, T. Ohto, J. Hunger, M. Bonn, and Y. Nagata Proc. Natl. Acad. Sci. USA 119, e2204156119 (2022).

3. Coexistence of Urbach-tail-like localized states and metallic conduction channels in nitrogen-doped 3D curved graphene
Y. Tanabe, Y. Ito, K. Sugawara, S. Jeong, T. Ohto, T. Nishiuchi, N. Kawada, S. Kimura, C. F. Aleman, T. Takahashi, M. Kotani, and M. Chen Adv. Mater. 34, 2205986 (2022).

4. Corrosion-resistant and high-entropic non-noble-metal electrodes for oxygen evolution in acidic media
A. A. H. Tajuddin, M. Wakisaka, T. Ohto, Y. Yu, H. Fukushima, H. Tanimoto, X. Li, Y. Misu, S. Jeong, J.-i. Fujita, H. Tada, T. Fujita, M. Takeguchi, K. Takano, K. Matsuoka, Y. Sato, and

Y. Ito Adv. Mater. 35, 2207466 (2023).

OHTSUKI, Tomi [C class; 5600 (B), 200 (C)] (239)
— *Localization-delocalization transition in non-Hermitian random system*

1. Deciphering quantum fingerprints in electric conductance
   Daimon, K. Tsunekawa, S. Kawakami, T. Kikkawa, R. Ramos, K. Oyanagi, T. Ohtsuki, and E. Saitoh Nat. Commun. **13**, 3160 (2022).

2. Universality classes of the Anderson transitions driven by quasiperiodic potential in the three-dimensional Wigner-Dyson symmetry classes
   X. Luo and T. Ohtsuki Phys. Rev. B **106**, 104205 (2022)

3. Unifying the Anderson Transitions in Hermitian and Non-Hermitian Systems
   X. Luo, Z. Xiao, K. Kawabata, T. Ohtsuki, and R. Shindou Phys. Rev. Res. **4**, L022035 (2022).

4. Topological Anderson Transitions in Chiral Symmetry Classes
   Z Xiao, K Kawabata, X Luo, T Ohtsuki, and R Shindou arXiv:2211.09999

5. Irrelevant Corrections at the Quantum Hall Transition
   K. Slevin and T. Ohtsuki Phys. Status Solidi RRL **2023**, 2300080 (2023).

OKUBO, Masashi [B class; 1100 (B), 170 (C)] (132)
— *Charge storage mechanism of layered transition metal carbides with regulated terminal groups*
— *Exploration of transition-metal carbides and nitrides*

OKUBO, Tsuyoshi [C class; 6200 (B), 500 (C)] (228)
— *Novel phenomena in frustrated magnets*

1. Hunting for quantum-classical crossover in condensed matter problems
   N. Yoshioka, T. Okubo, Y. Suzuki, Y. Koizumi, and W. Mizukami, arXiv:2210.14109
   DOI:10.48550/arXiv.2210.14109

2. TeNeS: Tensor Network Solver for Quantum Lattice Systems
   Y. Motoyama, T. Okubo, K. Yoshimi, S. Morita, T. Kato, and N. Kawashima, Comput. Phys. Commun. **279**, 108437 (2022).
   DOI:10.1016/j.cpc.2022.108437

3. 拡張キタエフ模型における熱ホール伝導度のテンソルネットワーク法による研究
   大久保毅、固体物理 **57**, 633 (2022).

OKUMURA, Hisashi [C class; 3800 (B), 350 (C)] (251)
— *Molecular dynamics simulation of disease-related biomolecules*

1. Molecular Dynamics Simulation Studies on the Aggregation of Amyloid-β Peptides and Their Disaggregation by Ultrasonic Wave and Infrared Laser Irradiation
   H. Okumura and S. G. Itoh, Molecules **27**, 2483 (2022).
   DOI:10.3390/molecules27082483

2. Key residue for aggregation of amyloid-β peptides
   S. G. Itoh, M. Yagi-Utsumi, K. Kato, and H. Okumura, ACS Chem. Neurosci. **13**, 31393151 (2022).
   DOI:10.1021/acschemneuro.2c00358

OKUMURA, Masahiko [B class; 500 (B), 90 (C)] (317)
— *Machine learning molecular dynamics studies of complex structural materials*

ONO, Atsushi [B class; 200 (B), 80 (C)] (212)
— *Photoinduced nonequilibrium dynamics in itinerant magnets*

1. Energy-band echoes: Time-reversed light emission from optically driven quasiparticle wave packets
   S. Imai, A. Ono, and S. Ishihara, Phys. Rev. Res. **4**, 043155 (2022).
   DOI:10.1103/PhysRevResearch.4.043155

ONO, Shota [B class; 900 (B), 130 (C)] (140)
— *Metastable structure map of Lennard-Jones cluster based on vibrational frequency analysis*
— *Stable structure of 2D metals on graphene substrate*
— *Surface Alloy Database*

1. Optimization of configurations of atomic species on two-dimensional hexagonal lattices for copper-based systems
   S. Ono, AIP Adv. **12**, 085313 (2022).
   DOI:10.1063/5.0098517

2. Two-Dimensional Ionic Crystals: The Cases of IA-VII Alkali Halides and IA-IB CsAu
   S. Ono, J. Phys. Soc. Jpn. **91**, 094606 (2022).
   DOI:10.7566/JPSJ.91.094606

3. Small atoms fall into bulk from non-close-packed metal surfaces?
   S. Ono, H. Satomi, and J. Yuhara, Comp. Mater. Sci. **218**, 111959 (2023).
   DOI:10.1016/j.commatsci.2022.111959

ONO, Tomoya [C class; 12800 (B), 1000 (C)] (53)
— *Development of first-principles calculation code RSPACE and design of highly functional interface*

1. Density functional theory calculations for investigation of atomic structures of 4H-SiC/SiO_2 interface after NO annealing
   N. Komatsu, M. Ohmoto, M. Uemoto, and T. Ono, J. Appl. Phys. **132**, 155701 (2022).

2. Density functional study of twisted graphene $L1_0$-FePd heterogeneous interface
   M. Uemoto, H. Adachi, H. Naganuma and T. Ono, J. Appl. Phys. **132**, 095301 (2022).

3. Unique electrical signature of phosphate for specific single-molecule detection of peptide phosphorylation
   T. Harashima, Y. Egami, K. Homma, Y. Jono, S. Kaneko, S. Fujii, T. Ono, and T. Nishino, J. Am. Chem. Soc. **144**, 17449 (2022).

OSHIKAWA, Masaki [B class; 600 (B), 90 (C)] (314)
— *Gapless symmetry-protected topological phase in anisotropic triangle strips*

1. Gapless symmetry-protected topological phase of quantum antiferromagnets on anisotropic triangular strip
   Y. Hidaka, S. C. Furuya, A. Ueda, and Y. Tada, Phys. Rev. B **106**, 144436 (2022).
   DOI:10.1103/PhysRevB.106.144436

2. Tensor network renormalization study on the crossover in classical Heisenberg and RP^2 models in two dimensions
   A. Ueda and M. Oshikawa Phys. Rev. E **106**, 014104 (2022).
   DOI:10.1103/PhysRevE.106.014104

OSHIYAMA, Atsushi [E class; 16500 (B), 1200 (C)] (48)
— *Clarification of Microscopic Mechanisms of Semiconductor Epitaxial Growth and Device-Interface Formation by Large-Scale Quantum-Theory-Based Computations*

1. An atomistic insight into reactions and free-energy profiles of NH_3 and Ga on GaN surfaces during the epitaxial growth
   M. Boero, K. M. Bui, K. Shiraishi, K. Ishisone, Y. Kangawa, and A. Oshiyama, Appl. Surf. Sci. **599**, 153935 (2022).

2. Microscopic identification of stepped SiC (0001) and the reaction site of hydrogen-rich epitaxial growth
   T. Kimura, K. Chokawa, K. Shiraishi, and A. Oshiyama, Phys. Rev. B **106**, 035309 (2022).

3. Chickens or Eggs in the Atomic World: Structures and Electronic Properties of Defects in Semiconductors
   A. Oshiyama JPSJ News and Comments **19**, 12 (2022).

4. Atomistic insight into initial stage of graphene formation on SiC (0001) surfaces
   M. Boero, F. Imoto and A. Oshiyama, Phys. Rev. Materials **6**, 093403 (2022).

5. Atomic and electronic structures of nitrogen vacancies in silicon nitride: Emergence of floating gap states
   F. Nanataki, K. Shiraishi, J.-I. Iwata, Y.-i. Matsushita, and A. Oshiyama, Phys. Rev. B **106**, 155201 (2022).

6. Insight into the Step Flow Growth of Gallium Nitride based on Density Functional Theory
   K. M. Bui, K. Shiraishi and A. Oshiyama, Appl. Surf. Sci. **613**, 155840 (2023).

7. Atomic and electronic structures of interfaces between amorphous $(Al_2O_3)_{1-x}(SiO_2)_x$ and GaN polar surfaces revealed by first-principles simulated annealing technique
   K. Chokawa, K. Shiraishi and A. Oshiyama, J. Appl. Phys **133**, 065301 (2023).

8. Microscopic physical origin of charge traps in 3D NAND flash memories
   F. Nanataki, J.-i. Iwata, K. Chokawa, M. Araidai, A. Oshiyama and K. Shiraishi, Jpn. J. Appl. Phys. **62**, SC1038 (2023).

OTANI, Minoru [C class; 5000 (B), 0 (C)] (87)
— *First-principles simulation of interfacial reactions using density functional theory and classical liquid theory*

1. Theoretical Consideration of Side Reactions between the VS4 Electrode and Carbonate Solvents in Lithiummetal Polysulfide Batteries
   S. Hagiwara、J. Haruyama, M. Otani, Y. Umemura, T. Takeuchi, and H. Sakaebe, Electrochemistry **90**, 107002 (2022).
   DOI:10.5796/electrochemistry.22-00087

2. Development of a dielectrically consistent reference interaction site model combined with the density functional theory for electrochemical interface simulations
   S. Hagiwara, S. Nishihara, F. Kuroda, and M. Otani, Phys. Rev. Mater. **6**, 093802 (2022).
   DOI:10.1103/PhysRevMaterials.6.093802

3. Theoretical Analysis on the Stability of 1-Pyrenebutanoic Acid Succinimidyl Ester Adsorbed on Graphene
   Y. Oishi, H. Ogi, S. Hagiwara, M. Otani, and K. Kusakabe, ACS Omega, bf 7, 31120 (2022).
   DOI:10.1021/acsomega.2c03257

OTSUKI, Junya [B class; 500 (B), 90 (C)] ()
— *Dynamical mean-field study of rare-earth ferromagnetic compounds*

OTSUKI, Michio [C class; 200 (B), 0 (C)] (350)
— *Shape dependence of macroscopic friction between solids*
1. Static friction coefficient depends on the external pressure and block shape due to precursor slip
   W. Iwashita, H. Matsukawa, and M. Otsuki, Sci. Rep. **13**, 2511 (2023).
   DOI:10.1038/s41598-023-29764-w

OYA, Yutaka [C class; 3200 (B), 300 (C)] (260)
— *Molecular dynamics simulation for chemical reactions in multicomponent systems of thermosetting resins*

OZAKI, Taisuke [C class; 6200 (B), 500 (C)] (72)
— *Computational materials discovery based on densest ternary sphere packings*
1. Diverse densest ternary sphere packings
   R. Koshoji and T. Ozaki J. Phys. Commun. 6, 075002 (2022).
   DOI:10.1088/2399-6528/ac7d38

2. Prediction of quaternary hydrides based on densest ternary sphere packings
   R. Koshoji, M. Fukuda, M. Kawamura and T. Ozaki Phys. Rev. Mater. 6, 114802 (2022).
   DOI:10.1103/PhysRevMaterials.6.114802

OZEKI, Yukiyasu [C class; 6000 (B), 0 (C)] (238)
— *Development and applications of scaling analysis for critical phenomena*
— *Gauss process regression applied to relaxation of fluctuation for estimations of critical exponents*
1. Size-Independent Scaling Analysis for Explosive Percolation
   K. Hagiwara and Y. Ozeki Phys. Rev E **106**, 054138 (2022).

PETERS, Robert [C class; 2400 (B), 100 (C)] (202)
— *Correlation induced phenomena in Kondo lattice systems*
1. Quantum metric on the Brillouin zone in correlated electron systems and its relation to topology for Chern insulators
   T. Kashihara, Y. Michishita, and R. Peters Phys. Rev. B 107, 125116 (2023).
   DOI:10.1103/PhysRevB.107.125116

2. Low-energyexcitations and transport functions of the one-dimensional Kondo insulator
   R. Peters and R. Rausch, submitted to SciPost Physics
   ,

RAEBIGER, Hannes [C class; 4000 (B), 350 (C)] ()
— *First Principles calculation of carrier doping in Mott Insulators*

SAITO, Shinji [C class; 1200 (B), 0 (C)] (283)
— *Theoretical stuidies on dynamics in biomolecular and liquid systems*

SAKAGUCHI, Norihito [C class; 7800 (B), 0 (C)] (70)
— *Reduction of Rare Metals in Fuel Cell and Formic Acid Decomposition Catalysts*

SAKAI, Masatoshi [B class; 300 (B), 70 (C)] (338)
— *Charge distribution in low excitation state of organic charge order materials*

SAKAI, Toru [C class; 6600 (B), 700 (C)] (223, 225)
— *Magnetization Plateau with Spontaneous Symmetry Breaking*
— *Numerical Study on Novel Spin Nematic Phase*

1. Field-induced spin nematic Tomonaga-Luttinger liquid of the $S = 1/2$ spin ladder system with anisotropic ferromagnetic rung interaction
   T. Sakai, R. Nakanishi, T. Yamada, R. Furuchi, H. Nakano, H. Kaneyasu, K. Okamoto and T. Tonegawa, Phys. Rev. B 106 (2022) 064433

2. S=2 Quantum Spin Chain with the Biquadratic Exchange Interaction
   T. Sakai, T. Yamada, R. Nakanishi, R. Furuchi, H. Nakano, H. Kaneyasu, K. Okamoto and T. Tonegawa, J. Phys. Soc. Jpn. 91 (2022) 074702

3. The Haldane Gap of the $S = 1$ Heisenberg Antiferromagnetic Chain
   H. Nakano, H. Tadano, N. Todoroki and T. Sakai, J. Phys. Soc. Jpn. 91 (2022) 074701

4. Field-Induced Quantum Spin Nematic Liquid Phase in the $S = 1$ Antiferromagnetic Heisenberg Chain with Additional Interactions
   T. Sakai, H. Nakano, R. Furuchi and K. Okamoto, J. Phys.: Conf. Ser. 2164 (2022) 012030

5. Magnetization plateau of the distorted diamond spin chain with anisotropic ferromagnetic interaction
   T. Sakai, K. Okamoto, H. Nakano and R. Furuchi, AIP Adv. 12 (2022) 035030

6. Spin Nematic Liquid of the $S = 1/2$ Distorted Diamond Spin Chain in Magnetic Field
   T. Sakai, H. Nakano, R. Fruchi and K. Okamoto, AIP Adv. 13 (2023) 015313

7. Quantum Phase Transition of the Shastry-Sutherland System and ESR Forbidden Transition
   T. Sakai, R. Furuchi and H. Nakano, to appear in JPS Conf. Proc.

8. Field-Induced Spin Nematic Liquid of the $S = 1/2$ Bond-Alternating Chain with the Anisotropy
   R. Nakanishi, T. Yamada, R. Furuchi, H. Nakano, H. Kaneyasu, K. Okamoto, T. Tonegawa and T. Sakai, to appear in JPS Conf. Proc.

9. Translational Symmetry Broken Magnetization Plateau of the $S = 2$ Antiferromagnetic Chain with Anisotropies
   T. Yamada, R. Nakanishi, R. Furuchi, H. Nakano, H. Kaneyasu, K. Okamoto, T. Tonegawa and T. Sakai, to appear in JPS Conf. Proc.

10. Numerical Study of $S = 1/2$ Heisenberg Antiferromagnet on the Floret Pentagonal Lttice
    R. Furuchi, H. Nakano and T. Sakai, to appear in JPS Conf. Proc.

11. Large-Scale Numerical Diagonalization Study of the Shastry-Sutherland Model
    H. Nakano and T. Sakai, to appear in JPS Conf. Proc.

12. Nematic Tomonaga-Luttinger Liquid Phase in an $S = 1/2$ Ferromagnetic-Antiferromagnetic Bond-Alternating Chain
    T. Tonegawa, K. Okamoto, K. Nomura and T. Sakai, to appear in JPS Conf. Proc.

13. Quantum spin nematic liquid in the low-dimensional anisotropic magnets -$S = 1/2$ delta spin chain with the anisotropic ferromagnetic interaction in magnetic field-
    T. Sakai, R. Furuchi, H. Nakano and K. Okamoto, to apper in SciPost Physics

SAKAKIBARA, Hirofumi [B class; 500 (B), 0 (C)] (172)
— *A study of nickelate superconductors in first-principles*

SAKASHITA, Tatsuya [B class; 200 (B), 60 (C)] (347)
— *Development of integrated interface of eigensolvers Rokko and application to quantum spin systems*

SASAKI, Takehiko [C class; 1200 (B), 200 (C)] (127)
— *Study on oxidation and sulfurization of platinum nanoparticles*

SATO, Masahiro [D class; 6000 (B), 250 (C)] (75)
— *Discovery of Super-Composite Electrical Insulating Materials Based on Multiscale Physics and Deep Learning of Polymers*

1. Extrapolative molecular property prediction using quantum chemistry-assisted machine learning for accelerated materials discovery
   H. Shimakawa, A. Kumada, and M. Sato, Nature Communications, in preparation

2. Direct measurement of charge trap depth in polymer nanocomposites
   H. Suzuki, Y. Kubo, Y. Sekiguchi, M. Kobayashi, A. Kumada, and M. Sato Journal of Physics D: Applied Physics, under review

3. Au/ポリプロピレン界面，Au/ポリイミド界面のバンドアラインメントの解明
   D. Katase, H. Suzuki, R. Yoshinaga, M. Kobayashi, A. Kumada, and M. Sato IEEJ Transactions on Fundamentals and Materials, accepted for publication

4. Probing the Band Alignment at the Metal/Dielectric Polymer interface
   D. Katase, H. Suzuki, M. Kobayashi, A. Kumada, and M. Sato Transactions on Dielectrics and Electrical Insulation, under review

SATO, Ryuhei [C class; 1200 (B), 0 (C)] (281)
— *the study on super ionic conduction and phase transition by disordering of complex hydride*

1. Topological Data Analysis of Ion Migration Mechanism
   R. Sato, K. Akagi, S. Takagi, K. Sau, K. Kisu, H. Li, and S.-i. Orimo, J. Chem. Phys. 158, 144116 (2023).
   DOI:10.1063/5.0143387

2. A Noise-Robust Data Assimilation Method for Crystal Structure Prediction Using Powder Diffraction Intensity
   S. Yoshikawa, R. Sato, R. Akashi, S. Todo, and S. Tsuneyuki, J. Chem. Phys. **157**, 224112 (2022).
   DOI:10.1063/5.0125553

SATO, Shunsuke [C class; 3200 (B), 0 (C)] (113)
— *First-principles analysis for nonlinear optical responses based on the transition current density*

1. Frequency-resolved microscopic current density analysis of linear and nonlinear optical phenomena in solids
   S. A. Sato, arXiv.2302.05859
   DOI:10.48550/arXiv.2302.05859

SAWABE, Kyoichi [C class; 5200 (B), 0 (C)] (85)
— *Prediction of CO adsorption energy on single atom catalysts embedded in TiO_2 by machine learning*

SEKI, Yuya [B class; 400 (B), 70 (C)] (328)
— *Analysis of Ising model in statistical-mechanical informatics*

1. Black-box optimization for integer-variable problems using Ising machines and factorization machines
   Y. Seki, R. Tamura, and S. Tanaka, arXiv.2209.01016
   DOI:10.48550/arXiv.2209.01016

SHAO, Cheng [C class; 3200 (B), 350 (C)] ()
— *Machine-learning optimization of ionic liquids for energy storage application*

SHIMADA, Toshihiro [B class; 400 (B), 80 (C)] (174)
— *Computational search for narrow bandgap organic charge transfer complex*

1. Molecular Dynamics Simulation of Poly(Ether Ether Ketone) (PEEK) Polymer to Analyze Intermolecular Ordering by Low Wavenumber Raman Spectroscopy and X-ray Diffraction
   X. Yang, S. Yokokura, T. Nagahama, M. Yamaguchi, and T. Shimada, Polymers **14**, 5406 (2022).
   DOI:10.3390/polym14245406

2. Synthesis of Epitaxial MoS_2/MoO_2 CoreShell Nanowires by Two-Step Chemical Vapor Deposition with Turbulent Flow and Their Physical Properties
   M. Goto, I. Yamane, S. Arasawa, T. YAnase, S. Yokokura, T. Nagahama, Y. Chueh, Y. Shin, Y. Kim, and T. Shimada, ACS Omega **7**, 39362 (2022).
   DOI:10.1021/acsomega.2c05586

SHIMAMURA, Kohei [C class; 4200 (B), 350 (C)] ()
— *Thermal Conductivity calculation with ANN potential for multi-component heterogeneous materials*

1. Thermal conductivity calculation based on GreenKubo formula using ANN potential for β-Ag_2Se
   Y. Takeshita, K. Shimamura, S. Fukushima, A. Koura, and F. Shimojo, J. Phys. Chem. Solids **163** (2022) 110580.

2. Importance of Adjusting Coefficients in Cost Function for Construction of High-Accuracy Machine-Learning Interatomic Potential
   A. Irie, K. Shimamura, A. Koura, and F. Shimojo, J. Phys. Soc. Jpn. **91** (2022) 045002.

SHIMOJO, Fuyuki [C class; 5000 (B), 400 (C)] (15)
— *First-Principles Molecular-Dynamics Study of Structural and Electronic Properties of Covalent Liquids and Glasses under Pressure*

SHIMOKAWA, Tokuro [C class; 4200 (B), 750 (C)] (245)
— *Thermal effects on quantum frustrated magnetisms*
— *Thermal effects on the frustrated magnets*

1. Quantum paramagnetic states in the spin-1/2 distorted honeycomb-lattice Heisenberg antiferromagnet:Application to $Cu_2(pymca)_3(ClO_4)$
   T. Shimokawa, K. Takano, Z. Honda, A. Okutani, and M. Hagiwara, Phys. Rev. B **106**, 134410 (2022).
   DOI:10.1103/PhysRevB.106.134410

SHINAOKA, Hiroshi [C class; 4200 (B), 400 (C)] (195)
— *First-principles calculations of dynamical susceptibilities for strongly correlated materials*

SHINODA, Wataru [E class; 29500 (B), 1300 (C)] (216)
— *Large-scale Molecular Simulation of Soft Materials using All-Atom and Coarse-Grained Model*

1. Adsorption characteristics of peptides on ω-functionalized self-assembled monolayers: a molecular dynamics study
H. O. S. Yadav, A.-T. Kuo, S. Urata, K. Funahashi, Y. Imamura, and W. Shinoda, Phys. Chem. Chem. Phys. **24**, 14805 (2022).
DOI:10.1039/D2CP01348G

2. SPICA Force Field for Proteins and Peptides
S. Kawamoto, H. Liu, Y. Miyazaki, S. Seo, M. Dixit, R. DeVane, C. MacDarmaid, G. Fiorin, M. L. Klein, and W. Shinoda, J. Chem. Theory Comput. **18**, 3204 (2022).
DOI:10.1021/acs.jctc.1c01207

3. Cooperative antimicrobial action of melittin on lipid membranes: A coarse-grained molecular dynamics study
Y. Miyazaki and W. Shinoda, Biochim. Biophys. Acta-Biomembr. **1864**, 183955 (2022).
DOI:10.1016/j.bbamem.2022.183955

4. Amphotericin B assembles into seven-molecule ion channels: An NMR and molecular dynamics study
Y. Umegawa, T. Yamamoto, M. Dixit, K. Funahashi, S. Seo, Y. Nakagawa, T. Suzuki, S. Matsuoka, H. Tsuchikawa, Sh. Hanashima, T. Oishi, N. Matsumori, W. Shinoda, and M. Murata, Sci. Adv. **8**, eabo2658 (2022).
DOI:10.1126/sciadv.abo2658

5. Fluorescence Turn - on of Tetraphenylethylene Derivative by Transfer from Cyclodextrin to Liposomes, HeLa cells, and E. coli
K. Masuda, R. Omokawa, R. Kawasaki, Y. Mise, Y. Ooyama, S. Harada, W. Shinoda, and A. Ikeda, Chem. Eur. J. **29**, e202203071 (2023).
DOI:10.1002/chem.202203071

6. Liquid Structures and Ion Dynamics of Ionic Liquids viewed from Intermolecular Interactions
S. Tsuzuki, and W. Shinoda, Chem. Rec. e202200272 (2023).
DOI:10.1002/tcr.202200272

7. Self-Assembly of Glycerol-Amphiphilic Janus Dendrimers Amplifies and Indicates Principles for the Selection of Stereochemistry by Biological Membranes
D. Zhang, Q. Xiao, M. Rahimzadeh, M. Liu, C. Rodriguez-Emmenegger, Y. Miyazaki, W. Shinoda, and V. Percec, J. Am. Chem. Soc. **145**, 4311 (2023).
DOI:10.1021/jacs.3c00389

SHINOHARA, Yasushi [C class; 1800 (B), 0 (C)] (124)
— *First-principles simulations for optical absorption of dielectrics under multi-color laser field*

1. Semiclassical description of electron dynamics in extended systems under intense laser fields
M. Tani, K. Sasaki, Y. Shinohara, and K. L. Ishikawa, Phys. Rev. B **106**, 195141 (2022).
DOI:10.1103/PhysRevB.106.195141

SHIOMI, Junichiro [C class; 9400 (B), 900 (C)] (59)
— *Development of Thermal Functional Materials Based on First-principles Simulations*

1. Anharmonic phonon renormalization and thermal transport in the type-I $Ba_8Ga_{16}Sn_{30}$ clathrate from first principles
M. Ohnishi, T. Tadano, S. Tsuneyuki, and J. Shiomi, Phys. Rev. B **106**, 24303 (2022).
DOI:10.1103/PhysRevB.106.024303

2. A Qualitative Study of the Disorder Effect on the Phonon Transport in a Two-Dimensional

Graphene/h-BN Heterostructure
Y Liu, W Ren, M An, L Dong, L Gao, X Shai, T Wei, L Nie, S Hu and C Zeng, Frontiers in Materials **9**, 913764 (2022).
DOI:10.3389/fmats.2022.913764

3. Photonic design for color compatible radiative cooling accelerated by materials informatics
Jiang Guo, Shenghong Ju, Yaerim Lee, A. Alperen Gunay, Junichiro Shiomi, International Journal of Heat and Mass Transfer **195**, 123193 (2022).
DOI:10.1016/j.ijheatmasstransfer.2022.123193

4. P-TRANS: A Monte Carlo ray-tracing software to simulate phonon transport in arbitrary nanostructures
C. Shao, T. Hori, and J. Shiomi, Comput. Phys. Commun. **276**, 108361 (2022).
DOI:10.1016/j.cpc.2022.108361

5. Negligible contribution of inter-dot coherent modes to heat conduction in quantum-dot superlattice
C. Shao and J. Shiomi, Mater. Today Phys. **22**, 100601 (2022).
DOI:10.1016/j.mtphys.2021.100601

SHIRAI, Tatsuhiko [B class; 1000 (B), 80 (C)] (290)
— *An Ising machine based on multi-spin flip method*
— *Quantum algorithm for an Ising machine*

1. Multi-spin-flip engineering in an Ising machine
T. Shirai and N. Togawa, IEEE Transactions on Computers **72** (2022) 759.

2. Spin-Variable Reduction Method for Handling Linear Equality Constraints in Ising Machines
T. Shirai and N. Togawa IEEE Transactions on Computers (Early Access)

SHIRAISHI, Kenji [C class; 10000 (B), 0 (C)] (62,63)
— *First Principles Studies on Si-rich a-SiN for Flash Memory Application*
— *First Principles Studies on Spin Tranfer Torque Magnetic Randum Access Memory (STT-MRAM)*

1. Atomic and electronic structures of nitrogen vacancies in silicon nitride: Emergence of floating gap states
F. Nanataki, K. Shiraishi, J. Iwata, Y. Matsushita, and A. Oshiyama, Phys. Rev. B, 106, (2022) 155201

2. Effect of interfacial nitrogen defects on tunnel magnetoresistance in an Fe/MgO/Fe magnetic tunnel junction
Y. Ogawa, M. Araidai, T. Endoh, and K. Shiraishi, J. Appl. Phys., 132, (2022) 213904

3. Microscopic physical origin of charge traps in 3D NAND flash memories
F. Nanataki, J. Iwata, K. Chokawa, M. Araidai, A. Oshiyama, and K. Shiraishi, Jpn. J. Appl. Phys., 62, (2023) SC1038

4. Effect of MgO Grain Boundaries on the Interfacial Perpendicular Magnetic Anisotropy in Spin-transfer torque Magnetic Random-Access Memory: A First-Principles Study
K. Morishita, Y. Harashima, M. Araidai, T. Endoh, and K. Shiraishi, IEEE Transactions on Magnetics, 59 (2023) 1

SHUDO, Ken-ichi [C class; 1200 (B), 50 (C)] (133)
— *Ultrafast adsorption states of two-dimensional metal-organic-frameworks and semiconductors*

1. K-point longitudinal acoustic phonons are responsible for ultrafast intervalley scattering in mono-

layer $MoSe_2$
S. Bae, K. Matsumoto, H. Raebiger, K.-i. Shudo, Y.-H. Kim, Ø. S. Handegård, T. Nagao, M. Kitajima, Y. Sakai, X. Zhang, R. Vajtai, P. Ajayan, J. Kono, J. Takeda, and I. Katayama, Nat. Commun. 13, 4279 (2022).
DOI:10.1038/s41467-022-32008-6

SUGINO, Osamu [E class; 16500 (B), 1300 (C)] (47)
— *Prediction of material properties using the density functional theory*

1. Roadmap on Machine Learning in Electronic Structure
   H. J. Kulik et al. Electron. Struct. 4, 023004 (2022).
   DOI:10.1088/2516-1075/ac572f

2. First-principles electronic structure investigation of $HgBa_2Ca_{n-1}Cu_nO_{2n+2+x}$ with the SCAN density functional
   A. N. Tatan, J. Haruyama, and O. Sugino AIP Adv. 12, 105308 (2022).
   DOI:10.1063/5.0098554

3. Effect of Nitrogen Doping and Oxygen Vacancy on the Oxygen Reduction Reaction on the Tetragonal Zirconia(101) Surface
   S. Muhammady, J. Haruyama, S. Kasamatsu, and O. Sugino J. Phys. Chem. C 126, 15662 (2022).
   DOI:10.1021/acs.jpcc.2c04132

SUWA, Hidemaro [C class; 5000 (B), 450 (C)] (240)
— *Large-scale simulation of spin dynamics in the vicinity of a phase transition point*

1. Lifted directed-worm algorithm
   H. Suwa, Phys. Rev. E **106**, 055306 (2022).
   DOI:10.1103/PhysRevE.106.055306

2. Reducing rejection exponentially improves Markov chain Monte Carlo sampling
   H. Suwa, submitted to Physica A: Statistical mechanics

SUZUKI, Takafumi [C class; 2800 (B), 300 (C)] (265)
— *Dynamical properties of the extended Kitaev-Γ model on a honeycomb lattice*

SUZUKI, Takehito [B class; 200 (B), 40 (C)] (348)
— *Determining the period of the mainshock repetition with foreshocks in terms of permeability profile*
— *Estimation of the transition time from slow to fast earthquakes and its mathematical implications*

1. Deriving the slip front propagation velocity with the slip-dependent and slip-velocity-dependent friction laws via the use of the linear marginal stability hypothesis
   T. Suzuki Phys. Rev. E **106**, 015002 (2022).
   DOI:10.1103/PhysRevE.106.015002

SUZUKI, Yoshikazu [B class; 100 (B), 30 (C)] ()
— *Electronic state calculation of inorganic energy materials using Quantum Espresso*

SUZUKI, Yuji [C class; 4400 (B), 0 (C)] (95)
— *Development of Polymer Electret Materials for Energy Harvesting Using Machine Learning*

1. Property Prediction of Polymer Electret Material with Physics-informed Neural Network
   Y. Zhang, K. Suzuki, and Y. Suzuki, 日本機械学会熱工学コンファレンス 2022, 東京, A234, (2022).

2. Intrinsically-stretchable Polymer Electret for Powering Skin Electronics

R. Wang, K. Suzuki, T. Miyoshi, and Y. Suzuki, 1th Int. Conf. on Micro and Nanotechnology for Power Generation and Energy Conversion Applications (PowerMEMS 2022), Salt Lake City, T1A-01 (2022).

3. エレクトレットを用いた環境発電
鈴木 雄二, 静電気学会誌, 49(2), 50 (2022).

TAKAYAMA, Akari [B class; 300 (B), 0 (C)] (344)
— *Structure analysis of borophene by using 2DMAT*

1. Structure of χ_3 borophene studied by total-reflection high-energy positron diffraction (TRHEPD)
Y. Tsujikawa, M. Shoji, M. Hamada, T. Takeda, I. Mochizuki, T. Hyodo, I. Matsuda, and A. Takayama Molecules **27**, 4219 (2022).
DOI:10.3390/molecules27134219

TAKETSUGU, Tetsuya [C class; 2200 (B), 250 (C)] (117)
— *Ab initio study on the structure and functions of nanomaterials*

1. Superior Multielectron-Transferring Energy Storage by π-d Conjugated Frameworks
D. Xia, K. Sakaushi, A. Lyalin, K. Wada, S. Kumar, M. Amores, H. Maeda, S. Sasaki, T. Taketsugu, and H. Nishihara Small, 18, 2202861 (2022).
DOI:10.1002/smll.202202861

TAMURA, Ryo [B class; 300 (B), 80 (C)] (334)
— *Development of black-box optimization method for phase diagram*

1. Machine-learning-based phase diagram construction for high-throughput batch experiments
R. Tamura, G. Deffrennes, K. Han, T. Abe, H. Morito, Y. Nakamura, M. Naito, R. Katsube, Y. Nose, and K. Terayama Science and Technology of Advanced Materials: Methods **2** (2022) 153.

2. Bayesian optimization package: PHYSBO
Y. Motoyama, R. Tamura, K. Yoshimi, K. Terayama, T. Ueno, and K. Tsuda, Comput. Phys. Commun. **278** (2022) 108405.

3. Automatic Rietveld refinement by robotic process automation with RIETAN-FP
R. Tamura, M. Sumita, K. Terayama, K. Tsuda, F. Izumi, and Y. Matsushita Science and Technology of Advanced Materials: Methods **2** (2022) 435.

TANAKA, Shu [B class; 300 (B), 70 (C)] (336)
— *Study on novel algorithm for Ising machines*

1. A phase-field model by an Ising machine and its application to the phase-separation structure of a diblock polymer
K. Endo, Y. Matsuda, S. Tanaka, and M. Muramatsu, Sci. Rep. **12**, 10794 (2022).
DOI:10.1038/s41598-022-14735-4

2. Black-box optimization for integer-variable problems using Ising machines and factorization machines
Y. Seki, R. Tamura, and S. Tanaka, submitted to IEEE Access.

3. Towards optimization of photonic-crystal surface-emitting lasers via quantum annealing
T. Inoue, Y. Seki, S. Tanaka, N. Togawa, K. Ishizaki, and S. Noda Opt. Exp. **30**, 43503 (2022).
DOI:10.1364/OE.476839

4. Quantum annealing and computation: challenges and perspectives
   B. K. Chakrabarti, H. Leschke, P. Ray, T. Shirai, and S. Tanaka Phil. Trans. Roy. Soc. A **381**, 20210419 (2023).
   DOI:10.1098/rsta.2021.0419

5. ISAAQ: Ising Machine Assisted Quantum Compiler
   S. Naito, Y. Hasegawa, Y. Matsuda, and S. Tanaka submitted to PRX Quantum.

TATETSU, Yasutomi [C class; 3600 (B), 350 (C)] (107)
— *Ab-initio research on nano structures of materials' surfaces and grain boundaries with magnetic elements*

TEN-NO, Seiichiro L. [D class; 10000 (B), 500 (C)] (57)
— *Theoretical study of point defects in visible-light-driven semiconductor photocatalysts using first-principles calculations*

TERAO, Takamichi [B class; 1000 (B), 170 (C)] (285)
— *Structural formation of inverse patchy particles*

1. Eigenstates in gainloss systems of metallic-mean quasiperiodic chains
   T. Terao, Physica D **444**, 133612 (2023).

TEZUKA, Masaki [C class; 3400 (B), 400 (C)] (257)
— *Measurement-induced phase transition and chaotic dynamics in quantum many-body systems*

1. Binary-coupling sparse Sachdev-Ye-Kitaev model: An improved model of quantum chaos and holography
   M. Tezuka, O. Oktay, E. Rinaldi, M. Hanada, and F. Nori, Phys. Rev. B **107**, L081103 (2023).
   DOI:10.1103/PhysRevB.107.L081103

2. Hayden-Preskill Recovery in Hamiltonian Systems
   Y. Nakata and M. Tezuka, submitted to Phys. Rev. Lett.

Data Repository
Dataset for "Binary-coupling sparse Sachdev-Ye-Kitaev model: an improved model of quantum chaos and holography"
https://zenodo.org/record/7514850
DOI:10.5281/zenodo.7514849

TODO, Synge [C class; 6400 (B), 500 (C)] (226)
— *Simulation of quantum many-body systems by tensor network and sampling*

1. Optimized Implementation for Calculation and Fast-Update of Pfaffians Installed to the Open-Source Fermionic Variational Solver mVMC
   R.Q. G. Xu, T. Okubo, S. Todo, and M. Imada Comp. Phys. Comm. **277**, 108375 (2022).
   DOI:10.1016/j.cpc.2022.108375

2. Nematicity and fractional magnetization plateaus induced by spin-lattice coupling in the classical kagome-lattice Heisenberg antiferromagnet
   M. Gen and H. Suwa, Phys. Rev. B **105**, 174424 (2022).
   DOI:10.1103/PhysRevB.105.174424

3. TeNeS: Tensor Network Solver for Quantum Lattice Systems
   Y. Motoyama, T. Okubo, K. Yoshimi, S. Morita, T. Kato, and N. Kawashima, Comp. Phys. Comm. **279**, 108437 (2022).

DOI:10.1016/j.cpc.2022.108437

4. Quasi-Two-Dimensional Anomalous Hall Mott Insulator of Topologically Engineered Jeff=1/2 Electrons
J. Yang, H. Suwa, D. Meyers, H. Zhang, L. Horak, Z. Wang, G. Fabbris, Y. Choi, J. Karapetrova, J.-W. Kim, D. Haskel, P. J. Ryan, M. P. M. Dean, L. Hao, and J. Liu Phys. Rev. X **12**, 031015 (2022).
DOI:10.1103/PhysRevX.12.031015

5. MateriApps LIVE! and MateriApps Installer: Environment for starting and scaling up materials science simulations
Y. Motoyama, K. Yoshimi, T. Kato, and S. Todo, Software X **20**, 101210 (2022).
DOI:10.1016/j.softx.2022.101210

6. Bond-weighting method for the Grassmann tensor renormalization group
S. Akiyama, J. High Energy Phys. **11**, 030 (2022).
DOI:10.1007/JHEP11(2022)030

7. Lifted directed-worm algorithm
H. Suwa, Phys. Rev. E **106**, 055306 (2022).
DOI:10.1103/PhysRevE.106.055306

8. A Noise-Robust Data Assimilation Method for Crystal Structure Prediction Using Powder Diffraction Intensity
S. Yoshikawa, R. Sato, R. Akashi, S. Todo, and S. Tsuneyuki, J. Chem. Phys. **157**, 224112 (2022).
DOI:10.1063/5.0125553

TOHYAMA, Takami [C class; 4200 (B), 0 (C)] (198)
— *Transient absorption spectrum in photo-excited one-dimensional Mott insulator*

1. Glassy dynamics of the one-dimensional Mott insulator excited by a strong terahertz pulse
K. Shinjo, S. Sota, and T. Tohyama, Phys. Rev. Res. **4**, L032019 (2022).
DOI:10.1103/PhysRevResearch.4.L032019

2. Controlling inversion and time-reversal symmetries by subcycle pulses in the one-dimensional extended Hubbard model
K. Shinjo, S. Sota, S. Yunoki, and T. Tohyama, arXiv:2211.08694, submitted to Phys. Rev. B
DOI:10.48550/arXiv.2211.08694

TOKUMOTO, Yuki [B class; 400 (B), 70 (C)] (177)
— *Exploring dopants aiming at achieving high bulk insulation in Pb-based topological insulators*

TONEGAWA, Takashi [B class; 800 (B), 0 (C)] (309)
— *Numerical Study of the One-Dimensional Quantum Spin Systems*

1. S=2 Quantum Spin Chain with the Biquadratic Exchange Interaction
T. Sakai, T. Yamada, R. Nakanishi, R. Furuchi, H. Nakano, H. Kaneyasu, K. Okamoto, and T. Tonegawa, J. Phys. Soc. Jpn. **91**, 074702 (2022).

2. Field-induced spin nematic Tomonaga-Luttinger liquid of the S=1/2 spin ladder system with anisotropic ferromagnetic rung interaction
T. Sakai, R. Nakanishi, T. Yamada, R. Furuchi, H. Nakano, H. Kaneyasu, K. Okamoto, and T. Tonegawa, Phys. Rev. B. **106**, 064433 (2022).

TOYODA, Masayuki [B class; 400 (B), 0 (C)] (182)
— *Electronic Structure of Novel 2D Boron Monosulfide and Design of Related Materials*

1. Rhombohedral Boron Monosulfide as a p-Type Semiconductor
   N. Watanabe, K. Miyazaki, M. Toyoda, K. Takeyasu, N. Tsujii, H. Kusaka, A. Yamamoto, S. Saito, M. Miyakawa, T. Taniguchi, T. Aizawa, T. Mori, M. Miyauchi, and T. Kondo, Molecules 28, 1896 (2023).
   DOI:10.3390/molecules28041896

2. Direct Imaging of Band Structure for Powdered Rhombohedral Boron Monosulfide by Microfocused ARPES
   K. Sugawara, H. Kusaka, T. Kawakami, K. Yanagizawa, A. Honma, S. Souma, K. Nakayama, M. Miyakawa, T. Taniguchi, M. Kitamura, K. Horiba, H, Kumigashira, T. Takahashi, S. Orimo, M. Toyoda, S. Saito, T. Kondo, and T. Sato, Nano Lett. 23, 1673 (2023).
   DOI:10.1021/acs.nanolett.2c04048

TRAN, Ba Hung [E class; 2200 (B), 300 (C)] (115)
— *Computational screening for magnetocaloric materials and permanent magnets*

1. Direct and inverse magnetocaloric effects in FeRh alloy
   H. B. Tran, T. Fukushima, H. Momida, K. Sato, Y. Makino, and T. Oguchi J. Alloys Compd. 926, 166718 (2022).
   DOI:10.1016/j.jallcom.2022.166718

2. Effect of magnetocrystalline anisotropy on magnetocaloric properties of $AlFe_2B_2$ compound
   H. B. Tran, H. Momida, Y. Matsushita, K. Sato, Y. Makino, K. Shirai, and T. Oguchi Phys. Rev. B 105, 134402 (2022).
   DOI:10.1103/PhysRevB.105.134402

3. Insight into anisotropic magnetocaloric effect of CrI_3
   H. B. Tran, H. Momida, Y. Matsushita, K. Shirai, and T. Oguchi Acta Mater. 231, 117851 (2022).
   DOI:10.1016/j.actamat.2022.117851

4. Dzyaloshinskii-Moriya interaction in $Nd_2Fe_{14}B$ as the origin of spin reorientation and rotating magnetocaloric effect
   H. B. Tran, and Y. Matsushita Appl. Mater. Today 32, 101825 (2023).
   DOI:10.1016/j.apmt.2023.101825

5. Skyrmions in van der Waals centrosymmetric materials with Dzyaloshinskii-Moriya interactions
   H. B. Tran, and Y. Matsushita under review
   DOI:10.48550/arXiv.2209.02333

TSUKAHARA, Noriyuki [B class; 200 (B), 60 (C)] (187)
— *DFT calculations of organic halogen molecules and their reaction products on metal surfaces*

1. Substrate-Selective Intermolecular Interaction and the Molecular Self-Assemblies: 1,3,5-Tris(4-bromophenyl)benzene Molecules on the Ag(111) and Si(111) ($\sqrt{3} \times \sqrt{3}$)-Ag Surfaces
   N. Tsukahara, and J. Yoshinobu, Langmuir **38**, 8881 (2022).
   DOI:10.1021/acs.langmuir.2c00991

2. Surface-supported 2D metal-organic framework as a template to arrange metal clusters
   N. Tsukahara, R. Arafune, and J. Yoshinobu, submitted to Langmuir

TSUNEYUKI, Shinji [C class; 6200 (B), 0 (C)] (76)
— *First-principle study of photoresponsive functional materials*

1. Lattice Dielectric Properties of Rutile TiO_2: First-Principles Anharmonic Self-Consistent Phonon Study
   T. Amano, T. Yamazaki, R. Akashi, T. Tadano, and S. Tsuneyuki, Phys. Rev. B **107**, 094305 (2023).
   DOI:10.1103/PhysRevB.107.094305

2. A noise-robust data assimilation method for crystal structure determination using powder diffraction intensity
   S. Yoshikawa, R. Sato, R. Akashi, S. Todo and S. Tsuneyuki, J. Chem. Phys. **157**, 224112 (2022).
   DOI:10.1063/5.0125553

3. First-Principles Study of the Optical Dipole Trap for Two-Dimensional Excitons in Graphane
   H. Katow, R. Akashi, Y. Miyamoto, and S. Tsuneyuki, Phys. Rev. Lett. **129**, 047401 (2022).
   DOI:110.1103/PhysRevLett.129.047401

4. Anharmonic phonon renormalization and thermal transport in the type-I $Ba_8Ga_{16}Sn_{30}$ clathrate from first principles
   M. Ohnishi, T. Tadano, S. Tsuneyuki, and J. Shiomi, Phys. Rev. B **106**, 024303 (2022).
   DOI:10.1103/PhysRevB.106.024303

UCHIDA, Ken [C class; 2800 (B), 400 (C)] ()
— *Calculation of thermal and electrical properties of tungsten bronze*

UCHIDA, Takashi [B class; 200 (B), 60 (C)] (346)
— *Magnetic structures of multiple-Q orders in inversion-symmetric Hubbard models*

UJIHARA, Toru [C class; 5200 (B), 0 (C)] ()
— *Analysis of the behavior of third elements to the solvent in the SiC solution method*

USUI, Hidetomo [B class; 500 (B), 90 (C)] (168)
— *First principles study on the band structures of high entropy compounds*

WAKABAYASHI, Daisuke [B class; 400 (B), 0 (C)] (331)
— *Large-scale molecular-dynamics simulation of pressure-induced coordination change in silica glass with ANN potentials*

WATANABE, Hiroshi [C class; 12200 (B), 950 (C)] (218)
— *Molecular dynamics study of dynamic properties of interface structure*
— *Non-equilibrium relaxation analysis on J1-J2 frustrated Ising model*

1. Effect of surfactants on the elasticity of the liquidliquid interface
   S. Kikuchi and H. Watanabe, J. Chem. Phys. 158, 124901 (2023).
   DOI:10.1063/5.0138733

2. Non-monotonic behavior of the Binder parameter in discrete spin systems
   H. Watanabe, Y. Motoyama, S. Morita, N. Kawashima, Prog. Theor. Exp. Phys. 2023, 033A02 (2023).
   DOI:10.1093/ptep/ptad022

WATANABE, Hiroshi [B class; 400 (B), 80 (C)] (207)
— *Unified description of cuprate high-temperature superconductors using multiband models*

1. Monte Carlo study of cuprate superconductors in a four-band *d-p* model: Role of orbital degrees of freedom
H. Watanabe, T. Shirakawa, K. Seki, H. Sakakibara, T. Kotani, H. Ikeda, and S. Yunoki, J. Phys.: Condens. Matter **35**, 195601 (2023).
DOI:10.1088/1361-648X/acc0bf

WATANABE, Satoshi [C class; 10800 (B), 900 (C)] (56)
— Analyses on local properties at complex structures such as surfaces interfaces and defects via machine-learning potentials
— Analyses related to atomic structures and atom dynamics at complex structures such as surfaces interfaces and defects

1. Using neural network potentials to study defect formation and phonon properties of nitrogen vacancies with multiple charge states in GaN
K. Shimizu, Y. Dou, E.F. Arguelles, T. Moriya, E. Minamitani, and S. Watanabe, Phys. Rev. B **106**, 054108 (2022).
DOI:10.1103/PhysRevB.106.054108

2. Realistic simulation of thermoelectric characteristics of organic semiconductors based on electronic structure calculations
M. Ohno, K. Shimizu, and S. Watanabe, Appl. Phys. Express **16**, 011005 (2023).
DOI:10.35848/1882-0786/acaaee

YAMADA, Atsuo [C class; 3200 (B), 350 (C)] (111)
— Theoretical Analysis on Structure/Electronic State of Novel Energy Storage Materials

1. Kinetic Square Scheme in Oxygen-Redox Battery Electrodes
K. Kawai, X. M. Shi, N. Takenaka, J. Jang, B. M. de Boisse, A. Tsuchimoto, D. Asakura, J. Kikkawa, M. Nakayama, M. Okubo, and A. Yamada, Energy Environ. Sci. **15**, 2591 (2022).
DOI:10.1039/D1EE03503G

2. Anhydrous Fast Proton Transport Boosted by the Hydrogen Bond Network in a Dense Oxide-Ion Array of α-MoO3
Z. Ma, X. M. Shi, S. Nishimura, S. Ko, M. Okubo, and A. Yamada, Adv. Mater. **34**, 2203335 (2022).
DOI:10.1002/adma.202203335

3. Electrode Potential Influences the Reversibility of Lithium-Metal Anodes
S. Ko, T. Obukata, T. Shimada, N. Takenaka, M. Nakayama, A. Yamada, and Y. Yamada Nat. Energy **7**, 1217 (2022).
DOI:10.1038/s41560-022-01144-0

YAMADA, Atsushi [C class; 800 (B), 200 (C)] ()
— Studies of the superconductivity and magnetic states in the strongly correlated electron systems using Hubbard models.

YAMADA, Masahiko [E class; 4000 (B), 850 (C)] (246)
— Density matrix renormalization group study of SU(N) Heisenberg models

1. Matrix Product Renormalization Group: Potential Universal Quantum Many-Body Solver
M. G. Yamada, T. Sanno, M. O. Takahashi, Y. Akagi, H. Suwa, S. Fujimoto, and M. Udagawa, submitted to Phys. Rev. Lett.

YAMAGUCHI, Naoya [B class; 700 (B), 100 (C)] (156)
— *Development of Efficient Evaluation Methods of Berry-phase-mediated Physical Properties for Large Scale Systems Using the First-principles LCPAO Method*

1. First-principles LCPAO approach for insulators under finite electric fields with forces
   N. Yamaguchi and F. Ishii, Comput. Phys. Commun. **280**, 108487 (2022).
   DOI:10.1016/j.cpc.2022.108487

2. First-principles calculation of anomalous Hall and Nernst conductivity by local Berry phase
   H. Sawahata, N. Yamaguchi, S. Minami, and F. Ishii, Phys. Rev. B **107**, 024404 (2023).
   DOI:10.1103/PhysRevB.107.024404

3. First-principles study of anomalous Hall effect and anomalous Nernst effect in Fe_2Si
   T. Tominaga, N. Yamaguchi, H. Sawahata, and F. Ishii, Jpn. J. Appl. Phys. **62**, SD1019 (2023).
   DOI:10.35848/1347-4065/acaca6

4. Persistent spin helix on a diamond surface
   H. P. Kadarisman, N. Yamaguchi, and F. Ishii, Appl. Phys. Express **16**, 023001 (2023).
   DOI:10.35848/1882-0786/acb486

5. Seebeck-induced anomalous Nernst effect in van der Waals $MnBi_2Te_4$ layers
   Y. Morishima, N. Yamaguchi, H. Sawahata, and F. Ishii, Appl. Phys. Express **16**, 043003 (2023).
   DOI:10.35848/1882-0786/accacc

6. Prediction of wide-gap topological insulating phase in metastable BiTeI
   Y. Zhang, N. Yamaguchi, H. Sawahata, and F. Ishii, Appl. Phys. Express, in press
   DOI:10.35848/1882-0786/acccd3

YAMAJI, Youhei [E class; 15000 (B), 1150 (C)] (189)
— *Phase competition induced by long-range Coulomb interactions in candidate materials of Kitaev's quantum spin liquid*

1. Superconductivity in Bilayer tt' Hubbard Models
   A. Iwano and Y. Yamaji, J. Phys. Soc. Jpn. **91**, 094702 (2022).
   DOI:10.7566/JPSJ.91.094702

YAMAMOTO, Tsuyoshi [D class; 1000 (B), 0 (C)] (297)
— *Theory of microwave scattering in a dissipative superconducting circuit element*

YAMASHITA, Tomoki [C class; 4000 (B), 350 (C)] (103)
— *Development of crystal structure prediction method and material search*

1. Hybrid algorithm of Bayesian optimization and evolutionary algorithm in crystal structure prediction
   T. Yamashita, H. Kino, K. Tsuda, T. Miyake, and T. Oguchi, Sci. Technol. Adv. Mater. Meth **2**, 67 (2022).
   DOI:10.1080/27660400.2022.2055987

2. Improvement of look ahead based on quadratic approximation for crystal structure prediction
   T. Yamashita and H. Sekine, Sci. Technol. Adv. Mater. Meth **2**, 84 (2022).
   DOI:10.1080/27660400.2022.2059335

YAMAUCHI, Kunihiko [C class; 3200 (B), 0 (C)] (112)
— *First-principles design of novel topological materials and evaluation of anomalous Hall conductivity*

1. Microscopic origin of magnetism in monolayer 3d transition metal dihalides

K. Riedl, D. Amoroso, S. Backes, A. Razpopov, T. P. T. Nguyen, K. Yamauchi, P. Barone, S. M. Winter, S. Picozzi, and R. Valenti Phys. Rev. B **106**, 035156 (2022).
DOI:10.1103/PhysRevB.106.035156

2. Rhombic Fermi surfaces in a ferromagnetic MnGa thin film with perpendicular magnetic anisotropy
M. Kobayashi, N. H. D. Khang, T. Takeda, K. Araki, R. Okano, M. Suzuki, K. Kuroda, K. Yaji, K. Sugawara, S. Souma, K. Nakayama, K. Yamauchi, M. Kitamura, K. Horiba, A. Fujimori, T. Sato, S. Shin, M. Tanaka, and P. N. Hai, Phys. Rev. Mater. **6**, 074403 (2022).
DOI:10.1103/PhysRevMaterials.6.074403

3. Influence of Orbital Character on the Ground State Electronic Properties in the van Der Waals Transition Metal Iodides VI_3 and CrI_3
a) A. De Vita, T. T. P. Nguyen, R. Sant, G. M. Pierantozzi, D. Amoroso, C. Bigi, V. Polewczyk, G. Vinai, L. T. Nguyen, T. Kong, J. Fujii, I. Vobornik, N. B. Brookes, G. Rossi, R. J. Cava, F. Mazzola, K. Yamauchi, S. Picozzi, and G. Panaccione, Nano Lett. **22**, 7034 (2022).
DOI:10.1021/acs.nanolett.2c01922

4. Ab initio prediction of anomalous Hall effect in antiferromagnetic $CaCrO_3$
T. P. T. Nguyen and K. Yamauchi, Phys. Rev. B **107**, 155126 (2023).
DOI:10.1103/PhysRevB.107.155126

YANAGISAWA, Susumu [C class; 8000 (B), 0 (C)] (68)
— *First-principles band structure calculation with the electron-phonon coupling at finite temperature*
— *First-principles bandstructure calculation of organic crystals with the electron-phonon coupling*

1. Phonon dispersion of the organic semiconductor rubrene
K. Takada, K. Yoshimi, S. Tsutsui, K. Kimura, K. Hayashi, I. Hamada, S. Yanagisawa, N. Kasuya, S. Watanabe, J. Takeya, and Y. Wakabayashi, Phys. Rev. B **105**, 205205 (2022).
DOI:10.1103/PhysRevB.105.205205

YANAGISAWA, Takashi [B class; 700 (B), 140 (C)] (205)
— *Numerical study of electronic states in strongly correlated electron systems*
— *Numerical study of electronic states of strongly correlated electron systems*

1. Ferromagnetic diagonal stripe states in the two-dimensional Hubbard model with $U \leq \infty$
M. Miyazaki, T Yanagisawa Phys. Lett. A 446 (2022) 128276

2. Quasi-flat-band in s1/s2 pyrochlore oxides and the effect of spin-orbit interaction
I. Hase, Y. Higashi, T. Yanagisawa J. Phys. Conf. Ser. 2164 (2022) 012063

3. Field resilient superconductivity in atomic layer crystalline materials
Y. Higashi, S. Yoshizawa, T. Yanagisawa et al. unpublished

YASUDA, Chitoshi [C class; 2400 (B), 0 (C)] (271)
— *Numerical study of magnetism in the honeycomb-lattice spin systems*

YASUDA, Yusuke [B class; 900 (B), 160 (C)] (295, 296)
— *Rheology Simulation of Dynamically Cross-linked Elastomers*
— *Structural Analysis and Mechanical Properties Simulations of Polymer Networks with Various Network Structures*

1. Coarse-grained Molecular Dynamics Simulations of Dynamic Bond Elastomers using Inter-bead Potentials for Entropy- and Enthalpy-driven Mechanisms in Their Dynamics and Mechanical Properties
Y. Yasuda, S. Nakagawa, H. Houjou, N. Yoshie and H. Morita, under review

YOKO, Akira [C class; 8600 (B), 800 (C)] (64)
— *Hydrogen production by water splitting on CeO2 (100) facet*
— *Theoretical study for structure and property of metal oxide nanoclusters*

YOKOI, Tatsuya [C class; 4000 (B), 350 (C)] (101)
— *High-accuracy machine-learning interactomic potential and massively large-scale molecular simulation for miscroscopic mechanisms of grain-boundary-dislocation interactions*

YOKOMORI, So [B class; 500 (B), 90 (C)] (166)
— *Study of effects of modulation of molecular arrangement for electronic structure of single-component molecular conductors with canted antiferromagnetism*

YOSHIMOTO, Yuta [C class; 8600 (B), 800 (C)] (220)
— *Constructing a dataset of frequency-dependent dielectric properties of polymeric materials*
— *Constructing a dataset of thermal and dielectric properties of fluoropolymers*

YUAN, Zhicheng [C class; 200 (B), 100 (C)] ()
— *Numerical study of the contact line dynamics on a hybrid hydrophilic surface*

○ A class

Since this class is for trial use, research reports are not required.
When other classes are also used, their publications are shown in the list of B–E classes.
Then, the pages of their reports and publications are given in ( ).

AKIYAMA, Ryota [A class; 100 (B), 50 (C)] ()
— *Band calculations of atomic-layer α-Sn on SnTe*

BUERKLE, Marius [A class; 100 (B), 50 (C)] (383)
— *First-principles computational study of nanocrystals for photovoltaic applications*

FUKUI, Kiyu [A class; 100 (B), 50 (C)] ()
— *Program development of functional renormalization group for spin models with nondiagonal interactions*

HASEGAWA, Taisuke [A class; 100 (B), 50 (C)] ()
— *Analyzing the pump-probe spectra by molecular dynamics simulations*

HATANO, Naomichi [A class; 100 (B), 50 (C)] ()
— *Dynamics of Quantum Walks in Higher Dimensions*

1. Proposal of multidimensional quantum walks to explore Dirac and Schrdinger systems
   M. Yamagishi, N. Hatano, K.-I. Imura, and H. Obuse Phys. Rev. A **107**, 042206 (2023).
   DOI:10.1103/PhysRevA.107.042206

HOSONO, Nobuhiko [A class; 100 (B), 50 (C)] ()
— *Molecular Dynamics Simulation of Molecular Diffusion in Metal-Organic Frameworks*

JESCHKE, Harald [A class; 100 (B), 50 (C)] (247, 248, 394)
— *FLEX computation of susceptibility and superconductivity of β''-$(ET)_2X$ charge transfer salts*

KAGAWA, Fumitaka [A class; 100 (B), 50 (C)] ()
— *Emergent Electric Field induced by current-driven ferromagnetic domain walls*

KATO, Yasuyuki [A class; 100 (B), 50 (C)] ()
— *Theoretical study of topological phase transition and emergent electromagnetic phenomena in magnetic metals*

1. Hidden topological transitions in emergent magnetic monopole lattices
   Y. Kato and Y. Motome, Phys. Rev. B. **107**, 094437 (2023).
   DOI:10.1103/PhysRevB.107.094437

KIM, Kang [A class; 100 (B), 50 (C)] ()
— *Molecular dynamics simulations for interfacial water in acrylate polymers*

KOBAYASHI, Yoshihiro [A class; 100 (B), 50 (C)] ()
— *Molecular dynamics of nanocarbon heterostructure*

MASAKI, Yusuke [A class; 100 (B), 50 (C)] ()
— *Non-axisymmetric vortices in topological nematic superfluids*

MATSUMOTO, Ryosuke [A class; 100 (B), 50 (C)] ()
— *Pre-study for the dislocation-core structure analyses by DFT and atomistic calculations*

NAKAZAWA, Kazuki [A class; 100 (B), 50 (C)] ()
— *Magnetization angle dependence of transport properties in ferromagnetic Weyl semimetal Co_3Sn_2S*

NODA, Yusuke [A class; 100 (B), 50 (C)] ()
— *Microstructure analysis of polycrystalline silicon using first-principles phase-field method*

OKITSU, Kouhei [A class; 100 (B), 50 (C)] ()
— *Calculation of X-ray difffraction intensities from protein crystals based on the n-beam dynamical diffraction therory*

SATO, Taku [A class; 100 (B), 50 (C)] ()
— *Quantum pyrochlore magnet*

TADA, Kohei [A class; 100 (B), 50 (C)] ()
— *Theoretical study for diradicals in solids and on surfaces*

TAKAHASHI, Osamu [A class; 100 (B), 50 (C)] ()
— *Electronic structure of aqueous ionic liquids*

TAKEMORI, Nayuta [A class; 100 (B), 50 (C)] ()
— *Band calculation of hypermaterials*

TSUJI, Yuta [A class; 100 (B), 50 (C)] ()
— *Theoretical study of methane conversion catalysts by first-principles calculations*

UCHIDA, Kazuyuki [A class; 100 (B), 50 (C)] ()
— *First-principles Study on Superstructures of Si(111)-r7xr3-In Surface*

UEHARA, Masatomo [A class; 100 (B), 50 (C)] ()
— *Throughput calculations of electron-lattice interactions*

UEMURA, Naoki [A class; 100 (B), 50 (C)] ()
— *A benchmark test using OpenMX for alloy materials*

YAMAMOTO, Go [A class; 100 (B), 50 (C)] ()
— *Machine learning-assisted high-throughput molecular dynamics simulation of high-mechanical performance CNT yarn structure*

YAMAMOTO, Sayoko [A class; 100 (B), 50 (C)] ()
— *Polymer Design by Quantum Chemical Calculation*

YANAGISHIMA, Taiki [A class; 100 (B), 50 (C)] ()
— *Origin and dynamics of devitrification in dense colloidal glasses*

YUKAWA, Ryu [A class; 100 (B), 50 (C)] ()
— *Study of spin structure changes at Sb_2Te_3 surfaces*

□ SCCMS Projects

FUJII, Mikiya [2000 (B), 200 (C)] (368)
— *Data driven analysis for impurity effects on photocatalysts*

FUJITA, Takatoshi [3500 (B), 100 (C)] (359)
— *Exciton Properties in Organic Optoelectronic Devices from Large-Scale Electronic Structure Calculations*
— *Exciton Dynamics in Organic Optoelectronic Devices from Large-Scale Electronic Structure Calculations and Time-Resolved Spectroscopy*

1. Ab Initio Study of Charge Separation Dynamics and PumpProbe Spectroscopy in the P3HT/PCBM Blend
   T. Fujita, T. Hoshi submitted
   DOI:10.26434/chemrxiv-2023-773xs

FUKUSHIMA, Tetsuya [4000 (B), 400 (C)] (364)
— *Development of fundamental simulation code for magnetic materials*
— *Materials design of high performance magnetic materials*

1. A first-principles study on the electrical conductivity of $Ag_2S_{1-x}Se_x$ ($x = 0, 0.25, 0.5$): Electron-phonon coupling
   H. N. Nam, K. Suzuki, A. Masago, T. Q. Nguyen, H. Shinya, T. Fukushima, and K. Sato Appl. Phys. Lett. **120**, 143903 (2022).
   DOI:10.1063/5.0086703

2. Direct and inverse magnetocaloric effects in FeRh alloy: A theoretical study
   H. B. Tran, T. Fukushima, H. Momida, K. Sato, and T. Oguchi, J. Alloys Compd. **926** 166718 (2022).
   DOI:10.1016/j.jallcom.2022.166718

3. Physics-informed machine learning combining experiment and simulation for the design of neodymium-iron-boron permanent magnets with reduced critical-elements content
   A. Kovacs, J. Fischbacher, H. Oezelt, A. Kornell, Q. Ali, M. Gusenbauer, M. Yano, N Sakuma, A. Kinoshita, T. Shoji, A. Kato, Y. Hong, S. Grenier, T. Devillers, N. Dempsey, T. Fukushima, H. Akai, N. Kawashima, T. Miyake, and T. Schrefl, Front. Mater. **9**, 1094055 (2023).
   DOI:https://doi.org/10.3389/fmats.2022.1094055

4. The role of electronphonon scattering on thermoelectric properties of intermetallic compounds XSi (X = Co, Rh)
   H. N. Nam, K. Suzuki, A. Masago, H. Shinya, T. Fukushima, K. Sato Jpn. J. Appl. Phys. **62**, 020904 (2023).
   DOI:10.35848/1347-4065/acb97a

GOHDA, Yoshihiro [2000 (B), 200 (C)] (74)
— *Strain effects at magnetic interfaces*

1. Giant converse magnetoelectric effect in a multiferroic heterostructure with polycrystalline Co_2FeSi
   S. Fujii, T. Usami, Y. Shiratsuchi, A.M. Kerrigan, A.M. Yatmeidhy, S. Yamada, T. Kanashima, R. Nakatani, V.K. Lazarov, T. Oguchi, Y. Gohda, and K. Hamaya, NPG Asia Mater. **14**, 43 (2022).
   DOI:10.1038/s41427-022-00389-1

2. Superconductivity in a two monolayer thick indium film on Si(111)$\sqrt{3} \times \sqrt{3}$-B

T. Ogino, I. Seo, H. Tajiri, M. Nakatake, S. Takakura, Y. Sato, Y. Hasegawa, Y. Gohda, K. Nakatsuji, and H. Hirayama, Phys. Rev. B **106**, 045423 (2022).
DOI:10.1103/PhysRevB.106.045423

3. Origin of anisotropic magnetoresistance tunable with electric field in $Co_2FeSi/BaTiO_3$ multiferroic inetrfaces
S. Tsuna, R. Costa-Amaral, and Y. Gohda, J. Appl. Phys. **132**, 234101 (2022).
DOI:10.1063/5.0128149

4. First-principles phonon calculations of neodymium-magnet compounds
S. Tsuna and Y. Gohda, J. Appl. Phys. **133**, 115103 (2023).
DOI:10.1063/5.0142945

5. Structures of Sm-Cu intermetallics with Fe as subphase candidates in $SmFe_{12}$-based permanent magnets studied by first-principles thermodynamics
S. Nishino and Y. Gohda, Jpn. J. Appl. Phys. **62**, 030902 (2023).
DOI:10.35848/1347-4065/acc0b8

IMADA, Masatoshi [10000 (B), 1000 (C)] (23)
— *Analysis on Superconducting Mechanism of high-Tc Superconductors*
— *Systematic Analyses on Multi—Layer Copper Oxide Superconductors*

1. Unconventional exciton evolution from the pseudogap to superconducting phases in cuprates
A. Singh, H. Y. Huang, J. D. Xie, J. Okamoto, C. T. Chen, T. Watanabe, A. Fujimori, M. Imada, and D. J. Huang, Nat. Commun. **13**, 7906 (2022).
DOI:10.1038/s41467-022-35210-8

2. *Ab initio*low-energy effective Hamiltonians for the high-temperature superconducting cuprates $Bi_2Sr_2CuO_6$, $Bi_2Sr_2CaCu_2O_8$, $HgBa_2CuO_4$, and $CaCuO_2$
Jean-Baptiste Morée, M. Hirayama, M. T. Schmid, Y. Yamaji, and M. Imada, Phys. Rev. B **106**, 235150 (2022).
DOI:10.1103/PhysRevB.106.235150

3. Unconventional dual 1D-2D quantum spin liquid revealed by *ab initio* studies on organic solids family
K. Ido, K. Yoshimi, T. Misawa, and M. Imada, npj Quantum Mater. **7**, 48 (2022).
DOI:0.1038/s41535-022-00452-8

4. Optimized implementation for calculation and fast-update of Pfaffians installed to the open-source fermionic variational solver mVMC
R.-Q. G. Xu, T. Okubo, S. Todo, and M. Imada, Compt. Phys. Commun., **277**, 108375 (2022).
DOI:10.1016/j.cpc.2022.108375

MATUBAYASI, Nobuyuki [2000 (B), 500 (C)] (360)
— *Development of an efficient method for calculating miscibility of long-chain polymer blends using molecular dynamics simulations*

MIYAKE, Takashi [1800 (B), 70 (C)] (366)
— *Development of high-performance permanent magnets by large-scale simulation and data-driven approach*

1. A First-principles study on the stability of $(R$,Zr$)$(Fe,Co,Ti$)_{12}$ against 2-17 and unary phases (R=Y, Nd, Sm)
T. Fukazawa, Y. Harashima, H. Akai, and T. Miyake, Phys. Rev. Mater. **6**, 054404 (2022).
DOI:10.1103/PhysRevMaterials.6.054404

2. Explainable active learning in investigating structure-stability of $SmFe_{12-\alpha-\beta}X_\alpha Y_\beta$ structures X, Y= {Mo, Zn, Co, Cu, Ti, Al, Ga}
D.-N. Nguyen, H. Kino, T. Miyake, and H.-C. Dam MRS Bulletin **48**, 1 (2023).
DOI:10.1557/s43577-022-00372-9

3. Pareto front analysis and multi-objective Bayesian optimization for $(R,Z)(Fe,Co,Ti)_{12}$ (R=Y, Nd, Sm; Z=Zr, Dy)
T. Fukazawa and T. Miyake, J. Phys. Soc. Jpn. **92**, 014801 (2023).
DOI:10.7566/JPSJ.92.014801

4. Evidence-based data mining method to reveal similarities between materials based on physical mechanisms
M.-Q. Ha, D.-N. Nguyen, H. Kino, Y. Ando, T. Miyake, T. Denœux, V.-N. Huynh, and H.-C. Dam J. Appl. Phys. **133**, 053904 (2023).
DOI:10.1063/5.0134999

OSHIYAMA, Atsushi [10000 (B), 1000 (C)] (48)
— *Quantum-theory-based multiscale simulation for next-generation power devices*

1. An atomistic insight into reactions and free-energy profiles of NH_3 and Ga on GaN surfaces during the epitaxial growth
M. Boero, K. M. Bui, K. Shiraishi, K. Ishisone, Y. Kangawa, and A. Oshiyama, Appl. Surf. Sci. **599**, 153935 (2022).

2. Microscopic identification of stepped SiC (0001) and the reaction site of hydrogen-rich epitaxial growth
T. Kimura, K. Chokawa, K. Shiraishi, and A. Oshiyama, Phys. Rev. B **106**, 035309 (2022).

3. Chickens or Eggs in the Atomic World: Structures and Electronic Properties of Defects in Semiconductors
A. Oshiyama JPSJ News and Comments **19**, 12 (2022).

4. Atomistic insight into initial stage of graphene formation on SiC (0001) surfaces
M. Boero, F. Imoto and A. Oshiyama, Phys. Rev. Materials **6**, 093403 (2022).

5. Atomic and electronic structures of nitrogen vacancies in silicon nitride: Emergence of floating gap states
F. Nanataki, K. Shiraishi, J.-I. Iwata, Y.-i. Matsushita, and A. Oshiyama, Phys. Rev. B **106**, 155201 (2022).

6. Insight into the Step Flow Growth of Gallium Nitride based on Density Functional Theory
K. M. Bui, K. Shiraishi and A. Oshiyama, Appl. Surf. Sci. **613**, 155840 (2023).

7. Atomic and electronic structures of interfaces between amorphous $(Al_2O_3)_{1-x}(SiO_2)_x$ and GaN polar surfaces revealed by first-principles simulated annealing technique
K. Chokawa, K. Shiraishi and A. Oshiyama, J. Appl. Phys **133**, 065301 (2023).

8. Microscopic physical origin of charge traps in 3D NAND flash memories
F. Nanataki, J.-i. Iwata, K. Chokawa, M. Araidai, A. Oshiyama and K. Shiraishi, Jpn. J. Appl. Phys. **62**, SC1038 (2023).

SHIBA, Hayato [4000 (B), 400 (C)] (353)
— *Graph neural network accelerated MD sampling*

— *Development of surrogate model for liquid molecular dynamics based on graph neural networks*

1. BOTAN: BOnd TArgeting Network for prediction of slow glassy dynamics by machine learning relative motion
   H. Shiba, M. Hanai, T. Suzumura, and T. Shimokawabe J. Chem. Phys. **158**, 084503 (2023).
   DOI:10.1016/j.cpc.2017.04.006

SUGINO, Osamu [2000 (B), 200 (C)] (362)

— *Fugaku Battery & Fuel-Cell (B-1: Electrode interface reaction in fuel cell)*

1. Effect of Nitrogen Doping and Oxygen Vacancy on the Oxygen Reduction Reaction on the Tetragonal Zirconia (101) Surface
   S. Muhammady, J. Haruyama, S. Kasamatsu, and O. Sugino, J. Phys. Chem. C126, 15662 (2022).
   DOI:10.1021/acs.jpcc.2c04132

TATEYAMA, Yoshitaka [5000 (B), 500 (C)] (370)

— *Computational and Data Materials Science Study for ET Revolution by Developing Next-Generation Battery and Fuel Cell*

1. Atomistic insight into the dopant impacts at the garnet $Li_7La_3Zr_2O_{12}$ solid electrolyte grain boundaries
   B. Gao, R. Jalem, and Y. Tateyama J. Mater. Chem. A, **10**, 10083 (2022).
   DOI:10.1039/d2ta00545j

2. Favorable Role of the MetalSupport Perimeter Region in Electrochemical NH_3 Synthesis: A Density Functional Theory Study on $Ru/BaCeO_3$
   A. Ishikawa, F. Murase, Y. Tateyama, and J. Otomo ACS Omega **7**, 26107 (2022).
   DOI:10.1021/acsomega.2c01222

3. Tuning the Electronic, Ion Transport, and Stability Properties of Li-rich Manganese-based Oxide Materials with Oxide Perovskite Coatings: A First-Principles Computational Study
   Z. Zhou, D. Chu, B. Gao, T. Momma, Y. Tateyama, and C. Cazorla ACS Appl. Mater. Interfaces **14**, 37009 (2022).
   DOI:10.1021/acsami.2c07560

4. High-Throughput Data-Driven Prediction of Stable High-Performance Na-Ion Sulfide Solid Electrolytes
   S.-H. Jang, Y. Tateyama, and R. Jalem Adv. Funct. Mater. **32**, 2206036 (2022).
   DOI:10.1002/adfm.202206036

5. Evaluation of battery positive-electrode performance with simultaneous ab-initio calculations of both electronic and ionic conductivities
   H. D. Luong, C. Xu, R. Jalem, and Y. Tateyama J. Power Sources **569**, 232969 (2023).
   DOI:10.1016/j.jpowsour.2023.232969

6. Nonequilibrium molecular dynamics for accelerated computation of ionion correlated conductivity beyond NernstEinstein limitation
   R. Sasaki, B. Gao, T. Hitosugi, and Y. Tateyama npj Comput. Mater. **9**, 48 (2023).
   DOI:10.1038/s41524-023-00996-8

TEN-NO, Seiichiro L. [2000 (B), 200 (C)] (371)

— *Theoretical study of hydrogen-evolution semiconductor photocatalysts using first-principles calculations*

1. Characterization of Planar Defect in Layered Perovskite Photocatalyst $Y_2Ti_2O_5S_2$ by Electron

Microscopy and First-Principles Calculations
M. Nakabayashi, K. Nishiguchi, X. Liang, T. Hisatomi, T. Takata, T. Tsuchimochi, N. Shibata, K. Domen, and S. L. Ten-no, J. Phys. Chem. C (in press).
DOI:10.1021/acs.jpcc.3c00820

YOSHIMI, Kazuyoshi [4000 (B), 400 (C)] (355, 357)
— *A systematic ab initio study of quasi-one-dimensional molecular conductors TM salts*
— *Development of an effective model estimation tool by Bayesian optimization*

1. Comprehensive *ab initio* investigation of the phase diagram of quasi-one-dimensional molecular solids
   Kazuyoshi Yoshimi, Takahiro Misawa, Takao Tsumuraya, and Hitoshi Seo, arXiv:2210.13726.

Data Repository
Ab initio Hamiltonians for molecular solids TMTTF and TMTSF salts
https://isspns-gitlab.issp.u-tokyo.ac.jp/k-yoshimi/tm-salts

□ Doctor Theses

1. **CHO, Sanghun**
   Theory of resonance-enhanced tunneling currents at semicondutor pn junctions
   Chiba University, 2023-03

2. **HANA, Pratiwi Kadarisman**
   First-principles study of diamond surfaces
   Kanazawa University, 2023-03

3. **HIDAKA, Yuichiro**
   Density Matrix Renormalization Group studies of quantum antiferromagnets on an anisotropic triangular strip
   The University of Tokyo, 2023-03

4. **INUI, Koji**
   Computational approaches in condensed matter physics using machine learning and automatic differentiation
   The University of Tokyo, 2022-09

5. **KOSHIRO, Hidehiko**
   Theoretical investigation of a frustrated spin ladder realizing multiple magnetization plateaus
   The University of Tokyo, 2023-03

6. **MA, Zihan**
   Decoding fast proton intercalation mechanism for electrochemical energy storage devices
   The University of Tokyo, 2022-09

7. **NARUTA, Hiroki**
   Constructing a high-pressure cell to go beyond 10 GPa using a multianvil press under high temperatures for in situ synchrotron x-ray measurements
   Ehime University, 2023-03

8. **OGINO, Takuhiro**
   Phase diagrams and phase transitions of spin-1/2 XXZ ladder systems
   The University of Tokyo, 2023-03

9. **OHNO, Masahiro**
   Exploration of organic thermoelectric materials via electronic structure calculations
   The University of Tokyo, 2023-03

10. **PHAM, Thanh Ngoc**
    First-principles investigations of NO chemistry on Cu surfaces and sintering-resistant properties of $Sr_3Ti_2O_7$-supported Pd: towards the development of novel NOx purification catalysts
    Osaka University, 2022-09

11. **TSUCHIMOTO, Akihisa**
    Mechanisms behind high-capacity generation in cathode materials for rechargeable batteries based on earth-abundant elements
    The University of Tokyo, 2023-03

12. **WICAKSONO, Yusuf**
    Theoretical Study of Gap Opening/Closing Control of Dirac Cone Using Spin-dependent Potentials in Graphene-based Magnetic Junctions

Osaka University, 2022-06

13. **YAMANE, Ichiro**
Synthesis and Function Exploration of New Composite Materials from Designable Precursors Containing Carbon Using Ultrahigh Pressure
Hokkaido University, 2023-03

14. **YANG, Xiaoran**
Experimental and Simulation Studies on Crystal Growth and Crystallinity Evaluation of Organic Materials and Polymers
Hokkaido University, 2023-03

15. **YOSHII, Kiwamu**
Studies on rheology of cohesive granular materials
Osaka University, 2023-03

□ Master Theses

1. **AKAMATSU, Katsuya**
   A Numerical Study on the Faithfulness of Real-Space Renormalization Group Maps
   The University of Tokyo, 2022-9

2. **AOYAMA, Rina**
   Rational design of neutralizing antibodies against SARS-CoV-2 variants
   The University of Tokyo, 2023-03

3. **ENOMOTO, Satoru**
   Evaluation of Thermodynamic Phase Stability of Sm-Fe-Cu Ternary Alloys by Cluster Expansion
   Tokyo Institute of Technology, 2023-03

4. **FENG, Peijie**
   Effect of Metal Nitride Formation on Ammonia Surface Reaction
   The University of Tokyo, 2023-03

5. **FURUTA, Tatsuhiro**
   Hidden Markov simulation for time series data: Application to blinking phenomenon of quantum dot
   Kyushu Institute of Technology, 2021-03

6. **HASE, Tsubas**
   O vacancy induced local structural distortion and suppression of superconductivity in Sr_2IrO_4
   Osaka University, 2023-03

7. **HAYAMA, Masaki**
   Friction Simulation of Semicrystalline Polymers by a Coarse-Grained Molecular Dynamics Method
   University of Hyogo, 2023-03

8. **HENDRAWAN, Juhri**
   First-Principles Study of Monolayer PbS on The Noble Metal Surfaces
   Kanazawa University, 2023-03

9. **HIRAHARA, Yuushi**
   Correlation between band structure and molecular arrangement in organic molecular crystals investigated by Van Der Waals Density Functional Theory and Wannier function
   University of the Ryukyus, 2023-03

10. **HIRAYAMA, Rumiko**
    Study of CO_2 photoreduction process on nickel metal nanoparticle-supported ZrO_2 catalyst surface
    Chiba University, 2023-03

11. **HOMMA, Kenji**
    Tensor Ring Decomposition Using Entanglement Branching Operator
    The University of Tokyo, 2022-9

12. **HORIE, Ryota**
    Estimation of the ground state energy of the triangular-lattice Heisenberg antiferromagnet by using the spinon representation
    Tokyo University of Science, 2023-03

13. **ITO, Sho**
Bayesian optimization of flow synthesis processes in radical polymerization reactions
Nara Institute of Science and Technology, 2023-03

14. **ITOMITSU, Yohei**
Ab initio calculations for structural stability of transition-metal oxide superlattice
Kyushu Institute of Technology, 2022-03

15. **IWAMURA, Kazuya**
First-principles study of atomic and molecular adsorption on the Ag-In-Yb quasicrystal surface
Kagoshima University, 2023-03

16. **JOO, Hankyul**
Study of Electron Correlation Effects on π-Electron-Proton Correlated Charge Ordering Transition in Cat-TTF-based Molecular Conductors
The University of Tokyo, 2023-03

17. **KAMURA, Yugo**
Numerical study on the control of gas-liquid interface geometry and pressure response
Ibaraki University, 2023-03

18. **KITAHARA, Shinpei**
Application of Machine Learning for Fast Evaluation of Chemisorption Energy Surface from the First Principles
Kagoshima University, 2023-03

19. **MAKI, Yoshikazu**
First-principles study on ferroelectricity of HfO2
Chiba University, 2023-03

20. **MATSUBARA, Dai**
Mesoscopic pattern formation of weakly-charged polyelectrolyte in binary solvent mixtures
Kyoto University, 2023-03

21. **MISUMI, Shoji**
Machine learning-assisted evaluation of phase transition temperature in antiferromagnetic quantum spin model with long-range interaction
University of Hyogo, 2022-03

22. **MIZUHAR, Aoi**
Study on initial interface formation in metal heteroepitaxial growth
Osaka City University, 2023-03

23. **MURASE, Nobuaki**
Microscopic origin of anomalous phase transition in self-propelled hard disk systems
Nagoya Institute of Technology, 2023-03

24. **NIIMI, Kazuki**
Effect of metal substrates on the catalytic properties of light-element-doped graphene-supported Pt single atoms
Hokkaido University, 2023-03

25. **OGA, Satoshi**
Sine-square deformation of Heisenberg model on polyhedra
The University of Tokyo, 2023-03

26. **OHUCHI, Ryoga**
First-Principles Theory of Photo-Excited Carriers Utilizing Maximally Localized Wannier Functions on GaAs Surface
Osaka University, 2023-03

27. **OOISHI, Yasuhiro**
Theoretical Study of Mechanical Characteristics of Linker Molecules Adsorbed on Graphene
Osaka University, 2023-03

28. **OSHIMA, Hisanori**
Measurement-induced criticality in a random quantum circuit with $U(1)$ symmetry
The University of Tokyo, 2023-03

29. **OTAKE, Yutaro**
Inside deep neural network: insight from statistical physics
The University of Tokyo, 2023-03

30. **SATO, Takumi**
Crystal structure prediction for oxide lithium-ion conductors using first-principles calculations
Nagaoka University of Technology, 2023-03

31. **SEKINE, Hirotaka**
Structure prediction of SrO on MgO substrate by first-principles calculations
Nagaoka University of Technology, 2023-03

32. **SHIBATA, Ukyo**
First-principles study of β Ti-Al
Tokyo Institute of Technology, 2023-03

33. **SHIMAMURA, Hirotaro**
Rational design of a small protein targeting the immune checkpoint receptor PD-1
The University of Tokyo, 2023-03

34. **SHINOHARA, Haru**
Molecular dynamics simulation of polyrotaxane and slide-ring networks
The University of Tokyo, 2023-03

35. **SOUNO, Kazuyoshi**
Simple and efficient method for local structure analysis in poly-disperse hard disk systems
Nagoya Institute of Technology, 2023-03

36. **SUDO, Kosuke**
First-Principles Studies on Atomic Structures of Oxidized Cu(111)Surfaces
Kagoshima University, 2023-03

37. **SUZUKI, Haruto**
Electrical Conduction Phenomena in Impurity-Doped Insulating Materials
The University of Tokyo, 2023-03

38. **SUZUKI, Ken**
Electronic structures and modulation spectroscopic properties of LiNbO2 thin films
University of Fukui, 2023-03

39. **TADOKORO, Arito**

Effect of Inter-site Coulomb Interactions on Superconducting Gap Functions of BiS_2-Based Layered Superconductors
Tokyo Metropolitan University, 2023-03

40. **TAKEDA, Masashi**
A series expansion study for magnon spectrum in Cs2Cu3SnF12 -estimations of exchange and Dzyaloshinskii-Moriya interactions-
Tokyo University of Science, 2023-03

41. **TAKEDA, Tomoya**
Surface structure analysis of layered materials with Van der Waals bonds by total-reflection high-energy positron diffraction
Waseda University, 2023-03

42. **TERANISHI, Mizuki**
Theoretical design of a novel protein for suppression of allergic diseases induced by interleukin-33
The University of Tokyo, 2023-03

43. **TERASHITA, Kodai**
First-principles calculation for hydrogen diffusion and solubility in amorphous α-Al2O3
Hokkaido University, 2023-03

44. **TEWENG, Yedija Yusua Sibuea**
First-principles study of the perovskite-phase CsPbI3
Kanazawa University, 2023-03

45. **TOMINAGA, Takahiro**
First-principles study of the magneto-thermoelectric effect in Fe-Si alloys
Kanazawa University, 2023-03

46. **TOMITA, Ami**
Formation and electronic structures of nanodots in perovskite semiconductors; first-principles study
Chiba University, 2023-03

47. **TSUNA, Shunsuke**
First-principles phonon calculations of Nd-magnet compounds
Tokyo Institute of Technology, 2023-03

48. **TSUNASHIMA, Mizuki**
Study on Li ion diffusion in lithium lanthanum niobate based on first-principles calculations
Tokyo University of Science, 2023-03

49. **UEDA, Ryo**
Machine Learning Molecular Dynamics Simulation of CO-driven Formation of Restructuring of Stepped Cu Surfaces
Osaka University, 2023-03

50. **URATA, Sora**
Reduction of thermal conductivity at crystalline Si/amorphous SiO2 interfaces and its understanding via phonon transmission analysis
Osaka University, 2023-03

51. **UZA, Ryo**
Determination of charge injection levels in organic semiconductor films by Van Der Waals Density

Functional Theory and GW approximation
Graduate School of Engineering and Science, University of the Ryukyus, 2023-03

52. **YAMAGUCHI, Takuma**
Electronic structures and vibrational properties of YO monoxide thin films
University of Fukui, 2023-03

53. **ZHAO, Difei**
First-principles study on the magnetic contribution to thermodynamics functions of Fe
Tokyo Institute of Technology, 2022-09

54. **ZHAO, Wenxuan**
Computational study for improving electrochemical stability of aqueous electrolytes
The University of Tokyo, 2023-03

55. **ZHAO, Xun**
Improved path-integral worm Monte Carlo method and its application to interacting bosons
The University of Tokyo, 2022-09